

AD-A266 216



(1)

**FINAL REPORT TO
OFFICE OF NAVAL RESEARCH**

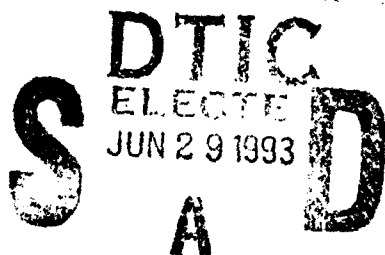
Publications Acknowledging

DARPA/ONR Contract # N00014-86-K-0033

TITLE: Electronic Theory of II-VI and Related
Semiconducting Materials and Structures

PRINCIPAL INVESTIGATOR: Professor Henry Ehrenreich
Clowes Professor of Science
205A Pierce Hall
Division of Applied Sciences
Cambridge, MA 02138
Phone: (617) 495-3213
FAX: (617) 495-9837

STARTING DATE: October 1, 1985

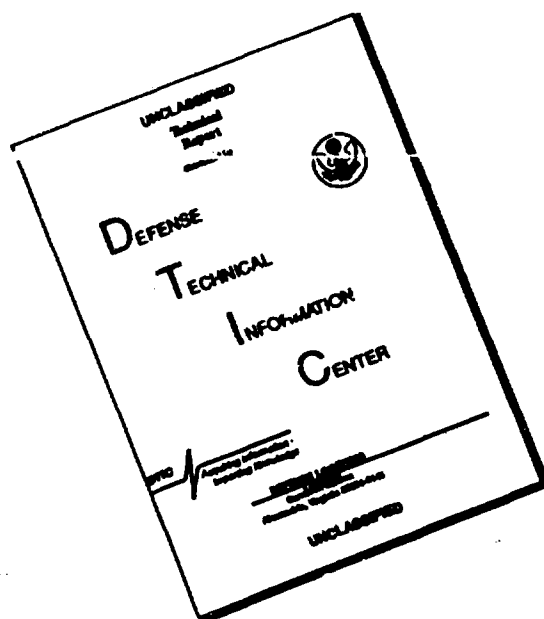


This document has been approved
for public release and sale; its
distribution is unlimited.

93 6 25 05 5

93-14645

DISCLAIMER NOTICE



**THIS DOCUMENT IS BEST
QUALITY AVAILABLE. THE COPY
FURNISHED TO DTIC CONTAINED
A SIGNIFICANT NUMBER OF
PAGES WHICH DO NOT
REPRODUCE LEGIBLY.**

TABLE OF CONTENTS

Electronic Structure and Magnetic Interactions in Diluted Magnetic Semiconductors <i>H. Ehrenreich, K.C. Hass, N.F. Johnson, B.E. Larson, and R.J. Lempert</i>	3.
Electronic Theory of Mn-Alloyed Diluted Magnetic Semiconductors <i>H. Ehrenreich, K.C. Hass, B.E. Larson, and N.F. Johnson</i>	7.
Molecular Coherent-Potential Approximation for Zinc-Blende Pseudobinary Alloys <i>R.J. Lempert, K.C. Hass, and H. Ehrenreich</i>	17.
Bond Relaxation in $\text{Hg}_{1-x}\text{Cd}_x\text{Te}$ and Related Alloys <i>K.C. Hass and D. Vanderbilt</i>	36.
Effective Masses and Optical Matrix Elements in Semiconductor Superlattices <i>N.F. Johnson, H. Ehrenreich, and K.C. Hass</i>	41.
<i>f</i> -Sum Rule and Effective Masses in Superlattices <i>N.F. Johnson, H. Ehrenreich, K.C. Hass, and T.C. McGill</i>	44.
Theory of Exchange Interactions and Chemical Trends in Diluted Magnetic Semiconductors <i>B.E. Larson, K.C. Hass, H. Ehrenreich, and A.E. Carlson</i>	48.
Carrier-Activated Light Modulation <i>N.F. Johnson, H. Ehrenreich, and R.V. Jones</i>	66.
Effective-Medium Theory for Weakly Nonlinear Composites <i>X.C. Zeng, D.J. Bergman, P.M. Hui, and D. Stroud</i>	68.
Superlattice $\mathbf{k} \cdot \mathbf{p}$ Models for Calculating Electronic Structure <i>N.F. Johnson, H. Ehrenreich, G.Y. Wu, and T.C. McGill</i>	72.
Valence-Band-Offset Controversy in HgTe/CdTe Superlattices: A Possible Resolution <i>N.F. Johnson, P.M. Hui, and H. Ehrenreich</i>	76.
Numerical Study of Optical Absorption in Two-Dimensional Metal-Insulator and Normal-Superconductor Composites <i>X.C. Zeng, P.M. Hui, D. Stroud</i>	79.
A Possible Resolution of the Valence-Band Offset Controversy in HgTe/CdTe Superlattices <i>P.M. Hui, H. Ehrenreich, and N.F. Johnson</i>	84.
Mean Field Theory for Weakly Nonlinear Composites <i>X.C. Zeng, P.M. Hui, D.J. Bergman, and D. Stroud</i>	87.
Correlation and Clustering in the Optical Properties of Composites: A Numerical Study <i>X.C. Zeng, P.M. Hui, D.J. Bergman, and D. Stroud</i>	93.
Enhancement in Nonlinear Effects in Percolating Nonlinear Resistor Networks <i>P.M. Hui</i>	100.
Optical and Magneto-Optical Absorption in Parabolic Quantum Wells <i>L. Brey, N.F. Johnson, and B.I. Halperin</i>	103.
Excitons in Superlattices <i>N.F. Johnson</i>	106.

Electronic and Optical Properties of III-V and II-VI Semiconductor Superlattices <i>N.F. Johnson, H. Ehrenreich, P.M. Hui, and P.M. Young</i>	112.
Infrared Optical Properties of III-V and II-VI Superlattices <i>N.F. Johnson and H. Ehrenreich</i>	127.
Infrared Optical Absorption in Imperfect Parabolic Quantum Wells <i>L. Brey, J. Dempsey, N.F. Johnson, and B.I. Halperin</i>	132.
Collective Modes in Quantum-Dot Arrays in Magnetic Fields <i>J. Dempsey, N.F. Johnson, L. Brey, and B.I. Halperin</i>	140.
Electronic and Optical Properties of a Superlattice in a Parabolic Potential <i>L. Brey, N.F. Johnson, and J. Dempsey</i>	146.
Additional Evidence Concerning the Valence-Band Offset in HgTe/CdTe <i>P.M. Young and H. Ehrenreich</i>	153.
Excitons and Interband Transitions in III-V Semiconductor Superlattices <i>P.M. Young, P.M. Hui, and H. Ehrenreich</i>	156.
Response and Transit Times in Quantum-Well Structures <i>E. Runge and H. Ehrenreich</i>	164.
Evidence for Quantum Well Asymmetry in Optical Absorption <i>P.M. Young and H. Ehrenreich</i>	168.
Non-equilibrium Transport in Alloy Based Resonant Tunneling Systems <i>E. Runge and H. Ehrenreich</i>	171.
Minority Carrier Lifetimes in Ideal InGaSb/InAs Superlattices <i>C.H. Grein, P.M. Young, and H. Ehrenreich</i>	194.
Noise in Alloy-Based Resonant-Tunneling Structures <i>E. Runge</i>	197.
Phonon Assisted Transport in Double-Barrier Resonant-Tunneling Structures <i>C.H. Grein, E. Runge, and H. Ehrenreich</i>	204.
Auger Lifetimes in Ideal InGaSb/InAs Superlattices <i>C.H. Grein, P.M. Young, H. Ehrenreich, and T.C. McGill</i>	232.
Temperature Limits on Infrared Detectivities of InAsIn _x Ga1 - xSb Superlattices and Bulk Hg _x Cd1 - xTe <i>P.M. Young, C.H. Grein, H. Ehrenreich, and R.H. Miles</i>	245.

DTIC QUALITY INSPECTED 2

Accession For	
NTIS	GENERAL
DTIC	TAB
Unannounced	
Justification	
By	
Date	
Approved	
Date	Approved
A-1	

ELECTRONIC STRUCTURE AND MAGNETIC INTERACTIONS IN DILUTED MAGNETIC SEMICONDUCTORS

H. Ehrenreich, K.C. Hass,* N.F. Johnson, B.E. Larson, and R.J. Lempert

Division of Applied Sciences and Department of Physics
Harvard University, Cambridge, Massachusetts 02138
USA

*Also at: Dept. of Physics, MIT, Cambridge, MA 02139

We summarize recent calculations of the electronic structure and exchange interactions in $\text{Cd}_{1-x}\text{Mn}_x\text{Te}$ and related alloys.

Mn-substituted II-VI diluted magnetic semiconductors (DMS) (e.g. $\text{Cd}_{1-x}\text{Mn}_x\text{Te}$) exhibit a variety of interesting phenomena¹⁾ of potential technological significance. This paper summarizes recent theoretical progress²⁻⁴⁾ made in understanding the electronic structure and magnetic interactions in these materials. The problem is complicated by the facts that DMS:¹⁾ (1) are random alloys exhibiting both compositional and structural disorder, (2) contain local moments due to narrow, strongly correlated Mn d bands, (3) are magnetically disordered due to the formation of a low temperature spin glass phase, and (4) have experimentally inaccessible $x = 1$ tetrahedral limiting crystals. The work described here overcomes these difficulties by combining a number of techniques developed previously for other transition metal and semiconductor alloys.

Figure 1 presents an overview of the emerging theoretical picture. We begin our discussion near the bottom to emphasize the chronological development of the subject. Most early theoretical studies¹⁾ of DMS were based on the phenomenological Hamiltonians H_H and H_K . The former is a spin 5/2 Heisenberg Hamiltonian which has been used extensively to examine the magnetic properties and phase diagrams of DMS. The Mn-Mn exchange constants J^{d-d} have been determined empirically^{1,5)} for most II-VI DMS and are known to be antiferromagnetic (AF) and of the order of -10 K for nearest neighbors (assuming a total interaction between two spins of $-2J^{d-d}\vec{S}_i\cdot\vec{S}_j$). The Kondo-like Hamiltonian H_K describes Mn d - sp band exchange. This has been combined¹⁾ with a $\vec{k}\cdot\vec{p}$ -virtual crystal approximation (VCA) treatment of the sp bands to describe the unique magneto-optical and magneto-transport properties of DMS. Typical values^{6,7)} for the $\vec{k}=0$ conduction and valence band edge exchange constants are $N_o\alpha \equiv J_c^{sp-d} \approx 0.2$ eV and $N_o\beta \equiv J_v^{sp-d} \approx -1.0$ eV, respectively.

Our work has focused on the development of a detailed electronic structure model designed to provide a more fundamental understanding of DMS. The starting point, in principle, is the many body Hamiltonian shown at the top of Fig. 1. For most purposes it is sufficient, and simpler, to consider an effective one electron Hamiltonian obtained in one of two ways. The left hand approach in Fig. 1 treats correlation effects in the linearized Hubbard approximation (LHA). This assumes that a Mn d electron of spin σ in orbital α has the energy $\epsilon_d + U_{eff} \langle n_{\alpha,-\sigma} \rangle$ where $\langle n_{\alpha,-\sigma} \rangle$ is one if the opposite spin state is occupied and zero if it is unoccupied. We use this approach in the alloy calculations below because it is applicable to disordered as well as ordered

systems. By contrast, the right hand approach in Fig. 1, the local spin density approximation⁸⁾ (LSDA), is easily implemented only in ordered systems. The LSDA forms the basis of most *ab initio* spin-polarized band calculations⁸⁾ and is thus useful for obtaining information on the hypothetical $x=1$ tetrahedral compounds.^{2-4,9)}

The schematic one electron Hamiltonian in Fig. 1 contains three terms. The first, H_{sp} , describes itinerant semiconducting sp bands and is similar to that which would occur in isoelectronic II-VI alloys.¹⁰⁾ H_d describes localized, half-filled Mn d shells which are spin-polarized on a given site. The $sp-d$ hybridization H_{sp-d} delocalizes the d states and broadens them into bands. H_{sp-d} is small compared to U_{eff} but has noticeable effects on the electronic structure and is the dominant source of magnetic interactions.^{2-4,11)}

We perform realistic electronic structure calculations for $Cd_{1-x}Mn_xTe$ using an empirical tight binding model (right side of Fig. 1). The basis consists of s^2, p^6, d^{10} orbitals for each cation and s^2, p^6 orbitals for Te. The Mn d electrons are treated in the LHA. Occupied d states are assumed to have either spin up (\uparrow) or spin down (\downarrow) at random. The alloy is thus modeled as the pseudo-ternary $Cd_{1-x}(Mn\uparrow)_{x/2}(Mn\downarrow)_{x/2}Te$.

The $Mn\uparrow$ and $Mn\downarrow$ concentrations are assumed equal to ensure zero net magnetization. Compositional and magnetic disorder in the alloy are treated in the coherent potential approximation (CPA). Parameters are obtained (assuming nearest neighbor hopping only) by fitting to the known CdTe band structure and the results of LSDA-augmented spherical wave calculations²⁾ for hypothetical AF zincblende MnTe. The values of ϵ_d and U_{eff} derived from the latter are adjusted to correct for errors in LSDA quasiparticle energies.⁴⁾

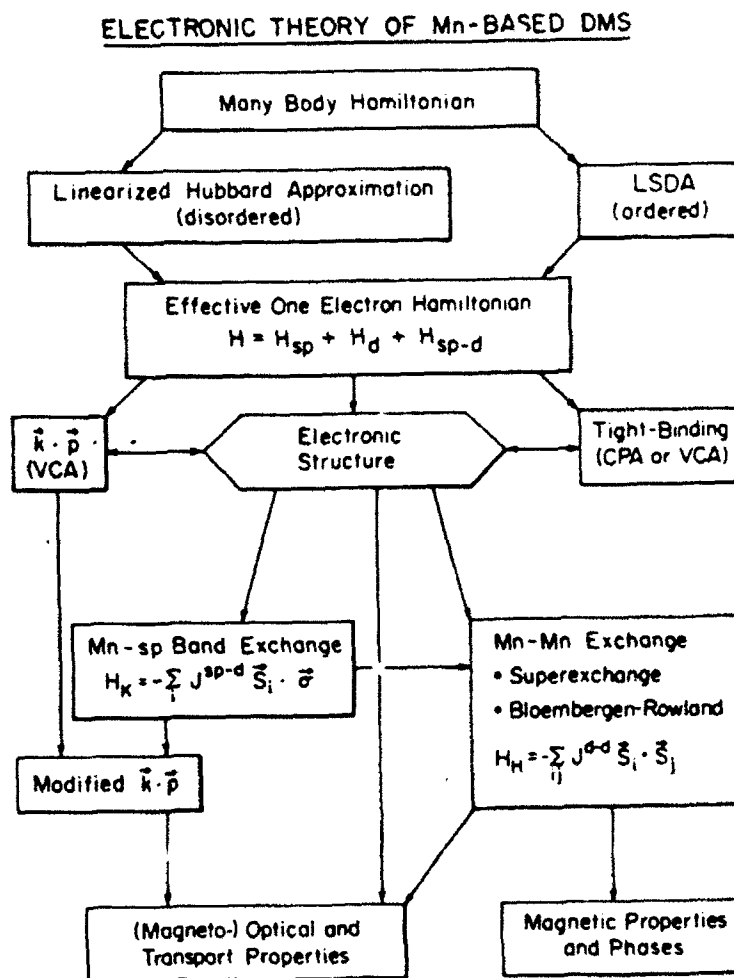


Fig. 1 - Schematic overview of theoretical developments summarized in the text.

Figure 2 shows the CPA total and projected d (shaded) densities of states for $x=0, 0.3, 0.6$. The zero of energy is fixed at the CdTe valence band maximum. The occupied Mn d states have been shifted down by ~ 1 eV from the LSDA results to place them near -3.4 eV, in agreement with photoemission experiments^{12,13)} The location of the unoccupied d states has yet to be determined definitively (e.g., by inverse photoemission). Here we have shifted them up by ~ 2 eV from the LSDA results. This places them at about 4.5 eV above the region of the upper valence band at L , a location which provides a possible explanation for the anomalous structure seen in optical data at this energy.¹⁴⁾

The occupied d states are split into two peaks due to $sp-d$ hybridization. The lower t_{2g} states hybridize more strongly in the tetrahedral environment and are shifted to lower energy due to a repulsion from the Te p -like upper valence bands. The corresponding d admixture in the upper valence region is responsible for the spectral change near -1 eV in Fig. 2 (which has been observed in photoemission experiments¹²⁾) and the slight shift of the valence band maximum. The cation s -like conduction band minimum is unaffected by $sp-d$ hybridization by symmetry. The energy of this state increases from 1.6 eV at $x=0$ to 2.6 eV at $x=0.6$ due to the difference between Cd and Mn atomic s levels.¹⁰⁾

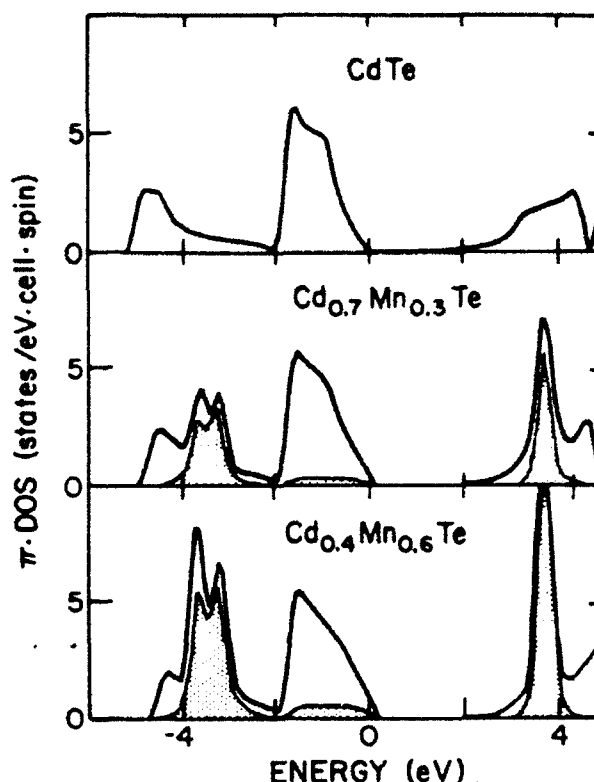


Fig. 2 - Calculated CPA total and projected d (shaded) densities of states.

The connections in Fig. 1 between the electronic structure and the Mn- sp band and Mn-Mn exchange interactions have been extensively discussed elsewhere.^{2,4)} The qualitative difference between $N_o\alpha$ and $N_o\beta$ results from the differing effects of $sp-d$ hybridization on the conduction and valence band edges.^{3,11)} The Mn-Mn exchange has been calculated quantitatively and shown to result primarily from hybridization-induced AF superexchange.^{2,4)} This accounts for about 95% of J^{d-d} at near neighbor distances with the Bloembergen-Rowland mechanism (resulting from H_K) accounting for most of the remaining 5%.

We have recently developed a physically transparent model⁴⁾ of both $N_o\beta$ and J^{d-d} in Mn-based II-VI DMS using only four parameters: ϵ_d , U_{eff} , the location of the valence band edge E_v , and a hybridization parameter V_{pd} . The analytic expressions

$$N_o\beta = -2V_{pd}^2\{(\epsilon_d + U_{eff} - E_v)^{-1} + (E_v - \epsilon_d)^{-1}\} \quad (1)$$

$$J^{d-d}(R) = -2V_{pd}^4\{(\epsilon_d + U_{eff} - E_v)^{-2}U_{eff}^{-1} + (\epsilon_d + U_{eff} - E_v)^{-3}\}f(R) \quad (2)$$

result from a Schrieffer-Wolff transformation^{4,11)} and an approximation to the formal results in Ref. 2, respectively. R here is the Mn-Mn separation and $f(R)$ is a universal function for II-VI DMS ($\approx 0.2 \exp(-4.89 R^2/a^2)$ where a is the cubic lattice constant). An application of these formulae to $\text{Cd}_{1-x}\text{Mn}_x\text{Te}$, $\text{Cd}_{1-x}\text{Mn}_x\text{Se}$ and $\text{Cd}_{1-x}\text{Mn}_x\text{S}$ is given in Table 1; the entries correspond to $x \approx 0.1$ but are not very sensitive to x . The $E_v - \epsilon_d$ values are taken from photoemission experiments.^{12,13)} The value $U_{\text{eff}} = 7.0$ eV for $\text{Cd}_{1-x}\text{Mn}_x\text{Te}$ is chosen from Fig. 2; the slight increase in U_{eff} down the column is estimated from simple electrostatic arguments⁴⁾ based on increasing Mn \rightarrow anion charge transfer. V_{pd} is obtained from Eq. (2) and the experiment $N_0\beta$ values^{6,7)} in the table. We attribute the increase in V_{pd} from telluride to sulfide to the decrease in Mn-anion bond length. Eq. (2) is seen to predict nearest neighbor (nn) J^{d-d} values in $\text{Cd}_{1-x}\text{Mn}_x\text{Te}$ and $\text{Cd}_{1-x}\text{Mn}_x\text{Se}$ in excellent agreement with experiment.⁵⁾ In view of the extremely large J^{d-d} value predicted for the sulfide, further experimental studies on this material would clearly be of interest.

Table 1 — Anion dependence of electronic structure parameters (defined in text) and exchange constants in Cd-based DMS.

	$E_v - \epsilon_d$	U_{eff}	V_{pd}	$N_0\beta$	J_{nn}^{dd} (theory)	J_{nn}^{dd} (expt.)
$\text{Cd}_{0.9}\text{Mn}_{0.1}\text{Te}$	3.4 eV	7.0 eV	0.88 eV	-0.88 eV	-8.0 K	-6.3 K
$\text{Cd}_{0.9}\text{Mn}_{0.1}\text{Se}$	3.4	7.6	1.01	-1.11	-9.0	-7.9
$\text{Cd}_{0.9}\text{Mn}_{0.1}\text{S}$	3.4	7.9	1.60	-2.7	-46	-

This work was supported by the Joint Services Electronics Program (No. N00014-84-K-0465), and the Defense Advanced Research Projects Agency (through ONR Contract N00014-86-K-003).

REFERENCES

- (1) N.B. Brandt and V.V. Moshchalkov, *Adv. in Phys.* **33**, 193 (1984) and references therein.
- (2) B.E. Larson, K.C. Hass, H. Ehrenreich and A.E. Carlsson, *Solid State Commun.* **56**, 347 (1985).
- (3) K.C. Hass, B.E. Larson, H. Ehrenreich and A.E. Carlsson, *J. Mag. Magn. Mat.* **54-57**, 1283 (1986).
- (4) B.E. Larson, K.C. Hass, H. Ehrenreich and A.E. Carlsson (unpublished).
- (5) B.E. Larson, K.C. Hass, and R.L. Aggarwal, *Phys. Rev.* **B33**, 1789 (1986).
- (6) D. Heiman, Y. Shapira and S. Foner, *Solid State Commun.* **51**, 603 (1984) and references therein.
- (7) V.G. Ambramishvili, S.I. Gubarev, A.U. Komarov and S.M. Ryabchenko, *Sov. Phys. Solid State* **26**, 666 (1984).
- (8) A.R. Williams and U. von Barth, in *The Inhomogeneous Electron Gas*, ed. by S. Lundquist and N.H. March (Plenum, New York, 1983).
- (9) S-H. Wei and A. Zunger, *Phys. Rev. Lett.* **56**, 2391 (1986).
- (10) K.C. Hass and H. Ehrenreich, *J. Vac. Sci. Technol.* **A1(3)**, 1678 (1983).
- (11) A.K. Bhattacharjee, G. Fishman and B. Coqblin, *Physica* **117&118B**, 449 (1983).
- (12) M. Taniguchi, *et al.*, *Phys. Rev.* **B33**, 1206 (1986).
- (13) A. Franciosi *et al.*, this conference.
- (14) P. Lautenschlager, S. Logothetidis, L. Viña and M. Cardona, *Phys. Rev.* **32**, 3811 (1985).

ELECTRONIC THEORY OF Mn - ALLOYED DILUTED MAGNETIC SEMICONDUCTORS

H. EHRENREICH, K.C. HASS*, B.E. LARSON AND N.F. JOHNSON
Harvard University, Division of Applied Sciences and Department of Physics,
Cambridge, Massachusetts 02138

* Also at MIT, Dept. of Physics, Cambridge, MA 02139

ABSTRACT

Recent calculations of the electronic structure and magnetic interactions in Mn - alloyed II-VI diluted magnetic semiconductors (DMS) are summarized. Detailed band structure results are obtained using an empirical tight-binding, coherent potential approximation approach with input from experiment and local spin density band calculations. The dominant magnetic interactions in these systems result from hybridization between spin-split Mn *d* states and *sp* valence bands. Superexchange between Mn moments is well described by a simple three-level model which yields accurate Mn - Mn exchange constants for a variety of II-VI DMS as well as the rocksalt insulators MnO and α -MnS.

INTRODUCTION

This paper summarizes recent theoretical contributions to the electronic structure and magnetic interactions in Mn - alloyed II-VI diluted magnetic semiconductors (DMS) (e.g. $\text{Cd}_{1-x}\text{Mn}_x\text{Te}$). These materials have generated considerable fundamental and technological interest because of their unusual magnetic properties (e.g. non-metallic spin glass phase) and because of their novel interplay between semiconductor physics and magnetism (e.g. enhanced band edge Zeeman splittings) [1]. The detailed microscopic picture reviewed here, which is in good agreement with experiment, is based on a variety of theoretical techniques developed previously for isoelectronic semiconducting alloys and transition metal oxides. Important issues resolved by this work include the effects of Mn *d* electrons on the electronic structure and the origin of Mn - *sp* band and Mn - Mn exchange interactions.

A brief overview of the developments discussed here and their relationship to previous theoretical models for DMS is presented in Fig. 1. The upper two-thirds of this figure, which will be described in detail, begins with the construction of a detailed electronic structure model based on a realistic microscopic Hamiltonian. Calculations of magnetic interactions within this framework provide fundamental support for the phenomenological spin Hamiltonians H_H and H_K used extensively in early theoretical studies of DMS [1]. A modified *k*·*p* approach, which combines the Kondo-like interaction H_K with a simple *k*·*p* virtual crystal approximation (VCA) treatment of *sp* band edge states, accounts well for the unique magneto-optical and magneto-transport properties of these materials [2]. The spin 5/2 Heisenberg Hamiltonian H_H similarly provides an excellent description of the magnetic properties and phase diagrams of DMS [3].

ELECTRONIC STRUCTURE

The description of the electronic structure of $\text{II}_{1-x}\text{Mn}_x\text{VI}$ alloys, in principle, is a complicated many body problem. Local magnetic moments in these systems result

ELECTRONIC THEORY OF Mn-BASED DMS

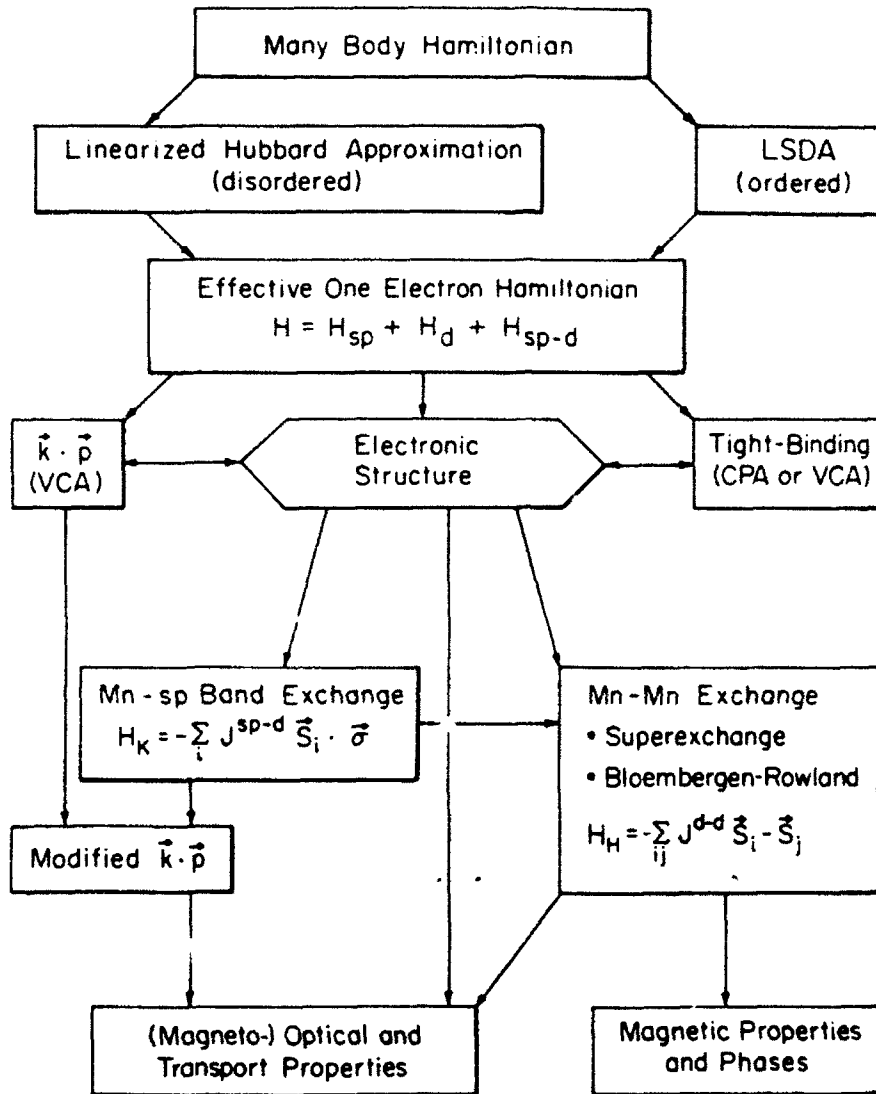


Fig. 1 — Schematic overview of the theoretical developments discussed in the text.

from strong exchange-correlation interactions among the Mn d electrons which strongly favor a spin-polarized d^5 configuration on each Mn site (Hund's rule). We treat these effects by considering the two commonly used approximations shown in the second line of Fig. 1. The linearized Hubbard approximation, on the left, assumes that a Mn d electron of spin σ in orbital α has the energy $\epsilon_d + U_{eff} \langle n_{\alpha,-\sigma} \rangle$ where $\langle n_{\alpha,-\sigma} \rangle$ is one if the opposite spin state is occupied and zero if it is unoccupied [4]. This approximation is particularly useful for the alloy tight-binding calculations described below because it is applicable to disordered as well as ordered systems. The second approach, the local spin density approximation (LSDA) [5], involves no adjustable parameters but is easily implemented only in ordered systems. *Ab initio*

spin-polarized band calculations based on the LSDA have successfully described the properties of a large number of magnetic compounds [6]. Such calculations are important in the present context for providing band structure information for hypothetical or metastable ordered configurations, particularly tetrahedral MnVI crystals [7-10].

Each of these approximations leads to an effective one electron Hamiltonian which is written schematically in Fig. 1 as the sum of three terms. The first term, H_{sp} , describes itinerant semiconducting sp bands. The similar behavior of these bands in $\text{II}_{1-x}\text{Mn}_x\text{VI}$ DMS and in isoelectronic II-VI alloys explains the similar semiconducting properties of these materials in the absence of a magnetic field. The second term, H_d , describes the local aspects of Mn d states, including the spin splitting U_{eff} at each site. The final term, H_{sp-d} , describes the hybridization between the two sets of electrons. This effect will be seen to be small compared to U_{eff} , but to represent the dominant source of magnetic interactions in these materials.

We have constructed a realistic electronic structure model based on this Hamiltonian by combining an empirical tight-binding (ETB) [11] description of the various terms with a coherent potential approximation (CPA) [12] treatment of disorder effects (fourth line of Fig. 1). The basis consists of two s , six p and ten d orbitals per cation, and two s and six p orbitals per anion. We first discuss the unperturbed sp band structure which results from H_{sp} acting alone. The effects of Mn d electrons will then be examined using information obtained from LSDA calculations and experimental data.

sp Bands

The first detailed calculations of the sp band structure of a DMS were performed by Hass and Ehrenreich for $\text{Hg}_{1-x}\text{Mn}_x\text{Te}$ [13]. This work was based on the ETB-CPA formalism developed previously for $\text{Hg}_{1-x}\text{Cd}_x\text{Te}$, which provides a sophisticated means of interpolating between tight-binding parametrizations for the limiting crystals [14]. For HgTe and CdTe in [14], the diagonal tight-binding parameters, which play the most important role, were fit to atomic levels [15], as suggested by Harrison [11]. Off-diagonal parameters (up to second neighbors) and a uniform shift of the diagonal parameters relative to the sp bands were chosen to provide the best overall fit to the known HgTe and CdTe band structures. The extension to $\text{Hg}_{1-x}\text{Mn}_x\text{Te}$ was accomplished by considering a hypothetical zincblende (zb) $x=1$ limiting crystal. Diagonal s and p tight binding parameters for Mn were again chosen from atomic levels on the same absolute energy scale. Off-diagonal parameters for zb-MnTe were assumed to be the same as those of CdTe . This approximation is reasonable in view of the small difference in bond lengths between the two crystals ($\sim 2\%$) and the fact that off-diagonal parameters in zincblende compounds are relatively insensitive to the chemical nature of the constituents [11].

Figure 2 shows the resulting placement of the sp ETB bands for HgTe , CdTe and zb-MnTe relative to the diagonal sp tight-binding parameters assumed in the calculations. (The lower energy Te $5s$ level and associated split-off valence band included in the calculations are not shown here.) The zero of energy corresponds to the valence band maxima which are assumed to be the same in the three crystals because of the large Te $5p$ component of the Γ_8 states. The increase in band gap from HgTe to CdTe results from the much higher cation s level in CdTe , which contributes significantly to the conduction band edge Γ_6 state. The still higher s level in Mn results in an even larger gap in zb-MnTe. The predicted gap value here of 3.2 eV is in good agreement with the extrapolated value obtained from low temperature measurements on $\text{II}_{1-x}\text{Mn}_x\text{Te}$ alloys [16]. The rise of the cation s levels also accounts for the slight decrease in the width of the upper valence region in the series $\text{HgTe} \rightarrow \text{CdTe} \rightarrow \text{MnTe}$.

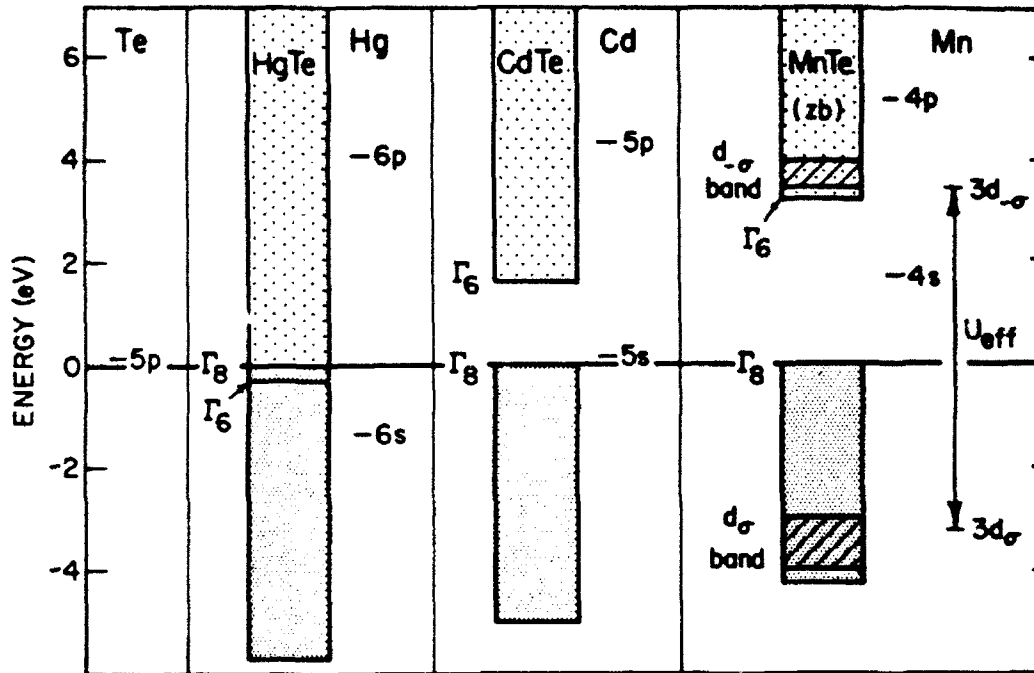


Fig. 2. — Limits of sp upper valence and lower conduction bands (darker and lighter boxes, respectively) for HgTe, CdTe and hypothetical zincblende (zb) MnTe relative to atomically-derived sp diagonal tight-binding parameters. Details of alignment are discussed in text. The Mn d levels are assumed to be spin split by an amount U_{eff} at each site with the occupied states having a spin σ . The resulting regions of large d state densities in zb-MnTe are shown as cross-hatched regions labeled d "bands."

For many purposes, the behavior of the sp bands at intermediate alloy compositions can be reasonably described by a simple VCA averaging scheme. The VCA predicts a nearly linear x dependence of the band features shown in Fig. 2. The additional effects of compositional disorder, included in the CPA, result primarily from the differences between cation s levels in the alloy constituents. The 1.4 eV difference between Hg and Cd s levels, for example, is known to affect the bowing of band gaps and electron mobilities in $Hg_{1-x}Cd_xTe$, and to give rise to a nearly split valence band density of states near -5 eV [14]. Qualitatively similar behavior is predicted for the sp bands of $Hg_{1-x}Mn_xTe$ and $Cd_{1-x}Mn_xTe$ with the most pronounced disorder effects occurring in the former system where the Hg and Mn s levels differ by ~ 3 eV. A consequence of this enhanced disorder is that, for a given band gap, the limiting electron mobility due to alloy scattering in $Hg_{1-x}Mn_xTe$ is estimated to be about a factor of three smaller than in $Hg_{1-x}Cd_xTe$, despite the smaller x value required to produce that gap [13].

Effects of Mn d Levels

The Hubbard-like treatment of Mn d levels described above is illustrated on the right hand side of Fig. 2. A simple perturbative analysis by Hass and Ehrenreich [13]

demonstrated that the principal effect of $sp-d$ hybridization is to broaden the spin-split d states into bands, denoted by cross-hatching in Fig. 2. The label σ ($-\sigma$) on the occupied (unoccupied) d band indicates that the associated extended wavefunction for a state of given spin has large amplitude only on those Mn sites whose net spin is in the same (opposite) direction. This basic picture holds regardless of whether the Mn spins are ordered antiferromagnetically, as would be expected for zb-MnTe at low temperatures, or are randomly oriented, as would occur at either higher temperatures or in the spin glass phase of $\text{II}_{1-x}\text{Mn}_x\text{VI}$ alloys.

We obtain ETB parameters describing the location of Mn d levels and the magnitude of $sp-d$ hybridization by fitting to the results of augmented spherical wave (ASW) - LSDA calculations for antiferromagnetic (AF) zb-MnTe [7,9]. The resulting hybridization parameters are in good agreement with previous estimates [13] obtained from Harrison's "universal" tight-binding scheme [11]. The location of Mn d levels relative to the sp bands is less reliable, however, since the LSDA is well known to underestimate quasiparticle excitation energies [17]. Both the ASW results of [7] and [9] and more recent linearized augmented plane wave calculations [10] for AF zb-MnTe place the occupied d states degenerate with the sp valence band near -2 eV and the unoccupied d states in the sp band gap. In our final ETB parametrization shown in Fig. 2 the $3d_\sigma$ level has been shifted to -3.4 eV to agree with the (x independent) location observed in photoemission experiments on $\text{Cd}_{1-x}\text{Mn}_x\text{Te}$ [18]. The $3d_{-\sigma}$ level has been similarly shifted to 3.6 eV to place it about 4.5 eV above the region of the L point of the upper valence band. This placement is consistent with the anomalous structure seen in ellipsometry [19] and reflectivity [20] data for $\text{Cd}_{1-x}\text{Mn}_x\text{Te}$ at 4.5 eV. The magnitudes and signs of the above d level adjustments are consistent with the expected corrections to LSDA eigenvalues [9,17].

The inclusion of d states on the same footing as sp bands in the ETB-CPA requires the consideration of magnetic as well as compositional disorder [21,22]. We model this effect for $\text{II}_{1-x}\text{Mn}_x\text{VI}$ alloys by assuming that the occupied d states have either spin up (\uparrow) or spin down (\downarrow) at random. The alloy is thus treated as the pseudo-ternary system $\text{II}_{1-x}(\text{Mn}\uparrow)_y(\text{Mn}\downarrow)_{x(1-y)}\text{VI}$. The constraint $y=0.5$ is imposed in the ground state calculations described below to ensure zero net magnetization. Variations in the value of y may also be considered to simulate the behavior in an external magnetic field.

Figure 3 shows the calculated CPA total and projected d (shaded) densities of states for $\text{Cd}_{1-x}(\text{Mn}\uparrow)_{x/2}(\text{Mn}\downarrow)_{x/2}\text{Te}$ with $x = 0.0, 0.3$ and 0.6 . The similar shape of the $x=0.3$ and $x=0.6$ results indicates that the d contribution to the density of states is determined primarily by the local environment of the Mn and is not strongly affected by the presence of magnetic disorder. Compositional disorder resulting from the difference between Cd and Mn s levels, on the other hand, does produce a slight change in the sp contribution to the density of states in the lower valence region shown in the figure. States contributing to the -4.5 eV peak in CdTe are composed primarily of Cd s and Te p orbitals. Upon alloying with Mn, this peak shifts to higher energy and decreases in magnitude while new structure appears in the alloy sp bands near -3.9 eV which is superimposed in Fig. 3 on the much larger Mn d contribution at this energy.

The splitting of the occupied Mn d peak in Fig. 3 is a consequence of $sp-d$ hybridization. The lower energy states, which have t_2 symmetry, hybridize more strongly in the tetrahedral environment than those of e symmetry and are repelled by the Te p -like upper valence region. The interaction in turn produces an appreciable d admixture throughout the upper valence region, including the valence band maximum. The resulting change in the structure of the density of states near -1 eV has been observed directly in photoemission experiments [18]. The small shift of the valence band maximum is overestimated in the CPA by the neglect of short ranged AF correlations. In contrast to the valence band behavior, the conduction bands in Fig. 3

are relatively unaffected by $sp-d$ hybridization except for a slight broadening of the unoccupied d peak. The d admixture in the conduction band minimum, in fact, is strictly zero by symmetry.

Much more detailed band structure information can be obtained from an analysis of k dependent properties in the ETB-CPA. Such calculations for $Cd_{1-x}Mn_xTe$ indicate that magnetic disorder causes an appreciable damping of states throughout the region of the upper valence peak in Fig. 3. The damping shows up in the calculations as a broadening of k dependent spectral densities which in the absence of disorder would reduce to series of δ - functions at the band energies. The calculated broadening and peak location of the upper valence band spectral density at L is qualitatively consistent with the anomalous behavior of the E_1 optical transition observed in recent ellipsometry experiments [19]. A more detailed analysis of spectral densities will be particularly important if more extensive angle-resolved photoemission data becomes available.

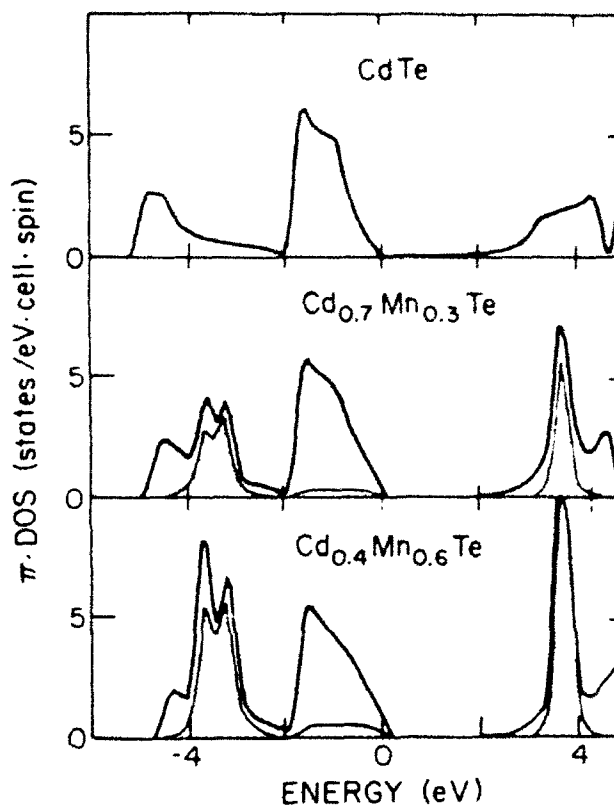


Fig. 3. — Calculated CPA total and projected (shaded) densities of states for $Cd_{1-x}(Mn\uparrow)_{x/2}(Mn\downarrow)_{x/2}Te$ with $x = 0.0, 0.3$ and 0.6 .

MAGNETIC INTERACTIONS

The preceding electronic structure model is now used to examine the principal magnetic interactions in $II_{1-x}Mn_xVI$ DMS along the lines indicated in Fig. 1.

Mn - sp Band Exchange

The Kondo-like interaction H_K between Mn local moments and the spins of band edge electrons and holes is the larger of the two exchange interactions considered here. The relevant exchange constants for most $II_{1-x}Mn_xVI$ DMS have been determined from experiment and found to be $N_0\alpha \equiv J_{sp-d}^c \approx 0.2$ eV for the conduction band edge and $N_0\beta \equiv J_{sp-d}^v \approx -1.0$ eV for the valence band edge [23]. The qualitative difference between these values can be understood in terms of the different effects of $sp-d$

hybridization on the two band edges [8,9,24]. For the conduction band edge, where no d admixture is allowed by symmetry, $N_0\alpha$ is a purely potential exchange interaction; this is a relatively weak effect in these systems, and always ferromagnetic. By contrast, the appreciable d admixture in the valence band edge gives rise, through the Schrieffer-Wolff transformation [25], to the much larger, antiferromagnetic exchange constant $N_0\beta$. Substitution of the above ETB parameters for $\text{Cd}_{1-x}\text{Mn}_x\text{Te}$ in the appropriate Schrieffer-Wolff expression yields an estimate of $N_0\beta$ within 20 % of experiment. Accurate values of both $N_0\alpha$ and $N_0\beta$ in $\text{II}_{1-x}\text{Mn}_x\text{VI}$ DMS have also been extracted from *ab initio* LSDA calculations of band edge spin splittings in hypothetical *ferromagnetic* compounds ($x = 1.0$ and 0.5) [8-10].

Mn - Mn Exchange

The weaker Mn - Mn exchange interaction H_H is known to be short-ranged and antiferromagnetic in $\text{II}_{1-x}\text{Mn}_x\text{VI}$ alloys [3]. Experimentally derived nearest neighbor exchange constants J_{nn}^{dd} are typically of the order of -10 K (-9×10^{-4} eV), assuming a total interaction between two spins of $-2J^{dd}(R_{ij})\mathbf{S}_i \cdot \mathbf{S}_j$ [26]. The hierarchy of Mn - Mn exchange mechanisms has recently been examined quantitatively by Larson, *et. al.* starting from a simplified version (VCA sp bands, single $sp-d$ band hopping parameter) of the effective one electron Hamiltonian discussed above [7,9]. The total Mn - Mn interaction in this work is calculated as a fourth order perturbation in H_{sp} with the contributions of various mechanisms classified by intermediate states. Processes which involve the creation of two holes in the sp valence band are associated with superexchange [27]. Processes which involve the creation of one electron and one hole are associated with the Bloembergen-Rowland mechanism [28] (RKKY in metals). Two-electron processes are also considered. The approach is superior to that of previous calculations of $J^{dd}(R_{ij})$ in DMS which considered only a second order perturbative treatment of H_K [29]. The retention of only spin degrees of freedom in H_K neglects many of the effects of $sp-d$ hybridization which play an important role in determining $J^{dd}(R_{ij})$.

Numerical calculations based on the above approach indicate that AF superexchange accounts for about 95 % of J_{nn}^{dd} in wide gap Cd and Zn DMS and remains dominant out to about fourth nearest neighbors [7,9]. The Bloembergen-Rowland mechanism makes an increasingly important contribution in narrower gap Hg systems (particularly for more distant neighbors) but is unlikely to ever become dominant. Exchange processes involving holes are more effective than those involving electrons because of the larger density of states and the larger degree of Mn d - sp band hybridization in the sp valence band. The net J_{nn}^{dd} values calculated by Larson, *et. al.* for $\text{Cd}_{1-x}\text{Mn}_x\text{Te}$ are -12 K in [7] and -8 K in [9] using a more refined set of parameters. The excellent agreement with experiment (-6.3 K [26]) is a clear indication of the validity of the resulting physical picture and the underlying electronic structure model.

Three-Level Model of Superexchange

We have recently developed a more physically transparent model of superexchange in Mn-based systems which involves only the essential features of the electronic structure [9]. The model contains four parameters: the occupied d level energy ϵ_d , the unoccupied d level energy $\epsilon_d + U_{eff}$, the energy of the valence band maximum E_v , and a Mn d - anion p hybridization parameter V_{pd} . The analytic expression

$$J^{dd}(R) = -2V_{pd}^4 [(\epsilon_d + U_{eff} - E_v)^{-2} U_{eff}^{-1} + (\epsilon_d + U_{eff} - E_v)^{-3}] f(R) \quad (1)$$

can be written down immediately in analogy with the full fourth order perturbation theory of [7]. The remarkable feature of this formula is that the function $f(R)$, which describes the dependence on the Mn - Mn separation R , is largely independent of the details of the electronic structure within a closely related class of materials.

For $\text{II}_{1-x}\text{Mn}_x\text{VI}$ DMS, with cubic lattice constant a , $f(R)$ is well approximated out to about fourth nearest neighbors by the Gaussian decay $0.2 \exp(-4.89 R^2/a^2)$ [7]. Trends in exchange constants upon variations in the group II or group VI element can thus be understood directly in terms of the corresponding trends in electronic structure parameters. By further supplementing this model with the Schrieffer-Wolff expression

$$N_0\beta = -2V_{pd}^2 [(\epsilon_d + U_{eff} - E_v)^{-1} + (E_v - \epsilon_d)^{-1}] \quad (2)$$

one can obtain a consistent description of *both* Mn - *sp* band and Mn - Mn exchange in these materials.

The utility of these expressions is first illustrated by considering those wide gap $\text{II}_{1-x}\text{Mn}_x\text{VI}$ DMS for which reliable experimental values of J_{nn}^{dd} have been reported [26]. The composition $x=0.1$ is chosen for clarity although none of the parameters or results depend strongly on x . The electronic structure parameters used in the model are given in the left-hand columns in Table I. The $E_v - \epsilon_d$ values for the two Cd alloys are taken from photoemission experiments [18]. The value $U_{eff} = 7.0$ eV in $\text{Cd}_{1-x}\text{Mn}_x\text{Te}$ is chosen from Fig. 2 and the increase in U_{eff} in $\text{Cd}_{1-x}\text{Mn}_x\text{Se}$ is estimated from the smaller dielectric constant in this system. Both $E_v - \epsilon_d$ and U_{eff} are assumed to be the same in the corresponding Zn alloys since these quantities are relatively insensitive to the cation species. The values of V_{pd} are determined from Eq. (2) and the experimental $N_0\beta$ values in the table [23].

Table I — Electronic structure parameters used as input in three-level model and associated experimental (exp.) and theoretical (th.) exchange constants for a variety of Mn-based DMS and rocksalt insulators.

	$E_v - \epsilon_d$	U_{eff}	V_{pd}	$N_0\beta$ (exp.)	J_{nn}^{dd} (th.)	J_{nn}^{dd} (exp.)
$\text{Cd}_{0.9}\text{Mn}_{0.1}\text{Te}$	3.4 eV	7.0 eV	0.88 eV	-0.88 eV	-8.0 K	-6.3 K
$\text{Cd}_{0.9}\text{Mn}_{0.1}\text{Se}$	3.4	7.6	1.01	-1.11	-9.0	-7.9
$\text{Zn}_{0.9}\text{Mn}_{0.1}\text{Te}$	3.4	7.0	0.99	-1.12	-13.0	-8.8
$\text{Zn}_{0.9}\text{Mn}_{0.1}\text{Se}$	3.4	7.6	1.06	-1.22	-11.0	-13
$\alpha\text{-MnS}$	0.5	8.0	1.08	-	-1.7	-4.4
MnO	-2.5	9.0	1.84	-	-5.0	-7.2

The resulting theoretical values of J_{nn}^{dd} obtained from Eq. (1) are compared to the corresponding experimental values [26] in the right-hand columns of the table. The simple model not only yields absolute values of the exchange constants within 50 % of experiment for each DMS considered, but it also accounts for the observed trends towards larger J_{nn}^{dd} in $\text{Cd}_{1-x}\text{Mn}_x\text{Se}$ compared to $\text{Cd}_{1-x}\text{Mn}_x\text{Te}$ and when Cd is replaced by Zn. Both of these trends result from an increase in V_{pd} which we attribute to a decrease in the Mn - anion bond length. The failure of the theory to account for the experimentally observed increase in J_{nn}^{dd} in $\text{Zn}_{1-x}\text{Mn}_x\text{Se}$ compared to $\text{Zn}_{1-x}\text{Mn}_x\text{Te}$ may be an artifact of our assumed constancy of $E_v - \epsilon_d$ and U_{eff} in Cd and Zn alloys.

The three-level model of superexchange outlined here is expected to have more general applicability to a variety of Mn - based non-metals. The function $f(R)$ will differ somewhat depending on the symmetry and sp bandwidths in a given class of materials but within each class $f(R)$ is expected to remain largely independent of the actual atomic constituents [9]. We illustrate this point by considering the Mn - based rocksalt insulators MnO and α -MnS. By coincidence, the appropriate $f(R)$ for Mn nearest neighbors in these materials (~ 0.017) turns out to be the same as in $\text{II}_{1-x}\text{Mn}_x\text{VI}$ DMS, despite the difference in symmetry and smaller sp bandwidths in the rocksalt systems [9]. The values of $E_v - \epsilon_d$, U_{eff} and V_{pd} for MnO and α -MnS given in Table I were obtained in [9] from a variety of theoretical ingredients including LSDA calculations [30] and tight-binding "scaling laws" [11]. The resulting theoretical values of J_{nn}^{dd} are again in reasonable agreement with experiment [31]. More importantly, the increase in J_{nn}^{dd} from α -MnS to MnO is well accounted for in the model and related directly through Eq. (1) to changes in the corresponding electronic structure parameters.

ACKNOWLEDGEMENTS

We are grateful to A. E. Carlsson and R. J. Lempert for their collaboration on some of the calculations reviewed here [7-9,21]. This work was supported by the Joint Services Electronics Program (N00014-84-K-0465), the Defense Advanced Research Projects Agency (through ONR Contract N00014-86-K-003) and the National Science Foundation (DMR 85-14638).

REFERENCES

1. N.B. Brandt and V.V. Moschalkov, Adv. in Phys. **33**, 193 (1984); J.K. Furdyna, J. Appl. Phys. **53**, 637 (1982) and references therein.
2. J. Kossut, Phys. Stat. Sol. (b) **78**, 537 (1976).
3. S.B. Oseroff and P.H. Keesom, to be published in *Semiconductors and Semimetals*, ed. by R.K. Willardson and A.C. Beer (Academic, New York).
4. J. Hubbard, Proc. Roy. Soc. (London) A **281** 401 (1964).
5. U. Von Barth and L. Hedin, J. Phys. C **5**, 1629 (1972).
6. A.R. Williams and U. Von Barth, in *The Inhomogeneous Electron Gas*, ed. by S. Lundqvist and N.H. March (Plenum, New York, 1983).
7. B.E. Larson, K.C. Hass, H. Ehrenreich and A.E. Carlsson, Solid State Commun. **56**, 347 (1985).
8. K.C. Hass, B.E. Larson, H. Ehrenreich and A.E. Carlsson, J. Mag. Magn. Mat. **54-57**, 1283 (1986).
9. B.E. Larson, K.C. Hass, H. Ehrenreich and A.E. Carlsson (unpublished).
10. S.H. Wei and A. Zunger, Phys. Rev. Lett. **56**, 2391 (1986) and unpublished.
11. W.A. Harrison, *Electronic Structure and the Properties of Solids* (Freeman.

- San Francisco, 1980).
12. H. Ehrenreich and L.M. Schwartz, in *Solid State Physics*, ed. by H. Ehrenreich, F. Seitz and D. Turnbull (Academic, New York, 1976) Vol. 31, p. 149.
 13. K.C. Hass and H. Ehrenreich, *J. Vac. Sci. Technol. A* **1**, 1678 (1983).
 14. K.C. Hass, H. Ehrenreich and B. Velický, *Phys. Rev. B* **27**, 1088 (1983).
 15. C.E. Moore, *Atomic Energy Levels* (U.S. G.P.O., Washington, D.C., 1949); F. Herman and S. Skillman, *Atomic Structure Calculations* (Prentice-Hall, Englewood Cliffs, 1963).
 16. N.T. Khoi and J.A. Gaj, *Phys. Stat. Sol. (b)* **83**, K133 (1977); R. Brun de Re, T. Donofro, J. Avon, J. Magid and J.C. Wooley, *Nuovo Cim.* **2D**, 1911 (1983).
 17. A.E. Carlsson, *Phys. Rev. B* **31**, 5178 (1985).
 18. M. Taniguchi, *et. al.*, *Phys. Rev. B* **33**, 1206 (1986); A. Franciosi, *et. al.*, *Proc. of the 18th Int. Conf. on the Phys. of Semicond.*, Stockholm, 1986 and references therein.
 19. P. Lautenschlager, S. Logothetidis, L. Viña and M. Cardona, *Phys. Rev. B* **32**, 3811 (1985).
 20. T. Kendelewicz, *J. Phys. C* **14**, 6407 (1981).
 21. H. Ehrenreich, K.C. Hass, N.F. Johnson, B.E. Larson and R.J. Lempert, *Proc. of the 18th Int. Conf. on the Phys. of Semicond.*, Stockholm, 1986.
 22. B. Velický, J. Mašek, V. Cháb and B.A. Orlowski, *Acta Physica Polonica A* **69**, 1059 (1986).
 23. D. Heiman, Y. Shapira and S. Foner, *Solid State Commun.* **51**, 603 (1984) and references therein.
 24. A.K. Bhattacharjee, G. Fishman and B. Coqblin, *Physica* **117/118B**, 449 (1983).
 25. J.R. Schrieffer and P.A. Wolff, *Phys. Rev.* **149**, 491 (1966).
 26. B.E. Larson, K.C. Hass and R.L. Aggarwal, *Phys. Rev. B* **33**, 1789 (1986); Y. Shapira, S. Foner, D.H. Ridgley, K. Dwight and A. Wold, *Phys. Rev. B* **30**, 4021 (1984); L.M. Corliss, J.M. Hastings, S.M. Shapiro, Y. Shapira and P. Becla, *Phys. Rev. B* **33**, 608 (1986).
 27. P.W. Anderson, in *Solid State Physics*, ed. by F. Seitz and D. Turnbull (Academic, New York, 1963) Vol. 14, p. 79; B. Koiller and L.M. Falicov, *J. Phys. C* **8**, 695 (1975).
 28. N. Bloembergen and T.J. Rowland, *Phys. Rev. B* **97**, 1697 (1955).
 29. G. Bastard and C. Lewiner, *Phys. Rev. B* **20**, 4265 (1979); V.C. Lee and L. Liu, *Phys. Rev. B* **29**, 2125 (1984).
 30. T. Oguchi, K. Terakura and A.R. Williams, *Phys. Rev. B* **28**, 6443 (1983).
 31. J.S. Smart, in *Magnetism*, ed. by G.T. Rado and H. Suhl (Academic, New York, 1963) Vol. 3, p. 63.

Molecular coherent-potential approximation for zinc-blende pseudobinary alloys

R. J. Lempert, K. C. Hass,* and H. Ehrenreich†

Division of Applied Sciences, Harvard University, Cambridge, Massachusetts 02138

(Received 15 January 1987)

A detailed description is presented of the recently developed molecular coherent-potential approximation (MCPA) theory of the electronic structure of zinc-blende pseudobinary alloys [K. C. Hass, R. J. Lempert, and H. Ehrenreich, *Phys. Rev. Lett.* **52**, 77 (1984)]. This approach is superior to previous CPA treatments because of its ability to treat the dominant effects of both random chemical and random bond-length variations. The two effects are modeled as diagonal and off-diagonal disorder, respectively, in an empirical tight-binding framework. A straightforward application of the MCPA is made possible by the presence of one chemically ordered sublattice. General consequences of this approach are illustrated through detailed applications to $\text{In}_{1-x}\text{Ga}_x\text{As}$ and $\text{ZnSe}_{1-x}\text{Te}_x$. The interference between chemically and structurally induced scattering in different energy regions is analyzed by comparing MCPA, site CPA, and virtual-crystal spectral densities and band-edge properties. Differences between the two materials are used to contrast the behavior in cation-substituted III-V and anion-substituted II-VI alloys. The merits of the MCPA are discussed in relation to some alternative alloy theories (bond-centered CPA, supercell, and recursion method).

I. INTRODUCTION

Isoelectronic semiconducting alloys have become increasingly important technologically because of their tailorable band gaps and other materials properties.¹ In recent years considerable effort has been devoted to examining the role that disorder plays in determining their electronic structure.² This issue is of practical as well as intrinsic interest since the presence of disorder may impose fundamental limits on device performance. While some progress has been made in understanding disorder effects in certain specific alloy semiconductors,^{3,4} no fully satisfactory theory has yet emerged which is capable of providing quantitatively accurate results for a variety of materials over a wide energy range.

This paper focuses on an important restricted class of semiconducting alloys known as zinc-blende pseudobinary alloys. These materials are of the form $A'_{1-x}A''_xB$ where the $A'B$ and $A''B$ limiting crystals are ordinary III-V or II-VI compound semiconductors having the zinc-blende structure. (The A' and A'' atoms may be either cations, as in $\text{Hg}_{1-x}\text{Cd}_x\text{Te}$, or anions, as in $\text{GaAs}_{1-x}\text{P}_x$.) Alloy disorder in these systems is conveniently divided into a chemical and a structural component. The former is associated with the different atomic potentials of the A' and A'' atoms, which we will assume to be randomly distributed.⁵ The latter is associated with local distortions in the underlying lattice structure which occur due to a difference in $A'-B$ and $A''-B$ bond lengths. The presence of structural disorder was first unambiguously identified by Mikkelsen and Boyce⁶ in extended x-ray-absorption fine-structure (EXAFS) measurements on $\text{In}_{1-x}\text{Ga}_x\text{As}$. There the $\text{In}-\text{As}$ and $\text{Ga}-\text{As}$ nearest-neighbor bond lengths were found to vary by less than 2% from their limiting-crystal values, despite a 7% Vegard's-law (linear) variation in the average x-ray lattice

constant. A similar near conservation of tetrahedral bond lengths⁷ has also been observed recently in EXAFS results for other zinc-blende pseudobinary systems.⁸ This effect is believed to be a general feature of these materials resulting from the much stronger bond-stretching forces compared to bond-bending forces in covalent systems.^{7,9}

Most previous band-structure calculations¹ for zinc-blende pseudobinary alloys have either neglected disorder entirely [as in the virtual-crystal approximation (VCA)], or else taken into account only the chemical component [e.g., in the coherent-potential approximation¹⁰ (CPA)]. A more comprehensive treatment, capable of including the dominant effects of both types of disorder, as well as the correlations between them, was outlined by the present authors in a recent Letter.¹¹ The approach is based on modeling of chemical and structural disorder as diagonal and off-diagonal disorder, respectively, in an empirical tight-binding framework.^{12,13} An unconventional unit cell is chosen so that the dominant disorder effects are "cell diagonal." The problem is then treated within the molecular coherent-potential approximation (MCPA).¹⁴ This simple matrix extension of the CPA retains the favorable analytic properties of the CPA.^{14(b)} A complex MCPA effective potential is defined by the condition that a single cell, as opposed to a single site, embedded in the effective medium, on average, produces no further scattering. (The imaginary part of the potential reflects the fact that alloy quasiparticle states are damped.) Early applications of the MCPA to binary metallic alloys were of limited validity because of the absence of an appropriate molecular unit.¹⁵ A natural unit exists in the case of zinc-blende pseudobinary alloys because of the presence of the chemically ordered B sublattice.¹⁶

This paper provides a much more complete account of the MCPA treatment of zinc-blende pseudobinary alloys. Important general consequences of this approach are discussed in detail and illustrated by specific applications to

$\text{In}_{1-x}\text{Ga}_x\text{As}$ and $\text{ZnSe}_x\text{Te}_{1-x}$. These materials were chosen both for the interesting contrasts they provide (the former is a III-V cation-substituted alloy and the latter is a II-VI anion substituted alloy) and because both are expected to exhibit appreciable chemical and structural disorder.¹⁷ While it is not our intent here to provide a definitive treatment of these materials, the detailed semi-quantitative descriptions which emerge may nevertheless be of interest in their own right.

The key assumptions of the MCPA model and its basic formalism are outlined in Sec. II. The disordered-alloy Hamiltonian is constructed by interpolating between Slater-Koster parameters¹² for the limiting crystals. Section III discusses the specific choice of parameters for the $\text{In}_{1-x}\text{Ga}_x\text{As}$ and $\text{ZnSe}_x\text{Te}_{1-x}$ systems. Constraints similar to those suggested by Harrison¹³ are imposed to ensure the physical reasonability of the MCPA scattering parameters.

The significance of structural disorder is illustrated by means of comparisons of the MCPA results to those of the VCA and site CPA (Ref. 4) (diagonal, or chemical, disorder only). Section IV examines this issue in the context of damping effects throughout the bands. Section V focuses on two band-edge properties: the alloy scattering mobility and band-gap "bowing."^{1,2} The principal conclusions are that (1) disorder effects are generally small, particularly near the band edges, (2) the effects of structural disorder in these alloys can be of comparable magnitude to those of chemical disorder, and (3) the interplay between the two types of disorder can either enhance or diminish the total scattering in a particular energy region. A preliminary discussion of these results based on more limited calculations for $\text{In}_{1-x}\text{Ga}_x\text{As}$ was given in Ref. 11.

The paper concludes in Sec. VI with a discussion of the relationship between the MCPA and some alternative alloy theories. Sections VIA and VIB present comparisons to results obtained within the bond-centered CPA and the supercell approach,^{7,18} respectively. Section VIC briefly comments on the recursion method.^{19,20} The bond-centered CPA is a limiting case of the MCPA similar to that used in many previous treatments of zinc-blende pseudobinary alloys.^{3,21} It is shown here to be unreliable for alloys with appreciable chemical disorder because it neglects an important distinction between *s*-like and *p*-like scattering. The former usually dominates because *s* states are more sensitive to the core.

Supercell and recursion-method calculations are conceptually different in that they do not involve configuration averaging. The former applies standard crystalline band-structure techniques to ordered alloy configurations. This approach is especially interesting in view of recent experimental^{5(a),(d)} and theoretical^{5(b)} indications that the growth of such ordered alloys may, in fact, be possible. The recursion method, by contrast, is a cluster approach. We argue that both this and the supercell method contain much of the same basic physics as the MCPA and lead to similar physical results. The supercell method, however, provides more limited band-structure information for random alloys because of its introduction of artificial periodicity.

II. DESCRIPTION OF THE MODEL

A. Tight-binding treatment of structural disorder

The basic idea illustrating the MCPA treatment of structural disorder is shown schematically in Fig. 1 for a two-dimensional analog of the zinc-blende structure.

The upper half of the figure shows the true structure expected for a concentrated $A'_{1-x}A''_x B$ alloy whose limiting crystals $A'B$ and $A''B$ are poorly lattice matched. We assume that the crystalline nearest-neighbor bond lengths $d_{A'B}$ and $d_{A''B}$ are such that $d_{A'B} > d_{A''B}$. The characteristic feature recently revealed by EXAFS is that the $A'-B$ and $A''-B$ bond lengths do not change very much in the alloy but instead retain mean values closer to $d_{A'B}$ and $d_{A''B}$ than to the average value $\bar{d}(x) = (1-x)d_{A'B} + xd_{A''B}$. The associated distortions are accommodated locally and preserve the zinc-blende topology. Such structural disorder is much simpler than that in amorphous semiconductors. An effective-medium approach is therefore more appropriate.

Within tight-binding theory, the actual locations of the atoms never need to be specified as long as the Hamiltonian contains the appropriate matrix elements and has the property connectivity.²² The alloy constituents in the MCPA are thus assumed to occupy the sites of an ordered zinc-blende "virtual lattice" with nearest-neighbor spacing $\bar{d}(x)$. Structural distortions are modeled by choosing the Hamiltonian matrix elements to be those appropriate to the actual distorted structure. This is done here by assuming that the structural disorder resides entirely in the variation of the dominant nearest-neighbor hopping integrals. The hopping associated with the longer $A'-B$ bond is assumed to be smaller in magnitude than that associated with the $A''-B$ bond, as illus-

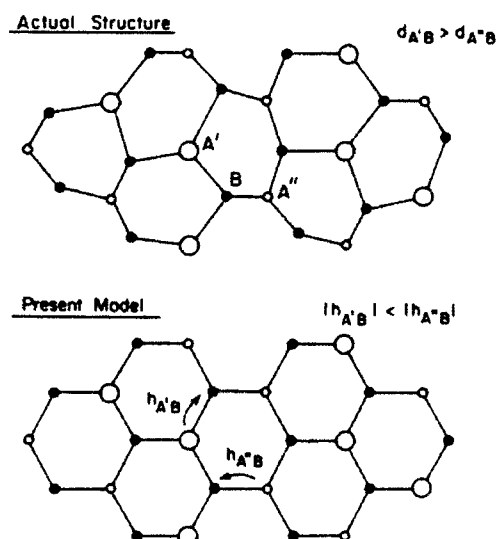


FIG. 1. Two-dimensional analogue of the true structure of an $A'_{1-x}A''_xB$ zinc-blende alloy and its corresponding "virtual lattice" model. The bond-length difference $d_{A'B} > d_{A''B}$ is modeled as a difference in hopping integrals $|h_{A'B}| < |h_{A''B}|$.

trated in the lower half of Fig. 1.

Additional effects associated with bond-angle variations and longer-range strain fields²³ are neglected to make the problem tractable.²⁴ Estimates indicate that for a general \mathbf{k} point this will usually be a good approximation. Near the band edges, however, angular variations and long-range strain fields play an increasingly important role²⁵ because of the higher symmetry and long wavelength of states near $\mathbf{k}=0$. We return to this issue in Sec. V as a possible explanation for some of the quantitative discrepancies in the MCPA band-edge results.

One additional feature of Fig. 1 is worth noting. Since the A' atoms are always surrounded by longer bonds than the A'' atoms, the structural and chemical disorder are strongly correlated. These correlations were neglected in many earlier treatments of structural disorder in zinc-blende alloys based on analogies with finite-temperature effects.^{21(c),26} They are naturally included in the present model and will give rise to novel interference effects between the two types of disorder.

B. Construction of the alloy Hamiltonian

A realistic alloy Hamiltonian based on these ideas is constructed by interpolating between Slater-Koster parametrizations of the electronic structure of the limiting crystals.¹² An orthonormal basis of one s and three p orbitals per site is employed with hopping integrals extending up to second-nearest neighbors. This is known to provide a reasonable description of the valence and lowest conduction bands in zinc-blende crystals.⁴ The truncation at second neighbors is not essential to the MCPA formalism but provides a useful compromise between ease of parametrization and the quality of the resulting band structures.

The alloy disorder is modeled most conveniently by performing a unitary transformation to an equivalent basis of sp^3 hybrid orbitals. Details of this procedure are presented in the Appendix. The unconventional unit cell shown in Fig. 2 is chosen for reasons described in more detail below. The cell is centered on an A sublattice site and consists of the four sp^3 hybrid orbitals from the central A atom plus those four from neighboring B atoms which point in the direction of the central site. The orbitals are labeled as $|\alpha, j\rangle$ where $\alpha=1-4$ correspond to A hybrid orbitals, $\alpha=5-8$ to B hybrid orbitals, and \mathbf{R}_j is a lattice vector. Orbitals 1 and 5, 2 and 6, 3 and 7, and 4 and 8 lie along the $[111]$, $[1\bar{1}\bar{1}]$, $[\bar{1}1\bar{1}]$, and $[\bar{1}\bar{1}1]$ directions, respectively.

Construction of the Bloch sums

$$|\alpha, \mathbf{k}\rangle = N^{-1/2} \sum_j e^{i\mathbf{k}\cdot\mathbf{R}_j} |\alpha, j\rangle, \quad (1)$$

where N is the number of unit cells in a normalization volume, reduces each limiting-crystal Hamiltonian to an 8×8 matrix for each \mathbf{k} point. The crystalline matrix elements are conveniently written in the form

$$\langle \alpha, \mathbf{k} | H | \beta, \mathbf{k} \rangle = \epsilon_{\alpha\beta} + \sum_{j(\neq 0)} h_{\alpha\beta}(0, j) e^{i\mathbf{k}\cdot\mathbf{R}_j} + \langle \alpha, \mathbf{k} | H_2 | \beta, \mathbf{k} \rangle. \quad (2)$$

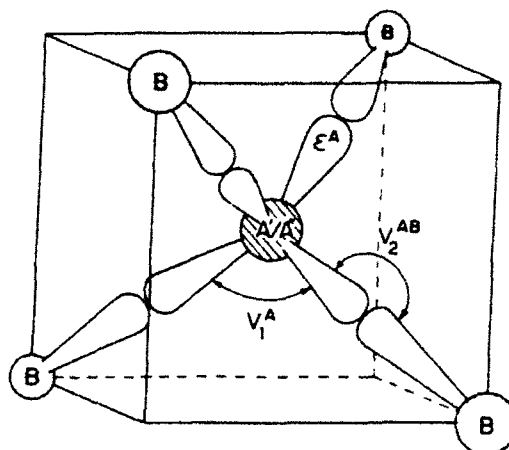


FIG. 2. Unit cell employed in the MCPA model of $A'_{1-x}A''_xB$ zinc-blende alloys. Lobes represent sp^3 hybrid orbitals on central A' or A'' atom and on neighboring B sites. Chemical disorder is modeled by random ϵ^A and V_1^A . Differences in $A'-B$ and $A''-B$ bond lengths are modeled by random V_2^{AB} .

The $\epsilon_{\alpha\beta}$ contain only intra-atomic and nearest-neighbor hopping integrals which couple orbitals within the same cell. The most important of these are the matrix elements ϵ^A , V_1^A , and V_2^{AB} shown in Fig. 2. The $h_{\alpha\beta}(0, j)$ contain intra-atomic and nearest-neighbor hopping integrals which couple orbitals in different cells. An example would be a V_1^B coupling (not shown) between two sp^3 hybrid orbitals on a B atom. The last term in Eq. (2) describes second, and in principle, more distant neighbor interactions. Explicit expressions for the $\epsilon_{\alpha\beta}$, $h_{\alpha\beta}(0, j)$, and $\langle \alpha, \mathbf{k} | H_2 | \beta, \mathbf{k} \rangle$ in terms of Slater-Koster parameters are presented in the Appendix.

The advantage of this unusual description is that it allows the dominant disorder effects in the alloy to be modeled entirely in terms of the randomly distributed cell-diagonal matrix elements $\epsilon_{\alpha\beta}$. This restriction is essential for straightforward application of the MCPA. The specific assumptions concerning the form of disorder made here are motivated by Harrison's universal tight-binding scheme¹³ and defect molecule calculations of isolated impurity levels in semiconductors.²⁷ The chemical component is represented by differences between the ϵ^A and V_1^A matrix elements for A' and A'' atoms. This is equivalent to assuming that the s and p atomic-level energies differ in A' and A'' atoms. The difference in $A'-B$ and $A''-B$ bond lengths is represented by different V_2^{AB} hopping integrals for the two types of bonds. Other interatomic matrix elements are an order of magnitude smaller and are treated in an averaged fashion, as are intra-atomic matrix elements $h_{\alpha\beta}$ for the B sites.

The $A'_{1-x}A''_xB$ alloy Hamiltonian can then be written as

$$H_{\text{alloy}} = \sum_j \sum_{\alpha, \beta} |\alpha, j\rangle v_{\alpha\beta}(j) \langle \beta, j| + \bar{H}, \quad (3)$$

where \bar{H} is a periodic reference Hamiltonian with \mathbf{k} -space

matrix elements

$$\langle \alpha, \mathbf{k} | \bar{H} | \beta, \mathbf{k} \rangle = \bar{\epsilon}_{\alpha\beta} + \sum_{j \neq 0} \bar{h}_{\alpha\beta}(0, j) e^{i\mathbf{k} \cdot \mathbf{r}_j} + \langle \alpha, \mathbf{k} | \bar{H}_2 | \beta, \mathbf{k} \rangle \quad (4)$$

and the

$$v_{\alpha\beta}(j) = \epsilon_{\alpha\beta}(j) - \bar{\epsilon}_{\alpha\beta}(j) \quad (5)$$

are fluctuations in the intracell matrix elements with respect to their average values at site \mathbf{R}_j . The averaged quantities in Eq. (4) are obtained using a scaled version³ of the VCA specified below. The $\epsilon_{\alpha\beta}(j)$ are assumed to take on two sets of values, with probabilities $1-x$ and x , respectively, depending on whether the central A atom in the cell is A' or A'' . For simplicity, we define these

quantities so that the matrix elements shown explicitly in Fig. 2 retain their limiting crystal values $\epsilon^{A'}$, $V_1^{A'}$, $V_2^{A'B}$ or $\epsilon^{A''}$, $V_1^{A''}$, $V_2^{A''B}$. A generalization to allow these matrix elements to vary with x could also be easily introduced. A variation in $V_2^{A'B}$, for example, could reflect the fact that the $A'-B$ bond lengths do change slightly in the alloy, although much less rapidly than the average bond length $\bar{d}(x)$.

The linear x dependence of $\bar{d}(x)$ and the corresponding virtual lattice constant are taken into account through an appropriate choice of reference Hamiltonian \bar{H} . Here we employ Harrison's ansatz¹³ that interatomic matrix elements in zinc-blende crystals scale as d^{-2} , the inverse square power of the bond length. Other scaling laws²⁸ produce only small quantitative changes. The averaged quantities in Eq. (4) are defined to be

$$\bar{\epsilon}_{\alpha\beta} = \begin{cases} (1-x)\epsilon_{\alpha\beta}^{A'B} + x\epsilon_{\alpha\beta}^{A''B} & \text{for } \epsilon^A, V_1^A, V_2^{A'B}, \text{ and } \epsilon^B, \\ (1-x)(r')\epsilon_{\alpha\beta}^{A'B} + x(r'')\epsilon_{\alpha\beta}^{A''B} & \text{for all other parameters,} \end{cases} \quad (6a)$$

$$\bar{h}_{\alpha\beta}(0, j) = \begin{cases} (1-x)h_{\alpha\beta}^{A'B}(0, j) + xh_{\alpha\beta}^{A''B}(0, j) & \text{for } V_1^B, \\ (1-x)(r')h_{\alpha\beta}^{A'B}(0, j) + x(r'')h_{\alpha\beta}^{A''B}(0, j) & \text{for all other parameters,} \end{cases} \quad (6b)$$

and

$$\langle \alpha, \mathbf{k} | \bar{H}_2 | \beta, \mathbf{k} \rangle = (1-x)(r')\langle \alpha, \mathbf{k} | H_2^{A'B} | \beta, \mathbf{k} \rangle + x(r'')\langle \alpha, \mathbf{k} | H_2^{A''B} | \beta, \mathbf{k} \rangle, \quad (6c)$$

where $r' = [d_{A'B}/\bar{d}(x)]^2$ and $r'' = [d_{A''B}/\bar{d}(x)]^2$. The superscripts indicate limiting-crystal values. The matrix elements ϵ^B and V_1^B are defined in an analogous fashion to ϵ^A and V_1^A (see the Appendix). The $V_2^{A'B}$ parameter in Eq. (6a) is not scaled in order to simplify the MCPA formalism. Since the actual choice of $\bar{\epsilon}_{\alpha\beta}$ is arbitrary as long as the $v_{\alpha\beta}(j)$ in Eq. (5) are properly specified, this has no bearing on the final results.

The $v_{\alpha\beta}(j)$ can now be written explicitly as

$$v_{\alpha\beta}(j) = \begin{cases} x\Delta_{\alpha\beta} & \text{if site } \mathbf{R}_j \text{ is occupied by an } A' \text{ atom,} \\ -(1-x)\Delta_{\alpha\beta} & \text{if site } \mathbf{R}_j \text{ is occupied by an } A'' \text{ atom.} \end{cases} \quad (7)$$

The $\Delta_{\alpha\beta}$ are elements of the scattering matrix

$$\bar{\Delta} = \begin{pmatrix} \Delta_0 & \Delta_1 & \Delta_1 & \Delta_1 & \Delta_2 & 0 & 0 & 0 \\ \Delta_1 & \Delta_0 & \Delta_1 & \Delta_1 & 0 & \Delta_2 & 0 & 0 \\ \Delta_1 & \Delta_1 & \Delta_0 & \Delta_1 & 0 & 0 & \Delta_2 & 0 \\ \Delta_1 & \Delta_1 & \Delta_1 & \Delta_0 & 0 & 0 & 0 & \Delta_2 \\ \Delta_2 & 0 & 0 & 0 & 0 & 0 & 0 & 0 \\ 0 & \Delta_2 & 0 & 0 & 0 & 0 & 0 & 0 \\ 0 & 0 & \Delta_2 & 0 & 0 & 0 & 0 & 0 \\ 0 & 0 & 0 & \Delta_2 & 0 & 0 & 0 & 0 \end{pmatrix}, \quad (8)$$

with scattering parameters

$$\Delta_0 = \epsilon^{A'} - \epsilon^{A''}, \quad (9a)$$

$$\Delta_1 = V_1^{A'} - V_1^{A''}, \quad (9b)$$

and

$$\Delta_2 = V_2^{A'B} - V_2^{A''B}. \quad (9c)$$

The signs of the "chemical parameters" Δ_0 and Δ_1 depend on the relative binding energies of atomic s and p levels

[cf. Eq. (A8)]. For $d_{A'B} > d_{A''B}$, we constrain the "structural parameter" Δ_2 to be positive since $V_2^{A'B}$ is generally negative and its magnitude decreases with increasing bond length.

This completes the description of the alloy Hamiltonian used in Ref. 11 and the present work. The form of $\bar{\Delta}$ may also be generalized to include disorder in other intracell matrix elements. The inclusion of additional diagonal elements in $\bar{\Delta}$ to reflect a dependence of B -site hybrid energies on the occupation of the central A site would be of particular interest. "Redistribution disorder" of this kind has been considered previously in studies of the alloy scattering mobility in zinc-blende alloys.²⁹ It is neglected here because (1) its importance is difficult to assess in an empirical scheme, and (2) more severe limitations on the accuracy of the present calculations are believed to result from the neglect of intercell disorder effects, particularly those resulting from bond-angle variations about the B sites.

C. Implementation of the MCPA

The alloy Hamiltonian, Eq. (3), is a simple matrix generalization of the one-band single-site Hamiltonian used

extensively in early CPA studies.¹⁰ The MCPA analysis proceeds in an analogous fashion. The present section serves only to outline the most basic features of the formalism as applied to the present problem. Additional details and the analytic properties of the MCPA Green's function are discussed in Ref. 14.

The disordered-alloy Hamiltonian is replaced in the MCPA by a periodic effective Hamiltonian

$$H_{\text{eff}}(z) = \bar{H} + \Sigma(z) \quad (10)$$

which is a function of the complex energy z . The effective potential, or self-energy $\Sigma(z)$, is itself complex and cell-diagonal. Its 8×8 matrix representation $\tilde{\Sigma}(z)$ in the basis $|\alpha, j\rangle$ or $|\alpha, \mathbf{k}\rangle$ is determined by the condition that the average t matrix associated with scattering from a single cell (as opposed to a single atom) embedded in the effective medium vanish. This leads to the self-consistency condition

$$\tilde{\Sigma}(z) = [(1-x)\bar{\Delta} + \tilde{\Sigma}(z)]\bar{F}(z)[x\bar{\Delta} - \tilde{\Sigma}(z)] \quad (11)$$

which is analogous to that obtained in the single-site, single-band CPA. Here $\bar{F}(z)$ is the cell-diagonal block of the Green's function with matrix elements

$$F_{\alpha\beta}(z) = N^{-1} \sum_{\mathbf{k}} [z\bar{I} - \bar{H}_{\text{eff}}(\mathbf{k}, z)]_{\alpha\beta}^{-1}, \quad (12)$$

\bar{I} is the 8×8 identity matrix, and $\bar{H}_{\text{eff}}(\mathbf{k}, z)$ has matrix elements

$$\langle \alpha, \mathbf{k} | H_{\text{eff}}(z) | \beta, \mathbf{k} \rangle = \langle \alpha, \mathbf{k} | \bar{H} | \beta, \mathbf{k} \rangle + \Sigma_{\alpha\beta}. \quad (13)$$

Symmetry conditions on the $\Sigma_{\alpha\beta}$ allow us to write $\tilde{\Sigma}(z)$ explicitly as

$$\tilde{\Sigma}(z) = \begin{pmatrix} \Sigma_0^A & \Sigma_1^A & \Sigma_2^A & \Sigma_3^A & \Sigma_2^{AB} & \Sigma_1^{AB} & \Sigma_3^{AB} & \Sigma_0^{AB} \\ \Sigma_1^A & \Sigma_0^A & \Sigma_1^A & \Sigma_2^A & \Sigma_3^{AB} & \Sigma_2^{AB} & \Sigma_0^{AB} & \Sigma_1^{AB} \\ \Sigma_2^A & \Sigma_1^A & \Sigma_0^A & \Sigma_3^A & \Sigma_2^{AB} & \Sigma_3^{AB} & \Sigma_1^{AB} & \Sigma_2^{AB} \\ \Sigma_3^A & \Sigma_2^A & \Sigma_1^A & \Sigma_0^A & \Sigma_1^{AB} & \Sigma_2^{AB} & \Sigma_3^{AB} & \Sigma_0^{AB} \\ \Sigma_2^{AB} & \Sigma_3^{AB} & \Sigma_2^{AB} & \Sigma_1^{AB} & \Sigma_0^B & \Sigma_1^B & \Sigma_2^B & \Sigma_3^B \\ \Sigma_1^{AB} & \Sigma_2^{AB} & \Sigma_3^{AB} & \Sigma_0^{AB} & \Sigma_1^B & \Sigma_0^B & \Sigma_3^B & \Sigma_2^B \\ \Sigma_3^{AB} & \Sigma_0^{AB} & \Sigma_1^{AB} & \Sigma_2^{AB} & \Sigma_2^B & \Sigma_3^B & \Sigma_0^B & \Sigma_1^B \\ \Sigma_0^{AB} & \Sigma_1^{AB} & \Sigma_2^{AB} & \Sigma_3^{AB} & \Sigma_3^B & \Sigma_2^B & \Sigma_1^B & \Sigma_0^B \end{pmatrix}. \quad (14)$$

The structure of $\bar{F}(z)$ is identical. [Note that all the elements of $\tilde{\Sigma}(z)$ are nonzero despite the sparseness of the scattering potential $\bar{\Delta}$. The level of complexity is thus not affected by the inclusion of additional intracell disorder effects.]

The matrix equation (11) is simplified considerably by exploiting the tetrahedral symmetry of the effective medium. Block diagonalization reduces the problem to two 2×2 matrix equations associated with the usual a_1 and t_2 symmetries:

$$\tilde{\Sigma}_\lambda(z) = [(1-x)\bar{\Delta}_\lambda + \tilde{\Sigma}_\lambda(z)]\bar{F}_\lambda(z)[x\bar{\Delta}_\lambda - \tilde{\Sigma}_\lambda(z)], \quad \lambda = a_1, t_2. \quad (15)$$

(Throughout this paper we use the single subscript t_2 to denote quantities whose t_{2x}, t_{2y}, t_{2z} components are all equal.) The scattering matrices in Eq. (15) are given by

$$\bar{\Delta}_{a_1} = \begin{pmatrix} \Delta_1 & \Delta_2 \\ \Delta_2 & 0 \end{pmatrix}, \quad \bar{\Delta}_{t_2} = \begin{pmatrix} \Delta_p & \Delta_2 \\ \Delta_2 & 0 \end{pmatrix}, \quad (16)$$

where $\Delta_s = \Delta_0 + 3\Delta_1$ and $\Delta_p = \Delta_0 - \Delta_1$. The quantities Δ_s and Δ_p are simply the differences in the A' and A'' s and p on-site energies in an atomic-orbital basis. The self-energy has the form

$$\tilde{\Sigma}_\lambda(z) = \begin{pmatrix} \Sigma_\lambda^A(z) & \Sigma_\lambda^{AB}(z) \\ \Sigma_\lambda^{AB}(z) & \Sigma_\lambda^B(z) \end{pmatrix}, \quad \lambda = a_1, t_2, \quad (17)$$

with

$$\begin{aligned} \Sigma_{a_1}^A(z) &= \Sigma_0^A + 3\Sigma_1^A, & \Sigma_{t_2}^A(z) &= \Sigma_0^A - \Sigma_1^A, \\ \Sigma_{a_1}^{AB}(z) &= \Sigma_0^{AB} + 3\Sigma_1^{AB}, & \Sigma_{t_2}^{AB}(z) &= \Sigma_0^{AB} - \Sigma_1^{AB}, \\ \Sigma_{a_1}^B(z) &= \Sigma_0^B + 3\Sigma_1^B, & \Sigma_{t_2}^B(z) &= \Sigma_0^B - \Sigma_1^B. \end{aligned} \quad (18)$$

The Green's-function matrices $\bar{F}_\lambda(z)$ are defined by expressions similar to Eqs. (17) and (18). These quantities couple the a_1 and t_2 equations since both \bar{F}_{a_1} and \bar{F}_{t_2} depend on both $\tilde{\Sigma}_{a_1}$ and $\tilde{\Sigma}_{t_2}$ through Eq. (12). If $\Delta_2 = 0$, Eq. (15) reduces to the scalar site CPA equations considered previously by Hass, Ehrenreich, and Velický.⁴ This limit of chemical disorder only will be used as a basis of comparison for the present MCPA results.

The alloy electronic structure in the MCPA is conveniently described by the spectral density function

$$A(\mathbf{k}, E) = -\pi^{-1} \text{Im} \sum_{\alpha} \langle \alpha, \mathbf{k} | [E^+ - H_{\text{eff}}(E^+)]^{-1} | \alpha, \mathbf{k} \rangle, \quad (19)$$

with $E^+ = E + i0^+$. $A(\mathbf{k}, E)$ represents the average probability of finding an electron with wave vector \mathbf{k} having an energy E . Denoting the eigenstates and corresponding eigenvalues of \bar{H} by $|n\mathbf{k}\rangle$ and $E_n(\mathbf{k})$, respectively, we can write Eq. (19) in the form

$$A(\mathbf{k}, E) = \sum_n \frac{-\sigma_n''(\mathbf{k}, E^+)}{[E^+ - E_n(\mathbf{k}) - \sigma_n'(\mathbf{k}, E^+)]^2 + [\sigma_n''(\mathbf{k}, E^+)]^2}, \quad (20)$$

where

$$\langle n\mathbf{k} | \Sigma(E^+) | n\mathbf{k} \rangle = \sigma_n'(k, E) + i\sigma_n''(k, E) \quad (21)$$

defines the real and imaginary parts of $\langle n\mathbf{k} | \Sigma(E^+) | n\mathbf{k} \rangle$. In the absence of disorder $\Sigma(E^+) = 0$ and $A(\mathbf{k}, E)$ reduces to a series of δ functions at the band energies $E_n(\mathbf{k})$. In the weak-scattering limit,¹⁰ which is often applicable in semiconductors, $\sigma_n''(\mathbf{k}, E)$ is small and the principal effect of the disorder is to shift the spectral density peaks and to broaden them into Lorentzians.

It is useful to express $\langle n\mathbf{k} | \Sigma(E^+) | n\mathbf{k} \rangle$ in terms of the self-energy components defined in Eq. (17). We first introduce the symmetrized orbitals

$$\begin{aligned}
|a_1^A, j\rangle &= (|1, j\rangle + |2, j\rangle + |3, j\rangle + |4, j\rangle)/2, & |t_{2x}^B, j\rangle &= (|5, j\rangle + |6, j\rangle - |7, j\rangle - |8, j\rangle)/2, \\
|t_{2x}^A, j\rangle &= (|1, j\rangle + |2, j\rangle - |3, j\rangle - |4, j\rangle)/2, & |t_{2y}^B, j\rangle &= (|5, j\rangle - |6, j\rangle + |7, j\rangle - |8, j\rangle)/2, \\
|t_{2y}^A, j\rangle &= (|1, j\rangle - |2, j\rangle + |3, j\rangle - |4, j\rangle)/2, & |t_{2z}^B, j\rangle &= (|5, j\rangle - |6, j\rangle - |7, j\rangle + |8, j\rangle)/2, \\
|t_{2z}^A, j\rangle &= (|1, j\rangle - |2, j\rangle - |3, j\rangle + |4, j\rangle)/2, & & \\
|a_1^B, j\rangle &= (|5, j\rangle + |6, j\rangle + |7, j\rangle + |8, j\rangle)/2, & &
\end{aligned} \quad (22)$$

the first four of which reduce to ordinary s and p atomic orbitals on the A sites. The appropriate expansion is then

$$\begin{aligned}
\langle nk | \Sigma(E^+) | nk \rangle &= \sum_{\lambda} [\langle nk | \lambda^A, j \rangle |^2 \Sigma_{\lambda}^A(E^+) + \langle nk | \lambda^B \rangle |^2 \Sigma_{\lambda}^B(E^+) \\
&\quad + 2 \operatorname{Re}(\langle nk | \lambda^A, j \rangle \langle \lambda^B, j | nk \rangle) \Sigma_{\lambda}^{AB}(E^+)], \quad (23)
\end{aligned}$$

where $\lambda = a_1, t_{2x}, t_{2y}, t_{2z}$ and all three t_2 components of the self-energy are equal to the values given in Eq. (18). In the weak-scattering limit, the Σ_{λ} themselves can be expanded as

$$\begin{aligned}
\Sigma_{\lambda}^A(z) &\approx x(1-x)[\Delta_{\lambda}^2 f_{\lambda}^A(z) + 2\Delta_{\lambda}\Delta_2 f_{\lambda}^{AB}(z) + \Delta_2^2 f_{\lambda}^B(z)], \\
\Sigma_{\lambda}^{AB}(z) &\approx x(1-x)[\Delta_{\lambda}\Delta_2 f_{\lambda}^A(z) + \Delta_2^2 f_{\lambda}^{AB}(z)], \\
\Sigma_{\lambda}^B(z) &\approx x(1-x)[\Delta_2^2 f_{\lambda}^B(z)]. \quad (24)
\end{aligned}$$

Here $\Delta_{a_1} = \Delta_s$, $\Delta_{t_2} = \Delta_p$ and the $f_{\lambda}(z)$'s are components of the VCA Green's functions $\tilde{F}_{a_1}(z)$ and $\tilde{F}_{t_2}(z)$ obtained by setting $\Sigma_{\alpha\beta} = 0$ in Eqs. (12) and (13). These expressions again reduce to those of Ref. 4 in the case $\Delta_2 = 0$. Only the A site-diagonal components then contribute. If, furthermore, $|\Delta_s| \gg |\Delta_p|$, which is often satisfied in practice, Eq. (23) becomes simply

$$\langle nk | \Sigma(E^+) | nk \rangle \approx x(1-x)\Delta_s^2 | \langle nk | a_1^A, j \rangle |^2 f_{a_1}^A(E^+). \quad (25)$$

This expression and Eqs. (23) and (24) will be helpful in Secs. IV and V for comparing the MCPA and site-CPA results.

The calculations are performed numerically by an iterative procedure using the full MCPA expressions. The first step is to obtain the cell local Green's function $\tilde{F}(z)$ for $\Sigma = 0$. This is done by inverting the effective Hamiltonian in Eq. (12) and summing over the Brillouin zone. The resulting matrix is then transformed into the a_1 and t_2 basis and the self-energies $\tilde{\Sigma}_{\lambda}(z)$ are calculated using a modified version³⁰ of Eq. (15). The $\tilde{\Sigma}_{\lambda}(z)$ are then transformed back into the hybrid basis and a new $\tilde{H}_{\text{eff}}(\mathbf{k}, z)$ is found. The process is repeated until convergence.

The most time-consuming aspect of the calculations involves the Brillouin-zone integrations. These are more difficult here than in the site CPA because additional off-diagonal Green's-function matrix elements are required. The computational effort is reduced considerably by a recently developed technique based on analytic continuation.³¹ All calculations are first performed off the real axis where the integrand of Eq. (12) is slowly varying. When full convergence is reached, usually after three to

five iterations, quantities of physical interest are analytically continued back to the real axis. A sampling of 444 \mathbf{k} points in the Brillouin zone was found to be sufficient for most of the numerical integrations required in this paper. Still, the MCPA was found to require about 3 times as much computer time as an equivalent site CPA calculation.

III. LIMITING-CRYSTAL PARAMETRIZATIONS

The success of the MCPA approach depends in large part on the choice of tight-binding parameters for the limiting crystals. It is physically simpler to address this problem in the more familiar atomic-orbital basis using the standard Slater-Koster notation.¹² Parameters in the sp^3 -hybrid basis follow from the transformation in the Appendix.

As in Sec. II, we formally neglect spin-orbit splitting for computational convenience. The MCPA formalism is easily generalized to include this interaction but the resulting matrices are then doubled in size. The empirical nature of the MCPA implies that scalar relativistic effects are automatically included as long as parameters are obtained by fitting to experimental data or relativistic calculations. However, the magnitudes of the spin-orbit splittings themselves in $\text{In}_{1-x}\text{Ga}_x\text{As}$ and $\text{ZnSe}_x\text{Te}_{1-x}$ are actually quite large [from $E(\Gamma_8^0) - E(\Gamma_6^0) = 0.35$ eV in GaAs to 0.9 eV in ZnTe; cf. Table I]. Suitable corrections must thus be included in comparing with experiment (cf. Sec. V).

To reduce the arbitrariness associated with the large number of tight-binding parameters (23 for each crystal), we require that the parametrizations satisfy various physical criteria in addition to providing a reasonable fit to the limiting-crystal bands. This is particularly important for the alloy scattering parameters Δ_s , Δ_p , and Δ_2 . This problem was discussed extensively in Ref. 4 for the case of chemical disorder alone.

The specific physical constraints imposed on each $A'_{1-x}A''_x B$ system are the following.

(1) The difference in A' and A'' on-site parameters in the atomic basis should closely approximate the differences in corresponding atomic-energy levels.

(2) The B on-site energies should be the same in the

TABLE I. Comparison of energy eigenvalues (in eV) at Γ , X , and L in present tight-binding model with empirical pseudopotential method (EPM) results of Ref. 33 for InAs and GaAs and experimental results for ZnSe and ZnTe. Symmetry labels including spin-orbit interactions are given in parentheses.

	InAs		GaAs		ZnSe		ZnTe	
	Present work	EPM	Present work	EPM	Present work	Expt.	Present work	Expt.
$\Gamma_1^s (\Gamma_1^s)$	-12.42	-12.42	-13.16	-12.55	-15.39	-15.2 ^b	-12.62	-12.6 ^b
$\Gamma_2^s (\Gamma_2^s)$		-0.26		-0.35		-0.43 ^c		-0.50 ^c
$\Gamma_{15}^s (\Gamma_6^s)$	0.03	0.17 ^a	-0.10	0.00	-0.15	0.00 ^b	0.11	0.43 ^e
$\Gamma_1^s (\Gamma_6^s)$	0.56	0.54	1.46	1.51	2.89	2.9 ^d	2.82	3.0 ^f
$\Gamma_2^s (\Gamma_6^s)$		4.56		4.55				
$\Gamma_{15}^s (\Gamma_6^s)$	3.89	4.80	4.18	4.71	7.48		6.56	
$X_1^s (X_1^s)$	-9.98	-10.03	-10.05	-9.83	-12.83	-12.5 ^b	-10.87	-11.2 ^b
$X_2^s (X_1^s)$	-6.33	-6.47	-7.09	-6.88	-5.43	-5.6 ^b	-4.85	-5.1 ^b
$X_3^s (X_1^s)$		-2.30		-2.99				
$X_4^s (X_1^s)$	-2.13	-2.20	-3.40	-2.89	-1.99	-2.1 ^b	-1.53	-2.0 ^b
$X_1^s (X_2^s)$	2.22	2.45	2.17	2.03	4.37	4.3 ^d	3.41	3.3 ^f
$X_2^s (X_2^s)$	2.47	2.83	2.87	2.38	4.56	5.1 ^d	4.92	
X_3^s	7.25		7.80		8.20		8.52	
$L_1^s (L_1^s)$	-10.50	-10.60	-10.97	-10.60	-13.41	-13.1 ^b	-11.31	-11.6 ^b
$L_2^s (L_1^s)$	-5.93	-6.06	-7.30	-6.83	-5.45	-5.6 ^b	-4.99	-5.1 ^b
$L_3^s (L_1^s)$		-1.09		-1.42				
$L_4^s (L_1^s)$	-1.43	-0.83	-1.73	-1.20	-1.09	-1.3 ^b	-0.45	-0.7 ^b
$L_1^s (L_2^s)$	1.92	1.70	1.49	1.82	4.10	3.7 ^d	3.40	3.1 ^f
$L_2^s (L_2^s)$		5.59		5.47				
$L_3^s (L_2^s)$	4.99	5.72	5.89	5.52	6.79		6.69	
L_4^s	6.33		6.11		7.42		7.30	

^aReference 34.

^bReference 38(a).

^cReference 39(f).

^dReference 39(a).

^eReference 40.

^fReference 39(c).

$A'B$ and $A''B$ crystals (consistent with our neglect of redistribution disorder).

(3) The difference in $V_1^{A'B}$ and $V_1^{A''B}$ should be in reasonable agreement with the value obtained from Harrison's universal parametrization scheme.¹³

(4) Other nearest-neighbor hoppings in the hybrid basis and all second-neighbor parameters for each crystal should be small relative to $V_1^{A'B}$.

(5) The alignment of $A'B$ and $A''B$ crystal bands on a common energy scale should correspond to the "natural" valence-band offset, as far as it is known (± 0.2 eV).

Constraints (1)–(3) are the most crucial since they ensure that the MCPA scattering parameters are reasonably unique to within a few tenths of an eV. Constraint (4) ensures that the 14 second-neighbor parameters used to improve the crystalline bands do not become unphysically large or strongly influence the results. Constraint (5) provides a common energy zero. The MCPA results are not very sensitive to the valence-band offset as long as the other constraints are satisfied. This contrasts with treatments of alloy disorder in which the scattering potentials are determined directly from the band alignment.³²

The specific input data and resulting parameters for the $\text{In}_{1-x}\text{Ga}_x\text{As}$ and $\text{ZnSe}_x\text{Te}_{1-x}$ systems are discussed below. A successive approximation approach is employed

in the fitting. The parametrizations appear to be fairly unique although no attempt is made at optimization.

A. InAs and GaAs

Accurate empirical pseudopotential band structures for InAs and GaAs have been calculated by Chelikowsky and Cohen.³³ These provide valence energies in good agreement with photoemission experiments and optical gaps in agreement with reflectivity and electroreflectance measurements. Table I lists the eigenvalues from Ref. 33 for the symmetry points Γ , X , and L . Spin-orbit splittings were included in Ref. 33 so the notation is that of the zincblende double group. The zero of energy is chosen as the GaAs valence-band maximum $E(\Gamma_6^s)$. The Γ_6^s level in InAs is assumed to be 0.17 eV higher, in accordance with recent heterojunction measurements³⁴ (assuming interface dipole effects to be negligible).

Tight-binding parameters for these systems are chosen to provide reasonable fits to the valence and lowest conduction states at Γ , X , and L (with the spin-orbit splittings averaged as $\frac{1}{2}[2E(\Gamma_6^s) + E(\Gamma_2^s)]$), in addition to satisfying the above physical criteria. The resulting eigenvalues are listed in the "present work" columns of Table I. The agreement for all states of interest is typically

better than ± 0.3 eV. The largest discrepancy (-0.6 eV) occurs for the GaAs Γ_1^+ level which could not be raised appreciably without violating either constraint (2) or (3). This may indicate that the As on-site parameters should actually differ slightly in InAs and GaAs as in some previous parametrizations.³⁵ The tight-binding description is further limited by the fact that the lowest conduction band exhibits too little dispersion (not shown) and the placement of higher conduction states is incorrect.

The parameters for InAs and GaAs are listed in Table II. The chemical scattering parameters $\Delta_1 = 0.92$ eV and $\Delta_p = 0.12$ eV are close to the values 0.8 and 0.1 eV which result from differences between relativistic In and Ga atomic levels.³⁶ (The corresponding nonrelativistic values are 1.25 and 0.21 eV.) The structural scattering parameter $\Delta_2 = 0.50$ eV (obtained by transforming to the hybrid parameters $V_{\frac{1}{2}^{\text{InAs}}}$ and $V_{\frac{1}{2}^{\text{GaAs}}}$) is close to the value 0.66 eV obtained from Harrison's approach¹³ using the InAs and GaAs bond lengths in Table II. The second-neighbor parameters are small, as required by constraint (4).

B. ZnSe and ZnTe

Much more limited band-structure information is available for ZnSe and ZnTe. Few theoretical calculations exist³⁷ and experimental data^{38,39} are quite widely scattered. To obtain parameters which are consistently determined we fit the valence eigenvalues of both crystals at Γ , X , and L to the x-ray photoemission results of Ley *et al.*,^{38,39} corrected for the measured spin-orbit splittings.^{39(c)} The lowest conduction states are fit to values obtained by adding the relevant low-temperature optical gaps.^{39(a),(c)} The resulting data are summarized in Table I. The ZnSe valence-band maximum $E(\Gamma_8^+)$ is chosen as the zero of energy; the Γ_8^+ level in ZnTe is assumed to be 0.43 eV higher, as suggested by the empirical tabulation of Katnani and Margaritondo.⁴⁰

The tight-binding eigenvalues and parameters for ZnSe and ZnTe are again listed in Tables I and II. The Γ_{15}^+ levels lie at -0.15 and 0.11 eV, respectively, in agreement with the spin-orbit averaged experimental results. The

TABLE II. Limiting-crystal bond lengths (d) and Slater-Koster parameters in eV used in present work and resulting MCPA scattering parameters Δ_1 , Δ_p , and Δ_2 for $\text{In}_{1-x}\text{Ga}_x\text{As}$ and $\text{ZnSe}_{1-x}\text{Te}_x$.

Parameter	InAs $d=2.61$ Å	GaAs $d=2.45$ Å	ZnSe $d=2.45$ Å	ZnTe $d=2.64$ Å
$E_{\pi}(000)_{ss}$	-8.53	-8.53	-11.50	-9.90
$E_{\pi}(000)_{cc}$	-3.21	-4.13	-1.00	-1.00
$E_{xx}(000)_{ss}$	0.87	0.87	0.93	1.33
$E_{xx}(000)_{cc}$	2.69	2.57	4.80	4.80
$E_{\pi}(\frac{1}{2}\frac{1}{2}\frac{1}{2})_{ss}$	-1.46	-1.70	-1.87	-1.47
$E_{xx}(\frac{1}{2}\frac{1}{2}\frac{1}{2})_{ss}$	1.01	1.01	1.15	0.90
$E_{xx}(\frac{1}{2}\frac{1}{2}\frac{1}{2})_{cc}$	1.05	1.10	1.24	1.17
$E_{xx}(\frac{1}{2}\frac{1}{2}\frac{1}{2})_{sc}$	0.39	0.49	0.77	0.65
$E_{xy}(\frac{1}{2}\frac{1}{2}\frac{1}{2})_{sc}$	1.15	1.37	1.17	1.12
$E_{\pi}(110)_{ss}$	-0.02	0.00	0.00	0.00
$E_{\pi}(110)_{cc}$	0.01	0.08	0.00	0.09
$E_{xx}(110)_{ss}$	0.00	0.00	0.00	0.00
$E_{xx}(110)_{cc}$	0.00	0.00	0.00	0.00
$E_{xx}(011)_{ss}$	-0.04	-0.10	0.08	0.00
$E_{xx}(011)_{cc}$	0.09	0.12	-0.12	-0.10
$E_{xx}(110)_{sc}$	0.09	0.06	0.08	0.00
$E_{xx}(110)_{cc}$	0.15	0.14	0.18	0.18
$E_{xx}(011)_{ss}$	-0.10	-0.04	-0.04	0.03
$E_{xx}(011)_{cc}$	-0.20	-0.20	-0.08	-0.24
$E_{xy}(110)_{ss}$	0.00	0.10	0.12	0.13
$E_{xy}(110)_{cc}$	0.00	0.08	0.03	0.05
$E_{xy}(011)_{ss}$	0.10	0.10	0.00	-0.10
$E_{xy}(011)_{cc}$	0.10	0.10	0.10	0.00
Δ_1	0.92		1.60	
Δ_p	0.12		0.40	
Δ_2	0.50		0.51	

quality of the fits elsewhere is comparable to that achieved in InAs. The chemical scattering parameters $\Delta_s = 1.60$ eV and $\Delta_p = 0.40$ eV are close to the values 2.0 and 0.5 eV obtained from relativistic atomic-level differences³⁶ (3.2 and 0.9 eV nonrelativistically). The structural parameter $\Delta_r = 0.51$ eV is comparable to the value 0.57 eV obtained from Harrison's universal scheme¹³ and the difference in ZnSe and ZnTe bond lengths.

IV. EFFECTS OF CHEMICAL AND STRUCTURAL DISORDER IN THE MCPA

The $x=0.5$ concentrations are chosen for this discussion, because disorder effects are maximized in these alloys. Emphasis is placed on the damping associated with $\sigma_n''(\mathbf{k}, E^+)$, which results from scattering on the energy shell. By contrast, disorder-induced energy shifts (discussed in Sec. VB) associated with $\sigma_n'(\mathbf{k}, E^+)$ are determined by scattering over a much wider energy range.

Figure 3 shows MCPA spectral densities for $\text{In}_{0.5}\text{Ga}_{0.5}\text{As}$ for several \mathbf{k} points along the $\langle 100 \rangle$ and $\langle 111 \rangle$ directions. The normalization $A(\mathbf{k}, E)/[A(\mathbf{k}, E) + 5 \text{ eV}^{-1} \text{ cell}^{-1} \text{ spin}^{-1}]$ is used to facilitate graphing; peak widths are thus slightly exaggerated. The VCA bands resulting from \bar{H} are also plotted for comparison. The fact that the MCPA results do not differ appreciably indicates that disorder effects in this system are relatively weak. The behavior is qualitatively different, however, in different energy regions. The strongest scattering is evident 5–7 eV below the valence-band maximum where the MCPA spectral densities are relatively broad and non-Lorentzian. Elsewhere in the valence band the

scattering is somewhat weaker, as evidenced by the more nearly Lorentzian behavior. The extremely sharp spectral densities in the conduction band indicated a virtual absence of disorder effects for states at these energies.

Figure 4 compares the $\text{In}_{1-x}\text{Ga}_x\text{As}$ density of states $g(E) = \sum_{\mathbf{k}} A(\mathbf{k}, E)$ calculated in the (a) VCA, (b) site CPA, and (c) MCPA. The differences between the VCA and site CPA result indicate that chemical disorder acting alone preferentially damps only states in the lowest conduction-band region and near -6 eV in the valence band. Similar behavior was found in previous site CPA calculations⁴ for $\text{Hg}_{1-x}\text{Cd}_x\text{Te}$. In both systems $|\Delta_r| \gg |\Delta_p|$ and only states with a large amplitude on cation s orbitals are strongly affected by the chemical disorder. The imaginary part of the VCA Green's-function matrix element,

$$\text{Im} f_{a_i}^j(E^+) = -N^{-1} \pi \sum_{\mathbf{k}} |\langle n\mathbf{k} | a_i^j | j \rangle|^2 \delta(E - E_n(\mathbf{k})), \quad (26)$$

plotted in Fig. 5(a), projects the total VCA density of states on cation s orbitals. The cation s component is clearly seen to be largest in Fig. 5(a) near -6 and +2 eV. The presence of strong chemical disorder effects in these regions follows from the weak-scattering expression Eq. (25).

Relative to the site CPA results, the MCPA density of states in Fig. 4(c) shows increased broadening throughout the upper valence bands. The peak near -6 eV, in fact, nearly splits in two. With increasing Ga concentration x , the lower peak in this region increases in height and the

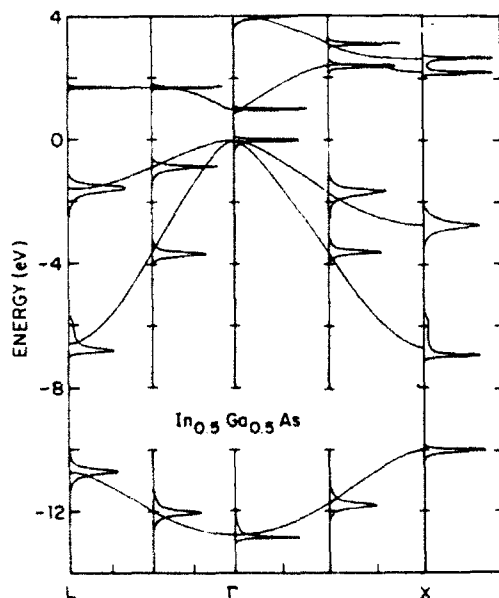


FIG. 3. Normalized MCPA spectral densities $(A(\mathbf{k}, E)/[A(\mathbf{k}, E) + 5 \text{ eV}^{-1} \text{ cell}^{-1} \text{ spin}^{-1}])$ for $\text{In}_{0.5}\text{Ga}_{0.5}\text{As}$ as a function of energy E for various \mathbf{k} points. VCA bands plotted as solid curves.

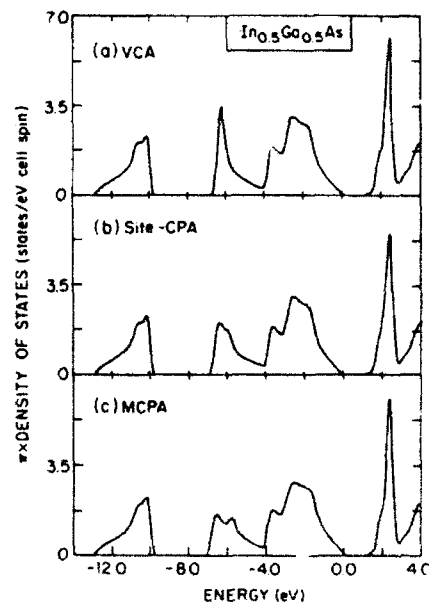


FIG. 4. Comparison of $\text{In}_{0.5}\text{Ga}_{0.5}\text{As}$ densities of states calculated in the (a) VCA, (b) site CPA (chemical disorder only), and (c) MCPA (both chemical and structural disorder).

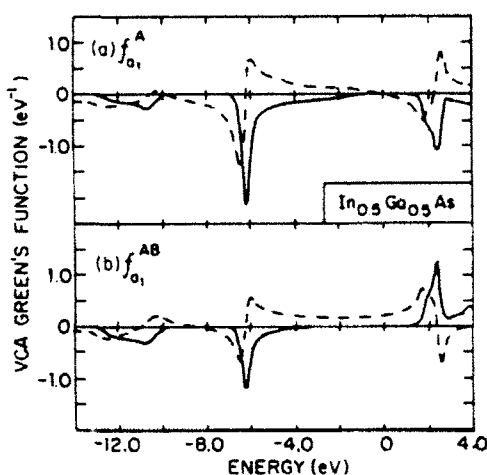


FIG. 5. Real (dashed) and imaginary (solid) parts of the VCA Green's-function matrix elements (a) f_{a1}^A and (b) f_{a1}^{AB} for $\text{In}_{0.5}\text{Ga}_{0.5}\text{As}$.

upper peak decreases. A similar strong scattering feature has recently been observed experimentally⁴¹ in the $\text{Hg}_{1-x}\text{Cd}_x\text{Te}$ system. There, however, the effect is purely a chemical one.⁴ Here the splitting only becomes appreciable due to the additional effects of structural disorder. Whether it is large enough to be resolved experimentally is unclear. Detailed photoemission studies on $\text{In}_{1-x}\text{Ga}_x\text{As}$ samples with varying x values would be useful.⁴²

A surprising feature of the MCPA conduction-band state density in Fig. 4(c) is that the broadening actually decreases and the peak height increases relative to the site CPA results. The absence of appreciable damping in the conduction-band spectral densities in Fig. 3 may be attributed to a destructive interference between chemically and structurally induced scattering. This effect was explained physically in Ref. 11 using the schematic energy-level diagram in Fig. 6. The mean energy for bonding and anti-

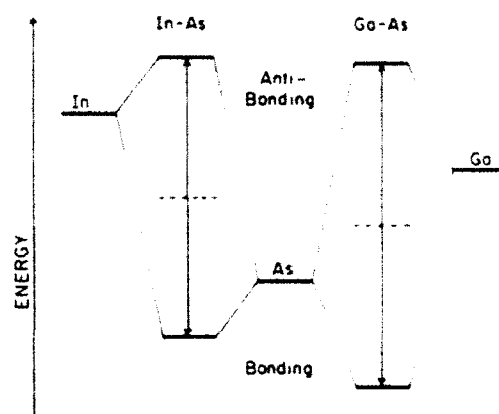


FIG. 6. Schematic representation of energy levels for single In—As and Ga—As bonds as derived from constituent atomic sp^3 hybrid energies (average values denoted by dashed line), and hybridization splittings (denoted by arrows).

bonding levels (dashed line) is lower for a Ga—As bond than an In—As bond because of the deeper Ga atomic levels (chemical disorder). The shorter Ga—As bond length, however, results in a larger $|V_{ij}^{AB}|$ value and, hence, a larger hybridization splitting. The two effects add to give an increased separation between In—As and Ga—As bonding levels, but essentially cancel for anti-bonding levels. The correlation between chemical and structural disorder thus results in stronger valence-band and weaker conduction-band scattering in the alloy than would occur if either type of disorder acted alone.

Formal insight can be obtained by examining the MCPA weak-scattering expressions. The analytic properties of the MCPA imply that the total imaginary part of $\langle n\mathbf{k} | \Sigma(E^+) | n\mathbf{k} \rangle$ is negative definite. Several of the terms appearing in the expansion of Eqs. (23) and (24), however, can be of either sign. The net imaginary part is given in the weak-scattering limit by

$$\sigma_n''(\mathbf{k}, E^+) \approx 2x(1-x) \sum_{\lambda} \Delta_{\lambda} \Delta_2 [|\langle n\mathbf{k} | \lambda^A, j \rangle|^2 \text{Im} f_{\lambda}^{AB}(E^+) + \text{Re}(\langle n\mathbf{k} | \lambda^A, j \rangle \langle \lambda^B, j | n\mathbf{k} \rangle) \text{Im} f_{\lambda}^A(E^+)] + \dots, \quad (27)$$

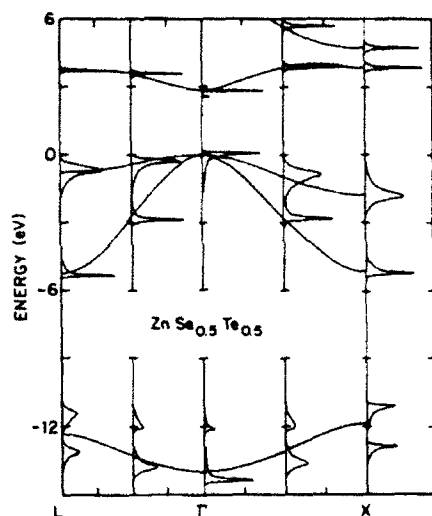
where the ellipsis represents additional negative definite terms. Since $f_{\lambda}^A(E^+)$ is a diagonal Green's-function matrix element, $\text{Im} f_{\lambda}^A(E^+)$ is negative definite. The imaginary part of the off-diagonal element $f_{\lambda}^{AB}(E^+)$, is a type of bond order,⁴³ given explicitly in the VCA by

$$\text{Im} f_{\lambda}^{AB}(E^+) = -\pi N^{-1} \sum_{n, \mathbf{k}} \text{Re}(\langle \lambda^A, j | n\mathbf{k} \rangle \langle n\mathbf{k} | \lambda^B, j \rangle) \times \delta(E - E_n(\mathbf{k})). \quad (28)$$

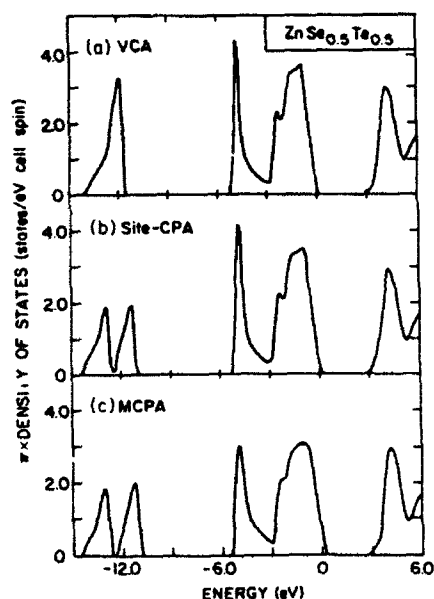
This quantity is also negative in the valence band, but positive in the conduction band, as seen in the example in Fig. 5(b). The sign change results from the fact that $\text{Re}(\langle \lambda^A, j | n\mathbf{k} \rangle \langle n\mathbf{k} | \lambda^B, j \rangle)$, which appears in both Eqs.

(27) and (28) is positive for states with bonding character and negative for states with antibonding character.⁴⁴ Since the terms in parentheses in Eq. (27) are generally of the same sign, the nature of the interference between chemically and structurally induced scattering (constructive or destructive) for a given state is determined by the signs of the products $\Delta_1 \Delta_2$ and $\Delta_p \Delta_2$. The qualitative picture developed in Fig. 6, in particular, depends on the fact that Δ_1 , Δ_p and Δ_2 in $\text{In}_{1-x}\text{Ga}_x\text{As}$ all have the same sign.

Figure 7 shows the normalized MCPA spectral densities and the corresponding VCA bands for the anion-substituted II-VI system $\text{ZnSe}_{1-x}\text{Te}_x$. The VCA, site CPA and MCPA densities of states are compared in Fig. 8. A striking feature of the MCPA results is the split-

FIG. 7. Same as Fig. 3 but for $\text{ZnSe}_{0.5}\text{Te}_{0.5}$.

band behavior observed in the lowest valence region in both the density of states and the spectral densities. This strong-scattering effect should be easily observable in photoemission experiments. With increasing Te concentration the upper ZnTe-like peak should grow and the lower ZnSe peak diminish. The fact that the splitting already appears in the site CPA results indicates that it is primarily chemically induced; the addition of structural disorder enhances the effect slightly. In other energy regions, the site CPA results are virtually indistinguishable from those of the VCA. The addition of structural disorder results in

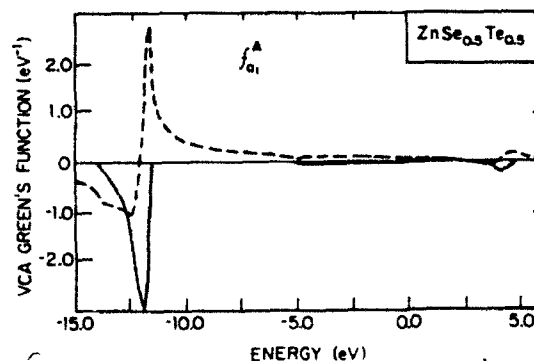
FIG. 8. Same as Fig. 4 but for $\text{ZnSe}_{0.5}\text{Te}_{0.5}$.

a weak Lorentzian broadening of states in the upper valence bands, but produces no appreciable damping of states in the conduction band.

Compared to $\text{In}_{1-x}\text{Ga}_x\text{As}$, the effects of chemical disorder in $\text{ZnSe}_x\text{Te}_{1-x}$ occur in a different energy region and are much more pronounced. In an anion-substituted alloy like $\text{ZnSe}_x\text{Te}_{1-x}$ the states which are affected most by chemical disorder are those with a large amplitude on anion s orbitals. That such states occur primarily in the lowest valence-band region in zinc-blende compounds can be seen from the imaginary part of the VCA Green's-function matrix element $f_{a1}^A(E^+)$ shown in Fig. 9. By contrast, the cation s projection for the cation-substituted alloy $\text{In}_{1-x}\text{Ga}_x\text{As}$ shown in Fig. 5(a) is not only peaked in a different region but is also more widely dispersed over a broad energy range. The concentration of $\text{Im}f_{a1}^A$ in a narrow energy range in $\text{ZnSe}_x\text{Te}_{1-x}$ is a consequence of the more polar, and less covalent, character of II-VI compared to III-V compounds. The combination of this feature with the larger chemical scattering parameter Δ_s accounts for the more pronounced effects of chemical disorder in $\text{ZnSe}_x\text{Te}_{1-x}$.

The additional effects of structural disorder are qualitatively similar in the two systems. The increased valence-band broadening in $\text{ZnSe}_x\text{Te}_{1-x}$ again results from the fact that Δ_s , Δ_p , and Δ_2 all have the same sign. A cancellation of conduction-band disorder effects also occurs in $\text{ZnSe}_x\text{Te}_{1-x}$ but is not apparent in Fig. 8 because neither chemically- nor structurally-induced scattering is appreciable in this region.

In summary, the damping of VCA eigenstates in different energy regions of zinc-blende pseudobinary alloys is determined qualitatively by the nature of the disordered sublattice (anion or cation) and the relative signs of Δ_s , Δ_p , and Δ_2 , and quantitatively by the magnitudes of the scattering parameters and the degree of polarity in the system. An examination of Harrison-derived scattering parameters¹³ for all possible III-V and II-VI pseudobinary alloys indicates that the relationships $|\Delta_s| \gg |\Delta_p|$ and $\Delta_s\Delta_2 > 0$ observed in both systems considered here are generally obeyed. Damping effects will thus usually be

FIG. 9. Real (dashed) and imaginary (solid) part of the VCA Green's-function matrix element f_{a1}^A for $\text{ZnSe}_{0.5}\text{Te}_{0.5}$. (Note that the A here denotes anion, unlike the case in Fig. 5.)

strongest in the valence band, particularly for states with large amplitude on the s orbitals of the disordered sublattice. The few exceptions are alloys of the form $\text{Hg}_{1-x}\text{Zn}_x\text{X}$ ($\text{X}=\text{S}, \text{Se}, \text{Te}$) and $\text{Al}_{1-x}\text{In}_x\text{Y}$ ($\text{Y}=\text{P}, \text{As}, \text{Sb}$). In these systems, $\Delta_1, \Delta_2 < 0$ and conduction-band damping should be more pronounced.

V. IMPLICATIONS FOR BAND-EDGE PROPERTIES

A. Limiting mobilities due to alloy scattering

Damping effects are particularly important near the band edges in semiconducting alloys because they impose fundamental limits on achievable electron and hole mobilities. For most direct-gap zinc-blende pseudobinary alloys, it is sufficient under low-field conditions to consider the weak-scattering or perturbation-theory limit,⁴⁵ rather than a full-MCPA two-particle Green's-function formalism analogous to that of Ref. 46. The solution of the transport equations then reduces to that of the Boltzmann equation with a current relaxation time given by

$$\tau^{-1}(E) = -(2/\hbar)\sigma''_n(\mathbf{k}, E^+).$$

Here $|n\mathbf{k}\rangle \approx |\Gamma_1^{\pm}\rangle$ for electrons (e) and $|n\mathbf{k}\rangle \approx |\Gamma_{15}^{\pm}\rangle$ for holes (h). The golden-rule expression

$$\tau_{e,h}^{-1}(E) \approx \frac{2\pi}{\hbar} x(1-x)(\Delta_{\text{eff}}^{e,h})^2 g(E) \quad (29)$$

follows by expanding the Green's-function matrix elements [e.g., Eqs. (26) and (28)] in Eqs. (23) and (24) near $\mathbf{k}=0$. The effective scattering parameters

$$\Delta_{\text{eff}}^e = \left[\frac{1+\alpha_s}{2} \right] \Delta_s - (1-\alpha_s^2)^{1/2} \Delta_2 \quad (30)$$

and

$$\Delta_{\text{eff}}^h = \left[\frac{1-\alpha_p}{2} \right] \Delta_p + (1-\alpha_p^2)^{1/2} \Delta_2 \quad (31)$$

are obtained by diagonalizing the VCA Hamiltonian at $\mathbf{k}=0$ to determine the coefficients $\langle n\mathbf{k} | \lambda^A, j \rangle$ and $\langle n\mathbf{k} | \lambda^B, j \rangle$. The "polarities" α_s and α_p are defined as

$$\alpha_\gamma = \frac{\epsilon_\gamma^A - \epsilon_\gamma^B}{[(\epsilon_\gamma^A - \epsilon_\gamma^B)^2 + 4V_\gamma^2]^{1/2}}, \quad \gamma = s, p, \quad (32)$$

with

$$\begin{aligned} \epsilon_\gamma^A &= \bar{E}_{ss}(000)_{vv} + 12\bar{E}_{ss}(110)_{vv}, \quad v = A, B \\ \epsilon_\gamma^B &= \bar{E}_{xx}(000)_{vv} + 8\bar{E}_{xx}(110)_{vv} + 4\bar{E}_{xx}(011)_{vv}, \quad v = A, B, \end{aligned} \quad (33)$$

$$V_s = 4\bar{E}_{ss}(\frac{1}{2}\frac{1}{2}\frac{1}{2})_{AB},$$

$$V_p = 4\bar{E}_{xx}(\frac{1}{2}\frac{1}{2}\frac{1}{2})_{AB}.$$

Note that $\alpha_\gamma > 0$ for cation-substituted alloys (A the cation), $\alpha_\gamma < 0$ for anion-substituted alloys (A the anion) and $0 \leq |\alpha_\gamma| \leq 1$. The quantities defined in Eqs. (30)–(32) are all weakly dependent on x through the VCA averages in Eq. (33).

The familiar Brooks formula⁴⁷ for the alloy scattering mobility at temperature T ,

$$\mu_{\text{alloy}}^{e,h} = \frac{\sqrt{2\pi e \hbar^4 N_0}}{3(m_{e,h}^*)^{5/2} x(1-x)(\Delta_{\text{eff}}^{e,h})^2 \sqrt{k_B T}} \quad (34)$$

follows from Eq. (29) by assuming nondegenerate statistics and parabolic band edges. Here k_B is Boltzmann's constant, N_0 is the number of atoms per unit volume, and m_e^* and m_h^* are the electron and hole effective masses, respectively. Most previous discussions⁴⁷ of Eq. (34) have been obscured by confusion concerning the appropriate choice of Δ_{eff}^e and Δ_{eff}^h . We emphasize that the MCPA provides a unique and consistent definition of these quantities in Eqs. (30) and (31) in terms of the previously defined tight-binding parameters.

A few general conclusions follow immediately. First, a clear difference exists between the effective scattering parameters for electrons and holes. Second, these quantities are not simply related to differences in limiting crystal band gaps or electron affinities. Third, the magnitudes of Δ_{eff}^e and Δ_{eff}^h depend sensitively on all of the factors discussed in Sec. IV which determine the interplay between chemical and structural disorder for particular eigenstates. The physical differences between Δ_{eff}^e and Δ_{eff}^h critically depend on the fact that $|\Gamma_1^{\pm}\rangle$ is an antibonding s state with a larger cation component and $|\Gamma_{15}^{\pm}\rangle$ is a bonding p state with a large anion component.

Table III lists the MCPA band-edge scattering parameters for the present $\text{In}_{1-x}\text{Ga}_x\text{As}$ and $\text{ZnSe}_x\text{Te}_{1-x}$ parametrizations for $x=0.5$ together with the corresponding site CPA results and values of α_s and α_p . The entries in Table III are relatively insensitive to x . In both materials the addition of structural disorder in the MCPA decreases the magnitude of Δ_{eff}^e by about a factor of 3 (an increase of a factor of 9 in μ_{alloy}^e) and increases the magnitude of Δ_{eff}^h by more than a factor of 5. These results are consistent with the conduction- and valence-band behavior discussed in Sec. IV.

Experimental values of $\mu_{\text{alloy}}^{e,h}$, in principle, can be extracted from detailed transport studies.⁴⁸ In practice, this is usually quite difficult because of uncertainties in the contributions of other scattering mechanisms (e.g., electron-phonon interactions), which usually dominate, even in good samples. Even the $T^{-1/2}$ dependence in Eq. (34), which is often used as a signature of alloy scattering,

TABLE III. Polarities α_s and α_p [cf. Eq. (32)] and effective electron and hole scattering parameters [Δ_{eff}^e and Δ_{eff}^h , respectively—cf. Eqs. (30) and (31)] for $\text{In}_{1-x}\text{Ga}_x\text{As}$ and $\text{ZnSe}_x\text{Te}_{1-x}$.

	$\text{In}_{0.5}\text{Ga}_{0.5}\text{As}$	$\text{ZnSe}_{0.5}\text{Te}_{0.5}$
α_s	0.4	-0.6
Δ_{eff}^e (site CPA)	0.64 eV	0.31 eV
Δ_{eff}^e (MCPA)	0.19 eV	-0.09 eV
α_p	0.5	-0.6
Δ_{eff}^h (site CPA)	0.03 eV	0.10 eV
Δ_{eff}^h (MCPA)	0.46 eV	0.51 eV

is not completely reliable since similar behavior can also result from space-charge or neutral-impurity scattering.⁴⁹

In general the MCPA is expected to overestimate $\mu_{\text{alloy}}^{\text{ch}}$ because of its inclusion of only short-range contributions to the alloy scattering potential. Previous calculations have demonstrated that states at $k=0$ are particularly sensitive to clustering effects⁵⁰ (both statistical and nonstatistical). Intercell disorder contributions such as bond-angle fluctuations and longer-ranged strain fields also tend to increase scattering and lead to a reduction in $\mu_{\text{alloy}}^{\text{ch}}$.

In the two alloy systems considered here, only the electron mobility in $\text{In}_{1-x}\text{Ga}_x\text{As}$ has been extensively analyzed.⁵¹ The experimental results are most consistent with a value of $|\Delta_{\text{eff}}^{\text{ch}}|$ in the range 0.5–1.0 eV. The MCPA value of 0.19 eV in Table III thus leads to an overestimate of $\mu_{\text{alloy}}^{\text{ch}}$ by about an order of magnitude.⁵² While this result is consistent with the above arguments, much of the present discrepancy may simply be due to subtraction errors in Eq. (30) due to uncertainties in Δ_1 and Δ_2 . One can also not rule out at this point the possible presence of uncharacterized defects which has frequently turned out to be the cause of theoretical overestimates of mobility in other systems.

B. Band-gap bowing

The "bowing," or nonlinear concentration dependence of band gaps in zinc-blende pseudobinary alloys is technologically important and frequently misinterpreted. Much of the confusion stems from the conventional separation^{2(a)} of bowing into an intrinsic VCA contribution plus an extrinsic disorder-induced contribution. In the context of a comprehensive alloy theory such as the MCPA, which contains both ingredients, this separation often provides useful physical insight. It is important to keep in mind, however, that (1) only the net bowing is physically observable, (2) VCA nonlinearities are highly model specific, and (3) the magnitude of the extrinsic bowing alone is a poor indicator of the importance of disorder effects for other physical properties.

The extrinsic bowing of a gap in the MCPA is determined by the real parts of $\langle nk | \Sigma(E_F^+(k)) | nk \rangle$ for the

individual VCA valence- and conduction-band states involved. The real part of Σ [cf. Eq. (21)] is given by a Hilbert transform of $\sigma_n''(k, E)$ which can be written in the form

$$\sigma_n'(k, E) = \pi^{-1} \int_{-\infty}^{E_F} \frac{\sigma_n''(k, \eta) d\eta}{E - \eta} + \pi^{-1} \int_{E_F}^{\infty} \frac{\sigma_n''(k, \eta) d\eta}{E - \eta}, \quad (35)$$

where E_F is the Fermi level. This separation into valence- and conduction-band contributions provides a rigorous basis for distinguishing between intraband and interband disorder-induced shifts²⁵ of VCA eigenstates within the MCPA.

We focus here on the bowing of the fundamental gaps in $\text{In}_{1-x}\text{Ga}_x\text{As}$ and $\text{ZnSe}_{1-x}\text{Te}_x$. In both systems this gap is direct (at $k=0$) for all concentrations and depends parabolically on x .^{53,54} Calculated results in the present work for both the individual Γ_{15}^{v} and Γ_{15}^{c} band-edge states and the spin-orbit-averaged Γ_{15}^{v} - Γ_{15}^{c} gaps are summarized in Table IV. The linear contributions listed in the top row are obtained by straightforward interpolations between limiting-crystal values. The remaining entries represent deviations from linearity at $x=0.5$. These deviations are a factor of 4 smaller than the so-called "bowing parameters" b , defined so that the net deviations from linearity are of the form $-bx(1-x)$. The intrinsic VCA nonlinearities which occur in both materials result primarily from the scaling in Eq. (6) and the $\sim 7\%$ variation in alloy lattice constants.⁵⁵

In $\text{In}_{0.5}\text{Ga}_{0.5}\text{As}$ the addition of chemical disorder (site CPA) has no effect on the anion p -like Γ_{15}^{v} state but produces a -20 meV extrinsic shift of the cation s -like Γ_{15}^{c} level. This shift is largely an intraband repulsion induced by the appreciable cation s scattering of conduction states in the site CPA. The addition of structural disorder (MCPA) shifts both the valence- and conduction-band edges up relative to the site CPA results by $+20$ meV and $+33$ meV, respectively. The former is an intraband effect caused by the increased valence-band scattering discussed in Sec. IV. The latter is due in part to a reduced intraband repulsion resulting from the decreased

TABLE IV. Linear interpolation formulae for x dependences of band edges and fundamental gaps in $\text{In}_{1-x}\text{Ga}_x\text{As}$ and $\text{ZnSe}_{1-x}\text{Te}_x$ compared to deviations from linearity at $x=0.5$ obtained in various theoretical approaches and experiment. All entries are in meV.

	$\text{In}_{1-x}\text{Ga}_x\text{As}$			$\text{ZnSe}_{1-x}\text{Te}_x$		
	Γ_{15}^{v}	Γ_{15}^{c}	E_{gap}	Γ_{15}^{v}	Γ_{15}^{c}	E_{gap}
Linear interpolation	$30 - 130x$	$560 + 900x$	$530 + 1030x$	$-150 + 260x$	$2890 - 70x$	$3040 - 330x$
Deviation from linearity ($x=0.5$)						
VCA	+12	-47	-59	-15	-5	+10
Site CPA	+12	-67	-79	0	-5	-5
MCPA	+32	-34	-66	+85	-5	-90
Supercell	+26	-34	-60	+43	-6	-49
Expt. ^a			$-123^b, -133^c$			-270^d

^aSpin-orbit averaged.

^bReference 53(a).

^cReference 53(b).

^dReference 54.

conduction-band scattering. The interplay between chemical and structural disorder also produces a strong interband repulsion of Γ_1^c which results in a *smaller net deviation from linearity in the MCPA than in the VCA*. This unusual behavior can be traced to the corresponding real parts of the two terms given explicitly in Eq. (27). Both real parts contribute positive shifts because of the same sign of Δ_1 and Δ_2 and the antibonding character of the Γ_1^c conduction-band edge. [Note, for example, that $\text{Re} f_{a1}^{AB}(E^+) > 0$ for $E > 0$.]

The behavior in $\text{ZnSe}_{0.5}\text{Te}_{0.5}$ differs quantitatively because of the anion substitution and larger value of Δ_p . In this system the Γ_1^c state is more strongly affected by the disorder while the Γ_1^v state experiences no disorder-induced shifts. The extrinsic shifts of Γ_1^c are +15 meV in the site CPA and +100 meV in the MCPA. The net extrinsic contribution to the MCPA gap, -100 meV, is much larger than the corresponding -7 meV in $\text{In}_{0.5}\text{Ga}_{0.5}\text{As}$.

In both materials the MCPA underestimates the bowing of the spin-orbit averaged experimental gaps^{53,54} by more than 50%. This is somewhat misleading since in absolute terms the experimental nonlinearities are extremely small (<0.3 eV). The same factors proposed at the end of Sec. V A as possible causes of the mobility overestimates in the MCPA (uncertainties in MCPA scattering parameters, intercell disorder effects, clustering⁵⁶) would also tend to increase the magnitude of the bowing beyond the MCPA prediction. The above analysis serves to emphasize, however, the intimate connection between extrinsic band-edge shifts and the effects of chemical and structural disorder elsewhere in the bands.

VI. COMPARISON WITH ALTERNATIVE ALLOY THEORIES

The present formulation of the MCPA is believed to be the most complete effective medium theory yet developed for zinc-blende pseudobinary alloys. The relationship of this approach to some alternative treatments of these materials is therefore of interest.

A. Bond-centered CPA

The first alternative, which we will refer to as the bond-centered CPA, is suggested by the simple molecular level diagram in Fig. 6. This scheme considers only diagonal disorder in a basis of bonding and antibonding orbitals. A similar approximation has been made in many previous effective medium calculations for zinc-blende pseudobinary alloys.^{3(a),21} It will be argued that while this approach includes structural disorder in the same manner as the MCPA, its treatment of chemical disorder will usually be inadequate for detailed applications.

We begin with a unitary transformation from the sp^3 hybrid orbital basis to a basis of bonding and antibonding orbitals

$$|\alpha, R_j\rangle_+ = \gamma_+ |\alpha, R_j\rangle + \gamma_- |\alpha + 4, R_j\rangle$$

and

$$|\alpha, R_j\rangle_- = \gamma_- |\alpha, R_j\rangle - \gamma_+ |\alpha + 4, R_j\rangle,$$

respectively ($\alpha=1-4$). We choose the coefficients $\gamma_+ = (1 + \alpha_h/2)^{1/2}$ and $\gamma_- = (1 - \alpha_h/2)^{1/2}$ to depend on the weakly x -dependent polarity

$$\alpha_h = \frac{\bar{\epsilon}_0^A - \bar{\epsilon}_0^B}{[(\bar{\epsilon}_0^A - \bar{\epsilon}_0^B)^2 + 4(V_1^A)^2]^{1/2}}. \quad (36)$$

Within this basis the MCPA scattering matrix becomes

$$\bar{\Delta}_{\text{bond}} = \begin{pmatrix} \Delta_b & \delta_b & \delta_b & \delta_b & \Delta_{ba} & \delta_{ba} & \delta_{ba} & \delta_{ba} \\ \delta_b & \Delta_b & \delta_b & \delta_b & \delta_{ba} & \Delta_{ba} & \delta_{ba} & \delta_{ba} \\ \delta_b & \delta_b & \Delta_b & \delta_b & \delta_{ba} & \delta_{ba} & \Delta_{ba} & \delta_{ba} \\ \delta_b & \delta_b & \delta_b & \Delta_b & \delta_{ba} & \delta_{ba} & \delta_{ba} & \Delta_{ba} \\ \Delta_{ba} & \delta_{ba} & \delta_{ba} & \delta_{ba} & \Delta_a & \delta_a & \delta_a & \delta_a \\ \delta_{ba} & \Delta_{ba} & \delta_{ba} & \delta_{ba} & \delta_a & \Delta_a & \delta_a & \delta_a \\ \delta_{ba} & \delta_{ba} & \Delta_{ba} & \delta_{ba} & \delta_a & \delta_a & \Delta_a & \delta_a \\ \delta_{ba} & \delta_{ba} & \delta_{ba} & \Delta_{ba} & \delta_a & \delta_a & \delta_a & \Delta_a \end{pmatrix}, \quad (37)$$

with

$$\begin{aligned} \Delta_b &= \gamma_+^2 \Delta_0 + 2\gamma_+ \gamma_- \Delta_2, & \delta_b &= \gamma_+^2 \Delta_1, \\ \Delta_{ba} &= \gamma_+ \gamma_- \Delta_0 + (\gamma_-^2 - \gamma_+^2) \Delta_2, & \delta_{ba} &= \gamma_+ \gamma_- \Delta_1, \\ \Delta_a &= \gamma_-^2 \Delta_0 - 2\gamma_+ \gamma_- \Delta_2, & \delta_a &= \gamma_-^2 \Delta_1. \end{aligned} \quad (38)$$

The transformed cell diagonal Green's function and MCPA self-energy matrices have structures identical to Eq. (37).

Two simplifying assumptions are then imposed. First, the disorder associated with each bond (value of α) is decoupled by setting $\delta_b = \delta_{ba} = \delta_a = 0$. This is equivalent to neglecting Δ_1 in Eq. (8). Second, the self-energy is restricted to having nonzero components only within the 2×2 blocks associated with each bond. This assumes that the Green's-function matrix elements between orbitals associated with different bonds are small compared to bond-diagonal elements. Numerical calculations confirm that this is usually the case. The self-consistency condition within the bond-centered CPA [analogous to Eq. (11)] thus reduces to four equivalent 2×2 matrix equations for the self-energy corrections associated with each pair of bonding and antibonding orbitals.⁵⁷

The approach is attractive in that it is computationally simpler than the MCPA and, unlike the MCPA, can be applied directly to group-IV alloys (e.g., $\text{Si}_x\text{Ge}_{1-x}$) and two-sublattice quaternary alloys^{21(b)} (e.g., $\text{In}_{1-x}\text{Ga}_x\text{As}_y\text{Pb}_{1-y}$). Its inadequacies are illustrated by comparing the MCPA and bond-centered CPA densities of states in parts (a) and (b) of Figs. 10 and 11. In both $\text{In}_{0.5}\text{Ga}_{0.5}\text{As}$ and $\text{ZnSe}_{0.5}\text{Te}_{0.5}$ the bond-centered CPA greatly underestimates the effects of disorder in strong scattering regions. This failure can be traced directly to the neglect of Δ_1 . Stated differently, the bond-centered CPA neglects the strong correlations in the disorder associated with the four bonds emanating from each A site (cf. Fig. 1). Since $\Delta_1 = (\Delta_1 - \Delta_p)/4$, this approximation is equivalent to assuming that s and p states are equally

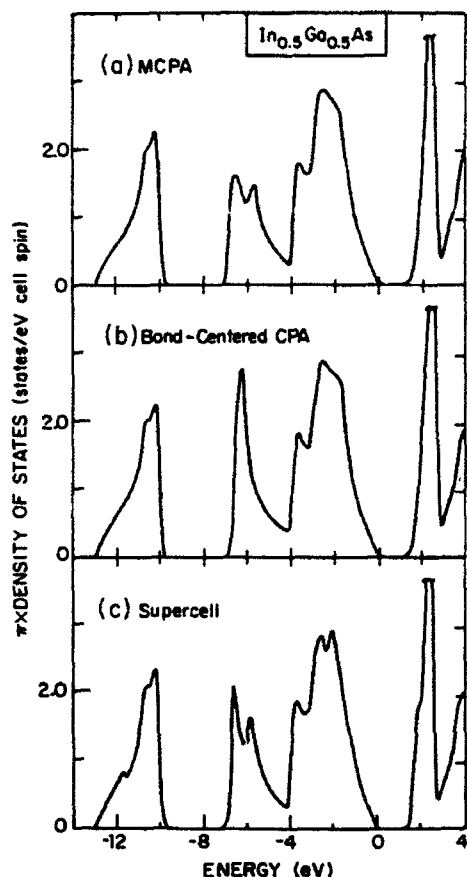


FIG. 10. Comparison of $\text{In}_{0.5}\text{Ga}_{0.5}\text{As}$ densities of states—calculated in the (a) MCPA, (b) bond-centered CPA, and (c) supercell approaches. [(a) is identical to Fig. 4(c)].

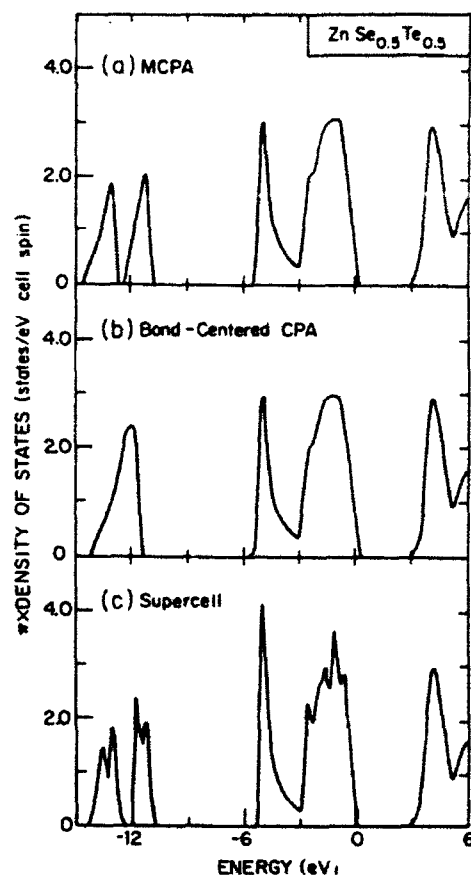


FIG. 11. Same as Fig. 10 but for $\text{ZnSe}_{0.5}\text{Te}_{0.5}$. [(a) is identical to Fig. 8(c)].

affected by the presence of chemical disorder. In $\text{In}_{1-x}\text{Ga}_x\text{As}$, $\text{ZnSe}_x\text{Te}_{1-x}$ and most other zinc-blende pseudobinary alloys, however, $|\Delta_s| \gg |\Delta_p|$. The bond-centered CPA thus tends to underestimate disorder effects for s states and to overestimate them for p states. Since the only chemical scattering parameter in the approach $\Delta_0 = (\Delta_s + 3\Delta_p)/4$ is weighted more heavily by the p disorder, the s -state discrepancies tend to be more severe.

B. Supercell approach

The other alternatives to be considered are conceptually different in that they forego configuration averaging entirely. The first of these, the supercell method,^{7,18} introduces an artificial periodic ordering to allow the use of standard crystalline band-structure techniques. The unit cell in this approach is chosen to represent the most probable local configuration in the alloy. A common example is the modeling of an $A'_{0.5}A''_{0.5}B$ zinc-blende pseudobinary as a chalcopyrite crystal.⁷ The larger chalcopyrite unit cell²⁸ accommodates two different types of A atom with each B atom having two A' and two A'' nearest neighbors.

The difference between $A'-B$ and $A''-B$ bond lengths is accommodated by a displacement of the B atoms from their ideal fcc lattice sites.

This approach is attractive because it permits the use of more accurate and sophisticated band-structure techniques than the empirical tight-binding method. Self-consistent density-functional-theory calculations,^{5(b),59} for example, have recently been shown to provide important information concerning local structure properties and charge-redistribution effects in zinc-blende pseudobinary alloys. The relevance of the associated band-structure information to random alloys is much less clear. This relationship is elucidated here by comparing the results of analogous MCPA and supercell calculations for $\text{In}_{0.5}\text{Ge}_{0.5}\text{As}$ and $\text{ZnSe}_{0.5}\text{Te}_{0.5}$.

To isolate the effects of ordering, we construct a supercell Hamiltonian which is locally equivalent to the random alloy Hamiltonian in Eq. (3). The specific assumptions employed are (1) an undistorted chalcopyrite lattice (eight atoms per unit cell) with all nearest-neighbor bond lengths equal to $\bar{d}(x=0.5)$, (2) A' and A'' intraatomic matrix elements and $V_2^{A'B}$ and $V_2^{A''B}$ parameters identical to those in the corresponding $A'B$ and $A''B$ zinc-blende

limiting crystals, and (3) scaled-VCA values [Eq. (6)] for all other matrix elements. The resulting Hamiltonian is 32×32 in k space. Band structures are obtained by direct diagonalization using the limiting-crystal parameters in Table II.

The associated supercell densities of states for $\text{In}_{0.5}\text{Ga}_{0.5}\text{As}$ and $\text{ZnSe}_{0.5}\text{Te}_{0.5}$ are plotted in Figs. 10(c) and 11(c), respectively. Except for some additional fine structure, the basic features are remarkably similar to the corresponding MCPA state densities. Even the nearly split-band behavior near -6 eV in $\text{In}_{0.5}\text{Ga}_{0.5}\text{As}$ and -12 eV in $\text{ZnSe}_{0.5}\text{Te}_{0.5}$ is well reproduced.^{18(b)} We conclude that the gross features of the electronic structure are determined primarily by local bonding properties and are relatively insensitive to long-range correlations. This behavior follows from Heine's invariance theorem⁴³ which states that local Green's functions are insensitive to the environment beyond a few electron wavelengths. Here the nearest-neighbor environments around each A' and A'' atom are identical in the two approaches and the nearest-neighbor environment around each B atom in the supercell is the most probable one in the MCPA. A similarity in local, and hence total, densities of states is thus to be expected, regardless of how the local environments are connected to form the alloy.

The long-range correlations in the supercell model do produce some observable differences, however. New structure appears in Figs. 10(c) and 11(c) due to new critical points in the smaller chalcopyrite Brillouin zone. This structure is spurious as far as random alloys are concerned but may be useful for detecting ordering in real materials (e.g., through an examination of optical spectra^{18(c)}). The supercell bands are also somewhat narrower than in the MCPA. This reflects the fact that, relative to the VCA, the MCPA perturbation produces a repulsion from states throughout the zinc-blende zone while the supercell perturbation produces a repulsion only from states with particular k vectors. An important consequence is that VCA band-edge states generally experience a smaller intraband repulsion in the supercell approach than in the MCPA. The predicted bowing of the fundamental gap is thus usually smaller in the supercell approach than in the MCPA, but still larger than that of the VCA.⁶⁰ The calculated supercell band-edge results in Table IV for $\text{In}_{0.5}\text{Ga}_{0.5}\text{As}$ and $\text{ZnSe}_{0.5}\text{Te}_{0.5}$ confirm this behavior. The much large discrepancy between the MCPA and supercell results for $\text{ZnSe}_{0.5}\text{Te}_{0.5}$ reflects the much larger extrinsic contribution to the bowing in this system.⁶¹

We conclude that the supercell approach is largely complementary to the MCPA. Both approaches are superior to the VCA in predicting properties sensitive to local bonding characteristics because both include two distinct types of $A-B$ bond instead of one bond of average character. The supercell approach is particularly useful if employed with more sophisticated band-structure techniques. The approach is only applicable to certain x values, however, and provides no information on damping effects and limiting mobilities due to alloy scattering. It is also unreliable in predicting k -dependent band-structure properties (e.g., effective masses, gaps at $k \neq 0$) which are unduly

influenced by the introduction of artificial periodicity and anisotropy.

C. Recursion method

The final alternative, the recursion method,¹⁹ has only recently been implemented in electronic structure calculations for semiconducting alloys.²⁰ This approach obviates the need for configuration averaging by the direct consideration of large clusters characteristic of the alloy environment. Spectral densities and local densities of states are calculated by a recursive solution to the Schrödinger equation.

Davis has demonstrated that for randomly generated clusters and similar tight-binding Hamiltonians the recursion method yields similar results to the MCPA.^{20(b),62} This result provides additional support for the reasonability of the MCPA mean-field approximation. The real power of the recursion method, however, lies in its ability to go beyond cell-diagonal disorder and to consider clusters with arbitrary degrees of short- or long-range correlations. These features have yet to be exploited for zinc-blende pseudobinary alloys but have been included in calculations^{20(c)} for $\text{Ge}_{2x}(\text{GaAs})_{1-x}$. The main disadvantage of the recursion method is that, like the MCPA, it is limited to an empirical tight-binding description at the present time. The approach is also more computationally intensive than the MCPA (Ref. 62) and somewhat less physically transparent.

ACKNOWLEDGMENTS

We are grateful to L. C. Davis for useful discussions and correspondence pertaining to the recursion method. This work was supported in part by the Joint Service Electronics Program (N00014-84-K-0465), the Defense Advanced Research Projects Agency (through Office of Naval Research Contract No. N00014-86-K-0033) and the National Science Foundation (Contract No. DMR-85-14638).

APPENDIX: TRANSFORMATION FROM ATOMIC TO sp^3 HYBRID BASIS

The standard Slater-Koster description¹² of zinc-blende semiconductors without spin-orbit interactions employs an orthonormal basis of atomiclike orbitals $\phi_\gamma(r-R_j-\tau_\nu)$ with $\gamma = s, x, y, z$; $\nu = A, B$; $\tau_A = 0$; and $\tau_B = a/4(111)$. (a is the cubic lattice constant.) This gives rise to an 8×8 Hamiltonian matrix $\bar{H}^{AO}(\mathbf{k})$ in the basis of corresponding Bloch sums. The matrix elements of $\bar{H}^{AO}(\mathbf{k})$ are

$$\langle \gamma \nu \mathbf{k} | H | \gamma' \nu' \mathbf{k} \rangle = \sum_j e^{i\mathbf{k} \cdot (\mathbf{R}_j + \tau_\nu - \tau_{\nu'})} E_{\gamma\gamma'}(l m n)_{\nu\nu'}, \quad (\text{A1})$$

where $a/2(l m n) = \mathbf{R}_j + \tau_\nu - \tau_{\nu'}$ and the $E_{\gamma\gamma'}(l m n)_{\nu\nu'}$ are Slater-Koster parameters such as those given in Table II. The explicit form of $\bar{H}^{AO}(\mathbf{k})$ for interactions up to second-nearest neighbors is given in the Appendix of Ref. 4 for the Hamiltonian labeled H^0 .

The equivalent description in the sp^3 hybrid basis described in Eq. (2) of Sec. II is obtained by performing the

unitary transformation

$$\bar{H}^{\text{hyb}}(\mathbf{k}) = \bar{S}_k^\dagger \bar{H}^{\text{AO}}(\mathbf{k}) \bar{S}_k. \quad (\text{A2})$$

Here \bar{S}_k is block diagonal in the index ν with the A block equal to

$$\frac{1}{2} \begin{bmatrix} 1 & 1 & 1 & 1 \\ 1 & 1 & -1 & -1 \\ 1 & -1 & 1 & -1 \\ 1 & -1 & -1 & 1 \end{bmatrix}, \quad (\text{A3})$$

and the B block equal to

$$\frac{1}{2} \begin{bmatrix} e^{-ik \cdot \tau_3} & e^{-ik \cdot \tau_6} & e^{-ik \cdot \tau_7} & e^{-ik \cdot \tau_8} \\ e^{-ik \cdot \tau_3} & -e^{-ik \cdot \tau_6} & e^{-ik \cdot \tau_7} & e^{-ik \cdot \tau_8} \\ e^{-ik \cdot \tau_3} & e^{-ik \cdot \tau_6} & -e^{-ik \cdot \tau_7} & e^{-ik \cdot \tau_8} \\ e^{-ik \cdot \tau_3} & e^{-ik \cdot \tau_6} & e^{-ik \cdot \tau_7} & -e^{-ik \cdot \tau_8} \end{bmatrix}. \quad (\text{A4})$$

The basis vectors in (A4) are

$$\tau_3 = (a/4)(1, 1, 1),$$

$$\tau_6 = (a/4)(1, \bar{1}, \bar{1}),$$

$$\tau_7 = (a/4)(\bar{1}, 1, \bar{1}),$$

and

$$\tau_8 = (a/4)(\bar{1}, \bar{1}, 1).$$

Equation (2) follows by dividing the atomic-orbital Hamiltonian as

$$\bar{H}^{\text{AO}}(\mathbf{k}) = \bar{H}_1^{\text{AO}}(\mathbf{k}) + \bar{H}_2^{\text{AO}}(\mathbf{k}) \quad (\text{A5})$$

with $\bar{H}_1^{\text{AO}}(\mathbf{k})$ containing only intra-atomic and nearest-neighbor interactions and $\bar{H}_2^{\text{AO}}(\mathbf{k})$ containing all longer-ranged interactions (second neighbors in the present case). The quantities $\langle \alpha, \mathbf{k} | H_2 | \beta, \mathbf{k} \rangle$ in Eq. (2) are matrix elements of $\bar{S}_k^\dagger \bar{H}_2^{\text{AO}}(\mathbf{k}) \bar{S}_k$ which never need to be explicitly written in the hybrid basis. The quantities $\epsilon_{\alpha\beta}$ and $h_{\alpha\beta}(0, j)$ in Eq. (2) are determined by analytically evaluating $\bar{S}_k^\dagger \bar{H}_1^{\text{AO}}(\mathbf{k}) \bar{S}_k$. The $\epsilon_{\alpha\beta}$ are elements of the matrix

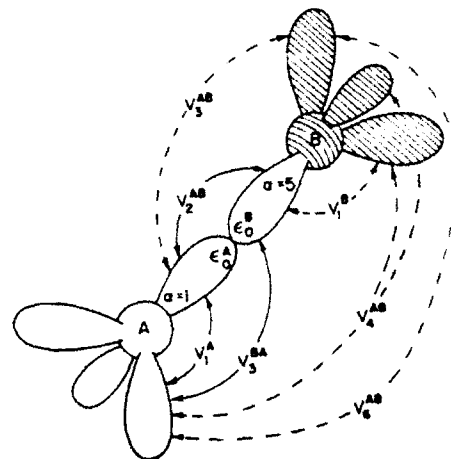


FIG. 12. On-site and nearest-neighbor hopping matrix elements in sp^3 hybrid orbital basis. Lobes $\alpha=1$ and $\alpha=5$ are labeled explicitly to illustrate convention introduced prior to Eq. (1). Intracell (intercell) hoppings (cf. Fig. 2) denoted by solid (dashed) lines. Elements V_1^A and V_1^B connect orbitals with dihedral angles of 60° and 180° , respectively.

$$\bar{\epsilon} = \begin{bmatrix} \epsilon_0^A & V_1^A & V_1^A & V_1^A & V_2^{AB} & V_3^A & V_3^A & V_3^A \\ V_1^A & \epsilon_0^A & V_1^A & V_1^A & V_3^A & V_2^{AB} & V_3^A & V_3^A \\ V_1^A & V_1^A & \epsilon_0^A & V_1^A & V_3^A & V_3^A & V_2^{AB} & V_3^A \\ V_1^A & V_1^A & V_1^A & \epsilon_0^A & V_3^A & V_3^A & V_3^A & V_2^{AB} \\ V_2^{AB} & V_3^A & V_3^A & V_3^A & \epsilon_0^B & 0 & 0 & 0 \\ V_3^A & V_2^{AB} & V_3^A & V_3^A & 0 & \epsilon_0^B & 0 & 0 \\ V_3^A & V_3^A & V_2^{AB} & V_3^A & 0 & 0 & \epsilon_0^B & 0 \\ V_3^A & V_3^A & V_3^A & V_2^{AB} & 0 & 0 & 0 & \epsilon_0^B \end{bmatrix} \quad (\text{A6})$$

and

$$h_{\alpha\beta}(0, j) = \begin{cases} V_1^B & \text{for } \alpha=5-8; \beta=5-8; \beta \neq \alpha; R_j = \tau_\alpha - \tau_\beta, \\ V_3^{AB} & \text{for } \alpha=1-4; \beta=5-8; \beta \neq \alpha+4; R_j = \tau_{\alpha+4} - \tau_\beta, \\ V_4^{AB} & \text{for } \alpha=1-4; \beta=5-8; \beta \neq \alpha+4, \beta'; R_j = \tau_\beta - \tau_{\beta'} \text{ where } \beta'=5-8; \beta' \neq \alpha+4, \\ & \text{and } \alpha=5-8; \beta=1-4; \alpha \neq \beta+4, \alpha'; R_j = \tau_\alpha - \tau_{\alpha'} \text{ where } \alpha'=5-8; \alpha' \neq \beta+4, \\ V_6^{AB} & \text{for } \alpha=1-4; \beta=\alpha+4; R_j = \tau_{\alpha'+4} - \tau_\beta \text{ where } \alpha'=1-4; \alpha' \neq \alpha, \\ & \text{and } \alpha=5-8; \beta=\alpha-4; R_j = \tau_\alpha - \tau_{\alpha'} \text{ where } \alpha'=5-8; \alpha' \neq \alpha, \\ 0 & \text{for all other matrix elements.} \end{cases} \quad (\text{A7})$$

The hybrid orbital matrix elements appearing in (A6) and (A7) [cf. Fig. (12)] are given by

$$\epsilon_0^A = [E_{xx}(000)_{vv} + 3E_{xx}(000)_{vv}]/4, \quad v = A, B,$$

$$V_1^A = [E_{xx}(000)_{vv} - E_{xx}(000)_{vv}]/4, \quad v = A, B,$$

$$V_2^{AB} = [E_{xx}(\frac{1}{2}\frac{1}{2}\frac{1}{2})_{AB} - 3E_{xx}(\frac{1}{2}\frac{1}{2}\frac{1}{2})_{AB} - 3E_{xx}(\frac{1}{2}\frac{1}{2}\frac{1}{2})_{AB} - 3E_{xx}(\frac{1}{2}\frac{1}{2}\frac{1}{2})_{BA} - 6E_{xy}(\frac{1}{2}\frac{1}{2}\frac{1}{2})_{AB}]/4,$$

$$V_3^{AB} = [E_{xx}(\frac{1}{2}\frac{1}{2}\frac{1}{2})_{AB} + E_{xx}(\frac{1}{2}\frac{1}{2}\frac{1}{2})_{AB} - 3E_{xx}(\frac{1}{2}\frac{1}{2}\frac{1}{2})_{AB} + E_{xx}(\frac{1}{2}\frac{1}{2}\frac{1}{2})_{BA} + 2E_{xy}(\frac{1}{2}\frac{1}{2}\frac{1}{2})_{AB}]/4, \quad (\text{A8})$$

$$V_3^A = [E_{xx}(\frac{1}{2}\frac{1}{2}\frac{1}{2})_{AB} + E_{xx}(\frac{1}{2}\frac{1}{2}\frac{1}{2})_{AB} + E_{xx}(\frac{1}{2}\frac{1}{2}\frac{1}{2})_{AB} - 3E_{xx}(\frac{1}{2}\frac{1}{2}\frac{1}{2})_{BA} + 2E_{xy}(\frac{1}{2}\frac{1}{2}\frac{1}{2})_{AB}]/4,$$

$$V_4^A = [E_{xx}(\frac{1}{2}\frac{1}{2}\frac{1}{2})_{AB} + E_{xx}(\frac{1}{2}\frac{1}{2}\frac{1}{2})_{AB} + E_{xx}(\frac{1}{2}\frac{1}{2}\frac{1}{2})_{AB} + E_{xx}(\frac{1}{2}\frac{1}{2}\frac{1}{2})_{BA} - 2E_{xy}(\frac{1}{2}\frac{1}{2}\frac{1}{2})_{AB}]/4,$$

$$V_6^A = [E_{xx}(\frac{1}{2}\frac{1}{2}\frac{1}{2})_{AB} - 3E_{xx}(\frac{1}{2}\frac{1}{2}\frac{1}{2})_{AB} + E_{xx}(\frac{1}{2}\frac{1}{2}\frac{1}{2})_{AB} + E_{xx}(\frac{1}{2}\frac{1}{2}\frac{1}{2})_{BA} + 2E_{xy}(\frac{1}{2}\frac{1}{2}\frac{1}{2})_{AB}]/4.$$

*Also at: Dept. of Physics, Massachusetts Institute of Technology, Cambridge, Massachusetts 02139.

†Author to whom all correspondence should be addressed.

¹For a recent review, see M. Jaros, *Rep. Prog. Phys.* **48**, 1091 (1985).

²Important contributions have been made using (a) dielectric theory: J. A. Van Vechten and T. K. Bergstresser, *Phys. Rev. B* **1**, 3351 (1970); (b) pseudopotential theory: D. Stroud and H. Ehrenreich, *ibid.* **2**, 3197 (1970); (c) k·p theory: E. D. Sigia, *ibid.* **10**, 5147 (1974); and (d) real-space techniques: A. B. Chen and A. Sher, *Phys. Rev. Lett.* **40**, 900 (1978).

³(a) A. B. Chen and A. Sher, *Phys. Rev. B* **23**, 5360 (1981); (b) J. Vac. Sci. Technol. **21**, 138 (1982).

⁴K. C. Hass, H. Ehrenreich, and B. Velický, *Phys. Rev. B* **27**, 1088 (1983).

⁵The present theory is thus most applicable to alloys which are quenched rapidly from high temperatures. At lower growth temperatures the actual distribution of A' and A'' atoms is expected to deviate from randomness and exhibit short-ranged and possibly long-ranged correlations. [See (a) T. S. Kuan, T. F. Keuch, W. I. Wang, and E. L. Wilkie, *Phys. Rev. Lett.* **54**, 201 (1985); (b) G. P. Srivastava, J. L. Martins, and A. Zunger, *Phys. Rev. B* **31**, 2561 (1985); (c) A. Sher, A. B. Chen, and M. van Schilfgaarde, *J. Vac. Sci. Technol. A* **4**, 1965 (1986); (d) H. R. Jen, M. J. Cherng, and G. B. Stringfellow, *Appl. Phys. Lett.* **48**, 1603 (1986).]

⁶J. C. Mikkelsen, Jr. and J. B. Boyce, *Phys. Rev. Lett.* **49**, 1412 (1982); *Phys. Rev. B* **28**, 7130 (1983).

⁷A. Zunger and J. E. Jaffe, *Phys. Rev. Lett.* **51**, 662 (1983).

⁸(a) ZnSe_{1-x}Te_x: J. C. Mikkelsen, Jr., *Bull. Am. Phys. Soc.* **29**, 202 (1984); (b) Cd_{1-x}Mn_xTe: A. Balzarotti *et al.*, *Phys. Rev. B* **30**, 2295 (1984); (c) Cd_{1-x}Zn_xTe: N. Motta *et al.*, *Solid State Commun.* **53**, 509 (1985).

⁹J. L. Martins and A. Zunger, *Phys. Rev. B* **30**, 6217 (1984); J. M. Baronowski, *J. Phys. C* **17**, 6287 (1984); C. K. Shih, W. E. Spicer, W. A. Harrison, and A. Sher, *Phys. Rev. B* **31**, 1139 (1985); A. B. Chen and A. Sher, *ibid.* **32**, 3695 (1985); T. Fukui, *J. Appl. Phys.* **57**, 5188 (1985).

¹⁰(a) H. Ehrenreich and L. M. Schwartz, in *Solid State Physics*, edited by H. Ehrenreich, F. Seitz, and D. Turnbull (Academic, New York, 1976), Vol. **31** p. 149; (b) H. Ehrenreich and K. C. Hass, *J. Vac. Sci. Technol.* **21**, 138 (1982).

¹¹K. C. Hass, R. J. Lempert, and H. Ehrenreich, *Phys. Rev. Lett.* **52**, 77 (1984).

¹²J. C. Slater and G. F. Koster, *Phys. Rev.* **94**, 1498 (1954).

¹³W. A. Harrison, *Electronic Structure and the Properties of Solids* (Freeman, San Francisco, 1980).

¹⁴(a) M. Tsukada, *J. Phys. Soc. Jpn.* **32**, 1475 (1972); (b) F. Ducastelle, *J. Phys. C* **7**, 1795 (1974).

¹⁵J. M. Ziman, *Models of Disorder* (Cambridge University Press, Cambridge, 1979), p. 342.

¹⁶A more complicated formalism which reduces to the present MCPA approach was introduced previously for zinc-blende pseudobinary alloys by S. Sakai and T. Sugano, *J. Appl. Phys.*

50, 4143 (1979).

¹⁷Atomic energy level differences are on the order of 1 eV and EXAFS results for both systems [Refs. 6 and 8(a)] indicate appreciable structural disorder because of the large lattice mismatches between limiting crystals ($\Delta a/a \sim 7\%$).

¹⁸(a) D. J. Stukel, *Phys. Rev. B* **3**, 3347 (1971); (b) J. E. Bernard and A. Zunger, *ibid.* **34**, 5992 (1986); (c) N. E. Christensen, E. Molinari, and G. B. Bachelet, *Solid State Commun.* **56**, 125 (1985).

¹⁹R. Haydock, in *Solid State Physics*, edited by H. Ehrenreich, F. Seitz, and D. Turnbull (Academic, New York, 1980), Vol. **35**, p. 215.

²⁰(a) L. C. Davis, *Phys. Rev. B* **28**, 6961 (1983); (b) L. C. Davis, *Mater. Sci. Forum* **4**, 197 (1985); (c) H. Holloway and L. C. Davis, *Phys. Rev. Lett.* **53**, 830 (1984).

²¹(a) A. B. Chen and A. Sher, *Phys. Rev. B* **17**, 4726 (1978); (b) *ibid.* **19**, 3057 (1979); (c) D. Z.-Y. Ting and Y.-C. Chang, *ibid.* **30**, 3309 (1984).

²²This is well known, for example, from (a) the treatment of amorphous semiconductors by D. Weaire and M. F. Thorpe, *Phys. Rev. B* **4**, 2508 (1971); and (b) calculations of electron-phonon interactions [e.g., C. M. Varma, E. I. Blount, P. Vashishta, and W. Weber, *Phys. Rev. B* **19**, 6130 (1979)].

²³The neglect of longer-ranged strain fields is similar to the neglect of Coulomb tails and inclusion of only "central cell corrections" in deep-level calculations for nonisoelectronic impurities [e.g., H. P. Hjalmarson, P. Vogl, D. J. Wolford, and J. D. Dow, *Phys. Rev. Lett.* **44**, 810 (1980)].

²⁴In practice, we also assume that the same finite basis set can be used for both the distorted and undistorted lattices and neglect possible changes in overlap integrals between basis functions [cf. Ref. 22(b)].

²⁵O. Berolo, J. C. Wooley, and J. A. Van Vechten, *Phys. Rev. B* **8**, 3794 (1973).

²⁶A. Baldereschi, E. Hess, M. Maschke, H. Neumann, K. R. Schulze, and K. Unger, *J. Phys. C* **10**, 4709 (1977).

²⁷C. A. Coulson and M. J. Kearsley, *Proc. R. Soc. London, Ser. A* **241**, 433 (1957); A. Baldereschi and J. J. Hopfield, *Phys. Rev. Lett.* **28**, 171 (1972); M. Lannoo and J. Bourgoin, in *Point Defects in Semiconductors*, edited by M. Cardona (Springer, Berlin, 1983), Vols. I and II.

²⁸(a) P. V. Smith and D. McMahon, *J. Phys. C* **16**, 6947 (1973); (b) L. Brey, C. Tejedor, and J. A. Verges, *Phys. Rev. B* **29**, 6840 (1984); (c) A. A. Mbaye, C. Verie, and F. Aymerich, *ibid.* **29**, 3756 (1984).

²⁹P. A. Fedders and C. W. Myles, *Phys. Rev. B* **29**, 802 (1984).

³⁰The modification is the matrix generalization of Eq. (14.9b) in *Solid State Physics*, Ref. 10(a).

³¹K. C. Hass, B. Velický, and H. Ehrenreich, *Phys. Rev. B* **29**, 3697 (1984).

³²M. Bugajski, A. M. Kontkiewicz, and H. Mariette, *Phys. Rev. B* **28**, 7105 (1983); J. Singh and K. K. Bajaj, *J. Appl. Phys.* **57**, 322 (1985).

³³J. R. Chelikowsky and M. L. Cohen, *Phys. Rev. B* **14**, 556

- (1979).
- ³⁴S. P. Kowalczyk, W. J. Schaffer, E. A. Kraut, and R. W. Grant, *J. Vac. Sci. Technol.* **20**, 705 (1982).
- ³⁵P. Vogl, H. P. Hjalmarson, and J. D. Dow, *J. Phys. Chem. Solids* **44**, 365 (1983); Y. Li and P. J. Lin-Chung, *ibid.* **46**, 241 (1985).
- ³⁶F. Herman and S. Skillman, *Atomic Structure Calculations* (Prentice-Hall, Englewood Cliffs, 1963).
- ³⁷To our knowledge the only theoretical calculations performed for both ZnSe and ZnTe by the same group are the orthogonalized plane wave (OPW) calculations described in S. I. Kurganskii, O. V. Farberovich, and E. P. Domashevskaya, *Fiz. Tekh. Poluprovodn.* **14**, 1315 (1980) [*Sov. Phys. Semicond.* **14**, 775 (1980)]. These results are in poor agreement, however, with the photoemission data of Ref. 39.
- ³⁸(a) L. Ley, R. A. Pollak, F. R. McFeely, S. P. Kowalczyk, and D. A. Shirley, *Phys. Rev. B* **9**, 600 (1974); (b) D. E. Eastman, W. D. Grobman, J. L. Freeouf, and M. Erbudak, *ibid.* **9**, 3473 (1974).
- ³⁹(a) M. Cardona, *J. Appl. Phys., Suppl.* **32**, 2151 (1961); (b) M. Aven, D. T. F. Maple, and B. Segall, *ibid.* **32**, 2261 (1961); (c) M. Cardona and D. L. Greenaway, *Phys. Rev.* **131**, 98 (1963); (d) J. P. Walter, M. L. Cohen, Y. Petroff, and M. Balkanski, *Phys. Rev. B* **1**, 2661 (1970); (e) J. L. Freeouf, *ibid.* **7**, 3810 (1973); (f) M. Cardona, in *Modulation Spectroscopy*, edited by H. Ehrenreich, F. Seitz, and D. Turnbull (Academic, New York, 1969), Suppl. 11.
- ⁴⁰A. D. Katnani and G. Margaritondo, *J. Appl. Phys.* **54**, 2522 (1983).
- ⁴¹J. A. Silberman, P. Morgen, W. E. Spicer, and J. A. Wilson, *J. Vac. Sci. Technol.* **21**, 142 (1982); W. E. Spicer, J. A. Silberman, P. Morgen, I. Lindau, J. A. Wilson, A. B. Chen, and A. Sher, *Phys. Rev. Lett.* **49**, 948 (1982).
- ⁴²Previous photoemission studies on this alloy system by K. Y. Cheng, A. Y. Cho, S. B. Christman, T. P. Pearsall, and J. E. Rowe, *Appl. Phys. Lett.* **40**, 423 (1982); and J. E. Rowe, T. P. Pearsall, and R. A. Logan, *Physica* **117&118B**, 347 (1983) have been concerned with structure near the top of the valence band. The slight deviations from VCA-like behavior observed in these experiments may be due to the broadening of upper valence-band spectral densities in the present MCPA results.
- ⁴³V. Heine, in *Solid State Physics*, edited by H. Ehrenreich, F. Seitz, and D. Turnbull (Academic, New York, 1980), Vol. 35, p. 85.
- ⁴⁴It is useful to note that the off-diagonal Green's-function matrix elements satisfy the general sum rule $\int dE \text{Im} f^{\text{AB}}(E^+) = 0$ and the Schwarz inequality $|\text{Im} f^{\text{AB}}(E^+)|^2 \leq |\text{Im} f^{\text{A}}(E^+)| |\text{Im} f^{\text{B}}(E^+)|$.
- ⁴⁵D. L. Rode and P. A. Fedders, *J. Appl. Phys.* **54**, 6425 (1983); D. S. Montgomery, *J. Phys. C* **16**, 2923 (1983).
- ⁴⁶B. Velický, *Phys. Rev.* **184**, 615 (1969).
- ⁴⁷H. Brooks (unpublished). See L. Makowski and M. Glicksman, *J. Phys. Chem. Solids* **34**, 487 (1973) and M. A. Littlejohn, J. R. Hauser, T. H. Glisson, D. K. Ferry, and J. W. Harrison, *Solid State Electron.* **21**, 107 (1978).
- ⁴⁸H. Ehrenreich, *J. Phys. Chem. Solids* **12**, 97 (1959).
- ⁴⁹A. Chandra and L. F. Eastman, *J. Appl. Phys.* **51**, 2669 (1980); E. M. Conwell and M. O. Vassell, *Phys. Rev.* **166**, 797 (1968).
- ⁵⁰F. Oosaka, T. Sugano, Y. Okabe, and Y. Okada, *Jpn. J. Appl. Phys.* **15**, 2371 (1976); J. H. Marsh, *Appl. Phys. Lett.* **41**, 732 (1982); P. Blood and A. D. C. Grassie, *J. Appl. Phys.* **56**, 1866 (1984).
- ⁵¹M. Glicksman, R. E. Enstrom, S. A. Mittelman, and J. R. Appert, *Phys. Rev. B* **9**, 1621 (1974); T. Katoda, F. Oosaka, and T. Sugano, *Jpn. J. Appl. Phys.* **13**, 561 (1974); J. R. Hayes, A. R. Adams, and P. D. Greene, in *GaInAsP Alloy Semiconductors*, edited by T. P. Pearsall (Wiley, New York, 1982), Ch. 8; P. P. Basu, D. Chattopadhyay, and C. K. Sarkar, *J. Phys. C* **19**, L173 (1986).
- ⁵²The strong asymmetry in the experimental x dependence of μ_{alloy} (Ref. 51) is nevertheless correctly described in the MCPA. The location of the minimum near $x=0.7$ results from the $x(1-x)$ factor in Eq. (29) and the nearly linear effective-mass variation $m^*(x)/m \approx (1-x)0.024 + 0.066x$ observed experimentally [D. Olego, T. Y. Chang, E. Silberg, E. A. Caridi, and A. Pinczuk, *Appl. Phys. Lett.* **41**, 476 (1982)].
- ⁵³(a) K. H. Goetz *et al.*, *J. Appl. Phys.* **54**, 4543 (1983); (b) K. Nakajima, A. Yamaguchi, K. Akita, and T. Kotani, *ibid.* **49**, 5944 (1978).
- ⁵⁴A. Ebina, M. Yamamoto, and T. Takahashi, *Phys. Rev.* **26**, 3786 (1972).
- ⁵⁵If the V_{f}^{AB} parameter in Eq. (6) is also scaled to correspond more closely to the "scaled-VCA" treatment of Refs. 3(a) and 28(c), the deviations from linearity become (in meV) $\Delta E(\Gamma_{\text{S}}) = +24$, $\Delta E(\Gamma) = -57$ in $\text{In}_{0.5}\text{Ga}_{0.5}\text{As}$ and $\Delta E(\Gamma_{\text{S}}) = -6$, $\Delta E(\Gamma) = -15$ in $\text{ZnSe}_{0.5}\text{Te}_{0.5}$. Since the net MCPA bowing is unaffected, this provides an example of the ambiguity associated with the separation between intrinsic and extrinsic contributions.
- ⁵⁶An extreme case of clustering is that of a superlattice which generally has a band gap smaller than that of the corresponding alloy. Some insight into the spectral limits expected in various types of disordered semiconductors is provided by the theorem of A. E. Carlsson, H. Ehrenreich, and K. C. Hass, *Phys. Rev. B* **28**, 4468 (1983).
- ⁵⁷In practice, the bonding and antibonding states are often assumed to be completely decoupled with $\Delta_{\text{AB}} = 0$ [e.g., Ref. 3(a)]. This further simplifies the bond-centered CPA formalism but introduces additional errors near the band edges, particularly in narrower gap systems.
- ⁵⁸For a description of the chalcopyrite structure, see A. Miller, A. MacKinnon, and D. Weaire, in *Solid State Physics*, edited by H. Ehrenreich, F. Seitz, and D. Turnbull (Academic, New York, 1981), Vol. 36, pp. 119.
- ⁵⁹P. Boguslawski and A. Baldereschi, in *Proceedings of the 17th International Conference on the Physics of Semiconductors*, edited by D. J. Chadi and W. A. Harrison (Springer, New York, 1984), p. 939; K. C. Hass and D. Vanderbilt, in *Proceedings of the 18th International Conference on the Physics of Semiconductors*, edited by O. Engström (World Scientific, Singapore, 1987), p. 1181.
- ⁶⁰Note that the net supercell bowing still contains an "extrinsic" (non-VCA) contribution despite the absence of any disorder. One must be careful to avoid potential semantic difficulties associated with the fact that the term disorder has conventionally been used to refer to any deviation from VCA behavior. It is incorrect, for example, to correct for "disorder" effects left out of the supercell approach by simply adding the extrinsic CPA or MCPA bowing as is done in Ref. 7.
- ⁶¹The present comparison between MCPA and supercell results is intended merely as an illustration of the types of differences that one expects, in principle, between random and ordered alloys. *Ab initio* supercell calculations for $\text{ZnSe}_{0.5}\text{Te}_{0.5}$ which include bond-angle changes [Ref. 18(b)] actually overestimate the bowing of the fundamental gap in this system by predicting a net deviation from linearity at $x=0.5$ of -490 meV.
- ⁶²L. C. Davis (private communication).

Bond relaxation in $\text{Hg}_{1-x}\text{Cd}_x\text{Te}$ and related alloys

K. C. Hass

Division of Applied Sciences, Harvard University, Cambridge, Massachusetts 02138 and Department of Physics, Massachusetts Institute of Technology, Cambridge, Massachusetts 02139

David Vanderbilt

Department of Physics, Harvard University, Cambridge, Massachusetts 02138

(Received 13 November 1986; accepted 8 December 1986)

The local structural properties of $\text{Hg}_{1-x}\text{Cd}_x\text{Te}$, $\text{Hg}_{1-x}\text{Zn}_x\text{Te}$, and $\text{Cd}_{1-x}\text{Zn}_x\text{Te}$ are examined using a self-consistent pseudopotential approach. An accurate description of the limiting crystals is obtained by adding empirical corrections to *ab initio* total energies calculated with the group-II *d* states included in the cores. Similar calculations for $x = 0.5$ ordered alloys confirm the presence of nearest-neighbor bond-length differences in these systems without violation of Vegard's law. An anomalously large "relaxation" is predicted here for $\text{Hg}_{1-x}\text{Cd}_x\text{Te}$ ($\sim 2\%$ bond-length difference in the alloy compared to only 0.3% between limiting crystals) due to the dominance of chemical effects neglected from simple valence force models. The implications of the present results for alloy mixing energies and possible deviations from randomness are discussed.

I. INTRODUCTION

The local structural properties of tetrahedrally bonded semi-conducting alloys play an important role in determining the electronic,^{1,2} thermodynamic,³⁻⁶ and defect properties^{7,8} of these materials. Recent extended x-ray absorption fine-structure (EXAFS) measurements⁹⁻¹¹ have demonstrated that in a variety of $\text{A}_{1-x}\text{B}_x\text{C}$ zinc-blende systems, the individual A-C and B-C nearest-neighbor bond lengths do not simply equalize to an average "virtual lattice" value but instead each bond length remains much closer to that of its limiting crystal. The "relaxation" of an A-C bond is conveniently described by the dimensionless parameter

$$\epsilon = (d_{\text{AC}}[\text{BC:A}] - d_{\text{BC}}^0) / (d_{\text{AC}}^0 - d_{\text{BC}}^0),$$

where d_{AC}^0 and d_{BC}^0 are the limiting crystal bond lengths and $d_{\text{AC}}[\text{BC:A}]$ is the A-C bond length associated with an isolated A impurity in a BC crystal. Typical values of ϵ measured in EXAFS experiments range from 0.6 to 0.8. An upper bound of $\epsilon = 1$ is predicted by classical valence force (VF) models^{3,5} which involve a competition between bond-stretching and bond-bending forces.

In the case of $\text{Hg}_{1-x}\text{Cd}_x\text{Te}$ (MCT), local structural distortions have generally been assumed to be unimportant in view of the excellent agreement between limiting crystal bond lengths ($\Delta d \sim 0.01 \text{ \AA}$). Tight-binding calculations⁴ presented at the 1983 MCT Workshop, however, suggested the possibility of an anomalously large relaxation ($\epsilon > 1$) in this system due to an additional chemically induced force omitted from simple VF models. We have recently confirmed this prediction using a more realistic self-consistent pseudopotential total energy minimization procedure.¹² In this paper we present a more detailed account of this work and its implications for other alloy properties (e.g., charge redistribution and mixing energies). Similar calculations are reported for the closely related $\text{Hg}_{1-x}\text{Zn}_x\text{Te}$ and $\text{Cd}_{1-x}\text{Zn}_x\text{Te}$ systems, which have become increasingly important in their own right.

II. THEORETICAL APPROACH

A. Limiting crystals

We begin with a straightforward application of the *ab initio* pseudopotential method¹³ to the limiting crystals HgTe , CdTe , and ZnTe . This approach has been extremely successful in describing the structural properties of group IV and III-V crystals and has recently yielded important insight into the effects of bond relaxation in $\text{In}_{1-x}\text{Ga}_x\text{P}^4$ and $\text{In}_{1-x}\text{Ga}_x\text{As}$.¹⁴ A complicating factor in the case of II-VI's is the presence of shallow group-II *d* states¹⁵ ($> -1 \text{ Ry}$). For computational convenience, we treat these states here as part of the core. We later add empirical corrections to the total energy to compensate for the errors introduced by this assumption.

Ab initio, "norm-conserving" pseudopotentials are generated for Hg^{2+} , Cd^{2+} , Zn^{2+} , and Te^{6+} using a slight modification¹⁶ of the Hamann-Schlüter-Chiang procedure.¹⁷ Relativistic effects, which play an important role in these heavy ions,¹⁸ are included in the scalar approximation of Ref. 19. Total energy calculations are performed within the local density approximation using a plane-wave basis²⁰ and a Hedin-Lundqvist exchange-correlation potential.²¹ Plane waves with energies up to 8 Ry are treated exactly and those between 8 and 12 Ry are treated perturbatively. Brillouin zone integrals are evaluated using two special *k* points²² for zinc-blende crystals and the corresponding *k* point sets for lower symmetry structures.

Total energies are obtained for each crystal at both a series of zinc-blende lattice constants and a series of (111) trigonal distortions. Results in the former case are used to calculate the equilibrium lattice constant (*a*), bulk modulus (*B*), and cohesive energy (E_{coh}). The latter results are used to calculate the zone-center transverse-optic phonon frequency²³ [$\nu_{\text{TO}}(\Gamma)$]. *Ab initio* predictions for these quantities are compared to experiment²⁴ in the upper part of Table I. The theoretical lattice constant in each case is too small by

TABLE I. Top: Comparisons of calculated and experimental (Ref. 24) lattice constants a (in Å), bulk moduli B (in kbar), cohesive energies E_{coh} (in eV/cell), and zone-center phonon frequencies $\nu_{\text{TO}}(\Gamma)$ (in 10^{12} Hz). Deviations from experiment are listed in parentheses. Bottom: Coefficients (in eV Å⁶) of nearest-neighbor (V_1) and cation second-neighbor (V_2) r^{-6} repulsions assumed in modified total energy results.

		ZnTe	CdTe	HgTe
a	<i>Ab initio</i>	5.618 (− 8%)	5.818 (− 10%)	5.616 (− 13%)
	modified; expt	6.103	6.482	6.462
B	<i>Ab initio</i> (at a_{expt})	273 (− 46%)	133 (− 69%)	47 (− 89%)
	modified	544 (+ 7%)	412 (− 3%)	447 (+ 2%)
	expt	509	424	437
E_{coh}	<i>Ab initio</i> (at a_{expt})	6.75 (+ 41%)	6.77 (+ 54%)	7.05 (+ 115%)
	modified	4.69 (− 2%)	4.23 (− 4%)	3.44 (− 5%)
	expt	4.80	4.40	3.28
$\nu_{\text{TO}}(\Gamma)$	<i>Ab initio</i> (at a_{expt})	4.41 (− 17%)	3.07 (− 27%)	2.20 (− 38%)
	modified; expt	5.30	4.20	3.54
V_1		90.530	193.350	230.733
V_2		1074.311	1482.937	2556.274

~10% and the other three quantities are predicted with even less accuracy. By comparison, similar calculations for group IV and III-V crystals¹³ typically yield errors of only 1% in a , 5% in B and E_{coh} , and 3% in $\nu_{\text{TO}}(\Gamma)$.

We attribute the much larger errors here to an inadequate treatment of the cation d states. The "frozen core" approximation breaks down because the large radii of these states make it impossible to choose fully satisfactory cutoff radii for the d components of the ionic pseudopotentials. In contrast to the present results, *ab initio* calculations for II-VI's which include the d electrons on the same footing as valence s and p electrons yield accuracies comparable to those for group IV and III-V systems.²⁵⁻²⁷

To compensate for the errors inherent in the frozen core approximation, we add empirical repulsive forces to the total energy which we assume to be independent of chemical environment. The particular choice of these interactions is motivated by a desire to provide an accurate description of the limiting crystal properties in Table I with as few empirical parameters as possible. The best compromise we have achieved assumes pairwise repulsions of the form $V_1 r^{-6}$ between nearest neighbors and $V_2 r^{-6}$ between cation second neighbors, where r is the separation between atoms. This introduces only two parameters for each crystal which we fit to the experimental lattice constants and $\nu_{\text{TO}}(\Gamma)$ values. The resulting V_1 and V_2 parameters are listed at the bottom of Table I. The increase in magnitudes from Zn → Cd → Hg is consistent with a corresponding increase in the d -state radius. The significant improvements achieved in the modified B and E_{coh} values in the upper part of the table support the validity of this approach and give us the confidence to employ the same empirical corrections in the alloy calculations described below.

B. Ordered alloys

A direct extension of this approach to intermediate alloy concentrations is practical only for ordered configurations with small unit cells. Here we consider only the simplest

such arrangement: the $\text{A}_{0.5}\text{B}_{0.5}\text{C}$ simple tetragonal structure shown in Fig. 1. We assume that the A and B atoms in this structure occupy alternating (001) planes of an undistorted fcc sublattice. The neglect of an overall tetragonal distortion is consistent with the relatively weak broadening of the cation-cation separation observed in EXAFS measurements on random alloys.⁹⁻¹¹ The C atom location in Fig. 1 is allowed to vary from its ideal tetrahedral position ($u = 0.25$) to accommodate a relaxation of nearest-neighbor bond lengths. The A-C and B-C bond lengths are given by $(u^2 + 0.125)^{1/2}a$ and $[(u - 0.5)^2 + 0.125]^{1/2}a$, respectively, where a is the lattice constant.

The modified total energy is minimized with respect to both u and a for each of the $\text{Hg}_{0.5}\text{Cd}_{0.5}\text{Te}$, $\text{Hg}_{0.5}\text{Zn}_{0.5}\text{Te}$, and $\text{Cd}_{0.5}\text{Zn}_{0.5}\text{Te}$ systems. *Ab initio* calculations are first performed for each system in exact analogy with those of Sec. II A. Empirical corrections are then added by assuming that the A-C, B-C, A-A, and B-B interactions in an $\text{A}_{0.5}\text{B}_{0.5}\text{C}$ alloy are well described by the same V_1 and V_2

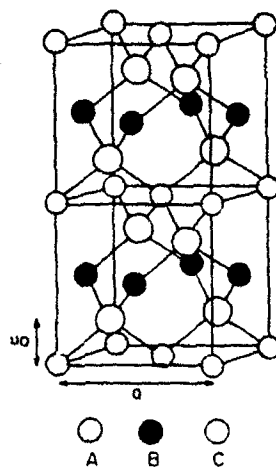


FIG. 1. Simple tetragonal structure assumed for an $\text{A}_{0.5}\text{B}_{0.5}\text{C}$ ordered alloy with lattice constant a . The parameter u is allowed to vary to accommodate a difference in A-C and B-C bond lengths.

parameters as in the limiting crystals. The only complication which arises concerns an A-B interaction, for which there is no crystalline counterpart. Here we assume that the appropriate V_2 parameter for this interaction is given by either an arithmetic or a geometric mean of the corresponding V_2 parameters for the A-A and B-B interactions. The two approximations will be seen in Sec. III B to lead to slightly different alloy mixing energies. The equilibrium bond lengths in the two cases are indistinguishable, however, since the cation-cation interaction plays no role in determining the equilibrium u value for a given lattice constant.

III. RESULTS AND DISCUSSION

A. Alloy structural properties

The calculated equilibrium lattice constants for $\text{Hg}_{0.5}\text{Cd}_{0.5}\text{Te}$, $\text{Hg}_{0.5}\text{Zn}_{0.5}\text{Te}$, and $\text{Cd}_{0.5}\text{Zn}_{0.5}\text{Te}$ are all found to be within 0.5% of the limiting crystal averages. This result is consistent with the nearly linear (Vegard's law) concentration dependencies observed in x-ray lattice constant measurements on $\text{Hg}_{1-x}\text{Cd}_x\text{Te}$,¹⁸ $\text{Hg}_{1-x}\text{Zn}_x\text{Te}$,²⁸ and $\text{Cd}_{1-x}\text{Zn}_x\text{Te}$.¹⁰

The predicted nearest-neighbor bond-length behavior is summarized in Fig. 2. The dashed lines represent the average variation $\bar{d}(x)$ expected for both bond types in an undistorted virtual lattice. The relaxed bond lengths calculated for the $x = 0.5$ ordered alloys are denoted by \times 's. In the corresponding random alloys, one expects a distribution of bond lengths due to variations in the local environment. We estimate the mean values in such systems (solid lines in Fig. 2) using a binomial distribution analysis similar to that of Ref. 4. The specific assumptions made are that (1) the A and B atoms in an $\text{A}_{1-x}\text{B}_x\text{C}$ system remain fixed on their fcc lattice sites, (2) the A-C bond length associated with a given nearest-neighbor environment of the C atom varies linearly with the number of B neighbors, (3) the A-C bond associated with a configuration of two A and two B nearest neighbors at $x = 0.5$ has the length $d_{\text{AC}}^{\text{ord}}$ calculated for the corresponding ordered alloy, and (4) the mean A-C bond length $d_{\text{AC}}^{\text{rand}}(x)$ varies linearly with x (as observed in EXAFS experiments). The resulting mean value at $x = 0.5$ is

$$d_{\text{AC}}^{\text{rand}}(0.5) = 3d_{\text{AC}}^{\text{ord}}/4 + \bar{d}(0.5)/4$$

The smaller relaxation compared to the ordered case is a consequence of the fact that, while the bond lengths relax coherently in the ordered systems, many of the local environments in the random alloys are more highly strained⁴ [e.g., the A-C bond length associated with a configuration of four A nearest neighbors in our model is always the virtual lattice value $\bar{d}(x)$].

The solid lines in Fig. 2 for $\text{Cd}_{1-x}\text{Zn}_x\text{Te}$ correspond to relaxation parameters of $\epsilon \approx 0.6$. This is in reasonable agreement with recent EXAFS experiments¹⁰ ($\epsilon \approx 0.75$) as well as with previous VF^{3,5} and tight-binding⁵ calculations. The slightly smaller relaxation predicted here may be an artifact of our assumed perfection of the cation sublattice.

Much more unusual behavior is found here for the two previously discussed systems. The anomalously large relaxation predicted for $\text{Hg}_{1-x}\text{Cd}_x\text{Te}$ ($\epsilon \approx 5.8$) supports the earlier tight-binding analysis of Ref. 8 ($\epsilon \approx 2$) and is in striking contrast to the predictions of VF models. The Hg-Te and Cd-Te bond lengths are found to differ by $\sim 2\%$ (0.05 Å) in this system, which should be easily resolvable in EXAFS experiments. By contrast, the relaxation predicted here for $\text{Hg}_{1-x}\text{Zn}_x\text{Te}$ ($\epsilon \approx 0.21$) is much smaller than that in previous VF^{3,5} and tight-binding⁵ calculations ($\epsilon > 0.70$). EXAFS results for this system would thus also be of interest.

We attribute the dramatic failure of VF predictions for $\text{Hg}_{1-x}\text{Cd}_x\text{Te}$ and $\text{Hg}_{1-x}\text{Zn}_x\text{Te}$ to the presence of an additional chemically induced force associated with a difference in cation electronegativities. Such a force has been discussed previously in the tight-binding analysis of Refs. 5 and 8 and shown to result from the difference in "metallic coupling" between the alloy and crystalline environments. The metallic coupling is defined as the interaction between a given bonding state and its neighboring antibonding states.²⁹ The fact that an A-C bonding state is coupled to some B-C antibonding states in an $\text{A}_{1-x}\text{B}_x\text{C}$ alloy produces a change in the effective A-C force constant. Relative to the virtual lattice structure, the presence of this effect generally drives a contraction of the less ionic bond in order to increase charge transfer from the less to the more electronegative cation. In the case of $\text{Hg}_{1-x}\text{Cd}_x\text{Te}$, Hg is more electronegative and the contraction of the Hg-Te bond results in a net Cd-Hg charge transfer, which is energetically favorable. The anomalous behavior in this system results from the unusual situation in which the limiting crystals have roughly the same bond length despite an appreciable difference in ionicities.³⁰ In systems which are poorly lattice matched (e.g., $\text{Hg}_{1-x}\text{Zn}_x\text{Te}$ and $\text{Cd}_{1-x}\text{Zn}_x\text{Te}$), the consequences of the chemical force are more difficult to predict due to additional complications associated with bond angle changes (e.g., rehybridization). The present calculations, which include these effects automatically, suggest that the chemical force has little effect on the resulting bond lengths in $\text{Cd}_{1-x}\text{Zn}_x\text{Te}$ but is responsible for the much smaller relaxation predicted here for $\text{Hg}_{1-x}\text{Zn}_x\text{Te}$ compared to previous VF estimates.

One final feature of Fig. 2 which is worth noting is the fact that the calculated bond lengths satisfy the transitivity relationship

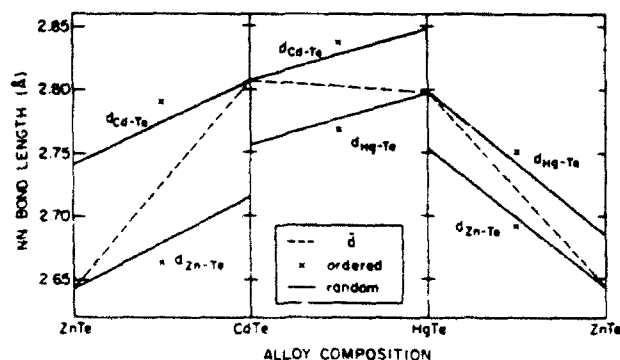


FIG. 2 Calculated nearest-neighbor (NN) bond lengths in ordered and random alloys compared to average behavior (\bar{d}) predicted for unrelaxed virtual lattice.

$$d_{\text{ZnTe}}[\text{CdTe:Zn}] + d_{\text{CdTe}}[\text{HgTe:Cd}] + d_{\text{HgTe}}[\text{ZnTe:Hg}] \\ = d_{\text{ZnTe}}^0 + d_{\text{CdTe}}^0 + d_{\text{HgTe}}^0$$

to within better than 0.2%. (This is equivalent to saying that the sum of the slopes of the solid lines in Fig. 2 is zero.) We are unable to provide a simple explanation for this behavior at this time but we note that simple VF estimates of impurity bond lengths in a wide variety of zinc-blende systems^{3,5} predict a similar relationship to hold in most common anion and common cation systems. Further EXAFS studies would be useful to test for such transitivity experimentally.

B. Alloy mixing energies

We conclude this paper by exploring some of the implications of the above bond-length calculations for the thermodynamic properties of $\text{Hg}_{1-x}\text{Cd}_x\text{Te}$, $\text{Hg}_{1-x}\text{Zn}_x\text{Te}$, and $\text{Cd}_{1-x}\text{Zn}_x\text{Te}$. The discussion is based on the total excess energies ΔE_0 of the $x = 0.5$ ordered alloys relative to their segregated crystals. Srivastava, Martins, and Zunger⁴ have recently shown that, contrary to previous expectations, the ΔE_0 's associated with various ordered phases of $\text{In}_{1-x}\text{Ga}_x\text{P}$ are actually negative which suggests that such phases may actually represent the stable low-temperature ground states of this system. Here we find a similar result for $\text{Hg}_{1-x}\text{Cd}_x\text{Te}$ but a much smaller tendency towards ordering in the two Zn alloys.

We proceed as in Ref. 4 by considering the formation of a relaxed $x = 0.5$ ordered alloy as a three-step process. In step one, the segregated crystals are appropriately expanded or contracted to the alloy lattice constant \bar{a} . This costs a valence distortion (VD) energy ΔE^{VD} which is always positive and is the only contribution considered in simple virtual lattice strain models of alloy mixing energies.³¹ Calculated values of ΔE^{VD} in the three systems considered here are listed in the top line of Table II. The negligible distortion energy in $\text{Hg}_{0.5}\text{Cd}_{0.5}\text{Te}$ is a consequence of the excellent lattice match in this system.

In the second step, the ordered alloy is formed with all atoms in their ideal tetrahedral locations ($u = 0.25$). The associated chemical energy contribution ΔE^{CE} results from a slight charge redistribution which occurs at this stage to smooth out any discontinuities in the charge densities at the

boundaries of the crystalline unit cells. ΔE^{CE} , in general, can be of either sign. Here we find negative values in each of the three systems in Table II with magnitudes which depend sensitively on the averaging procedure (arithmetic or geometric mean) used to treat the empirical repulsion between cation second neighbors.

In the final step, the individual nearest-neighbor bond lengths in the alloy are allowed to relax to their preferred equilibrium positions. This yields a structural energy contribution ΔE^{S} which is always negative. The magnitudes of ΔE^{S} are generally much larger than the predictions of simple VF models^{3,5} since the local distortions in the alloy are accompanied by the additional charge redistribution effects discussed in Sec. III A. The presence of these effects gives rise to a much larger $|\Delta E^{\text{S}}|$ value compared to $|\Delta E^{\text{VD}}|$ in $\text{Hg}_{0.5}\text{Cd}_{0.5}\text{Te}$ but is not sufficient to overcome the valence distortion energies in the Zn alloys.

The total excess energies in Table II are obtained by summing the ΔE^{VD} , ΔE^{CE} , and ΔE^{S} results. Despite the large uncertainties in these numbers, there does seem to be a much larger tendency towards ordering (negative ΔE_0) in the $\text{Hg}_{0.5}\text{Cd}_{0.5}\text{Te}$ system than in the two Zn alloys. Even in $\text{Hg}_{0.5}\text{Cd}_{0.5}\text{Te}$, however, the magnitude of ΔE_0 is probably too small to overcome entropy effects at typical growth temperatures. [It is important to note that, while the smaller ΔE_0 value in $\text{Hg}_{0.5}\text{Cd}_{0.5}\text{Te}$ compared to $\text{Hg}_{0.5}\text{Zn}_{0.5}\text{Te}$ means that the former *ordered* alloy is more "stable" in the technical sense, the present results provide no direct information on individual bond strengths in the two systems. The tight-binding prediction⁸ that the weak Hg-Te bond (cf. E_{coh} values in Table I) may be somewhat stronger in $\text{Hg}_{1-x}\text{Zn}_x\text{Te}$ than in $\text{Hg}_{1-x}\text{Cd}_x\text{Te}$ is thus not contradicted by our results.]

The bottom line of Table II lists experimentally determined enthalpies of formation ΔH_D for *disordered* $\text{Cd}_{1-x}\text{Zn}_x\text{Te}$, $\text{Hg}_{1-x}\text{Cd}_x\text{Te}$, and $\text{Hg}_{1-x}\text{Zn}_x\text{Te}$ alloys.³² Like ΔE_0 , ΔH_D is also found to be smallest in magnitude in $\text{Hg}_{1-x}\text{Cd}_x\text{Te}$, although its sign is positive. A possible origin of the positive ΔH_D value in $\text{Hg}_{1-x}\text{Cd}_x\text{Te}$ has recently been proposed in terms of the Coulomb energy associated with charge fluctuations in a disordered ionic system.³³ The present bond-length results suggest an additional contribu-

TABLE II. Contributions to the total excess energies ΔE_0 of the $x = 0.5$ ordered alloys. The valence distortion energies (ΔE^{VD}), chemical energies (ΔE^{CE}), and structural energies (ΔE^{S}) are defined in the text. Results are presented for both the arithmetic mean (a.m.) and geometric mean (g.m.) treatments of the empirical repulsion between unlike cation second neighbors. The final line gives the experimentally determined enthalpies of formation ΔH_D of the corresponding *disordered* alloys. All energies are in eV/(zinc-blende cell).

	$\text{Cd}_{0.5}\text{Zn}_{0.5}\text{Te}$	$\text{Hg}_{0.5}\text{Cd}_{0.5}\text{Te}$	$\text{Hg}_{0.5}\text{Zn}_{0.5}\text{Te}$
ΔE^{VD}	+ 0.075	+ 0.0002	+ 0.071
ΔE^{CE} (a.m.)	- 0.001	- 0.002	- 0.003
(g.m.)	- 0.009	- 0.034	- 0.085
ΔE^{S}	- 0.047	- 0.012	- 0.013
ΔE_0 (a.m.)	+ 0.027	- 0.014	+ 0.055
(g.m.)	+ 0.019	- 0.046	- 0.027
ΔH_D (expt)	+ 0.014	+ 0.007, + 0.015	+ 0.032

tion in terms of the strain associated with different local environments in the disordered alloy. This effect is believed to be the dominant source of the positive ΔH_D values in poorly lattice-matched systems⁴ (e.g., $\text{Cd}_{1-x}\text{Zn}_x\text{Te}$ and $\text{Hg}_{1-x}\text{Zn}_x\text{Te}$) but has previously been assumed to be negligible in $\text{Hg}_{1-x}\text{Cd}_x\text{Te}$. The fact that it may not be also suggests that deviations from randomness^{4,6} in $\text{Hg}_{1-x}\text{Cd}_x\text{Te}$ may also be larger than expected.

ACKNOWLEDGMENTS

This work was supported in part by the Defense Advanced Research Projects Agency (through ONR Contract No. N00014-86-K-0033), the Joint Services Electronics Program (N00014-84-K-0465), and the National Science Foundation (DMR-85-14638).

Conference on the Physics of Semiconductors, edited by O. Engstrom (World Scientific, Singapore, 1987), p. 1181.

¹⁵See, M. L. Cohen, Phys. Scr. T 1, 5 (1982), for a review.

¹⁶P. Boguslawski and A. Baldereschi, in *Proceedings of the 17th International Conference on the Physics of Semiconductors*, edited by D. J. Chadi and W. A. Harrison (Springer, New York, 1984), p. 939.

¹⁷N. J. Shevchik, T. Tejeda, M. Cardona, and D. W. Langer, Phys. Status Solidi B 59, 87 (1973).

¹⁸D. Vanderbilt, Phys. Rev. B 32, 8412 (1985).

¹⁹D. R. Hamann, M. Schluter, and C. Chiang, Phys. Rev. Lett. 43, 1494 (1979).

²⁰R. Dornhaus and G. Nuntz, in *Solid State Physics*, Vol. 78 of Springer Tracts in Modern Physics, edited by G. Hohler (Springer, Berlin, 1976), p. 1.

²¹G. B. Bachelet and M. Schluter, Phys. Rev. B 25, 2103 (1982).

²²J. Ihm, A. Zunger, and M. L. Cohen, J. Phys. C 12, 4409 (1979).

²³L. Hedin and B. I. Lundqvist, J. Phys. C 4, 2064 (1971).

²⁴D. J. Chadi and M. L. Cohen, Phys. Rev. B 8, 5747 (1973).

²⁵K. J. Chang and M. L. Cohen, Ref. 14, p. 1151.

²⁶R. Landolt-Bornstein, *Numerical Data and Functional Relationships in Science and Technology*, Vol. 18 in *Crystal and Solid State Physics* (Springer, Berlin, 1984).

²⁷N. A. Cade and P. M. Lee, Solid State Commun. 56, 637 (1985).

²⁸N. E. Christensen and O. B. Christensen, Phys. Rev. B 33, 4739 (1986).

²⁹S. H. Wei and A. Zunger, Phys. Rev. B 35, 2340 (1987).

³⁰A. Sher, D. Eger, A. Zemel, H. Feldstein, and A. Raizman, J. Vac. Sci. Technol. A 4, 2024 (1986).

³¹W. A. Harrison, *Electronic Structure and the Properties of Solids* (Freeman, San Francisco, 1980).

³²One measure of ionicity in zinc-blende crystals is the maximum charge density along the bonding direction. Here we find maxima of 30.02 in ZnTe, 34.59 in HgTe, and 35.14 in CdTe in units of electrons/cell.

³³P. A. Fedders and M. W. Muller, J. Phys. Chem. Solids 45, 685 (1984).

³⁴M. B. Panish and M. Ilegems, Prog. Solid State Chem. 7, 39 (1972); A. Langier, Rev. Phys. Appl. 8, 2959 (1973); G. B. Stringfellow, J. Cryst. Growth 27, 21 (1974); 58, 194 (1982).

³⁵M. van Schilfgaarde, A. Sher, and A. B. Chen, Phys. Rev. Lett. 57, 1149 (1986).

¹A. Zunger and J. E. Jaffe, Phys. Rev. Lett. 51, 662 (1983).

²K. C. Hass, R. J. Lempert, and H. Ehrenreich, Phys. Rev. Lett. 52, 77 (1984).

³J. L. Martins and A. Zunger, Phys. Rev. B 30, 6217 (1984).

⁴G. P. Srivastava, J. L. Martins, and A. Zunger, Phys. Rev. B 31, 2561 (1985).

⁵A. B. Chen and A. Sher, Phys. Rev. B 32, 3695 (1985).

⁶A. Sher, A. B. Chen, and M. van Schilfgaarde, J. Vac. Sci. Technol. A 4, 1965 (1986).

⁷H. Ehrenreich and J. P. Hirth, Appl. Phys. Lett. 46, 668 (1985).

⁸A. Sher, A. B. Chen, W. E. Spicer, and C. K. Shih, J. Vac. Sci. Technol. A 3, 105 (1985).

⁹J. C. Mikkelsen, Jr. and J. B. Boyce, Phys. Rev. Lett. 49, 1412 (1982).

¹⁰N. Motta, A. Balzarotti, P. Letardi, A. Kisiel, M. T. Czyzyk, M. Zinnal-Starnawska, and M. Podgorny, Solid State Commun. 53, 509 (1985).

¹¹B. A. Bunker, J. Vac. Sci. Technol. A 5, 3003 (1987) (this issue).

¹²K. C. Hass and D. Vanderbilt, in *Proceedings of the 18th International*

EFFECTIVE MASSES AND OPTICAL MATRIX
ELEMENTS IN SEMICONDUCTOR SUPERLATTICESN. F. Johnson and H. Ehrenreich
Division of Applied Sciences and Physics Department
Harvard University, Cambridge, Massachusetts 02138K. C. Hass
Research Staff, Ford Motor Company
Dearborn, Michigan 48121-2053

(Received 16 August 1987)

A novel analytic approach for calculating superlattice effective masses both perpendicular and parallel to the layer planes is summarized. The approach is based on the crystalline oscillator strength ("f-") sum rule and the envelope function approximation. Applications to GaAs/Ga_{1-x}Al_xAs and HgTe/CdTe yield excellent agreement with experiment for a conduction : valence band offset ratio of 70:30 and a valence band offset near zero, respectively.

A periodic superlattice (SL) containing an arbitrary number of constituents may be conveniently viewed as a crystalline solid having a large unit cell. While any bulk band structure technique is thus directly applicable to SL's, most realistic calculations are limited in practice either to relatively thin-layered systems¹ or to the dispersion only along the growth direction.² Recently, we presented a novel analytic approach for the calculation of SL effective masses which is valid for arbitrary directions and layer thicknesses in any system composed entirely of direct gap materials.³ The present note briefly summarizes the key ingredients of this method and its predictions for the GaAs/Ga_{1-x}Al_xAs and HgTe/CdTe systems. A more complete description of this work will be given elsewhere.

The approach is based on the well known *f*-sum rule relationship between effective masses and optical oscillator strengths. For a SL characterized by eigenstates $|L, \vec{K}\rangle$ and energies $E_L(\vec{K})$, where L and \vec{K} are the SL band index and wavevector, respectively, this relationship takes the form

$$\left(\frac{m}{m_a}\right)_L = 1 + \sum_{L' \neq L} \frac{2}{m} \frac{|(L, 0 | p_a | L', 0)|^2}{E_L(0) - E_{L'}(0)} \quad (1)$$

Here p_a is the momentum operator component either perpendicular ($a = \perp$) or parallel ($a = \parallel$) to the layer planes and $(m_a/m)_L$ is the corresponding $\vec{K} = 0$ effective mass of SL band L in units of the electron mass m . The quantities summed in Eq. (1) represent the oscillator strengths associated with optical transitions between SL states $|L, 0\rangle$ and $|L', 0\rangle$. Analytic solutions for the $|L, 0\rangle$'s and $E_L(0)$'s are easily obtained in terms of bulk band structure parameters using the Kane $\vec{k} \cdot \vec{p}$ model⁴ (including finite spin-orbit splitting) and the envelope function approximation;^{2,5} the treatment of band discontinuities and the boundary conditions are equivalent to those of Ref. 5. The relevant momentum matrix elements then reduce to integrals over the

envelope functions and their spatial derivatives. These integrals may also be evaluated analytically since the envelope functions themselves are simply trigonometric functions within each layer.

The sum in Eq. (1) is found to be dominated by only a small number of SL states whose energies lie well within the range which is adequately described by the Kane model. The use of only $\vec{K} = 0$ information allows m_{\parallel} to be calculated as easily as m_{\perp} without any of the previously reported difficulties² associated with the coupling of SL light and heavy hole bands for finite \vec{K} values parallel to the planes.

Values of both electron effective masses for an 80A GaAs/20A Ga_{1-x}Al_xAs SL were obtained in Ref. 3 using standard bulk parameters⁴ and a conduction : valence band offset ratio⁶ of 70:30. The results agree well with recent cyclotron resonance measurements⁷ and with previous theoretical calculations⁸ of m_{\perp} . The two masses start out at the same bulk GaAs value of 0.067 m for $x=0$ and increase to $m_{\perp}/m = 0.114$ and $m_{\parallel}/m = 0.070$ for $x = 0.3$. The relatively small increase in m_{\parallel} follows a slight increase in the SL band gap which results from the increasing barrier height in the Ga_{1-x}Al_xAs layers. The perpendicular mass, by contrast, is much more sensitive to the barriers; for thick Ga_{1-x}Al_xAs layers, $m_{\perp} \rightarrow \infty$. In terms of oscillator strengths, the difference between m_{\perp} and m_{\parallel} results primarily from the coupling between the conduction band minimum and the next highest $\vec{K} = 0$ conduction state which lies $\lesssim 160$ meV higher due to zone-folding. This transition has an appreciable oscillator strength only for the perpendicular direction⁹ where it makes a significant negative contribution to the sum in Eq. (1).

The *f*-sum rule approach has also been applied to HgTe/CdTe SL's using the bulk parameters of Ref. 9. While the appropriate value of the valence band offset A (defined to be positive if the valence band maximum of HgTe lies above that of CdTe) remains controversial,¹⁰ the calculated electron m_{\parallel} values in

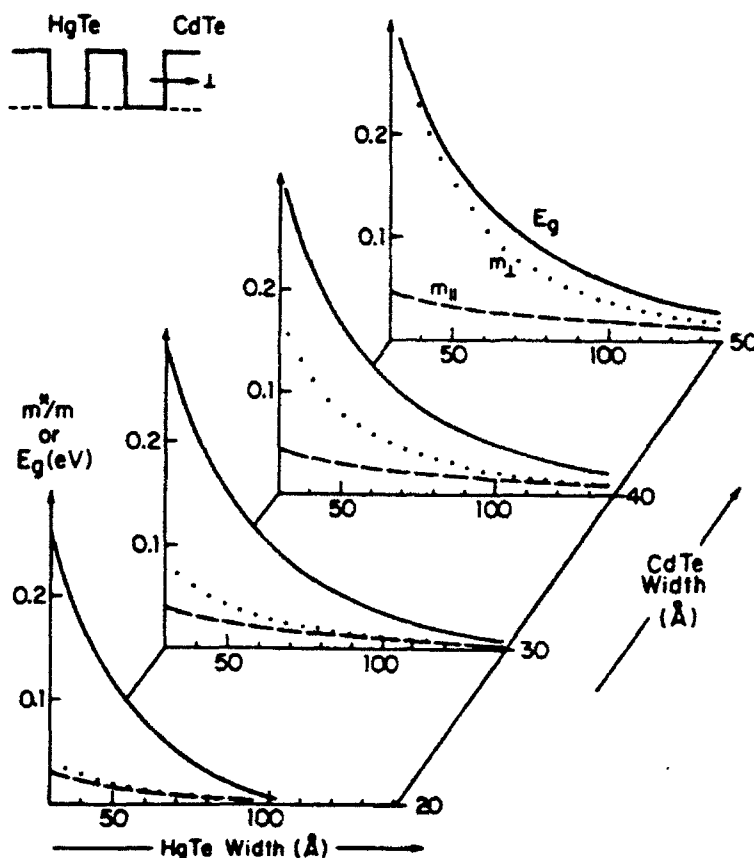


Fig. 1 Calculated variations of the superlattice electron effective masses m_{\perp} (dotted) and m_{\parallel} (dashed) and band gap E_g (solid) as functions of layer widths in the HgTe/CdTe system. The inset shows the

assumed alignment of the bulk conduction (solid) and valence (dashed) band edges (zero valence band offset).

Ref. 3 were found to be consistent with experimental magneto-absorption measurements¹¹ only if $\Delta \approx 0$. Theoretical predictions for m_{\perp} , m_{\parallel} and the SL energy gap E_g for $\Delta = 0$ are shown in Fig. 1 as a function of HgTe layer width for a series of CdTe widths. The results are consistent with previous theoretical calculations^{2,12} and with available experimental values^{11,13} of m_{\parallel} (for slightly different CdTe widths). The increase in E_g with decreasing HgTe width reflects the quantum confinement of the lowest SL conduction state. Both m_{\perp} and m_{\parallel} also increase monotonically in this direction in Fig. 1 although neither is, in general, proportional to E_g . For thin CdTe layers (e.g. 20 Å), $m_{\parallel} \approx m_{\perp}$ and both masses are within 10% of the value which would be obtained in a $\text{Hg}_{1-x}\text{Cd}_x\text{Te}$ alloy of equivalent composition. The perpendicular mass is extremely sensitive to the CdTe (barrier) width and increases by more than a factor of four from 20 Å CdTe to 50 Å CdTe widths for SL's whose HgTe width is allowed to vary slightly to fix E_g at 0.1 eV. This ability to tailor m_{\perp} independently of E_g has previously been suggested as a means of controlling reverse currents in HgTe/CdTe infrared detectors.¹⁴

Acknowledgements—We are indebted to T. C. McGill for his collaboration on Ref. 3. This work was supported by JSEP (through ONR contract N00014-84-K-0465) and DARPA (through ONR contracts N00014-86-K-0033 and N00014-86-K-0760).

REFERENCES

1. e.g. W. Andreoni and R. Car, *Physical Review B* **21**, 3334 (1980).
2. G. Bastard, *Physical Review B* **25**, 7584 (1982).
3. N. F. Johnson, H. Ehrenreich, K. C. Hass and T. C. McGill, *unpublished*.
4. E. O. Kane, in *Narrow Gap Semiconductors: Physics and Applications*, edited by W. Zawadzki (Springer-Verlag, New York, 1979) p. 13.
5. G. Bastard, in *Proceedings of the NATO Advanced Study Institute on Molecular Beam Epitaxy and Heterostructures*, edited by L. L. Chang and K. Ploog (Nijhoff, Dordrecht, 1985) p. 381.

- tenendes, A. Pinczuk, D. J. Werder, A. C. Goel and J. H. English, *Physical Review B* **33**, 3 (1986).
- Duffield, R. Bhat, M. Koza, F. DeRosa, D. M. ang, P. Grabbe and S. J. Allen, *Physical Review* **56**, 2724 (1986).
- Experimental evidence for an appreciable opticalillator strength has been obtained by J. West and S. J. English, *Applied Physics Letters* **46**, 1156 (1985).
- ong, in *Energy Bands in Semiconductors* (Wiley, New York, 1968).
10. e.g. C. K. Shih and W. E. Spicer, *Physical Review Letters* **58**, 2594 (1987) and references therein.
 11. J. M. Berroir, Y. Guldner, J. P. Vieren, M. Voos and J. P. Faurie, *Physical Review B* **34**, 891 (1986).
 12. J. N. Schulman and Y. C. Chang, *Physical Review B* **33**, 2594 (1986).
 13. Y. Guldner, G. Bastard, J. P. Vieren, M. Voos, J. P. Faurie and A. Million, *Physical Review Letters* **51**, 907 (1983).
 14. D. L. Smith, T. C. McGill and J. N. Schulman, *Applied Physics Letters* **43**, 180 (1983).

***f*-Sum Rule and Effective Masses in Superlattices**N. F. Johnson, H. Ehrenreich, and K. C. Hass^(a)*Division of Applied Sciences and Physics Department, Harvard University, Cambridge, Massachusetts 02138*

and

T. C. McGill

T. J. Watson, Sr., Laboratory of Applied Physics, California Institute of Technology, Pasadena, California 91125

(Received 29 June 1987)

The *f*-sum rule, relating effective masses to oscillator strengths, is extended to semiconducting superlattices and applied to GaAs-(Ga,Al)As and HgTe-CdTe. This novel approach is implemented analytically by use of the envelope-function approximation to calculate both parallel and perpendicular masses and is used to account for their difference physically. Agreement with experiment is excellent, but in HgTe-CdTe only if the valence-band offset is small.

PACS numbers: 73.20.Dx, 73.40.Kp, 73.40.Lq

The *f*-sum rule has been extremely useful for the extraction of a wide range of physical information pertaining to condensed matter. As shown here, this is equally true for superlattices, in particular, GaAs-(Ga,Al)As and HgTe-CdTe. Specifically, we (1) relate the parameters in the formal, exact expression for the *f*-sum rule to those of the bulk constituents using the envelope-function approximation¹; (2) obtain oscillator strengths relevant to optical absorption and show that only a small number of superlattice (SL) bands contribute to the sum; (3) derive values of both m_{\parallel} and m_{\perp} (the effective masses in the plane of the SL and along the growth or *z* axis, respectively) simultaneously and show that they compare well with experimental information; (4) comment on band-offset values that yield effective masses consistent with cyclotron resonance experiments. It should be emphasized that these results can all be obtained from physically transparent, analytic expressions without extensive numerical computation.

For superlattices characterized by eigenstates $|L, K\rangle$ and energies $E_L(K)$, where K and L are the SL wave vector and band index, respectively, the *f*-sum rule takes the form

$$(m/m_L)_\alpha = 1 + \sum_L f_{L'L}^\alpha, \quad (1)$$

where

$$f_{L'L}^\alpha = \frac{2}{m} \frac{|\langle L, 0 | p_\alpha | L', 0 \rangle|^2}{E_L(0) - E_{L'}(0)}$$

is the oscillator strength. The valence- and conduction-band extrema are assumed to be at $K=0$. p_α is the momentum operator component along the principal axis α ($\alpha=z$ or \perp for the growth axis and x, y , or \parallel within the layers, respectively), and $(m_L/m)_\alpha$ is the corresponding effective mass in units of the electron mass m .

Equation (1) is exact as it stands. Here we evaluate the relevant SL quantities analytically in terms of bulk electronic structure parameters using the envelope-function approximation.¹ The envelope function $F_n(L, K; r)$ is defined by the coefficients of the expansion of $\langle r | L, K \rangle$ in terms of bulk Bloch functions $\langle r | n \rangle$ for band n at $k=0$. $F_n(L, K; r)$ varies slowly with r on the scale of the unit-cell size. For the well-lattice-matched SL's considered here, $\langle r | n \rangle$ may be assumed the same in each constituent. This easily generalizable assumption is justified here by the similarity of the bulk pseudopotentials and momentum matrix elements.²

For the energy region of interest here, the envelope function may be calculated with the Kane model including finite spin-orbit coupling.³ A finite heavy-hole mass is obtained by the inclusion of the next higher conduction band by perturbation theory. The function $F(L, K; r)$ with components $F_n(L, K; r)$ in an A (B) layer is determined from

$$H_{A(B)}[k_x, k_y, k_z \rightarrow -i(\partial/\partial z)]F(L, K; r) = E_L(K)F(L, K; r),$$

where $H_{A(B)}$ is the 8×8 Hamiltonian matrix.³ For $K=(0,0,K_z)$ only bulk states with the same m_J mix, where J is the total angular momentum, and each F_n becomes independent of x and y . These simplifications¹ do not occur for $K=(K_x, 0, 0)$ since the bulk states being mixed correspond to $\Delta m_J = \pm 1, 0$. Both effective masses m_{\perp} and m_{\parallel} can be calculated from the *f*-sum rule if $F(L, 0; z)$ is known. The involvement of only $K=0$ states reduces the number of coupled differential equations,¹ thereby permitting an analytical solution to the problem for arbitrary direction. The boundary conditions used are equivalent to those of Bastard and Mailhot and co-workers.³⁻⁵

The relevant matrix elements are given by

$$\langle L, 0 | p_z | L', 0 \rangle = \sum_{nn'} [P_{nn'}^z a_{nn'} \langle L, L' \rangle + \delta_{nn'} \pi_n(L, L')], \quad \langle L, 0 | p_x | L', 0 \rangle = \sum_{nn'} P_{nn'}^x a_{nn'} \langle L, L' \rangle, \quad (2)$$




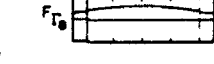
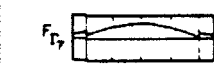
$E_{L',0} (eV)$	L'	Envelope Functions	$f_{L',C1}^{\perp} (\Sigma f^{\perp})$	$f_{L',C1}^{\parallel} (\Sigma f^{\parallel})$
1.72	C2		-0.17	~ 0
1.56	C1		-4.89	~ 0
			— (CB -5.06)	— (CB 0.00)
-0.006	HH1		0	6.85
-0.017	LH1		8.90	2.48
	LH2 → LH5		0.60	0.43
	HH2 → HH7		0	0.27
-0.36	LH16		3.36	3.35
	Lower Bands		~ 0 (VB 12.86)	~ 0 (VB 13.38)
			$m_{\perp}/m = 0.114$	$m_{\parallel}/m = 0.070$

FIG. 1. Contributions to f -sum rule for 80-Å GaAs, 20-Å $\text{Ga}_{0.7}\text{Al}_{0.3}\text{As}$ superlattice. Envelope functions shown for important superlattice $K=0$ states $|L',0\rangle$ at energies $E_{L',0}$. Partial sums of oscillator strengths over superlattice conduction and valence bands (CB and VB) in parentheses. Masses calculated from Eq. (1).

where $P_{nn'}^* = \langle n | p_x | n' \rangle$ is the bulk momentum matrix element, and

$$a_{nn'}(L, L') = d^{-1} \left[\int_{-l_A/2}^{l_A/2} + \int_{l_A/2}^{l_A/2+l_B} \right] dz F_n^*(L, 0; z) F_{n'}(L', 0; z), \quad (3)$$

$$\pi_n(L, L') = (\hbar/i) d^{-1} \left[\int_{-l_A/2}^{l_A/2} + \int_{l_A/2}^{l_A/2+l_B} \right] dz F_n^*(L, 0; z) (\partial/\partial z) F_n(L', 0; z).$$

Here l_A (l_B) is the A (B) layer width and $d = l_A + l_B$ is the superlattice period. The F_n 's are trigonometric functions within each layer; the integrations are therefore straightforward.

Figure 1 shows the dominant F 's for an 80-Å GaAs, 20-Å $\text{Ga}_{0.7}\text{Al}_{0.3}\text{As}$ SL over an energy range $-0.36 < E_{L',0} < 1.72$ eV. The condition-band-valence-band offset ratio is taken to be 70:30,⁶ and standard bulk input parameters are employed.² The large number of SL valence bands are associated with the zone-folding due to the smaller SL Brillouin zone. The few $|L',0\rangle$'s of primary importance to the f -sum rule, whose F 's are sketched in Fig. 1, have substantially the atomic symmetry of the bulk bands from which they originate, although small admixtures of other bands included in the Kane model are present. This behavior is associated with the small curvature of the F 's (for a bulk crystal they would be constant). The closely spaced SL conduction-band states $|C1,0\rangle$ and $|C2,0\rangle$ have F 's resembling the ground and first excited states of standing waves in a box. Even though they derive primarily from the same bulk symmetry Γ_6 , they can have nonvanishing momentum or optical matrix elements coupling them because of the crystal momentum supplied by the barriers.

Values for the electron masses m_{\perp} and m_{\parallel} may be cal-

culated with the oscillator strengths shown in Fig. 1. The results are shown in Fig. 2 as functions of Al concentration x for the layer widths used in Fig. 1 and compared to the $T=75$ K experimental cyclotron resonance values of Duffield *et al.*⁷ As expected, the m_{\perp} value increases with x , i.e., with the barrier height separating the GaAs layers, and agrees well with that obtained by differentiation of the dispersion relation derived in Ref. 3. By contrast, m_{\parallel} is nearly proportional to the band gap, also shown in Fig. 2, much as in bulk GaAs. The agreement between theory and experiment, although excellent, could be improved by the addition of temperature corrections to the $T=0$ K theoretical results.

It is clear that $m_{\perp} > m_{\parallel}$ because of the barriers. A more subtle explanation of this inequality is provided by consideration of the oscillator strengths $f_{L',C1}^{\perp}$ and their sums, as shown in Fig. 1. We note first that the principal contributions to the f -sum rule determining m_{\perp} and m_{\parallel} come from SL states near the GaAs bulk Γ_6 , Γ_7 , and Γ_8 levels. The total valence-band contributions to m_{\perp} and m_{\parallel} obtained by summation of $f_{L',C1}^{\perp}$ and $f_{L',C1}^{\parallel}$, respectively, are the same and are nearly to the bulk value. Individual f 's differ, however, just as in the bulk Kane model where the z direction is given special significance.

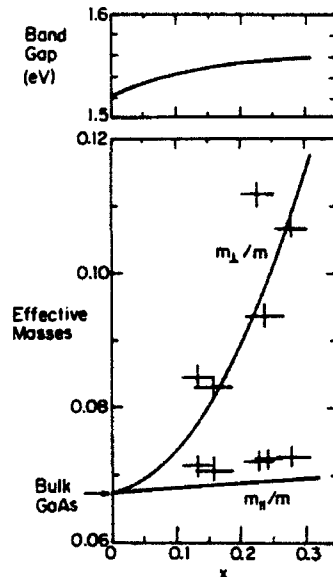


FIG. 2. Comparison of experimental (crosses, Ref. 7) and theoretical (solid lines) values of electron masses for 80-Å GaAs, 20-Å $\text{Ga}_{1-x}\text{Al}_x\text{As}$ superlattice. Top: theoretical superlattice band gap.

The difference between Σf^+ and Σf^+ is seen to arise from the negative contribution of C2 to Σf^+ , which has no analog in the bulk band structure. The $\langle C1,0 | p_z | C2,0 \rangle$ matrix element, while smaller than typical bulk values, gives rise to an appreciable oscillator strength because of the energy proximity of C1 and C2.

Results for HgTe-CdTe are obtained with standard bulk parameters² and a variable valence-band offset Λ (defined to be positive if the Γ_8 level of HgTe lies above that of CdTe). Values of m_{\perp}/m and m_{\parallel}/m calculated for the controversial common-anion-rule value $\Lambda = 0$ are plotted in Fig. 3 as functions of HgTe layer width (l_A) for a series of CdTe widths (l_B). The behavior of the SL band gap E_g is shown for a single representative CdTe width of 50 Å. For thick CdTe widths, E_g corresponds physically to the kinetic energy of confinement in the HgTe quantum well. E_g increases with decreasing l_A as expected. For narrow CdTe widths (e.g., $l_B = 20$ Å), for which the extent of the F 's is greater than l_B , the SL case can be shown to be substantially equivalent to that of the alloy $\text{Hg}_{1-x}\text{Cd}_x\text{Te}$ ($x = l_B/d$) and $m_{\parallel} \approx m_{\text{alloy}}$ to better than 10%.

The remarkable peak in m_{\perp} as a function of HgTe thickness for fixed CdTe width (e.g., $l_B = 50$ Å) can be explained by reference to the inset in Fig. 3 showing the complex band structure of bulk CdTe near $k=0$. Note that the SL gap $E_g(\text{SL})$ lies inside the CdTe gap $E_g(\text{CdTe})$. The imaginary wave vector κ , which characterizes the decay length of F in the CdTe barriers, increases as $E_g(\text{SL})$ becomes larger and causes F to decay

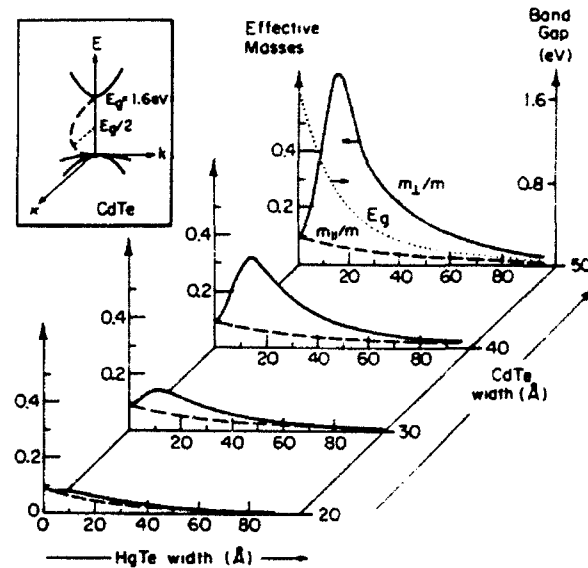


FIG. 3. Variation of effective masses as functions of layer widths in HgTe-CdTe superlattice. The superlattice band-gap behavior corresponds to 50-Å CdTe. Inset: Schematic complex band structure of bulk CdTe near $k=0$.

more rapidly. This effect is most pronounced when the SL gap is $\frac{1}{2} E_g(\text{CdTe})$, i.e., at $E_g(\text{SL}) = 0.8$ eV. Figure 3 shows the peak in m_{\perp} to occur at that energy. For l_A values smaller than that for which the peak occurs, m_{\perp} decreases and approaches the CdTe value as l_A approaches zero. Values of m_{\perp} are within 5% of those obtainable from the dispersion relation of Ref. 3.

Magnetoabsorption measurements of Berroir *et al.*⁸ for a 100-Å HgTe, 36-Å CdTe SL have yielded $m_{\parallel}/m = 0.017 \pm 0.003$. The present theoretical results for a positive band offset Λ (in electronvolts) can be empirically represented by $m_{\parallel}/m = 0.014 - 0.046\Lambda$. Good agreement with experiment is thereby achieved for small Λ but not for the value $\Lambda \approx 0.36$ eV suggested by recent photoemission experiments.⁹ We are not suggesting that any of these experiments is flawed; neither is it likely that the results of $k \cdot p$ calculations can be seriously in error. (Large band offsets, however, have been obtained from first-principles band calculations,¹⁰ which do not address effective mass values.) These inconsistencies pose an interesting dilemma which remains unresolved.¹¹

This work was supported by the Joint Services Electronics Program through U. S. Office of Naval Research (ONR) Contract No. N00014-84-K-0465, and by the Defense Advanced Research Projects Agency through ONR Contracts No. N00014-86-K-0033, No. N00014-86-K-0760, and No. N00014-86-K-0841.

(*)Present address: Research Staff, Ford Motor Co., Dear-

born MI 48121.

¹G. Bastard, Phys. Rev. B **25**, 7584 (1982).

²E. O. Kane, in *Narrow Gap Semiconductors: Physics and Applications*, edited by W. Zawadzki, Lecture Notes in Physics Vol. 133 (Springer-Verlag, New York, 1981), p. 19; D. Long, *Energy Bands in Semiconductors* (Wiley, New York, 1968), p. 195. The Kane momentum matrix energy (E_p) is taken as 18 eV for HgTe and CdTe, and 24 eV for (Ga,Al)As.

³G. Bastard, in *Proceedings of the NATO Advanced Study Institute on Molecular Beam Epitaxy in Heterostructures, Erice, Italy, 1983*, edited by L. L. Chang and K. Ploog (Martinus-Nijhoff, Dordrecht, 1984), p. 381.

⁴C. Mailhot, T. C. McGill, and D. L. Smith, J. Vac. Sci. Technol. B **2**, 371 (1984); D. L. Smith and C. Mailhot, Phys. Rev. B **33**, 8345 (1986).

⁵The results for $f_{L'L}^*$ are insensitive to the addition of a smoothing function guaranteeing continuity at the cell boundary.

⁶See, for example, J. Menendez, A. Pinczuk, D. J. Werder, A. C. Gossard, and J. H. English, Phys. Rev. B **33**, 8863 (1986).

⁷T. Duffield, R. Bhat, M. Koza, F. DeRosa, D. M. Hwang, P. Grabbe, and S. J. Allen, Phys. Rev. Lett. **56**, 2724 (1986).

⁸J. M. Berroir, Y. Guldner, J. P. Vieren, M. Voos, and J. P. Faurie, Phys. Rev. B **34**, 891 (1986).

⁹S. P. Kowalczyk, J. T. Cheung, E. A. Kraut, and R. W. Grant, Phys. Rev. Lett. **56**, 1605 (1986); T. M. Duc, C. Hsu, and J. P. Faurie, Phys. Rev. Lett. **58**, 1127 (1987); C. K. Shih and W. E. Spicer, Phys. Rev. Lett. **58**, 2594 (1987).

¹⁰See, for example, S. H. Wei and A. Zunger, Phys. Rev. Lett. **59**, 144 (1987), and references therein.

¹¹Note that while the recent empirical pseudopotential calculations of M. Jaros, A. Zoryk, and D. Ninno, Phys. Rev. B **35**, 8277 (1987), for $\Lambda=0.37$ eV claim consistency with experimental SL band gaps, we find that the present $k \cdot p$ model, in fact, yields much better agreement, particularly for small Λ .

Theory of exchange interactions and chemical trends in diluted magnetic semiconductors

B. E. Larson,* K. C. Hass,[†] and H. Ehrenreich

Division of Applied Sciences and Physics Department, Harvard University, Cambridge, Massachusetts 02138

A. E. Carlsson

Physics Department, Washington University in Saint Louis, Saint Louis, Missouri 63130

(Received 15 July 1987)

The electronic structure and magnetic properties of Mn-substituted II-VI diluted magnetic semiconductors are treated theoretically with emphasis on $\text{Cd}_{1-x}\text{Mn}_x\text{Te}$. The derived electronic structure is based on a combination of *ab initio* spin-polarized band calculations, a semiempirical tight-binding model containing the relevant experimental input, and consideration of alloying effects. The magnetic properties are calculated using a multisite Anderson Hamiltonian incorporating the derived electronic structure. The derived *sp*-band-Mn-*d* and Mn-Mn exchange constants compare as well with experiment as any previous calculations of this kind. The results establish the importance of *sp*-*d* hybridization and demonstrate superexchange as the dominant Mn-Mn exchange mechanism. A phenomenological three-level model for superexchange is constructed, which gives results in excellent agreement with the detailed calculations, provides physical insight, and permits exploration of chemical trends in the magnetic behavior for the series $M_{1-x}^{II}\text{Mn}_xX^{VI}$ ($M^{II}=\text{Cd}$ or Zn ; $X^{VI}=\text{Te}$, Se , or S). The same model, with minor modification, is found to be applicable to MnO and $\alpha\text{-MnS}$, which are insulating and have the rocksalt structure.

I. INTRODUCTION

This paper presents a comprehensive treatment of the electronic structure and magnetic properties of the Mn-substituted II-VI class of diluted magnetic semiconductors (DMS's).¹ The discussion of the electronic structure is based on a combination of *ab initio* band calculations, a semiempirical tight-binding model (ETBM) based on these results, carefully referenced relevant experimental input, and consideration of effects associated with alloying. The resulting electronic structure model is therefore consistent with currently available experimental and theoretical evidence and represents a suitable starting point for the formulation of a model Hamiltonian useful for calculating magnetic properties.

The magnetic properties to be considered here are Mn-(*sp*-band) exchange and Mn-Mn exchange. The results establish the importance of *p*-*d* hybridization and demonstrate superexchange as the dominant Mn-Mn exchange mechanism.² Related calculations of exchange anisotropy and spin-resonance linewidths will be discussed in a subsequent publication.³ Some of the present results have been briefly reported previously.^{4,5}

The first picture of the DMS electronic structure emerged from the empirical-tight-binding-method-coherent-potential-approximation (ETBM-CPA) calculations of Hass and Ehrenreich.⁶ These calculations emphasized the effect of chemical disorder on the *s* and *p* levels. The occupied Mn 3*d* states were included much in the same way as in the combined interpolation scheme⁷ for the transition metals and exhibited strong hybridization with the anion derived *p* states.

The results to be described here are based on self-consistent augmented-spherical-wave (ASW) band calculations⁸ utilizing the local-spin-density approximation⁹

(LSDA) for a hypothetical zinc-blende MnTe compound. (The structure of MnTe is nickel arsenide.) The derived electronic structure represents the $x=1$ limit of the $\text{Cd}_{1-x}\text{Mn}_x\text{Te}$, $\text{Zn}_{1-x}\text{Mn}_x\text{Te}$, and $\text{Hg}_{1-x}\text{Mn}_x\text{Te}$ alloys to be considered here. The spin-polarized band calculations for $\text{Cd}_{1-x}\text{Mn}_x\text{Te}$ will be described here in detail. In addition, we present new results for MnSe and MnS (Sec. II A). The inclusion of spin polarization in these calculations is of particular importance for the placement of occupied (spin-up) and unoccupied (spin-down) Mn *d* bands and for treating their hybridization with *sp* bands correctly. The derived band structures are fit by an appropriate parametrization of simplified ETBM results and then adjusted using optical¹⁰⁻¹³ and photoemission data¹⁴⁻¹⁶ (Sec. II B).

The magnetic interactions to be considered here are as follows.

(1) The (*sp*-band-edge)-Mn or *sp*-*d* exchange interaction having the Kondo form¹⁷

$$-\sum_i J_{sp-d}^{h,e} S_i \cdot \sigma_i^{h,e}, \quad (1.1)$$

where S_i is the Mn moment at site *i*, $\sigma_i^{h,e}$ is the spin operator associated with a valence-band-edge hole (*h*) or a conduction-band-edge electron (*e*), and $J_{sp-d}^e \approx -1.0$ eV, $J_{sp-d}^h \approx 0.2$ eV are the corresponding exchange constants.¹⁸⁻³⁰ The sum extends over Mn occupied sites only.

(2) The Mn-Mn or *d*-*d* exchange described by the spin- $\frac{1}{2}$ Heisenberg Hamiltonian

$$-\sum_{\langle i,j \rangle} J^{dd}(R_{ij}) S_i \cdot S_j, \quad (1.2)$$

where $J^{dd}(R_{ij}) \approx -1$ meV (Refs. 31-40) is the antiferro-

magnetic (AF) coupling between spins separated by R_{ij} . Again, the sum extends over Mn-occupied sites only. The exchange constants are determined by a random multisite Anderson Hamiltonian (Sec. II B), which incorporates the relevant features of the DMS electronic structure⁴ (Sec. II A), using second- and fourth-order perturbation theory^{41,42} for Eqs. (1.1) and (1.2), respectively (Secs. III and IV). $J_{sp-d}^{u,c}$ is theoretically determined from band-edge spin splittings of ferromagnetic ASW bands, or experimentally from magnetooptic experiments. The numerical relationship⁴³ between $J_{sp-d}^{u,c}$ and the hybridization parameter V_{pd} [Eq. (2.4)] determining the $sp-d$ band mixing, follows directly from a Schrieffer-Wolff transformation.⁴⁴ The detailed calculation of $J^{dd}(R_{ij})$ presented here establishes superexchange, resulting from $p-d$ hybridization, as the dominant mechanism at near-neighbor distances, and as significantly more important than the Bloembergen-Rowland interaction.⁴⁵ The latter has been previously suggested as responsible for Mn-Mn exchange.⁴⁶ Further support for the present view is provided by numerical estimates of the total ASW energy differences between ferromagnetic and antiferromagnetic configurations which are in surprisingly good agreement with the perturbation results. The excellent agreement between theory and experiment ($\sim 50\%$) results from the accuracy of the input parameters (most notably V_{pd} as determined by the experimental $J_{sp-d}^{u,c}$) and the detailed understanding of the electronic structure. The superexchange results are at least as accurate as any theoretical values previously obtained for other materials.

The detailed results for $\text{Cd}_{1-x}\text{Mn}_x\text{Te}$ are used to construct a three-level, four-parameter phenomenological model for superexchange which is able to reproduce them simply, thereby providing insight into their physical significance (Sec. V). More importantly, the model is applicable to other Mn-based DMS's and permits the exploration of chemical trends in magnetic behavior. This model expresses $J^{dd}(R_{ij})$ as a product of two factors. The first depends explicitly on the electronic level parameters; the second is a function $f(R_{ij}/a)$, where a is the lattice parameter, which is approximately the same for all members of a class of materials like the DMS's having a given chemical structure. The model is supported by the results of exchange constant estimates derived from ASW band and total-energy calculations. Applications are made to the DMS series $M_{1-x}^{II}\text{Mn}_xX^{VI}$ ($M^{II}=\text{Cd}$ or Zn ; $X^{VI}=\text{Te}$, Se , or S). Experimental information is used to fix the input parameters. The calculated exchange constants are in satisfactory agreement with experiment.

Somewhat surprisingly, the model turns out to be applicable as well to at least some materials (MnO and $\alpha\text{-MnS}$) which are largely ionic, insulating, and have the rocksalt rather than the zinc-blende structure. The function $f(R_{ij}/a)$, while quantitatively different from that appropriate for the zinc-blende materials, is again insensitive to the chemical composition for this crystal structure.

Discussion of theoretical matters pertaining to the accuracy of the LSDA, the ETBM model and its implementation, and the derivation and properties of the function $f(R_{ij}/a)$ are relegated to appendices.

II. ELECTRONIC STRUCTURE AND MODEL HAMILTONIAN

A. Electronic structure

As a guide to the electronic structure of DMS's, we have performed self-consistent spin-polarized band calculations for hypothetical stoichiometric antiferromagnetic MnTe, MnSe, and MnS compounds having the zinc-blende structure. This section discusses only results for MnTe; the results for MnSe and MnS are quite similar. The AF-I ordering, consisting of alternating (001) spin-up and spin-down planes, is chosen for simplicity, although the DMS's are believed to prefer the more complicated AF-III ordering. The zinc-blende lattice constant of 6.430 Å used here is obtained by linear extrapolation of measured values for $x < 1$.⁴⁷ Possible tetragonal distortions due to the antiferromagnetic ordering are neglected.

Exchange and correlation effects are treated in the local-spin-density approximation (LSDA) using an exchange-correlation functional of the von Barth-Hedin form.⁹ The LSDA is primarily a ground-state formalism and yields band gaps in semiconductors and insulators which are typically 40–60% too small. Relativistic effects are neglected.

The one-electron Schrödinger equation is solved using the augmented-spherical-wave (ASW) technique,⁸ with extra ASW spheres centered on the tetrahedral interstices.⁴⁸ This results in a bcc lattice of spheres for which the sphericalization of the Wigner-Seitz cell inherent in the ASW method is a good approximation. This radii of spheres are chosen to be equal. This procedure produces results for tetrahedrally coordinated materials which agree well with state-of-the-art linear-augmented-plane-wave (LAPW) and pseudopotential calculations.⁴⁹ Results for zinc-blende MnTe similar to those reported here have recently been obtained using an LSDA-LAPW approach.⁵⁰

The calculated ASW bands for AFI zinc-blende MnTe are shown in Fig. 1. The energy zero is fixed at the valence-band maximum. The corresponding density of states and the densities of states projected on the Mn sphere majority (\uparrow) and minority (\downarrow) spin d components are plotted in Fig. 2. We define the majority (minority) spin component to be that which contains a larger (smaller) percentage of the occupied d states at a given site. The magnitude of the net magnetic moment inside each Mn sphere is $4.2\mu_B$. This is less than the atomic value of $5\mu_B$ because of hybridization.

The states lying between -4 and 0 eV are derived primarily from Mn majority spin d levels and Te sp levels. Those between -4 and -3 eV and between -2 and 0 eV have the largest Te sp components but display strong $p-d$ hybridization effects. The Mn d content of the valence-band maximum E_v , for example, is roughly 50%. The bands are quite flat between -2 and -2.5 eV and consist of largely unhybridized d levels ($> 80\%$ Mn d content at Γ).

The states lying between $+1.0$ and $+2.5$ eV are derived primarily from unoccupied Mn minority spin d levels. The lower bands in this complex are only slightly hybridized with the Te levels ($> 80\%$ Mn d content at Γ).

while the upper bands exhibit stronger hybridization effects ($< 65\%$ Mn d content at Γ). The spin splitting, which is most directly associated with the splitting $\epsilon_d^+ - \epsilon_d^-$ in Fig. 2, is roughly 3.5 eV. The bands above 3 eV correspond to the conduction band in an ordinary sp -bonded semiconductor. The minimum at Γ contains roughly equal contributions from the s orbitals in the Mn spheres, the Te spheres, and the empty spheres neighboring the Mn spheres, and none from the Mn d levels.

It should be noted that LSDA band energies have no rigorous significance except for the highest occupied level and the lowest unoccupied level.⁵¹ Furthermore, the approximate LSDA one-electron potential does not contain the discontinuity^{52,53} between the valence and conduction bands which must be present in the exact density-functional potential. Some insight is gained⁵⁴ by associating the LSDA eigenvalues with hypothetical quasiparticles which are completely screened as they would be in a uniform electron gas. Since true Landau quasiparticles in an insulator are not completely screened in the absence of other quasiparticles the LSDA underestimates quasiparticle excitation energies: conduction bands are too low, valence bands are too high, and band gaps are too small. In the present case the occupied d states may be about 1 eV too high and the unoccupied d states about 1 eV too low. Appendix A contains a more detailed discussion of the errors associated with the LSDA and with the neglect

of relativistic effects.

In applying the crystalline MnTe and well-known CdTe results to $\text{Cd}_{1-x}\text{Mn}_x\text{Te}$, we use insight drawn from Hass and Ehrenreich's empirical tight-binding-method-coherent-potential-approximation (ETBM-CPA) calculations for $\text{Hg}_{1-x}\text{Mn}_x\text{Te}$ and $\text{Cd}_{1-x}\text{Mn}_x\text{Te}$.^{6,55} The ETBM-CPA calculations indicate that the important features of the alloy electronic structure for the present purposes are understandable within the virtual-crystal approximation (VCA), which will be made in Sec. II B.

The upper valence bands in both CdTe and zinc-blende MnTe are largely Te $5p$ derived. Using the common anion rule, it is assumed that these lie at the same absolute energy level before p - d hybridization. The ETBM calculations indicate that the effect of such hybridization on the valence-band edge is small. The valence-band edge thus remains largely independent of x . This assertion is supported by the observed x independence of the phototreshold in $\text{Cd}_{1-x}\text{Mn}_x\text{Te}$.¹⁴ It is also consistent with experimental evidence for a small valence-band offset in epitaxial $\text{Cd}_{1-x}\text{Mn}_x\text{Te}$ grown on CdTe.⁵⁶ The sp conduction-band edge, on the other hand, is predicted to increase linearly with x in the VCA due to the difference between the Cd $5s$ and Mn $4s$ atomic levels. This is consistent with the linear increase in the net sp band gap observed in optical absorption¹⁰ and reflectivity¹² measurements.

The location of the occupied and unoccupied Mn $3d$

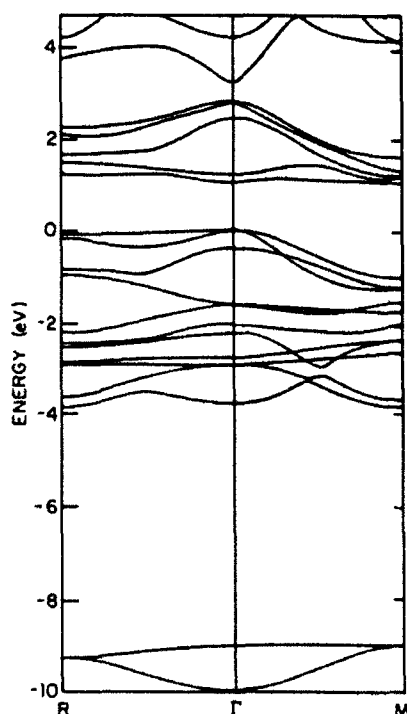


FIG. 1. Spin-polarized ASW band structure for hypothetical zinc-blende MnTe with AF-I ordering. The symmetry directions Γ - M and Γ - R in the tetragonal unit cell (shown) corresponding to Γ - X and Γ - L in the zinc-blende zone, respectively.

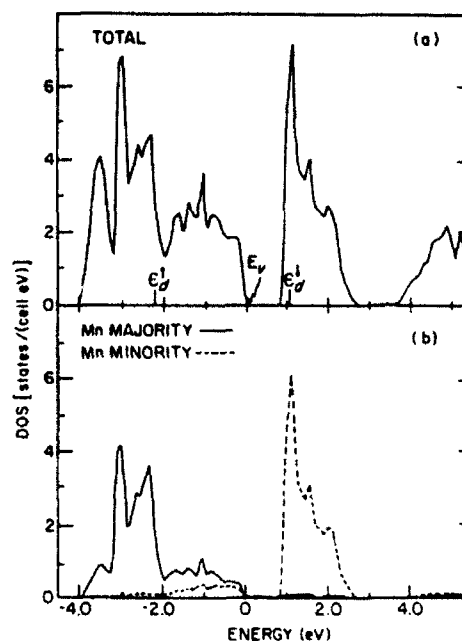


FIG. 2. Total and projected densities of states (per unit cell) of zinc-blende MnTe in the AF-I ordering. (a) Total density of states. (b) Mn d majority spin (solid line) and minority spin (dotted line) projected densities of states. Calculations employed the ASW-LSDA scheme described in the text. Majority and minority spin Mn d states of e_g symmetry at Γ are labeled by ϵ_d^+ and ϵ_d^- , respectively. The valence-band edge is labeled E_v .

states relative to the Te p -like valence-band maximum should not be very sensitive to x . Photoemission studies^{14,15} indeed show the growth of a Mn d peak approximately 3.4 eV below the valence-band edge for all concentrations. Angle-resolved measurements indicate that the occupied states contributing to this peak exhibit dispersion of about 1 eV,¹⁶ suggesting that they are actually bands resulting from p - d hybridization. Spectral changes higher in the valence band as a function of x are also attributable to hybridization. In addition, its presence provides a qualitative explanation¹¹ for the decrease of the E_1 optical transition energy observed in ellipsometry measurements with x .

The location of the unoccupied Mn d states has not yet been established definitively. Transitions from sp valence-band states to the unoccupied d states should be optically observable. Kendrewicz interprets structure at 4.5 eV in reflectivity measurements as arising from these transitions.¹² Structure at 4.5 eV has also been observed recently in ellipsometry data.¹¹ The most plausible initial-state energy for these transitions corresponds to the first maximum in the upper-valence-band density of states. This assignment would place the unoccupied d states 3.5 eV above the valence-band edge. The optical structure at lower energies can be explained in terms of standard interband transitions in zinc-blende semiconductors and Mn²⁺ multipletlike excitations,¹³ which are essentially Frenkel excitons and do not appear in a band picture.

B. Model Hamiltonian

The model Hamiltonian to be used in the determination of the magnetic exchange constants has the form of a multisite Anderson Hamiltonian containing the essential ingredients of the band structure. Explicitly,

$$H = H_0 + H_d + H_{pd} + H_X. \quad (2.1)$$

Here

$$H_0 = \sum_{n,k,\sigma} \epsilon_n(k) c_{nk\sigma}^\dagger c_{nk\sigma} \quad (2.2)$$

describes the virtual-crystal sp bands, $\epsilon_n(k)$; $c_{nk\sigma}^\dagger$ creates an electron in band n , with wave number k , and spin σ in the Bloch state $\psi_{nk}(r)$. The sp bands are determined by the ETBM using a basis of three anion p orbitals and one cation s orbital (Appendix B). With the proper choice of parameters this model yields band gaps in agreement with experiment as well as reasonable bandwidths and wave-function components for the highest valence bands and lowest conduction band.

The term

$$H_d = \sum_i \sum_{m,\sigma} (\epsilon_d + U_{eff}(n_{im-\sigma})) n_{im\sigma} \quad (2.3)$$

describes five degenerate Mn d levels per site i with site-localized linearized electron-electron interactions of the Hubbard form. Here $n_{im\sigma}$ is the number operator for d electrons of magnetic quantum number m on site i . The

prime indicates that the sum extends over only Mn-occupied sites. H_d acts on a subspace (per site) consisting only of d^4 , d^5 , and d^6 configurations.⁵⁷ We assume $\langle n_{im\sigma} \rangle = 0$ or 1, and that Hund's rule remains in effect, consistent with the observed magnetic moment of $5\mu_B$.⁵⁸ The parameter ϵ_d is taken to have the value -3.4 eV with respect to the valence-band-edge zero of energy. The parameter U_{eff} is assigned a value of 7.0 eV in accordance with the discussion at the end of Sec. II A. This is somewhat larger than the value 5.5 eV used in our previous calculations of $J^{dd}(R_{ij})$.⁴ The results of Sec. IV are not qualitatively sensitive to variations in U_{eff} of this magnitude.

The term

$$H_{pd} = \sum_i \sum_{m,\sigma} \sum_{n,k} [\bar{V}_{pd}(n,k) e^{ik \cdot R_i} d_{im\sigma}^\dagger c_{nk\sigma} + \text{H.c.}] \quad (2.4)$$

describes Mn $3d$ -Te $5p$ hybridization. Here $d_{im\sigma}^\dagger$ creates a d electron at site i in orbital m with spin σ . We define V_{pd} to be the real-space hopping amplitude from a Mn d to a neighboring p orbital, neglecting any m dependence. The four-orbital ETBM model of Appendix B then yields $\bar{V}_{pd}(n,0) = 4N^{-1/2}V_{pd}$ for the upper valence band and a general wave-vector-dependent hopping amplitude of

$$\bar{V}_{pd}(n,k) = \bar{V}_{pd}(n,0) \left[\sum_p \langle p, 1k | nk \rangle \right] \left[\frac{1}{4} \sum_{\delta} e^{ik \cdot \delta} \right]. \quad (2.5)$$

Here $\langle \alpha vk | nk \rangle$ is the coefficient in the Bloch function $|nk\rangle$ of the Bloch sum $|\alpha vk\rangle$ corresponding to orbital α of basis atom v [$=0$ (cation), 1 (anion)] in the unit cell. The δ_j are the four basis vectors to neighboring Te with respect to a Mn cation at $R=0$; N is the number of unit cells in a normalization volume. The value of V_{pd} is obtained in Sec. III from experimental sp - d exchange constants. As discussed in Appendix B, the numerical calculations in Sec. IV involve averaging Eq. (2.5) over principal directions.

The Mn- d - sp -band potential exchange is given by

$$H_X = -\frac{1}{4} \sum_i \sum_n \sum_{k,k'} J_n^{dir}(k,k') e^{i(k-k') \cdot R_i} \times S_i \cdot \left[\sum_{\mu,\nu} c_{nk\mu}^\dagger \sigma_{\mu\nu} c_{nk'\nu} \right]. \quad (2.6)$$

Here

$$J_n^{dir}(k,k') = \sum_m \int d^3r \int d^3r' \phi_{dm}^*(r) \psi_{nk}^*(r) v_{sc}(|r-r'|) \times \phi_{dm}(r') \psi_{nk'}(r') \quad (2.7)$$

is the ordinary exchange integral with screened Coulomb interaction $v_{sc}(|r-r'|)$ between a d wave function $\phi_{dm}(r)$ and sp Bloch states (n,k) and (n,k') ; $\sigma_{\mu\nu}$ are the Pauli matrices. H_X -derived terms are unimportant for d - d exchange, and become important for sp - d exchange only when the H_{pd} contribution vanishes by symmetry. Mn-Mn direct exchange is even smaller and is neglected.

III. *sp-d* EXCHANGE

The commonly used *sp-d* exchange Hamiltonian¹⁷

$$H_{sp-d} = -\frac{1}{2} \sum_i \sum_{n,k,k'} J_n^{sp-d}(\mathbf{k}, \mathbf{k}') e^{i(\mathbf{k}-\mathbf{k}') \cdot \mathbf{R}_i} \times \mathbf{S}_i \cdot \left[\sum_{\mu,\nu} c_{n\mu}^\dagger \sigma_{\mu\nu} c_{nk'\nu} \right] \quad (3.1)$$

involves $J_n^{sp-d}(\mathbf{k}, \mathbf{k}')$, the exchange between *sp* band states (n, \mathbf{k}) and (n, \mathbf{k}') and Mn local moments \mathbf{S}_i ($S = \frac{1}{2}$) for valence bands ($n = v$) and conduction band ($n = c$). Interband terms $n \neq n'$ in Eq. (3.1) are smaller and are neglected. The analysis below is restricted to the band-edge *sp-d* exchange constants $\alpha \equiv J_c^{sp-d}(0,0)$ and $\beta \equiv J_v^{sp-d}(0,0)$. The former will be seen to result exclusively from the term H_X in Eq. (2.1). The latter depends predominantly on H_{pd} and is thus more sensitive to details of the band structure.

Experimentally, α and β are determined from the enhanced Zeeman splittings of free-exciton lines in magnetooptic experiments.¹⁸ For an external magnetic field along the *z* direction, the spin \mathbf{S}_i is replaced in standard mean-field theory by an average spin \bar{S}_z proportional to the magnetization. Equation (3.1) is then diagonal in *k*. The effect of H_{sp-d} on band-edge states,

$$-\frac{1}{2} x N \bar{S}_z J_n^{sp-d}(0,0) (c_{n0\uparrow}^\dagger c_{n0\uparrow} - c_{n0\downarrow}^\dagger c_{n0\downarrow}) \quad (n = c, v), \quad (3.2)$$

can thus be considered independently of other *k* states in the same band. In all DMS's except Hg-based compounds, the splitting produced by an external magnetic field in the presence of H_{sp-d} is more than an order of magnitude larger than the intrinsic Zeeman splittings of these states.⁵⁹ The observed splittings therefore are nearly proportional to \bar{S}_z . From Eq. (3.2), the splitting of the $j = \frac{1}{2}$, $m_j = \frac{1}{2}$ (valence-band edge) to $j = \frac{1}{2}$, $m_j = \frac{1}{2}$ (conduction-band edge) exciton transition is seen to be $\Delta E_{3/2} = x N \bar{S}_z (\beta - \alpha)$. A different linear combination of α and β can be obtained from a different exciton transition.

Simultaneous measurements of such transitions together with magnetization data yield the experimental values given in Table I.

The exchange constants α and β can be determined within the mean-field approximation from the ASW bands for a hypothetical ferromagnetic zinc-blende MnTe compound.⁵ The ferromagnetic order is imposed only to model the effects of a magnetic field in producing finite magnetization and associated mean-field spin splittings. More-direct calculations of *sp-d* exchange constants for spin-disordered alloys are difficult. We believe the $x = 1$ case to be relevant because experimentally determined exchange constants are reasonably insensitive to *x*, at least for $x \leq 0.30$.⁶⁰ The ASW-LSDA calculation scheme is the same as that described in Sec. II. The results for the majority and minority spin bands are shown in Fig. 3. We take \bar{S}_z to be the calculated total magnetic moment ($4.8 \mu_B$). Assuming the conduction- and valence-band-edge spin splittings [$\Delta E^{c,v} \equiv E^{c,v}(\downarrow) - E^{c,v}(\uparrow)$] to be proportional to \bar{S}_z , we find

$$N\alpha = \Delta E^c / \bar{S}_z = 0.33 \text{ eV}, \quad N\beta = \Delta E^v / \bar{S}_z = -1.05 \text{ eV}. \quad (3.3)$$

Similar ASW calculations were performed for a ferromagnetic $\text{Cd}_{0.5}\text{Mn}_{0.5}\text{Te}$ alloy in an ordered simple tetragonal structure. These assume a basal-plane lattice constant of 6.414 Å and perfect tetrahedral coordination. The *x* independence of J^{sp-d} is supported by the good agreement between the calculated values $N\alpha = 0.32$ eV and $N\beta = -1.12$ eV and the results in Eq. (3.3).

The comparison of MnTe results with experiment in Table I shows satisfactory agreement. This agreement should be viewed with caution because (1) the perturbative treatment of $N\beta$ given below indicates that this exchange constant would be reduced in a calculation employing the correct *d* level locations; and (2) the experimental $N\beta$ is properly defined as the exchange constant for the Γ_8 level ($j = \frac{3}{2}$), whereas the present calculations

TABLE I. $M_{1-x}\text{Mn}_x\text{X}^{\text{VI}}$ *sp-d* exchange constants from experiment, and corresponding Mn-X^{VI} *sp-d* exchange constants from the ferromagnetic ASW band calculations.

	Experimental			ASW calculation	
	$N\alpha$ (eV)	$N\beta$ (eV)		$N\alpha$ (eV)	$N\beta$ (eV)
$\text{Cd}_{1-x}\text{Mn}_x\text{Te}$	0.22	-0.89 ^a	MnTe	0.33	-1.05
$\text{Zn}_{1-x}\text{Mn}_x\text{Te}$	0.18	-1.05 ^b			
$\text{Cd}_{1-x}\text{Mn}_x\text{Se}$	0.26	-1.11 ^c			
$\text{Zn}_{1-x}\text{Mn}_x\text{Se}$	0.26	-1.31 ^d	MnSe	0.33	-1.35
$\text{Cd}_{1-x}\text{Mn}_x\text{S}$	0.22 ^e	-1.80 ^f			
$\text{Zn}_{1-x}\text{Mn}_x\text{S}$			MnS	0.36	-1.50

^aReferences 18 and 20.

^bReferences 19, 21, 22, and 23.

^cReferences 19, 21, 24, and 25.

^dReferences 19, 21, and 26.

^eReference 30.

^fReference 27.

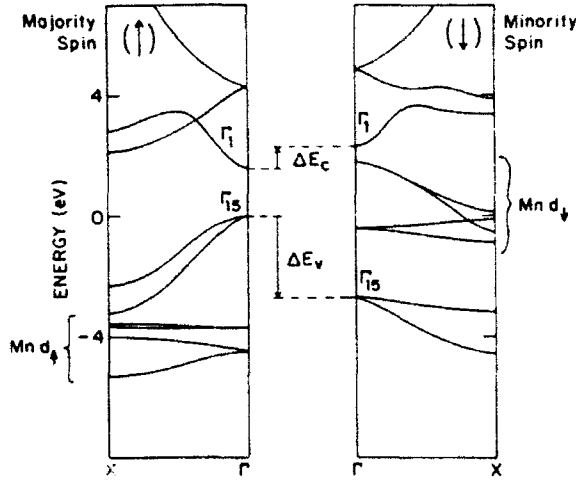


FIG. 3. Spin-polarized ASW energy bands for ferromagnetic MnTe along the symmetry direction Γ -X. Left (right) panel shows majority (minority) spin bands. Shown also are the valence- and conduction-band-edge spin splittings, ΔE_v and ΔE_c .

refer to a nonrelativistic Γ_{15} band edge. The neglect of spin-orbit splitting in the present calculations may be unimportant because of experimental evidence that the exchange constants of the Γ_8 and Γ_7 ($j = \frac{1}{2}$) levels are the same.⁶¹ The uncertainty due to effects (1) and (2) should not exceed 20%.

The qualitative difference between α and β reflects the importance of p - d hybridization and the different symmetry character of the conduction- and valence-band edges. The present ASW results support the analysis of Ref. 43. The presence of hybridization introduces an appreciable Mn d admixture in the Γ_{15} valence-band maximum. This is seen in Fig. 3 to give rise to a strong repulsion from lower, occupied Mn d states in the majority spin bands and higher, unoccupied Mn d states in the minority spin bands. Large negative values of ΔE_c and hence β result. By contrast, hybridization between the Γ_1 conduction-band edge and Mn d states is forbidden by symmetry. The much smaller, positive values of ΔE_v and α are thus determined exclusively by potential exchange [the H_X terms in Eq. (2.1)].

An explicit theoretical expression for β in terms of the parameters defined in Sec. II B permits the calculation of the hybridization parameter V_{pd} from experimental sp - d exchange constants. By neglecting H_X , and performing a Schrieffer-Wolff canonical transformation⁴⁴ to eliminate H_{pd} to first order in Eq. (2.1), we obtain

$$N\beta = -32V_{pd}^2[(\epsilon_d + U_{eff} - E_v)^{-1} + (E_v - \epsilon_d)^{-1}], \quad (3.4)$$

where E_v is the valence-band-edge energy. Substituting $N\beta = -0.88$ eV, $E_v - \epsilon_d = 3.4$ eV, and $U_{eff} = 7.0$ eV for $\text{Cd}_{1-x}\text{Mn}_x\text{Te}$ yields $V_{pd} = 0.22$ eV. The value of V_{pd} agrees very well with that (~ 0.2 eV) obtained from an ETBM fit to the ASW bands.⁶²

IV. Mn-Mn EXCHANGE

The spin- $\frac{1}{2}$ Heisenberg Hamiltonian describing the Mn-Mn, or d - d , exchange in $\text{Cd}_{1-x}\text{Mn}_x\text{Te}$ is given by

$$H_H = - \sum_{\langle i,j \rangle} J^{dd}(R_{ij}) \mathbf{S}_i \cdot \mathbf{S}_j. \quad (4.1)$$

$J^{dd}(R_{ij})$ is the exchange constant for Mn local moments \mathbf{S}_i and \mathbf{S}_j , separated by $R_{ij} \equiv |\mathbf{R}_i - \mathbf{R}_j|$, and the sum extends over Mn-occupied sites. [Note that with the present convention the total interaction between two spins is $-2J^{dd}(R_{ij})\mathbf{S}_i \cdot \mathbf{S}_j$.]

The value of $J_1^{dd} \equiv J^{dd}(\text{nearest neighbor } R_{ij})$ is estimated first from ASW-LSDA total-energy calculations. More extensive calculations of $J^{dd}(R_{ij})$ are then performed within fourth-order perturbation theory using the model Hamiltonian (2.1) and the electronic structure parameters obtained earlier.

The estimate of J_1^{dd} is based on the ASW-LSDA total-energy difference between (hypothetical) zinc-blende MnTe in antiferromagnetic and ferromagnetic orderings. We assume only nearest-neighbor interactions in the fcc Heisenberg Hamiltonian (4.1) leading to an energy per spin of $-24J_1^{dd}S^2$ in the totally aligned (ferromagnetic) state and $8J_1^{dd}S^2$ in the AF-I state. S is taken to be one-half the computed Mn-sphere moment: $S_F = \frac{1}{2}(4.47\mu_B)$ for ferromagnetic ordering and $S_{AF} = \frac{1}{2}(4.23\mu_B)$ for antiferromagnetic ordering. The difference in Heisenberg energies per spin, $J_1^{dd}(8S_{AF}^2 + 24S_F^2)$ is equated to ΔE^{ASW} , the difference between antiferromagnetic and ferromagnetic ASW-LSDA total energies per Mn. The computed ΔE^{ASW} of -0.23 eV yields an antiferromagnetic exchange constant of $J_1^{dd} = -17.1$ K.

This result can be directly compared to experimental $\text{Cd}_{1-x}\text{Mn}_x\text{Te}$ exchange constants since the latter are only weakly x dependent. The best evidence for the weak x dependence is the good agreement between the value of J_1^{dd}/k_B (≈ -7 K) obtained from magnetization step experiments^{31,32,34} for $x < 0.05$ and the value ($J_1^{dd}/k_B \approx -7.5$ K) obtained from neutron scattering experiments³⁵ for $x \approx 0.65$. The ASW-LSDA calculations overestimate $|J_1^{dd}|$. Similar overestimates result from ASW-LSDA calculations of d - d exchange constants in MnO, MnS, and NiO.⁶³ This effect is probably associated with the LSDA underestimate of the energy of unoccupied Mn $3d$ levels discussed in Sec. II.

The perturbative calculation of $J^{dd}(R_{ij})$ begins with the unperturbed Hamiltonian $H_0 + H_d$ in Eq. (2.1). The perturbation $H_{pd} + H_X$ partially lifts the large ground-state degeneracy of $H_0 + H_d$ associated with the moment directions on each Mn site. The resulting spectrum of low-lying states is described by the Heisenberg Hamiltonian (4.1). The lowest-order contributions to $J^{dd}(R_{ij})$ arising from H_{pd} and H_X are termed kinetic and potential exchange, respectively.² As pointed out in Sec. III, H_X is important only at k points where H_{pd} vanishes (e.g., the conduction-band edge). Since $J^{dd}(R_{ij})$ is determined by integrals over the entire zone, the contribution of H_X is significantly smaller and may be neglected.

Previous estimates of $J^{dd}(R_{ij})$ in DMS's have started

from H_0 and the sp - d exchange Hamiltonian (3.1).⁶⁴ This fundamentally different approach neglects important intermediate states in which the Mn d -shell occupations differ from five. The restriction to fixed occupancy is valid at near-neighbor distances only in materials in which potential exchange dominates kinetic exchange [e.g., EuO (Ref. 65)]. Since the opposite limit holds for $\text{Cd}_{1-x}\text{Mn}_x\text{Te}$ it is important to consider the effects of H_{pd} explicitly in calculating $J^{dd}(R_{ij})$ instead of starting from Eq. (3.1).

The kinetic exchange contributions are calculated by considering an initial state $|i\rangle = | \dots, M_i = \frac{5}{2}, M_j = \frac{1}{2}, \dots \rangle$ and final state $|f\rangle = | \dots, M_i = \frac{3}{2}, M_j = \frac{3}{2}, \dots \rangle$. The specification of $|i\rangle$ and $|f\rangle$ implicit-

ly includes the quantum numbers associated with filled sp -valence and empty sp -conduction bands, and the magnetic quantum numbers of S_i , $-\frac{1}{2} \leq M_i \leq \frac{1}{2}$. H_H of Eq. (4.1) connects $|i\rangle$ and $|f\rangle$:

$$\langle f | H_H | i \rangle = -2(\frac{1}{2})J^{dd}(R_{ij}). \quad (4.2)$$

Since H_H is an effective Hamiltonian representing the effects of the more fundamental Hamiltonian (2.1), $J^{dd}(R_{ij})$ can be calculated by computing the matrix element on the left-hand side of (4.2) in terms of H_{pd} . The first nonvanishing terms in H_{pd} connecting $|i\rangle$ and $|f\rangle$ are of fourth order. Thus,

$$-2(\frac{1}{2})J^{dd}(R_{ij}) = \sum_{I_1, I_2, I_3} \frac{\langle f | H_{pd} | I_1 \rangle \langle I_1 | H_{pd} | I_2 \rangle \langle I_2 | H_{pd} | I_3 \rangle \langle I_3 | H_{pd} | i \rangle}{(E_0 - E_1)(E_0 - E_2)(E_0 - E_3)}. \quad (4.3)$$

Here I_1, I_2, I_3 label intermediate states, to be described in more detail below, specified by the occupation of sp -band states and Mn d orbitals and sites i and j with four, five, or six electrons per site. E_1, E_2, E_3 , and E_0 are the energies of the intermediate states and the ground state, respectively. This method of calculating $J^{dd}(R_{ij})$ is very similar to the approach developed for rare-earth compounds and NiO by Falicov and co-workers.^{41,42}

The assumption in Sec. II B that $\tilde{V}_{pd}(n, k)$ is independent of the Mn orbital index m allows Eq. (4.3) to be factored into two terms. The first term depends only on the Mn-ion ground state, and is exactly one for the $\text{Mn}^{2+} (^6S_{5/2})$ configuration assumed here. The second term is a perturbation expression identical to Eq. (4.3) but for $S = \frac{1}{2}$. The calculation of $J^{dd}(R_{ij})$ thus proceeds exactly as in the case of a single d orbital per Mn.

Figure 4 shows a schematic representation of terms contributing to $J^{dd}(R_{ij})$. Each arrow represents the formation of one on the intermediate states I_1, I_2 , or I_3 through transfer of one electron between Mn ions at R_i or R_j and the sp bands. All permutations of the arrow labels consistent with particle conservation and the exclusion principle produce intermediate states that contribute to the exchange constants. The sums of terms with two-hole [Fig. 4(a)], hole-electron [Fig. 4(b)], and electron-electron (not shown) intermediate states are denoted by $J_{hh}^{dd}(R_{ij})$, $J_{he}^{dd}(R_{ij})$, and $J_{ee}^{dd}(R_{ij})$, respectively. Thus $J^{dd}(R_{ij}) = J_{hh}^{dd}(R_{ij}) + J_{he}^{dd}(R_{ij}) + J_{ee}^{dd}(R_{ij})$.

Let $[A, B, C, D]$ be the sum of the terms in Eq. (4.3) corresponding to the intermediate-state sequence shown in Fig. 4(a) plus the same term with i and j interchanged. The total contribution to $J_{hh}^{dd}(R_{ij})$ is then

$$\begin{aligned} J_{hh}^{dd}(R_{ij}) &= [A, B, C, D] + [C, D, A, B] + [A, C, D, B] + [A, C, B, D] + [C, A, D, B] + [C, A, B, D] \\ &= -2 \sum_{k, k'} \sum_{n, n'} |\tilde{V}_{pd}(n, k)|^2 |\tilde{V}_{pd}(n', k')|^2 \cos[(\mathbf{k} - \mathbf{k}') \cdot \mathbf{R}_{ij}] \\ &\quad \times \{ U_{eff}^{-1} [\epsilon_n(k) - \epsilon_d - U_{eff}]^{-1} [\epsilon_n(k') - \epsilon_d - U_{eff}]^{-1} - [\epsilon_n(k) - \epsilon_d - U_{eff}]^{-2} [\epsilon_n(k') - \epsilon_d - U_{eff}]^{-1} \}. \end{aligned} \quad (4.4)$$

Here the sum on bands is restricted to the upper valence bands, and the k, k' sums extend over the first Brillouin zone. Both terms in curly brackets are positive. The rapid decrease of $|\tilde{V}_{pd}(v, k)|^2$ away from $k = 0$ discussed in Appendix B implies that the integrals over k and k' are positive. $J_{hh}^{dd}(R_{ij})$ is thus negative or antiferromagnetic.

$J_{hh}^{dd}(R_{ij})$ will be seen below to be the dominant exchange mechanism in $\text{Cd}_{1-x}\text{Mn}_x\text{Te}$ at near-neighbor distances. Since $J_{hh}^{dd}(R_{ij})$ involves only the anion-derived upper-valence-band states, it is identified with superexchange. The present k -space description of superexchange is believed to be superior for $\text{Cd}_{1-x}\text{Mn}_x\text{Te}$ to more familiar real-space, path-counting schemes⁶⁷ because the upper valence bands are relatively broad. In materials with narrower valence bands (e.g., NiO), the sp hopping itself can be treated as a perturbation and only the shortest paths contribute significantly to $J^{dd}(R_{ij})$. Correlation effects within the valence band may also be important. In $\text{Cd}_{1-x}\text{Mn}_x\text{Te}$, however, the broader, uncorrelated valence bands require a relatively large number of paths to be retained. The appropriate summation over paths is taken care of automatically in Eq. (4.4) by the cosine factor and k -dependent hopping amplitudes $\tilde{V}_{pd}(n, k)$.

$J_{he}^{dd}(R_{ij})$ contains intermediate states involving the lowest conduction band and the upper valence bands. In analogy to Eq. (4.4), we find

$$\begin{aligned}
J_{he}^{dd}(R_{ij}) = & -2 \sum_{k,k'} \sum_{n,n'} |\bar{V}_{pd}(n,k)|^2 |\bar{V}_{pd}(n',k')|^2 \cos[(\mathbf{k}-\mathbf{k}') \cdot \mathbf{R}_{ij}] \\
& \times (U_{eff}^{-1} [\epsilon_n(k) - \epsilon_d - U_{eff}]^{-1} [\epsilon_d - \epsilon_{n'}(k')]^{-1} \\
& + \frac{1}{2} [\epsilon_n(k) - \epsilon_{n'}(k')]^{-1} [\epsilon_d - \epsilon_{n'}(k')]^{-1} + [\epsilon_n(k) - \epsilon_d - U_{eff}]^{-1})^2, \quad (4.5)
\end{aligned}$$

where $n=c$ and $n'=v$ refer to conduction and valence bands, respectively. In a metal $[\epsilon_n(k) - \epsilon_{n'}(k')]^{-1}$ is singular over the Fermi surface, leading to the oscillatory long-ranged Ruderman-Kittel-Kasuya-Yosida (RKKY) interaction at large distances. In systems with an energy gap, there is no singularity and the interaction (the Bloembergen-Rowland interaction⁶⁸) is characterized by a large-distance associated exponential decay. This interaction dominates asymptotically in DMS's. The superexchange contribution $J_{hh}^{dd}(R_{ij})$ also decays exponentially but with a larger decay constant. For first and second neighbors in $\text{Cd}_{1-x}\text{Mn}_x\text{Te}$ the calculations below indicate that $J_{he}^{dd}(R_{ij})$ (which in general can be of either sign) is antiferromagnetic and much smaller ($\sim 5\%$) than $J_{hh}^{dd}(R_{ij})$. The smaller magnitude results from (1) the smaller density of states in the lowest conduction band

compared to the upper valence band, and (2) the fact that $\bar{V}_{pd}(c,k)$ vanishes at $k=0$ and remains small throughout the Brillouin zone. These same factors cause the two-electron contribution $J_{ee}^{dd}(R_{ij})$, which is also antiferromagnetic, to be completely negligible.

Equation (4.3) for $J^{dd}(R_{ij})$ has been evaluated numerically for first and second neighbors in $\text{Cd}_{1-x}\text{Mn}_x\text{Te}$ ($0 \leq x \leq 0.70$), using the $\epsilon_n(k)$ and $\bar{V}_{pd}(n,k)$ determined by the four-orbital ETBM model described in Appendix B. The sphericalization procedure which is used assumes $\epsilon_n(k)$ and $\bar{V}_{pd}(n,k)$ depend on $|\mathbf{k}|$ according to analytic expressions obtained along $\Gamma-X$. This approximation is reasonable because the main contribution to $J^{dd}(R_{ij})$ arises from the central region of the Brillouin zone where $\epsilon_n(k)$ and $\bar{V}_{pd}(n,k)$ are isotropic.

For $x=0.30$, we find $J_1^{dd}/k_B \approx -8$ K and $J_2^{dd}/k_B \equiv J^{dd}(\text{second neighbor } R_{ij})/k_B \approx -0.9$ K (also antiferromagnetic). The ratio $J_2^{dd}/J_1^{dd} \approx 0.11$ is probably more accurate than the absolute values because it is independent of V_{pd} . Superexchange, or $J_{hh}^{dd}(R_{ij})$ contributes about 95% to the total J_1^{dd} and J_2^{dd} for $x=0.3$. The $J_{he}^{dd}(R_{ij})$ contribution accounts for most of the remaining 5%. If V_{pd} is assumed independent of x , the calculated values of J_1^{dd} and J_2^{dd} are nearly constant throughout the physically attainable concentration range ($0 \leq x \leq 0.70$). In Sec. V we argue that V_{pd} should actually increase slightly with x , leading to an increase of $\sim 20\%$ in the magnitude of J_1^{dd} and J_2^{dd} between $x=0$ and $x=0.7$.

The nearly complete x independence of J_1^{dd}/k_B (with V_{pd} assumed constant) results in part from a competition between J_{hh}^{dd}/k_B and J_{he}^{dd}/k_B . The former increases in magnitude for nearest neighbors from -7.6 K at $x=0.1$ to -8.1 K at $x=0.7$. This enhancement results from the increasing Te p character of the upper valence bands which accompanies the increase in band gap. The J_{he}^{dd}/k_B contribution for nearest neighbors decreases in magnitude over the same composition range from -0.6 to -0.3 K. The much larger percentage change in J_{he}^{dd} reflects the strong band-gap dependence of the energy denominator $[\epsilon_c(k) - \epsilon_v(k')]^{-1}$ in Eq. (4.5).

The principal uncertainty in our numerical results lies in the parameters V_{pd} and U_{eff} . The magnitude of V_{pd} is largely constrained by Eq. (3.4) and the values of ϵ_d , U_{eff} , and $N\beta$ but J^{dd} is proportional to V_{pd}^4 . Sample calculations show J_1^{dd} to vary by $\sim \pm 50\%$ for changes in U_{eff} of $\sim \pm 15\%$, and by $\sim \pm 30\%$ for changes in $N\beta$ or ϵ_d of $\sim \pm 15\%$. The overall accuracy of the calculation of J_1^{dd} is thus $\sim \pm 50\%$.

The most accurate experimental values of J_1^{dd}/k_B in $\text{Cd}_{1-x}\text{Mn}_x\text{Te}$ range from -6.1 to -7.7 K.^{31,32,34,35} As

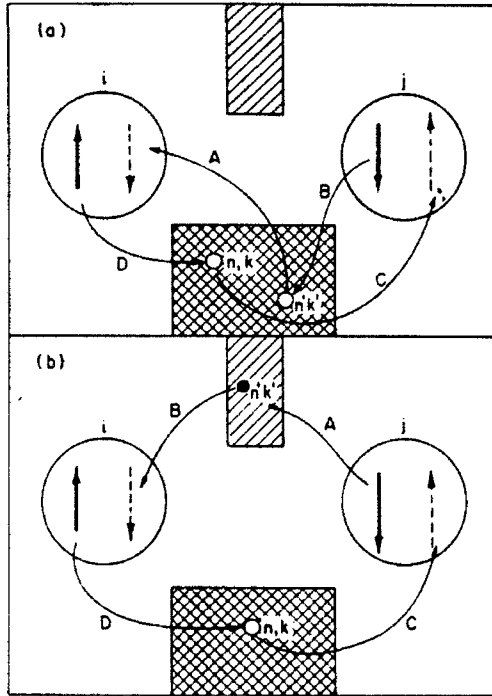


FIG. 4. Diagrammatic representation of fourth-order contributions to $J^{dd}(R_{ij})$. The filled valence bands, empty conduction band, and Mn d levels at R_i and R_j are shown. Solid (dashed) arrows at i and j represent the initial (final) Mn spin states. Terms contributing to (a) $J_{hh}^{dd}(R_{ij})$ and (b) $J_{he}^{dd}(R_{ij})$ correspond to allowable permutations of the spin-conserving transfers A, B, C, and D. The intermediate states of holes or electrons are labeled by (n,k) or (n',k') .

discussed earlier, no significant differences have been observed between experimental determinations for dilute ($x < 0.05$) and concentrated ($x \geq 0.6$) samples. Much of the experimental variation, in fact, may only reflect a difference in assumptions made concerning J_2^{dd} and more distant neighbor exchange constants. Direct experimental information on interactions beyond nearest neighbors is unavailable. An upper bound of $J_2^{dd}/J_1^{dd} < 0.5$ (Ref. 69) is imposed by the observation of short-ranged AF-III ordering in neutron scattering experiments.³⁵ Detailed analysis of the neutron scattering data as well as magnetization step data place this ratio in the narrower range 0.1–0.3.^{35,31} Overall, the agreement between the present perturbative calculations of J_1^{dd} and J_2^{dd} and experiment is excellent. This agreement strongly supports the basic validity of the electronic structure model used here and confirms superexchange as the dominant source of Mn-Mn interactions at near-neighbor distances. Conversely, the success of the present calculation of superexchange may be attributed to the detailed knowledge of the relevant parts of the electronic structure.

More-accurate calculations of J_{hh}^{dd} have been performed in connection with a recent study of *anisotropic* superexchange in DMS's.³ These calculations employ the Baldereschi "special k points" method, with 10 k points in the irreducible Brillouin zone (as well as more realistic e_g and t_{2g} symmetry d orbitals).^{70,71} The results are very similar to those reported here: $J_{hh}^{dd} = -5.6$ K ($\sim 25\%$ smaller), and relative chemical and compositional trends are effectively unchanged ($< 10\%$ difference). The good agreement supports the adequacy of the spherical approximation used in this section for treating J_1^{dd} . The same approximation also leads naturally to the simple three-level model for superexchange described in the following section.

V. THREE-LEVEL MODEL OF SUPEREXCHANGE IN Mn-BASED MATERIALS

A. Three-level model

A transparent expression for the superexchange contribution to $J^{dd}(R_{ij})$ that is unobscured by the elaborate

calculations of the preceding section provides physical insight for this and other Mn-based systems. The simplified expression to be developed here is based on a three-level model which contains only the most relevant characteristics of the electronic structure. The model contains four parameters: an occupied d level at energy ϵ_d , an unoccupied d level at energy $\epsilon_d + U_{\text{eff}}$, a p level at the energy of the sp -valence-band edge, E_v , and the single hopping parameter V_{pd} (defined in Sec. II) which connects the p level to both d levels. The three levels ϵ_d , E_v , and $\epsilon_d + U_{\text{eff}}$ correspond to ϵ_d^1 , E_v , and ϵ_d^2 in Fig. 2, respectively. (The numerical values of the parameters will be different from those indicated in Fig. 2.) The model neglects conduction states since these have been shown to be unimportant for superexchange (Sec. IV).

The expression for superexchange is first calculated strictly within the three-level model, where perturbation theory (in analogy to the development in Sec. IV) yields⁷²

$$J_{hh}^{dd}(R_{ij}) = -2V_{pd}^4 [U_{\text{eff}}^{-1}(E_v - \epsilon_d - U_{\text{eff}})^{-2} - (E_v - \epsilon_d - U_{\text{eff}})^{-3}] f(r). \quad (5.1)$$

The dimensionless function $f(r)$ describes the dependence of $J^{dd}(R_{ij})$ on $R_{ij}/a \equiv r$, where a is the cubic lattice constant. This dependence is trivial for the pure three-level problem: $f(r) = 1$ for nearest neighbors and vanishes for more distant neighbors.⁷³

The expression (5.1) is actually more widely applicable than its derivation above might suggest. It describes Mn-Mn exchange in both DMS's and the rocksalt insulators MnO and α -MnS. Within each class of materials a *single*—material insensitive—function $f(r)$ may be defined. Here "material insensitive" means independent of electronic structure details within a class of materials having the same or closely related symmetries. Variations of J^{dd} within a class are therefore controlled by the simple three-level-derived prefactor in Eq. (5.1).

An expression for $f(r)$ in DMS's which is exact within the fourth-order perturbation theory of Sec. IV may be obtained by comparing Eq. (5.1) with Eq. (4.4). We denote the result by $\tilde{f}(r)$:

$$\begin{aligned} \tilde{f}(r) = & \sum_{n,k} \sum_{n',k'} \cos(ak \cdot r) \cos(ak' \cdot r) V_{pd}^{-4} |\tilde{V}_{pd}(n,k)|^2 |\tilde{V}_{pd}(n',k')|^2 \{ U_{\text{eff}}^{-1} [\epsilon_n(k) - \epsilon_d - U_{\text{eff}}]^{-1} - [\epsilon_n(k) - \epsilon_d - U_{\text{eff}}]^{-2} \} \\ & \times [\epsilon_{n'}(k') - \epsilon_d - U_{\text{eff}}]^{-1} \{ U_{\text{eff}}^{-1} (E_v - \epsilon_d - U_{\text{eff}})^{-2} - (E_v - \epsilon_d - U_{\text{eff}})^{-3} \}^{-1}. \end{aligned} \quad (5.2)$$

In the limit of flat valence bands, $\tilde{f}(r)$ becomes 9 for nearest neighbors and vanishes at larger r . Thus the flat band case reproduces the results of the three-level model as generalized to include valence-band degeneracy. For finite band dispersion the sums in Eq. (5.2) are dominated by the region near $k=0$. The discussion in Appendix B shows that both $|\tilde{V}_{pd}(n,k)|^2$ and the energy denominator factors decrease away from $k=0$. Phase cancellation due to the $\cos(k \cdot r)$ factors further enhance the zone-center contribution. Because these features are common

to all tetrahedrally bonded Mn-based DMS's, $\tilde{f}(r)$ is approximately material insensitive.

By making the following approximations to $\tilde{f}(r)$ we obtain a form for $f(r)$ which is explicitly insensitive to variations in the DMS energy bands $\epsilon_n(k)$ and electronic structure parameters ϵ_d , U_{eff} , and V_{pd} .

(1) The energy bands and $|\tilde{V}_{pd}(n,k)|^2$ are assumed to depend isotropically on k as discussed in Appendix B. The result for $|\tilde{V}_{pd}(n,k)|^2$ is [Eq. (B8)] $|\tilde{V}_{pd}(0)|^2 z^2(k) \cos^2(ak/4)$, where $z(k)$ is the averaged

projection of the periodic part of a valence-band Bloch function onto the anion p orbitals [Eq. (B7) and following; $z(0)=1$, $z(2\pi/a)\approx 0.8$]. The $\cos^2(ak/4)$ factor arises from the interference of hopping amplitudes to different anions.

(2) The energy denominators in Eq. (5.2) and $z(k)$ are each averaged over the Brillouin zone, weighted by $\cos^2(ak/4)$. This averaging is performed by first interpolating the k dependence and is carried out explicitly in Appendix C. Denoting this average for a quantity $A(k)$ by $\langle A(k) \rangle$, we define

$$a_n \equiv \left\langle \frac{E_v - \epsilon_d - U_{\text{eff}}}{\epsilon_n(k) - \epsilon_d - U_{\text{eff}}} \right\rangle, \quad b_n \equiv \left\langle \left(\frac{E_v - \epsilon_d - U_{\text{eff}}}{\epsilon_n(k) - \epsilon_d - U_{\text{eff}}} \right)^2 \right\rangle, \quad (5.3)$$

and $z \equiv \langle z(k) \rangle$.

(3) Terms containing $a_n - b_n$ are neglected relative to those containing $a_n + b_n$. For DMS parameters this approximation is accurate to better than 10%.

With these approximations

$$f(r) \approx \frac{1}{2} z^4 \left[\sum_n a_n \right] \left[\sum_m a_m + b_m \right] \times \left[\frac{1}{2} \left(\frac{a}{\pi} \right)^3 \int d^3k \cos(ak \cdot r) \cos^2\left(\frac{1}{4}ak\right) \right]^2. \quad (5.4)$$

The integral on the right-hand side is expressible in terms of special functions, but for the physically interesting region $r < 1.5$, including out to fourth nearest neighbors, it is well approximated by $3.3e^{-2.58r^2}$ (Appendix C). Thus,

$$f(r) \approx \frac{1}{2} z^4 \left[\sum_n a_n \right] \left[\sum_m a_m + b_m \right] (3.3e^{-2.58r^2})^2 \approx 30.7e^{-5.16r^2}. \quad (5.5)$$

Here $\frac{1}{2}(\sum_n a_n)(\sum_m a_m + b_m)$ is approximately 4.5 for a

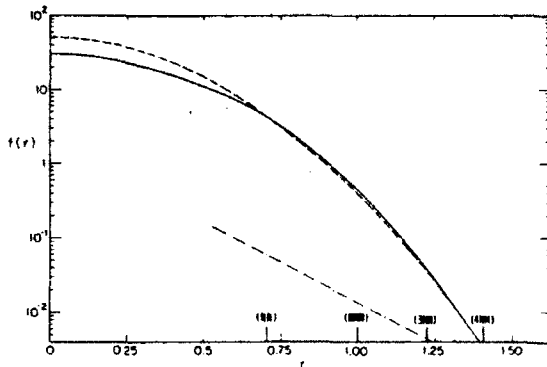


FIG. 5. The dimensionless functions $\tilde{f}(r)$ (solid line), $f(r)$ (dotted line) of Eq. (5.5), and the empirical $f(r)$ (dashed line) of Eq. (5.6), as a function of $r \equiv R/a$. Here a is the cubic lattice constant. Parameters correspond to those of $\text{Cd}_{0.7}\text{Mn}_{0.3}\text{Te}$. Also shown is the asymptotically valid exponential form of $f(r)$ (dot-dashed line) for the same parameters. The first four nearest neighbors on the fcc magnitude lattice are indicated by NN, NNN, 3NN, and 4NN.

wide range of DMS parameters (Appendix C), including those of Sec. IV. Finite valence-band dispersion is responsible for the 50% reduction from the flat band value of 9.

Figure 5 shows $f(r)$ (dotted line), and the $\tilde{f}(r)$ (solid line; Eq. (5.2)) corresponding to $\text{Cd}_{0.7}\text{Mn}_{0.3}\text{Te}$ parameters. The functions f and \tilde{f} agree at small r where the averaging assumption (2) is most accurate. At larger r the neglect of k dependence in the energy denominators causes f to fall off somewhat too quickly. The reasonableness of the functional form given by Eq. (5.5) suggests fitting $f(r)$ empirically as

$$f(r) \approx 51.2e^{-4.89r^2} \quad (5.6)$$

(the dashed line in Fig. 5). This function reproduces $\tilde{f}(r)$ to 20% for first through fourth nearest neighbors⁷⁴ with $f(\text{NN})=4.4$ and $f(\text{NNN})=0.4$. (Here NN and NNN denote nearest and next-nearest neighbors, respectively.) Also shown in Fig. 5 is the exponential asymptotic form for $\tilde{f}(r)$ obtained analytically as described in Ref. 68. The exponential is apparently inapplicable for $r < 1.5$. Table II contains parameters and the resulting $J^{dd}(R_{ij})$ value for $\text{Cd}_{1-x}\text{Mn}_x\text{Te}$ using empirical $f(r)$ of Eq. (5.6). [The $\sim 5\%$ difference between this value of J^{dd} and the result in Sec. IV is due to the discrepancy between $f(\text{NN})$ and $\tilde{f}(\text{NN})$, and the neglect of J_{he}^{dd} terms.]

B. Chemical trends in DMS's

The usefulness of the three-level model will be illustrated first by applying it to DMS's other than $\text{Cd}_{1-x}\text{Mn}_x\text{Te}$. Although much less experimental information is presently available for these materials, a consistent set of input data will be obtained here using what is available together with simple theoretical estimates. An additional consistency check on anion trends is provided by the results of first-principles ASW calculations.

For clarity the comparisons will be restricted to a single concentration, $x=0.1$. Calculations not discussed here indicate that the chemical trends are characteristic of a wide range of concentrations. The material insensitivity of $f(r)$ implies that the J_2^{dd}/J_1^{dd} ratio will be constant. Therefore we focus on changes in J_1^{dd} .

1. Anion substitutions

Changes in the anion species are particularly significant since both $d-d$ and $sp-d$ exchange in DMS's are primarily determined by the anion-derived upper valence bands. Chemical trends in the series $\text{Cd}_{0.9}\text{Mn}_{0.1}\text{Te} \rightarrow \text{Cd}_{0.9}\text{Mn}_{0.1}\text{Se} \rightarrow \text{Cd}_{0.9}\text{Mn}_{0.1}\text{S}$ are summarized in the first three columns of Table II. The input parameters $E_v - \epsilon_d$, U_{eff} , and V_{pd} for the selenide and sulfide are obtained as follows.

(1) $E_v - \epsilon_d$ is obtained from photoemission data.^{14,75-78} The surprising constancy of this difference in Cd-based DMS's presumably results from two competing effects. E_v shifts to lower energy (by about 1 eV between the telluride and selenide and 0.80 eV between the selenide and sulfide⁷⁹) due to the deeper anion potential seen by the outer valence p electrons. For the same sequence the ma-

TABLE II. Chemical trends for $M_{1-x}^{II}Mn_xX^{VI}$, computed using the three-level model, compared with experiment. The calculations of J_1^{dd} employed Eq. (5.1) with $f(r)=4.4$ for nearest neighbors as given by Eq. (5.6).

	$Cd_{0.9}Mn_{0.1}Te$	$Cd_{0.9}Mn_{0.1}Se$	$Cd_{0.9}Mn_{0.1}S$	$Zn_{0.9}Mn_{0.1}Te$	$Zn_{0.9}Mn_{0.1}Se$	$Zn_{0.9}Mn_{0.1}S$
Input parameters						
$E_v - \epsilon_d$ (eV)	3.4 ^a	3.4 ^b	3.4 ^c	3.4	3.4 ^d	3.4
U_{eff} (eV)	7.0 ^e	7.6	7.9	7.0	7.6	7.9
V_{pd} (eV)	0.219	0.255	0.330	0.240	0.277	0.351 ^f
$d_{Mn-X^{VI}}$ (Å)	2.759	2.572	2.453	2.722	2.533	2.411
Theoretical estimates						
[Eq. (5.1)] J_1^{dd}/k_B (K)	-7.6	-9.0	-21.0	-11.0	-13.0	-27.0
Experiment						
J_1^{dd}/k_B (K)	-6.3 ^g	-7.9 ^h	-8.6 ⁱ	-8.8 ^k	-9.9 ^l	-16.1 ^m
	-6.1 ^h	-8.1 ^j	-10.6 ⁱ	-9.3 ^l	-12.3 ^m	

^aReference 14.

^bReference 76.

^cReferences 75 and 77.

^dReference 78.

^eReference 11.

^fEstimated in text.

^gReference 31.

^hReference 32.

ⁱReference 37.

^jReference 36.

^kReference 38.

^lReference 39.

^mReference 40.

terials become more ionic and the d -level energy ϵ_d also shifts to lower energy because of the larger Mn-to-anion charge transfer.

(2) The variations in U_{eff} are estimated using a simple electrostatic argument. Although information on this parameter is not available for DMS's other than $Cd_{1-x}Mn_xTe$, the value of U_{eff} is not expected to change appreciably as a function of anion substitution since it is largely an intra-atomic property of Mn. A slight increase is expected in the series telluride \rightarrow selenide \rightarrow sulfide due to the reduced screening associated with the increasing Mn to anion charge transfer. We estimate U_{eff} by assuming a linear dependence on the inverse dielectric constant ϵ_0^{-1} and fitting to $Cd_{1-x}Mn_xTe$ and MnO . ($U_{eff}=7$ and 9 eV and $\epsilon_0=0.14$ and 0.25, respectively, for the two materials.^{2,80,81}) The values⁸⁰ $\epsilon_0^{-1}=0.17$ for CdSe and 0.19 for CdS lead immediately to the U_{eff} entries in Table II. The estimated variations from the telluride to the sulfide is less than 15%.

(3) The p - d hybridization parameter V_{pd} is determined from Eq. (3.4) using the above parameters and the experimental sp - d exchange constants $N\beta$ listed in Table I. The increase in V_{pd} from the telluride to the sulfide is qualitatively consistent with scaling arguments for V_{pd} given a decrease in the Mn-anion bond length. Different scaling theories^{82,83} predict a bond length d dependence of either d^{-4} or $d^{-7/2}$. Recent extended x-ray absorption fine-structure (EXAFS) studies of a number of semiconducting alloys including $Cd_{1-x}Mn_xTe$ (Ref. 84) provide some further information. They show individual cation-anion bond lengths in the alloy to retain values close to those of the limiting crystals. A simple central-force model⁸⁵ based on those results suggests that the Mn-anion bond length in $M_{1-x}^{II}X^{VI}$ DMS's should exhibit the weak x dependence

$$d_{Mn-X^{VI}}(x) \approx d_{Mn-X^{VI}} + \frac{1}{4}(1-x)(d_{Mn-X^{VI}}^0 - d_{Mn-X^{VI}}^1). \quad (5.7)$$

Here $d_{Mn-X^{VI}}^0$ and $d_{Mn-X^{VI}}^1$ are the nearest-neighbor bond lengths in the limiting $x=0$ and $x=1$ zinc-blende crystals. The values of $d_{Mn-X^{VI}}(x=0.1)$ listed in Table II are obtained from Eq. (5.7) and the tabulated crystalline bond lengths in Ref. 86. With the value of V_{pd} determined in Sec. III for $Cd_{0.9}Mn_{0.1}Te$ scaled by the $d_{Mn-X^{VI}}(x=0.1)$ of Table II, the scaling theories yield V_{pd} in $Cd_{0.9}Mn_{0.1}Se$, $Cd_{0.9}Mn_{0.1}S$ as 0.31, 0.36 eV (d^{-4}), or 0.29, 0.34 eV ($d^{-7/2}$). Neither set of values agrees particularly well with the experimentally determined entries in Table II, probably because chemical differences between the anions are neglected.

Substitution of $E_v - \epsilon_d$, U_{eff} , and V_{pd} determined in (1)–(3) above into Eq. (5.1) yields the theoretical prediction for J_1^{dd} listed in Table II. The 18% increase from the telluride to the selenide is in reasonable agreement with the 25% increase observed experimentally.^{31,34} The larger predicted increase in $|J_1^{dd}|$ from selenide to sulfide somewhat overestimates the experimental trend. The discrepancy is still within the accuracy of the model, and may be corrected when more-accurate input parameters (e.g., U_{eff}) become available. (To aid comparison, the experimental J_1^{dd} entries in Table II are all taken from experiments in which the effects of second and more-distant neighbor exchanges are approximately corrected for.)

The results of ASW-LSDA calculations listed in Table III for the limiting crystalline compounds $MnTe$, $MnSe$, and MnS are qualitatively consistent with the anion trends. The calculations assume that all three have the zinc-blende structure and an AF-I antiferromagnetic ordering. (At small Mn concentrations $Cd_{1-x}Mn_xSe$ and $Cd_{1-x}Mn_xS$ actually have the wurtzite structure.) The spin splitting $\epsilon_d^{\uparrow} - \epsilon_d^{\downarrow}$, or U_{eff} in the present model, increases somewhat from the telluride to the sulfide although the magnitude of this splitting is known to be seriously underestimated in the LSDA (Sec. II and Appendix A). The difference $E_v - \epsilon_d$ is roughly constant

TABLE III. ASW-LSDA results for zinc-blende MnTe, MnSe, and MnS in the AF-I ordering. Here a is the cubic lattice constant, and M_{loc} is the Mn-sphere magnetic moment. The meaning of $\epsilon_d^j - \epsilon_d^i$ and $E_v - \epsilon_d^j$ in all three systems is the same as indicated in Fig. 2 for MnTe.

	a (Å)	M_{loc} (μ_B)	$\epsilon_d^j - \epsilon_d^i$ (eV)	$E_v - \epsilon_d^j$ (eV)	J_1^{dd}/k_B (K)
MnTe	6.34	4.23	3.2	2.2	-17
MnSe	5.82	4.15	3.4	2.1	-24
MnS	5.60	4.14	3.9	2.4	-26

across the series, although the values are $\sim 30\%$ smaller than those listed in Table II. The increasing $|N\beta|$ values in the ASW results in Table I provide support for an increasing V_{pd} from the telluride to the sulfide. The J_1^{dd} values in Table III are obtained as before from ASW total-energy differences between AF-I and ferromagnetic orderings. The increase in magnitude is smaller than that given in Table II. As was found for the larger discrepancy in J_1^{dd} magnitudes, the discrepancy in the telluride-to-selenide J_1^{dd} trend is probably associated with the LSDA underestimate of the energy of unoccupied Mn 3d levels (Sec. II and Appendix A).

2. Cation substitutions

Changes in the cation species play a far less important role in determining the magnetic properties. Here we consider only the replacement of Cd with Zn. Hg-based DMS's are omitted because of larger experimental uncertainties in $sp-d$ exchange constants. Furthermore, J_{he}^{dd} associated with the Bloembergen-Rowland interaction, neglected in this section, plays a more important role in the zero-gap case. Nevertheless, superexchange is believed to be dominant in Hg-based alloys.⁸⁷

The substitution of Zn for Cd has only an indirect effect on the band-structure features relevant to superexchange. We estimate the associated changes in J_1^{dd} using Eq. (5.1) and the input data listed in Table II. $E_v - \epsilon_d$ and U_{eff} are assumed to be the same in the corresponding Cd and Zn alloys since these parameters are determined primarily by the Mn and the anion. (Experimental information is presently available only for $\text{Zn}_{1-x}\text{Mn}_x\text{Se}$, when $E_v - \epsilon_d$ is 3.5 ± 0.1 eV, consistent with this assumption.⁷⁸)

V_{pd} values in $\text{Zn}_{0.9}\text{Mn}_{0.1}\text{Te}$ and $\text{Zn}_{0.9}\text{Mn}_{0.1}\text{Se}$ are determined from the experimental $N\beta$ values in Table I. Small but definite increases in V_{pd} are observed relative to the corresponding Cd alloys. We interpret this trend as an indirect effect of the cation on the Mn-anion bond length. The $d_{\text{Mn-X}}$ values in Table II indeed decrease slightly as Cd is replaced by Zn. The variations in V_{pd} for $\text{Cd}_{0.9}\text{Mn}_{0.1}\text{Te} \rightarrow \text{Zn}_{0.9}\text{Mn}_{0.1}\text{Te}$ and $\text{Cd}_{0.9}\text{Mn}_{0.1}\text{Se} \rightarrow \text{Zn}_{0.9}\text{Mn}_{0.1}\text{Se}$ in fact are well described by a $d^{-7/2}$ or d^{-4} power law. (Scaling works better here than for the anion trends because the chemical nature of the anion is unchanged and the variation in d is smaller.) In the absence of an experimental $N\beta$ value, we estimate V_{pd} for $\text{Zn}_{1-x}\text{Mn}_x\text{S}$ by scaling the $\text{Cd}_{0.9}\text{Mn}_{0.1}\text{S}$ value.

The J_1^{dd} results in Table II indicate a clear trend towards a larger superexchange interaction in Zn-substituted DMS's. Quantitative agreement with experiment is achieved for $\text{Zn}_{0.9}\text{Mn}_{0.1}\text{Te}$ and $\text{Zn}_{0.9}\text{Mn}_{0.1}\text{Se}$. The value of $|J_1^{dd}|$ in $\text{Zn}_{0.9}\text{Mn}_{0.1}\text{S}$ is found to be the largest of any of the DMS's considered here. This prediction agrees with a recent neutron scattering experiment.⁴⁰ By using the experimental values of J_1^{dd} given in Table II for $\text{Cd}_{1-x}\text{Mn}_x\text{S}$ and $\text{Zn}_{1-x}\text{Mn}_x\text{S}$ together with $N\beta$ for $\text{Cd}_{1-x}\text{Mn}_x\text{S}$ in Eqs. (5.1) and (3.4), we predict $N\beta$ for $\text{Zn}_{1-x}\text{Mn}_x\text{S}$ to be $-(2.2 \text{ to } 2.4)$ eV. This prediction should be checked experimentally.

An alternative model of cation trends has recently been proposed by Spalek *et al.*⁸⁸ They assume that J_1^{dd} is affected principally by the change in the Mn—anion—Mn bond angle due to the structural distortions associated with different cations. This undoubtedly has some effect, but is neglected here, since, as in the case of amorphous covalent semiconductors, we regard changes in V_{pd} due to small variations in bond length to be considerably more important.

The present approach provides a consistent interpretation of the increase in both $N\beta$ and J_1^{dd} as Cd is replaced by Zn. In addition, this interpretation implies a dependence of V_{pd} on x within the Cd and Zn alloy systems, since both must extrapolate to the same value at $x = 1$. If $d_{\text{Mn-X}}$ follows Eq. (5.7), a 6.2% increase in V_{pd} is predicted in $\text{Cd}_{1-x}\text{Mn}_x\text{Te}$ between $x = 0$ and $x = 0.75$. This leads to a 13% increase in $N\beta$ and a 27% increase in J_1^{dd} (if other factors are neglected).

C. MnO and α -MnS

It is remarkable that the three-level expression (5.1) is applicable to a quite different class of materials, illustrated by the insulators MnO and α -MnS. This is seen by calculating the Mn-Mn exchange interaction in these materials. The $f(r)$ appropriate to the rocksalt structure, hereafter denoted $f_{\text{RS}}(r)$, is again insensitive to the specific material.

The main differences between the electronic structure of DMS's and MnX ($X = \text{O, S}$) result primarily from the increased ionicity of the rocksalt compounds. They are (1) the anion p -derived levels lie primarily below the occupied Mn d levels and are significantly narrower than in DMS's; (2) U_{eff} is larger than in DMS's, because the screening charge on the Mn cation is decreased; (3) the higher symmetry of the rocksalt structure leads to $|\bar{V}_{pd}(v, k)|^2 = 0$ at both Γ and X .

Although we would expect the three-level model to apply generally to Mn-based nonmetals, the corresponding $f(r)$ for different classes of materials will generally depend on their point-group symmetry. For example, selection rules (Goodenough-Kanamori rules⁸⁹) reduce the region of the Brillouin zone where $p-d$ hybridization occurs, thereby decreasing $f(r)$. For DMS's these selection rules impose no restrictions; however, the higher symmetry of the rocksalt structure causes a reduction of nearest-neighbor superexchange by $\sim \frac{1}{2}$. The effect on $f(r)$ will generally depend both on the functional form of $\bar{V}_{pd}(v, k)$ and on the location of critical points in the ener-

TABLE IV. Chemical trends for the rocksalt compounds MnO and α -MnS, computed using the three-level model, compared with experiment. The calculations of J_1^{dd} employed by Eq. (5.1) with $f_{RS}(r)=4.4$ for nearest neighbors as given by Eq. (5.6).

	$E_v - \epsilon_d$ (eV)	U_{eff} (eV)	V_{pd} (eV)	d (Å)	$J_1^{dd}(\text{theory})/k_B$ (K)	$J_1^{dd}(\text{expt.})/k_B$ (K)
MnO	-2.5 ^a	9.0 ^b	0.46	2.225 ^a	-5.0	-7.2 ^a
α -MnS	0.5 ± 1.0 ^a	8.0	0.27	2.605 ^a	-1.7 ± 0.4	-4.4 ^a

^aReference 63, and references therein.

^bReference 2.

gy denominators of Eq. (5.2). For example, in DMS's the minima in energy denominators [Eq. (5.2)] and in $|\tilde{V}_{pd}(v, k)|^2$ both occur at Γ , causing $f(\text{NN})$ to be reduced by $\sim \frac{1}{2}$ from the flat-band result (cf. Sec. V A). By contrast, in the perovskite compound KMnF_3 , the minimum in the energy denominators at Γ corresponds to a zero in $\tilde{V}_{pd}(v, k)$, leading to a larger reduction, estimated at $\sim \frac{1}{4}$.

In MnX the flat-band limit should correspond to a good approximation for $f_{RS}(r)$ since $W(E_v - \epsilon_d - U_{eff})^{-1} \ll 1$. (W is the average bandwidth of the sp valence bands.⁹⁰) In contrast to DMS's, this limit here implies $f_{RS}(r)$ is nonzero for both first and second neighbors on the fcc magnetic lattice, since superexchange to both is mediated by p orbitals of the nearest-neighbor anions. Second neighbor superexchange is reduced by the same factor $\frac{1}{2}$ as first neighbor superexchange because only one anion mediates these processes, compared to two anions for first neighbors. In DMS's, $f(\text{NN})$ is reduced by $\frac{1}{2}$ due to the presence of broad bands (see preceding paragraph). It therefore turns out by accident that $f_{RS}(\text{NN}) \approx f(\text{NN})$. However, f_{RS} and f differ for second and more-distant neighbors. The function $f_{RS}(r)$ is expected to be similar in MnO and α -MnS because $W(E_v - \epsilon_d - U_{eff})^{-1} \ll 1$ in both. As in DMS's, f_{RS} is material insensitive because the k integrations are dominated by $|\tilde{V}_{pd}(v, k)|^2$.

Table IV contains parameters and calculated values of J_1^{dd} for MnO and α -MnS using Eq. (5.1) and (5.6) with $f_{RS}(\text{NN}) \approx f(\text{NN}) \approx 4.4$. $E_v - \epsilon_d$ was taken from the ASW-LSDA calculations of Terakura *et al.*;⁹¹ U_{eff} for α -MnS was estimated as in Sec. V B; V_{pd} was calculated from V_{pd} for $\text{Cd}_{1-x}\text{Mn}_x\text{Te}$ and was assumed to obey the $d^{-7/2}$ scaling law.

The good agreement of the calculated J_1^{dd} with experimental results given in Table IV in both magnitude and trend indicates that the three-level model is applicable to

MnX, and that a single function $f_{RS}(r)$, which needs to be calculated only once for each class of materials, can be defined. The calculations, like those for DMS's (Sec. V B), are remarkably simple, requiring only the electronic structure input parameters ($E_v - \epsilon_d$, U_{eff} , and V_{pd}) and the function f_{RS} . As a result it is reasonable to expect that the three-level model will also provide useful numerical estimates of exchange constants in other Mn-based nonmetals.

ACKNOWLEDGMENTS

This work was supported by U.S. Defense Advanced Research Agency (DARPA) through U.S. Office of Naval Research (ONR) Contracts Nos. ONR-N00014-86-K-0760 and 0033, by U.S. Joint Service Electronics Program (JSEP) through ONR Contract No. ONR-N00014-86-K-0465, and (for A.E.C.) the U.S. Department of Energy (Grant No. DE-FG02-84ER45130). One of us (B.E.L.) acknowledges partial support by the National Science Foundation during the beginning stages of this work. We have benefited from helpful discussions with R. L. Aggarwal, M. Cardona, A. Franciosi, J. K. Furdyna, T. M. Giebultowicz, A. V. Nurmikko, A. K. Ramdas, and Y. Shapira.

APPENDIX A: CORRECTIONS TO THE LSDA

To quantify the discussion of Sec. II, corrections to the LSDA eigenvalues has been estimated, employing a simple method based on empirical dielectric constants.⁵⁴ Corrections to the MnTe conduction and valence sp band edges, and the majority and minority spin levels of e_g symmetry at Γ , were computed. The value $\epsilon_0 = 7$ was derived by linear extrapolation from dielectric constants in the alloy for $x \leq 0.7$. The estimated difference between the LSDA eigenenergies, ϵ^{LSDA} , and the true quasiparticle energies,⁹² ϵ , is given by⁵⁴

$$\epsilon - \epsilon^{\text{LSDA}} = \frac{e^2}{2\epsilon_0} \int_{\text{unit cell}} d^3r d^3r' \frac{\delta n(r) \delta n(r') - \delta n^{\text{LSDA}}(r) \delta n^{\text{LSDA}}(r')}{|r - r'|} \quad (\text{A1})$$

Here

$$\delta n(r) = |\psi_\epsilon(r)|^2 \left[\int_{\text{unit cell}} |\psi_\epsilon(r)|^2 d^3r \right]^{-1}, \quad (\text{A2})$$

$\psi_\epsilon(r)$ is the LSDA wave function corresponding to ϵ^{LSDA} ,

and $\delta n^{\text{LSDA}}(r) = \delta n(r) + \delta n_{\text{scr}}(r)$. The LSDA screening charge $\delta n_{\text{scr}}(r)$ is given by

$$\delta n_{\text{scr}}(r) = \bar{n} \int d^3r' [g(|r - r'|; \bar{n}) - 1] \delta n(r'). \quad (\text{A3})$$

where $g(|r-r'|; \bar{n})$ is the pair distribution function (taken to be spin independent) for a uniform electron gas having the weighted average density

$$\bar{n} = \left| \int \delta n(r) n^{1/3}(r) d^3r \right|^3. \quad (\text{A4})$$

To aid comparison with experiment, scalar-relativistic corrections were also estimated. The MnTe sp -conduction and valence-band-edge shifts were approximated using the corresponding shifts for a Te atom:

$$\begin{aligned} (\text{energy shift of } \psi)_{\text{band}} &\approx \frac{(\text{core charge of } \psi)_{\text{band}}}{(\text{core charge of } \psi)_{\text{atom}}} \\ &\times (\text{energy shift of } \psi)_{\text{atom}}. \end{aligned} \quad (\text{A5})$$

These calculations lead to the following results.

(1) The LSDA correction is largest for the d levels since the associated orbitals are most localized. The occupied d levels are shifted to lower energies by 1.5 eV and the unoccupied levels to higher energies by 1.0 eV. Thus the energy required to create a separated d -electron- d -hole pair is underestimated by the LSDA spin splitting. Since the LSDA eigenvalues are computed using the ground-state potential, the LSDA spin splitting may actually correspond more closely to the energy of an intra-atomic $S = \frac{1}{2} \rightarrow S = \frac{3}{2}$ transition.⁹³ The corrections increase U_{eff} from 3.2 to 5.7 eV. This improves agreement with the value $U_{\text{eff}} = 7$ eV, derived from experiment, which was used in the magnetic calculations.

(2) The valence-band edge is shifted to lower energy by 0.5 eV due to the LSDA corrections, and by a further 0.4 eV by scalar-relativistic corrections. These shifts, combined with (1), cause the energy required to remove an electron from the top of the valence band and place it in an unoccupied d level infinitely far away in the crystal to increase from 1 to 2.9 eV. Additionally, the valence-band-edge-to-occupied d energy splitting increases to 0.6 eV from 2.3 to 2.9 eV. This value is closer to the 3.4 eV (for $x \leq 0.6$) value discussed in Sec. II.

APPENDIX B: ETBM MODEL AND SPHERICAL APPROXIMATION FOR H_0 AND H_{pd}

The empirical tight-binding model used to obtain the explicit forms of the H_0 and H_{pd} terms in Eq. (2.1) employs a minimal basis set consisting of one s orbital per cation and three p orbitals per anion. The resulting sp Hamiltonian H_0 provides a good semiquantitative description of the Te p -like upper valence bands in $\text{Cd}_{1-x}\text{Mn}_x\text{Te}$. The lowest conduction band is also reasonably described although this is less important for the numerical calculations of $J^{dd}(R_{ij})$ in Sec. IV. Scalar-relativistic effects are included in the model by the empirical choice of parameters. The neglect of spin-orbit splitting is not believed to lead to serious errors in $J^{dd}(R_{ij})$.

We consider interactions for first- and second-nearest neighbors. H_0 is then completely characterized by six Slater-Koster parameters⁹⁴ for which we introduce a

simplified notation in Table V. The parameter values for $\text{Cd}_{1-x}\text{Mn}_x\text{Te}$ listed in the third column of the table are obtained as follows.

(1) The cation on-site energy ϵ_c is assumed to exhibit the linear VCA variation

$$\epsilon_c = \Delta_c + x(\epsilon_c(\text{Mn}) - \epsilon_c(\text{Cd})). \quad (\text{B1})$$

Here $\epsilon_c(\text{Cd}) = 0.12$ eV and $\epsilon_c(\text{Mn}) = 1.72$ eV are the Cd 5s and Mn 4s on-site energy levels, respectively, and $\Delta_c = 3.16$ eV is chosen to reproduce the experimental $x = 0$ band gap.

(2) The anion on-site energy ϵ_a and the single nearest-neighbor hopping parameter V_{ca} are assumed to be independent of x and have the same value as in more-extensive ETBM parametrizations of CdTe.⁹⁵ The x independence of ϵ_a reflects a common anion assumption.

(3) The second-neighbor parameters (C, A_1, A_2) are also assumed to be x independent and are required to be no larger than $\sim 10\%$ of V_{ca} . The chosen values yield conduction and valence bandwidths in reasonable agreement with experiment.

The spherical approximation used in the calculation of $J^{dd}(R_{ij})$ assumes that the sp bands are isotropic and have the k dependence given by the diagonalization of H_0 along $\Gamma-X$. This direction is chosen because the resulting eigenvalues

$$\epsilon_{2,3}(k) = \epsilon_a + 4A_1[1 + \cos(\frac{1}{2}ak)] + 4A_2\cos(\frac{1}{2}ak) \quad (\text{B2})$$

and

$$\begin{aligned} \epsilon_{4,1}(k) &= \frac{1}{2}[g_1(k) + g_2(k)] \\ &\pm \left\{ \frac{1}{4}[g_1(k) - g_2(k)]^2 + 16V_{ca}^2 \sin^2(\frac{1}{4}ak) \right\}^{1/2} \end{aligned} \quad (\text{B3})$$

can be obtained analytically. Here

$$\begin{aligned} g_1(k) &= \epsilon_c + 4C[1 + 2\cos(\frac{1}{2}ak)], \\ g_2(k) &= \epsilon_a + 4A_2 + 8A_1\cos(\frac{1}{2}ak). \end{aligned} \quad (\text{B4})$$

Bands 2 and 3 are degenerate valence bands with an x -independent bandwidth of 2.2 eV. Band 1 is the wider valence band, with a bandwidth of 5.1 eV at $x = 0$ and 4.8 eV at $x = 1$. Band 4 is the sp conduction band, with a bandwidth of 2.8 eV at $x = 0$ and 2.5 eV at $x = 1$. The band gap is given by $(1.6 + 1.6x)$ eV.

TABLE V. ETBM parameters for $\text{Cd}_{1-x}\text{Mn}_x\text{Te}$. The table also establishes the correspondence between the Slater-Koster notation and the notation used in this work.

Slater-Koster	Parameter	Value (eV)
$E_{ss}(000)_{cc}$	ϵ_c	$3.16 + 1.6x$
$E_{ss}(000)_{aa}$	ϵ_a	0.10
$E_{ss}(\frac{1}{2}\frac{1}{2}\frac{1}{2})_{ca}$	V_{ca}	1.103
$E_{ss}(110)_{cc}$	C	0.015
$E_{ss}(110)_{aa}$	A_1	0.13
$E_{ss}(011)_{aa}$	A_2	0.15

We now consider H_{pd} , for which we compute $\tilde{V}_{pd}(n, \mathbf{k})$ within the ETBM. Let $|d(i)\rangle$ be a d function at site i . We assume a Löwdin orthogonalization^{9b} has made this function orthogonal to the other basis functions. In the VCA

$$\begin{aligned} \langle d(i) | H | n \mathbf{k} \rangle &= e^{i\mathbf{k} \cdot \mathbf{R}_i} N^{-1/2} \sum_{\alpha=x,y,z} a_{p_i, \alpha}^{(n)}(\mathbf{k}) \sum_{\delta_j} e^{i\mathbf{k} \cdot \delta_j} V_{pd} \\ &\equiv e^{i\mathbf{k} \cdot \mathbf{R}_j} \tilde{V}_{pd}(n, \mathbf{k}). \end{aligned} \quad (\text{B5})$$

Here δ_j is one of the four \mathbf{R}_{ij} associated with nearest-neighbor anions to the Mn, and $a_{\alpha v}^{(n)}(\mathbf{k})$ is the coefficient in the expansion of the Bloch function $|n \mathbf{k}\rangle$ of the Bloch sum $|\alpha v \mathbf{k}\rangle$ corresponding to the α th basis function ϕ_α at τ_v . ($\alpha = s, p_x, p_y, p_z$; $v = a, c$ for anion and cation.) Our basic approximation is that the hopping integral V_{pd} is (1) only nonzero for nearest-neighbor anion p orbitals, and (2) independent of the type of p and d orbitals involved. We thus define

$$V_{pd} \equiv \int \phi_d^*(\mathbf{r}) H \phi_{p_i}(\mathbf{r} - \delta_j - \tau_a) d^3r. \quad (\text{B6})$$

Here $\phi_{p_i}(\mathbf{r} - \delta_j - \tau_a)$ is a p_i orbital centered at $\delta_j + \tau_a$. The basic reason for this is a good approximation for DMS's is that V_{pd} is determined from experiments which give an orbitally averaged quantity. On the other hand, orbital indices are summed over in the calculation of $J^{dd}(R_{ij})$, so that the averaged parameter should provide a good approximation.

$|\tilde{V}_{pd}(n, \mathbf{k})|^2$, which occurs in the calculation of $J^{dd}(R_{ij})$, contains the factor

$$\begin{aligned} \left| \sum_{\delta_j} e^{i\mathbf{k} \cdot \delta_j} \right|^2 &= 4 \left[1 + \cos(\tfrac{1}{2}ak_x) \cos(\tfrac{1}{2}ak_y) \right. \\ &\quad \left. + \cos(\tfrac{1}{2}ak_y) \cos(\tfrac{1}{2}ak_z) \right. \\ &\quad \left. + \cos(\tfrac{1}{2}ak_z) \cos(\tfrac{1}{2}ak_x) \right]. \end{aligned} \quad (\text{B7})$$

This has a maximum at $\mathbf{k} = 0$ and decreases in all directions away from $\mathbf{k} = 0$, vanishing at the X point. This decrease comes from the interference of hopping amplitudes to different anion neighbors as k^{-1} becomes comparable with the Mn-anion distance. The factor $|\sum_{\alpha=x,y,z} a_{p_i, \alpha}^{(n)}(\mathbf{k})|^2 \equiv |\hat{\mathbf{z}}_n(\mathbf{k})|^2$ is the square of the projection of the periodic part of the Bloch function at \mathbf{k} onto the anion p orbitals. For the upper valence bands, this factor is just 1 at $\mathbf{k} = 0$ and decreases along $\Gamma-X$. For the lowest conduction band $a_{p_i, 1}^{(n)}(\mathbf{k} = 0) = 0$. (This remains true for a more general basis than we consider here, because it follows from a selection rule.) The net effect of the two \mathbf{k} dependencies is to suppress hopping through the conduction band relative to the valence bands, and to emphasize hopping through the states near the zone center.

We adopt an approximation to $\tilde{V}_{pd}(n, \mathbf{k})$ which preserves these features and is consistent with the assumed spherical energy bands (calculated along $\Gamma-X$).

The $a_{p_i, 1}^{(n)}(\mathbf{k})$ are calculated along $\Gamma-X$, $|\tilde{V}_{pd}(n, \mathbf{k})|^2$ is averaged over principal directions, and the result is taken to be a function of $|\mathbf{k}|$ in a spherical Brillouin zone:

$$|\tilde{V}_{pd}(n, \mathbf{k})|^2 \approx 16 V_{pd}^2 N^{-1} z^2(k) \cos^2(\tfrac{1}{4}ak). \quad (\text{B8})$$

Here $z^2(k)$ is the average of $|\hat{\mathbf{z}}_n(\mathbf{k})|^2$ over principal directions. (For the three sp valence bands the result of this averaging is independent of n .)

APPENDIX C: DERIVATION AND PROPERTIES OF $f(r)$

Beginning with the definition of $\tilde{f}(r)$ given in Eq. (5.2), with the isotropic approximation made for the \mathbf{k} dependence of energy bands and $|\tilde{V}_{pd}(n, \mathbf{k})|^2$ [Eq. (B7) and following], the energy denominators are averaged next over the Brillouin zone. Averaging is reasonable because the energy denominators are weakly \mathbf{k} dependent compared to $|\tilde{V}_{pd}(n, \mathbf{k})|^2$. The average is weighted by the dominant $\cos^2(ak/4)$ factor in $|\tilde{V}_{pd}(n, \mathbf{k})|^2$ [Eq. (B8)]. This choice of weighting ensures that $f(r)$ has the correct limit as $r \rightarrow 0$. The average of a quantity $A(k)$, denoted by $\langle A(k) \rangle$, is given explicitly by

$$\langle A(k) \rangle \equiv \left[\int d^3k \cos^2(\tfrac{1}{4}ak) \right]^{-1} \int d^3k \cos^2(\tfrac{1}{4}ak) A(k). \quad (\text{C1})$$

In order to perform this averaging on Eq. (5.2), the \mathbf{k} dependence of the energy denominators and of the factor $z(k)$ [Eq. (B7) and following] are approximated by

$$\begin{aligned} [\epsilon_n(k) - \epsilon_d - U_{\text{eff}}]^{-1} &\approx (E_v - \epsilon_d - U_{\text{eff}})^{-1} \\ &\quad \times [y_n + (1 - y_n) \cos^2(\tfrac{1}{4}ak)], \end{aligned} \quad (\text{C2})$$

and

$$z(k) \approx z \left[\frac{2\pi}{a} \right] + \left[1 - z \left[\frac{2\pi}{a} \right] \right] \cos^2(\tfrac{1}{4}ak). \quad (\text{C3})$$

The y_n are defined by

$$y_n \equiv (E_v - \epsilon_d - U_{\text{eff}}) / (E_v - W_n - \epsilon_d - U_{\text{eff}}),$$

where W_n is the bandwidth of the valence band $\epsilon_n(k)$ [Eqs. (B2) and (B3)]. The interpolation of Eq. (1.2) is chosen to reproduce the correct values and first derivatives of the energy denominators at Γ and X . Using

$$\langle \cos^2(\tfrac{1}{4}ak) \rangle \approx 0.46 \quad \text{and} \quad \langle \cos^4(\tfrac{1}{4}ak) \rangle \approx 0.28, \quad (\text{C4})$$

we compute the quantities a_n , b_n , and z defined in Eq. (5.3):

$$a_n = y_n + 0.46(1 - y_n), \quad (\text{C5})$$

$$b_n = y_n^2 + 0.92y_n(1 - y_n) + 0.28(1 - y_n)^2, \quad (\text{C6})$$

and

$$z = z \left[\frac{2\pi}{a} \right] + 0.46 \left[1 - z \left[\frac{2\pi}{a} \right] \right] \approx 0.89. \quad (\text{C7})$$

Inserting Eqs. (C5)–(C7) in Eq. (5.2) and neglecting

$a_n - b_n$ relative to $a_n + b_n$ (accurate to $\sim 10\%$ for y_n corresponding to a wide range of the parameters $E_v - \epsilon_d$, U_{eff} , and W_n), we obtain Eq. (5.4).

The integral on the right-hand side of Eq. (5.4) is

$$\frac{1}{2} \left[\frac{a}{\pi} \right]^3 \int d^3k \cos(ak \cdot r) \cos^2(\frac{1}{4}ak) \\ = - \frac{2}{\pi r} \frac{\partial}{\partial r} \{ [\Gamma(2+2r)\Gamma(2-2r)]^{-1} \}. \quad (\text{C8})$$

By expanding

$$\ln[\Gamma(2 \pm 2r)] \approx \pm 2r\psi(2) + 1/2(2r)^2\psi'(2),$$

where $\psi(r) \equiv d(\ln\Gamma)/dr$ is the digamma function, the in-

tegral is approximated by

$$\frac{16}{\pi} \psi'(2) \exp[-4\psi'(2)r^2]. \quad (\text{C9})$$

Using⁹⁷ $\psi'(2) \approx 0.645$ yields Eq. (5.5) for $f(r)$.

The results of the averaging appear in Eq. (5.4) as the factors z^4 and $\frac{1}{2}(\sum_n a_n)(\sum_m a_m + b_m) \equiv Q$. The factor Q is insensitive to changes in valence bandwidth. To show this, we compute Q assuming all valence bands have the average bandwidth W , with $E_v - \epsilon_d - U_{\text{eff}} = 3.6$ eV. For $W=0$, one has $Q=9$, but for the range $W=2$ eV to $W=6$ eV relevant to DMS's, Q changes only from 5.5 to 3.8.

*Present address: Department of Physics, Boston University, 590 Commonwealth Ave., Boston, MA 02215.

†Present address: Research Staff, Ford Motor Company, Dearborn, MI 48121-2053.

¹For recent reviews, see J. K. Furdyna, J. Appl. Phys. 53, 637 (1982); and N. B. Brandt and V. V. Moshchakov, Adv. Phys. 33, 193 (1984).

²P. W. Anderson, in *Solid State Physics*, edited by F. Seitz and D. Turnbull (Academic, New York, 1963), Vol. 14, p. 99.

³B. E. Larson (unpublished).

⁴B. E. Larson, K. C. Hass, H. Ehrenreich, and A. E. Carlsson, Solid State Commun. 56, 347 (1985).

⁵K. C. Hass, B. E. Larsson, H. Ehrenreich, and A. E. Carlsson, J. Magn. Magn. Mater. 54-57, 1283 (1986).

⁶K. C. Hass and H. Ehrenreich, J. Vac. Sci. Technol. A 1, 1678 (1983).

⁷H. Ehrenreich and L. Hodges, in *Methods in Computational Physics*, edited by B. J. Alder (Academic, New York, 1968), Vol. 8, p. 149.

⁸A. R. Williams, J. Kübler, and C. D. Gelatt, Phys. Rev. B 19, 6094 (1979).

⁹U. von Barth and L. Hedin, J. Phys. C 5, 1629 (1972).

¹⁰See, e.g., N. T. Khoi and J. A. Gaj, Phys. Status Solidi B 83, K133 (1977).

¹¹P. Lautenschlager, S. Logothetidis, L. Viña, and M. Cardona, Phys. Rev. B 32, 3811 (1985).

¹²T. Kendlewick, J. Phys. C 14, L407 (1981).

¹³Y. R. Lee, A. K. Ramdas, and R. L. Aggarwal, Phys. Rev. B 33, 7383 (1985).

¹⁴M. Taniguchi, L. Ley, R. L. Johnson, J. Ghijsen, and M. Cardona, Phys. Rev. B 33, 1206 (1986).

¹⁵C. Webb, M. Kaminska, M. Lichtensteiger, and J. Lagowski, Solid State Commun. 40, 609 (1981).

¹⁶P. Oelhafen, M. P. Vecchi, J. L. Freeouf, and V. L. Moruzzi, Solid State Commun. 44, 1547 (1982).

¹⁷J. Kossut, Phys. Status Solidi B 78, 536 (1976).

¹⁸J. A. Gaj, R. Planel, and G. Fishman, Solid State Commun. 29, 435 (1979).

¹⁹D. Heiman, Y. Shapira, and S. Foner, Solid State Commun. 51, 603 (1984), and references therein.

²⁰R. L. Aggarwal, S. N. Jaspersion, P. Becla, and R. R. Galazka, Phys. Rev. B 32, 5132 (1985).

²¹A. Twardowski, T. Dietl, and M. Demianiuk, Solid State Commun. 48, 845 (1983), and references therein.

²²A. Twardowski, P. Swiderski, M. von Ortenburg, and R.

Pauthenet, Solid State Commun. 50, 509 (1984).

²³G. Barilero, C. Rigaux, M. Menant, Nguyen Hy Hau, and W. Giriat, Phys. Rev. B 32, 5144 (1986).

²⁴Y. Shapira, D. Heiman, and S. Foner, Solid State Commun. 44, 1243 (1982).

²⁵R. L. Aggarwal, S. N. Jaspersion, J. Stankiewicz, Y. Shapira, S. Foner, B. Khazai, and A. Wold, Phys. Rev. B 28, 6907 (1983).

²⁶A. Twardowski, M. von Ortenburg, M. Demianiuk, and R. Pauthenet, Solid State Commun. 51, 849 (1984).

²⁷M. Nawrocki, J. P. Lascaray, D. Coquillat, and M. Demianiuk, in *Proceedings of the MRS Symposium on Diluted Magnetic (Semimagnetic) Semiconductors, Boston 1986*, edited by R. L. Aggarwal, J. K. Furdyna, and S. von Molnar (Materials Research Society, Boston, 1987), p. 65.

²⁸Y. B. Abramishvili, S. I. Gubarev, A. V. Komarov, and S. M. Ryabchenko, Fiz. Tverd. Tela (Leningrad) 26, 1095 (1984) [Sov. Phys.—Solid State 26, 666 (1984)].

²⁹D. A. Alov, S. I. Gubarev, V. B. Timofeev, and B. N. Shepel, Pis'ma Zh. Eksp. Teor. Fiz. 34, 76 (1981) [JETP Lett. 34, 71 (1981)].

³⁰D. Heiman, Y. Shapira, and S. Foner, Solid State Commun. 45, 899 (1983).

³¹B. E. Larson, K. C. Hass, and R. L. Aggarwal, Phys. Rev. B 33, 1789 (1986).

³²Y. Shapira and N. F. Olivera, Jr., Phys. Rev. B 35, 6888 (1987).

³³Y. Shapira, S. Foner, D. H. Ridgley, K. Dwight, and A. Wold, Phys. Rev. B 30, 4021 (1984).

³⁴R. L. Aggarwal, S. N. Jaspersion, Y. Shapira, S. Foner, T. Sakakibara, T. Goto, N. Miura, K. Dwight, and A. Wold, in *Proceedings of the 17th International Conference on the Physics of Semiconductors*, edited by J. D. Chadi and W. A. Harrison (Springer, New York, 1985), p. 1419.

³⁵T. Giebultowicz, B. Lebeck, B. Buras, W. Minor, H. Kepa, and R. R. Galazka, J. Appl. Phys. 55, 2305 (1984).

³⁶J. P. Lascaray, M. Nawrocki, J. M. Broto, M. Rakoto, and M. Demianiuk, Solid State Commun. 61, 401 (1987).

³⁷D. E. Bartholomew, E.-K. Suh, S. Rodriguez, A. K. Ramdas, and R. L. Aggarwal, Solid State Commun. 62, 35 (1987).

³⁸L. M. Corliss, J. M. Hastings, S. M. Shapiro, Y. Shapira, and P. Becla, Phys. Rev. B 33, 608 (1986).

³⁹G. Barilero, C. Rigaux, Nguyen Hy Hau, J. C. Picoche, and W. Giriat, Solid State Commun. 62, 345 (1987).

⁴⁰T. M. Giebultowicz, J. J. Rhyne, and J. K. Furdyna, J. Appl.

- Phys. 61, 3537 (1987).
- ⁴¹C. E. T. Gonçalves da Silva and L. M. Falicov, J. Phys. C 5, 63 (1972).
 - ⁴²B. Koiller and L. M. Falicov, J. Phys. C 8, 695 (1975).
 - ⁴³A. K. Bhattacharjee, G. Fishman, and B. Coqblin, Physica B + C 117-118B, 449 (1983).
 - ⁴⁴J. R. Schrieffer and P. A. Wolff, Phys. Rev. 149, 491 (1966); J. R. Schrieffer, J. Appl. Phys. 38, 1143 (1967). We have corrected a factor-of-2 error in the latter [in Eq. (2.13a), $(4S)^{-1}$ should be $(2S)^{-1}$].
 - ⁴⁵N. Bloembergen and T. J. Rowland, Phys. Rev. 97, 1697 (1955).
 - ⁴⁶Most recently, in M. A. Novak, O. G. Symko, D. J. Zheng, and S. Oseroff, Phys. Rev. B 33, 6391 (1986). See also Ref. 64 and the reviews of Ref. 1.
 - ⁴⁷J. K. Furdyna, W. Giriat, D. F. Mitchell, and G. I. Sproule, J. Solid State Chem. 46, 349 (1983).
 - ⁴⁸T. Jarlborg and A. J. Freeman, Phys. Lett. 74A, 349 (1979).
 - ⁴⁹For example, the ASW indirect gaps for Si and C are 0.51 and 4.11 eV, respectively [P. A. Fedders and A. E. Carlsson (unpublished)]. The pseudopotential gaps are 0.56 and 4.05 eV [C. S. Wang and W. E. Pickett, Phys. Rev. Lett. 51, 597 (1983); W. E. Pickett and C. S. Wang, Phys. Rev. B 30, 4719 (1984)]. The LAPW gap for Si is 0.5 eV [D. R. Hamann, Phys. Rev. Lett. 42, 662 (1979)].
 - ⁵⁰S.-H. Wei and A. Zunger, Phys. Rev. Lett. 56, 2391 (1986); Phys. Rev. B 35, 2340 (1987).
 - ⁵¹For a discussion of the meaning of density-functional eigenvalues, see J. P. Perdew, in *Density Functional Methods in Physics*, edited by R. M. Dreizler and J. da Providencia (Plenum, New York, 1985).
 - ⁵²J. P. Perdew and M. Levy, Phys. Rev. Lett. 51, 1884 (1983).
 - ⁵³L. J. Sham and M. Schlüter, Phys. Rev. Lett. 51, 1888 (1983).
 - ⁵⁴A. E. Carlsson, Phys. Rev. B 31, 5178 (1985).
 - ⁵⁵ETBM-CPA calculations for $\text{Cd}_{1-x}\text{Mn}_x\text{Te}$ including d levels are described in H. Ehrenreich, K. C. Hass, N. F. Johnson, B. E. Larson, and R. J. Lempert, in *Proceedings of the 17th International Conference on the Physics of Semiconductors*, edited by O. Engström (World-Scientific, Singapore, 1987).
 - ⁵⁶M. Pessa and O. Jylhä, Appl. Phys. Lett. 45, 646 (1984).
 - ⁵⁷Atomic spectra indicate that other occupations (d^3, d^7) involve large energy costs [C. E. Moore, *Atomic Energy Levels* (U.S. GPO, Washington, D.C., 1971), Vol. II]. Within this subspace, H_d is equivalent within Hartree-Fock to the usual (per site): $H = U \sum_m n_{m\uparrow} n_{m\downarrow} + \frac{1}{2} U' \sum_{m \neq m'} n_{m\uparrow} n_{m'\uparrow} + \sum_{m \neq m'} \epsilon_d n_{m\uparrow} n_{m'\downarrow} + \frac{1}{2} J \sum_{m \neq m'} n_{m\uparrow} n_{m'\downarrow}$. In this notation, $\epsilon_d = \epsilon_d^0 + 4U'$, $U_{\text{eff}} = U + 4J$, modified by screening effects in the solid. H_d is thus parametrized in terms of an ionization potential (ϵ_d) and electron affinity ($\epsilon_d + U_{\text{eff}}$) for Mn in the solid.
 - ⁵⁸See the review articles of Ref. 1 and also S. B. Oseroff, R. Calvo, and W. Giriat, Solid State Commun. 35, 539 (1980).
 - ⁵⁹J. A. Gaj, J. Ginter, and R. R. Galazka, Phys. Status Solidi B 89, 655 (1978).
 - ⁶⁰This is verified for $\text{Cd}_{1-x}\text{Mn}_x\text{Te}$ in Ref. 18. Since the position of the d level relative to the valence-band edge is expected to be independent of x , the only change anticipated in extrapolating to $x=1$ is a change in hybridization strength. The similarity of $N\beta$ for $\text{Cd}_{1-x}\text{Mn}_x\text{Te}$ and $\text{Zn}_{1-x}\text{Mn}_x\text{Te}$ indicates that this is a minor effect.
 - ⁶¹A. Turandowski, E. Rokita, and J. A. Gaj, Solid State Commun. 36, 927 (1980).
 - ⁶²R. J. Lempert (private communication).
 - ⁶³T. Oguchi, K. Terakura, and A. R. Williams, Phys. Rev. B 28, 6443 (1983).
 - ⁶⁴See, e.g., V. C. Lee and L. Liu, Phys. Rev. B 29, 2125 (1984).
 - ⁶⁵T. Kasuya, IBM J. Res. Develop. 14, 214 (1970).
 - ⁶⁶The energy denominators of the process [ABCD] are easily determined from the figure: the first transfer out of a valence-band state (n', k') onto the Mn at site i has an excitation energy of $\epsilon_{n'}(k') - (\epsilon_d + U_{\text{eff}})$. After the transfer B , the valence band is filled again, but there has been a net transfer of one electron from j to i . The excitation energy here is just U_{eff} . The last two steps transfer an electron back from i to j via the valence-band state (n, k) , reversing the transfers of the previous two steps. Thus the last excitation energy is just $\epsilon_n(k) - (\epsilon_d + U_{\text{eff}})$.
 - ⁶⁷See, e.g., D. J. Newman, J. Phys. C 5, 1089 (1972).
 - ⁶⁸See Ref. 45, and also R. Sokel and W. A. Harrison, Phys. Rev. Lett. 36, 61 (1976); and A. A. Abrikosov, J. Low Temp Phys. 39, 217 (1980). In these theories the effective-mass approximation is made, and then the exponential decay is controlled by the pole closest to the real axis in the complex k plane. For direct gap at Γ this gives a ferromagnetic interaction at large R . The applicability of the effective-mass treatment has been questioned by S. J. Frisken and D. J. Miller, Phys. Rev. B 33, 7134 (1986). More generally, repeated partial integration and use of the Riemann-Lebesgue Lemma [see, e.g., M. J. Lighthill, *Introduction to Fourier Analysis and Generalized Functions* (Cambridge University Press, Cambridge, 1958), p. 46] shows that $J_{\text{eff}}^{dd}(R)$ must decay faster than any power of R at asymptotic distances. Beyond the first few nearest neighbors this interaction becomes so small, for realistic parameters, that the weaker but long-ranged ($\sim R_j^{-3}$) dipolar interaction rapidly becomes more important. The precise form of the asymptotic decay may therefore be physically irrelevant.
 - ⁶⁹This condition is based on molecular-field theory for a fully occupied fcc lattice. [J. S. Smart, *Effective Field Theories of Magnetism* (Saunders, Philadelphia, 1966), p. 74.] We assume the same conditions apply locally in the concentrated alloy.
 - ⁷⁰A. Baldereschi, Phys. Rev. B 7, 5212 (1973).
 - ⁷¹D. J. Chadi and Marvin L. Cohen, Phys. Rev. B 8, 5747 (1973).
 - ⁷²This calculation assumes that selection rules do not force $\bar{V}_{\text{pd}}(0)=0$.
 - ⁷³This result is not based on the spherical approximation since the flat bands demand that the orthogonality relation $\sum_k e^{i(k \cdot R_i - R_j)} = N \delta_{R_i, R_j}$ be satisfied exactly [R. Sokel and W. A. Harrison, Phys. Rev. Lett. 36, 61 (1976)].
 - ⁷⁴Beyond the first few neighbors other exchange mechanisms may become important. Therefore estimates of $J^{dd}(R)$ in this region should not be based on Eq. (5.6), which reflects only the superexchange contribution.
 - ⁷⁵M. Taniguchi, M. Fujimori, M. Fujisawa, T. Mori, I. Souma, and Y. Oka, Solid State Commun. 62, 431 (1987).
 - ⁷⁶A. Franciosi, S. Chang, R. Reifengerger, U. Debska, and R. Riedel, Phys. Rev. B 32, 6682 (1985).
 - ⁷⁷A. Franciosi, in *Proceedings of the MRS Symposium on Diluted Magnetic (Semimagnetic) Semiconductors, Boston, 1986*, Ref. 27, p. 175.
 - ⁷⁸A. Franciosi, S. Chang, C. Caprile, R. Reifengerger, and U. Debska, J. Vac. Sci. Technol. A 3, 926 (1985).
 - ⁷⁹W. A. Harrison, *Electronic Structure and the Properties of Solids* (Freeman, San Francisco, 1980), p. 253 (and references therein).
 - ⁸⁰W. A. Harrison, *Electronic Structure and the Properties of Solids*, Ref. 79, p. 253.

- ⁸¹*Handbook of Chemistry and Physics*, 54th ed., edited by R. C. Weast (CRC Press, Cleveland, 1973), p. B-108.
- ⁸²O. K. Anderson, W. Klose, and H. Nohl, *Phys. Rev. B* **17**, 1209 (1978); D. G. Pettifor, *J. Phys. F* **7**, 613 (1977).
- ⁸³W. A. Harrison, *Electronic Structure and the Properties of Solids*, Ref. 79, pp. 514-519.
- ⁸⁴A. Balzarotti, N. Motta, A. Kisiel, M. Zimnal-Starnawska, M. T. Czyzyk, and M. Podgorny, *Phys. Rev. B* **31**, 7526 (1985).
- ⁸⁵C. K. Shih, W. E. Spicer, W. A. Harrison, and A. Sher, *Phys. Rev. B* **31**, 1139 (1985).
- ⁸⁶D. R. Yoder-Short, U. Debska, and J. K. Furdyna, *J. Appl. Phys.* **58**, 4056 (1985).
- ⁸⁷In the zero-gap case, $J_{he}^{dd}(R_{ij})$ is modified at large r , becoming polynomial instead of exponential [G. Bastard and C. Lewiner, *Phys. Rev. B* **20**, 4256 (1979)]. At near-neighbor distances, however, antiferromagnetic $J_{hh}^{dd}(R_{ij})$ will be dominant because for small R_{ij} , $J_{dd}(R_{ij})$ is determined by integrals over the entire Brillouin zone, whereas the region of narrow gap is only a small fraction of the zone.
- ⁸⁸J. Spałek, A. Lewicki, Z. Tarnawski, J. K. Furdyna, R. R. Gałazka, and Z. Obuszko, *Phys. Rev. B* **33**, 3407 (1986).
- ⁸⁹J. B. Goodenough, *Phys. Rev.* **100**, 564 (1955); J. Kanamori, *Phys. Chem. Solids* **10**, 87 (1959).
- ⁹⁰This quantity is the weight of each anion-anion step in a path model of superexchange.
- ⁹¹K. Terakura, T. Oguchi, A. R. Williams, and J. Kübler, *Phys. Rev. B* **30**, 4734 (1984).
- ⁹²By true quasiparticles we mean those incorporating the electron-electron Coulomb interaction in a fixed lattice potential. We are thus ignoring all other interactions of the electrons such as the electron-phonon coupling in defining these quasiparticles.
- ⁹³This interpretation (for NiO) was suggested by G. A. Sawatzky and J. W. Allen, *Phys. Rev. Lett.* **53**, 2339 (1984).
- ⁹⁴J. C. Slater and G. F. Koster, *Phys. Rev.* **94**, 1498 (1954).
- ⁹⁵K. C. Hass, H. Ehrenreich, and B. Velicky, *Phys. Rev. B* **27**, 1088 (1983).
- ⁹⁶P. O. Löwdin, *J. Chem. Phys.* **18**, 365 (1950).
- ⁹⁷P. J. Davis, in *Handbook of Mathematical Functions*, edited by Milton Abramowitz and Irene A. Stegun (Dover, New York, 1965), p. 270.

Carrier-activated light modulation

N. F. Johnson, H. Ehrenreich,^{a)} and R. V. Jones

Division of Applied Sciences, Harvard University, Cambridge, Massachusetts 02138

(Received 29 February 1988; accepted for publication 16 May 1988)

A variety of superlattices is predicted to exhibit high-speed carrier-activated light modulation. The proposal is based on the large, tunable, and very narrow absorption peak for transitions between the two lowest conduction subbands. The theory, which is demonstrated to be predictive, also suggests correspondingly large variations of the refractive index.

Recent reports have highlighted the potential importance of intersubband transitions between the two lowest conduction subbands ($C1, C2$) of a semiconductor superlattice (SL) in optoelectronic applications.¹⁻³ Two factors are of key significance: intersubband transitions are spectrally tunable and exceptionally strong. The VB (valence band) $\rightarrow C1$ band gap and the $C1 \rightarrow C2$ subband gap are determined independently by choice of superlattice period and alloy composition. The absorption coefficient and change in refractive index associated with the $C1 \rightarrow C2$ transitions depend directly on the number of electrons in the $C1$ subband and may be adjusted to exceed the values associated with the fundamental absorption of a direct gap bulk semiconductor. These considerations also apply to silicon-based SL's, although the effects are a factor of 10 smaller.

The carrier dependence of the intersubband optical properties is the basis of a novel class of *carrier-activated light modulators*. A light beam tuned to the miniband gap energy propagates through an undoped superlattice without appreciable attenuation since there are no carriers in the $C1$ subband. If, however, the beam is polarized perpendicular to the superlattice planes (the z direction) and electrons are electrically injected into or optically generated within the superlattice, the beam can be modulated by the induced intersubband absorptive and/or refractive effects. In view of the polarization restriction, carrier-activated modulation is most simply realized in integrated optical configurations where the light signals are guided by planar waveguide channels aligned parallel to the planes of the superlattice. One particularly promising configuration, which would be useful in communications and computer applications, is that of a crossed waveguide switch wherein the cross-channel coupling is controlled by carrier-activated index changes at the intersection of waveguides.^{4,5} A second promising configuration, which would be useful in signal processing applications, is that of a one-dimensional spatial modulator wherein a planar beam is diffracted by an induced spatially varying carrier distribution within the planar channel.⁶ Picosecond response of these modulators is expected if the electrons are electrically injected normal to the superlattice planes by resonant tunneling. The response of optically activated devices would be limited to the nanosecond range by carrier recombination, but the independent tunability of the VB $\rightarrow C1$ band gap makes possible three-dimensional stacking of switching structures in which the signal at a given level is controlled by

a light distribution propagating normal to the superlattice and tuned to the band gap at that level. The analysis that follows demonstrates that useful carrier-activated modulation is possible under practicable circumstances.⁷

These considerations are firmly based on the theoretical envelope function description of superlattices which has previously yielded quantitative results for effective masses and oscillator strengths in 3-5 and 2-6 superlattices.⁸ The optical absorption is equally well described. As shown in Fig. 1 for the InAs/GaSb type II SL, the results, which depend only on input pertaining to the bulk parent compounds within the Kane model, (1) agree as well with experiments as Kane's original calculations for bulk InSb and (2) provide a quantitative description of the structure due to both VB $\rightarrow C1$ and $C1 \rightarrow C2$ transitions. Similar quantitative results have been obtained for HgTe/CdTe and GaAs/GaAlAs superlattices. The illustration presented here provides a particularly stringent test since the VB envelope functions peak in the GaSb layers, whereas those associated with the conduction bands peak in the InAs layers. This effect leads to relatively low values of $\alpha(E)$, where E is the photon energy. Formal difficulties connected with satisfying envelope function boundary conditions at the interface, when the bulk band structure used as input is limited to only those bands considered in the Kane model, have been shown to have very small numerical effects. These considerations provide confidence that the present theoretical approach is indeed predictive.

Figure 2 shows the $C1 \rightarrow C2, K=0$ gap $E_g^{C2,C1}$, the corresponding oscillator strength $f_{C1,C2}^1 = (2/m)$

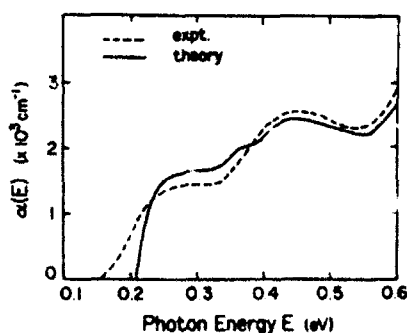


FIG. 1. Comparison of experimental (dashed line) of Chang *et al.* (see Ref. 9) and theoretical (solid line) fundamental absorption coefficients $\alpha(E)$ as function of photon energy E for 37 Å InAs/37 Å GaSb at $T = 4$ K. The theory contains only bulk input parameters.

^{a)} To whom all correspondence should be addressed.

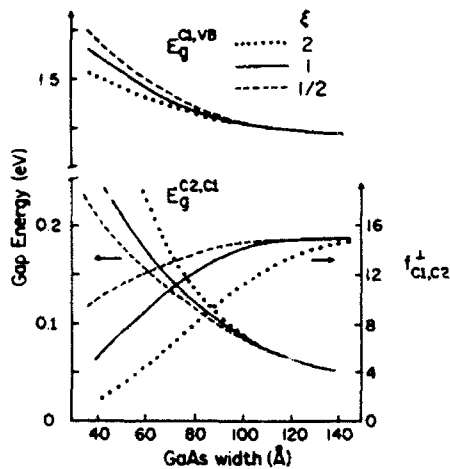


FIG. 2. Calculated VB \rightarrow C1 fundamental superlattice band gap $E_g^{C1,VB}$ and C1 \rightarrow C2 subband gap $E_g^{C2,C1}$ vs GaAs layer width for GaAs/Ga_{0.7}Al_{0.3}As superlattice having 300 K bulk parameters. Relative layer widths are specified by ratio $\xi = (l_{\text{GaAs}})/(l_{\text{Ga}_{0.7}\text{Al}_{0.3}\text{As}}) = 2$ (dotted), 1 (solid), and 1/2 (dashed). Corresponding oscillator strengths $f_{C1,C2}$ are given on the right-hand scale.

$\times |C2,0|p_1|C1,0\rangle^2/E_g^{C2,C1} \equiv E_p/E_g^{C2,C1}$, and the SL band gap $E_g^{C1,VB}$ as a function of GaAs layer width l_{GaAs} for three width ratios $\xi = l_{\text{GaAs}}/l_{\text{Ga}_{0.7}\text{Al}_{0.3}\text{As}}$, where $l_{\text{Ga}_{0.7}\text{Al}_{0.3}\text{As}}$ is the width of Ga_{0.7}Al_{0.3}As layers. The matrix element of p_1 refers to light polarized along the z direction. Layer width adjustment leads to a $E_g^{C2,C1}$ tunability extending from 0.05 eV (25 μm) to 0.2 eV (6 μm). This fact suggests that the infrared band-aligned SL lattice suggested by Yuh and Wang³ is more practically achievable by adjusting layer widths than by well shaping. The limiting oscillator strength is ~ 15 (in agreement with the estimates of West and Eglash¹) and is greater than the value ~ 10 associated with the fundamental optical absorption. The decrease of $f_{C1,C2}$ with decreasing $l_{\text{Ga}_{0.7}\text{Al}_{0.3}\text{As}}$ reflects the diminished effectiveness of the barriers as they become thinner. Similar effects are found in related superlattices. The value of $f_{C1,C2}$ for HgTe/CdTe and InAs/GaSb of comparable thickness is similar to that found in GaAs/GaAlAs.

For $l_{\text{GaAs}} = 80$ Å and $\xi = 1/2$, we find E_p is 1.6 eV for C1 \rightarrow C2 compared to the fundamental absorption value VB \rightarrow C1 of 15 eV; however, the ratio $E_g^{C1,VB}/E_g^{C2,C1} = 12.3$ more than compensates for this reduction in $f_{C1,C2}$. The size of $f_{C1,C2}$ together with the large joint density of states, due to the fact that C1 and C2 are nearly parallel and form critical surfaces along the \parallel direction, leads to an exceptionally large optical absorption coefficient $\alpha(E)$. The two-dimensional joint density of states $m_{r,\parallel}/\pi\hbar^2 d$ is constant and proportional to the reduced mass $m_{r,\parallel}^{-1} = m_{C1,\parallel}^{-1} - m_{C2,\parallel}^{-1}$ which is large (d is the SL period). We find $m_{C1,\parallel} = 0.066m$ and $m_{C2,\parallel} = 0.074m$, $m_{r,\parallel} = 0.61m$, and $\alpha(E) \approx 4 \times 10^4 \text{ cm}^{-1}$ when the C1 filling corresponds to $n_{C1} = 5 \times 10^{17} \text{ cm}^{-3}$ (Fig. 3). At $T = 0$ K the range for which $\alpha(E)$ is nonvanishing is $E_g^{C1,C2} (k=0) > E > E_g^{C1,C2} (k=k_F)$, where k and k_F , the Fermi wave vector, are parallel to the planes. Because

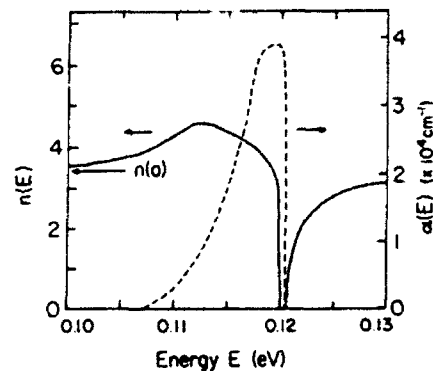


FIG. 3. Calculated refractive index $n(E)$ (solid line; left-hand scale) and absorption coefficient $\alpha(E)$ (dashed line; right-hand scale) vs photon energy E for 80 Å GaAs/160 Å Ga_{0.7}Al_{0.3}As at $T = 300$ K, for C1 electron concentration $n_{C1} = 5 \times 10^{17} \text{ cm}^{-3}$.

of the near parallelism of the C1, C2 bands, the linewidth ΔE for which $\alpha(E)$ is nonzero is very narrow. Specifically, $\Delta E = (10^{-20} n) \text{ eV}$, where n is the carrier concentration (e.g., 0.005 eV for $n = 5 \times 10^{17} \text{ cm}^{-3}$). Temperature effects, causing broadening of the electron distribution and $\alpha(E)$, are small for the same reason. The index of refraction $n(E)$ and $\alpha(E)$, corresponding to $T = 300$ K and $n_{C1} = 5 \times 10^{17} \text{ cm}^{-3}$, which specify the optical constants completely, are shown in Fig. 3. The total absorption width of 0.01 eV is comparable to semiconductor laser widths.

Figure 3 also shows that the value of $n(E)$ below the absorption peak, which is nearly the same as $n(0)$ when C1 is unpopulated, is significantly larger (~ 0.6) than the value above the peak. This variation suggests that the current and optical power requirements for refractive applications are modest. To switch a beam in a cross waveguide configuration by carrier activation requires a minimum injection current of order 10 μA (i.e., a current density of 10 A/cm²) or a light input of 10 μW .

This work was supported by the Defense Advanced Research Projects Agency through U. S. Office of Naval Research (ONR) contract No. N00014-86-K-0033 and by the Joint Services Electronics Program through ONR contract No. N00014-84-K-0465.

¹L. C. West and S. J. Eglash, Appl. Phys. Lett. 46, 1156 (1985).

²B. F. Levine, K. K. Choi, C. G. Bethea, J. Walker, and R. J. Malik, Appl. Phys. Lett. 50, 1092 (1987).

³Peng-fei Yuh and K. L. Wang, Appl. Phys. Lett. 51, 1404 (1987).

⁴K. Ishida, H. Nakamura, H. Matsumura, T. Kadoi, and H. Inoue, Appl. Phys. Lett. 50, 141 (1987).

⁵Y. Silberberg, P. Perlmutter, and J. E. Baran, Appl. Phys. Lett. 51, 1230 (1987).

⁶For example, R. Arrathoon, E. R. Schroeder, and L. D. Hutcheson, Opt. Lett. 10, 244 (1985).

⁷Full details of the relevant theory will appear elsewhere. Further information is available from the authors.

⁸N. F. Johnson, H. Ehrenreich, K. C. Hass, and T. C. McGill, Phys. Rev. Lett. 59, 2352 (1987).

⁹L. L. Chang, G. A. Sai-Halasz, L. Esaki, and R. L. Aggarwal, J. Vac. Sci. Technol. 19, 589 (1981).

Effective-medium theory for weakly nonlinear composites

X. C. Zeng

Department of Physics, Ohio State University, Columbus, Ohio 43210

D. J. Bergman

*Department of Physics, Ohio State University, Columbus, Ohio 43210
and School of Physics and Astronomy, Raymond and Beverly Sackler Faculty of Exact Sciences,
Tel Aviv University, Tel Aviv 69978, Israel*

P. M. Hui

Division of Applied Sciences, Harvard University, Cambridge, Massachusetts 02138

D. Stroud

Department of Physics, Ohio State University, Columbus, Ohio 43210

(Received 6 July 1988)

We propose an approximate general method for calculating the effective dielectric function of a random composite in which there is a weakly nonlinear relation between electric displacement and electric field of the form $\mathbf{D} = \epsilon \mathbf{E} + \chi |\mathbf{E}|^2 \mathbf{E}$, where ϵ and χ are position dependent. In a two-phase composite, to first order in the nonlinear coefficients χ_1 and χ_2 , the effective nonlinear dielectric susceptibility is found to be $\chi_e = \sum_{i=1,2} (\chi_i/p_i) (\partial \epsilon_i / \partial \epsilon_e)_0 | \partial \epsilon_e / \partial \epsilon_i |_0$, where $\epsilon_e^{(0)}$ is the effective dielectric constant in the linear limit ($\chi_i = 0, i = 1, 2$) and ϵ_i and p_i are the dielectric function and volume fraction of the i th component. The approximation is applied to a calculation of χ_e in the Maxwell-Garnett approximation (MGA) and the effective-medium approximation. For low concentrations of nonlinear inclusions in a linear host medium, our MGA reduces to the results of Stroud and Hui. An exact calculation of χ_e is carried out for the Hashin-Shtrikman microgeometry and compared to our MG approximation.

I. INTRODUCTION

There are many phenomena in composite media in which nonlinearity plays an important role. Among these are dielectric breakdown in metal-insulator composites, and the nonlinear optical susceptibility of composite media. In this paper we will be concerned with determining the effective nonlinear dielectric susceptibility of a two-phase, weakly nonlinear, inhomogeneous composite.

For linear composites, the effective dielectric ϵ_e is a function of the geometry of the composite, and the volume fraction and the physical properties of each component. There have been numerous approximations developed to calculate ϵ_e in the linear regime. Two of the most widely used methods are the Maxwell-Garnett approximation¹ (MGA) and the effective-medium approximation² (EMA). Both methods involve an approximation which results in a uniform field inside one or more of the pure components.

In a nonlinear composite, unlike a linear one, the dielectric function depends on the applied electric field. If the applied electric field is sufficiently low, however, the relevant nonlinear effective susceptibilities can be obtained by a perturbation approach. This perturbation approach can be used to give an *exact* expression for the nonlinear susceptibility in terms of the electric field distribution in the related *linear* medium.³ Recently, Stroud and Hui³ have used this result in the low-concentration limit to obtain an exact expression for the cubic nonlinear

susceptibility of a composite medium in the limit of a small concentration of nonlinear inclusions in a linear host.

In this paper, we derive a more general type of approximation for the nonlinear susceptibility—one which is not limited to a system of dilute nonlinear inclusions in a linear host. The resulting approximation for nonlinear media is similar in spirit to the well-known effective-medium approximation² for linear composite media. Besides this generalization, we also present an *exact* calculation of the nonlinear susceptibility for a composite that has the special geometry first discussed by Hashin and Shtrikman.⁴

The remainder of the paper is organized as follows. In Sec. II, we present our general method of approximation, and apply it to obtain a number of specific results. Section III describes an exact calculation of the nonlinear susceptibilities for the Hashin-Shtrikman microgeometry and compares this result with the Maxwell-Garnett approximation. A brief discussion and summary follows in Sec. IV.

II. GENERAL APPROXIMATION METHOD AND ITS APPLICATIONS

We consider a two-component composite in which each component is described by a weakly cubic nonlinear relation between the electric displacement \mathbf{D} and electric field

E of the form

$$D_i = \epsilon_i^{(0)} E_i + \chi_i |E|^2 E. \quad (1)$$

Such an expansion will always be possible provided that $\chi_i |E|^2 \ll \epsilon_i^{(0)}$ ($i=1,2$). The term quadratic in electric field will vanish unless the constituents lack inversion symmetry. The space-averaged fields and displacements $\langle E \rangle$ and $\langle D \rangle$ are related by an equation of the same form:

$$\langle D \rangle = \epsilon_e \langle E \rangle + \chi_e |\langle E \rangle|^2 \langle E \rangle. \quad (2)$$

Our goal is to find approximations for χ_e .

Now in a binary composite, the linear effective dielectric function can always be written in the form

$$\epsilon_e^{(0)} = F(\epsilon_1^{(0)}, \epsilon_2^{(0)}, p_1), \quad (3)$$

where p_1 is the volume fraction of the ϵ_1 component, and F is some function which will, in general, depend on the geometry of the composite. In order to obtain our approximation for χ_e , we initially assume that only component 1 is nonlinear, so that $\epsilon_2 = \epsilon_2^{(0)}$. We then invoke an approximate nonlinear form of Eq. (3):

$$\epsilon_e = F(\epsilon_1, \epsilon_2, p_1). \quad (4)$$

Here $\epsilon_i = \epsilon_i^{(0)} + \chi_i \langle |E_i|^2 \rangle$ and $\langle |E_i|^2 \rangle$ is the mean square of the electric field in the i th component in the linear limit. Equation (4) is strictly valid only if ϵ_1 and ϵ_2 are constant in each component. Thus, our use of Eq. (4) here involves making the approximation that the field E is uniform in the nonlinear component. This assumption is consistent with the spirit of linear effective-medium approximations.

Next, we expand the function F in a Taylor series about the linear $\epsilon_e^{(0)}$, to obtain

$$\epsilon_e \approx F(\epsilon_1^{(0)}, \epsilon_2, p_1) + F'(\epsilon_1^{(0)}, \epsilon_2^{(0)}, p_1) \chi_1 \langle |E_1|^2 \rangle, \quad (5)$$

where χ_1 is the nonlinear coefficient of the component 1 and $F' = \partial F / \partial \epsilon_1$. Now this partial derivative can be expressed exactly in terms of the average squared electric field in component 1 in the linear limit; the relation is⁵

$$p_1 \langle |E_1|^2 \rangle / E_0^2 = (\partial \epsilon_e / \partial \epsilon_1)_{(0)} \equiv F'(\epsilon_1^{(0)}, \epsilon_2^{(0)}, p_1), \quad (6)$$

where E_0 is the external field. Therefore, we have

$$\epsilon_e = \epsilon_e^{(0)} + \frac{\chi_1}{p_1} F' |F| E_0^2, \quad (7)$$

and by the definition of the effective nonlinear coefficient χ_e , we obtain

$$\chi_e = \frac{\chi_1}{p_1} \left[\frac{\partial \epsilon_e}{\partial \epsilon_1} \right]_0 \left[\frac{\partial \epsilon_e}{\partial \epsilon_1} \right]_0. \quad (8)$$

These considerations are easily generalized to the case where both components are nonlinear. In this instance, we simply expand Eq. (1) around both $\epsilon_1^{(0)}$ and $\epsilon_2^{(0)}$, so

that

$$\epsilon_e = \epsilon_e^{(0)} + \frac{\chi_1}{p_1} F'_1 |F'_1| E_0^2 + \frac{\chi_2}{p_2} F'_2 |F'_2| E_0^2, \quad (9)$$

where $F'_i = (\partial \epsilon_e / \partial \epsilon_i)$ ($i=1,2$). We now find that χ_e is given by

$$\chi_e = \frac{\chi_1}{p_1} F'_1 |F'_1| + \frac{\chi_2}{p_2} F'_2 |F'_2|. \quad (10)$$

Equation (10) is our principal result. It is based on the assumption that the fluctuations $\langle |E_i|^4 \rangle - \langle |E_i|^2 \rangle^2$ within the i th component are small, compared to $\langle |E_i|^4 \rangle$ itself. This approximation will be most accurate in geometries, such as the Hashin-Shtrikman geometry discussed below, for which the electric field is nearly uniform within the nonlinear component, and less accurate when these fluctuations are large, such as near a percolation threshold. To illustrate its predictions, we proceed to apply this general formula to various binary composites with different geometric configurations and different densities of inclusions.

A. Low-density limit

We first consider a linear host containing a very small volume fraction of nonlinear inclusions. In this case, we recover the known results of the low-density theory.³ The argument is the following: in the low-density regime, the effective dielectric function of such a composite in the linear limit is

$$\epsilon_e^{(0)} = \epsilon_2 + 3\epsilon_2 p_1 \frac{\epsilon_1^{(0)} - \epsilon_2}{\epsilon_1^{(0)} + 2\epsilon_2}, \quad (11)$$

where ϵ_2 is the host material and ϵ_1 the nonlinear inclusion. $\partial \epsilon_e^{(0)} / \partial \epsilon_1^{(0)}$ is then

$$\left[\frac{\partial \epsilon_e}{\partial \epsilon_1} \right]_0 = p_1 \left[\frac{3\epsilon_2}{\epsilon_1^{(0)} + 2\epsilon_2} \right]^2. \quad (12)$$

Substituting Eq. (12) into Eq. (8), we obtain

$$\chi_e = \chi_1 p_1 \left[\frac{3\epsilon_2}{\epsilon_1^{(0)} + 2\epsilon_2} \right]^2 \left[\frac{3\epsilon_2}{\epsilon_1^{(0)} + 2\epsilon_2} \right]^2. \quad (13)$$

This is the same as the result of Stroud and Hui.³

B. Maxwell-Garnett approximation

Next, we obtain χ_e for a composition which in the linear regime is described by the Maxwell-Garnett approximation. As is well known, the MG approximation is most appropriate for a composite in which one of the constituents plays the role of a host medium and the other acts as an inclusion. If medium 2 is then host, then the MG approximation takes the form⁶

$$\frac{\epsilon_e^{(0)}}{\epsilon_2^{(0)}} = \frac{\epsilon_1^{(0)}(1+2p_1) + 2\epsilon_2^{(0)}(1-p_1)}{\epsilon_1^{(0)}(1-p_1) + \epsilon_2^{(0)}(2+p_1)} \quad (14)$$

From this we obtain

$$F_1' = \frac{\partial \epsilon_e}{\partial \epsilon_1} \bigg|_0 = \frac{9p_1\epsilon_2^{(0)2}}{[\epsilon_1^{(0)}(2+p_1) + \epsilon_1^{(0)}(1-p_1)]^2}, \quad (15)$$

and

$$F_2' \equiv \frac{\partial \epsilon_e}{\partial \epsilon_2} \bigg|_0 = p_2 \frac{2\epsilon_2^{(0)2}p_1 - 4\epsilon_1^{(0)}\epsilon_2^{(0)}p_1 + 2\epsilon_1^{(0)2}p_1 + 4\epsilon_2^{(0)2} + 4\epsilon_1^{(0)2} + \epsilon_2^{(0)} + \epsilon_1^{(0)2}}{[\epsilon_2^{(0)}(2+p_1) + \epsilon_1^{(0)}(1-p_1)]^2}. \quad (16)$$

From these two formulas, we can calculate χ_e using Eq. (10).

C. Exactly solvable microgeometry: Parallel cylinders and slabs

There exist a number of special microgeometries for which $\epsilon_e^{(0)}$ can be calculated exactly. The first of these is the case where the components are arranged in the form of (not necessarily circular) cylinders parallel to the external field. Another soluble geometry is one in which the constituents are arranged in the form of flat slabs perpendicular to the applied field. The effective dielectric constant takes the form

$$\epsilon_e^{(0)} = p_1\epsilon_1^{(0)} + p_2\epsilon_2^{(0)} \quad (17)$$

for parallel cylinders and

$$\epsilon_e^{(0)} = 1 / \left[\frac{p_1}{\epsilon_1^{(0)}} + \frac{p_2}{\epsilon_2^{(0)}} \right] \quad (18)$$

for parallel slabs. These results are analogous to the effective capacitance for capacitors in parallel and in series.

Using Eq. (10), we obtain for the effective nonlinear dielectric susceptibility

$$\chi_e = p_1\chi_1 + p_2\chi_2 \quad (19)$$

for parallel cylinders and

$$\chi_e = \frac{\chi_1 p_1}{[p_1 + (\epsilon_1^{(0)} p_2 / \epsilon_2^{(0)})]^4} + \frac{\chi_2 p_2}{[p_2 + (\epsilon_2^{(0)} p_1 / \epsilon_1^{(0)})]^4} \quad (20)$$

for parallel slabs. Both of these results are exact for a weakly nonlinear medium, since the local field is in fact uniform in each component in these two cases, even if the components are weakly nonlinear. [The local field may be uniform in these geometries even if the components are strongly nonlinear, but in such cases the results (19) and (20) will no longer apply.]

D. Effective-medium approximation

In the effective-medium approximation^{2,6} (EMA), the effective dielectric function $\epsilon_e^{(0)}$ is one of the solutions of the quadratic equation

$$p_1 \frac{\epsilon_1^{(0)} - \epsilon_e^{(0)}}{\epsilon_e^{(0)} + g(\epsilon_1^{(0)} - \epsilon_e^{(0)})} + (1-p_1) \frac{\epsilon_2^{(0)} - \epsilon_e^{(0)}}{\epsilon_e^{(0)} + g(\epsilon_2^{(0)} - \epsilon_e^{(0)})} = 0. \quad (21)$$

Here g is a geometric factor related to the depolarization factor of the inclusions and dependent on their shape. For a three-dimensional composite with compact, roughly spherical inclusions, $g = \frac{1}{3}$, while for a two-dimensional composite with circular inclusions, $g = \frac{1}{2}$. If $\epsilon_1^{(0)}$ and $\epsilon_2^{(0)}$ are real and positive, then the physically relevant solution is the positive one.

The required derivatives F_1' and F_2' can readily be computed from this equation, with the results

$$F_1' = \frac{1}{2(g-1)} \{ [2(\epsilon_1^{(0)} - \epsilon_2^{(0)})p_1^2 + 2(\epsilon_2^{(0)} - 2\epsilon_1^{(0)}g)p_1 + 2(\epsilon_1^{(0)} - \epsilon_2^{(0)})g^2 + 2\epsilon_2^{(0)}g] / [2\{(\epsilon_2^{(0)} - \epsilon_1^{(0)})^2 p_1^2 + [2(\epsilon_2^{(0)2} - \epsilon_1^{(0)2})g - 2\epsilon_2^{(0)2} + 2\epsilon_1^{(0)}\epsilon_2^{(0)}]p_1 + (\epsilon_2^{(0)} - \epsilon_1^{(0)})^2 g^2 + 2\epsilon_2^{(0)}(\epsilon_1^{(0)} - \epsilon_2^{(0)})g + \epsilon_2^{(0)2}\}^{1/2} - p_1 + g] \}, \quad (22)$$

and

$$F_2' = \frac{1}{2(g-1)} \{ [2(\epsilon_2^{(0)} - \epsilon_1^{(0)})p_1^2 + 2(2\epsilon_2^{(0)}g - 2\epsilon_2^{(0)} + \epsilon_1^{(0)})p_1 + 2(\epsilon_2^{(0)} - \epsilon_1^{(0)})g^2 + 2(\epsilon_1^{(0)} - 2\epsilon_2^{(0)})g + 2\epsilon_2^{(0)}] \times [2\{(\epsilon_2^{(0)} - \epsilon_1^{(0)})^2 p_1^2 + [2(\epsilon_2^{(0)2} - \epsilon_1^{(0)2})g - 2\epsilon_2^{(0)2} + 2\epsilon_1^{(0)}\epsilon_2^{(0)}]p_1 + (\epsilon_2^{(0)} - \epsilon_1^{(0)})^2 g^2 + 2\epsilon_2^{(0)}(\epsilon_1^{(0)} - \epsilon_2^{(0)})g + \epsilon_2^{(0)2}\}^{1/2} - 1 + p_1 + g] \}. \quad (23)$$

Given these formulas for F_1' and F_2' , one can readily calculate the effective dielectric nonlinear susceptibility χ_e using

Eq. (10). The resulting expression for χ_e exhibits interesting behavior, especially near the percolation threshold, which will be discussed elsewhere.

III. EXACT RESULTS FOR THE HASHIN-SHTRIKMAN MICROGEOMETRY

In the Hashin-Shtrikman microgeometry,⁴ the entire binary composite is composed of coated spheres with a core made of one component ϵ_1 and a concentric spherical shell made of the other component ϵ_2 [see Fig. 1(a)]. These composite spheres must come in a variety of sizes in order to fill up the entire volume, but all must have the same ratio of core volume to shell volume. It is easy to show⁴ that for this microgeometry the bulk effective linear dielectric constant $\epsilon_e^{(0)}$ is exactly equal to the MG result. Furthermore, in the linear limit it is possible to evaluate the local electric field $E(r)$ exactly within both the cores (where it is uniform but different from the average field E_0) and the shells [where it is not uniform; see Fig. 1(b)]. Given these fields, we can exactly evaluate the nonlinear susceptibility χ_e from the expression³

$$\chi_e = \frac{1}{V} \int dV \chi(r) (E/E_0)^4. \quad (24)$$

The result is

$$\chi_e = \chi_1 p_1 \left[\frac{3\epsilon_2^{(0)}}{(1-p_2)\epsilon_1^{(0)} + (2+p_1)\epsilon_2^{(0)}} \right]^4 + \frac{\chi_2(1-p_1)}{[(1-p_1)\epsilon_1^{(0)} + (2+p_1)\epsilon_2^{(0)}]^4} \\ \times [(\epsilon_1^{(0)} + 2\epsilon_2^{(0)})^4 + \frac{3}{2}p_1\epsilon_1^{(0)2}(\epsilon_1^{(0)} + 2\epsilon_2^{(0)})^2 - \frac{1}{2}p_1(1+p_1)\epsilon_1^{(0)3}(\epsilon_1^{(0)} + 2\epsilon_2^{(0)}) + \frac{1}{2}p_1(1+p_1+p_1^2)\epsilon_1^{(0)4}]. \quad (25)$$

Comparing this to the MG result found earlier, and given implicitly by Eqs. (14)–(16), we can show that the coefficient of χ_1 is the same, but that of χ_2 is different. This difference has a simple explanation: The MGA for χ_e is based on the assumption that E is uniform in each component, while in the Hashin-Shtrikman geometry E is uniform within the cores but not the shells of the composite spheres.

IV. DISCUSSION AND CONCLUSIONS

We have presented a simple approximation for the nonlinear susceptibility χ_e of a weakly nonlinear dielectric composite. The approximation consists of assuming that the field is uniform in each of the nonlinear components. Given this approximation, we have easily obtained expressions for χ_e based on the MG and EM approximations for a linear dielectric composite. We have also calculated χ_e exactly for several simple, solvable microgeometries.

Our results are applicable not only to nonlinear media

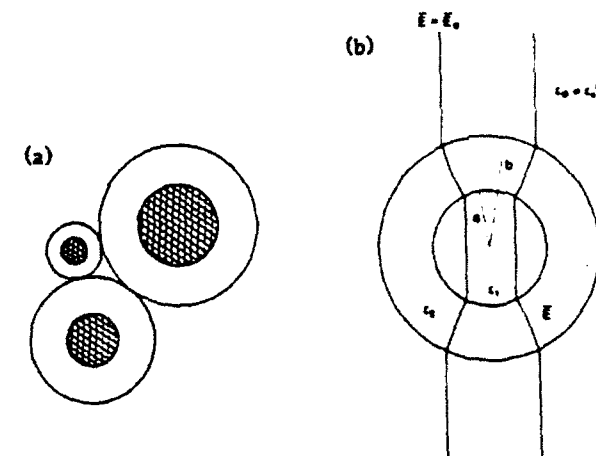


FIG. 1. (a) Schematic representation of the Hashin-Shtrikman microgeometry. The cores are described by ϵ_1, χ_1 ; the shells by ϵ_2, χ_2 . The ratio of core-to-shell volume is the same for each composite sphere, and equal to the ratio of volume fractions $p_1/(1-p_1)$. (b) Schematic showing the solution for the local electric field in the Hashin-Shtrikman microgeometry. The field E remains undistorted and equal to the applied field E_0 outside the inclusion, is uniform but $\neq E_0$ in the core, and has a dipolar form in the shell.

but also to $1/f$ noise or resistance fluctuations in composite conductors. The connection arises because the mean-square resistance fluctuations are given by an expression similar to Eq. (24).^{3,7,8} Our EMA result thus provides an approximate calculation for the noise power spectrum. The result proves to differ from that of Ref. 7. In particular, our result exhibits no divergence of the relative noise at the EMA percolation threshold. A detailed comparative discussion of the various types of effective-medium approximations that can be developed for this problem will be given elsewhere.⁸

ACKNOWLEDGMENTS

This work was supported by National Science Foundation Grant No. DMR-87-18874, U.S. Defense Advanced Research Projects Agency Grant No. ONR-NO00014-86-K-0033, and the U.S.-Israel Binational Science Foundation under Grant No. 354/85.

¹J. C. M. Garnett, *Philos. Trans. R. Soc. London* **203**, 385 (1904); 205, 237 (1906).

²D. A. G. Bruggeman, *Ann. Phys. (Leipzig)* **24**, 636 (1935).

³D. Stroud and P. M. Hui, *Phys. Rev. B* **37**, 8719 (1988).

⁴Z. Hashin and S. Shtrikman, *J. Appl. Phys.* **33**, 3125 (1962).

⁵D. J. Bergman, *Phys. Rep.* **43**, 377 (1978) [also published in *W. E. Lamb Festschrift*, edited by D. ter Haar and M. O. Scully

(North-Holland, Amsterdam, 1978)].

⁶R. Landauer, in *Electrical Transport and Optical Properties of Inhomogeneous Media*, edited by J. C. Garland and D. B. Tanner, AIP Conf. Proc. No. 40 (American Institute of Physics, New York, 1978).

⁷R. Rammal, *J. Phys. (Paris) Lett.* **46**, L129 (1985).

⁸D. J. Bergman (unpublished).

Superlattice $k \cdot p$ models for calculating electronic structure

N. F. Johnson, H. Ehrenreich,* and G. Y. Wu

Division of Applied Sciences, Harvard University, Cambridge, Massachusetts 02138

T. C. McGill

Thomas J. Watson, Sr., Laboratory of Applied Physics, California Institute of Technology, Pasadena, California 91125

(Received 6 July 1988)

A quantitative comparison is presented of two realistic superlattice $k \cdot p$ electronic structure calculations. The first is an analytic approach based on an extended bulk Kane model; the second is an extended-basis treatment, developed by McGill and collaborators, based on bulk pseudopotential calculations. Both approaches are applied to HgTe/CdTe superlattices. Energies, wave functions, effective masses, and oscillator strengths are found to agree within 10%. The limited-basis approach based on the Kane model is seen to be adequate for superlattices whose bulk constituents have direct gaps in the conduction- and valence-band regions near the superlattice band gap.

INTRODUCTION

The electronic properties of semiconductor superlattices are most conveniently calculated using the bulk electronic structures of the constituent materials obtained by the $k \cdot p$ method as a starting point.¹ In this approach,² the superlattice (SL) wave function for SL band L at wave vector K is expanded in terms of a Luttinger basis as

$$\langle r|L, K \rangle = \sum_n F_n(L, K; r) \langle r|n \rangle,$$

where $\langle r|n, k=0 \rangle \equiv \langle r|n \rangle$ is the bulk Bloch function of band n at $k=0$. Both constituents will be regarded as direct-band-gap materials with valence-band maxima and conduction-band minima at $k=0$. $F_n(L, K; r)$ is the envelope function.²

The correct microscopic boundary conditions demand that at each interface $\langle r|L, K \rangle$ and its derivative be continuous for all r . In practice, however, most calculations employ approximate boundary conditions which are obtained after averaging the SL wave function over a bulk unit cell. This practice derives from the fact that the bulk basis set $\{\langle r|n \rangle\}$ must be truncated for tractable computations. The bulk band structure therefore must be chosen so as to include the most important physical features in their simplest form and the basis set must be sufficiently complete that the boundary conditions are satisfied to a suitable level of approximation.

This paper compares the results of two such calculations involving quite different levels of basis-set truncations. One model, developed by McGill and collaborators, to be termed the extended-basis model considers an extended basis containing 54 $\langle r|n \rangle$'s.³⁻⁵ The other simpler model, to be termed the limited-basis model, considers only the eight fold basis contained in the Kane model but yields analytic results.^{2,6} It will be seen, in reference to the HgTe/CdTe SL, that the simpler approach is sufficient for a quantitative description of the SL electronic properties over the energy region subsumed by the lowest band gaps. At the same time we emphasize that for SL having constituents with indirect band gaps,

or for properties (e.g., optical) involving larger energy ranges, a more elaborate approach, such as the extended-basis model, is required.

DESCRIPTION OF MODELS

We begin with a precise specification of the two models. The limited-basis model (LBM) considers only the eight $\langle r|n \rangle$ in Eq. (1) that are contained in the bulk Kane model including spin-orbit splitting. A finite heavy-hole mass results from the inclusion of the antibonding conduction-band p state by perturbation theory. The LBM has been used successfully to calculate SL gaps,² effective masses⁶ using the f sum rule, and the optical absorption coefficients in various III-V compound and II-VI compound superlattices.⁷

Specifically, the features associated with the model are the following.

- (1) The bulk band structures are assumed isotropic.
- (2) The bulk $k \cdot p$ parameters are taken from experiment. This applies to the effective masses m^* and band gaps E_g for both constituents. The optical matrix elements $P_{nn'} = \langle n, k=0 | p | n', k=0 \rangle$ are deduced from the Kane model and the experimental bulk m^* and E_g . The difference between the $P_{nn'}$ for HgTe and CdTe is less than 10%. A single value of $P_{nn'}$, applicable to either constituent, is obtained from an arithmetic mean.
- (3) The $\langle r|n \rangle$ are assumed the same for each constituent. The procedure for obtaining the parameters described in (2) is essentially equivalent to that assumption.
- (4) Superlattice $K=0$ energies, masses, and envelope functions can be obtained analytically.

The extended-basis model³⁻⁵ (EBM) contains many bands in addition to those considered within the Kane model. These bands are folded down using Löwdin perturbation theory. The EBM is properly regarded as the "state of the art" of the superlattice $k \cdot p$ approaches.

Specifically, the model contains the following features.

- (1) The bulk band structure and the $\langle r|n \rangle$ are obtained from an empirical pseudopotential calculation that contains the full zinc-blende symmetry.
- (2) The bulk $k \cdot p$ parameters are calculated utilizing these pseudopotential results.

(3) The $\langle r|n \rangle$, and hence the parameters calculated from them, differ for the two constituents, in contrast to the LBM.

(4) The boundary conditions, as expected, are better satisfied by the EBM than by the LBM.

The results for HgTe/CdTe obtained from each of these two approaches as described above will be compared by using the bulk band gaps and effective masses resulting from the pseudopotential calculations of the EBM as input for the LBM as a common base.

CRITIQUE OF THE LIMITED-BASIS MODEL

The possible shortcomings of the LBM should be considered before proceeding to a detailed comparison. There are three major points of criticism.

The first concerns the adequacy of the LBM bulk band structure and the limited number of bulk bands involved in the description. Figure 1 compares the bulk band structure as a function of complex k for $\text{Hg}_{0.5}\text{Cd}_{0.5}\text{Te}$ for the two models in the virtual crystal approximation. (This bulk band structure is appropriate here since the SL to be considered have equal layer widths.) The results agree well near $k=0$. For finite real k , the LBM light hole band (Γ_8) flattens out too rapidly, as does the split-off band (Γ_7) along the $\text{Im}(k)$ direction. These discrepancies are associated with the absence of higher and lower bulk bands in the LBM. For example, in the case of the split-off band (Γ_7) along $\text{Im}(k)$ the higher band to which it connects is missing in the LBM. By contrast, since Γ_8 and Γ_6 are present in both models, the curvature along $\text{Im}(k)$ is very similar in the two cases. These differences are of little concern even in a narrow

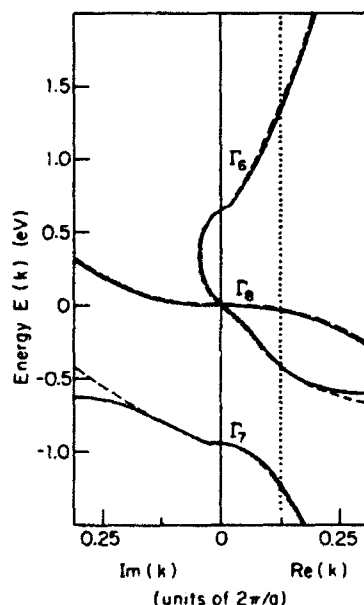


FIG. 1. Virtual crystal $\text{Hg}_{0.5}\text{Cd}_{0.5}\text{Te}$ bulk band structure $E(k)$ for a limited-basis (LBM—solid line) and extended-basis (EBM—dashed line) model vs real k and imaginary k ; k is in units of $2\pi/a$, where a is bulk lattice constant. EBM calculation is for k parallel to $[100]$. Dotted vertical line denotes Brillouin-zone boundary for $(13 \text{ \AA} \text{ HgTe})/(13 \text{ \AA} \text{ CdTe})$ SL.

layer width SL, since for the SL Brillouin zone of the $(13 \text{ \AA} \text{ HgTe})/(13 \text{ \AA} \text{ CdTe})$ SL, demonstrated by a dotted vertical line in Fig. 1, and for the same region along the $\text{Im}(k)$ axis the two sets of results are in very good agreement.

The consequences of neglecting the full zinc-blende symmetry, as exemplified by the choice of different growth axes, are discussed in Ref. 4. The differences are on the meV scale, and are smaller than those resulting from the neglect of basis states in the LBM.

The second concern is the assumption that the $\langle r|n \rangle$ are the same for each SL constituent. This assumption implies that the $P_{nn'}$ are material independent in the LBM description of the superlattice. The substantial constancy of direct gap momentum matrix elements in the III-V compound and II-VI compound bulk semiconductors has been long recognized and is by now well documented.^{1,8} However, this assumption, while certainly valid for HgTe/CdTe, requires reexamination for superlattices whose constituents involve different rows of the Periodic Table. These assertions are supported also by the pseudopotentials given in the review by Cohen and Heine.⁹

The third question concerns the interface boundary conditions and whether they are adequately satisfied in the LBM. The current averaged over a bulk unit cell is continuous across the interface for both models considered in this paper at $K=0$. However, the extent to which the microscopic boundary conditions are satisfied in the LBM because of the more severe basis-set truncations and the neglect of pseudo-wave-function differences requires detailed examination. This matter will be discussed in the next section. The implementation of the LBM boundary conditions is equivalent to that in Refs. 2 and 10, while that of the EBM is equivalent to that described in Ref. 4.

DETAILED COMPARISON

HgTe/CdTe is a type-III superlattice because of the inverted bulk band structure of HgTe. The s - p mixing accordingly is much larger than that characteristic of the wide gap type-I superlattices, many (but not all) of whose features can be described by the continuum approximation exemplified by the Kronig-Penney model. The strong s - p admixture in the SL under consideration amplifies the difficulty of satisfying the boundary conditions. The situation is made yet more difficult in the thin-layer limit, to be considered here, in which the interface region comprises a significant fraction of the SL period. Strain effects will be neglected because the superlattice under consideration is well lattice matched.

The $(13 \text{ \AA} \text{ HgTe})/(13 \text{ \AA} \text{ CdTe})$ SL contains only eight molecular layers per period. The results for the envelope functions to be presented assume a valence band offset of 40 meV. While this value is now widely believed to be too small, the quantitative aspects of the comparison made here are little affected by the choice of a larger offset.

The unit-cell average used in obtaining the approximate boundary conditions implies that they can be expressed entirely in terms of the envelope functions

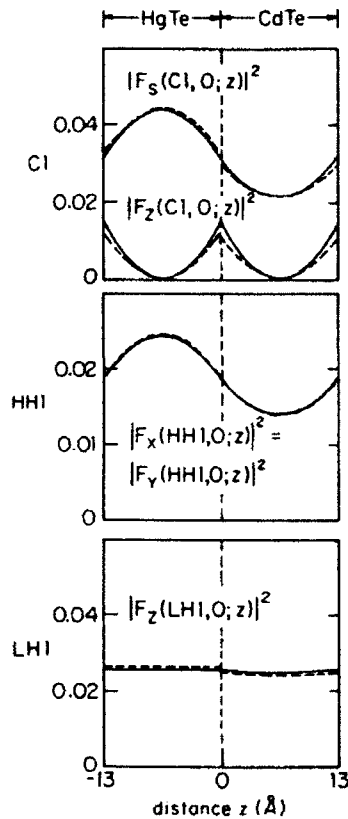


FIG. 2. Square of absolute value of dominant envelope functions vs distance along growth (z) axis for the $K=0$ (13 Å HgTe)/(13 Å CdTe) superlattice states for superlattice bands C1, HH1, and LH1. Solid and dashed lines correspond to limited-basis and extended-basis models, respectively. The superlattice wave function is normalized to unity over the 26-Å period.

$F_n(L, K; z)$. These correspond to the bulk basis states [cf. Eq. (1)] $|n\rangle = |S\rangle, |X\rangle, |Y\rangle$, and $|Z\rangle$ in the notation of Ref. 1 or equivalently to the linear combinations appropriate to the band edges under consideration as defined by Kane.

Figure 2 shows the most important $|F_n(L, 0; z)|^2$ for the (13 Å HgTe)/(13 Å CdTe) SL as a function of distance

along the growth axis on either side of the HgTe/CdTe interface, which is taken to correspond to $z=0$. The envelope functions shown correspond to the conduction-band minimum ($L=C1$) and the bands nearest the valence-band maximum ($L=HH1$, light-hole band; $L=HH1$, heavy-hole band). In both models the envelope functions are continuous to a good approximation. The discontinuities in the $|F_n(L, 0; z)|^2$ are seen to be larger for the EBM. This discrepancy is only apparent: The continuity conditions apply to quantities involving $F_n(L, 0; z)\langle r|n\rangle$, and are still satisfied within the EBM since the difference between the $\langle r|n\rangle$ on either side of the interface in the EBM compensates for the discontinuity in the F_n . The magnitude of the two sets of F_n are in excellent overall agreement. Significant differences extend over only a small region of the distance $z=26$ Å shown in the figure. For a (39 Å HgTe)/(39 Å CdTe) superlattice that region becomes a smaller fraction of the total. Properties, such as optical matrix elements and tunneling probabilities, depending only on integrals involving the F_n will therefore be well described in both approximations.¹¹ $|F_Z(C1, 0; z)|^2$ exhibits evanescent character, as does $|F_Z(LH1, 0; z)|^2$ to a lesser extent. (LH1 is commonly termed the "interface state" for that reason.) The HH1 envelope function is seen to be more confined within the HgTe layer than the LH1 function. This is because the bulk heavy-hole mass is larger than the bulk light-hole mass, and hence the tunneling probability out of the HgTe layer (which acts as the quantum well for the hole states) is smaller for the heavy hole than for the light hole. This effect is amplified if the band offset is made larger.

Table I compares energies, masses, and oscillator strengths for (13 Å HgTe)/(13 Å CdTe) and (39 Å HgTe)/(39 Å CdTe) superlattices, as given by the LBM and EBM. $E_L(0)$ is the $K=0$ energy of SL band L , m_L^\perp is the corresponding effective mass perpendicular to the layers, and $f_{VB, C1}^\perp$ is the total $K=0$ oscillator strength (polarization parallel to the layers) between the superlattice valence bands LH1 and HH1, and C1. The agreement of m_L^\perp and $f_{VB, C1}^\perp$ illustrates the ability of the LBM to predict superlattice properties analytically both perpendicular and parallel to the layers.¹² (References 2 and 4

TABLE I. Comparison of superlattice energies $E_L(0)$, masses m_L^\perp perpendicular to the planes, and total valence-band to conduction-band oscillator strengths $f_{VB, C1}^\perp$, where polarization is parallel to the planes for (13 Å HgTe)/(13 Å CdTe), and (39 Å HgTe)/(39 Å CdTe) superlattices as calculated in the limited-basis (LBM) and extended-basis (EBM) models. m_0 is the free-electron mass.

	(13 Å HgTe)/(13 Å CdTe)		(39 Å HgTe)/(39 Å CdTe)	
	EBM	LBM	EBM	LBM
$E_{C1}(0)$ (eV)	0.48	0.50	0.21	0.23
$E_{HH1}(0)$ (eV)	-0.018	-0.018	-0.0085	-0.0095
$E_{LH1}(0)$ (eV)	-0.020	-0.019	-0.019	-0.019
m_{C1}^\perp	$0.050m_0$	$0.047m_0$	$0.092m_0$	$0.099m_0$
m_{HH1}^\perp	$-1.1m_0$	$-1.0m_0$	∞	∞
m_{LH1}^\perp	$-0.055m_0$	$-0.052m_0$	$-0.055m_0$	$-0.058m_0$
$f_{VB, C1}^\perp$	21	20	27	26

speculate that parallel properties, e.g., $f/v_{B,C1}$ would not be reliably given within the Kane model without extensive numerical computation.) The agreement between the models for a given layer thickness is generally better for the hole states (LH1, HH1) than for the electron state (C1). This is a consequence of the small valence-band offset which causes the hole states to lie in an energy region where the bulk band structures of the constituent materials are well described by both models, i.e., close to $k=0$. (This conclusion will not be appreciably modified for offsets as large as 350 meV.)

Since the HgTe/CdTe case considered here is one in

which the LBM is put to a particularly stringent test, one would expect this model to be applicable to other SL as well. This observation is confirmed by our experience.^{6,7}

ACKNOWLEDGMENTS

This work was supported by the Joint Services Electronics Program through U.S. Office of Naval Research (ONR) Contract No. N00014-84-K-0465, and by the Defense Advanced Research Projects Agency through ONR Contracts Nos. N00014-86-K-0033, N00014-86-K-0760, and N00014-86-K-0841.

*To whom all correspondence should be addressed.

¹E. O. Kane, in *Narrow Gap Semiconductors: Physics and Applications*, Vol. 133 of Lecture Notes in Physics, edited by W. Zawadzki (Springer-Verlag, New York, 1981), p. 13.

²G. Bastard, in *Proceedings of the NATO Advanced Study Institute on Molecular Beam Epitaxy in Heterostructures*, Erice, Italy, 1983, edited by L. L. Chang and K. Ploog (Martinus-Nijhoff, Dordrecht, 1984), p. 381. See also, G. Bastard, *Phys. Rev. B* **25**, 7584 (1982).

³C. Mailhot, T. C. McGill, and D. L. Smith, *J. Vac. Sci. Technol. B* **2**, 371 (1984).

⁴D. L. Smith and C. Mailhot, *Phys. Rev. B* **33**, 8345 (1986).

⁵C. Mailhot and D. L. Smith, *Phys. Rev. B* **33**, 8360 (1986).

⁶N. F. Johnson, H. Ehrenreich, K. C. Hass, and T. C. McGill, *Phys. Rev. Lett.* **59**, 2352 (1987).

⁷N. F. Johnson, H. Ehrenreich, and R. V. Jones, *Appl. Phys. Lett.* **53**, 180 (1988).

⁸H. Ehrenreich, *J. Appl. Phys.* **32**, 2155 (1961).

⁹M. L. Cohen and V. Heine, in *Solid State Physics*, edited by H. Ehrenreich, F. Seitz, and D. Turnbull (Academic, New York, 1970), Vol. 24, p. 37.

¹⁰R. I. Taylor and M. G. Burt, *Semicond. Sci. Technol.* **2**, 485 (1987).

¹¹This applies to the optical matrix element involving dF_x/dz , as we have verified, if the discontinuity at the interface is neglected or a suitable "smoothing function" is introduced.

¹²Although the present comparison involves $K=0$ quantities, the LBM does successfully predict finite- K properties using superlattice $K \cdot p$ perturbation theory. See N. F. Johnson, P. M. Hui, and H. Ehrenreich, *Phys. Rev. Lett.* (to be published).

Valence-Band-Offset Controversy in HgTe/CdTe Superlattices: A Possible Resolution

N. F. Johnson, P. M. Hui, and H. Ehrenreich^(a)

Division of Applied Sciences, Harvard University, Cambridge, Massachusetts 02138

(Received 12 July 1988)

The valence-band-offset controversy in HgTe/CdTe superlattices can be simply resolved. It is shown that, while the superlattice becomes semimetallic with increasing valence-band offset, it reverts to semiconducting behavior as the offset is increased yet further. The observed electron-cyclotron mass and the band gap can be better explained for the offset of 350 meV measured by photoemission than for the smaller offset ~ 40 meV which coincidentally is also in fair agreement with the magneto-optical data.

PACS numbers: 73.40.Lq, 73.20.A1, 73.20.Dx

The dilemma posed by the differing valence-band offsets Λ in HgTe/CdTe superlattices (SL) obtained from room-temperature photoemission ($\Lambda \approx 350$ meV)¹ and low-temperature magneto-optical experiments ($\Lambda \approx 40$ meV)² can be resolved in favor of the larger Λ by showing, as we do here, that the effective mass and the band gap obtained by Berroir *et al.*² are consistent with the value $\Lambda \approx 350$ meV. As noted previously³ the conduction and valence bands of the semiconducting superlattices cross as Λ is increased from small values and render the material semimetallic. What has been missed is the fact that the superlattice again becomes semiconducting as Λ is increased further for the layer widths corresponding to the SL described in Ref. 2.

These results are obtained with use of the envelope-function approach which has recently been criticized^{4,5} because of its reliance on $k \cdot p$ perturbation theory. Indeed, the bulk $k=0$ basis set used here is limited to that of the Kane model. The results have been questioned on the grounds that a broader width of the bulk Brillouin zone than that adequately described by the model would play a role in the SL electronic structure. However, as we have recently shown,⁶ the results obtained using the extended basis comprising ~ 50 bulk wave functions at $k=0$, which would be expected to describe the requisite region of the Brillouin zone adequately, are essentially the same as those for the limited

basis set exemplified by the Kane model, even for narrow layer width. This approach has been shown to yield quantitative results for effective masses and optical-absorption coefficients for a variety of 3-5 and 2-6 SL's.^{7,8} The theoretical approach outlined in Ref. 7 can therefore be regarded as applicable to the present considerations. The calculations, however, neglected strain effects.

Figure 1 shows the relative alignment of the bulk HgTe and CdTe band edges (Γ_6 and Γ_8) schematically. The band offset Λ is defined to be positive. The potential well formed by the Γ_6 edge (solid line) becomes shallower with increasing Λ , whereas that for the Γ_8 edge (dashed line) becomes deeper.

The present calculations refer to the 100-Å HgTe/36-Å CdTe SL considered in the magneto-optical experiments of Ref. 2. The only input consists of the constituent bulk parameters listed in Table I. These parameters determine the bulk momentum matrix elements for each material within the Kane model. They differ by less than 10% and will therefore be taken to have the same average value for both materials.

Figure 2 shows the energies of the C1, LH1, HH1, HH2, and HH3 (C denotes conduction, LH light hole, and HH heavy hole) bands at $K=0$ (K is the SL wave vector) as a function of band offset Λ . The zero of energy is taken to be the valence-band maximum for $\Lambda=0$. At zero offset the electrons are located in a quantum well of finite depth, whereas the holes see no potential varia-

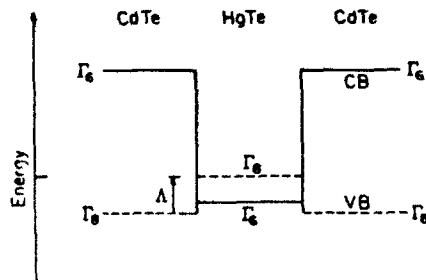


FIG. 1. The relative alignment of the bulk HgTe and CdTe band edges. The valence-band offset Λ is defined as the difference between the HgTe and CdTe Γ_8 valence-band maxima.

TABLE I. Parameters for bulk CdTe and HgTe used in the present calculations.

	CdTe	HgTe
Electron mass (m_0)	0.11	0.031 ^a
$E(\Gamma_6) - E(\Gamma_8)$ (eV)	1.6	-0.3
Spin-orbit splitting (eV)	0.9	1.0
Heavy-hole mass (m_0) ^b	0.7	0.7

^aReference 9.

^bReference 10. We use the heavy-hole masses along the [111] direction.

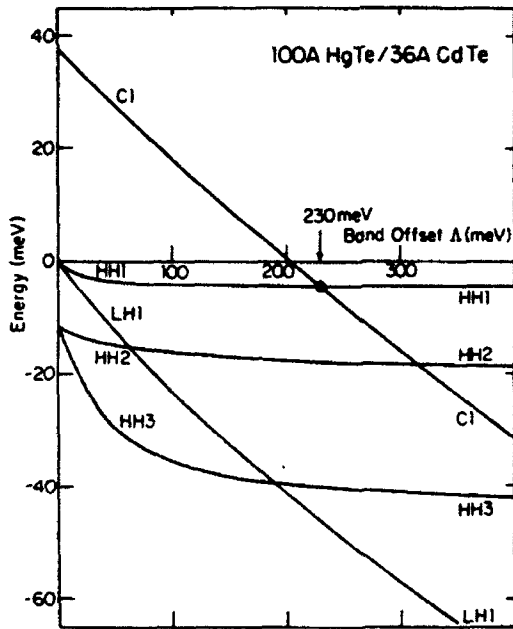


FIG. 2. The energies of the bands C1, LH1, HH1, HH2, and HH3 at $K=0$ as a function of band offset Δ for 100-Å HgTe/36-Å CdTe superlattice (see Ref. 2).

tion. With increasing Δ the electron energies become less positive, whereas the hole energies become more negative as the well becomes more substantial. The most dramatic feature is the rapid variation of the C1 and LH1 bands relative to the HH bands. This behavior is associated with the light bulk effective masses characterizing the former bands. The heavy-hole bulk mass is sufficiently large that the potential well seen by the HH particles is effectively infinite for $\Delta \geq 100$ meV and the values become virtually constant. The C1 and HH1 bands cross at 230 meV, the HH1 electrons are transferred to the C1 band, and the SL becomes semimetallic.

The behavior of the minimum band gap E_g is determined by the SL band structure along K_\perp perpendicular to the layers. Figure 3 shows E_g as a function of Δ and directly above the appropriate energies a sketch of the SL band structure for the offset indicated by the arrows. The figure divides itself into three regimes. For $0 < \Delta < 230$ meV the SL is a semiconductor (SC) with a direct gap at $K=0$ and with C1 and HH1 the lowest conduction band and highest valence band, respectively. For $230 < \Delta < 295$ meV the superlattice is semimetallic.¹¹

The new and remarkable feature we note here is the third region in which the SL becomes semiconducting once again for $\Delta > 295$ meV as a result of the continued downward shift of the C1 band and a resulting uncrossing of the C1 and HH1 bands. The band gap in this region is still direct but, as shown in Fig. 3, it occurs at the

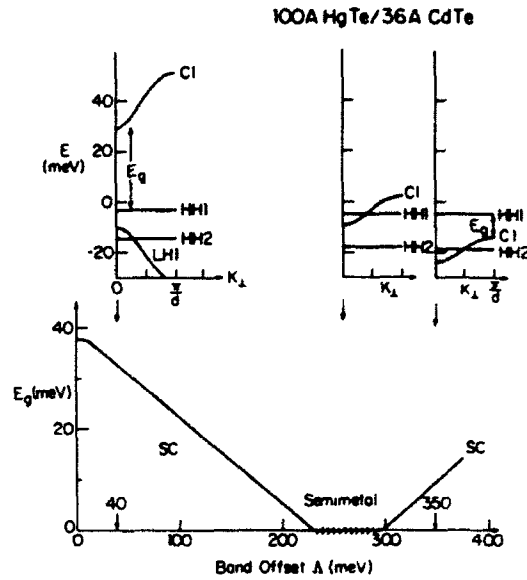


FIG. 3. The band gap, E_g , as a function of the band offset Δ for 100-Å HgTe/36-Å CdTe superlattice. Also shown are the band structures in the \perp direction at $K_\perp=0$ for $\Delta=40$, 260, and 350 meV.

SL Brillouin-zone face $K_\perp = \pi/d$, where d is the SL period. (C1 and HH1 just touch at $\Delta=295$ meV.) In this region C1 becomes a valence and HH1 a conduction miniband. In the absence of conduction-band electrons, $E_g = 10$ meV for $\Delta=350$ meV.

The behavior of the in-plane electron effective mass m_i and the corresponding band structure along K_\parallel as a function of band offset is shown in Fig. 4 using the same format as that of Fig. 3. The behavior of the band structure is quite reminiscent of that encountered in $\text{Hg}_x\text{Cd}_{1-x}\text{Te}$ alloys as a function of Hg concentration x . With increasing band offset the band gap decreases until the C1 and HH1 bands just touch at 230 meV and the E vs K dispersion becomes linear. Subsequently they exchange roles in that HH1 becomes the conduction band and C1 the valence band. This behavior results from the $k \cdot p$ interaction between the two bands along the \parallel direction. They do not interact along the \perp direction. For $\Delta < 230$ meV, m_i is roughly proportional to E_g , and formally vanishes at the intersection. The effective mass m_i shown in the subsequent region is that of the new conduction band HH1 at $K=0$.

The experimental electron-cyclotron mass ($m_e^*/m_0 = 0.017 \pm 0.003$) at 1 T,² extrapolated to vanishing magnetic field (0.015 ± 0.003) is also shown with its error bars at both $\Delta=40$ and 350 meV. The magnitude is somewhat larger than the band-edge, $K=0$, value at $\Delta=350$ meV. The energy gap is seen from Fig. 3 to have a value 10 meV as compared to the quoted² "20 meV." Since unintentionally doped n -type samples have

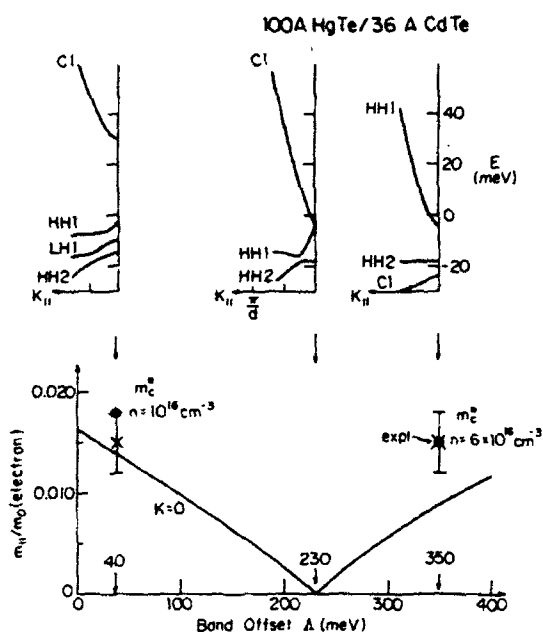


FIG. 4. Bottom: The in-plane effective mass $m_{||}$ at $K_{\perp}=0$ (solid line) as a function of the band offset Λ for 100-Å HgTe/36-Å CdTe superlattice. The experimental value (crosses) of the cyclotron mass m_c^* in the limit of zero field is shown with its error bars, together with the theoretical values (solid circles) of m_c^* with use of $6 \times 10^{16} \text{ cm}^{-3}$ for $\Lambda=350$ meV and 10^{16} cm^{-3} for $\Lambda=40$ meV. Top: The band structures in the \parallel direction at $K_{\perp}=0$ for $\Lambda=40$, 230, and 350 meV.

carrier densities $n \gtrsim 10^{16} \text{ cm}^{-3}$, an electron density was calculated that would produce a value of m_c^*/m_0 consistent with the experimental mass (Ref. 2 does not cite a precise value of n). As shown in Fig. 4 the requisite electron concentration for $\Lambda=350$ meV is $6 \times 10^{16} \text{ cm}^{-3}$. (The extremal values of m_c^*/m_0 at $K_{\perp}=0$ and π/d are almost identical because the HH1 constant energy surfaces are calculated to be nearly cylindrical. This point will be fully discussed elsewhere.) The corresponding Fermi energy lies 17 meV above the band minimum. Thus no interband transitions should be observed below 27 meV, in accord with experiment.² The same calculation for $\Lambda=40$ meV and $n=10^{16} \text{ cm}^{-3}$ yields $m_c^*/m_0=0.018$, quite close to the $\Lambda=350$ meV value. This observation provides some insight into the cause of the band-offset controversy: Both values of Λ coincidentally lead to similar results. The value of E_g , however, is 33 meV for $\Lambda=40$ meV and therefore larger than the approximate experimental value cited in Ref. 2.

Note that for $\Lambda=350$ meV, a smaller unintentional doping corresponding to $n=2 \times 10^{16} \text{ cm}^{-3}$ yields $m_c^*/m_0=0.012$. This result still falls within the experimental error² cited for m_c^* , and shows the precise value of n to be relatively unimportant.

Because of the unexpected semimetal to semiconductor transition at $\Lambda=295$ meV, the data of Ref. 2 are seen to be better explained by an offset $\Lambda \approx 350$ meV (or possibly even a slightly larger value) than the smaller $\Lambda=40$ meV. The semiconductor and semimetal transitions described here depend sensitively on the quantum well width for a given narrow barrier and band offset. For $\Lambda=350$ meV and the well width of the SL in Ref. 2 reduced to 50 Å, Cl would be above HH1 and E_g would lie at $K=0$, as is commonly assumed. The dependence of E_g on composition, strain, and temperature¹² requires further investigation.

We are grateful to K. C. Hass and J. R. Meyer for helpful discussions. We also thank R. J. Wagner for correcting our interpretation of the magneto-optical data. This research was supported by the U.S. Defense Advanced Research Projects Agency under Contract No. ONR N00014-86-K-0033 and the Joint Services Electronics Project under Contract No. ONR N00014-84-K-0465.

(a) To whom all correspondence should be addressed.

¹S. P. Kowalczyk, J. T. Cheung, E. A. Kraut, and R. W. Grant, Phys. Rev. Lett. **56**, 1605 (1986); T. M. Duc, C. Hsu, and J. P. Faurie, Phys. Rev. Lett. **58**, 1127 (1987); C. K. Shih and W. E. Spicer, Phys. Rev. Lett. **58**, 2594 (1987).

²J. M. Berroir, Y. Guldner, J. P. Vieren, M. Voos, and J. P. Faurie, Phys. Rev. B **34**, 891 (1986); see also J. M. Berroir, Y. Guldner, and M. Voos, IEEE J. Quantum Electron. **22**, 1793 (1986).

³C. A. Hoffman, J. R. Meyer, F. J. Bartoli, J. W. Han, J. W. Cook, Jr., J. F. Schetzina, and J. N. Schulman, to be published. We are grateful to J. R. Meyer for communicating these results prior to publication.

⁴M. Jaros, Phys. Rev. Lett. **60**, 2560 (1988).

⁵G. Bastard, Phys. Rev. Lett. **60**, 2561 (1988).

⁶N. F. Johnson, H. Ehrenreich, G. Y. Wu, and T. C. McGill, Phys. Rev. B (to be published).

⁷N. F. Johnson, H. Ehrenreich, K. C. Hass, and T. C. McGill, Phys. Rev. Lett. **59**, 2352 (1987).

⁸N. F. Johnson, H. Ehrenreich, and R. V. Jones, Appl. Phys. Lett. **53**, 180 (1988).

⁹Y. Guldner, C. Rigaux, M. Grynberg, and A. Mycielski, Phys. Rev. B **8**, 3875 (1973).

¹⁰J. N. Schulman and Y. C. Chang, Phys. Rev. B **33**, 2594 (1986).

¹¹This discussion assumes that the band crossings and uncrossings responsible for the semiconductor and semimetal transitions are confined to the region around $K=0$ considered here and that other regions of the Brillouin zone have larger gaps. This is inferred from the bulk band structures, their relative energetic positions, and the fact that the SL bands are described qualitatively by folding bulk bands into the new Brillouin zone.

¹²D. H. Chow, J. O. McCaldin, A. R. Bonnefoi, T. C. McGill, I. K. Sou, and J. P. Faurie, Appl. Phys. Lett. **51**, 2230 (1987).

Numerical study of optical absorption in two-dimensional metal-insulator and normal-superconductor composites

X. C. Zeng

Department of Physics, Ohio State University, Columbus, Ohio 43210-1106

P. M. Hui

Division of Applied Sciences, Harvard University, Cambridge, Massachusetts 02138

D. Stroud

Department of Physics, Ohio State University, Columbus, Ohio 43210-1106

(Received 22 April 1988; revised manuscript received 18 July 1988)

We analyze a random resistor-inductor-capacitor (*RLC*) lattice model for the optical properties of a two-dimensional normal-metal-insulator composite, using the *Y-Δ* transformation algorithm developed by Frank and Lobb. Within such a model, the surface plasmon resonances of a Drude-metal-insulator composite are modeled by the ac resonances of a random *RLC* network. The real part of the effective conductance is found to show a broad surface plasmon resonance peak below and above the metal percolation threshold, and a Drude peak above the threshold. An effective-medium-approximation (EMA) calculation is in excellent agreement with the results of the simulations. We also calculate the far-infrared absorption in a model composite of normal metal and superconductor, using a lattice model. The absorption shows a strong absorption below the superconducting energy gap. An approximate calculation based on the EMA is again in excellent agreement with these results.

I. INTRODUCTION

The ac conductivity of granular materials is very different from that of ordinary bulk materials. These differences are particularly pronounced in composites of normal metal and insulator or of superconductor and normal metal near the percolation threshold p_c , at which one of the two components first forms a connected path extending through the system. Numerous recent studies have been devoted to this problem, both theoretically¹⁻⁵ and experimentally.⁶⁻¹² Recently, Bug *et al.*⁸ have studied the anomalous frequency dependence of the ac response in two-dimensional networks of conductors and insulators near the percolation threshold. Laugier *et al.*⁹ have investigated the scaling laws followed by the complex dielectric function in the critical regime.

Many numerical studies have benefited from the transfer-matrix algorithm,¹³⁻¹⁵ which is a widely used method for calculating the transport properties of random systems numerically on a two-dimensional strip. But despite its efficiency, this technique has certain disadvantages. For example,⁸ in order to get a reasonably accurate result for some properties, one must consider a strip of length 10^5 – 10^6 for strip of width 20. This requires a considerable amount of computer time. The surface plasmon modes in a two-dimensional normal metal-insulator composite have recently been studied by Koss and Stroud¹⁰ using this technique. But because of the limitations imposed by computing time, they carried out the simulation only on a rather small strip (10×100). Not surprisingly, the results showed large numerical fluctuations.

In this paper we present the results of a numerical study on two-dimensional normal-metal-insulator composites on square lattice, using an efficient numerical algorithm¹⁶ recently proposed by Lobb and Frank for calculation of the effective response of the networks. This algorithm is considerably faster than the transfer matrix method. It has been shown to work efficiently not only for problems involving dc conductivity but also for calculating the critical current of a normal-metal-superconducting composite. When we apply the Lobb-Frank algorithm to ac problems in normal-metal-insulator composites, we see the surface plasma peak both above and below p_c and the Drude peak above p_c . Using the same algorithm to simulate far-infrared absorption in two-dimensional normal-metal-superconductor composites, we find a strong absorption below twice the superconducting gap. The analytic effective-medium approximation¹⁷ (EMA) is in excellent agreement with all the results of our simulations.

The remainder of this paper is organized as follows. Our lattice models for composite media are described in Sec. II. Numerical results are presented in Sec. III followed by a brief discussion in Sec. IV.

II. MODEL COMPOSITE MEDIA

We consider two types of binary composite media: normal metal and insulator, and normal metal and superconductor. Both are two dimensional in the sense that the networks are confined to a plane, and that the relevant Kirchhoff's equations (which are the discrete version of the electrostatic equations for these problems)

are two dimensional. But real composite films are, of course, embedded in a three-dimensional space. This distinction should be remembered in comparing these results with experiments on real films.

A. Metal-insulator composite

It is well known that normal-metal-insulator composites possess surface plasmon modes or Mie resonances.¹⁸ In a bulk (three-dimensional) composite, such modes are easily understood by considering a small spherical metal particle described by a Drude dielectric function

$$\epsilon_m(\omega) = 1 - \frac{\omega_p^2}{\omega(\omega - i/\tau)}, \quad (1)$$

embedded in an insulating matrix of dielectric constant of value unity. Here ω_p is the plasma frequency and τ is a characteristic relaxation time. If we imagine that the medium is subjected to an applied electric field $E_0 \exp(+i\omega t)$ in the long-wavelength limit, the field inside the small particle is uniform and is given by

$$E_m = \frac{3E_0}{\epsilon_m + 2} \exp(+i\omega t). \quad (2)$$

In the limit $\omega_p \tau \gg 1$, the real part of $3/(\epsilon_m + 2)$ becomes very large at frequencies $\omega \sim \omega_p/\sqrt{3}$, which is the surface plasmon frequency of a small spherical metal particle. Near this frequency, the small metal particle will show strong energy absorption—that is, the absorption coefficient $\alpha_s = (\omega/c) \text{Im} \sqrt{\epsilon(\omega)}$ will exhibit a strong peak near $\omega = \omega_p/\sqrt{3}$.

We will model a composite of Drude metal and insulator by means of a two-dimensional random lattice of resistors, inductors, and capacitors, following the previous work of Koss and Stroud.¹⁰ The composite is represented by a random network which consists of insulating bonds and metallic bonds. An insulating bond is represented simply as a capacitor, with admittance

$$\sigma_I = i\omega C', \quad (3)$$

while a metallic bond is represented as a series of a resistor and inductor in parallel with a capacitor. The metallic bond has total admittance

$$\sigma_M = \frac{1 + i\omega RC - \omega^2 LC}{R + i\omega L}. \quad (4)$$

Here R is the resistance of the conducting element, L is its inductance, C is a capacitance, and C' is the capacitance of the insulating element. If we put $L = C = C' = 1$, then the ratio σ_M/σ_I takes the form

$$\sigma_M/\sigma_I = 1 - 1/[\omega(\omega - i/\tau)], \quad (5)$$

where $\tau = L/R$ is a characteristic relaxation time.

The connection between this lattice model and a composite of Drude metal and insulator can be seen in the following way. For the latter composite, if we choose the dielectric function of insulator to be $\epsilon_I = 1$, then the ratio $\epsilon_M/\epsilon_I = 1 - \omega_p^2/[\omega(\omega - i/\tau)]$. This ratio is identical to σ_M/σ_I for the lattice model, provided we choose fre-

quency units such that $\omega_p = 1$. Thus the various properties of the lattice model, and, in particular, the frequency-dependent absorption, should be the same as those of the metal-insulator composite.

Halperin, Feng, and Sen¹⁹ have recently noted that real composites may differ significantly from lattice models of composites, especially near the percolation threshold. In particular, the critical exponents which describe the power-law variation of transport properties, such as the dc conductivity, near the percolation threshold of real composites may differ from those of lattice models. To represent a real composite, therefore, one should probably use a different network than the one described above—for example, a continuous distribution of admittances, rather than a unique admittance for the conducting elements. We will not consider such refinements in this paper, although their inclusion would be straightforward.

B. Normal-superconductor composite

To model a composite of normal metal and superconductor, we use the description of Garner and Stroud.¹⁷ These workers described the conductivity of the superconducting component in the Mattis-Bardeen²⁰ form. Using the effective-medium approximation, they predicted a strong absorption in such composites below the optical superconducting gap $2\Delta/\hbar$, where Δ is the superconducting energy gap. The extra absorption was found to be particularly pronounced near the percolation threshold, at which the superconducting component first forms an infinite connected path. At these concentrations, the absorption was found to be considerably enhanced, relative to that of the normal state.

In order to simulate a two-dimensional composite of normal metal and superconductor, we consider a square lattice containing bonds of two kinds. The "normal" bonds are modeled as resistors with conductance g_n . The "superconducting" bonds have a conductance of the Mattis-Bardeen form,

$$\sigma_s = iG_0/\omega + \sigma'_s(\omega). \quad (6)$$

Here $G_0 = \sigma'_n(\pi\Delta/\hbar)$, where σ'_n is the frequency-independent real conductance of the superconducting component in its normal state. The function σ'_s is given in terms of elliptic integrals of the second kind; its real part vanishes except for frequencies greater than the optical gap $2\Delta/\hbar$.

III. RESULTS

We have carried out extensive calculations for the two models described in Sec. II, using the propagation algorithm described by Frank and Lobb.¹⁶ In this method, one can exactly calculate the equivalent conductance of a square network of arbitrary size, using a sequence of network reductions familiar to electrical engineers, known as "Y-Δ transformations." The propagation starts from the square in the first column and first row. After each propagation, one square is deleted. The Y-Δ algorithm is then used to delete successively all the other squares in the

first column. Once the first column is deleted, the propagation algorithm comes to the next column. After approximately $N^3/3$ propagations on an $N \times N$ network, the whole network is reduced to just a single conductor, which gives the effective conductance of the whole network. It has been shown that this algorithm is highly

efficient for reducing a large square network to a single effective conductance.^{16,21} Indeed, it is considerably faster than the transfer matrix algorithm applied to the same square networks.

Our simulations are done on 100×100 square networks. For the model normal-metal-insulator compos-

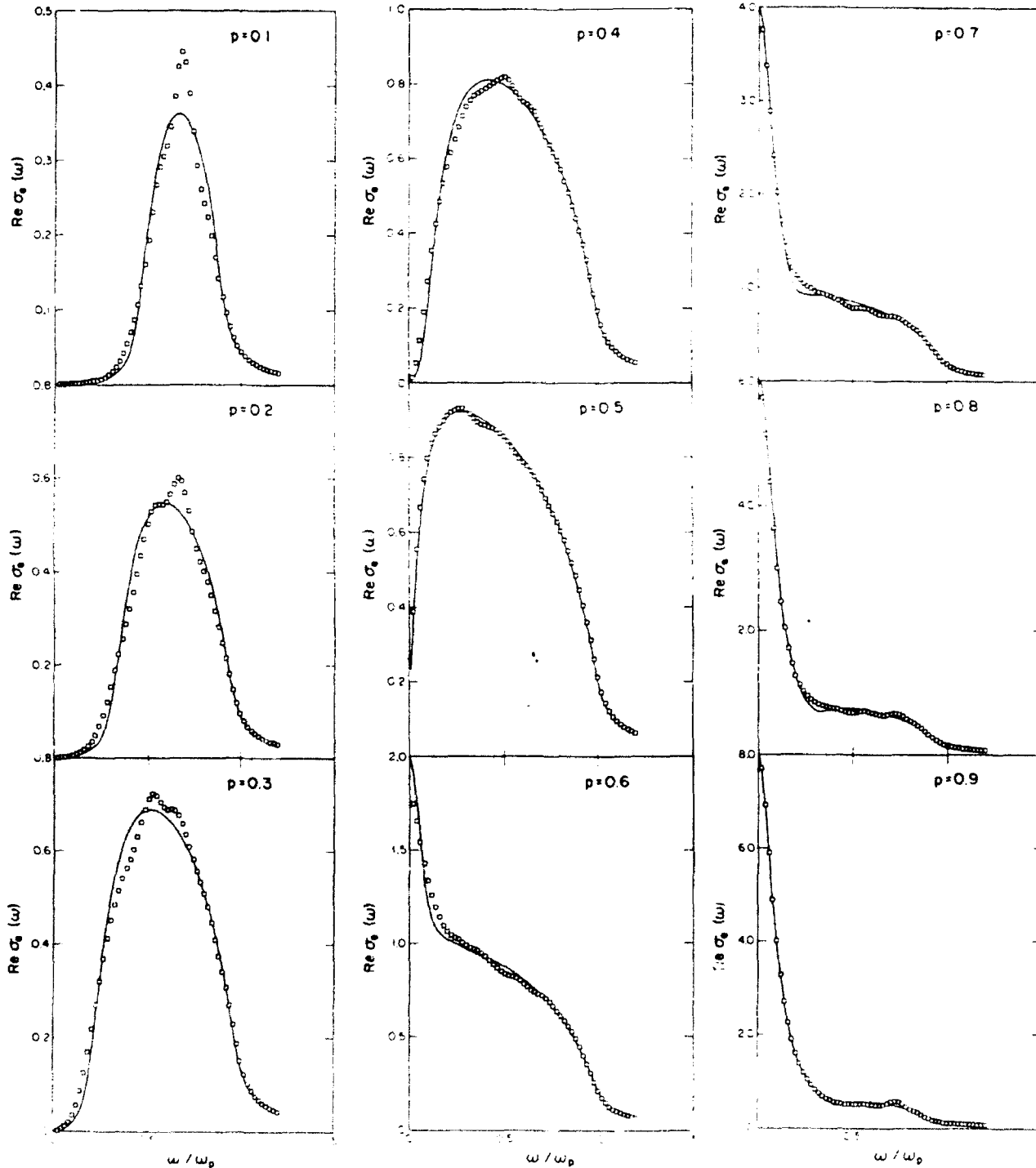


FIG. 1. Real part of the effective conductance, $\text{Re } \sigma_0(\omega)$, for a model composite of Drude metal and insulator, as calculated by numerical simulation on a 100×100 lattice, for metal volume fractions p from 0.1 to 0.9. The squares represent the results of simulation, and the solid lines denote the effective-medium calculations. The simulation results shown represent an average of five realizations for each concentration. The relaxation time is taken to be $\tau = 10$ in all calculations.

ites, we carry out the calculations for metal fractions from $p=0.1$ to 0.9 . In each case, we use bond percolation—that is, the admittance of each bond is chosen randomly and independently. The characteristic relaxation time is taken as $\tau=10$ in all our calculations.

Figure 1 shows the real part of the effective conductance, $\text{Re}\sigma_e(\omega)$, for this two-dimensional metal-insulator composite as a function of frequency. This quantity, of course, corresponds to absorption in these composites. For each value of the metal filling fraction p , we have averaged five realizations of each composite. (We also have averaged 20 realizations for a few metal filling fractions p , and find that the results change little from averaging five realizations.) Also shown are the effective-medium calculations for the same model.

As in Ref. 10, the results show both an "impurity band," which is the network analog of the band of surface plasmon resonances in a bulk metal insulator composite, and a "Drude peak." The surface plasmon peak is broadened as the metal fraction increases. The Drude peak, corresponding to nonzero dc conductivity, appears only at concentrations above the percolation threshold. In contrast to the results of Ref. 10, we obtain a relatively smooth impurity band (both because of the larger samples and because of the several realizations), and a correspondingly better agreement with the effective-medium predictions. In principle, the fluctuations in the structure can be averaged out with yet larger number of realizations. We believe that, if a few thousand realizations were to be run for each concentration, rather than about 10, the resulting absorption curves would be quite smooth.

To show the effects of averaging over realizations, we show in Fig. 2 the calculated $\text{Re}\sigma_e(\omega)$ for a single realization of a 100×100 lattice at $p=0.6$. There is somewhat more structure than in the ensemble-averaged calculations, which are effectively considering much larger lattices. However, even this curve is much smoother than that obtained by Koss and Stroud for a 10×100 lattice.

In Fig. 3 we show the calculated $\text{Re}\sigma_e(\omega)$ for the two-dimensional normal-superconductor composite at several values of the superconductor fraction p . The results are plotted in terms of the ratio $\text{Re}\sigma_e(\omega)/\sigma_\infty$, where $\sigma_\infty = \text{Re}\sigma_e(\infty)$. The effective-medium predictions are also shown on the same plot. For p sufficiently near p_c , a noticeable bump develops in this ratio at frequencies below $2\Delta/\hbar$, which shows that there is strong absorption as predicted by the effective-medium approximation.¹⁷

IV. DISCUSSION

The present results show that two-dimensional metal-insulator and normal-metal-superconductor composites are both well represented within the effective-medium approximation, provided that the geometries of these composites satisfy the assumptions of randomness implicit in the effective-medium theory. Our results also demonstrate the efficiency of the Lobb-Frank algorithm for ac as well as dc problems. In the case of the metal-insulator composite, only a propagation algorithm, such as the

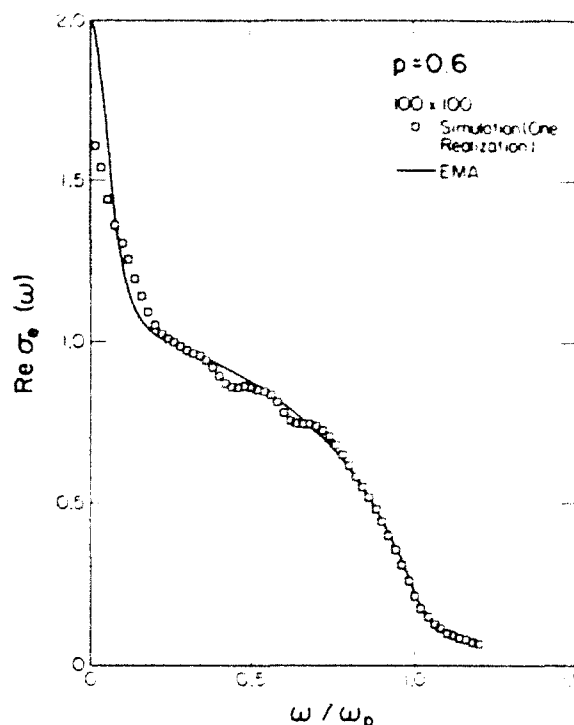


FIG. 2. Same as Fig. 1, but with only $p=0.6$ and a single realization.

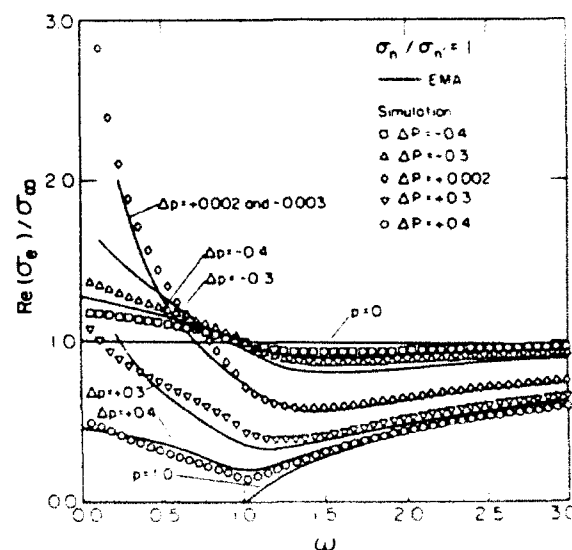


FIG. 3. The ratio $\text{Re}\sigma_e(\omega)/\text{Re}\sigma_e(\infty)$, as calculated by the numerical simulation on a 100×100 lattice (open symbols), and by effective-medium approximation (solid lines). The quantity shown is the ratio of the composite conductance to that of the superconducting component in its normal state. The quantity p_c is the percolation threshold, and $\Delta p = p - p_c$. Frequency units are such that $2\Delta/\hbar = 1$.

transfer matrix method or the present technique, can deal with the *RLC* resonances (Gaussian overrelaxation or underrelaxation techniques, as used in older papers, do not converge at all near the resonance). Of the two propagation algorithms, the Lobb-Frank method is by far the faster.

Our results for films of normal metal and superconductor show that the effective-medium theory works well in this case also. Since this approximation has been extensively used in recent months to calculate the ac properties of high- T_c superconductors,²² it is useful to have a

confirmation that this approximation is accurate for such materials, even though our model is slightly different from that studied in the literature.²²

ACKNOWLEDGMENTS

We are grateful for useful conversations with Professor C. J. Lobb. This work was supported by National Science Foundation Grant No. DMR-87-18874 and U.S. Defense Advanced Research Projects Agency Contract No. DARPA-ONR-N00014-86-K-0033.

- ¹E. L. Efros and B. I. Shklovskii, *Phys. Status Solidi B* **76**, 475 (1976).
- ²D. J. Bergman and Y. Imry, *Phys. Rev. Lett.* **39**, 1222 (1977).
- ³I. Webman, J. Jortner, and M. H. Cohen, *Phys. Rev. B* **16**, 2593 (1977).
- ⁴D. Stroud and D. J. Bergman, *Phys. Rev. B* **25**, 2067 (1982).
- ⁵D. Wilkinson, J. S. Langer, and P. N. Sen, *Phys. Rev. B* **28**, 1081 (1983).
- ⁶L. Benguigui, *J. Phys. (Paris) Lett.* **46**, L1015 (1985).
- ⁷Y. Song, T. W. Noh, S.-I. Lee, and J. R. Gaines, *Phys. Rev. B* **33**, 904 (1986).
- ⁸A. L. R. Bug, G. S. Grest, M. H. Cohen, and I. Webman, *J. Phys. A* **19**, L323 (1986).
- ⁹J. M. Langier, J. P. Clerc, G. Giraud, and J. M. Luck, *J. Phys. A* **19**, 3153 (1986).
- ¹⁰R. S. Koss and D. Stroud, *Phys. Rev. B* **35**, 9004 (1987).
- ¹¹B. N. J. Persson and A. Liebsch, *Phys. Rev. B* **28**, 4247 (1983).
- ¹²V. A. Davies and L. Schwartz, *Phys. Rev. B* **33**, 6627 (1986).
- ¹³B. Derrida and J. Vannimenus, *J. Phys. A* **15**, L557 (1982).
- ¹⁴H. J. Herrmann, B. Derrida, and J. Vannimenus, *Phys. Rev. B* **33**, 4080 (1984).
- ¹⁵G. Zabolitzky, *Phys. Rev. B* **30**, 4076 (1984).
- ¹⁶C. J. Lobb and D. J. Frank, *Phys. Rev. B* **30**, 4090 (1984); D. J. Frank and C. J. Lobb, *ibid.* **37**, 302 (1988).
- ¹⁷J. Garner and D. Stroud, *Phys. Rev. B* **28**, 2447 (1983); R. Landauer, in *Electrical Transport and Optical Properties of Inhomogeneous Media* (Ohio State University, 1977), Proceedings of the First Conference on the Electrical Transport of Optical Properties of Inhomogeneous Media, AIP Conf. Proc. No. 40, edited by J. C. Garland and D. B. Tanner (AIP, New York, 1978), pp. 2-43.
- ¹⁸F. Wooten, *Optical Properties of Solids* (Academic, New York, 1972).
- ¹⁹B. I. Halperin, Schechao Feng, and P. N. Sen, *Phys. Rev. Lett.* **54**, 2391 (1985).
- ²⁰D. C. Mattis and J. Bardeen, *Phys. Rev.* **111**, 412 (1958); M. Tinkham, *Introduction to Superconductivity* (McGraw-Hill, New York, 1975).
- ²¹M. Octavio, A. Octavio, J. Aponte, R. Medina, and C. J. Lobb, *Phys. Rev. B* **37**, 9292 (1988).
- ²²T. W. Noh, P. E. Sulewski, and A. J. Sievers, *Phys. Rev. B* **36**, 8866 (1987).

A possible resolution of the valence-band offset controversy in HgTe/CdTe superlattices

P. M. Hui, H. Ehrenreich, and N. F. Johnson

Division of Applied Sciences, Harvard University, Cambridge, Massachusetts 02138

(Received 11 October 1988; accepted 9 November 1988)

The valence-band offset controversy in HgTe/CdTe superlattices can be simply resolved by showing, as we do here, that a large offset value ($\Lambda > 300$ meV) is indeed consistent with the magneto-optical data of Berroir *et al.* [Phys. Rev. B **34**, 891 (1986)]. The superlattice (100 Å HgTe/36 Å CdTe) becomes semimetallic (SM) when Λ is increased from small values, but reverts to semiconducting (SC) behavior for $\Lambda > 300$ meV. The band gap in this new regime occurs at the superlattice Brillouin zone face. The sensitivity to layer thicknesses of such SC \rightarrow SM \rightarrow SC transitions is discussed and experiments suggested.

The controversy surrounding the differing values of the valence-band offset Λ in HgTe/CdTe superlattices (SL's) obtained from room-temperature photoemission¹⁻³ ($\Lambda \sim 350$ meV) and low-temperature magneto-optical experiments⁴ ($\Lambda \sim 40$ meV) is here resolved in favor of the large Λ by showing that the effective mass and band gap obtained by Berroir *et al.*⁴ are consistent with the value $\Lambda \sim 350$ meV. The experimental and theoretical results in Refs. 1-4 are completely correct; however, it was not recognized until our theoretical calculations⁵ that the particular sample chosen by Berroir *et al.*⁴ becomes semiconducting again for $\Lambda > 300$ meV (see Fig. 2).

The present calculations employ the envelope function approximation, with a modified Kane model⁶ as input, to obtain the SL $\mathbf{K} = 0$ energies and envelope functions analytically (where \mathbf{K} is the SL wave vector). $\mathbf{K} \cdot \mathbf{p}$ perturbation theory with respect to the SL $\mathbf{K} = 0$ states is then used to obtain the SL band structure for finite \mathbf{K} . This approach has been shown to yield quantitative results for effective masses and optical absorption coefficients for a variety of III-V and II-VI SL's⁶⁻⁸ and agrees well with more complicated $\mathbf{k} \cdot \mathbf{p}$ approaches.⁹

Figure 1 shows the relative alignment of the bulk HgTe and CdTe band edges (Γ_6 and Γ_8) schematically. The band offset Λ is defined to be positive. Even though the superlattice electron and hole states contain both Γ_6 and Γ_8 components, one can roughly associate the solid line with the quantum well appropriate to electrons, and the dashed line that appropriate to holes.

Figure 2 shows the SL band structure for the 100 Å HgTe/36 Å CdTe (111) SL of Ref. 4 as a function of Λ . K_1 is along the growth axis. The zero of energy is taken to be the valence-band maximum of bulk HgTe. The most dramatic feature with increasing Λ is the rapid downward variation of the lowest conduction miniband C_1 and highest light-hole band LH_1 relative to the heavy-hole bands HH_1 and HH_2 . This behavior is associated with the light bulk effective masses characterizing the former bands. The heavy-hole bulk mass is sufficiently large that the potential well seen by the bulk heavy hole is effectively infinite for $\Lambda > 100$ meV. Thus the HH minibands are virtually independent of Λ . As a result, the C_1 and HH_1 bands cross at $\Lambda = 230$ meV as shown; the HH_1 electrons are transferred to the C_1 band, and the SL

becomes semimetallic. The new and remarkable feature we note here is the third region ($\Lambda > 295$ meV) in which the SL becomes semiconducting once again as a result of the uncrossing of the C_1 and HH_1 bands. The band gap in this region is still essentially direct¹⁰ but it occurs at the SL Brillouin zone face $K_1 = \pi/d$, where d is the SL period.

Figure 3 shows the behavior of the minimum band gap E_g between C_1 and HH_1 as a function of both Λ and HgTe layer thickness for a fixed CdTe layer thickness of 36 Å. The zero gap ($E_g = 0$) regions correspond to semimetallic behavior, while nonzero E_g corresponds to semiconducting regimes. The bold curve (100 Å HgTe) corresponds to the sample thickness of Ref. 4. Values of the band gap for $\Lambda > 350$ meV are seen to be in better agreement with the experimental quoted ~ 20 meV⁴ than the value for $\Lambda \sim 40$ meV.

It is clear from Fig. 3 that the 100 Å HgTe/36 Å CdTe SL accidentally gives similar results for small and large Λ because of the nearly symmetrical location of the semimetallic regime between the high and low values of Λ . Such symmetry only occurs for HgTe thicknesses near 100 Å (given a 36-Å CdTe barrier thickness). As expected, E_g tends to decrease with increasing HgTe "well" thickness for fixed Λ . Figure 3 suggests that an optical study of band gaps in undoped HgTe/CdTe SL's having 36-Å CdTe layer width but varying HgTe layer widths should detect semiconducting \rightarrow semimetallic \rightarrow semiconducting transitions if Λ is indeed large.

Figure 4 shows the corresponding behavior of the in-plane

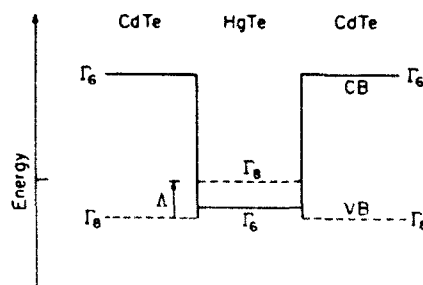


FIG. 1. The relative alignment of the bulk HgTe and CdTe band edges. The valence-band offset Λ is defined as the difference between the HgTe and CdTe Γ_8 valence-band maxima.

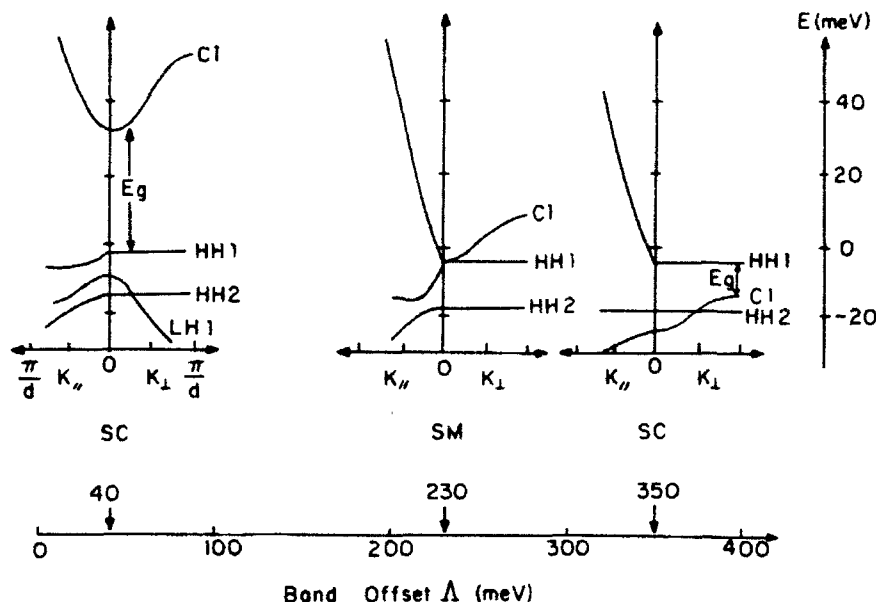


FIG. 2. The band structures for 100 Å HgTe/36 Å CdTe superlattice as a function of band offset Δ . As Δ increases, the system changes from semiconducting (SC) to semimetallic (SM) and back to semiconducting (SC) due to the crossing and uncrossing of the C1 and HH1 bands.

electron effective mass m_{\parallel} at $K = 0$. The bold curve again corresponds to the sample thickness of Ref. 4. For small Δ (below the semimetallic region) the value of m_{\parallel} corresponds to the C1 band, while the value in the large Δ region is that of the new conduction band HH1 at $K = 0$. The behavior of m_{\parallel} can be readily understood by referring back to the band structures in Fig. 2. With increasing band offset, the band gap decreases until the C1 and HH1 bands just touch at $\Delta = 230$ meV and the $E(K_{\parallel})$ dispersion becomes linear. The large $K \cdot p$ interaction between these two bands in the parallel direction implies that m_{\parallel} is roughly proportional to E_g , and formally vanishes at the intersection. (These two bands do not interact along the \perp direction.) The dependence of m_{\parallel} on HgTe layer thickness (for a given Δ and a

CdTe layer thickness of 36 Å) is reminiscent of that encountered in $\text{Hg}_x\text{Cd}_{1-x}\text{Te}$ alloys as a function of Hg concentration x .

The experimental electron cyclotron mass ($m_c^*/m_0 = 0.017 \pm 0.003$ at 1 T⁴) extrapolated to vanishing magnetic field (0.015 ± 0.003) is also shown in Fig. 4 for 100 Å HgTe with its error bars at both $\Delta = 40$ and 350 meV. The experimental value is somewhat larger than the calculated $K = 0$ value at $\Delta = 350$ meV. Since unintentionally doped n -type samples have carrier densities $n > 10^{16}$, an electron density was calculated that would produce a value of m_c^*/m_0

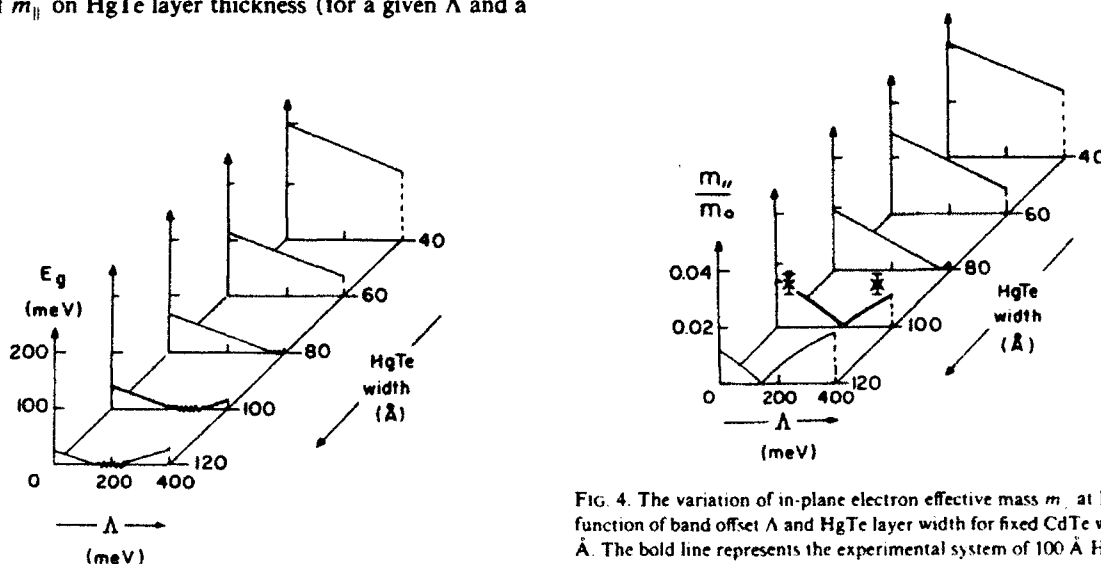


FIG. 3. The variation of band gap E_g between C1 and HH1 as a function of band offset Δ and HgTe layer width for fixed CdTe width of 36 Å. The bold line represents the experimental system of 100 Å HgTe/36 Å CdTe superlattice (see Ref. 4).

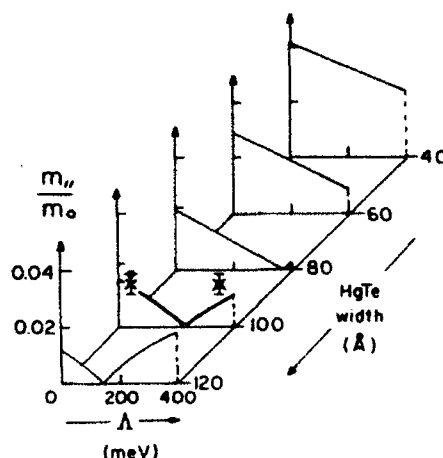


FIG. 4. The variation of in-plane electron effective mass m_{\parallel} at $K = 0$ as a function of band offset Δ and HgTe layer width for fixed CdTe width of 36 Å. The bold line represents the experimental system of 100 Å HgTe/36 Å CdTe superlattice (see Ref. 4). The experimental value (crosses) of the cyclotron mass m_c^*/m_0 in the limit of zero field is shown with its error bars, together with the theoretical values (solid circles) of m_c^*/m_0 using doping concentrations of $6 \times 10^{16} \text{ cm}^{-3}$ for $\Delta = 350$ meV and 10^{16} cm^{-3} for $\Delta = 40$ meV (see Ref. 5).

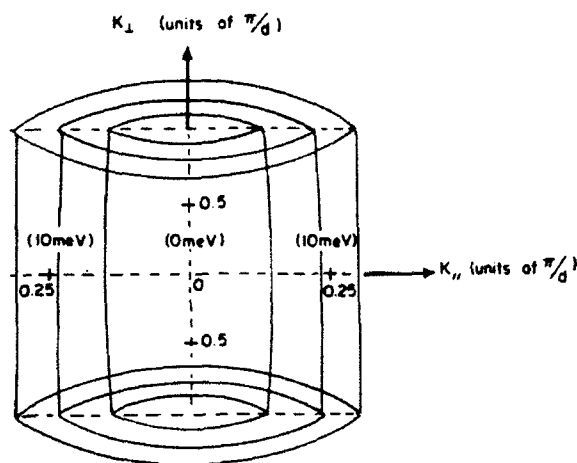


FIG. 5. Constant energy surfaces along K_{\parallel} and K_{\perp} of HH1 for 100 Å HgTe/36 Å CdTe superlattice with $\Lambda = 350$ meV.

consistent with the experimental mass. Reference 4 does not cite a value of n . As shown in Fig. 4, the requisite electron concentration for $\Lambda = 350$ meV is $6 \times 10^{16} \text{ cm}^{-3}$. The extremal values of m_c^*/m_0 at $K_{\perp} = 0$ and π/d are almost identical. This can be seen from Fig. 5, which shows HH1 constant energy surfaces to be nearly cylindrical. Indeed they are cylindrical at the corresponding Fermi energy of 17 meV above the conduction-band minimum. Thus no interband transitions should be observed below 27 meV, in accord with experiment.⁴

Calculations for $\Lambda = 40$ meV and $n = 10^{16} \text{ cm}^{-3}$ yield $m_c^*/m_0 = 0.018$, again quite close to the $\Lambda = 350$ meV value. The cause of the band offset controversy can now be understood: the sample of Berroir *et al.*⁴ accidentally gives similar results for both small and large offsets because of its particular layer thicknesses. For $\Lambda = 40$ meV, a higher concentration of $n = 4 \times 10^{16} \text{ cm}^{-3}$ yields $m_c^*/m_0 = 0.021$, a value of 0.003 outside the experimental error. For $\Lambda = 350$ meV, on the other hand, the same concentration gives $m_c^*/m_0 = 0.014$, a value close to the experimental result.

Baukus *et al.*¹¹ compared experimental infrared photoluminescence data with energy gaps calculated using a two-band tight-binding method and found that a value $\Lambda = 40$ meV gives better agreements. However, recent measurements¹² of the energy gaps on a series of HgTe/CdTe superlattices indicate better agreement for $\Lambda = 350$ meV on the basis of a tight-binding analysis.

The effects of strain due to the 0.5% lattice mismatch are neglected in the present calculations. However, from previous calculations,^{13,14} we expect that the inclusion of strain will only affect the band structure quantitatively on the meV scale, and will not alter the cyclotron mass by more than

20%. The conclusion of a large band offset is further supported by recent tight-binding calculations including strain.¹⁵

Using finite temperature bulk parameters as input,¹⁶ we find the band structure at 300 K for $\Lambda = 350$ meV to have a direct gap of 48 meV at $K = 0$. The C1 and HH1 bands, respectively, correspond to the lowest conduction band and the highest valence band. When the doping concentration is taken into account, the gap is found to be consistent with the experimental result⁴ of ~ 90 meV obtained optically at 300 K.

The effect of Hg concentration x in the CdTe barrier has also been examined. Using the virtual-crystal approximation for the alloy barrier and assuming that Λ is 350 (1 - x) meV, we found that the band gap is fairly insensitive to the composition, with the band gap at $K_{\perp} = \pi/d$ decreasing by < 2 meV for $x = 0.15$.

Acknowledgments: This work was supported in part by the Defense Advanced Research Projects Agency under Contract No. ONR N00014-86-K-0033 and the Joint Services Electronics Project under Contract No. ONR N00014-84-K-0465.

¹S. P. Kowalczyk, J. T. Cheung, E. A. Kraut, and R. W. Grant, *Phys. Rev. Lett.* **56**, 1605 (1986).

²T. M. Duc, C. Hsu, and J. P. Faurie, *Phys. Rev. Lett.* **58**, 1127 (1987).

³C. K. Shih and W. E. Spicer, *Phys. Rev. Lett.* **58**, 2594 (1987).

⁴J. M. Berroir, Y. Guldner, J. P. Vieren, M. Voos, and J. P. Faurie, *Phys. Rev. B* **34**, 891 (1986).

⁵N. F. Johnson, P. M. Hui, and H. Ehrenreich, *Phys. Rev. Lett.* **61**, 1993 (1988).

⁶N. F. Johnson, H. Ehrenreich, K. C. Hass, and T. C. McGill, *Phys. Rev. Lett.* **59**, 2352 (1987).

⁷N. F. Johnson, H. Ehrenreich, and R. V. Jones, *Appl. Phys. Lett.* **53**, 180 (1988).

⁸J. Schetzina (unpublished). Theoretical calculations using our $K \cdot p$ approach give results in excellent agreement with experimental optical absorption data. We are grateful to Professor Schetzina for making his results available prior to publication.

⁹N. F. Johnson, H. Ehrenreich, G. Y. Wu, and T. C. McGill, *Phys. Rev. B* (in press).

¹⁰The valence-band maximum may be slightly away from $K_{\parallel} = 0$.

¹¹J. P. Baukus, A. T. Hunter, J. N. Schulman, and J. P. Faurie, *J. Appl. Phys.* **64**, 283 (1988); J. P. Baukus, A. T. Hunter, O. J. Marsh, C. E. Jones, G. Y. Wu *et al.*, *J. Vac. Sci. Technol. A* **4**, 2110 (1986).

¹²C. A. Hoffman, J. R. Meyer, F. J. Bartoli, J. W. Han, J. W. Cook, Jr. *et al.* (preprint).

¹³J. M. Berroir and J. A. Brum, *Superlattices Microstructures* **3**, 239 (1987).

¹⁴J. N. Schulman and Y. C. Chang, *Phys. Rev. B* **33**, 2594 (1986).

¹⁵J. R. Meyer, F. J. Bartoli, C. A. Hoffman, and J. N. Schulman, *Phys. Rev. B* **38**, 12457 (1988).

¹⁶We assume that the valence-band offset is temperature independent. However, the interpretation of recent single-barrier tunneling experiments suggests that Λ may depend on temperature [D. H. Chow *et al.*, *Appl. Phys. Lett.* **51**, 2230 (1987)].

MEAN FIELD THEORY FOR WEAKLY NONLINEAR COMPOSITES

X.C. ZENG^a, P.M. HUI^b, D.J. BERGMAN^{ac} and D. STROUD^a

^a*Department of Physics, Ohio State University, Columbus, OH 43210, USA*

^b*Division of Applied Sciences, Harvard University, Cambridge, MA 02138, USA*

^c*School of Physics and Astronomy, Raymond and Beverly Sackler Faculty of Exact Sciences, Tel Aviv University, Tel Aviv 69978, Israel*

We discuss the nonlinear behavior of a random composite material characterized by a weakly nonlinear relation between the electric displacement of the form $D = \epsilon E + \chi |E|^2 E$, where ϵ and χ are position dependent. A general expression for the effective nonlinear susceptibility to first order in the nonlinear susceptibility of the constituents in the composite is given. A general method of approximation is introduced which gives the effective nonlinear susceptibility in terms of the solution of the linear dielectric function of the random composite. Various applications of the proposed approximation are demonstrated.

1. Introduction

There are many electrical-transport phenomena in solids in which nonlinearity plays an important role. At zero frequency, such nonlinearities show up in such effects as dielectric breakdown and the burning out of fuses. At finite frequencies, the nonlinear dependence of displacement current on electric field in some materials is the basis of nonlinear optical phenomena.

In this paper we consider some aspects of nonlinear behavior in granular materials and other composites. In particular, we consider various approximations for calculating the effective nonlinear susceptibility of a composite in which one or more of the components has nonlinear behavior.

The plan of the paper is as follows. In section 2, we give a general expression for the nonlinear susceptibility which is correct to first order in the nonlinear susceptibility of the constituents; and apply it to the case of a dilute composite. In section 3, we propose an effective medium approximation for weakly nonlinear composites, and explore its applications. We discuss our results in section 4. More details of the results presented here can be found in recent articles by the present authors [1, 2].

2. Nonlinear susceptibility

We consider the system of a two-component composite in which each component is described by a weakly cubic nonlinear relation between the electric displacement D and the electric field E of the form

$$D_i = \epsilon_i^0 E_i + \chi_i |E_i|^2 E_i. \quad (1)$$

Such an expansion will always be possible provided that $\chi_i |E_i|^2 \ll \epsilon_i^0$ ($i = 1, 2$). The term quadratic in electric field will vanish unless the constituents lack inversion symmetry. The space-averaged fields and displacements, $\langle E \rangle$ and $\langle D \rangle$, are related by an equation of the same form.

$$\langle D \rangle = \epsilon_c^0 \langle E \rangle + \chi_c |\langle E \rangle|^2 \langle E \rangle, \quad (2)$$

where ϵ_c^0 and χ_c are the effective linear dielectric function and the effective nonlinear susceptibility of the composite, respectively.

To first order in the nonlinear susceptibility of the constituents, the effective nonlinear susceptibility of a composite has been shown by two of the present authors [1] to be of the form

$$\chi_c = \frac{1}{V |E_0|^4} \int \chi(x) |E_{lin}(x)|^2 E_{lin}(x) \cdot E_{lin}(x) d^3x. \quad (3)$$

where E_0 is the average field [1] and $E_{lin}(x)$ is the electric field taken from the solution of the linear problem (i.e. by solving the same composite problem with $\chi_i = 0$), and V is the volume of the system.

The above formula can easily be applied to the case of a composite in which a small concentration of spheres of nonlinear material is included in a linear host. In this case, the effective nonlinear susceptibility is exactly

$$\chi_c = p \chi_1 [3\epsilon_2^0 / (\epsilon_1^0 + 2\epsilon_2^0)]^2 [3\epsilon_2^0 / (\epsilon_1^0 + 2\epsilon_2^0)]^2. \quad (4)$$

where χ_1 is the nonlinear susceptibility of material 1, present in volume fraction $p \ll 1$ in a host of linear material 2 (i.e. $\chi_2 = 0$). This result is valid to first order in χ_1 .

An interesting feature in eq. (4) is the vast enhancement of nonlinearity at frequencies such that $\epsilon_1^0 + 2\epsilon_2^0 \approx 0$. This is the condition for the occurrence of a surface-plasmon resonance which leads to a great increase in electric field near certain characteristic frequencies. This field enhancement is responsible for the enhancement of the nonlinearity.

3. Weakly nonlinear composite: a general approximation method

Consider the two-component composite defined in the previous section. The linear effective dielectric function can always be written in the form

$$\epsilon_e^0 = F(\epsilon_1^0, \epsilon_2^0, p_1), \quad (5)$$

where p_1 is the volume fraction of the component 1, and F is some function which will, in general, depend on the geometry of the composite. We invoke an approximate nonlinear form of eq. (5).

$$\epsilon_e = F(\epsilon_1, \epsilon_2, p_1). \quad (6)$$

Here $\epsilon_i = \epsilon_i^0 + \chi_i \langle |E_i|^2 \rangle$ and $\langle |E_i|^2 \rangle$ is the mean-square of the electric field in the i th component in the linear limit. Eq. (6) is strictly valid only if ϵ_1 and ϵ_2 are constant in each component. Our use of eq. (6) here thus involves making the approximation that the electric field is uniform in the nonlinear component.

For simplicity, we assume that only component 1 is nonlinear, so that $\epsilon_2 = \epsilon_2^0$. We then expand the function F in a Taylor series about the linear ϵ_e^0 to obtain

$$\epsilon_e \approx F(\epsilon_1^0, \epsilon_2^0, p_1) + F'_1(\epsilon_1^0, \epsilon_2^0, p_1) \chi_1 \langle |E_1|^2 \rangle. \quad (7)$$

where $F'_1 = \partial F / \partial \epsilon_1^0$. Now this partial derivative can be expressed *exactly* in terms of the average squared electric field in component 1 in the *linear* limit; the relation is [3]

$$p_1 \langle |E_1|^2 \rangle / |E_0|^2 = (\partial \epsilon_e^0 / \partial \epsilon_1^0) = F'_1(\epsilon_1^0, \epsilon_2^0, p_1), \quad (8)$$

where E_0 is the external field. Therefore, we have

$$\epsilon_e = \epsilon_e^0 + \frac{\chi_1}{p_1} F'_1 |F'_1| |E_0|^2. \quad (9)$$

and by the definition of the effective nonlinear coefficient χ_e , we obtain

$$\chi_e = \frac{\chi_1}{p_1} F'_1 |F'_1|. \quad (10)$$

These results can readily be generalized to the case where both components are nonlinear. In this case, we simply expand eq. (6) around both ϵ_1^0 and ϵ_2^0 and obtain for χ_e

$$\chi_e = \frac{\chi_1}{p_1} F'_1 |F'_1| + \frac{\chi_2}{p_2} F'_2 |F'_2|, \quad (11)$$

where $F'_i = (\partial \epsilon_i^0 / \partial \epsilon_i^0)$ ($i = 1, 2$). Eq. (11) is our principal result. It is based on the assumption that the fluctuations $\langle |E_i|^4 \rangle - \langle |E_i|^2 \rangle^2$ within the i th component are small, compared to $\langle |E_i|^4 \rangle$ itself. This approximation is valid for many, but not all weakly non-linear systems.

Eq. (11) gives the effective nonlinear susceptibility in terms of the function F , which can take on several forms according to different approximations for the solution of the linear problem. In the following, we apply eq. (11) to obtain χ_e for different forms of the function F .

3.1. Low density limit

For the case of a small concentration p_1 of spheres of nonlinear material 1 embedded in a linear host of material 2. The effective linear dielectric function can be written as [4]

$$\epsilon_e^0 = \epsilon_2^0 + 3\epsilon_2^0 p_1 \frac{\epsilon_1^0 - \epsilon_2^0}{\epsilon_1^0 + 2\epsilon_2^0}. \quad (12)$$

Given this form of the function F , application of eq. (11) leads to the same result as eq. (4), discussed in the previous section.

3.2. Exactly solvable microgeometries

For the case where the components are arranged in the form of cylinders (not necessarily circular) parallel to the external field, the function F can be obtained from the result

$$\epsilon_e^0 = p_1 \epsilon_1^0 + p_2 \epsilon_2^0. \quad (13)$$

Eq. (11) then leads to

$$\chi_e = p_1 \chi_1 + p_2 \chi_2 \quad (14)$$

for parallel cylinders.

For the case in which the constituents are arranged in the form of flat slabs perpendicular to the applied field, the function F is given by

$$\epsilon_e^0 = 1 / \left(\frac{p_1}{\epsilon_1^0} + \frac{p_2}{\epsilon_2^0} \right), \quad (15)$$

and χ_e is then found from eq. (11) to be

$$\chi_e = \frac{\chi_1 p_1}{(p_1 + \epsilon_1^0 p_2 / \epsilon_2^0)^4} + \frac{\chi_2 p_2}{(p_2 + \epsilon_2^0 p_1 / \epsilon_1^0)^4}. \quad (16)$$

3.3. Maxwell-Garnett approximation and effective medium approximation

The most successful approximations for the linear effective dielectric function of a binary composite are the Maxwell-Garnett approximation (MGA) for dilute concentrations and the effective medium approximation (EMA) for general values of concentration. Within MGA, ϵ_e^0 is given by [5]

$$\frac{\epsilon_e^0}{\epsilon_2^0} = \frac{\epsilon_1^0(1 + 2p_1) + 2\epsilon_2^0(1 - p_1)}{\epsilon_1^0(1 - p_1) + \epsilon_2^0(2 + p_1)}. \quad (17)$$

Within EMA, ϵ_e^0 is given by [6] solving the following quadratic equation:

$$p_1 \frac{\epsilon_1^0 - \epsilon_e^0}{\epsilon_e^0 + g(\epsilon_1^0 - \epsilon_e^0)} + (1 - p_1) \frac{\epsilon_2^0 - \epsilon_e^0}{\epsilon_e^0 + g(\epsilon_2^0 - \epsilon_e^0)} = 0. \quad (18)$$

where g is a geometric factor related to the depolarization factor of the inclusions and dependent on their shape. From these expressions for ϵ_e^0 , eq. (11) can be applied to calculate the nonlinear susceptibility of a binary composite, whether host or inclusions (or both) are nonlinear.

4. Discussion

Besides the present approximations, one can also prove exact results. For materials with cubic nonlinearities, it can be shown [1, 7] that the effective nonlinear susceptibility is closely related to the relative resistance fluctuations in the linear composite [8], as both of these problems can be related to the fourth moment of the current distributions in the linear problem. Hence, results for the divergence of the relative fluctuations (noise) near the percolation threshold of a random composite are immediately applicable to the nonlinear susceptibility.

Some of the most potentially interesting applications of this work lie in the field of nonlinear optics. One important goal of nonlinear optical studies is to obtain new materials with large nonlinear susceptibilities χ_e . The use of the present formalism may help in the design of such materials by suitable choices of nonlinear constituents, particle shapes, and other geometrical factors.

Acknowledgments

This work was supported by the US National Science Foundation under Grant DMR-87-18874 (DS, XCZ, DJB), the Defense Advanced Research Projects Agency under ONR Contract N00014-86-K-0033 (PMH), and the US-Israel Binational Science Foundation under Grant No. 354/85 (DJB).

References

- [1] D. Stroud and P.M. Hui, *Phys. Rev. B* 37 (1988) 8719.
- [2] X.C. Zeng, D.J. Bergman, P.M. Hui and D. Stroud, *Phys. Rev. B* (in press).
- [3] D.J. Bergman, *Phys. Rep.* 43 (1978) 377.
- [4] See, for example, L.D. Landau, E.M. Lifshitz and L.P. Pitaevskii, *Electrodynamics of Continuous Media*, 2nd edition (Pergamon, Oxford, 1984) p. 44.
- [5] J.C. Maxwell-Garnett, *Philos. Trans. R. Soc. London* 203 (1904) 385, 205; (1906) 237.
- [6] D.A.G. Bruggeman, *Ann. Phys. (Leipzig)* 24 (1935) 636; D. Stroud, *Phys. Rev. B* 12 (1975) 3368. See also R. Landauer, in *Electrical Transport and Optical Properties of Inhomogeneous Media*, J.C. Garland and D.B. Tanner, eds. (AIP, New York, 1977).
- [7] A. Aharony, *Phys. Rev. Lett.* 58 (1987) 2726.
- [8] R. Rammal, C. Tannous, P. Breton and A.-M.S. Tremblay, *Phys. Rev. Lett.* 54 (1985) 1718; R. Rammal, C. Tannous and A.-M.S. Tremblay, *Phys. Rev. A* 31 (1985) 2662.

Correlation and clustering in the optical properties of composites: A numerical study

X. C. Zeng

Department of Physics, Ohio State University, Columbus, Ohio 43210-1106

P. M. Hui*

Division of Applied Sciences, Harvard University, Cambridge, Massachusetts 02138

D. J. Bergman

*School of Physics and Astronomy, Raymond and Beverly Sackler Faculty of Exact Sciences,**Tel Aviv University, 69 978 Tel Aviv, Israel*

D. Stroud

Department of Physics, Ohio State University, Columbus, Ohio 43210-1106

(Received 3 February 1989)

We have numerically investigated the effects of correlation and clustering on the far-infrared (FIR) absorption and surface-plasmon modes of a model two-dimensional metal-insulator composite. We model the composite as a diluted resistor-inductor-capacitor (RLC) network. Two-site and nearest-neighbor-site correlations among the conducting bonds are found to enhance the FIR absorption per metallic bond by a factor of 5 relative to a network of the same concentration with a purely random distribution of metallic bonds. Ring-shaped clusters (which model insulating particles with a metallic coating), and percolation clusters are found to produce a FIR absorption enhanced by more than 2 orders of magnitude per metallic bond. The surface-plasmon absorption peak in a percolation cluster is found to be strongly broadened relative to the predictions of the Maxwell Garnett approximation. In the two-site correlation model, the surface-plasmon absorption peak is weakly split, whereas in the nearest-neighbor site-correlation model, it is weakly red shifted. Ring-shaped clusters are found to produce double and triple peaks in the surface-plasmon frequency range. Possible explanations for these novel features are briefly discussed.

I. INTRODUCTION

The optical properties of granular materials have attracted much attention in recent years. Many experimental studies¹⁻⁵ of the far-infrared (FIR) absorption by small metallic particles embedded in an insulating matrix have shown unusual results. Earlier studies show that the magnitude of the FIR absorption is a few orders of magnitude larger than the predictions of classical electromagnetic theory, even though the classical theory gives correctly the frequency, size, and concentration dependence of the absorption. This discrepancy remains even when magnetic dipole absorption is taken into account.⁶ Many theoretical explanations for this discrepancy⁷⁻²³ have been proposed. Among these are a broad distribution of particle sizes, absorption due to resistive coating on particles, quantum size effects, clustering of small metal particles into clumps, and the formation of percolation clusters and fractal clusters of various geometries.

In this article, we study numerically the effects of correlation and clustering on the optical properties of two-dimensional metal-insulator (M/I) composites. The composite is modeled as a resistor-inductor-capacitor (RLC) network, such as has been used previously²⁴ to describe random metal-insulator composites. The ac response of this network is calculated using a very fast

numerical algorithm proposed by Lobb and Frank,²⁵ based on the Y - Δ transformation familiar to electrical engineers. Various models with short-range order are then studied numerically and are shown to give widely varying responses both in the far-infrared and in the optical frequency ranges.

We turn now to the body of the paper. The model and the numerical algorithm are described in Sec. II, and numerical results are given in Sec. III. A brief discussion follows in Sec. IV.

II. MODEL

We study a thin-film composite of Drude metal and insulator, modeled as a two-dimensional random lattice of resistors, inductors, and capacitors. Several studies of this nature have already been carried out,^{24,26-30} but for purely random lattices. Each bond in the network is either an insulating bond or a metallic bond. The former is represented by a capacitor with admittance

$$\sigma_I = i\omega C'. \quad (1)$$

A metallic bond is represented by a series of resistor and inductor in parallel with a capacitor, and has admittance

$$\sigma_M = \frac{1 + i\omega RC - \omega^2 LC}{R + i\omega L}. \quad (2)$$

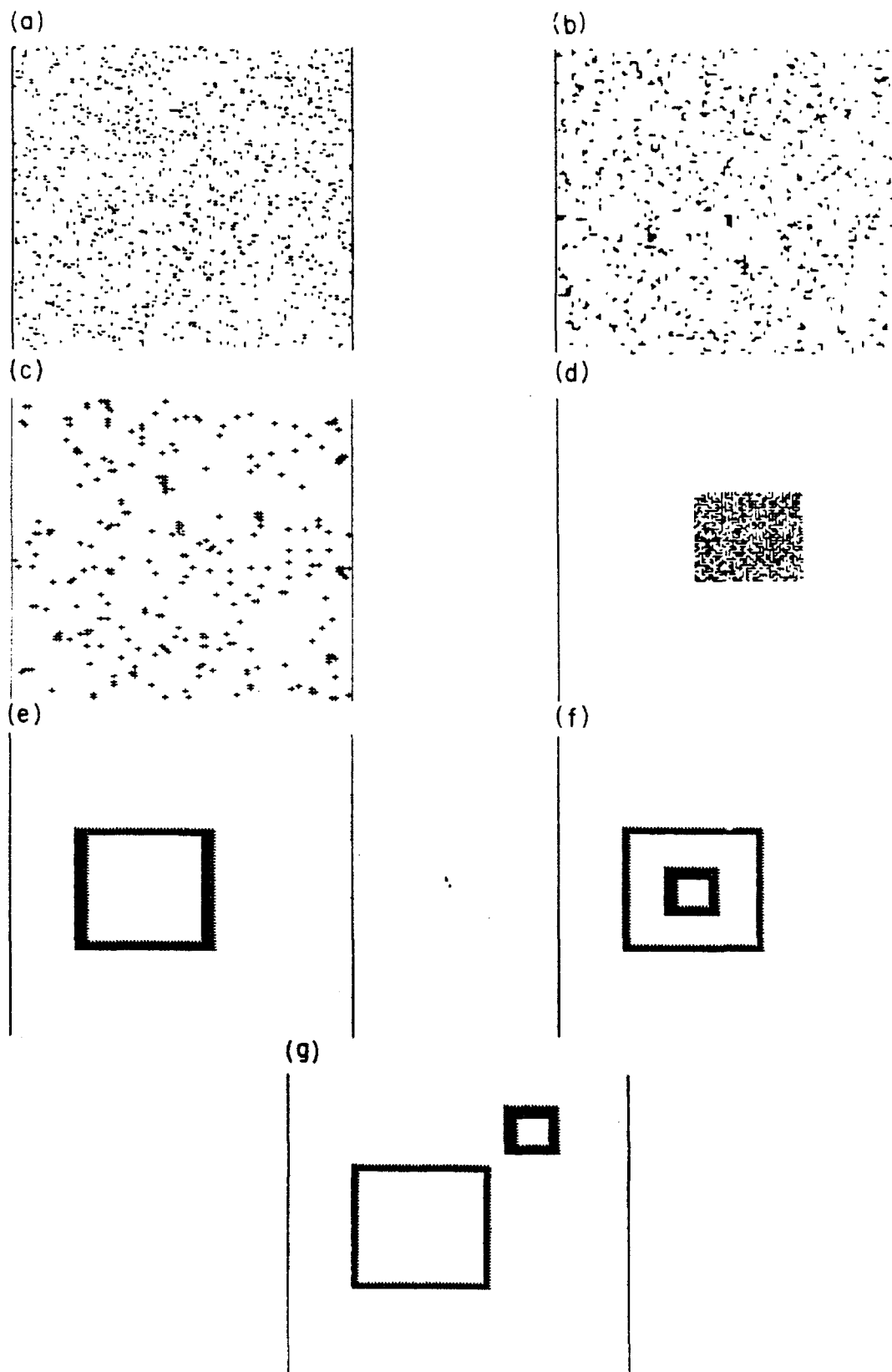


FIG. 1. Typical distribution of metallic bonds for the various models discussed in the text: (a) randomly distributed bonds, (b) two-site correlation model, (c) NNS correlation model, (d) percolation cluster, (e) single ring-shaped cluster, (f) sandwich of two ring-shaped clusters, and (g) double ring-shaped cluster. In all cases, the nominal fraction of metallic bonds is 0.05. The two vertical lines represent the superconducting bars to which the external voltage is applied.

Here R , L , and C are the resistance, inductance, and capacitance of the conducting element, and C' is the capacitance of the insulating element. For simplicity, we set $C=C'$, and introduce the plasma frequency $\omega_p=(LC)^{-1/2}$ and the relaxation time $\tau=L/R$. The ratio σ_M/σ_I then takes the form

$$\sigma_M/\sigma_I = 1 - \frac{\omega_p^2}{\omega(\omega - i/\tau)}, \quad (3)$$

which is identical to the ratio of dielectric functions of a Drude metal and insulator with dielectric function $\epsilon_I=1$. For convenience, we hereafter use units such that $\omega_p=1$.

To determine the ac response of an RLC network, we use the propagation algorithm developed by Frank and Lobb,²⁵ based on the Y - Δ transformation, to calculate the effective admittance σ_e of the entire network. This method has been used previously to study the surface plasmon modes in random metal-insulator composites below and above the metal percolation threshold p_c ,²⁴ and to investigate ac transport properties in a model for continuum percolation.³⁰ A detailed description of this model can be found in Refs. 24 and 30.

The new feature of the present calculation is the inclusion of clustering. The characteristic feature of clustering is the existence of nonrandom short-range order among the metallic bonds. We have carried out two types of calculations. The first involves the effects of a very local short-range order, which gives rise primarily to small clusters consisting of only a few metallic bonds. The second kind leads to large clusters of metallic bonds, including ringlike clusters and percolation clusters.¹⁵

To treat short-range correlations, we introduce two models, to be labeled the two-site model and the nearest-neighbor-site (NNS) model, which modify the random method of bond assignment. In a purely bond-random RLC network, one would assign a random number between zero and one (say n_i) to each bond in the network. If n_i is smaller than some metallic bond fraction, say p_1 ($0 < p_1 < 1$), one would label the i th bond as metallic; otherwise, it would be insulating. In the two-site model, the character of a particular bond is determined by the values of random numbers assigned to the two sites (the "site numbers") connected by the bond. If the sum of the two-site numbers exceeds a certain number $2p_1$ ($0 < p_1 < 1$), the bond between these two sites is chosen to be conducting; otherwise, the bond is insulating. In the NNS correlation model, one initially sets all the bonds in the lattice to be insulating. Each site is then assigned a random number n_i (the site number) between zero and one. One then scans sequentially through all the sites in the lattice. For each site scanned, if the site number of a center site is larger than a certain number p_2 ($0 < p_2 < 1$) and the sum of nearest-neighbor-site numbers is larger than $4p_2$, then all four bonds attached to the center site are chosen to be conducting.

Figures 1(a)–1(c) show lattices with typical metallic bond distributions produced by a purely random algorithm, the two-site model, and the NNS model. The latter two do, indeed, produce correlations between neighboring metallic bonds, but the bond morphologies

are quite different in the two cases.

We have also calculated the ac response of several metal-insulator composites with percolation or ring-shaped clusters [see Figs. 1(d)–1(g)]. A number of theoretical studies^{8,15,21,23} suggest that such clusters will tend to enhance the FIR absorption considerably, relative to purely random configurations. Other studies^{17,19–23} have predicted double absorption peaks or red-shifted surface-plasmon peaks in the optical frequency range. All these studies are based on various analytical models. In order to confirm these predictions, we have carried out numerical simulations in RLC networks on which such clusters are generated.

III. RESULTS

We carry out our simulations on 100×100 RLC networks. For all our calculations, we have used approximately the same concentration $\approx 5\%$ metallic bonds. The characteristic relaxation time τ is chosen as $\tau=10/\omega_p$. For all those configurations generated by random numbers, we average over five to ten realizations to obtain an effective conductance. Previous experience²⁴ indicates that such averages are sufficient to eliminate most of the fluctuation structure produced by small samples.

Figure 2 shows the real part of the effective conductance per metallic bond, $\text{Re}(\sigma_e)/\text{bond}$, plotted as a function of frequency in the FIR region. As can be seen, short-range correlations (both in the two-site and the NNS correlation models) enhance FIR absorption by about a factor of 5 relative to that of a purely random network. This enhancement is even more striking in the larger clusters. For example, ring-shaped clusters, which

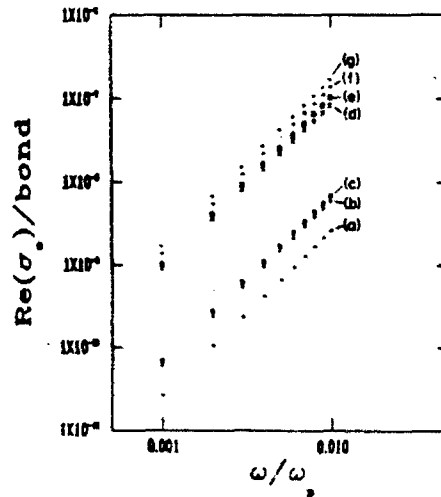


FIG. 2. Real part of the effective conductance per metallic bond, $\text{Re}(\sigma_e)/\text{bond}$, plotted as a function of frequency. The frequency range shown, $0.001\omega_p < \omega < 0.01\omega_p$, is typically within the far infrared in a free-electron metal. Calculations are carried out on 100×100 networks. For those configurations generated by random number, the plots represent averages over five realizations. The legends (a)–(g) correspond to the morphologies of Fig. 1.

represent metal-coated insulating particles, and percolation clusters each produce an enhancement of about 2 orders of magnitude relative to that of a random network of the same concentration. These results are consistent with some previous theoretical calculations^{8,15,17} based on effective-medium and renormalization-group analyses. Note that in all the FIR calculations the absorption is found to have a nearly ω^2 frequency dependence, independent of short-range order. This dependence is consistent with experiments.¹⁻⁵

Figures 3(a)–3(g) show $\text{Re}(\sigma_c)/\text{bond}$ for frequencies near ω_p . The absorption bands in these figures are the network analogs of the surface-plasmon resonances seen in bulk metal-insulator composites; the figures show how these bands are affected by short-range order and clustering. The purely random composite [Fig. 3(a)] has a surface-plasmon band with a single peak, as predicted by the Maxwell Garnett approximation. For samples with two-site correlations [Fig. 3(b)], the surface-plasmon band is split, and, for those with NNS correlations [Fig.

3(c)], it is weakly red shifted but not split. The percolation cluster [Fig. 3(d)] exhibits a surface-plasmon peak which is strongly broadened, relative to the purely random configuration [Fig. 3(a)]. Perhaps the most intriguing results are those shown in Figs. 3(e)–3(g). The single ring-shaped cluster shows a conspicuous double peak [Fig. 3(e)], while for the "sandwich" cluster a triple peak is obtained [Fig. 3(f)]. The double ring-shaped cluster shows a double-peaked structure [Fig. 3(g)], in which one of the two peaks is itself weakly split in two.

IV. DISCUSSION

Many of our numerical results can be understood, at least roughly, by simple qualitative arguments. For example, the FIR absorption is enhanced by clustering because clustering produces regions in the composite where the metal concentration is locally much greater than average. It is well known, both theoretically and experimentally,³¹ that the FIR absorption coefficient $\alpha(\omega)$ of a

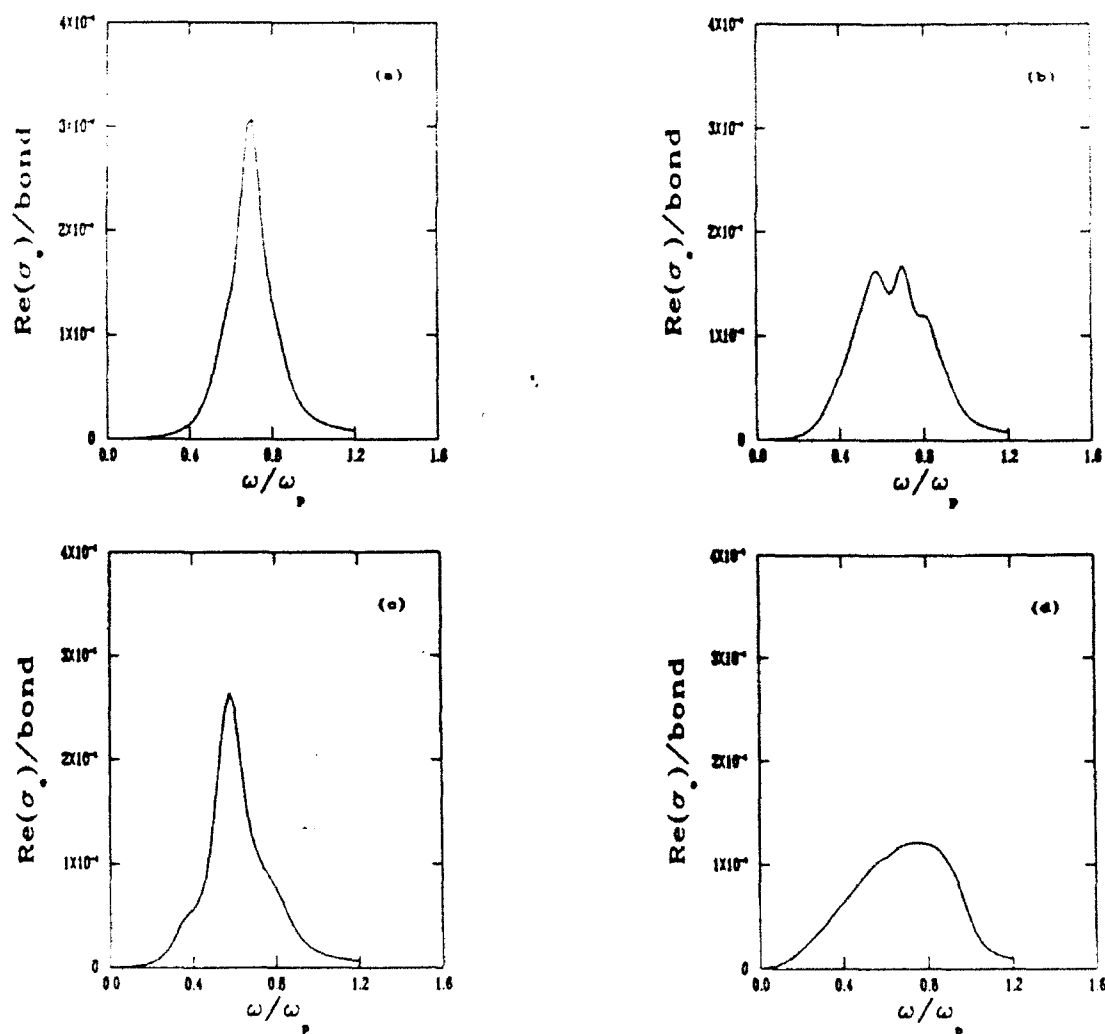


FIG. 3. Same as Fig. 2, but for a frequency range corresponding to the optical region in a typical metal. For those configurations generated by random number, the plots represent averages over ten realizations.

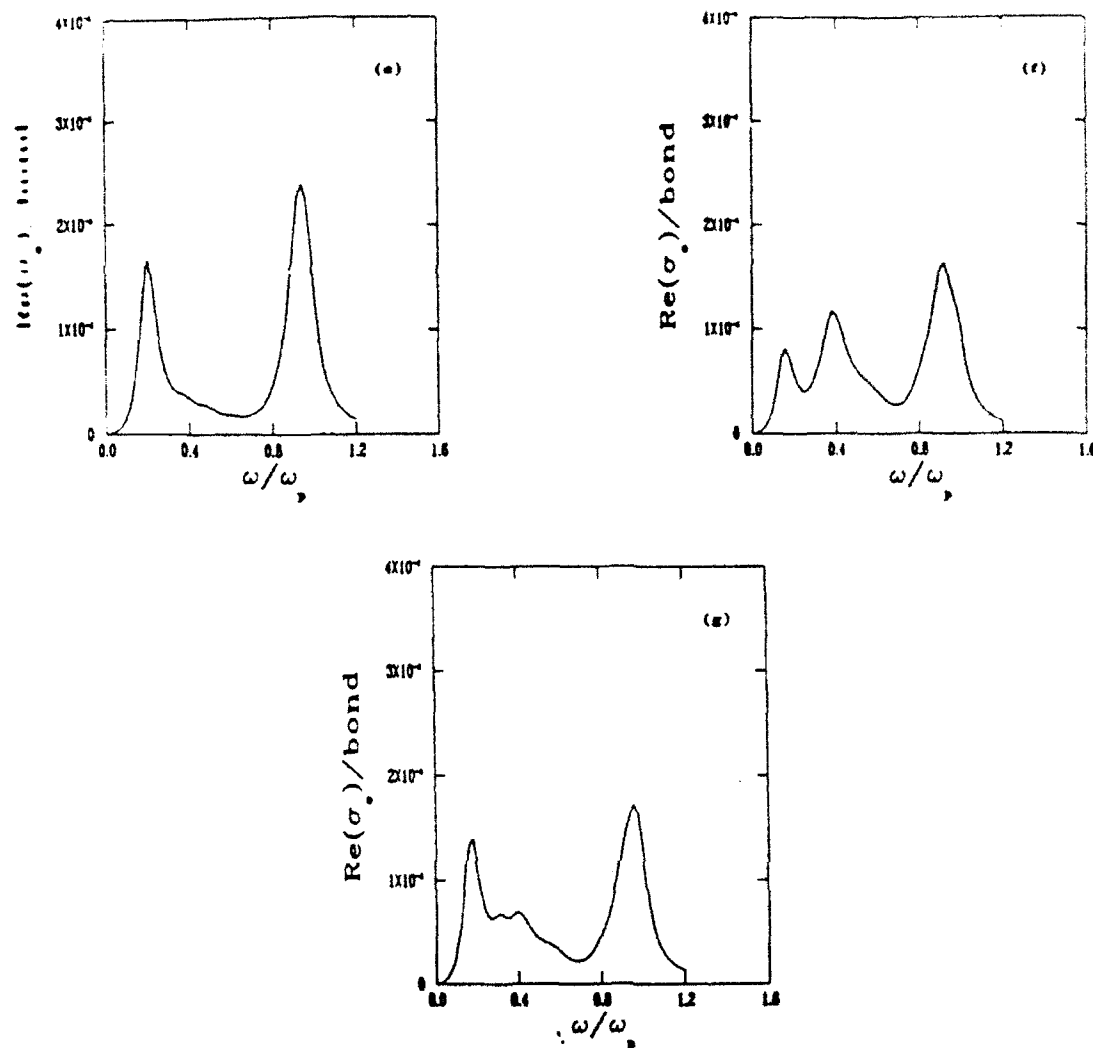


FIG. 3. (Continued).

metal-insulator composite varies as $\alpha(\omega) \approx A(p)\omega^2$, where the coefficient $A(p)$ tends to diverge as the metal volume fraction p approaches the percolation threshold p_c from below. As this concentration is approached, of course larger and larger clusters are formed. When short-range order or other clustering mechanisms are introduced, such large clusters can form even at low metal concentrations. Hence, the strongly enhanced FIR absorption expected near the percolation threshold can occur at much smaller metal volume fractions.

Likewise, the structure seen in the surface-plasmon frequency range can be simply understood. The two-site configurations depicted in Fig. 1(b), for instance, lead to a cluster of small, chain-shaped clusters. These can be thought of as the discrete versions of ellipses. Such ellipses are characterized by two different depolarization factors and have, therefore, two distinct surface-plasmon resonances.^{32,33} One thus expects the composite of Fig. 1(b) to have a split surface-plasmon peak, as observed. The two peaks correspond to the two different orientations of the chain-shaped clusters. In the NNS

configuration [Fig. 1(c)], many metallic clusters are symmetric crosses. The absorption peak in this instance is weakly red shifted relative to the purely random case [Fig. 1(a)]. The red shift may perhaps be understood from a model proposed by Liebsch and González (LG).¹¹ LG model a cermet composite as a diluted cubic lattice of metal spheres in an insulating host. Using the coherent-potential approximation, they find that, as the average spacing between particles is reduced (at fixed metal concentration), the disorder-induced red shift of the surface-plasmon peak is increased. By analogy, the symmetric crosses of Fig. 1(c) might be viewed as spherical clumps of particles with relatively small interparticle spacing for the given concentration. Then, by analogy with the results of LG, one might expect that the surface-plasmon peak would be red shifted relative to that of the purely random distribution of Fig. 1(a).

For percolating clusters, several effective-medium calculations have been carried out.^{15,17} Hui and Stroud¹⁷ have shown that for such a cluster, the surface-plasmon absorption peak will be strongly broadened, in qualitative

agreement with our numerical simulation.

At least two explanations seem plausible for the multiple absorption peaks seen in the case of the ring-shaped clusters [Figs. 1(e)–1(g)]. In the case of the simple ring-shaped clusters [Fig. 1(e)], one possible explanation is that the double absorption peak is due to the two orientations of the ring frame. The parts of the frame parallel to the external field produce the lower peak, while those perpendicular to the field generate the upper peak. We have attempted to check this analysis by moving one of the ring arms far from the remaining three, leaving a U-shaped metal particle and a needle; the resulting absorption spectrum is still very similar to that of Fig. 3(e). This picture suggests no simple explanation for the structures seen in Figs. 3(f) and 3(g). Another possibility is suggested by considering the standard electrostatic problem of a sphere with multiple alternating coatings, placed in a uniform external field. If the innermost sphere has the same dielectric constant as the (insulating) host medium, and if it is coated by alternate layers of Drude metal and insulator (all of equal thickness), so that there are an odd number (say, $2n+1$) of coating layers in all, then it can be shown that the composite particle exhibits exactly $2n+2$ surface-plasmon resonances. If we view the two-dimensional particles of Figs. 1(e) and 1(f) as having one and three layers, respectively, then this analysis would predict a Drude peak split into two and four subpeaks. The two peaks are indeed clearly visible. The geometry of Fig. 1(f) exhibits only three, but perhaps two of the four have coalesced into a single peak, given the rather substantial damping included in our calculation.

Note that all the results described in this paper are obtained in the so-called quasistatic approximation, in

which it is assumed that $\nabla \times \vec{E} = 0$, \vec{E} being the electric field. In some granular metals, it is well known⁶ that magnetic dipole absorption, which is absent in the quasistatic approximation, can greatly enhance far-infrared absorption. This absorption would have to be added to the clustering effects considered here, to obtain a complete theory in the far infrared. It should also be emphasized that the present calculations are two dimensional in a literal sense, and thus may not strictly apply to realistic thin granular films. In the experimental case, electric field lines may not be confined to the plane, and thus some account should probably be taken of the "three-dimensional" character of these films.

In summary, we have presented an efficient method for analyzing the effects of short-range order on the ac properties of composite media and described some initial results which show that clustering is of great importance, both in the far-infrared and in the optical frequency ranges. Although our method is applicable thus far only in two dimensions, the Y - Δ transformation can be extended to three dimensions also. Thus, the present method is a very promising tool for analyzing the ac response of a variety of granular materials.³⁴

ACKNOWLEDGMENTS

This work was supported by National Science Foundation (NSF) Grant No. DMR-87-18874, by the U.S. Defense Advanced Projects Agency through Grant No. DARPA-ONR-N00014-86-K-0033, and by the U.S. Israel Binational Science Foundation (Jerusalem, Israel) under Grant No. 354/85.

*Present address: Department of Physics, National Central University, Chung-li, Taiwan 32054, Republic of China.

¹D. B. Tanner, A. J. Sievers, and R. A. Buhrman, *Phys. Rev. B* **11**, 1330 (1975).

²C. G. Granqvist, R. A. Buhrman, J. Wyns, and A. J. Sievers, *Phys. Rev. Lett.* **37**, 625 (1976).

³N. E. Russell, J. C. Garland, and D. B. Tanner, *Phys. Rev. B* **23**, 632 (1981); G. L. Carr, R. L. Henry, N. E. Russell, J. C. Garland, and D. B. Tanner, *ibid.* **24**, 777 (1981).

⁴R. P. Devaty and A. J. Sievers, *Phys. Rev. Lett.* **52**, 1344 (1984).

⁵S. I. Lee, T. W. Noh, and J. R. Gaines, *Phys. Rev. B* **32**, 3580 (1985); S. I. Lee, T. W. Noh, K. Cummings, and J. R. Gaines, *Phys. Rev. Lett.* **55**, 166 (1985); Y. Song, T. W. Noh, S.-I. Lee, and J. R. Gaines, *Phys. Rev. B* **33**, 904 (1986); T. W. Noh, S. I. Lee, Y. Song, and J. R. Gaines, *ibid.* **34**, 2882 (1986).

⁶D. Stroud and F. P. Pan, *Phys. Rev. B* **17**, 1602 (1978).

⁷R. Rupp, *Phys. Rev. B* **19**, 1318 (1979).

⁸P. N. Sen and D. B. Tanner, *Phys. Rev. B* **26**, 3582 (1982).

⁹D. M. Wood and N. W. Ashcroft, *Phys. Rev. B* **25**, 6255 (1982).

¹⁰P. Chylek, D. Boice, and R. G. Pinnick, *Phys. Rev. B* **27**, 5107 (1983).

¹¹B. N. J. Persson and A. Liebsch, *Phys. Rev. B* **28**, 4247 (1983); A. Liebsch and P. V. Gonzalez, *ibid.* **29**, 6907 (1984).

¹²D. B. Tanner, *Phys. Rev. B* **30**, 1042 (1984).

¹³G. S. Agarwal and R. Ingura, *Phys. Rev. B* **30**, 6108 (1984).

¹⁴A. Bittar, S. Berthier, and J. Lafait, *J. Phys. (Paris)* **45**, 623 (1984).

¹⁵W. A. Curtin, R. C. Spitzer, N. W. Ashcroft, and A. J. Sievers, *Phys. Rev. Lett.* **54**, 1071 (1985); W. A. Curtin and N. W. Ashcroft, *Phys. Rev. B* **31**, 3287 (1985).

¹⁶R. S. Koss and D. Stroud, *Phys. Rev. B* **32**, 3456 (1985).

¹⁷P. M. Hui and D. Stroud, *Phys. Rev. B* **33**, 2163 (1986).

¹⁸G. A. Niklasson and C. G. Granqvist, *Phys. Rev. Lett.* **56**, 256 (1986).

¹⁹V. A. Davis and L. Schwartz, *Phys. Rev. B* **31**, 5155 (1985); **33**, 6627 (1986).

²⁰R. Fuchs, *Phys. Rev. B* **11**, 1732 (1975); **35**, 3722 (1987); R. Fuchs and F. Claro, *ibid.* **35**, 7700 (1987).

²¹R. Rojas, F. Claro, and R. Fuchs, *Phys. Rev. B* **37**, 6799 (1988).

²²Zhe Chen, Ping Sheng, D. A. Weitz, H. M. Lindsay, M. Y. Lin, and P. Meakin, *Phys. Rev. B* **37**, 5232 (1988); Zhe Chen and Ping Sheng (unpublished).

²³R. G. Barrera, G. Monsivais, and W. L. Mochan, *Phys. Rev. B* **38**, 5371 (1988).

²⁴X. C. Zeng, P. M. Hui, and D. Stroud, *Phys. Rev. B* **39**, 1063 (1989).

²⁵C. J. Lobb and D. J. Frank, *Phys. Rev. B* **30**, 4090 (1984); D. J. Frank and C. J. Lobb, *ibid.* **37**, 302 (1988).

- ²⁶J. P. Clerc, A.-M. S. Tremblay, G. Albiat, and C. D. Mitescu, *J. Phys. (Paris) Lett.* **45**, L913 (1984).
- ²⁷J. M. Langier, J. P. Clerc, G. Girand, and J. M. Luck, *J. Phys. A* **19**, 3153 (1986).
- ²⁸A. L. Bug, G. S. Grest, M. H. Cohen, and I. Webman, *J. Phys. A* **19**, L323 (1986); *Phys. Rev. B* **36**, 3675 (1987).
- ²⁹R. S. Koss and D. Stroud, *Phys. Rev. B* **35**, 9004 (1987).
- ³⁰X. C. Zeng, D. J. Bergman, and D. Stroud, *J. Phys. A* **21**, L949 (1988).
- ³¹See, for example, D. Stroud and P. M. Hui, in *Physics and Chemistry of Small Clusters*, Vol. 158 of *NATO Advanced Study Institute, Series B: Physics*, edited by P. Jena, B. K. Rao and S. N. Khanna (Plenum, New York, 1987), pp. 547-564.
- ³²L. D. Landau, E. M. Lifshitz, and L. P. Pitaevskii, *Electrodynamics of Continuous Media*, 2nd ed. (Pergamon, Oxford, 1984).
- ³³M. J. Bloemer, T. L. Ferrell, M. C. Buncick, and R. J. Warrmack, *Phys. Rev. B* **37**, 8015 (1988).
- ³⁴U. Kreibig and L. Genzel, *Surf. Sci.* **106**, 308 (1981); **156**, 678 (1985).

Enhancement in nonlinear effects in percolating nonlinear resistor networks

P. M. Hui

*Division of Applied Sciences, Harvard University, Cambridge, Massachusetts 02138
and Department of Physics, National Central University, Chung-li, Taiwan 32054, Republic of China**
(Received 18 August 1989)

The nonlinear response is studied in a percolating network of superconductor and normal conductor with nonlinear I - V characteristic below the percolation threshold of the superconductor. The crossover current density $J_{L,NL}$, defined as the current density at which the linear and nonlinear responses of the network become comparable, is found to have a power-law dependence $J_{L,NL} \sim (p_c - p)^H$ as the percolation threshold is approached from below. With use of a model of the percolating network below p_c analogous to the nodes-links-blobs picture, H is found to be $H = \nu_d(d-1)-1$, where ν_d is the correlation-length exponent and d is the dimensionality of the lattice.

I. INTRODUCTION

The subject of percolation phenomena has attracted much attention over the past decade.^{1,2} Studies in the geometric aspects of percolating systems, for example, has led to the use of the idea of fractal objects in physical systems. Transport properties in percolating systems are usually studied within models of random resistor networks.² In a network which consists of randomly occupied normal conducting and insulating bonds (N/I systems), the network conducts only above the percolation threshold where there exists a connected path of conducting bonds. Similarly, in a network with superconducting and normal conducting or insulating bonds (S/N or S/I systems), the network becomes superconducting above the percolation threshold of the superconducting bonds. For linear I - V response for the conducting bonds, one can define critical exponent $t(s)$ describing the divergence of the network resistance (conductance) in a N/I (S/N) system in the vicinity of the threshold. It is these richnesses in the interplay between geometric and transport properties that have led to a deeper understanding of the physics in macroscopic disordered systems.

In this Brief Report, we consider the geometrical effects of a percolating system on the nonlinear transport properties in a superconductor-normal-conductor nonlinear resistor network. Nonlinear composite systems have recently attracted much interest.³ Stroud and Hui studied the finite-frequency nonlinear dielectric response of a mixture of nonlinear dielectric in a linear host in the dilute limit of nonlinear constituent, and demonstrated the relation between the nonlinear-random-network problem and the noise problem in linear random network.⁴ Zeng *et al.*⁵ proposed a general effective-medium-type approximation for calculating the effective nonlinear susceptibility of a mixture for all concentrations. Recently, Blumenfeld and Bergman⁶ pointed out that the results in Ref. 4 can be used to derive a characteristic value of the current at which the nonlinear and linear responses in a N/I mixture become comparable. It is the purpose of this paper to study the effects of percolation on the

effective nonlinear response of a S/N network below the percolation threshold of the superconductor.

Below the percolation threshold p_c , the conductivity of the whole network is still finite. The I - V response of the network, however, is nonlinear due to the nonlinearity of the individual nonlinear bonds. We define a crossover current density $J_{L,NL}$ as the current density at which the linear response and the nonlinear response of the network become comparable. Using a picture of the percolating network below p_c analogous to the nodes-links-blobs picture often used above p_c , a power-law dependence of $J_{L,NL}$ is derived. It is found that, near the percolation threshold, $J_{L,NL} \sim (p_c - p)^H$, where $H = \nu_d(d-1)-1$, where p is the fraction of superconducting bonds, ν_d is the correlation-length exponent in d dimension, and d is the dimensionality. This result shows that the nonlinear response of the network becomes more pronounced as the threshold is approached due to the restricted geometry of the path through which current flows in the vicinity of the threshold.

II. DERIVATION

We consider a d -dimensional hypercubic lattice with fraction p of superconducting bonds and fraction $1-p$ of normal conducting bonds. Each normal bond is assumed to have identical I - V response of the form

$$v = ri + bi^\alpha \quad (\alpha > 1), \quad (1)$$

where v and i are the voltage across the bond and the current in the bond, respectively. The second term in Eq. (1) represents the nonlinear response of the nonlinear normal bond. Response of the form Eq. (1) has been studied previously in a N/I mixture and also in the finite-frequency regime,^{4,7} although most studies in nonlinear percolating systems assumed nonlinear response of the form *without* the linear term in Eq. (1).⁸ The form of Eq. (1) is of interest because most materials have linear response in the limit of small current and become nonlinear in the presence of large current. For materials with inversion symmetry, the lowest order nonlinearity

refers to $\alpha=3$.

We first consider the case of a full lattice of nonlinear bonds. Let L be the linear dimension of the lattice and a be the lattice constant. If a current I is injected into the lattice, the voltage V across the network is given by

$$V = rI/(L/a)^{d-1} + b[I/(L/a)^{d-1}]^a, \quad (2)$$

as $I/(L/a)^{d-1}$ is the current in each path connecting the lattice from one side to another in a full lattice. The injected current density is given by $J = I/L^{d-1}$. Let J_{L-NL}^0 be the current density at which the linear response and the nonlinear response in Eq. (2) become equal in magnitude, then for a full lattice

$$J_{L-NL}^0 = (r/b)^{1/(a-1)} a^{-(d-1)}. \quad (3)$$

As more and more normal bonds are removed and replaced by superconducting bonds, the percolation threshold p_c of the superconductor is approached. Below p_c , the conductance of the network is still finite. The I - V characteristic of the network is nonlinear due to the assumed nonlinearity in each of the individual normal bonds. To consider the percolation effect on the nonlinear response, we invoke a picture⁹ for the percolating S/N network similar to that of the "nodes-links-blobs" picture in N/I networks.¹⁰ For $p \leq p_c$, the percolating material (superconducting clusters in this case) can be approximated by an array of nodes separated by the correlation length ξ . Each node is the center of a superconducting cluster of linear size of order ξ . Adjacent clusters are separated by a thin layer of normal bonds. At some places, there is only one normal bond separating the superconducting clusters. These bonds are the "singly disconnected bonds" (SDB's). The number of SDB's diverges as $(p_c - p)^{-1}$ as the percolation threshold is approached from below.^{10,11} This picture of the percolating network below p_c has been used successfully to study the problem of fluctuations in resistance,¹¹ i.e., the noise problem, in percolating networks. Also, the present author and co-workers used this model to study the nonuniversal breakdown behavior in superconducting and dielectric composites.¹²

Using this model of percolating systems below p_c , the nonlinearity of the network can be studied. Let I be the current injected into the lattice, the current passes through each path from one side to another in the array of superconducting clusters and thin layers of normal bonds is approximately given by $I/(L/\xi)^{d-1}$, as there are $(L/\xi)^{d-1}$ paths assuming a regular array. Let L_1 be the number of SDB's in the thin layer separating adjacent superconducting clusters. As mentioned above, $L_1 \sim (p_c - p)^{-1}$. The current in each SDB is thus given by $\tilde{I} = I/(L/\xi)^{d-1} L_1$, if we neglect the effects of multiply connected regions, i.e., places where adjacent clusters are separated by more than one bond.¹³ The voltage \tilde{V} across the layer of normal bonds separating two adjacent clusters is given by

$$\tilde{V} = r\tilde{I} + b\tilde{I}^a. \quad (4)$$

The voltage V across the system is then given by

$$V = (L/\xi)\tilde{V} \quad (5)$$

due to the assumed geometry of the percolating network below p_c .

Substituting the form of \tilde{I} and Eq. (4), Eq. (5) can be rewritten as

$$V = r \frac{L}{\xi} \frac{\xi^{d-1}}{L_1} J + b \frac{L}{\xi} \left[\frac{\xi^{d-1}}{L_1} J \right]^a, \quad (6)$$

where $J = I/L^{d-1}$ is the injected current density. We define the crossover current density J_{L-NL} as the current density at which the linear and nonlinear terms in Eq. (6) become equal in magnitude. Hence,

$$J_{L-NL} = \left[\frac{r}{b} \right]^{1/(a-1)} L_1 \xi^{-(d-1)}. \quad (7)$$

The correlation length ξ diverges as $\xi \sim a(p_c - p)^{-v_d}$, where v_d is the exponent characterizing the divergence in a d -dimensional system. Substituting this result and $L_1 \sim (p_c - p)^{-1}$ into Eq. (7), we obtain

$$J_{L-NL} = J_{L-NL}^0 (p_c - p)^H, \quad (8)$$

with the exponent H given by

$$H = v_d(d-1) - 1. \quad (9)$$

The crossover current density J_{L-NL} thus decreases to zero following a power law as the percolation threshold is approached from below and H is the exponent characterizing the power-law behavior. Note that with the present model for the percolating network, H does not depend on α , i.e., the crossover current density behaviors the same way independent of the detail of the nonlinear behavior of individual normal bonds.

III. DISCUSSION

Near the percolation threshold, J_{L-NL} vanishes with a power law with exponent $H = v_d(d-1) - 1$. To show that this is the case, we use the standard values for v_d ,^{14,15} which give $H = \frac{1}{3}$ and 0.76 for $d = 2$ and 3, respectively.¹⁶ The exponent H increases as dimensionality increases and takes on the value $H = \frac{1}{3}$ for $d = 6$, the upper critical dimension of percolation. Hence, $H > 0$ for all d .

The result Eqs. (8) and (9) implies that due to the restricted geometry near the threshold, the nonlinear behavior is enhanced relative to the case of a full lattice of nonlinear bonds. This result will be of potential practical use because such percolating S/N composite has a high conductance and yet is highly nonlinear. It is well known that the system of N/S composites can be related to a N/I composite if the dielectric constants are considered instead of the conductivities, as the imaginary part of the dielectric function of a normal component diverges at the low-frequency limit and thus plays the role of superconductor in a S/N composite.¹⁷ Thus, with slight modification, the result here can be used in N/I composites in the low-frequency regime. It will be interesting to see if other methods such as the effective-medium ap-

proximation,⁵ real-space renormalization analysis,¹⁸ and computer stimulations give similar result as the simple scaling theory presented here.

ACKNOWLEDGMENTS

This work was supported in part by the National Science Council of the Republic of China through Contract No. NSC79-0208-M008-17. The author thanks Professor D. Stroud of the Ohio State University for many useful

discussions on the subject of nonlinear response in composites. He also wishes to thank Professor H. Ehrenreich of Harvard University for his hospitality. The work at Harvard University was supported in part by the U.S. Defense Advanced Research Projects Agency through Contract No. DARPA-ONR-N00014-86-K-0033 and by the Joint Services Electronics Program (JESP) through the U.S. Office of Naval Research (ONR) through Contract No. N00014-89-J-1023.

*Present address.

¹See, for example, the articles in the *Proceedings of the Second International Conference on Electrical Transport and Optical Properties of Inhomogeneous Media* [Physica A 157, No. 1, 1 (1989)]; *Percolation Structures and Processes*, edited by G. Deutscher, R. Zallen, and J. Adler (Hilger, Bristol, 1983).

²D. Stauffer, *Introduction to Percolation Theory* (Taylor and Francis, London, 1985).

³See the articles in Ref. 1 on this subject; and see also D. Stroud and Van E. Wood, *J. Opt. Soc. Am. B* 6, 778 (1989); A. E. Neeves and M. H. Birnboim, *ibid.* 6, 787 (1989); Y. Q. Li, C. C. Sung, R. Inguva, and C. M. Bowden, *ibid.* 6, 814 (1989).

⁴D. Stroud and P. M. Hui, *Phys. Rev. B* 37, 8719 (1988), and references therein.

⁵X. C. Zeng, D. J. Bergman, P. M. Hui, and D. Stroud, *Phys. Rev. B* 38, 10970 (1988); X. C. Zeng, P. M. Hui, D. J. Bergman, and D. Stroud, *Physica A* 157, 192 (1989).

⁶R. Blumenfeld and D. J. Bergman, *Phys. Rev. B* (to be published).

⁷D. Stroud and Van E. Wood, in Ref. 3, and references therein.

⁸See, e.g., S. W. Kenkel and J. P. Straley, *Phys. Rev. Lett.* 49, 767 (1982); J. P. Straley and S. W. Kenkel, *Phys. Rev. B* 29, 6299 (1984); R. Blumenfeld and A. Aharony, *J. Phys. A* 18, L443 (1985); Y. Meir, R. Blumenfeld, A. B. Harris, and A.

Aharony, *Phys. Rev. B* 34, 3424 (1986), and references therein; *Phys. Rev. B* 36, 3950 (1987); R. Blumenfeld and D. J. Bergman, *Physica A* 157, 428 (1989).

⁹A. Coniglio and H. E. Stanley, *Phys. Rev. Lett.* 52, 1068 (1984).

¹⁰A. Coniglio, *Phys. Rev. Lett.* 46, 250 (1982); J. P. Straley, *J. Phys. C* 15, 2333 (1982); J. Machta, R. A. Gruyer, and S. M. Moore, *Phys. Rev. B* 33, 4818 (1986).

¹¹D. C. Wright, D. J. Bergman, and Y. Kanter, *Phys. Rev. B* 33, 396 (1986).

¹²C. J. Lobb, P. M. Hui, and D. Stroud, *Phys. Rev. B* 36, 1956 (1987).

¹³Strictly speaking, \bar{l} should be less than $l/(L/\xi)^d - 1$, equality holds if the multiply connected regions are neglected.

¹⁴C. J. Lobb and K. R. Karasek, *Phys. Rev. B* 25, 492 (1982), and references therein.

¹⁵D. W. Heermann and D. Stauffer, *Z. Phys. B* 44, 449 (1981).

¹⁶The values given here are the upper bounds for the exponent H , due to the reason stated in Ref. 13, and is equivalent to putting $\xi_G = 1$ in the nodes-links-blobs picture (see Ref. 11).

¹⁷D. J. Bergman and Y. Irmay, *Phys. Rev. Lett.* 39, 1222 (1977); see also D. Stroud and D. J. Bergman, *Phys. Rev. B* 25, 2062 (1982).

¹⁸See, e.g., R. B. Stinchcombe and B. P. Watson, *J. Phys. C* 9, 3221 (1976).

Optical and magneto-optical absorption in parabolic quantum wells

L. Brey, N. F. Johnson, and B. I. Halperin

Physics Department, Harvard University, Cambridge, Massachusetts 02138

(Received 17 July 1989)

We show that an n -doped parabolic quantum well absorbs far infrared radiation at the bare harmonic-oscillator frequency ω_0 independently of the electron-electron interaction and the number of electrons in the well. In the presence of a magnetic field tilted with respect to the plane of the quantum well, we find that the cyclotron resonance becomes coupled to this ω_0 frequency mode. The absorption then occurs at two frequencies, which are again independent of the electron-electron interaction and the fractional filling of the well.

Wide parabolic quantum wells have been proposed¹⁻⁴ as structures in which a high-mobility quasi-three-dimensional electron gas can be realized. A parabolic potential of width W and height Δ_1 is equivalent to the potential created by a uniform slab of positive charge with a thickness W and density $n_0 = 2\epsilon\Delta_1/W^2e^2\pi$, where e is the electron charge and ϵ is the dielectric constant (taken to be constant in the well). Electrons, which arise from donor impurities located away from the well, enter the well and screen this "fictitious" potential, forming a uniform layer of density n_0 (see Fig. 1). By increasing the number of electrons per unit area n_s between zero and n_0W , the thickness of the electron layer will increase linearly between zero and W , and a thick slab of electrons (> 2000 Å) can be achieved.

These wide parabolic quantum wells have recently been grown^{2,3} by tailoring the conduction-band edge of a graded $\text{Ga}_{1-x}\text{Al}_x\text{As}$ semiconductor, and magnetotransport experiments on these systems^{2,3} confirm the existence of a thick slab of high-mobility electron gas. In addition Karrai *et al.*⁵ have reported measurements⁵ of far-infrared magnetotransmission in these parabolic wells. These experiments reveal a coupling between the cyclotron resonance and a frequency Ω_x , as the magnetic field is tilted

with respect to the electron-slab plane. The experiments suggest that Ω_x corresponds to the plasma frequency [$\Omega_x = (4\pi n_0 e^2 / \epsilon m^*)^{1/2}$] of a three-dimensional electron gas of density n_0 , which by construction is equal to the frequency of the bare harmonic oscillator potential. This frequency Ω_x is very different from the energy separation between the subbands of the self-consistent Hartree potential. Karrai *et al.*⁵ therefore conclude that the three-dimensional character of the electron gas tends to predominate over the two-dimensional properties.⁵

In this paper we study the optical absorption of an n -doped parabolic quantum well. In addition we investigate the coupling between the excitations of this system and the cyclotron energy in the presence of a magnetic field which is tilted with respect to the quantum-well plane. We find that in the ideal parabolic well the absorption spectrum is independent of the electron-electron interaction, and also independent of the number of electrons in the well.

First, in the absence of any magnetic field, the Hamiltonian of our system (with electrons in the x - y plane) is given within the effective-mass approximation by

$$H = \frac{1}{2m^*} \sum_{i=1}^N (p_{i,x}^2 + p_{i,y}^2 + p_{i,z}^2) + \sum_{i=1}^N \frac{\omega_0^2 m^*}{2} z_i^2 + U, \quad (1)$$

where p_i and r_i are respectively the momentum and position operators of the i th particle, m^* is the electron effective mass of the host semiconductor, $\omega_0 = (8\Delta_1 / W^2 m^*)^{1/2}$ is the bare harmonic-oscillator frequency of the parabolic well, and U is the interaction between electrons

$$U = \sum_{i < j} u(r_i - r_j).$$

We define raising and lowering operators,

$$\hat{c}^\pm = \sum_{i=1}^N (m^* \omega_0 z_i \mp i p_{i,z}). \quad (2)$$

It then follows from the quadratic form of the man-made potential that

$$[H, \hat{c}^\pm] = \pm \hbar \omega_0 \hat{c}^\pm. \quad (3)$$

If Ψ_n is an eigenstate of H with eigenenergy E_n , Eq. (3) implies

$$H \hat{c}^\pm \Psi_n = (\pm \hbar \omega_0 + E_n) \hat{c}^\pm \Psi_n. \quad (4)$$

Defining $\Psi_{n\pm 1} \equiv \hat{c}^\pm \Psi_n$, it is clear that $\Psi_{n\pm 1}$ is an exact eigenstate of our Hamiltonian with energy $E_{n\pm 1} = E_n$.

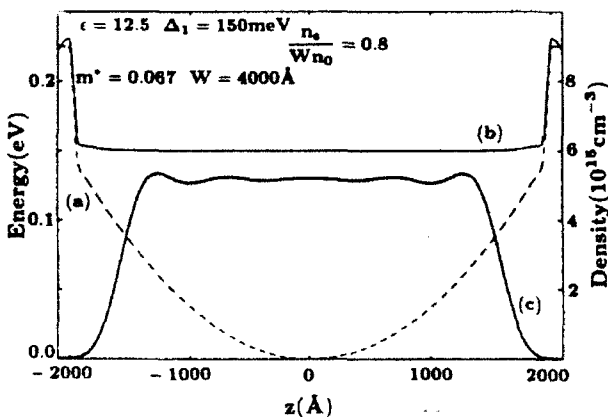


FIG. 1. Calculated electron density profile and self-consistent potential for an 80% full $\text{Al}_x\text{Ga}_{1-x}\text{As}$ parabolic well of total width 4000 Å. (a) Potential for the empty well. (b) Self-consistent total potential in the Hartree approximation. (c) Self-consistent charge density profile as obtained in the Hartree approximation. The parameters of the well are given in the figure.

$\pm \hbar \omega_0$.

When the system is placed in an electric field E applied in the z direction, the following term must be added to the Hamiltonian:

$$H' = \sum_{i=1}^N E e^{-i\omega_i z_i} = E \frac{e^{-i\omega_i}}{2m^* \omega_0} (\hat{c}^+ + \hat{c}^-). \quad (5)$$

This perturbation will only connect the state Ψ_N with the states $\Psi_{N \pm 1}$. A sharp peak in the absorption spectra is therefore expected at the frequency ω_0 . This result is not affected by the electron-electron interaction U . The parabolic well consequently absorbs light at the frequency ω_0 independently of the number of electrons in the well. We conclude that in the case of a parabolic quantum well the dielectric function diverges at the bare harmonic-oscillator frequency ω_0 , and not at the frequencies of the intersubband separation obtained in a Hartree or more sophisticated calculation.

The bare harmonic-oscillator frequency ω_0 is equal by

$$H = \frac{1}{2m^*} \sum_{i=1}^N \{p_{i,x}^2 + [p_{i,y} + (eB/c)(x \cos \theta - z \sin \theta)]^2 + p_{i,z}^2\} + \sum_{i=1}^N \frac{\omega_0^2 m^*}{2} z_i^2 + U. \quad (6)$$

This Hamiltonian can be simplified through a change of coordinates $x \rightarrow x'$ and $z \rightarrow z'$ corresponding to a rotation of angle α with respect to the y axis,^{9,10}

$$H = \frac{1}{2m^*} \sum_{i=1}^N (p_{i,x'}^2 + p_{i,y}^2 + p_{i,z'}^2) + \frac{m^*}{2} \sum_{i=1}^N (\omega_1^2 x_i'^2 + \omega_2^2 z_i'^2) + U + \omega_c \sum_{i=1}^N [\sin(\alpha - \theta) z_i' p_{i,y} + \cos(\alpha - \theta) x_i' p_{i,z}]. \quad (7)$$

The rotation angle α is obtained from

$$\tan(2\alpha) = \frac{\omega_c^2 \sin 2\theta}{\omega_c^2 \cos 2\theta - \omega_0^2}. \quad (8)$$

The frequencies $\omega_{1,2}$ are

$$\omega_{1,2} = [\frac{1}{2} (\omega_c^2 + \omega_0^2) \pm \frac{1}{2} (\omega_c^4 + \omega_0^4 - 2\omega_c^2 \omega_0^2 \cos 2\theta)^{1/2}]^{1/2}, \quad (9)$$

and $\omega_c = eB/m^*c$ is the cyclotron frequency. Defining the raising and lowering operators

$$\begin{aligned} \hat{a}^\pm &= \sum_{i=1}^N \left[m^* \omega_1 x_i' \mp i p_{i,x} + \frac{\omega_c}{\omega_1} \cos(\alpha - \theta) p_{i,y} \right], \\ \hat{b}^\pm &= \sum_{i=1}^N \left[m^* \omega_2 z_i' \mp i p_{i,z} + \frac{\omega_c}{\omega_2} \sin(\alpha - \theta) p_{i,y} \right], \end{aligned} \quad (10)$$

it follows from Eq. (7) that

$$\begin{aligned} [\hat{a}^\pm, \hat{b}^\pm] &= 0, \\ [H, \hat{a}^\pm] &= \pm \hbar \omega_1 \hat{a}^\pm, \\ [H, \hat{b}^\pm] &= \pm \hbar \omega_2 \hat{b}^\pm. \end{aligned} \quad (11)$$

If Ψ_{n_1, n_2} is an eigenstate of H with eigenvalue E_{n_1, n_2} , then

$$\begin{aligned} \hat{H} \hat{a}^\pm \Psi_{n_1, n_2} &= (\pm \hbar \omega_1 + E_{n_1, n_2}) \hat{a}^\pm \Psi_{n_1, n_2}, \\ \hat{H} \hat{b}^\pm \Psi_{n_1, n_2} &= (\pm \hbar \omega_2 + E_{n_1, n_2}) \hat{b}^\pm \Psi_{n_1, n_2}. \end{aligned} \quad (12)$$

Defining $\Psi_{n_1 \pm 1, n_2} \equiv \hat{a}^\pm \Psi_{n_1, n_2}$ and $\Psi_{n_1, n_2 \pm 1} \equiv \hat{b}^\pm \Psi_{n_1, n_2}$, we see that $\Psi_{n_1 \pm 1, n_2}$ and $\Psi_{n_1, n_2 \pm 1}$ are both exact eigenstates with energies $E_{n_1 \pm 1, n_2} = E_{n_1, n_2} \pm \hbar \omega_1$ and $E_{n_1, n_2 \pm 1} = E_{n_1, n_2} \pm \hbar \omega_2$, respectively. When illuminated with long wave-

length light, polarized in the z direction (x direction), the optical absorption of the parabolic well will present two peaks at ω_1 and ω_2 with intensities proportional to $\sin^2 \alpha$ ($\cos^2 \alpha$) and $\cos^2 \alpha$ ($\sin^2 \alpha$), respectively. Once again this result is independent of the electron-electron interaction and is a direct consequence of the parabolic form of the bare quantum-well potential. If the term corresponding to the parabolic well is dropped from the Hamiltonian equation (6), then $\omega_1 = \omega_c$, $\omega_2 = 0$ and we recover the Kohn result¹¹ that the cyclotron resonance ω_c in a bulk three-dimensional gas is not affected by the electron-electron interaction U .

In the experimental samples the width of the parabolic well is finite, and the well is confined by an additional barrier (see Fig. 1). This extra confinement will not affect our results as long as the number of electrons in the well is small enough so that the self-consistent charge-density profile remains essentially unchanged. We have checked this numerically in the case of no magnetic field by calculating the dynamical conductivity^{12,13} for the potential profile shown in Fig. 1. For a density of electrons per unit area n_s bigger than $0.9Wn_0$, we find that small satellites appear in the optical absorption close to ω_0 . Of course, impurities or other imperfections in the well can lead to

additional absorption even at smaller values of n_s . Variation of m^* across the parabolic well will also give corrections to these results.

In conclusion, we have shown that an ideal parabolic well absorbs light at the bare harmonic-oscillator frequency $\omega_0 = (8\Delta_1/W^2 m^*)^{1/2}$ independently of the electron-electron interaction. In addition, the presence of a tilted magnetic field couples the cyclotron frequency with ω_0 and *not* with the frequency corresponding to the self-consistent intersubband separation.

We thank D. Vanderbilt, J. Dempsey, R. Westervelt, A. C. Gossard, and R. Meade for useful discussions. L. Brey wishes to acknowledge support from Spain's Ministerio de Educacion y Ciencia. This work was supported by the National Science Foundation through the Harvard Materials Research Laboratory and Grant No. DMR88-17291, U.S. Defense Advanced Research Projects Agency (DARPA) through U.S. Office of Naval Research (ONR) Contract No. N00014-86-K-0033, and by St. John's College, Cambridge, England.

¹B. I. Halperin, Jpn. J. Appl. Phys. **26**, Suppl. 26-3, 1913 (1987).

²E. G. Gwinn, R. M. Westervelt, P. F. Hopkins, A. J. Rimberg, M. Sundaram, and A. G. Gossard, Phys. Rev. B **39**, 6260 (1989); A. J. Rimberg and R. M. Westervelt, *ibid.* **40**, 3970 (1989).

³T. Sajoto, J. Jo, L. Engel, M. Santos, and M. Shayegan, Phys. Rev. B **39**, 10464 (1989).

⁴L. Brey and B. I. Halperin, in *Proceedings of the Eighth International Conference on the Electronic Properties of Two Dimensional Systems, Grenoble, France, 1989* (to be published); Phys. Rev. B (to be published).

⁵K. Karrai, H. D. Drew, M. W. Lee, and M. Shayegan, Phys. Rev. B **39**, 1426 (1989).

⁶See, e.g., N. W. Ashcroft and N. D. Mermin, *Solid State Physics* (Holt, New York, 1976), p. 19.

⁷D. A. Dahl and L. J. Sham, Phys. Rev. B **16**, 651 (1977).

⁸D. Pines, *The Many-Body Problem* (Dunod-Wiley, New York, 1959), p. 202.

⁹J. C. Maan, in *Two-Dimensional Systems, Heterostructures and Superlattices*, edited by G. Bauer, F. Kuchar, and H. Heinrich, Solid State Sciences, Vol. 53 (Springer-Verlag, Berlin, 1984).

¹⁰R. Merlin, Solid State Commun. **64**, 99 (1987).

¹¹W. Kohn, Phys. Rev. **123**, 1242 (1961).

¹²T. Ando, Z. Phys. B **26**, 263 (1977).

¹³K. S. Yi and J. J. Quinn, Phys. Rev. B **27**, 2396 (1983).

LETTER TO THE EDITOR

Excitons in superlattices

N F Johnson

Division of Applied Sciences, Harvard University, Cambridge, MA 02138, USA and
Cavendish Laboratory, Cambridge University, Cambridge CB3 0HE, UK

Received 20 November 1989

Abstract. A simple, non-variational approach for calculating exciton binding energies in superlattices is developed. The approach is sufficiently versatile that it applies in the limits of strongly coupled and isolated quantum wells, and in the presence of external fields. Excellent agreement is obtained with experimental binding energies in GaAs/GaAlAs using only bulk $k \cdot p$ parameters as input.

Many experimental and theoretical studies have been reported of excitons in single quantum wells [1]. Increasing attention is now being paid to the properties of excitons in superlattices with finite barrier thicknesses [2-5], such that the exciton can spread over several superlattice periods. In particular, experimental values of superlattice exciton binding energies both with [2] and without [3] external electric fields have recently been reported. Theoretical studies of excitons in superlattices have however primarily utilised variational 'particle-in-a-box' approaches or the computationally intensive k -space sampling technique of Chu and Chang [6].

In this letter we present a simple and versatile non-variational approach for calculating superlattice binding energies based on the crystal coordinate representation (CCR) using a basis consisting of *superlattice* Wannier functions. The formalism underlying the present approach exploits the 3D superlattice periodicity, as in the case of the one-electron f-sum rule [7], and is applicable to semiconductor superlattices (types I, II and III) with arbitrary layer widths. The exciton equation in the CCR representation yields a 1D tight-binding equation involving the growth axis. An approximate solution yields excellent agreement with recently measured binding energies in GaAs/GaAlAs superlattices as a function of (i) layer widths spanning the range from strongly coupled to isolated quantum wells [3] and (ii) electric field strength [2]. Preliminary results from this work have been briefly reported [8]. The effects of other (e.g. magnetic) fields will be considered in a future publication [9].

The eigenstates of the superlattice single-particle Hamiltonian H_{SL} are defined for band L at wavevector K by

$$H_{SL} |LK\rangle = E_L(K) |LK\rangle. \quad (1)$$

As in the bulk, the superlattice Wannier function at *superlattice* lattice vector $R = (X, Y, Z)$ is defined as

$$\langle r | LR \rangle = (\Omega/8\pi^3)^{1/2} \int dK e^{-iK \cdot R} \langle r | LK \rangle \quad (2)$$

where Ω is the normalisation volume. The superlattice growth (\perp) axis is taken to be

the Z axis while the in-plane (\parallel) directions are described by X and Y . The superlattice period in the \perp (\parallel) direction is d (a), where d is typically of the order of 100 Å while $a \approx 6$ Å. The superlattice Wannier function will have a spatial extent of the order of d (a) in the \perp (\parallel) direction [9].

The many-body Hamiltonian is given by

$$H = \sum_i H_{SL}(r_i) + \sum_{i>j} v(r_i - r_j) \quad (3)$$

where the latter term is the Coulomb interaction. We are only interested in electron-hole excitations and expand the exciton wavefunction in a basis of two-particle Wannier states $|LR + R'; L'R'\rangle$ each consisting of a symmetrised product of electron (hole) Wannier functions [10] for band L (L') centred at $R + R'$ (R'). To simplify notation we only consider two superlattice bands although the formalism can be easily generalised. The total exciton state $|\Psi\rangle$ at zero exciton wavevector (i.e. the optically active exciton) can be written [10] as

$$|\Psi\rangle = (\Omega/8\pi^3)^{1/2} \sum_R U(R) \sum_{R'} |LR' + R; L'R'\rangle \quad (4)$$

where $U(R)$ is the exciton CCR wavefunction. The sum over R' includes all two-particle states with a given electron-hole separation R while the sum over R accounts for all possible electron-hole separations. Evaluating the many-body Hamiltonian of (3) in the two-particle basis leads to a set of difference equations [10]

$$\sum_{R'} \left((\Omega/8\pi^3) \int dK e^{iK \cdot (R-R')} (E_L(K) - E_{L'}(K)) \right) U(R') - V(R)U(R) = EU(R). \quad (5)$$

Here E is the excitation energy of the superlattice and $V(R)$ is the direct Coulomb term [11] given by

$$V(R) = \iint |\langle r_e | LR \rangle|^2 \frac{e^2}{\epsilon |r_e - r_h|} |\langle r_h | L'0 \rangle|^2 dr_e dr_h \quad (6)$$

where r_e (r_h) defines the electron (hole) coordinates and ϵ is the static dielectric constant.

To evaluate (5) for the superlattices of interest, we write

$$E_L(K) - E_{L'}(K) = \frac{\hbar^2 K_{\parallel}^2}{2\mu_{\parallel}} + E_g - \sum_{n=1}^{\infty} 2W(n)(\cos(nK_{\perp}d) - 1) \quad (7)$$

where μ_{\parallel} is the parallel reduced mass and E_g is the $K = 0$ gap between bands L and L' . The parabolic approximation has been made in the parallel direction. The expansion of the perpendicular dispersion as a cosine series with coefficients $W(n)$ exploits the approximate inversion symmetry of superlattice energy bands under $K_{\perp} \rightarrow -K_{\perp}$. The equivalent of the effective mass approximation is then made in the parallel direction where the exciton radius (typically 100 Å in the bulk semiconductors of interest) is much greater than the underlying superlattice unit cell size ($a \approx 6$ Å). The lattice vector coordinates X , Y can therefore be treated as continuous variables. Notice that the effective mass approximation *cannot* be made in the growth direction since d is of the

order of the exciton radius. Using (7) and the above approximations, equation (5) yields a set of coupled differential equations

$$\left[\frac{-\hbar^2}{2\mu_1} \left(\frac{\partial^2}{\partial X^2} + \frac{\partial^2}{\partial Y^2} \right) - V(X, Y, jd) \right] U(X, Y, jd) - \sum_{n=1}^{\infty} W(n) (U(X, Y, (j+n)d) + U(X, Y, (j-n)d)) = \left(\epsilon - \sum_{n=1}^{\infty} 2W(n) \right) U(X, Y, jd) \quad (8)$$

where $\epsilon = (E - E_g)$ represents the exciton binding energy. The two possible cases of (8) are as follows.

(i) $W(n) = 0$ in (8) for all n , which is characteristic of a thick barrier limit in which the electron and hole cannot tunnel between adjacent wells. Equation (8) becomes

$$\left[\frac{-\hbar^2}{2\mu_1} \left(\frac{\partial^2}{\partial X^2} + \frac{\partial^2}{\partial Y^2} \right) - V(X, Y, jd) \right] U_0^m(X, Y, jd) = \epsilon_j^{0,m} U_0^m(X, Y, jd) \quad (9)$$

which yields the m th (excited state) exciton solution for a given electron-hole separation of j periods. The corresponding binding energies $\epsilon_j^{0,m}$ for a given j are analogous to the energy levels of a hydrogenic atom. For convenience we can represent the eigenstate of (9) for a given j and m in terms of an orthonormal basis $\{\hat{e}_{X,Y,jd}\}$ corresponding to the superlattice lattice points; hence

$$\Psi_{\text{ex}}^{0,j,m} = \sum_{X,Y,j'} U_0^m(X, Y, j'd) \delta_{jj'} \hat{e}_{X,Y,jd}.$$

(ii) $W(n) \neq 0$; here the exciton is characterised by a distribution of js . The eigenstate of (8) can therefore be represented as

$$\Psi_{\text{ex}} = \sum_{j,m} c_j^m \Psi_{\text{ex}}^{0,j,m}. \quad (10)$$

It then follows formally from (8) that [9]

$$\sum_{j,m} \left[\left(\epsilon_j^{0,m} - \epsilon + \sum_{n=1}^{\infty} 2W(n) \right) \delta_{jj'} \delta_{mm'} - \sum_{n=1}^{\infty} \tilde{W}_{jj'}^{m,m}(n) \delta_{j'j \pm n} \right] c_j^m = 0 \quad (11)$$

where

$$\tilde{W}_{jj'}^{m,m}(n) = W(n) \iint dX dY (U_0^m(X, Y, j'd))^* U_0^m(X, Y, jd).$$

Equation (11) is identical to a 1D tight-binding equation where $\epsilon_j^{0,m}$ is the on-site energy at site j and $\tilde{W}_{jj'}^{m,m}(n)$ is the hopping term. Equation (11) is the main result of the formalism for the zero-field binding energy ϵ and is applicable to superlattices of arbitrary width.

We now solve (11) approximately to compare with the experimental results for GaAs/GaAlAs [3]. Only the nearest-neighbour hopping $\tilde{W}_{jj'}^{m,m}(1)$ will be retained since we are mostly interested in superlattices with barrier thicknesses greater than 30 Å. In order to obtain values of $\epsilon_j^{0,m}$, the potential function $V(X, Y, jd)$ needs to be specified (see (6)). Explicit forms for the electron and hole Wannier functions ($\langle r_e | LR \rangle$ and $\langle r_h | L'0 \rangle$ respectively) must therefore be used. Since the electron-hole Coulomb interaction is slowly varying on the atomic scale a , the rapidly varying portion of the superlattice Wannier functions in (6) can be integrated out [9], leaving an envelope function

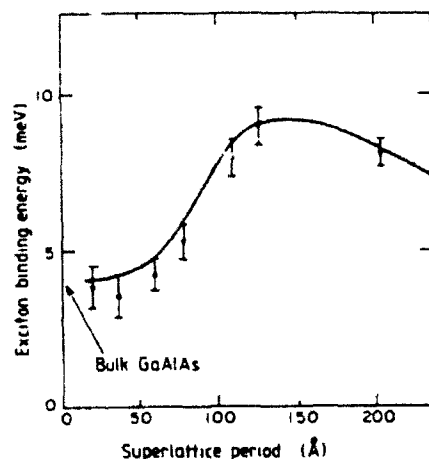


Figure 1. Binding energies of the heavy-hole (CI-HH1) exciton versus superlattice period d for $(d/2)$ GaAs/ $(d/2)$ Ga_{0.7}Al_{0.3}As. Full curve: present theory; experimental points: from [3].

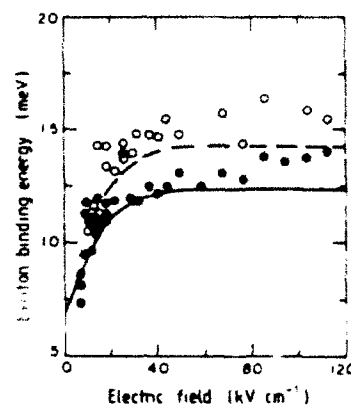


Figure 2. Experimental [2] and theoretical exciton binding energies for the 40 Å GaAs/40 Å Ga_{0.45}Al_{0.55}As superlattice versus electric field strength F . Binding energies of the heavy-hole (CI-HH1) exciton are shown by the full curve (theory) and full circles (experiment). Light-hole (CI-LH1) exciton binding energies are shown by the broken curve (theory) and open circles (experiment).

modulation of each Wannier function on the scale of d (a) in the \perp (\parallel) direction. We then assume for simplicity that the charge distribution associated with the electron (hole) Wannier function is well described by a uniformly charged rod of X - Y cross section equal to $a \times a$ and length l_e (l_h), where l_e (l_h) corresponds to the spatial extent of the electron (hole) Wannier function in the growth direction. We take l_e (l_h) to be equal to the well width plus twice the electron (hole) envelope function decay length in the barrier layers. This simplification leads to an analytic expression for $V(X, Y, jd)$. The resulting nearest-neighbour tight-binding equation is then easily solved. Values of the electron and hole bandwidths and the superlattice in-plane masses [12] are obtained using the envelope function approach of [7] which accounts for valence-band mixing. The bulk $k \cdot p$ input parameters for GaAlAs are the same as in [7].

Figure 1 compares the experimental [3] and present theoretical binding energies for 1s excitons formed from the lowest conduction band C1 and the topmost valence band HH1 in the $(d/2)$ GaAs/ $(d/2)$ Ga_{0.7}Al_{0.3}As superlattice at low temperature. The excellent agreement between theory and experiment implies that the simplifying assumptions made in the previous paragraph are reasonable. For small d , the superlattice exciton binding energy is nearly equal to that of the bulk alloy Ga_{0.85}Al_{0.15}As chosen to have the same Al concentration as the superlattice. The exciton CCR wavefunction $U(X, Y, jd)$ is non-zero over many superlattice periods in this regime. An increase in d implies an increase in the barrier thickness for holes and electrons. As a result the total electron-hole bandwidth given by $4W(1)$ decreases, and the binding energy increases. For $d > 140$ Å, $W(1)$ is zero; hence the electron and hole are localised in the same layer. The superlattice exciton binding energy becomes equal to the value for a single quantum well which gradually decreases as d increases [13].

The presence of a finite electric field F along the growth direction adds

$$-eF \sum_i z_i$$

to the total exciton Hamiltonian (3). A term $eFjd$ consequently appears in the CCR exciton equation, and corresponds to *intra-sub-band* transitions induced by the electric field. Contributions arising from *inter-sub-band* transitions are neglected. The effect of the electric field on the zero-wavevector exciton energy spectrum is then described in the present theory by

$$\sum_{i,m} \left[\left(\epsilon_i^{0,m} - eFjd - \epsilon + \sum_{n=1}^{\infty} 2W(n) \right) \delta_{ij} \delta_{mm} - \sum_{n=1}^{\infty} W_{ij}^{m,m}(n) \delta_{j,j-n} \right] c_i^m = 0. \quad (12)$$

In the zero-field limit, (12) is identical to (11). In the absence of the Coulomb interaction, $\epsilon_i^{0,m} = 0$ and (12) leads to the formation of a Stark ladder [14].

Figure 2 compares the experimental [2] and theoretical exciton binding energies for the 40 Å GaAs/40 Å Ga_{0.65}Al_{0.35}As superlattice as a function of increasing electric field F . The heavy-hole (C1-HH1) and light-hole (C1-LH1) binding energies shown correspond to the *intra-well* exciton, which is characterised by the electron and hole becoming localised in the same well at high electric fields. The total bandwidth of the electron and heavy hole ($4W(1)$) is 15 meV while that of the electron and light hole is 28 meV. At low fields the exciton binding energy tends to the zero-field result (cf figure 1). As F increases the binding energy increases due to the enhanced electron and hole localisation associated with the formation of the Stark ladder [14]. At high fields ($eFd \gg 4W(1)$) the exciton binding energies become those of an isolated quantum well of width 40 Å. The reason that the theoretical binding energies lie below the experimental values at high fields is most likely due to the neglect of *inter-sub-band* transitions and tunnelling effects.

The author is very grateful to Professor H Ehrenreich for stimulating the research. He is also very grateful to J Dempsey, P M Hui, R D Meade, S Tyč and P M Young for invaluable discussions. This work was supported by the Joint Service Electronics Program through US Office of Naval Research (ONR) Contract Nos N00014-84-K-0465 and N00014-89-J-1023, Defense Advanced Research Agency through ONR Contract No N00014-86-K-0033, and by a St John's College (Cambridge, UK) Fellowship.

References

- [1] See, for example,
Saunders G D and Bajaj K K 1987 *Phys. Rev. B* **35** 2308
Schmitt-Rink S, Chemla D S and Miller D A B 1985 *Phys. Rev. B* **32** 6601
- [2] Agullo-Rueda F, Mendez E E and Hong J M 1989 *Phys. Rev. B* **40** 1357
Agullo-Rueda F, Mendez E E, Brum J A and Hong J M 1990 *Proc. 4th Int. Conf. on Modulated Semiconductor Structures (Ann Arbor, 1989)* at press
- [3] Chomette A, Lambert B, Devaud B, Clerot F, Regreny A and Bastard G 1987 *Europhys. Lett.* **4** 461
- [4] Song J J, Jung P S, Yoon Y S, Chu H, Chang Y C and Tu C W 1989 *Phys. Rev. B* **39** 5562
- [5] Yang S R E and Das Sarma S 1988 *Phys. Rev. B* **37** 4007
- [6] Chu H and Chang Y C 1989 *Phys. Rev. B* **39** 10861
- [7] Johnson N F, Ehrenreich H, Hass K C and McGill T C 1987 *Phys. Rev. Lett.* **59** 2352
- [8] Johnson N F, Hui P M and Ehrenreich H 1989 *Bull. Am. Phys. Soc.* **34** 634
- [9] Johnson N F, Ehrenreich H and Young P M unpublished
- [10] Callaway J 1974 *Quantum Theory of the Solid State* (New York: Academic) p 544

- [11] The exchange term has been neglected. We have estimated it to be an order of magnitude smaller than the direct term for the superlattices of interest.
- [12] Average values of the superlattice in-plane masses were taken over an energy range corresponding to the exciton binding energy.
- [13] See, for example,
Ekenberg U and Altarelli M 1987 *Phys. Rev. B* **35** 7585
- [14] Bleuse J, Bastard G and Voisin P 1988 *Phys. Rev. Lett.* **60** 220

Electronic and optical properties of III-V and II-VI semiconductor superlattices

N. F. Johnson, H. Ehrenreich,* P. M. Hui, and P. M. Young

Division of Applied Sciences, Harvard University, Cambridge, Massachusetts 02138

(Received 11 July 1989)

The electronic structure and optical properties of III-V and II-VI semiconductor superlattices are treated theoretically using a superlattice-representation formalism. The band structure is obtained from superlattice $\mathbf{K} \cdot \mathbf{p}$ theory. The theory is based on closed analytic calculations of the superlattice states at wave vector $\mathbf{K} = 0$ and the envelope-function approach. The known parameters of the bulk constituents represent the only input. The electron effective masses and gaps of GaAs/Ga_{1-x}Al_xAs (type I), InAs/GaSb (type II), and HgTe/CdTe (type III) are investigated for a wide range of layer widths using the recently deduced large valence-band offset of HgTe/CdTe. The behavior of the masses is also discussed in terms of the f -sum rule. The calculated fundamental absorption coefficients for InAs/GaSb and HgTe/CdTe are in excellent agreement with experimental data. The intersubband absorption between the lowest two superlattice conduction bands is investigated. In the thick-barrier limit of GaAs/Ga_{1-x}Al_xAs the absorption can be larger than the fundamental absorption and as narrow as a laser linewidth. In the thin-barrier limit the absorption is smaller and broader, as illustrated for In_xGa_{1-x}As/In_yAl_{1-y}As.

I. INTRODUCTION

This paper presents a detailed treatment of the electronic structure and optical properties of III-V and II-VI semiconductor superlattices (SL's) based on and extending previous brief publications.¹⁻³ The present theoretical approach describes the superlattice as a perfectly periodic system within the envelope-function approximation.^{4,5} The standard formalism for bulk periodic solids, including $\mathbf{K} \cdot \mathbf{p}$ theory, is then directly applicable. The only input parameters for the theory are those of the bulk materials involved in the superlattice. This approach has previously been used (i) to extend the well-known bulk f -sum rule to superlattices,¹ (ii) to predict large intersubband optical absorption between the lowest two superlattice conduction bands,² and (iii) to propose a resolution of the valence-band offset controversy in HgTe/CdTe SL's.³ The results presented in this paper exhibit the excellent agreement obtained between the experimental values of quantities such as the fundamental absorption coefficients for InAs/GaSb and HgTe/Hg_{1-x}Cd_xTe and the results obtained using this theoretical approach.

The present approach, described in Sec. II, is easy to implement without large scale computation and yields reliable results for superlattice properties (e.g., effective masses) both perpendicular and parallel to the planes in the energy region of interest. The superlattice states at superlattice wave vector $\mathbf{K} = 0$ are first expressed in terms of known bulk $\mathbf{k} \cdot \mathbf{p}$ parameters using the envelope-function approach and a modified bulk Kane model as input. The adequacy of this limited-basis $\mathbf{k} \cdot \mathbf{p}$ model has recently been verified by comparison with the state-of-the-art extended-basis model of McGill and co-workers.⁶ The $\mathbf{K} = 0$ masses can then be obtained analytically using the f -sum rule.¹ Superlattice $\mathbf{K} \cdot \mathbf{p}$ theory is employed to yield the SL band structure at finite \mathbf{K} . The optical properties are then obtained from knowledge of the finite \mathbf{K}

electronic properties.

Sections III and IV present a quantitative comparison of the electronic and optical properties of several technologically important SL's. Section III A describes the layer width dependencies of the SL electron mass and gap in GaAs/Ga_{1-x}Al_xAs (type I), InAs/GaSb (type II), and HgTe/CdTe (type III). The behavior of the masses is then discussed in terms of the f -sum rule for the InAs/GaSb SL (Sec. III B), which is of theoretical interest because the electron and hole wave functions are concentrated in separate layers. Section III C compares the band structures of the three SL's.

The discussion of optical properties in Sec. IV is essentially self-contained. The primary motivation for studying HgTe/CdTe, and to a lesser extent InAs/GaSb, is for use in infrared detectors. This application makes use of fundamental SL absorption in the 10- μm range. The present theory yields fundamental absorption coefficients in excellent agreement with experimental data^{7,8} for both HgTe/Hg_{1-x}Cd_xTe and InAs/GaSb (Sec. IV A). The type-I SL's considered here have been recently proposed for use in optoelectronics owing to the large intersubband oscillator strength between the lowest two SL conduction bands, C1 and C2.^{2,9-12} In particular, the C1 \rightarrow C2 absorption in GaAs/Ga_{1-x}Al_xAs with thick Ga_{1-x}Al_xAs barriers has been suggested for use in carrier-activated light modulation in the 10- μm range.² The corresponding absorption coefficient is shown here to be sharply peaked with magnitude $\sim 10^4 \text{ cm}^{-1}$ (Sec. IV B). In the thin-barrier SL limit the absorption coefficient is predicted to be broader and smaller ($\sim 10^3 \text{ cm}^{-1}$), as illustrated in Sec. IV B for In_xGa_{1-x}As/In_yAl_{1-y}As.

II. FORMALISM

The Hamiltonian in an A/B superlattice is given by

$$H(\mathbf{r}) = \frac{p^2}{2m} + V(\mathbf{r}) + \frac{\hbar}{4m^2c^2} [\boldsymbol{\sigma} \times \nabla V(\mathbf{r})] \cdot \mathbf{p} \quad (1)$$

where $V(r)$ is the microscopic SL potential, p is the momentum operator, and the last term describes the spin-orbit coupling. The SL wave function at SL wave vector \mathbf{K} in band L satisfies

$$H(r)\langle r|L\mathbf{K}\rangle = E_L(\mathbf{K})\langle r|L\mathbf{K}\rangle \quad (2)$$

where $E_L(\mathbf{K})$ is the corresponding energy. The z (or \perp) axis is chosen as the SL growth direction with $z=0$ defined as the center of a given layer of material A . For lattice-matched SL's having the xy interface plane coincident with a crystal plane, $\mathbf{K}=(k_x, k_y, K_z) \equiv (\mathbf{K}_\parallel, K_\perp)$ where k_x and k_y are bulk wave vectors.

We employ the envelope-function approach⁵ to express SL quantities in terms of bulk electronic structure parameters. The envelope-function expansion is given by

$$\langle r|L\mathbf{K}\rangle = \sum_n F_n(L, \mathbf{K}; r) \langle r|n0\rangle \quad (3)$$

where $\langle r|n0\rangle$ is the bulk Bloch function for band n at $\mathbf{k}=0$ in either material A or B and $F_n(L, \mathbf{K}; r)$ is the envelope function. For the well-lattice-matched SL's considered here, $\langle r|n0\rangle$ may be assumed to be the same in A and B . This assumption is justified here by the similarity of the bulk pseudopotentials and momentum-matrix elements for the A and B bulk materials under consideration.^{5,13} The envelope function $F_n(L, \mathbf{K}; r)$ is taken to be slowly varying on the scale of the bulk unit-cell size, and can therefore be cell averaged. This approximation together with the substitution of Eq. (3) into Eq. (1) yields a multiband effective-mass-like Hamiltonian

$$H_A^{k p}(k_x, k_y, k_z \rightarrow -i(\partial/\partial z))F(L, \mathbf{K}; r) = E_L(\mathbf{K})F(L, \mathbf{K}; r) \quad (4)$$

governing the envelope functions at r in a layer of material A (B). The matrix $H_A^{k p}(\mathbf{k})$ is the general $\mathbf{k} \cdot \mathbf{p}$ matrix for bulk A (B) material and $F(L, \mathbf{K}; r)$ is a column vector with components $F_n(L, \mathbf{K}; r)$. The boundary conditions for $F(L, \mathbf{K}; r)$, to be specified explicitly later, are obtained by integrating Eq. (4) across an interface, and are consistent with continuity of the cell-averaged current.¹⁴

The bulk momentum-matrix elements of $H_A^{k p}(\mathbf{k})$ contain the effects of the rapidly varying $\langle r|n0\rangle$'s.

The envelope-function equation [Eq. (4)] is truncated here to a limited number of bulk bands by using the specific form of $H_A^{k p}(\mathbf{k})$ corresponding to the modified Kane model¹³ including finite-spin-orbit splitting.¹⁵ A finite bulk heavy-hole mass is obtained though inclusion of remote band effects via perturbation theory. The eight bulk $\mathbf{k}=0$ basis states $\langle r|n0\rangle$ being considered are defined in Table I in terms of the states $|S\rangle$, $|X\rangle$, $|Y\rangle$, and $|Z\rangle$ using the notation of Ref. 13. The corresponding $\mathbf{k}=0$ energies $E_n(0)$ in material A are also given. Each $\langle r|n0\rangle$ can be characterized by $|J, M_J\rangle$ as shown in Table I, where M_J is the z component of the total angular momentum J .¹³

The SL states at $\mathbf{K}=(0,0,K_z)$ can be labeled by M_J which remains a good quantum number.⁵ Specifically $M_J = \pm \frac{1}{2}$ for the light particle SL states, and $M_J = \pm \frac{3}{2}$ for the heavy-hole SL states. The resulting 8×8 matrix equation obtained from Eq. (4) at $\mathbf{K}=(0,0,K_z)$ consists of two equivalent 4×4 blocks corresponding to positive and negative M_J values, respectively. Table II shows the 4×4 block corresponding to positive M_J (i.e., $M_J = +\frac{1}{2}$ and $+\frac{3}{2}$). The 4×4 block corresponding to negative M_J can be obtained from Table II by replacing F_1 by F_2 , F_3 by F_4 , F_5 by F_6 , and F_7 by F_8 . Each F_n is independent of x and y . The Kane-matrix element $P = -i\sqrt{2/3}\langle S|p_z|Z\rangle$ which appears in Table II is deduced from experimental bulk masses and gaps. The function $m^{\text{HH}}(z)$ corresponds to the bulk heavy-hole mass $m_{A(B)}^{\text{HH}}$ when z is in material A or B , respectively. The quantities $V_{\Gamma_6}(z)$, $V_{\Gamma_7}(z)$, and $V_{\Gamma_8}(z)$ are set equal to zero in material A . They are given in material B by the differences V_{Γ_6} , V_{Γ_7} , and V_{Γ_8} between the corresponding bulk band edges of material A and B as shown in Fig. 1. The quantities $m^{\text{HH}}(z)$, $V_{\Gamma_6}(z)$, $V_{\Gamma_7}(z)$, and $V_{\Gamma_8}(z)$ are assumed to change abruptly at an interface on the macroscopic length scale of the SL period.

The coupled differential equations for $F_n(L, K_z; z)$ in Table II can be rewritten equivalently as

TABLE I. Bulk modified Kane model $\mathbf{k}=0$ states $|n0\rangle$, energies $E_n(0)$ in material A , and angular momentum labels $|J, M_J\rangle$ for Γ_6 , Γ_7 , and Γ_8 bulk band edges, using the notation of Refs. 5 and 13. The origin of energy is defined as the Γ_6 edge. The bulk band gap and spin-orbit splitting in bulk A material are E_A and Δ_A , respectively.

	$n: n0\rangle$	$E_n(0)$	$ J, M_J\rangle$
Γ_6	1: $ S\uparrow\rangle$	0	$ \frac{1}{2}, +\frac{1}{2}\rangle$
	2: $ S\downarrow\rangle$	0	$ \frac{1}{2}, -\frac{1}{2}\rangle$
Γ_8	3: $\sqrt{2/3} Z\uparrow\rangle - \sqrt{1/6} X+Y\downarrow\rangle$	$-E_A$	$ \frac{3}{2}, +\frac{1}{2}\rangle$
	4: $\sqrt{2/3} Z\downarrow\rangle + \sqrt{1/6} X-Y\uparrow\rangle$	$-E_A$	$ \frac{3}{2}, -\frac{1}{2}\rangle$
	5: $\sqrt{1/2} X+Y\uparrow\rangle$	$-E_A$	$ \frac{3}{2}, +\frac{3}{2}\rangle$
	6: $\sqrt{1/2} X-Y\downarrow\rangle$	$-E_A$	$ \frac{3}{2}, -\frac{3}{2}\rangle$
Γ_7	7: $\sqrt{1/3} Z\uparrow\rangle + \sqrt{1/3} X+Y\downarrow\rangle$	$-E_A - \Delta_A$	$ \frac{1}{2}, +\frac{1}{2}\rangle$
	8: $\sqrt{1/3} Z\downarrow\rangle - \sqrt{1/3} X-Y\uparrow\rangle$	$-E_A - \Delta_A$	$ \frac{1}{2}, -\frac{1}{2}\rangle$

TABLE II. Superlattice envelope-function equation [Eq. (4)] at $\mathbf{K}=(0,0,K_1)$ using modified Kane model as input. Only the positive M_j block is shown. The operator $\hat{\mathbf{K}}_1 = -i(d/dz)$. The $\mathbf{K}=(0,0,K_1)$ superlattice energy is defined as $E_L(K_1)$.

$$\begin{bmatrix} V_{r_0}(z) \\ -iP\hat{\kappa}\hat{\kappa}_z \\ m \\ 0 \\ -iP\hat{\kappa}\hat{\kappa}_z \\ \sqrt{2}m \end{bmatrix} \begin{bmatrix} \frac{iP\hat{\kappa}\hat{\kappa}_z}{\sqrt{2}m} \\ 0 \\ 0 \\ -E_A + V_{r_8}(z) \\ 0 \\ 0 \end{bmatrix} \begin{bmatrix} F_1(L, K_{1;2}) \\ F_3(L, K_{1;2}) \\ F_5(L, K_{1;2}) \\ F_7(L, K_{1;2}) \end{bmatrix} = E_L(K_1) \begin{bmatrix} F_1(L, K_{1;2}) \\ F_3(L, K_{1;2}) \\ F_5(L, K_{1;2}) \\ F_7(L, K_{1;2}) \end{bmatrix}$$

TABLE III. Superlattice quantities $A_{\pm}(z, E(K))$, $B_{\pm}(z, E(K))$, and $\bar{V}_{\pm}(z)$ which appear in the differential equations for the envelope functions [Eq. (5)].

n	1	2	3	4	5	6	7	8
$ J, M_J\rangle$	$ \frac{1}{2}, +\frac{1}{2}\rangle$	$ \frac{1}{2}, -\frac{1}{2}\rangle$	$ \frac{3}{2}, +\frac{1}{2}\rangle$	$ \frac{1}{2}, -\frac{1}{2}\rangle$	$ \frac{3}{2}, +\frac{1}{2}\rangle$	$ \frac{1}{2}, -\frac{1}{2}\rangle$	$ \frac{5}{2}, +\frac{1}{2}\rangle$	$ \frac{3}{2}, -\frac{1}{2}\rangle$
$B_n(z, E_L(K_1))$	$\frac{\hbar^2 p^2}{2m^2} \left[\frac{E_L(K_1) + E_A - V_{r_8}(z)}{2} + \frac{1}{E_L(K_1) + E_A + \Delta_A - V_{r_7}(z)} \right]$	$\frac{\hbar^2 p^2}{2m^2} \left[\frac{E_L(K_1) + E_A - V_{r_8}(z)}{2} + \frac{1}{E_L(K_1) + E_A + \Delta_A - V_{r_7}(z)} \right]$	$\frac{\hbar^2 p^2}{m^2} \left[\frac{E_L(K_1) + E_A + \Delta_A - V_{r_7}(z)}{2} + \frac{1}{E_L(K_1) + E_A + \Delta_A - V_{r_8}(z)} \right]$	$\frac{\hbar^2 p^2}{m^2} \left[\frac{E_L(K_1) + E_A + \Delta_A - V_{r_7}(z)}{2} + \frac{1}{E_L(K_1) + E_A + \Delta_A - V_{r_8}(z)} \right]$	$\frac{\hbar^2 p^2}{m^2} \left[\frac{E_L(K_1) + E_A + \Delta_A - V_{r_7}(z)}{2} + \frac{1}{E_L(K_1) + E_A + \Delta_A - V_{r_8}(z)} \right]$	$\frac{\hbar^2 p^2}{m^2} \left[\frac{E_L(K_1) + E_A + \Delta_A - V_{r_7}(z)}{2} + \frac{1}{E_L(K_1) + E_A + \Delta_A - V_{r_8}(z)} \right]$	$\frac{\hbar^2 p^2}{m^2} \left[\frac{E_L(K_1) + E_A + \Delta_A - V_{r_7}(z)}{2} + \frac{1}{E_L(K_1) + E_A + \Delta_A - V_{r_8}(z)} \right]$	$\frac{\hbar^2 p^2}{m^2} \left[\frac{E_L(K_1) + E_A + \Delta_A - V_{r_7}(z)}{2} + \frac{1}{E_L(K_1) + E_A + \Delta_A - V_{r_8}(z)} \right]$
$A_n(z, E_L(K_1))$	$\frac{3E_L(K_1) + 3E_A + 2\Delta_A - 2V_{r_7}(z) - V_{r_8}(z)}{2[E_L(K_1) + E_A + \Delta_A - V_{r_7}(z)]}$	$\frac{3E_L(K_1) + 3E_A + 2\Delta_A - 2V_{r_7}(z) - V_{r_8}(z)}{2[E_L(K_1) + E_A + \Delta_A - V_{r_7}(z)]}$	$\frac{3E_L(K_1) + 3E_A + 2\Delta_A - 2V_{r_7}(z) - V_{r_8}(z)}{2[E_L(K_1) + E_A + \Delta_A - V_{r_7}(z)]}$	$\frac{3E_L(K_1) + 3E_A + 2\Delta_A - 2V_{r_7}(z) - V_{r_8}(z)}{2[E_L(K_1) + E_A + \Delta_A - V_{r_7}(z)]}$	$\frac{3E_L(K_1) + 3E_A + 2\Delta_A - 2V_{r_7}(z) - V_{r_8}(z)}{2[E_L(K_1) + E_A + \Delta_A - V_{r_7}(z)]}$	$\frac{3E_L(K_1) + 3E_A + 2\Delta_A - 2V_{r_7}(z) - V_{r_8}(z)}{2[E_L(K_1) + E_A + \Delta_A - V_{r_7}(z)]}$	$\frac{3E_L(K_1) + 3E_A + 2\Delta_A - 2V_{r_7}(z) - V_{r_8}(z)}{2[E_L(K_1) + E_A + \Delta_A - V_{r_7}(z)]}$	$\frac{3E_L(K_1) + 3E_A + 2\Delta_A - 2V_{r_7}(z) - V_{r_8}(z)}{2[E_L(K_1) + E_A + \Delta_A - V_{r_7}(z)]}$
$\bar{V}_n(z)$	$V_{r_8}(z)$	$V_{r_8}(z)$	$V_{r_8}(z)$	$V_{r_8}(z) - E_A$	$V_{r_8}(z) - E_A$	$V_{r_8}(z) - E_A$	$V_{r_8}(z) - E_A$	$V_{r_8}(z) - E_A$

TABLE IV. Analytic solutions for the envelope function $F_n(L, 0; z)$ in layer A (width l_A) and layer B (width l_B) corresponding to the superlattice $K = 0$ states $|L, 0\rangle_{M, P}$ which are labeled by the z component of angular momentum M_J and parity P . Only the $|L, 0\rangle_{M, P}$ states with positive M_J are shown. For each $|L, 0\rangle_{M, P}$ shown, only the nonvanishing F_n 's are given. γ_A is defined to be $E_L(0) \text{Im} / i P \hbar k_A$. N is the normalization constant. The bulk wave vectors k_A, k_B may be real or imaginary. The superlattice period $d = l_A + l_B$.

$(L, 0)_{M, P}$	Im A: $-l_A/2 < z < l_A/2$	Im B: $l_A/2 < z < l_A/2 + l_B$
$M_J = +\frac{1}{2}$		
$P = +$	$F_1(L, 0; z): N \cos k_A z$ $F_3(L, 0; z): N i \gamma_A \frac{2[E_A + \Delta_A + E_L(0)] \sin k_A z}{3E_L(0) + 3E_A + 2\Delta_A}$ $F_5(L, 0; z): N i \gamma_A \frac{\sqrt{2}[E_A + E_L(0)] \sin k_A z}{3E_L(0) + 3E_A + 2\Delta_A}$	$N \frac{\cos k_A l_A / 2}{\cos k_B l_B / 2} \cos k_B (z - d/2)$ $- N i \gamma_A \frac{\sin k_A l_A / 2}{\sin k_B l_B / 2} \frac{2[E_A + \Delta_A + E_L(0) - V_{\Gamma_1}]}{3E_L(0) + 3E_A + 2\Delta_A - 2V_{\Gamma_1} - V_{\Gamma_2}} \sin k_B (z - d/2)$ $- N i \gamma_A \frac{\sin k_A l_A / 2}{\sin k_B l_B / 2} \frac{\sqrt{2}[E_A + E_L(0) - V_{\Gamma_1}]}{3E_L(0) + 3E_A + 2\Delta_A - 2V_{\Gamma_1} - V_{\Gamma_2}} \sin k_B (z - d/2)$ $- N \frac{i \sin k_A l_A / 2}{\gamma_A \sin k_B l_B / 2} \sin k_B (z - d/2)$
$M_J = +\frac{1}{2}$		
$P = -$	$F_1(L, 0; z): N \frac{i \sin k_A z}{\gamma_A}$ $F_3(L, 0; z): N \frac{2[E_A + \Delta_A + E_L(0)] \cos k_A z}{3E_L(0) + 3E_A + 2\Delta_A}$ $F_5(L, 0; z): N \frac{\sqrt{2}[E_A + E_L(0)] \cos k_A z}{3E_L(0) + 3E_A + 2\Delta_A}$	$N \frac{\cos k_A l_A / 2}{\cos k_B l_B / 2} \frac{2[E_A + \Delta_A + E_L(0) - V_{\Gamma_1}]}{3E_L(0) + 3E_A + 2\Delta_A - 2V_{\Gamma_1} - V_{\Gamma_2}} \cos k_B (z - d/2)$ $N \frac{\cos k_A l_A / 2}{\cos k_B l_B / 2} \frac{\sqrt{2}[E_A + E_L(0) - V_{\Gamma_1}]}{3E_L(0) + 3E_A + 2\Delta_A - 2V_{\Gamma_1} - V_{\Gamma_2}} \cos k_B (z - d/2)$ $- N \frac{\sin k_A l_A / 2}{\sin k_B l_B / 2} \sin k_B (z - d/2)$
$M_J = +\frac{3}{2}$		
$P = +$	$F_5(L, 0; z): N \sin k_A z$	
$M_J = +\frac{1}{2}$	$F_5(L, 0; z): N \cos k_A z$	
$P = -$		

$$\Pi_n(L, L') = \frac{1}{d} \left[\int_{-l_{A/2}}^{l_{A/2}} + \int_{l_{A/2}}^{l_{A/2}+l_B} \right] dz \\ \times F_n^*(L, 0; z) p_z F_n(L', 0; z). \quad (13)$$

The selection rules within the modified Kane model are $\langle L, 0 | p_z | L', 0 \rangle = 0$ unless (i) $M_j - M_{j'} = 0(\pm 1)$, and (ii) $|L, 0\rangle$ and $|L', 0\rangle$ have different parities.

For the SL's considered here, the $\alpha_{nn'}(L, L') p_{nn'}$ terms dominate over the $\Pi_n(L, L')$ terms in $\langle L, 0 | p_z | L', 0 \rangle$. Therefore the Kronig-Penney model is inadequate for calculating SL momentum-matrix elements since that model only contains Π terms. It can be shown^{14,18} that for type-I SL's such as GaAs/Ga_{1-x}Al_xAs having a gap much larger than the conduction- and valence-band offsets,

$$\langle L, 0 | p_z | L', 0 \rangle \sim (m/m_e^*) \Pi_n(L, L'), \quad n = 1, 2 \quad (14)$$

where $L = C1, C3, \dots$, $L' = C2, C4, \dots$, and m_e^* is the bulk electron mass. (C1 is the lowest SL conduction band.) The effect of $\Pi_n(L, L')$ in Eq. (11) is therefore smaller by about m/m_e^* than the first term. In the bulk limit (i.e., l_A or $l_B \rightarrow 0$) the F_n 's for C2 become sine or cosine waves with period d while the F_n 's for C1 become constant. The α and Π integrals for $L = C1$ and $L' = C2$ vanish and $\langle C1, 0 | p_z | C2, 0 \rangle$ is therefore zero. This behavior is consistent with that of a bulk intraband transition which vanishes in the absence of scattering. In a superlattice, the barrier layer supplies crystal momentum in the $\perp(z)$ direction. Hence $\langle C1, 0 | p_z | C2, 0 \rangle$ will be larger than $\langle C1, 0 | p_x | C2, 0 \rangle$.

III. ELECTRONIC PROPERTIES

The three types of superlattice (SL) being considered are shown in Fig. 2. The relative alignments of the Γ_6 and Γ_8 bulk band edges are shown for type-I (GaAs/Ga_{1-x}Al_xAs), type-II (InAs/GaSb), and type-III (HgTe/CdTe) A/B superlattices. Λ is the valence-band

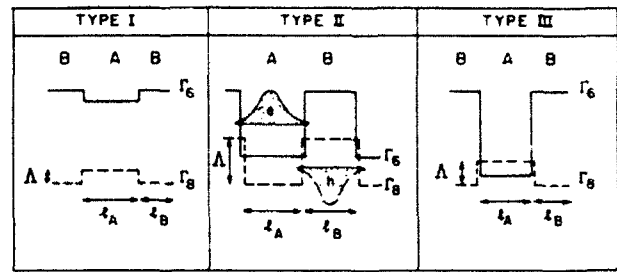


FIG. 2. Schematic band alignments for the three types of superlattice. The electron well associated with the Γ_6 conduction-band maximum (solid line) and the inverted hole well associated with the Γ_8 valence-band maximum (dashed line) are shown. The electron and hole envelope functions are shown schematically for a type-II superlattice, where the two are concentrated in adjacent layers. Λ is the valence-band offset.

offset. Although the SL electron and hole states contain both Γ_6 and Γ_8 components, the solid line (Γ_6) can be associated roughly with the quantum well appropriate to electrons, and the dashed line (Γ_8) with that appropriate to holes. As indicated by the sketched envelope functions, the electron and hole in type-II SL's are therefore concentrated in layers A and B, respectively. By contrast both electron and hole are concentrated in layer A in type-I and -III SL's. The spectral limit theorem¹⁹ implies that a positive SL gap always exists in type-I SL since there is a gap region common to both materials A and B. For type-II and -III SL's the gap may be zero.

Table V gives the bulk $k \cdot p$ parameters and valence-band offsets Λ used as input to the envelope-function equations [Eq. (5)]. Λ is taken as 350 meV for HgTe/CdTe (Ref. 3) in contrast to our previous zero offset analysis.¹ Although the qualitative features of Fig. 3 in Ref. 1 are unchanged, m_1 in the HgTe/CdTe SL is

TABLE V. Bulk $k \cdot p$ parameters and valence-band offsets (Λ) used as input to the superlattice envelope-function equations. $m_e^*(m_{HH}^*)$ is the bulk electron (heavy-hole) mass. $E(\Gamma_6)$, $E(\Gamma_7)$, and $E(\Gamma_8)$ are the energies of the Γ_6 , Γ_7 , and Γ_8 edges, respectively.

	Type I		Type II		Type III			
	GaAs (A)	Ga _{0.7} Al _{0.3} As ^a (B)	In _{0.53} Ga _{0.47} As (A)	In _{0.52} Al _{0.48} As (B)	InAs (A)	GaSb (B)	HgTe ^b (A)	CdTe ^b (B)
	T=0 K		T=60 K		T=0 K		T=0 K	
E(Γ ₆)-E(Γ ₈) (eV)	1.52 ^c	1.98	0.76 ^d	1.47 ^d	0.42 ^c	0.81 ^c	-0.30	1.60
E(Γ ₈)-E(Γ ₇) (eV)	0.34 ^c	0.32	0.35 ^a	0.32 ^a	0.38 ^c	0.75 ^c	1.0	0.90
Λ (eV)		0.138 ^f		0.16 ^d		0.57 ^e		0.35
m _e [*] /m ₀	0.067 ^g	0.084	0.042 ^d	0.075 ^d	0.022	0.042 ^h	0.031	0.11
m _{HH} [*] /m ₀	0.7 ^g	0.7	0.5 ^a	0.5 ^a	0.4 ^c	0.4 ^c	0.7	0.7

^aVirtual crystal alloy values.

^bReference 3.

^cReference 13.

^dReference 10.

^eReference 20.

^f70:30 conduction-band:valence-band ratio (Ref. 21).

^gReference 22.

roughly twice as large for $\Lambda = 350$ meV than for $\Lambda = 0$ while m_{\perp} and E_g^{SL} both tend to be slightly smaller.

A. $K=0$ gaps and masses

Figure 3 shows the SL band gap E_g^{SL} and the $K=0$ C1 electron masses m_{\perp} (solid line), m_{\parallel} (short-dashed line) as functions of layer width. The behavior can be understood qualitatively by considering the quantum well (QW)

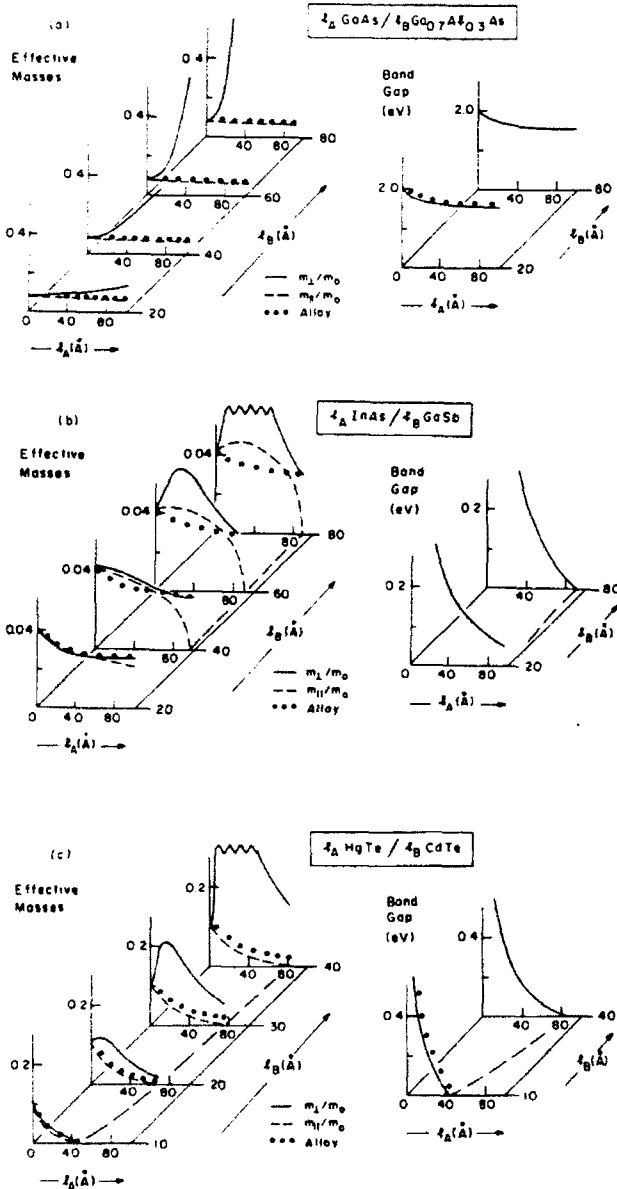


FIG. 3. Superlattice gap E_g^{SL} and the $K=0$ C1 electron masses m_{\perp} (solid line), m_{\parallel} (short-dashed line) as functions of layer widths l_A , l_B in (a) GaAs/Ga_{0.7}Al_{0.3}As, (b) InAs/GaSb, and (c) HgTe/CdTe. The locus of $E_g^{\text{SL}}=0$ is indicated by a long-dashed line for InAs/GaSb and HgTe/CdTe. VCA masses and gaps for the alloy A_xB_{1-x} with $x = l_A/d$ are shown by dotted lines.

and homogeneous virtual crystal alloy (VCA) limits (dotted lines). The behavior of the effective masses will be discussed again in Sec. III B on the basis of the f -sum rule.

The QW picture is appropriate in the thick-barrier limit where m_{\perp} is large. The SL band gap E_g^{SL} is then determined by the kinetic energies of confinement of the electrons and holes in their respective wells. In the QW picture, the energies of the electrons and holes are more sensitive to their respective well widths than the corresponding barrier widths. Furthermore, because of its lighter bulk mass, the electron confinement energy is more sensitive to the electron well width than the hole energy is to the model well width.

The VCA picture is appropriate in the thin-barrier SL limit where the envelope-function decay length in the barrier is much greater than the barrier thickness. In this limit the A/B SL is expected to behave like a homogeneous alloy A_xB_{1-x} where $x = l_A/d$ is the concentration of material A assumed to be uniformly dispersed throughout the sample. The VCA picture predicts that m_{\parallel} and m_{\perp} will be equal and follow E_g^{SL} as in the bulk.

For fixed barrier width l_B in each SL system, E_g^{SL} decreases as l_A increases, due to a reduction in the QW electron kinetic energy of confinement. In GaAs/Ga_{1-x}Al_xAs [Fig. 3(a)] E_g^{SL} tends to the bulk GaAs gap with increasing l_A . Figure 2, on the other hand, suggests that in InAs/GaSb [Fig. 3(b)] and HgTe/CdTe [Fig. 3(c)] the gap E_g^{SL} becomes zero for large l_A because the decreasing electron confinement energy causes the electron energy level to fall below that of the hole level. In the VCA picture an increase in l_A is equivalent to an increase in x . Since the bulk A gap is less than that of bulk B , the VCA gap also decreases. The variation of the VCA gap for GaAs/Ga_{1-x}Al_xAs and HgTe/CdTe using $x = l_A/d$ is shown by the dotted line in Fig. 3.²³ As expected the VCA gap agrees well with E_g^{SL} for thin barriers l_B .

In GaAs/Ga_{1-x}Al_xAs and HgTe/CdTe, E_g^{SL} increases with increasing barrier thickness l_B at fixed l_A and saturates at the isolated quantum-well value. For InAs/GaSb the confinement energy of the electron increases as l_B becomes larger, but the hole confinement energy decreases. Hence E_g^{SL} may increase or decrease with increasing l_B depending on whether the electron or hole energy shift dominates.

Figure 3 shows that m_{\parallel} , indicated by the short-dashed line, decreases somewhat with increasing l_A in GaAs/Ga_{1-x}Al_xAs and HgTe/CdTe for fixed l_B . This corresponds to the expected bulklike behavior for which $E_g^{\text{SL}} \sim m_{\parallel}$. In HgTe/CdTe m_{\parallel} becomes zero for sufficiently large l_A as indicated by the long-dashed line in Fig. 3(c). As l_A is increased further, m_{\parallel} actually becomes nonzero once more. A detailed account of the behavior of m_{\parallel} and E_g^{SL} for HgTe/CdTe in this layer width regime is given in Ref. 3. The VCA masses, shown by a dotted line, agree well with m_{\parallel} for thin barriers l_B . As shown in Fig. 3(b), m_{\parallel} in InAs/GaSb exhibits a peak at $l_A \approx 25$ Å for GaSb widths greater than 40 Å. The corresponding electron energy level coincides with the max-

imum imaginary wave vector in the bulk GaSb gap [see the cross labeling "Max Im(k)" in Fig. 1]. The decay length of the electron wave function in GaSb is therefore a minimum, and the electron is maximally confined to the InAs layer. As a result the in-plane SL mass m_{\parallel} resembles the bulk InAs electron mass $m_{\text{InAs}}^*(E_{C1}(0))$ at a finite energy $E_{C1}(0)$ corresponding to the electron confinement energy above the InAs conduction-band edge. However the $l_A \rightarrow 0$ limit of m_{\parallel} is given by the bulk GaSb electron mass $m_{\text{GaSb}}^*(0)$ which is smaller than $m_{\text{InAs}}^*(E_{C1}(0))$ due to the large conduction-band nonparabolicity in bulk InAs. This effect gives rise to a peak in m_{\parallel} .²⁴

Turning now to the case where l_A is fixed and l_B is varying, we see that the behavior of m_{\parallel} in all three SL systems is again similar to that of E_g^{SL} as described above.

Figure 3(a) shows that m_{\perp} in GaAs/Ga_{1-x}AlAs increases with l_A at fixed l_B . The electron energy is lowered and as a result the effective barrier height is increased, and the tunneling probability is decreased. As indicated in Figs. 3(b) and 3(c) m_{\perp} in InAs/GaSb and HgTe/CdTe exhibits a peak which occurs at the value of l_A for which the electron decay length in layer B is a minimum. The corresponding tunneling probability through layer B is therefore a minimum.²⁵

Finally for fixed l_A , m_{\perp} increases with increasing barrier thickness l_B in all the materials due to a decrease in tunneling probability.

B. f -sum rule

The behavior of m_{\perp} and m_{\parallel} of SL band C1 at $\mathbf{K}=0$ can also be understood in terms of the f -sum rule, Eq. (8),

with $f_{L,C1}^{\alpha}$ given by Eq. (9). Type-I SL's have already been discussed in Ref. 1. We focus here on the somewhat more complicated type-II case, InAs/GaSb, for which the electron and hole envelope functions are confined in separate layers. Figure 4 shows the variation of $E_L(0)$, $(2/m)|P_{L,C1}^{\alpha}|^2$, and $f_{L,C1}^{\alpha}$ ($\alpha=\perp, \parallel$) for $L=C2, C1, \text{HH1}$, and LH1 (where HH denotes heavy hole and LH denotes light hole) as a function of well and barrier widths for InAs/GaSb. Three typical sets of layer widths (60 Å/40 Å, 40 Å/40 Å and 40 Å/60 Å) are considered to illustrate the behavior. The (40 Å InAs)/(40 Å GaSb) SL is used as a reference. The f -sum rule contributions to C1 from bands other than those given above are also listed, as are the values of m_{\perp} and m_{\parallel} obtained from Eq. (8). As shown by sketches for the (40 Å InAs)/(40 Å GaSb) SL, the $F_n(L,0;z)$'s are concentrated in InAs (layer A) for the electron states (C1, C2) and in GaSb (layer B) for the hole states (HH1, LH1). The Γ_8 (VB) edge of GaSb is taken to be the zero of energy.

We first focus on C2 and C1. The C1 \rightarrow C2 properties of InAs/GaSb are representative of those of type-I and type-III SL's. As indicated by the upward arrow in the C2 column, increasing l_A (the electron well width) from 40 to 60 Å at fixed $l_B=40$ Å causes $E_{C2}(0)$ to decrease from 0.67 to 0.42 eV, and $E_{C1}(0)$ to decrease from 0.16 to 0.052 eV due to a reduction in the electron confinement energy. Hence the energy difference $\Delta E_{C2,C1}(0)=E_{C2}(0)-E_{C1}(0)$ decreases. The energy $(2/m)|P_{C2,C1}^{\perp}|^2=(2/m)|\langle C2,0|p_{\perp}|C1,0\rangle|^2$ decreases from 4.9 to 4.5 eV as l_A increases since $(2/m)|P_{C2,C1}^{\perp}|^2$ vanishes in the bulk limit of pure A material. However,

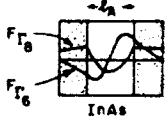
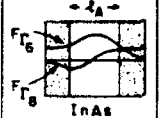
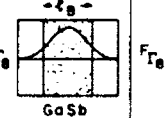
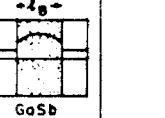
L	C2	C1	HH1	LH1		
$F_n(L,0;z)$						
$E_L(0)$ (eV)	l_A, l_B 60:40 \rightarrow 0.42 40:40 \rightarrow 0.67 40:60 \rightarrow 0.64	0.052 0.16 0.18	-0.040 -0.040 -0.020	-0.16 -0.16 -0.10		
$\frac{2}{m} P_{L,C1}^{\perp} ^2$ (eV)	60:40 4.5 40:40 4.9 40:60 7.1		0	7.0 8.5 6.2	Other Bands	m_{\perp}/m_0
$f_{L,C1}^{\perp}$	60:40 -12 40:40 -9.6 40:60 -15		0	30 27 22	14 9.8 11	0.031 0.036 0.057
$\frac{2}{m} P_{L,C1}^{\parallel} ^2$ (eV)	60:40 0.10 40:40 0.15 40:60 0.19		0.88 1.6 1.1	0.35 0.71 0.35	Other Bands	m_{\parallel}/m_0
$f_{L,C1}^{\parallel}$	60:40 -0.28 40:40 -0.29 40:60 -0.42		9.6 8.4 5.3	1.5 2.2 1.2	24 18 19	0.029 0.034 0.040

FIG. 4. Energies $E_L(0)$, $(2/m)|P_{L,C1}^{\perp}|^2=(2/m)|\langle L,0|p_{\perp}|C1,0\rangle|^2$, and oscillator strengths $f_{L,C1}^{\alpha}$ for l_A InAs/ l_B GaSb superlattice. Results are given for three sets of layer widths: 60 Å/40 Å, 40 Å/40 Å, and 40 Å/60 Å. The upward and downward arrows indicate increasing InAs (l_A) and GaSb (l_B) width, respectively. Dominant envelope functions are shown for the important $\mathbf{K}=0$ superlattice states $L=C2, C1, \text{HH1}$, and LH1 in the (40 Å InAs)/(40 Å GaSb) superlattice. The total contribution from other superlattice bands is also listed. Superlattice masses are calculated using the f -sum rule Eq. (8).

$f_{C2,C1}^{\perp}$ increases in magnitude (from -9.6 to -12) because of the dominating variation of the energy denominator.

Along the same lines, as indicated by the downward arrow in the C2 column, increasing l_B (the electron barrier) from 40 to 60 Å at fixed $l_A = 40$ Å causes $\Delta E_{C2,C1}(0)$ to decrease. This change is small because the electron energies are insensitive to l_B for sufficiently thick barriers. The energy $(2/m)|P_{C2,C1}^{\perp}|^2$ increases from 4.9 to 7.1 as l_B increases because the deviation from bulk A behavior becomes larger. Alternatively, the increase in $(2/m)|P_{C2,C1}^{\perp}|^2$ can be viewed as resulting from the increased effectiveness of the barriers in supplying crystal momentum. The net result is an increase in the magnitude of $f_{C2,C1}^{\perp}$ from -9.6 to -15 . The quantities $(2/m)|P_{C2,C1}^{\perp}|^2$ and $f_{C2,C1}^{\perp}$ are negligible since the parallel direction is essentially bulklike. We note in passing that a $(40$ Å GaAs)/(40 Å $\text{Ga}_{1-x}\text{Al}_x\text{As}$) SL has a smaller energy $(2/m)|P_{C2,C1}^{\perp}|^2$ ($=1.5$ eV) associated with the C1-C2 matrix element¹ than $(40$ Å InAs)/(40 Å GaSb) because InAs, where the C1 \rightarrow C2 transition occurs, is far more nonparabolic than its GaAs counterpart.

There are several differences between the intersubband C1 \rightarrow C2 and valence-conduction-band VB \rightarrow C1 properties (where VB \equiv HH1, LH1) of InAs/GaSb. In contrast to the electron energies $E_{C1}(0)$ and $E_{C2}(0)$, the hole energy $E_{VB}(0)$ is more sensitive to l_B than l_A for large l_B , since the hole is located in the B layer. Furthermore, the energies $(2/m)|P_{VB,C1}^{\perp}|^2 = (2/m)|\langle \text{VB}, 0 | p_{\perp} | C1, 0 \rangle|^2$ are small compared to the bulk VB \rightarrow CB value of 15 eV since the electron and hole are in adjacent layers. (Recall that $(2/m)|P_{C2,C1}^{\perp}|^2$ is smaller because of its intraband character.) The oscillator strength $f_{VB,C1}^{\perp}$ can however still be appreciable since $\Delta E_{C1,VB}(0) = E_{C1}(0) - E_{VB}(0)$ is also small. The quantity $f_{HH1,C1}^{\perp}$ vanishes because of the selection rules mentioned in Sec. II.

Unlike $(2/m)|P_{C2,C1}^{\perp}|^2$ which increases as l_B increases, the energies $(2/m)|P_{VB,C1}^{\perp}|^2$ decrease as either l_A or l_B is made larger. Specifically, for fixed $l_A = 40$ Å, increasing l_B from 40 to 60 Å causes both the electron and hole barriers to become more effective since the electron barrier thickness and the effective hole barrier height increase. As a result the electron-hole overlap is reduced. The decrease in $(2/m)|P_{VB,C1}^{\perp}|^2$ as l_A is increased for fixed $l_B = 40$ Å can be understood using a similar argument. In this case the hole barrier thickness and the effective electron barrier height increase.

In contrast to type-I SL's (Ref. 1) the values of m_1 shown in Fig. 4 are small and comparable to the VCA mass [see Fig. 3(b)] despite the fact that $f_{C2,C1}^{\perp}$ is large. Furthermore the contributions to the f -sum rule from HH1 and LH1 are small. The contributions from the excited hole states are therefore important as indicated in the column "Other Bands." For type-II SL, excited hole states near the top of the (Γ_8) hole well can leak into layer A thereby increasing the electron-hole overlap which leads to an appreciable contribution to the f -sum rule.

C. Finite \mathbf{K} properties

The results for the SL energies and matrix elements at $\mathbf{K} = 0$ can be used to obtain the band structure $E_L(\mathbf{K})$ for

$\mathbf{K} \neq 0$ by diagonalizing the SL $\mathbf{K} \cdot \mathbf{p}$ matrix in Eq. (7). The SL matrix elements $P_{LL'}(\mathbf{K}) = \langle L, \mathbf{K} | p | L', \mathbf{K} \rangle$ for finite \mathbf{K} are then calculated using the relationship $P_{LL'}(\mathbf{K}) = \sum_{MM'} c_{LM}^*(\mathbf{K}) c_{LM'}(\mathbf{K}) \langle M0 | p | M'0 \rangle$, which follows from Eq. (6). The resulting SL properties are illustrated in Fig. 5 which shows $E_L(\mathbf{K})$ and $(2/m)|P_{LL'}(\mathbf{K})|^2 = (2/m)|\langle L, \mathbf{K} | p | L', \mathbf{K} \rangle|^2$ for $(190$ Å GaAs)/(200 Å $\text{Ga}_{0.75}\text{Al}_{0.25}\text{As}$), $(37$ Å InAs)/(37 Å GaSb), and $(58$ Å HgTe)/(42 Å $\text{Hg}_{0.15}\text{Cd}_{0.85}\text{Te}$) along the K_x and K_z directions. Both $E_L(\mathbf{K})$ and $(2/m)|P_{LL'}(\mathbf{K})|^2$ are independent of the direction of \mathbf{K} within the present model.

The valence-band structure calculated by Chang and Schulman²⁰ utilizing an elaborate tight-binding approach, which has been widely used, is shown by the dashed line for the GaAs/ $\text{Ga}_{1-x}\text{Al}_x\text{As}$ SL. The agreement with the present results is good for both the band structure and matrix elements even though only eight $|L, 0\rangle$'s were explicitly included in the SL $\mathbf{K} \cdot \mathbf{p}$ matrix of Eq. (7), all other $|L, 0\rangle$'s lying in the energy range from -2 to 2 eV being treated perturbatively. Sixteen $|L, 0\rangle$'s were explicitly included in Eq. (7) in the cases of the InAs/GaSb and HgTe/ $\text{Hg}_{1-x}\text{Cd}_x\text{Te}$ SL's in order to facilitate the calculation of optical properties, to be discussed in Sec. IV, over a wider energy range.

The C1 energy band for $K_z = 0$, given by $E_{C1}(K_x)$, is reasonably parabolic in the K_x direction for each of the three SL's. However, the topmost valence bands show large nonparabolicity beyond π/d as a result of hybridization. The relative ordering of the LH1 and HH2 bands for each SL depends on the particular choice of SL layer widths. At $\mathbf{K} = 0$ HH1 and LH1 are repelled strongly by C1 in the K_x direction. The repulsion between LH1 and HH2 is also appreciable since the bands are close in energy. LH1 therefore bends upward in the parallel direction for the InAs/GaSb SL due to the ordering of the LH1 and HH2 bands but bends down for the GaAs/ $\text{Ga}_{1-x}\text{Al}_x\text{As}$ and HgTe/ $\text{Hg}_{1-x}\text{Cd}_x\text{Te}$ SL's. At finite K_x in the three SL's, the HH1 band contains a $|C1, 0\rangle$ component to first order in the $\mathbf{K} \cdot \mathbf{p}$ interaction, and hence indirectly acquires a $|LH1, 0\rangle$ component to second order in the $\mathbf{K} \cdot \mathbf{p}$ interaction. This leads to an anticrossing of HH1 and HH2 in the GaAs/ $\text{Ga}_{1-x}\text{Al}_x\text{As}$ SL and the HgTe/ $\text{Hg}_{1-x}\text{Cd}_x\text{Te}$ SL at finite K_x . In the InAs/GaSb SL the anticrossing involves LH1 and HH1. The HH3 band is flat in the parallel direction for the GaAs/ $\text{Ga}_{1-x}\text{Al}_x\text{As}$ SL since HH3 is not included in the more limited set used for this SL.

The energies $(2/m)|P_{LL'}(\mathbf{K})|^2 = (2/m)|\langle L, \mathbf{K} | p | L', \mathbf{K} \rangle|^2$ shown in Fig. 5 are relevant to the calculation of fundamental optical absorption discussed in Sec. IV, where the incident light propagates along the $z(1)$ axis and the polarization vector lies in the $xy(11)$ plane. At $K_z = 0$ the energies $(2/m)|P_{LL'}(\mathbf{K})|^2$ depend sensitively on K_x due to the significant hybridization of the SL valence bands. In the GaAs/ $\text{Ga}_{1-x}\text{Al}_x\text{As}$ SL the crossing of LH1 and HH3 causes $(2/m)|P_{C1,LH1}^{\perp}(\mathbf{K})|^2$ to drop abruptly to zero at the LH1-HH3 crossing point. For larger K_x the now uppermost HH3 band does not interact with C1. The values of

$(2/m)|P_{LL'}^{\parallel}(\mathbf{K})|^2$ for the HgTe/Hg_{1-x}Cd_xTe SL are seen to be smaller than those of the GaAs/Ga_{1-x}Al_xAs SL. The state |C1,0> in the HgTe/Hg_{1-x}Cd_xTe SL has an appreciable F_{Γ_8} component since the bulk HgTe conduction-band edge has Γ_8 symmetry, thereby reducing the matrix element between C1 and the SL valence bands. By contrast the InAs/GaSb matrix elements are small because the electron and hole are separated, as discussed in Sec. III B. In the HgTe/Hg_{1-x}Cd_xTe SL the value of $(2/m)|P_{C2,HH2}^{\parallel}(\mathbf{K})|^2$ is nearly equal to that of $(2/m)|P_{C1,HH1}^{\parallel}(\mathbf{K})|^2$ because the envelope functions corresponding to C2 and HH2 both resemble first excited states in the same well.

The perpendicular band structure for $K_{\parallel}=0$, given by $E_L(K_{\perp})$, shows essentially no dispersion for the GaAs/Ga_{1-x}Al_xAs SL since the Ga_{1-x}Al_xAs layer is thick. The $K_{\parallel}=0$ energy $(2/m)|P_{LL'}^{\parallel}(K_{\perp})|^2$ shows a weak dependence on K_{\perp} for GaAs/Ga_{1-x}Al_xAs and HgTe/Hg_{1-x}Cd_xTe, in contrast to the InAs/GaSb SL. The stronger dependence in InAs/GaSb is associated with the electron and hole lying in different wells and has been discussed previously by Voisin *et al.*²⁷ In the InAs/GaSb SL, the interchange of $(2/m)|P_{C1,LH1}^{\parallel}(K_{\perp})|^2$ and $(2/m)|P_{C1,HH2}^{\parallel}(K_{\perp})|^2$ at finite K_{\perp} is associated with

the crossing of the LH1 and HH2 bands.

The preceding results all pertain to the valence-band offsets Λ listed in Table V. One of the remarkable properties of the HgTe/CdTe electronic structure is that a semiconductor \rightarrow semimetal \rightarrow semiconductor transition occurs as the valence-band offset Λ (cf. Fig. 2) is increased from $\Lambda=0$. This behavior underlies our recently proposed resolution of the valence-band offset controversy in HgTe/CdTe SL's.³ Explicitly it was shown in Ref. 3 that a large offset value ($\Lambda \approx 350$ meV) is indeed consistent with the magneto-optical data of Berroir *et al.*²⁸ obtained from an unintentionally doped (100 Å HgTe)/(36 Å CdTe) SL sample. The experimental data had previously been interpreted as being uniquely associated with a small offset $\Lambda \approx 40$ meV.

Figure 6 shows the band structure for the (100 Å HgTe)/(36 Å CdTe) SL for $\Lambda=40, 230$, and 350 meV. For small Λ (~ 40 meV) C1 lies above HH1 and the SL is semiconducting. As Λ is increased C1 drops in energy until it touches HH1 for $\Lambda=230$ meV, and the SL becomes semimetallic. For $\Lambda > 295$ meV the SL is semiconducting once again as a result of the uncrossing of the C1 and HH1 bands. The band gap in this region is still direct but it occurs at the SL Brillouin-zone face $K_{\perp}=\pi/d$, as shown for $\Lambda=350$ meV.

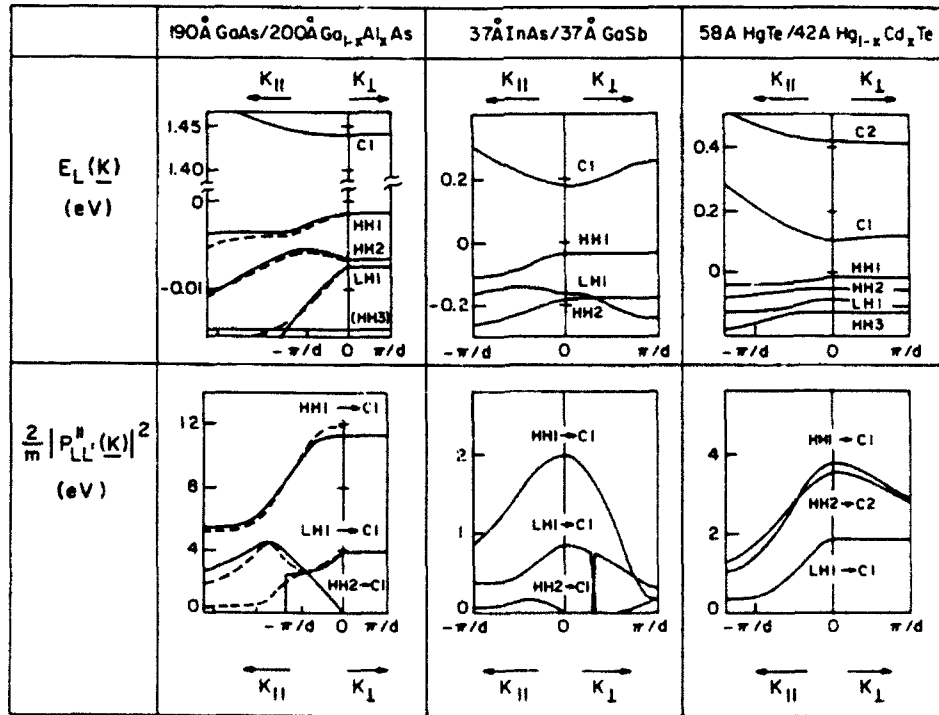


FIG. 5. Band structures $E_L(\mathbf{K})$ and energies $(2/m)|P_{LL'}^{\parallel}(\mathbf{K})|^2 = (2/m)|\langle L, \mathbf{K} | p_{\parallel} | L', \mathbf{K} \rangle|^2$ for (190 Å GaAs)/(200 Å Ga_{0.75}Al_{0.25}As), (37 Å InAs)/(37 Å GaSb), and (58 Å HgTe)/(42 Å Hg_{0.15}Cd_{0.85}Te) superlattices shown as functions of K_{\parallel} and K_{\perp} . The origin of energy is defined as the valence-band (Γ_8) edge of GaAs, GaSb, and HgTe, respectively. The label $L' \rightarrow L$ indicates the transition corresponding to $(2/m)|P_{LL'}^{\parallel}(\mathbf{K})|^2$. The superlattice growth axis is along the \perp direction. The tight-binding results of Chang and Schulman (Ref. 26) are shown (dashed line) for comparison.

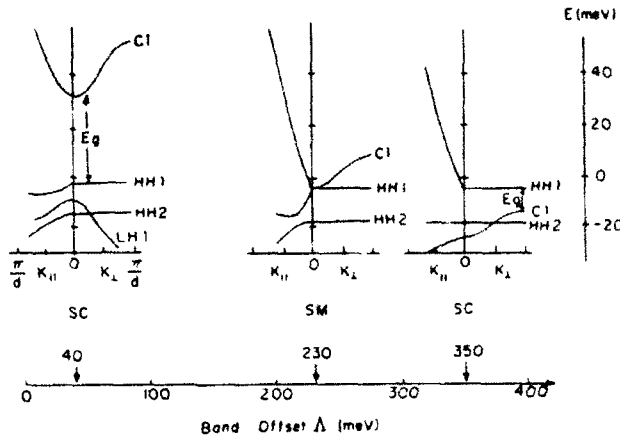


FIG. 6. The band structures for a (100 Å HgTe)/(36 Å CdTe) superlattice as a function of band offset Δ . As Δ increases, the system changes from semiconducting (SC) to semimetallic (SM) and back to semiconducting due to the crossing and uncrossing of the C1 and HH1 bands.

Figure 7 shows the nearly cylindrical constant energy surfaces of HH1 along $K_{||}$ and K_{\perp} for the (100 Å HgTe)/(36 Å CdTe) SL with $\Delta = 350$ meV. Energies are measured from the bottom of the HH1 band (0 meV). The bulges are a consequence of the K_{\perp} dependence of the in-plane band structure. Assuming reasonable values of the intrinsic electron concentration ($n_c \geq 2 \times 10^{16} \text{ cm}^{-3}$) the calculated cyclotron mass is consistent with the zero field experimental value of 0.015 ± 0.003 . Recently, unintentional doping concentrations of $n_c \sim 5 \times 10^{15} \text{ cm}^{-3}$ have been measured in other HgTe/CdTe samples.²⁹ Using $n_c = 5 \times 10^{15} \text{ cm}^{-3}$, the calculated cyclotron mass becomes consistent with the experimental value for a band offset of $\Delta \approx 370$ meV,³⁰ or possibly even a somewhat larger value.³¹

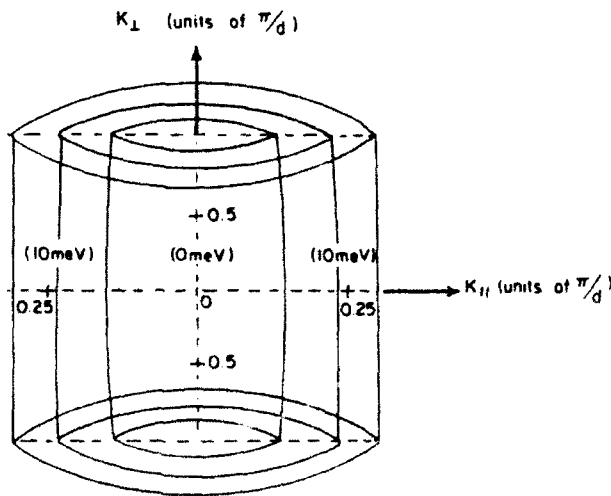


FIG. 7. Constant energy surfaces along $K_{||}$ and K_{\perp} of HH1 for a (100 Å HgTe)/(36 Å CdTe) superlattice with $\Delta = 350$ meV.

IV. OPTICAL PROPERTIES

The results of Sec. III C permit evaluation of the imaginary part of the dielectric function at frequency ω given by

$$\epsilon_2(\omega) = \frac{4\pi^2 e^2}{\hbar m^2 \omega^2} \sum_{LL'} \int \frac{d\mathbf{K}}{(2\pi)^3} \langle L\mathbf{K} | \hat{\mathbf{e}} \cdot \mathbf{p} | L'\mathbf{K} \rangle^2 \times \delta \left[\omega - \frac{E_L(\mathbf{K}) - E_{L'}(\mathbf{K})}{\hbar} \right] \times [f(E_L(\mathbf{K})) - f(E_{L'}(\mathbf{K}))] = 2n(\omega)\kappa(\omega) \quad (15)$$

where $L(L')$ is the SL band index of the initial (final) state, \mathbf{K} is the SL wave vector and $f(E)$ is the Fermi-Dirac distribution. The unit vector $\hat{\mathbf{e}}$ defines the polarization of incoming light. The quantities $n(\omega)$ and $\kappa(\omega)$ are the real and imaginary parts of the refractive index.

The two optical processes of interest are fundamental absorption involving transitions between SL valence and conduction bands (Sec. IV A), and intersubband absorption involving transitions between the lowest two SL conduction bands C1 and C2 (Sec. IV B). Fundamental absorption in SL's is appreciable regardless of the polarization of the incident light, although for the cases of interest in Sec. IV A the polarization vector $\hat{\mathbf{e}}$ lies in the plane of the layers. Intersubband absorption is only appreciable if the polarization vector $\hat{\mathbf{e}}$ is perpendicular to the plane of the layers, and if there are carriers in C1.

The imaginary part of the dielectric function $\epsilon_2(\omega) = 2n(\omega)\kappa(\omega)$ can be written as

$$\epsilon_2(\omega) = \epsilon_2^0(\omega) + \delta\epsilon_2^{C2,C1}(\omega) + \delta\epsilon_2^{CB,VB}(\omega) \quad (16)$$

where $\delta\epsilon_2^{C2,C1}(\omega)$ is associated with C1 \rightarrow C2 absorption, $\delta\epsilon_2^{CB,VB}(\omega)$ is associated with fundamental absorption between SL valence (VB) and conduction (CB) bands within ~ 0.5 eV of the onset, and $\epsilon_2^0(\omega)$ is the contribution associated with other occupied states. The real part of the dielectric function $\epsilon_1(\omega) \equiv n^2(\omega) - \kappa^2(\omega)$ is given by

$$\epsilon_1(\omega) = \epsilon_1^0(\omega) + \delta\epsilon_1^{C2,C1}(\omega) + \delta\epsilon_1^{CB,VB}(\omega) \quad (17)$$

where the individual contributions $\delta\epsilon_1^{C2,C1}(\omega)$, $\delta\epsilon_1^{CB,VB}(\omega)$, and $\epsilon_1^0(\omega)$ are obtained from $\delta\epsilon_2^{C2,C1}(\omega)$, $\delta\epsilon_2^{CB,VB}(\omega)$, and $\epsilon_2^0(\omega)$, respectively, using a Kramers-Kronig relation. The real part of the refractive index $n(\omega)$ is related to $\epsilon_1(\omega)$ and $\epsilon_2(\omega)$ by

$$n(\omega) = \left[\frac{\epsilon_1(\omega)}{2} + \frac{1}{2} [\epsilon_1^2(\omega) + \epsilon_2^2(\omega)]^{1/2} \right]^{1/2} \quad (18)$$

The absorption coefficient is defined as

$$\alpha(\omega) = \omega \epsilon_2(\omega) / n(\omega) c \quad (19)$$

For light polarized perpendicular to the layers the C1 \rightarrow C2 contribution to $\epsilon_2(\omega)$, given by $\delta\epsilon_2^{C2,C1}(\omega)$ in Eq. (16), is appreciable over a narrow energy range and at energies far below the onset of VB \rightarrow CB transitions for the cases of interest. The corresponding contribution to $\epsilon_1(\omega)$, given by $\delta\epsilon_1^{C2,C1}(\omega)$ in Eq. (17), is a strong function

of ω in this frequency range and is equal to the principal part of $(2/\pi) \int_0^\infty d\omega' \omega' \delta\epsilon_2^{C2,C1}(\omega')/(\omega'^2 - \omega^2)$. The frequency dependence of the refractive index $n(\omega)$ [Eq. (18)] must therefore be taken into account in calculating the intersubband absorption $\alpha(\omega)$ [Eq. (19)].

By contrast, the contribution $\epsilon_2^0(\omega)$ in Eq. (16) has a broad structure regardless of the polarization of incident light and only becomes appreciable at high energies (> 2 eV). The corresponding contribution to $\epsilon_1(\omega)$, given by $\epsilon_1^0(\omega)$ in Eq. (17), is therefore reasonably independent of frequency ω over the energy range of interest $0 < \hbar\omega < 0.5$ eV. In addition $\epsilon_1^0(\omega)$ dominates $\delta\epsilon_1^{CB,VB}(\omega)$. For fundamental absorption with light polarized within the layer plane $\delta\epsilon_2^{C2,C1}(\omega)$ and $\delta\epsilon_1^{C2,C1}(\omega)$ are negligible; hence the refractive index $n(\omega)$ can be taken to be constant near the fundamental absorption edge. We have estimated the actual variation in $n(\omega)$ to be less than 10% using a two-band SL model.

A. Fundamental absorption

Figure 8 compares the experimental absorption curve (dashed line) for a (37 Å InAs)/(37 Å GaSb) SL at $T=4$ K (Ref. 8) with the present theoretical results (solid line). The agreement is seen to be satisfactory. The absorption coefficient $\alpha(E)$ is an order of magnitude smaller than that of a direct-gap bulk material because the electron and hole in the SL are concentrated in separate layers resulting in reduced overlap. The structure in $\alpha(E)$ mainly arises from the transitions HH1→C1 and LH1→C1 whose onsets are indicated by arrows. The corresponding partial contributions are indicated by long-dashed lines. The tail of the experimental absorption curve, which is

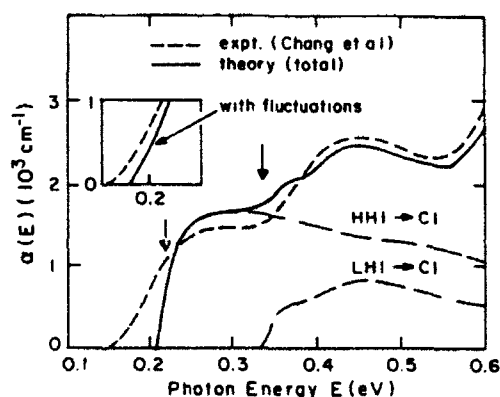


FIG. 8. Comparison of experimental coefficients (short-dashed line) of Chang *et al.* (Ref. 8) and theoretical (solid line) fundamental absorption coefficients $\alpha(E)$ as functions of photon energy E for (37 Å InAs)/(37 Å GaSb) at $T=4$ K. Dominant partial contributions are shown (long-dashed line). Inset: experimental vs theoretical tail of $\alpha(E)$ including a ± 4 -Å layer width fluctuation in the theory, at constant superlattice period.

not reproduced by the theory, is possibly due to disorder in the SL layer widths. The inset in Fig. 8 shows the modified theoretical absorption curve allowing for a randomly distributed ± 4 -Å fluctuation (corresponding to about a monolayer) in the individual layer widths, but keeping the SL period constant at 74 Å.

Figure 9 shows a similar comparison between the experimental⁷ and theoretical absorption curves for a (58 Å HgTe)/(42 Å Hg_{1-x}Cd_xTe) SL at room temperature. The experimental results of Lansari *et al.*⁷ (dashed line) are demonstrably reproducible in the sense that two separate samples grown under the same conditions yield an identical $\alpha(E)$ curve.⁷ The experimental data show no evidence of a theoretically inexplicable tail, possibly indicating that the corresponding disorder in the InAs/GaSb sample is absent in the HgTe/Hg_{1-x}Cd_xTe samples. The theoretical curve for $\Lambda=350$ meV (solid line) is in remarkable agreement with the experimental data. Although $\alpha(E)$ is not very sensitive to Λ the agreement between experiment and theory is better for $\Lambda=350$ meV than for $\Lambda=40$ meV (dashed-dotted line). The partial contributions for $\Lambda=350$ meV, shown by long-dashed lines, are again dominated by the HH1→C1 and LH1→C1 transitions at energies near the fundamental SL gap. The HH2→C2 contribution near $E \sim 0.5$ eV becomes comparable in magnitude to that of HH1→C1 since the corresponding matrix elements are nearly equal (Sec. III C). The HH3→C3 contribution is large for $E \sim 0.8$ eV. Calculation of $\alpha(E)$ for $E > 0.55$ eV is difficult since many SL bands contribute, and $E_L(K)$ is required for large K_{\parallel} values. The HH3→C3 contribution, shown by the dotted lines, was therefore included

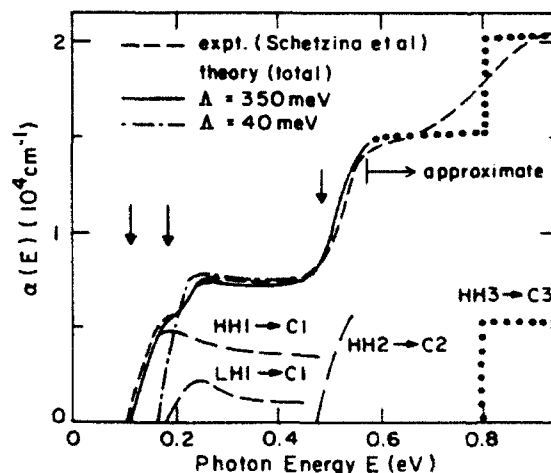


FIG. 9. Comparison of experimental coefficients (short-dashed line) of Lansari *et al.* (Ref. 7) and theoretical (solid line) fundamental absorption coefficients $\alpha(E)$ as a function of photon energy E for (58 Å HgTe)/(42 Å Hg_{0.15}Cd_{0.85}Te) at $T=300$ K. Λ is taken as 350 meV. Dominant partial contributions are shown (long-dashed line). Theoretical curve above $E=0.55$ eV is approximate (shown dotted). The theoretical absorption curve using $\Lambda=40$ meV is indicated by a dashed-dotted line.

approximately in Fig. 9 using a two-dimensional density of states and a \mathbf{K} -independent SL matrix element. The observed structure in all cases, even the last, coincides with theoretically expected transitions.

The fundamental absorption in the GaAs/Ga_{1-x}Al_xAs SL was not considered due to the importance of excitons which are not included in the present theory.

B. Intersubband absorption

In contrast to fundamental absorption, the C1→C2 absorption is only appreciable if the C1 band contains carriers, and the incident light is polarized perpendicular to the layers. The dependence of the C1→C2 absorption on the light polarization follows from the anisotropy of the C1→C2 oscillator strength $f_{C2,C1}^{\perp}$ discussed in Sec. III B (cf. Fig. 4). Several practical applications of the strong C1→C2 absorption have recently been suggested.

a. Carrier-activated light modulators. High-speed carrier-activated light modulation is possible in thick-barrier SL's (Ref. 2) where the C1→C2 absorption is large ($\sim 10^4 \text{ cm}^{-1}$) and narrow ($\sim 10 \text{ meV}$) as a result of the large C1→C2 oscillator strength $f_{C2,C1}^{\perp}$ and the fact that the C1 and C2 bands are essentially parallel in all directions. The properties of $\alpha(E)$ and $n(E)$ will be illustrated here by considering an (80 Å GaAs)/(160 Å Ga_{1-x}Al_xAs) SL.

b. Infrared detectors. Levine *et al.*¹² have proposed an infrared detector consisting of GaAs/Ga_{1-x}Al_xAs quantum wells with sufficiently thin well layers such that C2

lies in the continuum. The C1→C2 absorption of Ref. 12 is smaller and broader than for the case of Ref. 2 where both C1 and C2 are below the top of the well. As shown here, a thin-barrier SL also gives rise to a broad $\alpha(E)$ having a magnitude comparable to that of Ref. 12 ($\sim 10^3 \text{ cm}^{-1}$). This is because the oscillator strength $f_{C2,C1}^{\perp}$ is small in the thin-barrier SL (Sec. III B) and the C1 and C2 bands have finite dispersions along the perpendicular direction. The specific thin layer SL system chosen here, (40 Å In_xGa_{1-x}As)/(20 Å In_yAl_{1-y}As) which corresponds to the bulk materials suggested by Levine *et al.*,¹⁰ exhibits a larger high-energy cutoff for $\alpha(E)$ than a GaAs/Ga_{1-x}Al_xAs SL of comparable layer widths. In the GaAs/Ga_{1-x}Al_xAs SL, the Ga_{1-x}Al_xAs X-point minimum imposes a lower wavelength limit of $\sim 5 \mu\text{m}$,¹⁰ whereas in In_xGa_{1-x}As/In_yAl_{1-y}As the limit is $\sim 2 \mu\text{m}$.

1. Thick-barrier limit

Equation (15) can be used to obtain a simple analytic form for $\delta\epsilon_2^{C2,C1}(\omega)$ for wide-gap SL's such as GaAs/Ga_{1-x}Al_xAs in the thick-barrier limit. The C1 and C2 bands are dispersionless along the perpendicular direction. The in-plane dispersions of C1 and C2 are parabolic to a good approximation, with masses $m_{C1,\parallel}$ and $m_{C2,\parallel}$, respectively. In addition the matrix element $|\langle C1, \mathbf{K} | p_{\parallel} | C2, \mathbf{K} \rangle|^2$ is essentially independent of \mathbf{K} because the two bands are nearly parallel.

At $T=0 \text{ K}$ the expression for $\delta\epsilon_2^{C2,C1}(\omega)$ reduces to

$$\delta\epsilon_2^{C2,C1}(\omega) = \begin{cases} \frac{4\pi^2 e^2}{m^2 \omega^2} \left[\frac{m_{r,\parallel}}{\pi \hbar^2 d} \right] |\langle C1, 0 | p_{\parallel} | C2, 0 \rangle|^2 & \text{if } E_g^{C2,C1}(0) > \hbar\omega > E_g^{C2,C1}(K_{\parallel} = K_F) \\ 0 & \text{otherwise} \end{cases} \quad (20)$$

where $(m_{r,\parallel}/\pi \hbar^2 d)$ is the C1→C2 joint density of states with $m_{r,\parallel}/m = (m/m_{C1,\parallel} - m/m_{C2,\parallel})^{-1}$. The in-plane masses $m_{C1,\parallel}$ and $m_{C2,\parallel}$ differ slightly because of nonparabolic band effects in the bulk. The low-energy cutoff for $\delta\epsilon_2^{C2,C1}(\omega)$ is $E_g^{C2,C1}(K_{\parallel} = K_F)$ where $E_g^{C2,C1}(K_{\parallel}) = E_{C2}(K_{\parallel}) - E_{C1}(K_{\parallel})$ and K_F is the Fermi wave vector along the parallel direction. It follows that the absorption width $E_g^{C2,C1}(0) - E_g^{C2,C1}(K_{\parallel} = K_F)$ is $\pi n_{C1} \hbar^2 d / m_{r,\parallel}$ where n_{C1} is the concentration of electrons in C1 and $n_{C2} = 0$.

Since C1 and C2 are essentially parallel, $m_{r,\parallel}$ is large, and therefore $\delta\epsilon_2^{C2,C1}(\omega)$ is large and narrow. Figure 10 shows the corresponding $\alpha(E)$ (dashed line) and $n(E)$ (solid line) for (80 Å GaAs)/(160 Å Ga_{0.7}Al_{0.3}As) at $T=300 \text{ K}$ with $n_{C1} = 5 \times 10^{17} \text{ cm}^{-3}$. The 5-meV width is comparable to a laser linewidth. The sharp structure in $\alpha(E)$ is accompanied by a large variation in the refractive index $n(E)$. The sensitivity of $n(E)$ to the photon energy E has potential application in high-speed light modulation.² The slight smearing on the low-energy side of $\alpha(E)$ is due to the finite temperature Fermi distribution.

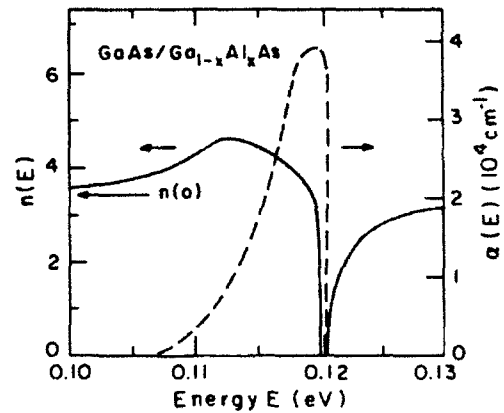


FIG. 10. Calculated refractive index $n(E)$ (solid line; left-hand scale) and absorption coefficient $\alpha(E)$ (dashed line; right-hand scale) vs photon energy E for (80 Å GaAs)/(160 Å Ga_{0.7}Al_{0.3}As) at $T=300 \text{ K}$, for C1 electron concentration $n_{C1} = 5 \times 10^{17} \text{ cm}^{-3}$. The incident light is polarized perpendicular to the layers.

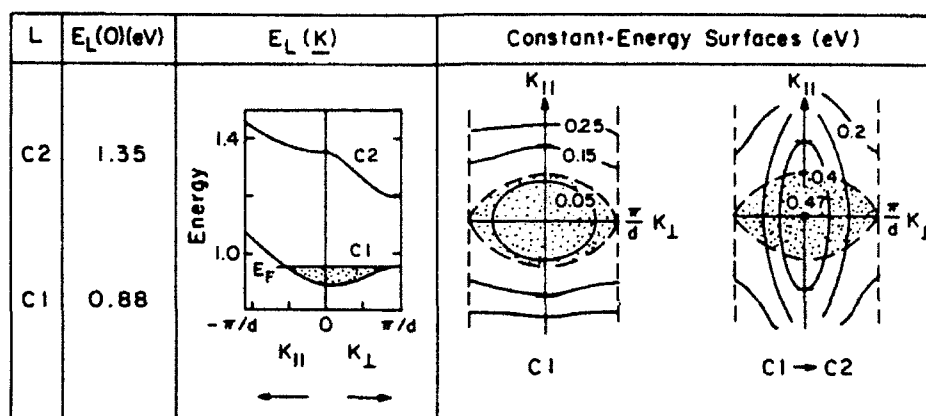


FIG. 11. C1 and C2 band structure for $(40 \text{ \AA In}_{0.53}\text{Ga}_{0.47}\text{As})/(20 \text{ \AA In}_{0.52}\text{Al}_{0.48}\text{As})$, together with C1 constant energy surfaces and C1 \rightarrow C2 constant energy surfaces. The chemical potential $E_F(T=60 \text{ K})=0.065 \text{ eV}$ corresponds to a C1 electron concentration of $n_{C1}=1.4 \times 10^{18} \text{ cm}^{-3}$. The shaded region of \underline{K} space corresponds to \underline{K} points at which the probability of occupation of C1 is greater than $\frac{1}{2}$.

The results plotted in Fig. 10 obey the sum rule

$$\int_0^\infty \omega \delta \epsilon_2^{C2,C1}(\omega) d\omega \approx \frac{2n_c \pi^2 e^2}{m_c^*} = \frac{\pi}{2} \omega_p^2, \quad (21)$$

where n_c is the electron density, m_c^* is the bulk electron mass ($m_c^* \sim 0.07m$), and the plasma frequency $\omega_p^2 = 4\pi n_c e^2 / m_c^*$, to a good approximation. This will not be the case for the thin-barrier SL to be discussed later. The magnitude of the absorption curve in the thick-barrier SL, which is larger than that for the interband bulk absorption, is a consequence of its narrow energy range. Substituting the general expression for $\delta \epsilon_2^{C2,C1}(\omega)$ in a thick-barrier SL [Eq. (20)] into Eq. (21) yields $|f_{C2,C1}^1| \approx m/m_c^*$. This approximate result for $|f_{C2,C1}^1|$ is verified for the $(80 \text{ \AA GaAs})/(160 \text{ \AA Ga}_{1-x}\text{Al}_x\text{As})$ SL in Fig. 10 where $|f_{C2,C1}^1| = 13.5$ compared to $m/m_c^* = 15$.

Physically, the magnitude of $\alpha(E)$ in Fig. 10 can be understood using a bulk free carrier absorption model for the C1 \rightarrow C2 transition. Explicitly, the barrier (B) atoms are imagined to be homogeneously distributed throughout the SL sample giving rise to scattering of the electrons. The impurity concentration of B atoms required for a bulk free carrier absorption of magnitude $\sim 10^4 \text{ cm}^{-1}$ roughly corresponds to the concentration of barrier atoms within the spatial extent of the C1 envelope function in the barrier ($\sim 30 \text{ \AA}$).

2. Thin-barrier limit

Figure 11 shows the C1 and C2 band structure for $(40 \text{ \AA In}_{0.53}\text{Ga}_{0.47}\text{As})/(20 \text{ \AA In}_{0.52}\text{Al}_{0.48}\text{As})$ together with the C1 constant energy surfaces, and the C1 \rightarrow C2 constant energy surfaces. The nonzero dispersion of C1 and C2 along the perpendicular direction gives reduced nesting between the C1 and C2 bands compared to the thick-barrier case. The energy difference $E_{C2}(\underline{K}) - E_{C1}(\underline{K})$ is a maximum at $\underline{K}=0$ which represents a high-energy cutoff of 0.47 eV (2.6 \mu m) for the C1 \rightarrow C2 transition. The

$\underline{K}=0$ oscillator strength $f_{C2,C1}^1$ is -4.0 and therefore smaller than the thick-barrier GaAs/Ga $_{1-x}$ Al $_x$ As value of -13.5 . We consider the situation with carriers in C1 at temperature T , and a Fermi level at energy $E_F(T)$ above the C1 edge. The shaded portions in Fig. 11 correspond to the region in \underline{K} space where the C1 band is occupied for an electron concentration $n_{C1}=1.4 \times 10^{18} \text{ cm}^{-3}$ at $T=60 \text{ K}$ [$E_F(T)=0.065 \text{ eV}$]. The C2 band is empty, hence C1 \rightarrow C2 transitions will occur at wave vectors \underline{K} within this shaded region. As seen from the C1 \rightarrow C2 constant energy surfaces in Fig. 11, the number of C1 \rightarrow C2 transitions occurring at a given incident photon energy E is a weak function of E over the range

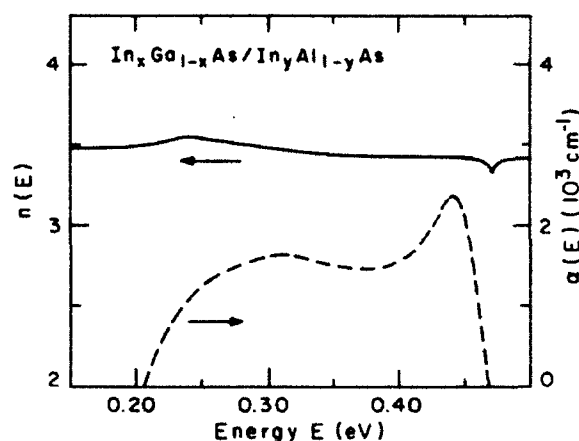


FIG. 12. Calculated refractive index $n(E)$ (solid line; left-hand scale) and absorption coefficient $\alpha(E)$ (dashed line; right-hand scale) vs photon energy E for $(40 \text{ \AA In}_{0.53}\text{Ga}_{0.47}\text{As})/(20 \text{ \AA In}_{0.52}\text{Al}_{0.48}\text{As})$ at $T=60 \text{ K}$, for C1 electron concentration $n_{C1}=1.4 \times 10^{18} \text{ cm}^{-3}$. The incident light is polarized perpendicular to the layers.

$0.25 < E < 0.45$ eV, therefore the absorption curve will be reasonably flat. Figure 12 shows the corresponding $\alpha(E)$ (dashed line) and $n(E)$ (solid line) for $(40 \text{ \AA} \text{ In}_x\text{Ga}_{1-x}\text{As})/(20 \text{ \AA} \text{ In}_y\text{Al}_{1-y}\text{As})$. The broad structure in $\alpha(E)$ yields a weaker variation in $n(E)$ than for the thick-barrier SL. The small peak in $\alpha(E)$ near 0.45 eV is reminiscent of a one-dimensional joint density of states and is associated with the near parallelism of $C1$ and $C2$ in the two in-plane (K_{\parallel}) directions.

In the thin-barrier limit considered in Fig. 12 the ϵ_2 -sum rule of Eq. (21) is only approximately half exhausted by the $C1 \rightarrow C2$ transition as a result of the finite band dispersion along the perpendicular direction. This effect causes nonzero free carrier absorption within $C1$ and also gives greater relative weight to transitions to higher minibands. The ϵ_2 -sum rule therefore provides an upper bound to the $C1 \rightarrow C2$ absorption strength in the thin-

barrier SL. The important consequence of the sum rule is that a narrow, large $C1 \rightarrow C2$ absorption in thick-barrier SL's becomes not only broader, but also considerably smaller for thin-barrier SL's than would be the case if the $C1 \rightarrow C2$ transition still exhausted the sum rule.

ACKNOWLEDGMENTS

This work was supported by the U.S. Defense Advanced Research Agency (DARPA) through U.S. Office of Naval Research (ONR) Contract No. N00014-86-K-0033 and by the U.S. Joint Service Electronics Program (JSEP) through ONR Contract Nos. N00014-84-K-0465 and N00014-89-J-1023. One of us (P.M.Y.) would like to acknowledge the Fannie and John Hertz Foundation for partial financial support.

*To whom all correspondence should be addressed.

¹N. F. Johnson, H. Ehrenreich, K. C. Hass, and T. C. McGill, *Phys. Rev. Lett.* **59**, 2352 (1987).

²N. F. Johnson, H. Ehrenreich, and R. V. Jones, *Appl. Phys. Lett.* **53**, 180 (1988).

³N. F. Johnson, P. M. Hui, and H. Ehrenreich, *Phys. Rev. Lett.* **61**, 1993 (1988); P. M. Hui, H. Ehrenreich, and N. F. Johnson, *J. Vac. Sci. Technol. A* **7**, 424 (1989).

⁴M. Altarelli, *Phys. Rev. B* **28**, 842 (1983).

⁵G. Bastard, in *Proceedings of the NATO Advanced Study Institute on Molecular Beam Epitaxy in Heterostructures, Erice, Italy, 1983*, edited by L. L. Chang and K. Ploog (Martinus-Nijhoff, Dordrecht, 1984), p. 381.

⁶N. F. Johnson, H. Ehrenreich, G. Y. Wu, and T. C. McGill, *Phys. Rev. B* **38**, 13095 (1988).

⁷Y. Lansari, J. W. Hans, S. Hwang, L. S. Kim, J. W. Cook, Jr., and J. F. Schetzina, *J. Vac. Sci. Technol. A* **7**, 241 (1989).

⁸L. L. Chang, G. A. Sai-Halasz, L. Esaki, and R. L. Aggarwal, *J. Vac. Sci. Technol.* **19**, 589 (1981).

⁹L. C. West and S. J. Eglash, *Appl. Phys. Lett.* **46**, 1156 (1985).

¹⁰B. F. Levine, K. K. Choi, C. G. Bethea, J. Walker, and R. J. Malik, *Appl. Phys. Lett.* **52**, 1481 (1988).

¹¹P. Yuh and K. L. Wang, *Appl. Phys. Lett.* **51**, 1404 (1987).

¹²B. F. Levine, C. G. Bethea, K. K. Choi, J. Walker, and R. J. Malik, *J. Appl. Phys.* **64**, 1591 (1988).

¹³E. O. Kane, in *Narrow Gap Semiconductors: Physics and Applications*, Vol. 133 of *Lecture Notes in Physics*, edited by W. Zawadzki (Springer-Verlag, New York, 1981), p. 13.

¹⁴N. F. Johnson, Ph.D. thesis, Harvard University, 1989.

¹⁵Inclusion of finite spin-orbit splitting, Δ , is necessary for an accurate description of excited SL hole states with energies comparable to Δ .

¹⁶In fact Eq. (5) holds for a general heterostructure state at $K_{\parallel} = 0$, if the SL labels L and K_{\perp} are dropped.

¹⁷The expressions for the F_n 's reduce to those of M. de Dias Leyva and J. Lopez Gondar, *Phys. Status Solidi B* **128**, 575 (1985) in the limit of infinite spin-orbit splitting.

¹⁸The derivation of Eq. (14) is similar to the bulk impurity problem considered by W. Kohn, in *Solid State Physics*, edited by F. Seitz and D. Turnbull (Academic, New York, 1967), Vol. 5, p. 284.

¹⁹H. Ehrenreich and L. Schwartz, in *Solid State Physics*, edited by H. Ehrenreich, F. Seitz, and D. Turnbull (Academic, New York, 1976), Vol. 31, p. 149.

²⁰G. Bastard, *Acta Electron.* **25**, 147 (1983).

²¹See, for example, J. Menendez, A. Pinczuk, D. J. Werder, A. C. Gossard, and J. H. English, *Phys. Rev. B* **33**, 8863 (1986).

²²D. Long, *Energy Bands in Semiconductors* (Wiley, New York, 1968), p. 195.

²³For an InAs/GaSb SL (type II), the electron and hole do not have common barriers. Therefore both layers must be thin before the VCA gap ($x = l_A/d$) will adequately describe the actual SL gap in InAs/GaSb. The VCA gap lies above the energy scale shown in Fig. 3(b) for the ranges of SL layer widths considered.

²⁴The HgTe/CdTe SL does not exhibit a distinguishable peak in m_{\parallel} as a function of HgTe width l_A since the bulk CdTe mass m_{CdTe}^* , which represents the $l_A \rightarrow 0$ limit of m_{\parallel} , is large ($m_{\text{CdTe}}^* = 0.11m_0$).

²⁵The peaks in m_{\perp} and m_{\parallel} for InAs/GaSb both occur near $l_A = 25 \text{ \AA}$.

²⁶Y. C. Chang and J. N. Schulman, *Phys. Rev. B* **31**, 2069 (1985).

²⁷P. Voisin, G. Bastard, and M. Voos, *Phys. Rev. B* **29**, 935 (1984).

²⁸J. M. Berroir, Y. Guldner, J. P. Vieren, M. Voos, and J. P. Faurie, *Phys. Rev. B* **34**, 891 (1986).

²⁹M. Voos (private communication).

³⁰P. Young, H. Ehrenreich, and N. F. Johnson (unpublished).

³¹Further evidence for a large band offset has recently been provided by M. Voos, J. Manasses, J. M. Berroir, Y. Guldner, J. P. Vieren, X. Chu, and J. P. Faurie, in *Proceedings of the 4th International Conference on Modulated Semiconductor Structures*, Ann Arbor, 1989 (Surf. Sci., to be published).

INFRARED OPTICAL PROPERTIES OF III-V AND II-VI SUPERLATTICES

N.F. JOHNSON and H. EHRENREICH *

Division of Applied Sciences, Harvard University, Cambridge, MA 02138, USA

Received 23 May 1989; accepted for publication 31 October 1989

The infrared optical properties arising from fundamental and intersubband absorption in III-V and II-VI semiconductor superlattices (SL) are calculated using a superlattice representation formalism. The SL electronic structure at finite wavevector K is obtained from the known $K = 0$ solutions using SL $K \cdot p$ theory. The theoretical fundamental absorption curves for HgTe/HgCdTe SL are in excellent agreement with recent experimental data. Intersubband absorption between the lowest conduction subbands C1 and C2 is large in both the thick and thin barrier limit, and of potential technological importance.

This paper discusses aspects of the infrared optical properties of III-V and II-VI semiconductor superlattices (SL) associated with fundamental and intersubband absorption. The present theoretical approach, summarized in fig. 1, employs a superlattice representation which is obtained from the Bloch representation describing the bulk constituents using envelope functions. The standard formalism for bulk periodic solids, including $K \cdot p$ theory, is then directly applicable to the superlattice [1].

Fig. 2 shows the resulting band structures and optical (momentum) matrix element energies for $190\text{\AA}\text{GaAs}/200\text{\AA}\text{Ga}_{0.75}\text{Al}_{0.25}\text{As}$, $37\text{\AA}\text{InAs}/37\text{\AA}\text{GaSb}$ and $58\text{\AA}\text{HgTe}/42\text{\AA}\text{Hg}_{0.15}\text{Cd}_{0.85}\text{Te}$ along the K_{\parallel} and K_{\perp} directions, where \perp denotes the SL growth axis. The valence band structure calculated by Chang and Schulman [2] utilizing their widely-used tight-binding approach, is shown by the dashed line for the GaAs/GaAlAs SL. The present results for both the band structure and matrix elements agree well. The relative ordering of the LH1 and HH2 bands for each SL depends on the particular choice of SL layer widths (and valence band offset). The energies $(2/m) \times |P_{LL'}^{\parallel}(K)|^2 = (2/m) |\langle L, K | p_{\parallel} | L', K \rangle|^2$ shown in fig. 2 are relevant to the calculation of

fundamental optical absorption, where the incident light propagates along the z (\perp) axis and the polarization vector lies in the xy (\parallel) plane for the case of interest. The values of $(2/m) |P_{LL'}^{\parallel}(K)|^2$ for the HgTe/HgCdTe SL are seen to be smaller than those of the GaAs/GaAlAs SL because the state $|C1, 0\rangle$ in the HgTe/HgCdTe SL has an appreciable p -component associated with the p -like character of the bulk HgTe conduction band edge. By contrast the InAs/GaSb matrix elements are small because the electron and hole lie in different layers. The valence band offset of HgTe/CdTe was taken to be 350 meV. One remarkable feature of the HgTe/CdTe electronic structure is that a semiconductor \rightarrow semimetal \rightarrow semiconductor transition can occur as the valence band offset Δ is increased from $\Delta = 0$. This behavior led to our recently proposed resolution of the valence band offset controversy in HgTe/CdTe SL's [3].

Fig. 3 shows a comparison between the experimental [4] and theoretical fundamental absorption curves for $58\text{\AA}\text{HgTe}/42\text{\AA}\text{Hg}_{0.15}\text{Cd}_{0.85}\text{Te}$ SL at room temperature. The experimental (dashed line) results of Lansari et al. [4] were shown to be reproducible in the sense that two separate samples grown under the same conditions yielded identical absorption coefficients $\alpha(E)$. The theoretical curve for $\Delta = 350$ meV (solid line) is in excellent agreement with the experimental data.

* To whom all correspondence should be addressed.

• Envelope Functions: $F_n(L, K; r)$

$$\langle r | L, K \rangle = \sum_n F_n(L, K; r) \langle r | n, k=0 \rangle$$

SL Wave Functions
Band L, Wavenumber K

Bulk Bloch Functions
Band n, Wavenumber k = 0

• SL Band Energy $E_L(K)$ from:

$$H_{SL} |L, K\rangle = E_L(K) |L, K\rangle$$

Slowly varying $F_n(L, K; r)$

$$H_{A(B)}^{k \cdot p}(k_x, k_y, -i \frac{\partial}{\partial z}) F(L, K; r) = E_L(K) F(L, K; r)$$

Bulk A(B) $k \cdot p$
matrix

$F = \{F_n\}$

• Effective-Mass Like Eqs. for F_n 's

- Install Standard Boundary Conditions at Interfaces
- Use Bulk A(B) Modified Kane Model
- Solve analytically at $K = 0$

• Superlattice Representation $|L, 0\rangle$:

$$\{F_n(L, 0; z)\}, E_L(0)$$

• Momentum/Optical Matrix Elements

$$\langle L, 0 | p | L', 0 \rangle$$

SL $k \cdot p$ Theory

f-Sum Rule

SL Bands $E_L(K)$
 $\langle L, K | p | L', K \rangle$

$K = 0$ Effective Masses
 m_{\perp}, m_{\parallel}

• Optical Properties

Absorption Coefficient $\alpha(\omega)$

Refractive Index $n(\omega)$

Fig. 1. Theoretical approach to calculation of superlattice electronic and optical properties.

Although $\alpha(E)$ is not very sensitive to Λ the agreement between experiment and theory is better for $\Lambda = 350$ meV than for $\Lambda = 40$ meV (dashed-dotted line). The partial contributions for $\Lambda = 350$ meV, shown by long-dashed lines, are

dominated by the HH1 \rightarrow C1 and LH1 \rightarrow C1 transitions at energies near the fundamental SL gap. Calculation of $\alpha(E)$ for $E > 0.55$ eV is difficult since many SL bands contribute, and $E_L(K)$ is required for large K_{\parallel} values. The HH3 \rightarrow C3

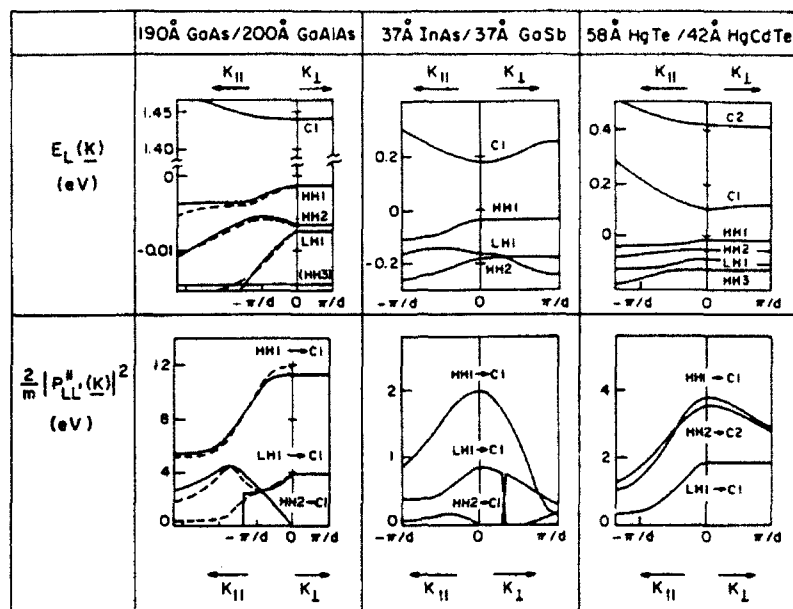


Fig. 2. Band structures $E_L(K)$ and energies $(2/m)|P_{L'L''}^{\parallel}(K)|^2 = (2/m)|\langle L, K | p_{\parallel} | L', K \rangle|^2$ for 190ÅGaAs/200ÅGa_{0.75}Al_{0.25}As, 37ÅInAs/37ÅGaSb and 58ÅHgTe/42ÅHg_{0.15}Cd_{0.85}Te superlattices shown as functions of K_{\parallel} and K_{\perp} . The origin of energy is defined as the valence band (Γ_8) edge of GaAs, GaSb and HgTe respectively. The label $L' \rightarrow L$ indicates the transition corresponding to $(2/m)|P_{L'L''}^{\parallel}(K)|^2$.

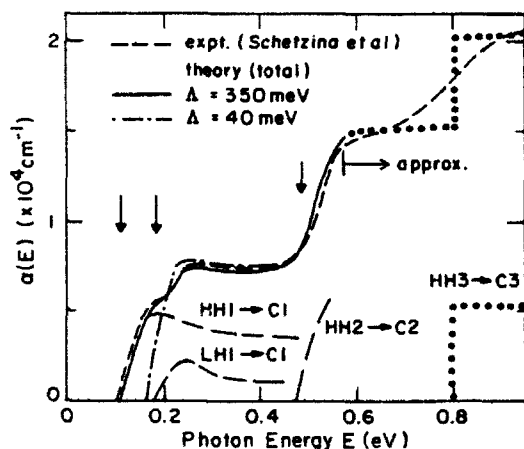
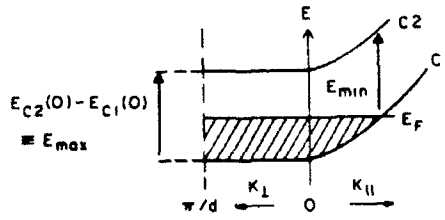


Fig. 3. Comparison of experimental (short dashed line) of Lansari et al. [4] and theoretical (solid line) fundamental absorption coefficients $\alpha(E)$ as a function of photon energy E for 58ÅHgTe/42ÅHg_{0.15}Cd_{0.85}Te at $T = 300$ K. Dominant partial contributions are shown (long dashed line). Theoretical curve above $E = 0.55$ eV is approximate (shown dotted). Δ is taken 350 meV. The theoretical absorption curve using $\Delta = 40$ meV is indicated by a dashed-dotted line.

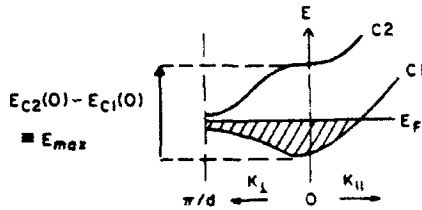
contribution, shown by dotted lines, was therefore included approximately in fig. 3 using a two-dimensional density of states and a K -independent SL matrix element. The observed structure in all cases, even the last, coincides with theoretically expected transitions. Similar agreement has also been obtained for the InAs/GaSb system [5].

Unlike fundamental absorption, the intersub-band absorption between conduction subbands C1 and C2 is only appreciable if the incident light is polarized perpendicular to the layers and the C1 band contains carriers. The dependence of the C1 \rightarrow C2 absorption on the light polarization follows from the anisotropy of the C1 \rightarrow C2 oscillator strength $f_{C2,C1}$ [6]. Several practical applications of the strong C1 \rightarrow C2 absorption, in particular carrier activated light modulators [5] and infrared detectors [7], have recently been suggested.

Fig. 4 shows the schematic band structure of C1 and C2 in the thick and thin barrier SL limits.

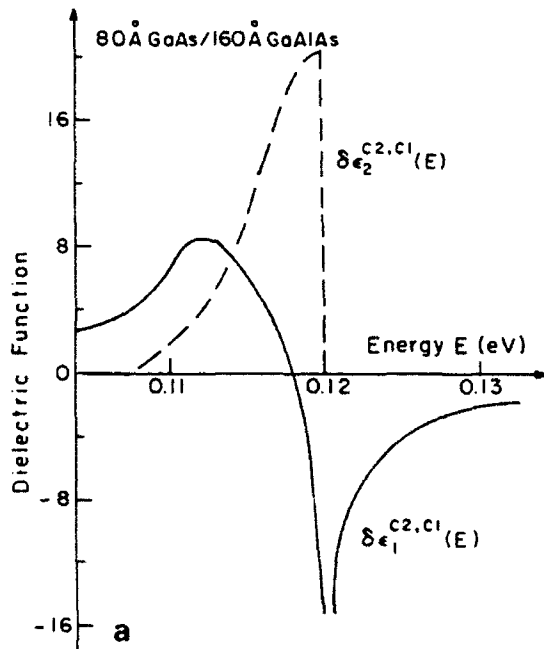


(a) Thick Barriers (QW)



(b) Thin Barriers

Fig. 4. Schematic band structure of the lowest two superlattice conduction bands C1 and C2 in the (a) thick and (b) thin barrier SL limits. Carriers are present in C1 with an associated Fermi level E_F . The maximum and minimum energies for photon absorption are indicated by E_{max} and E_{min} respectively.



with carriers filled up to the Fermi level E_F . For thick barriers the bands C1 and C2 are essentially parallel in all directions assuming both C1 and C2 lie energetically below the top of the barrier. The joint density of states is a sharply peaked function of energy. In addition the C1 \rightarrow C2 oscillator strength $f_{C2,C1}^\perp$ is large since the thick barriers are effective in supplying crystal momentum along the growth axis. The resulting intersubband absorption coefficient is therefore sharply peaked [5]. For thin barriers, the SL bands have finite dispersion along the growth axis. The joint density of states between C1 and C2 is smaller in magnitude for the thin barrier SL, but is also non-zero over a wider energy range as a result of reduced nesting. The oscillator strength $f_{C2,C1}^\perp$ is also smaller for the thin barrier SL since thin barriers are less effective at supplying crystal momentum.

Fig. 5a shows the C1 \rightarrow C2 contribution to the imaginary part of the dielectric function $\delta\epsilon_2^{C2,C1}(E)$ (dashed line) as a function of energy E for the thick barrier SL 80 Å GaAs / 160 Å GaAlAs at $T = 300$ K. The tail of $\delta\epsilon_2^{C2,C1}(E)$ on the low-energy

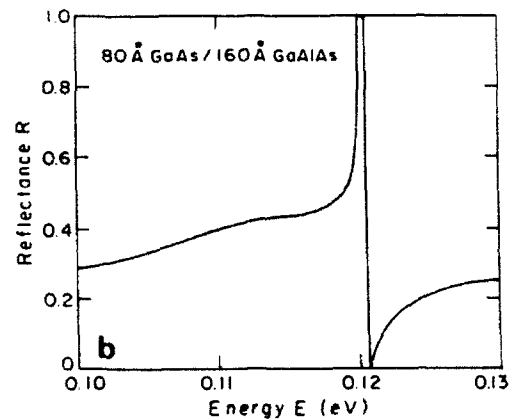


Fig. 5. Intersubband C1 \rightarrow C2 optical properties in 80 Å GaAs / 160 Å Ga_{0.7}Al_{0.3}As superlattice with C1 carrier concentration $n_c = 5 \times 10^{17} \text{ cm}^{-3}$ at temperature $T = 300$ K: (a) contributions to the real ($\delta\epsilon_1^{C2,C1}(E)$; solid line) and imaginary ($\delta\epsilon_2^{C2,C1}(E)$; dashed line) parts of the total dielectric function, and (b) reflectance R .

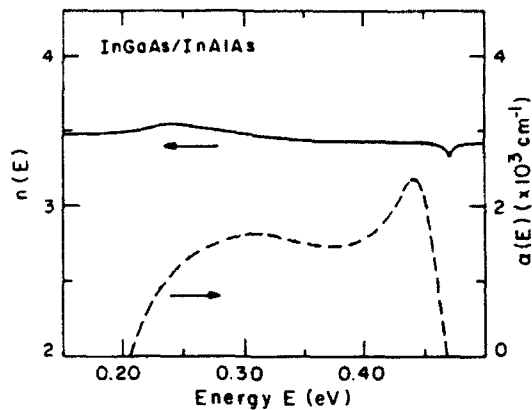


Fig. 6. Calculated refractive index $n(E)$ (solid line; left-hand scale) and absorption coefficient $\alpha(E)$ (dashed line; right-hand scale) versus photon energy E for $40\text{\AA}\text{In}_{0.53}\text{Ga}_{0.47}\text{As}/20\text{\AA}\text{In}_{0.52}\text{Al}_{0.48}\text{As}$ at $T = 60\text{ K}$, for C1 electron concentration $n_c = 1.4 \times 10^{18}\text{ cm}^{-3}$.

side is due to finite temperature smearing of the Fermi-Dirac distribution in C1. The contribution to the real part of the dielectric function $\delta\epsilon_1^{C2,C1}(E)$ is also shown (solid line). The corresponding reflectance is shown in fig. 5b. Fig. 3 of ref. [5] shows the resulting sharply peaked absorption coefficient (magnitude $\sim 10^4\text{ cm}^{-1}$; width $\sim 5\text{ meV}$) and refractive index.

Fig. 6 shows the smaller but broader $\alpha(E)$ (dashed line) for the *thin* barrier $40\text{\AA}\text{InGaAs}/20\text{\AA}\text{InAlAs}$ SL together with the corresponding refractive index $n(E)$ (solid line). The broad

structure in $\alpha(E)$ results in a weaker variation of $n(E)$ than in the thick barrier SL case. The near parallelism of C1 and C2 in the two in-plane (K_{\parallel}) directions gives rise to a small peak in $\alpha(E)$ near 0.45 eV which is reminiscent of a one-dimensional joint density of states. The magnitude of $\alpha(E)$ in fig. 6 is comparable to that of ref. [7].

This work was supported by JSEP (ONR contract N00014-84-K-0465 and N00014-89-J-1023) and DARPA (ONR contract N00014-86-K-0033).

References

- [1] A detailed account of the approach, together with specific input parameters and a complete list of references, can be found in an extended paper being submitted to Phys. Rev. B.
- [2] Y.C. Chang and J.N. Schulman, Phys. Rev. B 31 (1985) 2069.
- [3] N.F. Johnson, P.M. Hui and H. Ehrenreich, Phys. Rev. Lett. 61 (1988) 1993; P.M. Hui, H. Ehrenreich and N.F. Johnson, J. Vac. Sci. Technol. A 7 (1989) 424.
- [4] Y. Lansari, J.W. Han, S. Hwang, L.S. Kim, J.W. Cook, Jr. and J.F. Schetzina, J. Vac. Sci. Technol. A 7 (1989) 241.
- [5] N.F. Johnson, H. Ehrenreich and R.V. Jones, Appl. Phys. Lett. 53 (1988) 180.
- [6] N.F. Johnson, H. Ehrenreich, K.C. Hass and T.C. McGill, Phys. Rev. Lett. 59 (1987) 2352.
- [7] B.F. Levine, C.G. Bethea, K.K. Choi, J. Walker and R.J. Malik, J. Appl. Phys. 64 (1988) 1591.

Infrared optical absorption in imperfect parabolic quantum wells

L. Brey, Jed Dempsey, N. F. Johnson, and B. I. Halperin

Lyman Laboratory of Physics, Harvard University, Cambridge, Massachusetts 02138

(Received 26 February 1990)

The effects of possible imperfections on the infrared optical absorption and on the charge-density profile of wide parabolic quantum wells (WPQW's) are studied. We consider effects that can arise from the finite width of WPQW's, from the existence of a quartic component in the confining potential, and from the existence of a region of flat potential in the center of the well. Within the local-density approximation, we confirm that a perfect WPQW absorbs light only at the bare harmonic-oscillator frequency, and show that the effects of small imperfections of the types considered on the absorption spectrum are twofold: a shift in the location of the main peak and the appearance of new peaks nearby.

I. INTRODUCTION

The properties of an interacting three-dimensional (3D) electron gas in a uniform positive background have been widely studied over the years¹ and different many-body effects have been predicted. In particular, the ground state of this system in an external magnetic field is expected to be a spin-density wave or a Wigner crystal when the electron density is low enough.² In order to observe these broken-symmetry ground states, a lower density of electrons than that found in normal metals is required. For this reason, *n*-type doped semiconductors with small effective mass and low carrier density might seem the best candidates to exhibit exotic ground states. Unfortunately, the interaction between the electrons and the neutralizing charged impurities in these systems is strong enough³ to preclude any broken-symmetry ground state favored by the electron-electron interaction. In contrast, the study of a high-mobility, two-dimensional (2D) electron gas has been possible experimentally,⁴ due in part to the development of modulation-doping techniques, which reduce the electron-ionized impurity interaction by separating the 2D electron gas spatially from the neutralizing positive charges.

To achieve an almost-3D electron gas while reducing the electron-impurity interaction, a remotely doped wide-parabolic-quantum-well (WPQW) structure has been proposed.² In such a well, the parabolic potential, $V(z) = Az^2$, mimics the potential created by a uniform slab of positive charge of density $n_0 = A\epsilon/2\pi e^2$. In this expression, e is the electron charge and ϵ is the (uniform) static dielectric constant of the host semiconductor. Electrons are introduced remotely in the WPQW by placing donors at some distance from either side of the well. The electrons enter the well to screen the parabolic potential and distribute themselves in a uniform layer of density n_0 over the fictitious positive charge. In practice, the WPQW's are ~ 4000 Å wide, and uniform electron layers of thickness > 2000 Å have been obtained. Because the donors can be separated by several hundred angstroms from the electrons in such a system, the

electron-random impurity potential can be considerably smaller than is possible in the usual doped semiconductors. The mobility of these samples, even in the presence of alloy-disorder scattering, should be significantly higher than that of doped semiconductors with the same concentration of carriers.

In the experimental samples, the parabolic potential is achieved by tailoring the conduction-band edge of an alloy semiconductor, usually $\text{Ga}_{1-x}\text{Al}_x\text{As}$. Since the band offset between GaAs and $\text{Ga}_{1-x}\text{Al}_x\text{As}$ is proportional⁵ to x , it is possible to obtain a parabolic potential by varying the fraction of aluminum quadratically with position. Recently, structures of this type were grown using molecular-beam epitaxy by Gossard and co-workers,⁶ and independently by Shayegan and co-workers.⁷ Magneto-transport experiments^{6,7} on these WPQW's reveal that they hold a thick, high-mobility slab of electron gas. In addition, recent theoretical studies of these systems have discussed electron energy levels and charge-density profiles,⁸ electronic structure in the presence of a longitudinal magnetic field,⁹ and the existence of a spin-density-wave instability in the presence of a longitudinal magnetic field.¹⁰

The infrared optical absorption and magneto-optical absorption in WPQW have been studied experimentally¹¹ and theoretically.¹² It has been shown¹² that, in the absence of an applied magnetic field, an ideal *n*-type doped parabolic quantum well absorbs far-infrared radiation only at the bare harmonic oscillator frequency, independent of the electron-electron interaction and of the number of electrons in the well. For this reason, it has been thought that optical-absorption measurements might be useful in characterizing departures from ideal parabolicity in experimental samples.

The aim of the present work is to study, within the framework of the Hohenberg-Kohn-Sham local-density approximation (LDA), how the optical absorption of a WPQW changes from its ideal form when different imperfections are present. We also report the influence of imperfections on the charge-density profile and on the electronic states. In Sec. II we describe the method used

in our calculations, and in Sec. III we discuss three experimentally relevant⁶ effects: the effect of the finite width of the well, the effect of a quartic term added to the parabolic potential, and the effect of a region of flat potential in the center of the well. Finally, in Sec. IV, we summarize our results.

In the present paper we confine ourselves to the case of zero applied magnetic field. If one can neglect the scattering of electrons by impurities and phonons, the absorption in this case is produced only by the component of the electric field in the z direction (perpendicular to the layer). Thus, to see the effect, one must use radiation that is incident at an angle far from normal incidence.

II. METHOD OF CALCULATION

We consider a WPQW with the geometry used in Ref. 6, where the well has a finite width W , a depth Δ_1 , and is bounded by an additional barrier of height Δ_2 . To describe the electrons in the host semiconductor, we use the effective-mass approximation. We take the static dielectric constant and the effective mass to be uniform across the well. In the actual WPQW,^{6,7} these quantities vary by only 11 and 7%, respectively, from the center to the edge of the well, and including this variation in the calculation produces only small changes in the results. Also omitted from the calculation are the nonparabolicity of the conduction band and the band-mixing effects induced by confinement. These effects, again, have only a small influence on the electronic properties of the system.

The interactions between electrons in the conduction band can be separated into a Hartree term due to the electrostatic potential of the total electron density and an exchange-correlation term.¹ The exchange-correlation part of the ground-state energy can be described as a functional of the electron density.¹³ In the LDA this functional is assumed to have only local dependence on the electron density. The LDA has been used very successfully to obtain ground-state properties of many systems.¹⁴ Making this local approximation leads to a one-

body Schrödinger-type equation, where the electrons move in a potential that is the sum of the external (parabolic) potential, the Hartree potential, and an exchange-correlation potential. Although the energy eigenvalues of this one-particle equation do not correspond to the quasi-particle energies, one can consider the exchange-correlation potential as a local, energy-independent self-energy.¹⁵ The LDA gives good results for conduction electrons in silicon inversion layers and GaAs/Ga_{1-x}Al_xAs heterostructures, and for quantum wells.^{4,16}

In our system, we replace the localized donor charges by a z -dependent charge density that has been averaged over the x - y plane. If we restrict ourselves to self-consistent solutions that respect translational symmetry in the x - y plane, the one-electron equation describing the motion of the electrons separates, and the wave functions and eigenvalues are

$$E_{n,k_x,k_y} = \epsilon_n + \frac{\hbar^2 k_x^2}{2m^*} + \frac{\hbar^2 k_y^2}{2m^*}, \quad (1a)$$

$$\Psi_{n,k_x,k_y}(\mathbf{r}) = \frac{1}{\sqrt{S}} e^{i(k_x x + k_y y)} \varphi_n(z), \quad (1b)$$

where we have supposed spin degeneracy and omitted the spin index. In the above expression, S is the sample area, $\mathbf{k} = (k_x, k_y)$ is the wave vector of the electron, m^* is the effective mass, and ϵ_n and $\varphi_n(z)$ are obtained from the one-dimensional Schrödinger equation

$$\left[-\frac{\hbar^2}{2m^*} \frac{d^2}{dz^2} + V(z) + V_H(z) + V_{xc}(z) \right] \varphi_n(z) = \epsilon_n \varphi_n(z). \quad (2)$$

In this expression, $V(z)$ is the bare well potential, which depends on the Al concentration at the position z , and which corresponds to the position of the bottom of the conduction band in the absence of doping; $V_{xc}(z)$ is the exchange-correlation potential¹⁷

$$V_{xc}(z) = -0.985 \frac{e^2}{\epsilon} n^{1/3}(z) \left[1 + \frac{0.034}{a_B^* n^{1/3}(z)} \ln \{ 1 + 18.376 a_B^* n^{1/3}(z) \} \right], \quad (3)$$

where $a_B^* = \epsilon \hbar^2 / m^* e^2$; $V_H(z)$ is the Hartree term due to the electrostatic interaction of the electrons with themselves and with the $[(x,y)\text{-averaged}]$ impurity charge,

$$\frac{d^2 V_H(z)}{dz^2} = -\frac{4\pi e^2}{\epsilon} [n(z) - N_D(z)], \quad (4)$$

where $N_D(z)$ is the density of positive charge necessary to maintain charge neutrality. The electron density $n(z)$ is given by

$$n(z) = \sum_i n_i(z), \quad (5)$$

$$n_i(z) = \frac{m^*}{\pi \hbar^2} (\epsilon_F - \epsilon_i) |\varphi_i(z)|^2 \Theta(\epsilon_F - \epsilon_i),$$

where $n_i(z)$ is the contribution of the i th subband to the charge density, $\Theta(\epsilon)$ is the Heaviside unit-step function ($\Theta=0$ for $\epsilon < 0$ and $\Theta=1$ for $\epsilon > 0$), and ϵ_F is the Fermi energy obtained from the condition

$$n_s = \sum_i N_i, \quad (6)$$

$$N_i = \frac{m^*}{\pi \hbar^2} (\epsilon_F - \epsilon_i) \Theta(\epsilon_F - \epsilon_i),$$

N_i being the number of electrons per unit area in the i th subband. Consistent with our use of a dielectric constant that is uniform across the well, we have neglected the effect of image potentials in Eq. (2).

The self-consistent solution of Eqs. (2)–(6) gives us the charge-density profile, the Fermi energy, the subband energies, and the total potential, which is defined as $V_T(z) \equiv V(z) + V_H(z) + V_{xc}(x)$. From the eigenfunctions and eigenvalues, we can obtain the infrared (ir) optical spectrum of the system.

The peaks in the ir optical absorption do not appear at frequencies corresponding to the quasiparticle energy separation. Instead, the resonances are shifted from the self-consistent subband separation by the depolarization effect,¹⁸ due to the Hartree screening of the resonance, and by the excitoniclike¹⁹ or vertex-correction effect. In fact, the absorption peaks correspond to the collective modes of the system, which must be determined from the poles of the appropriate response function.²⁰ In the case of a quantum well, in the long-wavelength limit, the movement of the confined electrons can only be coupled to an electric field perpendicular to the electronic sheet, and the charge in the well absorbs ir radiation only if the electric field has a component in the perpendicular direction. We are able to use the dipole approximation in describing the interaction between light and the electrons and to neglect retardation effects²¹ because the thickness of the typical WPQW is much smaller than the wavelength of the light with frequency corresponding to the self-consistent subband separation.

We obtain the optical absorption by using the self-consistent-field approximation²² together with the LDA. In the form derived by Ando,¹⁹ the optical absorption per unit area can be written as

$$P(\omega) = \frac{1}{2} \text{Re}[\bar{\sigma}_z(\omega) D^2], \quad (7)$$

where D is the external electric field directed in the z direction and $\bar{\sigma}_z$ is the modified two-dimensional dynamical conductivity

$$\bar{\sigma}_z(\omega) = \frac{e^2}{m^*} (-i\omega) n_s \sum_l \frac{\tilde{f}_l}{\tilde{E}_l^2 - (\hbar\omega)^2 - 2i\hbar\omega/\tau}, \quad (8)$$

where we have introduced a phenomenological relaxation time τ and

$$\tilde{f}_l = \left[\sum_{n,n'} \left[\frac{2m^*}{\hbar^2} (\epsilon_n - \epsilon_{n'}) \right]^{1/2} \times Z_{n'n} \left[\frac{N_n - N_{n'}}{n_s} \right]^{1/2} U_{n'n,l} \right]^2, \quad (9)$$

where $Z_{n'n}$ is the matrix element of the z coordinate between the states $\varphi_{n'}$ and φ_n . \tilde{E}_l^2 in Eq. (8) and $U_{n'n,l}$ in Eq. (9) are the eigenvalues and eigenfunctions of the matrix

$$\Lambda_{nn',mm'} = E_{n'n}^2 \delta_{n'm} \delta_{nm} + (N_n - N_{n'})^{1/2} (N_m - N_{m'})^{1/2} \times (E_{m'm} E_{n'n})^{1/2} (\alpha_{nn',mm'} - \beta_{nn',mm'}). \quad (10)$$

In the above expressions, the indices n , n' , m , and m' refer to the eigenvalues and eigenvectors of the one-dimensional equation (2). The matrix elements α and β in

Eq. (9) represent the depolarization and excitonic effects, respectively, and are given by the expressions

$$\alpha_{nn',mm'} = -2 \frac{4\pi e^2}{\epsilon} \int_{-\infty}^{+\infty} dz \varphi_n(z) \varphi_{n'}^*(z) \times \int_{-\infty}^z dz' \int_{-\infty}^{z'} dz'' \varphi_m(z'') \times \varphi_{m'}^*(z''), \quad (11)$$

$$\beta_{nn',mm'} = -2 \int_{-\infty}^{+\infty} \varphi_n(z) \varphi_{n'}^*(z) \frac{\partial V_{xc}}{\partial n(z)} \varphi_m(z) \varphi_{m'}^*(z) dz. \quad (12)$$

It is also easy to show that the two-dimensional dynamical conductivity satisfies the sum rule

$$\int \bar{\sigma}_z(\omega) d\omega = \frac{e^2 \pi}{m^*} n_s. \quad (13)$$

In this model the vertex corrections are given by the functional derivative of the exchange-correlation potential with respect to the density. That this correction is independent of frequency is consistent with the lack of dependence of the exchange-correlation potential on the quasiparticle energy. It is important to note that, to be consistent, the use of the exchange-correlation potential in the calculation of the excitoniclike effects must be accompanied by the inclusion of V_{xc} in the one-dimensional Schrödinger equation, and vice versa.

III. NUMERICAL RESULTS

We are interested in the electronic and optical properties of the model parabolic potential

$$V_1(z) = \frac{4\Delta_1 z^2}{W^2} \Theta(W/2 - |z|) + (\Delta_1 + \Delta_2) \Theta(|z| - W/2) \quad (14)$$

and in the effects that different perturbations, when added to this potential, have on those properties. In our calculations we use the following set of parameters: $\epsilon = 12.5$, $\Delta_1 = 150$ meV, $\Delta_2 = 75$ meV, and $m^* = 0.067$ times the free electron mass. The positively charged donor impurities are in two layers of equal charge density, 200 Å thick, located just outside the well on either side. We have checked that our results are insensitive to the precise location of the positive charges for reasonable choices of the parameters.

In some of the actual WPQW the parabolic potential is created by changing the relative thickness of alternating GaAs and $\text{Al}_{0.3}\text{Ga}_{0.7}\text{As}$ layers in a superlattice of period 20 Å, so that the average aluminum composition changes quadratically across the well.⁶ Since the resulting potential is very difficult to handle numerically, we have used the averaged potential in our calculations. To check the sensitivity of our results to short-wavelength variations in the potential, we have compared the results for another fine superlattice with those for its averaged parabolic potential. The fine superlattice we considered had a period

of 20 Å, a fixed barrier thickness of 10 Å, and a barrier height which changed quadratically from one period to the next. The differences between the charge-density profiles obtained for the fine superlattice and for the averaged potential are very small. The superlattice produces an oscillation of very small amplitude in the charge-density profile, with the same period as the superlattice. There are also small differences in the charge-density distribution at the center of the well, due to the region of flat potential that the superlattice produces in the center of the well. This flat region typically corresponds to 3 or 5 periods of the fine superlattice. The effects on the energy levels and on the optical absorption are also small. The insensitivity of our results to fine structure in the potential arises because the reciprocal lattice vector corresponding to the superlattice period has an associated kinetic energy much larger than the energy spacing between the parabolic-well states in which we are interested. In summary, we have checked that the use of the averaged potential instead of the fine superlattice potential does not affect our results.

A. Size effects

In this subsection we study the effects of the finite width W and the additional confining potential Δ_2 on the properties of the system. We apply the method described in Sec. II to the potential of Eq. (14), $V(z) = V_1(z)$, and we study the variation of the properties of the system with the fractional occupation η defined by $\eta = n_s / (n_0 W)$, where n_s is the number of electrons per unit area in the system. We have found, in agreement with Ref. 8, that the number of occupied subbands increases with the number of electrons in the well, that the separation in energies between occupied subbands decreases with n_s , and that the separation between the Fermi energy and the first subband occupied goes quickly to the 3D value $\epsilon_F = \hbar^2 (3\pi^2 n_0)^{2/3} / 2m^*$. We have also checked that the thickness of the electron slab increases linearly with the fractional occupation η . Our calculations show that a very uniform slab of electrons is formed when only two subbands are occupied.

Size effects become important when the fractional occupation is near 1 and the electrons feel the abrupt change in potential at the edge of the well. In Fig. 1 we plot the charge-density profile for $\eta = 0.6$ and for $\eta = 1$. In the $\eta = 0.6$ case the charge is almost uniform in the occupied part of the well. The small bumps at the edges of the slab are Friedel-type oscillations, similar to those which appear at metal-vacuum interfaces.²³ As the WPQW moves toward complete filling ($\eta = 1$), the electrons start to feel the nonparabolic confining potential (Δ_2), and the amplitude of the oscillations at the edge of the charge-density profile increases. For $\eta > 1$, extra charge accumulates at the edges of the well, and the distribution of electrons becomes more and more like two 2D sheets.

Figure 2 shows the infrared optical absorption for different values of the fractional occupation η . When the number of electrons in the well is small enough, so that the charge does not feel the edges of the well ($\eta \leq 0.8$),

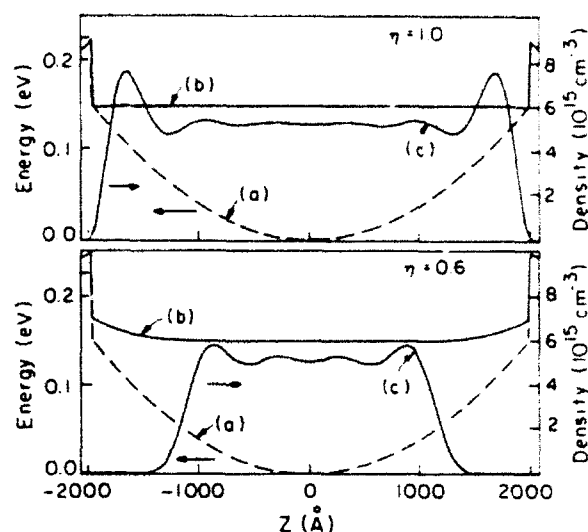


FIG. 1. Potential and charge density in a WPQW for two different fractional occupations, $\eta = 0.6$ and $\eta = 1$. Curve (a) shows the bare potential $V(z)$ for the well, and curve (b) shows the total self-consistent potential $V_T(z)$. Curve (c) shows the self-consistent charge-density profile $n(z)$. The parameters of the WPQW are given in the text.

the system absorbs light only at the bare frequency $\omega_0 = (8\Delta_1 / W^2 m^*)^{1/2}$. This frequency can be identified with the plasmon frequency of a 3D electron gas of density n_0 , since by construction $\omega_0 = (4\pi n_0 e^2 / \epsilon m^*)^{1/2}$. This result is expected from the analysis of Ref. 12. In the parabolic potential there is an *exact* cancellation of the depolarization term and the vertex-correction term by

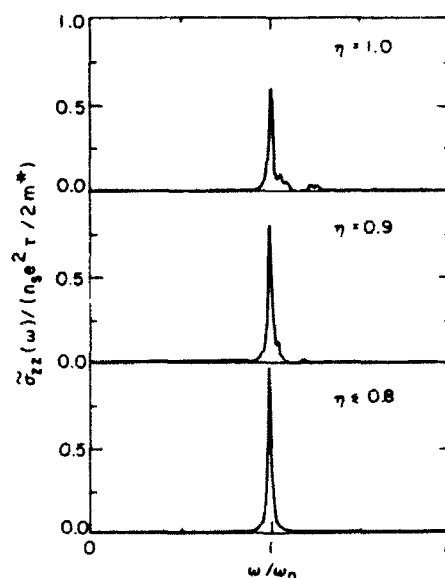


FIG. 2. Calculated real part of the dynamical conductivity $\sigma_{xx}(\omega)$ in a WPQW for different values of the fractional occupation η . The parameters of the WPQW are given in the text. The value of the phenomenological relaxation time, τ , is $0.01\omega_0$.

the corrections to the quasiparticle energy spacing due to the electron-electron interaction.

The effects of the finite width of the parabolic well begin to appear when $\eta \geq 0.8$. The effect of the finite width is negligible for fractional occupations smaller than 0.8 but increases quickly for higher values. For values of η smaller than 1, the perturbation is still relatively small and has two main effects on the optical absorption of the WPQW. First, the main peak in the absorption spectrum is shifted to a slightly higher frequency because the extra confinement increases the oscillation frequency of the center of mass of the electrons. Second, small satellites appear around the main peak because the electric field of the incident light can now couple to the internal motion of the electrons as well as to the motion of the center of mass.

B. Effect of a quartic term added to the parabolic potential

In this subsection we study the effect that a quartic term of the form

$$V_q(z) = \frac{16\Delta_q z^4}{W^4} \Theta(W/2 - |z|) \quad (15)$$

has on the properties of the WPQW. We apply the method described in Sec. II to the potential $V(z) = V_1(z) + V_q(z)$. In order to exclude effects due to the finite width of the well, we fix the fractional occupation at $\eta = 0.6$. Note that with this value of η , the ratio of the quartic potential to the parabolic potential at the edges of the electronic slab is only one-third the same ratio at the edges of the well.

In Fig. 3, we show the subband energies and the Fermi energy as a function of Δ_q . Figure 4 shows the initial potential, the self-consistent potential, and the charge-density profile for the cases $\Delta_q = -40$ and 75 meV. The

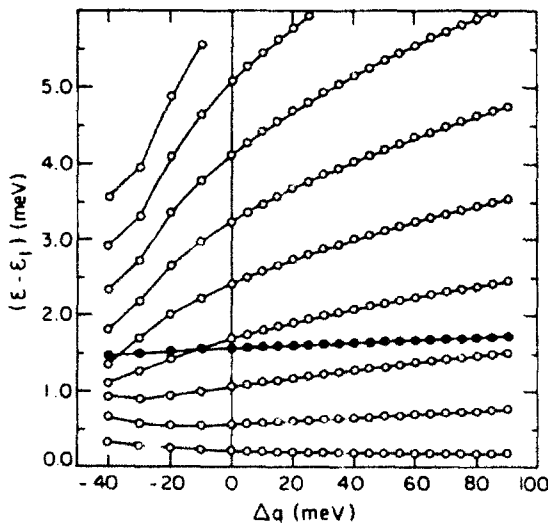


FIG. 3. Fermi level $\epsilon_F - \epsilon_1$ (solid circles) and energy-level separation $\epsilon_i - \epsilon_1$ (open circles) as a function of the strength of the quartic term Δ_q (see text). The fractional occupation η is 0.6. The parameters of the WPQW are given in the text.

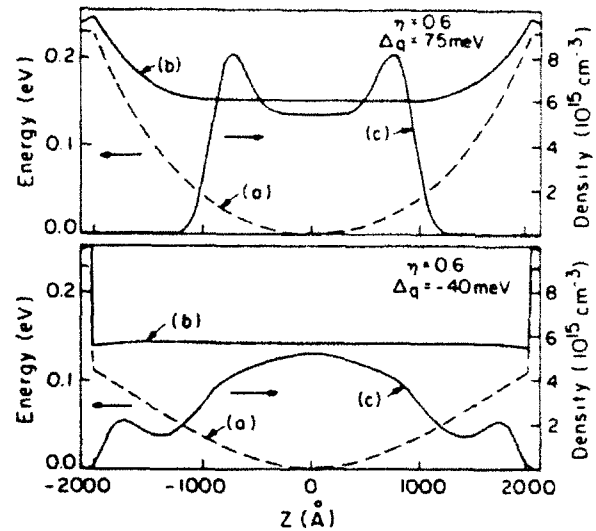


FIG. 4. Potential and charge density in a WPQW for two different values of the quartic term added to the potential: $\Delta_q = 75$ meV and $\Delta_q = -40$ meV. The fractional occupation is $\eta = 0.6$. Curve (a) shows the bare potential $V(z) = V_1(z) + V_q(z)$ for the well, curve (b) shows the total self-consistent potential $V_T(z)$. Curve (c) shows the self-consistent charge-density profile $n(z)$. The parameters of the WPQW are given in the text.

behavior is quite different for different signs of Δ_q . For positive values, the quartic potential induces a convex parabolic correction to the nearly uniform charge distribution produced by the parabolic potential alone. The positive quartic potential also increases the confinement of the electrons in the well, so the subband energy spacing increases with increasing Δ_q .

For negative values of Δ_q , the quartic potential adds a concave parabolic component to the charge distribution. Even a moderate negative Δ_q causes the charge to spread out considerably in the well and destroys the uniform charge-density profile. For small negative values of Δ_q , the main effect of the perturbation is to reduce the confinement of the electrons and, thus, the intersubband separation. For values of Δ_q more negative than those shown in Fig. 3, the charge builds up more and more at the edges of the well, and the energy levels approach those of two 2D electron gases.

In Fig. 5(a) we show the real part of the dynamical conductivity for different positive values of Δ_q . For small values of Δ_q the effect of the perturbation on the optical-absorption spectrum is twofold: a small shift to higher frequencies of the main peak and the appearance of small satellites around it. This is similar to the effect produced by the finite width of the well. But now instead of several peaks at higher frequencies than ω_0 there is only one additional peak. This shows that the step-potential Δ_2 allows more different transitions than the smoother quartic potential. At larger values of Δ_q the quartic term is comparable to the parabolic term and several transitions, with similar intensities, appear around ω_0 .

Figure 5(b) shows the optical absorption for negative values of Δ_q . In this case, as mentioned above, moderate

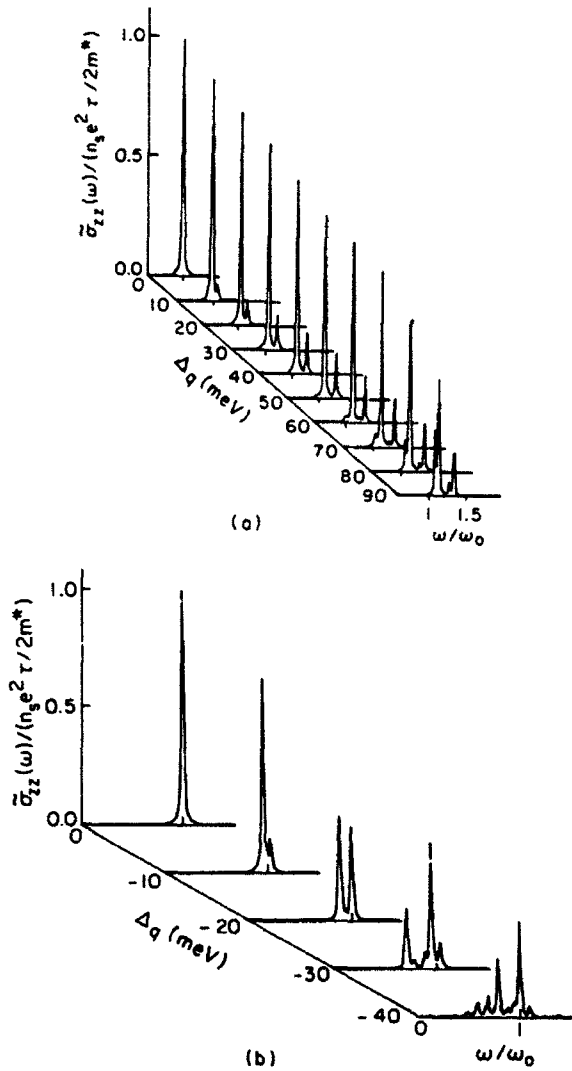


FIG. 5. Calculated real part of the dynamical conductivity $\tilde{\sigma}_{xx}(\omega)$ in a WPQW for (a) positive and (b) negative strengths of quartic term added to the potential. The fractional occupation η is 0.6. The parameters of the WPQW are given in the text. The value of the phenomenological relaxation time, τ , is $0.01\omega_0$.

values of Δq produce large changes in the charge-density profile, and the ir spectrum shows several peaks of comparable intensity around a main peak that is shifted down slightly from ω_0 .

C. Effect of a region of flat potential in the center of the well

In this section we apply the method of Sec. II to the potential $V(z) = V_1(z) + V_n(z)$, where $V_n(z)$ is given by

$$V_n(z) = -\frac{4\Delta_1 z^2}{W^2} \Theta(W_n/2 - |z|) - \frac{4\Delta_1}{W^2} \left[\frac{W_n}{2} \right]^2 \Theta(|z| - W_n/2). \quad (16)$$

$V_n(z)$ cancels $V_1(z)$ in the center of the well, producing a

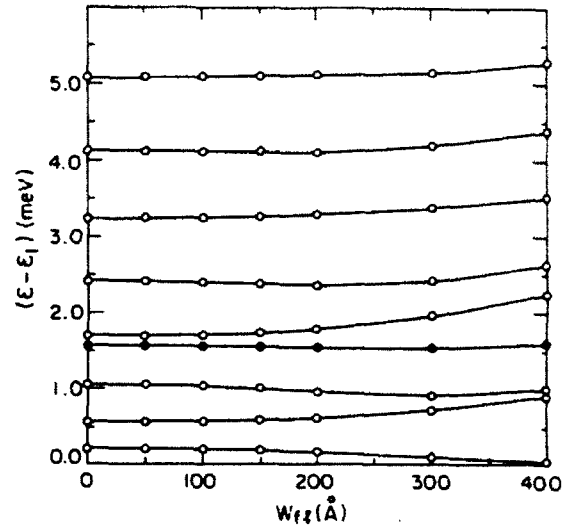


FIG. 6. Fermi level $\epsilon_F - \epsilon_1$ (solid circles) and energy-level separation $\epsilon_i - \epsilon_1$ (open circles) as a function of the width of the region of flat potential, W_{fl} (see text). The fractional occupation η is 0.6. The parameters of the WPQW are given in the text.

flat segment of potential of width W_n centered about $z=0$. When added to the perfect parabolic potential, $V_n(z)$ acts as a barrier in the center of the well which tends to separate the electron gas into two 2D systems. In Fig. 6 we plot the subband energies and the Fermi energy as a function of W_n , having fixed η at 0.6 as before to eliminate finite-width effects. As W_n increases, the

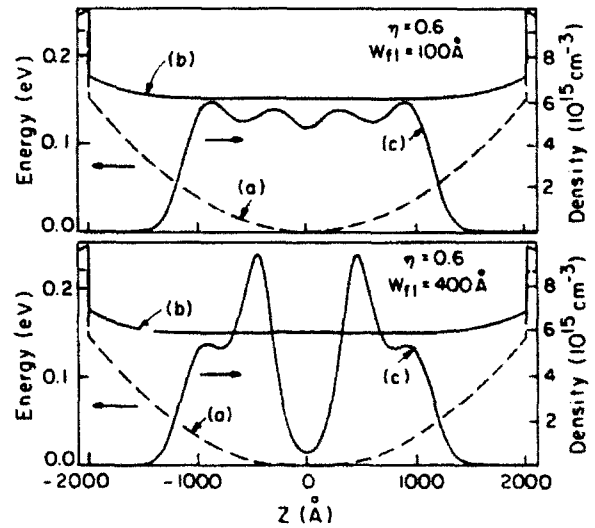


FIG. 7. Potential and charge density in a WPQW for two different widths of the region of flat potential $W_n = 100$ and 400 Å. The fractional occupation is $\eta = 0.6$. Curve (a) shows the bare potential $V(z) = V_1(z) + V_n(z)$ for the well, and curve (b) shows the total self-consistent potential $V_T(z)$. Curve (c) shows the self-consistent charge-density profile $n(z)$. The parameters of the WPQW are given in the text.

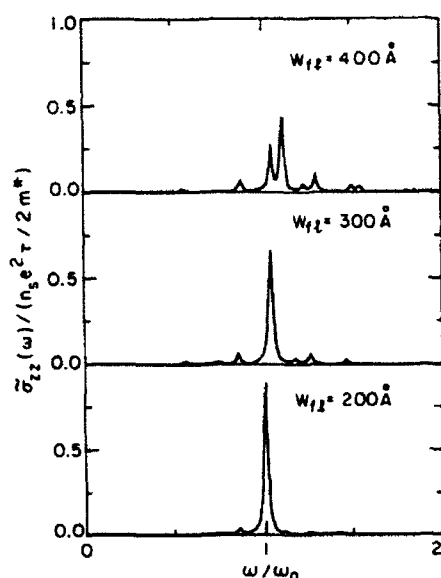


FIG. 8. Calculated real part of the dynamical conductivity $\sigma_{xx}(\omega)$ in a WPQW for different values of the width of the region of flat potential. The fractional occupation η is 0.6. The parameters of the WPQW are given in the text. The value of the phenomenological relaxation time, τ , is $0.01\omega_0$.

levels tend to become degenerate, as expected for two 2D electron gases. This is seen more clearly in Fig. 7, where the self-consistent charge-density profile is plotted for two values of W_{fl} . For $W_{fl}=400$ Å, the charge lies mostly to the sides of the barrier created by $V_{fl}(z)$.

As in the case of negative quartic term, the splitting of the charge-density profile strongly affects the optical-absorption spectrum, shown in Fig. 8. As W_{fl} increases, different peaks, with comparable intensities, appear around the frequency ω_0 .

IV. SUMMARY

An electron gas in a perfect parabolic quantum well absorbs light only at the bare harmonic oscillator frequency.¹² In this work we have studied the changes that different perturbations induce on the ir optical-absorption spectrum of wide parabolic quantum wells. Three different types of effects have been considered: size effects, important when the well is overfilled; effects of a quartic term added to the confining potential; and effects of a region of flat potential in the center of the well. When the strength of any of these perturbations is small enough, the effect on the ir absorption spectrum is the

same, namely (i) a shift of the main peak due to a shift in the frequency of oscillation of the center of mass of the electrons, and (ii) the appearance of new peaks around the main peak. The additional peaks had zero intensity in the ideal parabolic case, because they correspond to forbidden transitions. With the perturbations, the wave functions change and the transitions are no longer forbidden. The number of additional peaks and their positions depend on the particular form of the perturbation.

When the strength of the perturbation increases, the importance of the parabolic potential decreases, and the charge density in the electron slab becomes less and less uniform. When the uniformity is lost, several peaks with comparable intensities appear in the ir absorption spectrum.

Our LDA calculations are consistent with the result of Ref. 12, in that the optical-absorption spectrum we calculate in the absence of imperfections shows only one peak, which falls at precisely the expected frequency. On the other hand, one should not view this as strong confirmation that the LDA treats the electron-electron interaction accurately. The result of Ref. 12 holds for any interaction of the form $V(r-r')$, whether Coulombic or not. Our agreement with the general result shows only that, as we have used it, the LDA respects the translational invariance of the electron-electron interaction.

Also, the result of Ref. 12 implies that we must find an exact cancellation in our calculations of the depolarization term and the vertex-correction term by the corrections to the quasiparticle energy spacing due to the electron-electron interaction. In fact, we find that the cancellation also occurs when the vertex-correction term, Eq. (12), and the exchange-correlation potential, V_{xc} , are simultaneously omitted. This occurs because the depolarization term, Eq. (11), and the vertex-correction term separately cancel the effects of the Hartree and the exchange-correlation potentials, respectively.

ACKNOWLEDGMENTS

We thank P. F. Hopkins, R. Westervelt, A. C. Gosard, H. Ehrenreich, S. Das Sarma, and R. D. Meade for useful discussions. One of us (L.B.) wishes to acknowledge support from Spain's Ministerio de Educación y Ciencia. This work was supported by the U.S. National Science Foundation (NSF) through the Harvard University Materials Research Laboratory and Grant No. DMR-88-17291, by U.S. Defense Advanced Research Projects Agency (DARPA) through Office of Naval Research (ONR) Contract No. N00014-86-K-0033, and by St. John's College, Cambridge, England.

¹D. Pines, *The Many-Body Problem* (Dunod-Wiley, New York, 1959).

²A. C. Gosard, B. I. Halperin, and R. M. Westervelt (unpublished work); B. I. Halperin, *Jpn. J. Appl. Phys.* 26, Suppl. 26-3, 1913 (1987).

³See, for example, K. Ploog, *J. Cryst. Growth* 81, 304 (1987) and references therein.

⁴See, e.g., T. Ando, A. B. Fowler, and F. Stern, *Rev. Mod. Phys.* 54, 437 (1982); *The Physics of the Two-Dimensional Electron Gas*, edited by J. T. Devreese and F. M. Peeters (Plenum, New York, 1987).

⁵We restrict ourselves to concentrations of aluminum lower than 0.44, at which value the X valley becomes the minimum of the conduction band. See, for example, F. Flores and C.

- Tejedor, J. Phys. C 20, 145 (1987).
- ⁶M. Sundaram, A. C. Gossard, J. H. English, and R. M. Westervelt, Superlatt. Microstruct. 4, 683 (1988); E. G. Gwinn, R. M. Westervelt, P. F. Hopkins, A. J. Rimberg, M. Sundaram, and A. C. Gossard, Phys. Rev. B 39, 6260 (1989); E. G. Gwinn, P. F. Hopkins, A. J. Rimberg, R. M. Westervelt, M. Sundaram, and A. C. Gossard, in *High Magnetic Fields in Semiconductors Physics II*, edited by G. Landwehr (Springer-Verlag, New York, 1989).
- ⁷M. Shayegan, T. Sajoto, M. Santos, and C. Silvestre, Appl. Phys. Lett. 53, 791 (1988); T. Sajoto, J. Jo, L. Engel, M. Santos, and M. Shayegan, Phys. Rev. B 39, 10464 (1989); M. Shayegan, T. Sajoto, J. Jo, M. Santos, and H. D. Drew, *ibid.* 40, 3476 (1989).
- ⁸A. J. Rimberg and R. M. Westervelt, Phys. Rev. B 40, 3970 (1989).
- ⁹M. P. Stopa and S. Das Sarma, Phys. Rev. B 40, 10048 (1989).
- ¹⁰L. Brey and B. I. Halperin, in Proceedings of the Eighth International Conference on the Electronic Properties of Two-Dimensional Systems, Grenoble, France, 1989 [Surf. Sci. (to be published)]; Phys. Rev. B 40, 11 634 (1989).
- ¹¹K. Karraï, H. D. Drew, M. W. Lee, and M. Shayegan, Phys. Rev. B 39, 1426 (1989); K. Karraï, X. Ying, H. D. Drew, and M. Shayegan, *ibid.* 40, 12 020 (1989).
- ¹²L. Brey, N. F. Johnson, and B. I. Halperin, Phys. Rev. B 40, 10 647 (1989).
- ¹³P. Hohenberg and W. Kohn, Phys. Rev. 136, B864 (1964); W. Kohn and L. J. Sham, *ibid.* 140, A1133 (1965).
- ¹⁴See, e.g., R. O. Jones and O. Gunnarson, Rev. Mod. Phys. 61, 689 (1989).
- ¹⁵L. J. Sham and W. Kohn, Phys. Rev. 145, 561 (1966).
- ¹⁶F. Stern and S. Das Sarma, Phys. Rev. B 30, 840 (1984).
- ¹⁷We use the exchange-correlation potential suggested by L. Hedin and B. I. Lundqvist, J. Phys. C 4, 2064 (1971). Since we suppose a constant effective mass and dielectric constant across the well, this potential is continuous across the parabolic well. See the discussion in Ref. 16.
- ¹⁸W. B. Chen, Y. J. Chen, and E. Burstein, Surf. Sci. 58, 263 (1976); S. J. Allen, D. C. Tsui, and B. Vinter, Solid State Commun. 20, 425 (1976).
- ¹⁹T. Ando, Z. Phys. B 26, 263 (1977).
- ²⁰A. Tselis and J. J. Quinn, Surf. Sci. 113, 362 (1982); K. S. Yi and J. J. Quinn, Phys. Rev. B 27, 1184 (1983); 27, 2396 (1983).
- ²¹D. A. Dahl and L. J. Sham, Phys. Rev. B 16, 651 (1977).
- ²²H. Ehrenreich and M. H. Cohen, Phys. Rev. 115, 786 (1959); F. Stern, Phys. Rev. Lett. 18, 546 (1967); E. D. Siggia and P. C. Kwok, Phys. Rev. B 2, 1024 (1970).
- ²³W. Kohn and L. J. Sham, Phys. Rev. 137, A1697 (1965). N. D. Lang, in *Solid State Physics*, edited by H. Ehrenreich, F. Seitz, and D. Turnbull (Academic, New York, 1973), Vol. 28, p. 225.

Collective modes in quantum-dot arrays in magnetic fields

Jed Dempsey, N. F. Johnson, L. Brey,* and B. I. Halperin

Lyman Laboratory of Physics, Harvard University, Cambridge, Massachusetts 02138

(Received 13 August 1990)

We study collective excitations in a model array of parabolically confined quantum dots in an applied magnetic field. Treating the interactions between electrons on the same dot exactly and those between electrons on different dots in a simple approximation, we find that the Hamiltonian separates into a term involving center-of-mass coordinates of the electrons on each dot and a term that depends on the relative coordinates on each dot. We diagonalize the center-of-mass Hamiltonian exactly and discuss retardation effects and interactions between the array and far-infrared radiation.

In recent years there has been growing interest in the electronic properties of quantum-dot systems.¹⁻⁶ Most often these structures are formed when the quasi-two-dimensional electron gas (2DEG) at a semiconductor heterojunction or in a narrow quantum well is confined further, so that the electron motion is constrained in all three dimensions. In many of the experimental samples, particularly those where the dots are defined by metallic gates near the 2DEG,^{1,3,4,6} or by "deep-mesa" etching,^{2,6} the confinement in the plane is expected to be nearly parabolic.^{7,8} To provide adequate signal strength in measurements of optical transmission and of capacitance, arrays of as many as 10^8 dots covering several square millimeters are fabricated. In this paper, we discuss collective modes in a model array of quantum dots with two-dimensional parabolic confinement in an applied magnetic field, treating the interactions between electrons on the same dot exactly and those between electrons on different dots within a simple and often accurate approximation. We also investigate the interaction of the collective modes with far-infrared radiation and calculate the effects of retardation in a system where the array is embedded in a semiconductor crystal so that the dielectric constant is the same on both sides of the dot layer.

It has been shown recently⁹ that parabolically confined electron layers with or without an external magnetic field have center-of-mass collective modes that can be treated exactly. More recently, it has been noted that the techniques of Ref. 9 apply also to single quantum dots with general three-dimensional parabolic confinement¹⁰ and to single parabolic dots in external magnetic fields.¹¹ These results for single parabolic dots have also been obtained recently by other techniques.¹² On the other hand, theoretical work on arrays of parabolic quantum dots¹³ has failed to treat the interactions between electrons on the same dot accurately. Moreover, previous work on arrays has not considered the case of an applied magnetic field and has ignored effects due to retardation.

We begin with the model Hamiltonian $H = H_0 + H_{ee}^{(1)} + H_{ee}^{(2)}$, where

$$H_0 = \sum_{\alpha} \sum_i \left[\frac{1}{2m} \left(\mathbf{p}_{\alpha i} + \frac{e}{c} \mathbf{A}(\mathbf{r}_{\alpha i}) \right)^2 + \frac{1}{2} m \omega_0^2 \mathbf{u}_{\alpha i}^2 \right], \quad (1)$$

$$H_{ee}^{(1)} = \frac{1}{2} \sum_{\alpha} \sum_{i,j \neq i} V^{(1)}(|\mathbf{r}_{\alpha i} - \mathbf{r}_{\alpha j}|), \quad (2)$$

$$H_{ee}^{(2)} = \frac{1}{2} \sum_{\alpha, \beta \neq \alpha} \sum_{ij} V^{(2)}(|\mathbf{r}_{\alpha i} - \mathbf{r}_{\beta j}|). \quad (3)$$

In these expressions m is the effective mass, \mathbf{R}_{α} is the center position of the α th dot, $\mathbf{r}_{\alpha i} = \mathbf{R}_{\alpha} + \mathbf{u}_{\alpha i}$ is the position of the i th electron on the α th dot, and we take $\mathbf{A}(\mathbf{r}_{\alpha i}) = \mathbf{A}_0(\mathbf{r}_{\alpha i}) = B x_{\alpha i} \hat{y}$. The terms $H_{ee}^{(1)}$ and $H_{ee}^{(2)}$ represent the interactions between electrons on the same dot and on different dots, respectively. The Hamiltonian H incorporates the following characteristics: (i) a parabolic potential *before* electrons are added, (ii) no tunneling between dots, (iii) a uniform external magnetic field $\mathbf{B} = B \hat{z}$, and (iv) instantaneous interactions of the form $V(|\mathbf{r}_{\alpha i} - \mathbf{r}_{\beta j}|)$. We shall later relax the last of these assumptions. We also point out that the quantity $m \omega_0^2$ in Eq. (1) is the curvature of the parabolic potential confining the electrons on each dot when the dot is part of the array. In principle, this should be slightly different than the curvature of the confining potential of an isolated dot because of a small contribution from the fixed positive charges on the neighboring dots. We also ignore the Zeeman energy, which does not affect our results.

We define center-of-mass position and momentum operators for each site and for the system as a whole: $\mathbf{U}_{\alpha} = n_{\alpha}^{-1} \sum_i \mathbf{u}_{\alpha i}$, $\mathbf{P}_{\alpha} = \sum_i \mathbf{p}_{\alpha i}$, $\mathbf{U} = N^{-1} \sum_{\alpha} n_{\alpha} \mathbf{U}_{\alpha}$, and $\mathbf{P} = \sum_{\alpha} \mathbf{P}_{\alpha}$, where N is the total number of electrons and n_{α} is the number of electrons on the α th site. Defining

$$C_{\lambda}^{\pm} \equiv [2M\hbar(4\omega_0^2 + \omega_c^2)^{1/2}]^{-1/2} \\ \times \left[M\omega_{\lambda} U^{\pm} \mp i P^{\pm} + \lambda (\pm i M \omega_{-\lambda} U^{\mp} + P^{\mp}) \right. \\ \left. + m \omega_c \sum_{\alpha} n_{\alpha} X_{\alpha} \right], \quad (4)$$

where $M \equiv Nm$, $X_\alpha \equiv \mathbf{R}_\alpha \cdot \hat{\mathbf{x}}$, $\lambda = \pm 1$, and $\omega_\lambda = \lambda(\omega_c/2) + (\omega_0^2 + \omega_c^2/4)^{1/2}$, we find that $[H, C_\lambda^\pm] = \pm \hbar \omega_\lambda C_\lambda^\pm$ and that the $\{C_\lambda^\pm\}$ obey the commutation relations $[C_\lambda^+, C_\lambda^-] = \delta_{\lambda, \lambda'}$ and $[C_\lambda^+, C_{\lambda'}^-] = 0 = [C_\lambda^-, C_{\lambda'}^-]$. Thus C_λ^+ and C_λ^- are the creation and annihilation operators for exact excitations of our Hamiltonian. These excitations correspond to the classical modes in which all the electrons on all the dots move together in phase, maintaining their relative positions. This represents a generalization of the results for single dots¹⁰⁻¹² to arrays of dots.

To study modes where the electrons on different dots do not move in phase, we make a harmonic approximation to the interaction between pairs of electrons that lie on different dots. We note that although our treatment up to this point has assumed that $V^{(2)}$ in Eq. (3) depends only on $|\mathbf{r}_{ai} - \mathbf{r}_{bj}|$, the interactions in actual dot arrays may be more complicated, due, for example, to the effects of image charges on gate structures that do not possess translational symmetry in the xy plane. Then the interaction between electrons on different dots must be written in the more general form $V^{(2)}(\mathbf{r}_{ai}, \mathbf{r}_{bj})$. Image charges on gate structures will also cause modifications in the confining potential for an electron on a single dot and will modify the interactions between two electrons on the same dot, thereby affecting the assumptions that enabled us to solve exactly for the center-of-mass motion for a single dot. Nevertheless, under many conditions a simple-harmonic-oscillator approximation will be valid for small displacements.

For simplicity, we assume that the $\{\mathbf{R}_\alpha\}$ lie on a periodic lattice and that $V^{(2)}$ is invariant under reflections as well as under translations through lattice vectors, and write $V^{(2)}(\mathbf{r}_{ai}, \mathbf{r}_{bj}) = V^{(2)}(\mathbf{R}_{ab}, \mathbf{u}_{ai}, \mathbf{u}_{bj}) = V^{(2)}(\mathbf{R}_{ab}, -\mathbf{u}_{bj}, -\mathbf{u}_{ai})$, where $\mathbf{R}_{ab} \equiv \mathbf{R}_b - \mathbf{R}_a$. Using these symmetries and assuming that \mathbf{u}_{ai} and \mathbf{u}_{bj} are small compared to the scale of variation of $V^{(2)}(\mathbf{r}_{ai}, \mathbf{r}_{bj})$, we write $V^{(2)}(\mathbf{r}_{ai}, \mathbf{r}_{bj}) = \tilde{V}_{ai\beta j}^{(2)} + O(u^3)$ where

$$\tilde{V}_{ai\beta j}^{(2)} \equiv V^{(2)}(\mathbf{R}_a, \mathbf{R}_\beta) + (\mathbf{u}_{ai} - \mathbf{u}_{\beta j}) \cdot \mathbf{f}_{a\beta} + \frac{1}{2}(\mathbf{u}_{ai} \cdot \mathbf{w}_{a\beta} \cdot \mathbf{u}_{ai} + \mathbf{u}_{\beta j} \cdot \mathbf{w}_{a\beta} \cdot \mathbf{u}_{\beta j}) + \mathbf{u}_{ai} \cdot \mathbf{d}_{a\beta} \cdot \mathbf{u}_{\beta j}, \quad (5)$$

and $\mathbf{f}_{a\beta} \equiv (\partial V^{(2)}/\partial \mathbf{u}_{ai})$, $\mathbf{w}_{a\beta} \equiv (\partial^2 V^{(2)}/\partial \mathbf{u}_{ai} \partial \mathbf{u}_{ai})$, $\mathbf{d}_{a\beta} \equiv (\partial^2 V^{(2)}/\partial \mathbf{u}_{ai} \partial \mathbf{u}_{\beta j})$, with all derivatives evaluated at $\mathbf{u}_{ai} = 0 = \mathbf{u}_{\beta j}$. We emphasize that because the effective diameter d of the dots is generally much smaller than their nominal diameter and very much smaller than the spacing R_0 between dots, the replacement of $V^{(2)}$ by $\tilde{V}^{(2)}$ is often an excellent approximation. For example, if $V^{(2)}$ is a Coulomb interaction and $d/R_0 = 0.1$, then the worst case fractional error $(\tilde{V}^{(2)} - V^{(2)})/V^{(2)}$ is of order 10^{-3} for electrons on neighboring dots and decreases rapidly for dots that are not nearest neighbors.

Substituting $\tilde{H}_{ee}^{(2)} \equiv \frac{1}{2} \sum_{\alpha, \beta} \sum_{ij} \tilde{V}_{ai\beta j}^{(2)}$ for $H_{ee}^{(2)}$, one can show that the resulting Hamiltonian separates into two parts:

$$\tilde{H} \equiv H_0 + H_{ee}^{(1)} + \tilde{H}_{ee}^{(2)} = \tilde{H}_{c.m.} + \tilde{H}_{rel}, \quad (6)$$

where $\tilde{H}_{c.m.}$ depends only on the center-of-mass coordi-

nates $\{\mathbf{U}_\alpha\}$ and momenta $\{\mathbf{P}_\alpha\}$ of the electrons on each dot and \tilde{H}_{rel} depends only on the $n_\alpha - 1$ relative coordinates on each dot and on their conjugate momenta. The importance of this result is that the only coupling between dots is in $\tilde{H}_{c.m.}$, which is the Hamiltonian for lattice vibrations of charged ions in a magnetic field in the harmonic approximation. Specializing to the case when $n_\alpha = n$ for all α , $\tilde{H}_{c.m.}$ is given by

$$\tilde{H}_{c.m.} = \sum_\alpha \left\{ \frac{1}{2nm} [(P_\alpha^x)^2 + [P_\alpha^y + nm\omega_c(X_\alpha - U_\alpha^x)]^2] + \frac{1}{2} nm\omega_0^2 U_\alpha^2 \right\} + \frac{nm}{2} \sum_{\alpha\beta} \mathbf{U}_\alpha \cdot \mathbf{D}_{\alpha\beta} \cdot \mathbf{U}_\beta, \quad (7)$$

where

$$\mathbf{D}_{\alpha\beta} = \begin{cases} (n/m) \mathbf{d}_{\alpha\beta}, & \beta \neq \alpha \\ (n/m) \sum_{\gamma \neq \alpha} \mathbf{w}_{\alpha\gamma}, & \beta = \alpha \end{cases}. \quad (8)$$

Using the equation-of-motion method or techniques similar to those of Tikochinsky,¹⁴ $\tilde{H}_{c.m.}$ can be diagonalized exactly: $\tilde{H}_{c.m.} = \sum_{\mathbf{k}\lambda} \hbar \omega_{\mathbf{k}\lambda} C_{\mathbf{k}\lambda}^+ C_{\mathbf{k}\lambda}^- + \text{const.}$ where $\omega_{\mathbf{k}\lambda}$ is given by

$$\omega_{\mathbf{k}\lambda}^2 = \frac{1}{2} \{ \alpha_{11} + \alpha_{22} + \lambda [(\alpha_{11} + \alpha_{22})^2 - 4(\alpha_{11}\alpha_{22} - \alpha_{12}^2 - \omega_c^2\alpha_{22})]^{1/2} \}, \quad (9)$$

with $\lambda = \pm 1$, $\alpha_{11} \equiv (\omega_0^2 + \omega_c^2) + D_{\mathbf{k}}^{xx}$, $\alpha_{12} \equiv 2D_{\mathbf{k}}^{xy}$, $\alpha_{22} \equiv \omega_0^2 + D_{\mathbf{k}}^{yy}$, and $D_{\mathbf{k}}^{\mu\nu} = \sum_\alpha e^{i\mathbf{k} \cdot \mathbf{R}_{\alpha\beta}} D_{\alpha\beta}^{\mu\nu}$. Here $C_{\mathbf{k}\lambda}^+$ and $C_{\mathbf{k}\lambda}^-$ are

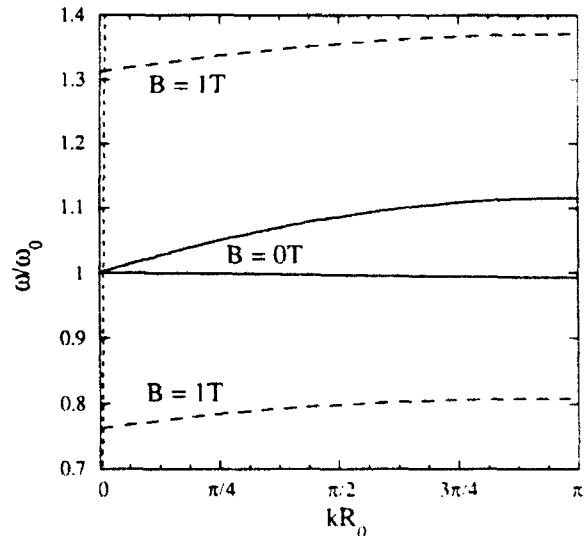


FIG. 1. Dispersion of center-of-mass collective modes $\omega_{\mathbf{k} \pm 1}$ for square lattice of lattice constant $R_0 = 5000 \text{ \AA}$ for $\mathbf{k} = k \hat{\mathbf{x}}$ in the first Brillouin zone, with $B = 0 \text{ T}$ (solid lines) and $B = 1 \text{ T}$ (dashed lines). Parameters are $\hbar\omega_0 = 3 \text{ meV}$, $n = 200$, $\epsilon = 12$, and m equals 0.07 times the electron mass. We assume Coulomb interactions. The nearly vertical dotted line at left is the line $\omega = kc/\epsilon^{1/2}$.

creation and annihilation operators which satisfy the commutation relations $[C_{\mathbf{k}\lambda}^-, C_{\mathbf{k}\lambda}^+] = \delta_{\mathbf{k}\lambda} \delta_{\mathbf{k}\lambda}$ and $[C_{\mathbf{k}\lambda}^-, C_{\mathbf{k}'\lambda'}^+] = 0 = [C_{\mathbf{k}\lambda}^+, C_{\mathbf{k}'\lambda'}^+]$. In the special case when $V^{(2)} = V^{(2)}(|\mathbf{r}_{\alpha i} - \mathbf{r}_{\beta j}|)$, one can show that $d_{\alpha\beta} = -\mathbf{w}_{\alpha\beta}$ and that $D_{\mathbf{k}=0}^{\alpha\beta} = 0$. In this case, $\omega_{\mathbf{k}=0,\lambda}$ is identical to ω_{λ} , $C_{\mathbf{k}=0,\lambda}^+$ is identical to C_{λ}^+ , and our approximation reproduces the exact result. In Fig. 1 we plot the frequencies $\omega_{\mathbf{k},\pm 1}$ for a square lattice of lattice constant $R_0 = 5000 \text{ \AA}$ for $\mathbf{k} = k\hat{x}$ in the first Brillouin zone, with no magnetic field (solid lines) and with $B = 1 \text{ T}$ (dashed lines). We have assumed Coulomb interactions and have taken $\hbar\omega_0 = 3 \text{ meV}$, $n = 200$, $\epsilon = 12$, and m equal to 0.07 times

the electron mass. The dynamical matrix has been calculated using the results of Bonsall and Maradudin.¹⁵

Having diagonalized $\hat{H}_{c.m.}$, we now consider the interaction of light with an array described by the Hamiltonian \hat{H} . We choose light incident obliquely on the array with $\mathbf{q} = q_z \hat{z} + \mathbf{q}$ and $\hat{\epsilon} = \epsilon_z \hat{z} + \hat{\epsilon}$. One way to take the light into account is to add a time-dependent component $\mathbf{A}_1(\mathbf{r}_{\alpha i}) = \text{Re}[\hat{\epsilon}(E_0 c / i\omega) \exp(i\mathbf{q} \cdot \mathbf{r}_{\alpha i} - i\omega t)]$ to the vector potential in our Hamiltonian. If we treat this as a small perturbation, neglect the \mathbf{A}_1^2 term, and make the dipole approximation $\exp(i\mathbf{q} \cdot \mathbf{u}_{\alpha i}) = 1$, we can write the perturbing Hamiltonian as

$$\begin{aligned} H' &= \frac{E_0}{2} e^{-i\omega t} \sum_{\alpha i} e^{i\mathbf{q} \cdot \mathbf{R}_{\alpha i}} \epsilon_{\alpha i} \cdot \mathbf{u}_{\alpha i} + \text{H.c.} = \frac{E_0}{2} e^{-i\omega t} N \epsilon_{\alpha} \cdot \mathbf{U}_{-\mathbf{q}} + \text{H.c.} \\ &= N^{1/2} \frac{E_0}{2} e^{-i\omega t} \sum_{\lambda\sigma} \left[\frac{\hbar}{2m\omega_{\mathbf{q},\lambda}} \right]^{1/2} (\epsilon_{\alpha x} + i\epsilon_{\alpha y} a_{\mathbf{q},\lambda}^{\sigma}) C_{\sigma\mathbf{q},\lambda}^{\sigma} + \text{H.c.} \end{aligned} \quad (10)$$

where $\sigma = \pm$, $\lambda = \pm 1$,

$$a_{\mathbf{q},\lambda}^{\sigma} = -\sigma \frac{[\omega_{\mathbf{q},\lambda}(\omega_{\mathbf{q},\lambda}^2 - \alpha_{11}) - i\sigma\omega_c\alpha_{12}]}{\omega_c\alpha_{22} - i\sigma\omega_{\mathbf{q},\lambda}\alpha_{12}}, \quad (11)$$

and

$$\begin{aligned} \omega_{\mathbf{q},\lambda}^2 &\equiv \omega_{\mathbf{q},\lambda}^2 \{ 1 + (\omega_{\mathbf{q},\lambda}^2 - \alpha_{11}) \\ &\quad \times [\alpha_{22}(\omega_{\mathbf{q},\lambda}^2 - \alpha_{11}) \\ &\quad + \alpha_{12}^2] / (\omega_c^2\alpha_{22} + \omega_{\mathbf{q},\lambda}^2\alpha_{12}^2) \}. \end{aligned} \quad (12)$$

We see that, in the dipole approximation, light couples only to the center-of-mass excitations of \hat{H} . For first-order processes, the perturbation H' can cause transitions only to states that differ in energy by $\pm\hbar\omega_{\mathbf{q},\pm 1}$ or $\pm\hbar\omega_{\mathbf{q},-1}$ from the original state. Because the wavelength of light of frequency $\omega_0 \sim 5 \times 10^{12} \text{ s}^{-1}$ is $(2\pi c / \epsilon^{1/2}\omega_0) \sim 10^{-2} \text{ cm} \sim 200R_0$, the dipole approximation is very well justified throughout the optical absorption region. In the special case of normal incidence ($q_z = 0$) with $V^{(2)}$ of the form $V^{(2)}(|\mathbf{r}_{\alpha i} - \mathbf{r}_{\beta j}|)$, the dipole approximation is exact in our two-dimensional model and the light couples only to the exact center-of-mass excitations of H with frequencies $\omega_{\pm 1}$. Thus, within this perturbative picture, the optical response at normal incidence of an array of quantum dots described by our original Hamiltonian with any number of electrons on the dots is exactly the same as for a single dot¹⁰⁻¹² with the same total number of electrons. For non-normal incidence, within the dipole approximation, perturbation theory predicts sharp peaks in the infrared optical absorption at $\omega_{\mathbf{q},\pm 1}$.

This analysis, however, is inadequate. It is known from the study of polar crystals¹⁶ that the optical properties of such systems are not given accurately by first-order perturbation theory because the radiation mixes strongly with the dynamical degrees of freedom of the

lattice. For small q_z , the modes created by $C_{\mathbf{q},\lambda}^+$ in fact lie in a continuum of radiation modes and thus become resonances with finite widths and with central frequencies that are shifted from $\omega_{\mathbf{q},\lambda}$. These changes in the modes are known as "retardation" effects because they result when the instantaneous interactions in our model Hamiltonian are replaced by the correct retarded interactions. Because the wavelength of light of frequency ω_0 is so large compared to the lattice spacing, the region where retardation effects are important is a very small fraction of the Brillouin zone, the region to the left of the nearly vertical dotted line in Fig. 1. On the other hand, it is precisely this region that is probed by infrared optical absorption, so we must understand the effects of retardation to understand the optical response of our quantum dot array.

To study retardation effects, we consider the classical electrodynamics of our array in the long-wavelength limit.¹⁶ For simplicity, we consider a system where the dot array is embedded in an infinite semiconductor crystal so that the dielectric constant ϵ is the same for $z > 0$ and $z < 0$. Because the radiation interacts only with the dipole moment on each dot in the long-wavelength limit, we treat our array as a two-dimensional lattice of two-dimensional harmonic oscillators, where each oscillator has charge $-ne$, mass nm , and natural frequency ω_0 (including the effects of any fixed positive charges in the array). The dynamics of the α th dot are given by

$$\ddot{\mathbf{U}}_{\alpha} = -\frac{e}{m} \left[\mathbf{E}_{\alpha} + \frac{\dot{\mathbf{U}}_{\alpha}}{c} \times \mathbf{B} \right] - \omega_0^2 \mathbf{U}_{\alpha}, \quad (13)$$

where \mathbf{E}_{α} is the component of the macroscopic electric field \mathbf{E} that lies in the plane of the array.¹⁷ Taking the continuum limit, we incorporate the charged oscillators through a polarization $\mathbf{P} = \chi \mathbf{E}$, where we use Eq. (13) to write

$$\chi = \delta(z) \frac{(n_s e^2 / m)}{(\omega_0^2 - \omega^2)^2 - \omega^2 \omega_c^2} \begin{pmatrix} \omega_0^2 - \omega^2 & i\omega\omega_c & 0 \\ -i\omega\omega_c & \omega_0^2 - \omega^2 & 0 \\ 0 & 0 & 0 \end{pmatrix}, \quad (14)$$

where $\delta(z)$ is the Dirac delta function and $n_s = (n/R_0^2)$ is the number of electrons per unit area in our array. We assume $\mathbf{E} = \mathbf{E}(z)\exp(iq_{\parallel}x - i\omega t)$ and $\mathbf{B} = \mathbf{B}(z)\exp(iq_{\parallel}x - i\omega t)$, and solve Maxwell's equations subject to the appropriate boundary conditions. Outside the continuum, we require that $E(z) \rightarrow 0$ as $z \rightarrow \pm\infty$. Inside the continuum, we require that $E(z)$ be an outgoing wave. In both cases we get the dispersion relation

$$1 = \frac{1}{(\omega_0^2 - \omega^2)^2 - \omega^2 \omega_c^2} \times \left[\omega_i^2 \omega^2 - \omega_i (\omega_0^2 - \omega^2) \frac{(q_{\parallel}^2 c^2 / \epsilon - 2\omega^2)}{(q_{\parallel}^2 c^2 / \epsilon - \omega^2)^{1/2}} \right], \quad (15)$$

where $\omega_i \equiv (2\pi n_s e^2 / \epsilon^{1/2} mc)$. Outside the radiation continuum, $\alpha_0^2 \equiv (q_{\parallel}^2 c^2 / \epsilon - \omega^2)\epsilon/c^2$ is positive and we take the positive square root. Inside the continuum, α_0^2 is complex near the roots of the dispersion relation and we take the square root with negative imaginary part.

Two special cases deserve mention. When $q_{\parallel} = 0$, the dispersion relation given by Eq. (15) factors, yielding

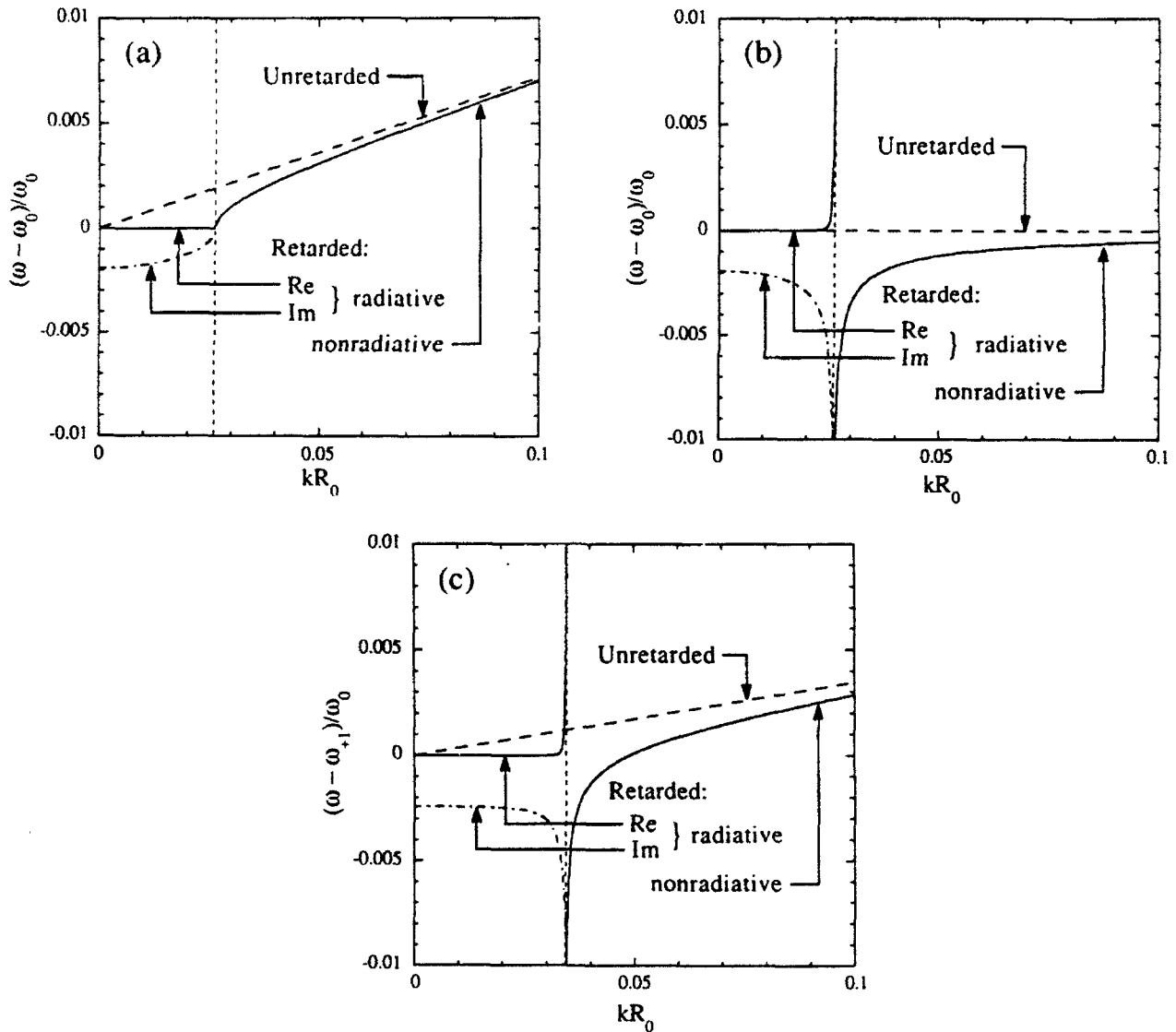


FIG. 2. (a) Small- k behavior of longitudinal mode frequencies ($B=0$ T): unretarded (diagonal dashed line), and retarded (real part, solid line; imaginary part, dash-dotted line). (b) Small- k behavior of transverse mode frequencies ($B=0$ T): unretarded (horizontal dashed line), and retarded (real part, solid line; imaginary part, dash-dotted line). (c) Small- k behavior of high-frequency mode ($B=1$ T): unretarded (slanted dashed line), and retarded (real part, solid line; imaginary part, dash-dotted line). Nearly vertical dotted line in (a)–(c) is the edge of the radiation continuum $\omega = kc/\epsilon^{1/2}$. Modes outside the continuum are nonradiative and have real frequencies. Modes inside the continuum are radiative and have complex frequencies.

$$\omega_{\lambda}^{\text{ret}} = \lambda(\omega_c/2) + (\omega_0^2 + \omega_c^2/4 - \omega_i^2/4 - i\lambda\omega_c\omega_i/2)^{1/2} - i\omega_i/2$$

with $\lambda = \pm 1$, where the square root is taken with positive real part. For $n_s \sim 10^{11} \text{ cm}^{-2}$ and $\epsilon \sim 12$, we find $\omega_i \sim 10^{10} \text{ s}^{-1} \ll \omega_0$, so $\omega_{\lambda}^{\text{ret}} \approx \omega_{\lambda}$ and the B -field dispersion of the frequencies at $q_{\parallel} = 0$ is hardly affected by retardation.

When $B=0$, Eq. (15) factors again and we get separate dispersion relations for the longitudinal and transverse modes. For the longitudinal mode we find $\omega_l^2 = \omega_0^2 - \omega_i^2/2 + \omega_i(-\omega_0^2 + \omega_i^2/4 + q_{\parallel}^2 c^2/\epsilon)^{1/2}$. This is complex with constant real part for $q_{\parallel}^2 < (\omega_0^2 - \omega_i^2/4)\epsilon/c^2$, so $\text{Re}\omega_l$ is almost dispersionless in this region. Thus retardation effects strongly suppress the dispersion of the longitudinal mode for q_{\parallel} in the radiation continuum. As q_{\parallel}^2 increases beyond the critical value $(\omega_0^2 - \omega_i^2/4)\epsilon/c^2$, ω_l becomes real and rises toward its nonretarded value. Figure 2(a) shows the small- q_{\parallel} dispersion of $\text{Re}\omega_l$ (solid line), $\text{Im}\omega_l$ (dash-dotted line), and the unretarded longitudinal frequency $\omega_{q_{\parallel} \rightarrow 1}$ (dashed line). The edge of the radiation continuum is indicated by the nearly vertical dotted line. Figures 2(b) and 2(c) are similar plots for the transverse mode and for the higher-frequency mode when $B=1 \text{ T}$, respectively.

With the addition of a small dissipative term in χ , the complex-frequency modes will appear as resonant peaks in the infrared optical absorption spectrum.¹⁶ If the electrons on different dots are screened from each other, as may be the case in samples with a metallic gate very close to the array,^{1,3,4} the optical absorption spectrum is that for isolated single dots, with no dispersion. Even when there is no such screening, however, we see that, when retardation is taken into account, the optical absorption spectrum is essentially unchanged by interactions between dots, except that the peaks acquire finite natural widths on the order of ω_i . These widths are much smaller than those shown in the experimental data,¹⁻⁴ which

presumably arise from impurity scattering and from imperfections in the dot array. The same conclusions hold with or without external magnetic fields. Thus it is very difficult to observe effects of interdot interactions with infrared optical absorption, even when the effects are large outside the optical absorption regime. It may, however, be possible to observe the dispersion outside the radiation continuum by Raman scattering or by other techniques such as the use of a grating.¹⁸

In summary, we have studied collective excitations in an array of parabolically confined quantum dots, with and without an external magnetic field. Using instantaneous interactions and a harmonic approximation to the interaction between electrons on different dots, we have found that the Hamiltonian separates into a term that depends only on the coupled center-of-mass motions of different dots and a term that depends only on the relative coordinates within each dot. Diagonalizing the center-of-mass portion of the Hamiltonian, we have shown that light couples only to the center-of-mass modes to an excellent approximation. Although the modes show dispersion at short wavelengths, the dispersion would be very difficult to observe via far infrared optical absorption—first, because the wave vector in such an experiment is always very small compared to the reciprocal lattice vectors of the dot array, and second, because the effects of retardation serve to reduce still further the dispersion in the optical region.

We are grateful to S. Das Sarma, P. M. Young, and especially R. D. Meade for several helpful discussions and suggestions. One of us (L.B.) wishes to acknowledge support from Spain's Ministerio de Educacion y Ciencia. This work was supported by the National Science Foundation through the Harvard Materials Research Laboratory and Grant No. DMR88-17291, by U.S. Defense Advanced Research Projects Agency through U.S. Office of Naval Research Contract No. N00014-86-K0033, and by St. John's College, Cambridge, England.

*Present address: Dpt. Física de la Materia Condensada, Facultad de Ciencias C-XII, Universidad Autónoma de Madrid, Madrid 28049, Spain.

¹Ch. Sikorski and U. Merkt, Phys. Rev. Lett. **62**, 2164 (1989).

²T. Demel, D. Heitmann, P. Grambow, and K. Ploog, Phys. Rev. Lett. **64**, 788 (1990).

³J. Alsmeier, E. Batke, and J. P. Kotthaus, Phys. Rev. B **41**, 1699 (1990).

⁴C. T. Liu, K. Nakamura, D. C. Tsui, K. Ismail, D. A. Antoniadis, and Henry I. Smith, Appl. Phys. Lett. **55**, 168 (1989).

⁵M. A. Reed, J. N. Randall, R. J. Aggarwal, R. J. Matyi, T. M. Moore, and A. E. Wetsel, Phys. Rev. Lett. **60**, 535 (1988).

⁶W. Hansen, T. P. Smith III, K. Y. Lee, J. A. Brum, C. M. Knoedler, J. M. Hong, and D. P. Kern, Phys. Rev. Lett. **62**, 2168 (1989); K. Ismail, T. P. Smith III, W. T. Masselink, and Henry I. Smith, Appl. Phys. Lett. **55**, 2766 (1989); W. Hansen, T. P. Smith III, K. Y. Lee, J. M. Hong, and C. M. Knoedler, *ibid.* **56**, 168 (1990); J. Cibert, P. M. Petroff, G. J. Dolan, S. J. Pearton, A. C. Gossard, and J. H. English, *ibid.* **49**, 1275

(1986).

⁷Arvind Kumar, Steven E. Laux, and Frank Stern, Phys. Rev. B **42**, 5166 (1990); S. E. Laux, D. J. Frank, and Frank Stern, Surf. Sci. **196**, 101 (1988).

⁸One can see this through simple electrostatic models. For the gated structures, consider the potential near a circular hole in an infinite conducting sheet [see J. D. Jackson, *Classical Electrodynamics*, 2nd ed. (Wiley, New York, 1975), Sec. 3.13]. For mesa-etched structures, consider the potential near a uniformly charged circular disk. In both cases the potential is very close to parabolic, except near the boundaries.

⁹L. Brey, N. F. Johnson, and B. I. Halperin, Phys. Rev. B **40**, 10647 (1989).

¹⁰L. Brey, N. F. Johnson, Jed Dempsey, and B. I. Halperin, in *Proceedings of the NATO Advanced Research Workshop on Light Scattering in Semiconductor Structures and Superlattices*, Mont Tremblant, Quebec, 1990 (Plenum, New York, in press).

¹¹F. M. Peeters, Phys. Rev. B **42**, 1486 (1990).

- ¹²P. A. Maksym and Tapash Chakraborty, *Phys. Rev. Lett.* **65**, 108 (1990); A. V. Chaplik and A. V. Govorov (unpublished).
- ¹³Wei-ming Que and George Kirczenow, *Phys. Rev. B* **38**, 3614 (1988).
- ¹⁴Yoel Tikochinsky, *J. Math. Phys.* **20**, 406 (1979).
- ¹⁵Lynn Bonsall and A. A. Maradudin, *Phys. Rev. B* **15**, 1959 (1977).
- ¹⁶See, e.g., Ronald Fuchs, K. L. Kliewer, and W. J. Pardee, *Phys. Rev.* **150**, 1966.
- ¹⁷The behavior of a collection of interacting harmonic oscillators is often formulated in terms of the response to the local electric field E_{loc} at the site of the oscillator, rather than to the long-wavelength macroscopic field E , which we have used in Eq. (13). The difference between E and E_{loc} is already taken into account, however, by our definition of ω_0 .
- ¹⁸D. N. Mirlin, *Surface Polaritons* (North-Holland, Amsterdam, 1982), p. 3.

Electronic and optical properties of a superlattice in a parabolic potential

L. Brey, N. F. Johnson, and Jed Dempsey

Lyman Laboratory of Physics, Harvard University, Cambridge, Massachusetts 02138

(Received 17 April 1990)

The electronic and optical properties of a superimposed parabolic and superlattice potential are calculated within the local-density approximation for a range of superlattice periods d . For small d , the properties are similar to those of a parabolic quantum well containing electrons with effective masses corresponding to the underlying superlattice. The "effective-mass approximation" is valid in this regime. For large d , the spacing of the ideal-parabolic-well energy levels becomes comparable to the superlattice miniband width, and the effective-mass approximation breaks down.

I. INTRODUCTION

Remotely doped wide parabolic quantum wells (WPQW's) have recently been proposed¹ as systems where an almost three-dimensional electron gas can be obtained without significant electron-impurity interaction. Several experimental and theoretical studies of the properties of WPQW's have recently been reported.²⁻⁷ In particular, the infrared optical absorption and magneto-optical absorption in WPQW's have been studied experimentally⁶ and theoretically.⁷ It has been shown⁷ that, in the absence of an applied magnetic field, an n -type doped parabolic quantum well absorbs far-infrared radiation at the bare harmonic-oscillator frequency, independent of the electron-electron interaction and the number of electrons in the well. For this reason, it has been thought that optical-absorption measurements might be useful in characterizing departures from ideal parabolicity in experimental samples.

Experimentally, WPQW's have been created from a thin layer $\text{GaAs}/\text{Ga}_{1-x}\text{Al}_x\text{As}$ superlattice by changing the relative GaAs and $\text{Ga}_{1-x}\text{Al}_x\text{As}$ layer thicknesses in a 20-Å-period superlattice so that the average Al concentration varies parabolically along the growth axis.² The implicit assumption being made is that an electron in a short-period superlattice "sees" an average "effective" potential (defined by the bottom of the superlattice conduction band) which varies quadratically along the growth axis. This assumption subsumes the properties of the underlying superlattice into a renormalized electron mass equal to the superlattice conduction-band-edge mass. The effective-mass approximation has essentially been made.

The aim of the present work is to study the electronic and optical properties of a combined parabolic-quantum-well (PQW) and superlattice (SL) potential for an arbitrary superlattice⁸ period d . For simplicity only periodic superlattices are investigated. We find the following results. (i) the superlattice potential introduces oscillations in the self-consistent charge-density profile with spatial period equal to that of the superlattice. (ii) For superlattices with thin barriers (such that the superlattice band-

width is much greater than the parabolic-well subband spacing) the properties of the combined superlattice and parabolic quantum well correspond to those of a parabolic well with a renormalized mass equal to the superlattice mass. In particular, the self-consistent energy levels show a fairly weak dependence on the superlattice-layer period. The static dielectric screening of the superlattice potential by the electron gas in the parabolic potential is similar to the screening obtained from a bulk three-dimensional electron gas. The combined PQW and SL absorbs infrared light with the electric field along the growth axis at only one frequency, independent of the electron-electron interaction or the electron concentration. (iii) For superlattices with thick barriers the spacing of the ideal parabolic energy levels becomes comparable to the superlattice miniband width, and the effective-mass approximation begins to break down. In particular, the self-consistent energy levels show dramatic variation with superlattice-layer period. The optical-absorption spectrum for light with the electric field along the growth axis shows increasing structure with increasing superlattice period. Satellites appear around the fundamental absorption peak, which itself becomes shifted to lower frequencies. Effective masses, obtained from the area under the fundamental peak, and the position of the fundamental peak, respectively, are shown to differ increasingly from each other and from the bare superlattice band-edge mass with increasing superlattice period.

In Sec. II we describe the calculational approach, which is the self-consistent-field approximation within the Hohenberg-Kohn-Sham local-density approximation (LDA). In Sec. III the calculated electronic and optical properties of the combined SL and PQW potentials are presented. Finally, in Sec. IV we summarize our results. In the present paper we restrict ourselves to the case of zero applied magnetic field. If one can neglect the scattering of electrons by impurities and phonons, the absorption in this case is produced only by the component of the electric field in the z direction (perpendicular to the layer). Thus, to see the described effects experimentally, one must use radiation which is incident at an angle far from normal incidence.

II. FORMALISM

We use the effective-mass approximation in order to describe the electrons in the host semiconductor. We take the static dielectric constant to be constant along the well. The nonparabolicity of the conduction band and the band-mixing effects induced by the confinement are omitted from the calculation. These effects only have small influence on the electronic properties of the system.

The interactions between electrons in the conduction band can be separated into a Hartree term due to the electrostatic potential of the total electron density and an exchange-correlation term. The exchange-correlation part of the ground-state energy can be described as a functional of the electron density.⁹ In the LDA this functional is assumed to have only local dependence on the electron density. Making this local approximation leads to a one-body Schrödinger-type equation, where the electrons move in a potential that is the sum of the external (e.g., parabolic plus superlattice) potential, the Hartree potential, and an exchange-correlation potential. Although the energy eigenvalues of this one-particle equation do not correspond to the quasiparticle energies, one can consider the exchange-correlation potential as a local, energy-independent self-energy.¹⁰ The LDA gives good results for conduction electrons in silicon inversion layers and GaAs-Ga_{1-x}Al_xAs heterostructures, and for quantum wells.^{11,12}

Specifically, within these approximations the motion of the electrons in directions parallel (x, y) and perpendicular (z) to the electron sheet are separable. The electrons are free to move in the plane perpendicular to the confining direction, and the wave function and eigenvalues are given by

$$E_{n,k_x,k_y} = \epsilon_n + \frac{\hbar^2 k_x^2}{2m^*} + \frac{\hbar^2 k_y^2}{2m^*}, \quad (1a)$$

$$\Psi_{n,k_x,k_y}(\mathbf{r}) = \frac{1}{\sqrt{S}} e^{i(k_x x + k_y y)} \varphi_n(z). \quad (1b)$$

Spin degeneracy has been assumed, and the spin index omitted. In the above expression, S is the sample area, $\mathbf{k} = (k_x, k_y)$ is the wave vector of the electron, m^* is the effective mass, and ϵ_n and $\varphi_n(z)$ are obtained from the one-dimensional Schrödinger equation,

$$\left[-\frac{\hbar^2}{2m^*} \frac{d^2}{dz^2} + V(z) + V_H(z) + V_{xc}(z) \right] \varphi_n(z) = \epsilon_n \varphi_n(z). \quad (2)$$

In this expression $V(z)$ is the bare potential, $V_{xc}(z)$ is the exchange-correlation potential,¹³ and $V_H(z)$ is the Hartree term due to the electrostatic interaction of the electrons with themselves and with the ionized impurities. Consistent with the approach of a constant value of the dielectric constant, we have neglected the effect of the image potentials in Eq. (2). The self-consistent solution of Eq. (2) gives us the charge-density profile, the Fermi energy, the total potential—defined as $V_T(z) \equiv V(z) + V_H(z) + V_{xc}(z)$ —and the subband energies. From the eigenfunctions and eigenvalues, we can obtain the infrared (ir) optical spectrum of the system.

The electrons absorb light at the frequencies corresponding to the collective modes of the system which must be determined from the poles of the appropriate response function. Within the LDA, the resonances are shifted from the self-consistent subband separation by the depolarization effect¹⁴ due to the Hartree screening of the resonance, and by the excitoniclike¹⁴ or vertex-correction effect due to the exchange-correlation screening of the resonance. If one can neglect the scattering of electrons by impurities and phonons, the absorption of light is produced only by the component of the electric field perpendicular to the electron layer. In this case, and within the dipole approximation, we obtain the optical absorption by using the self-consistent-field approximation together with the LDA.¹⁴ In the form derived by Ando,¹⁴ the optical absorption per unit area can be written as

$$P(\omega) = \frac{1}{2} \text{Re}[\partial_{xx}(\omega) D^2], \quad (3)$$

where D is the external electric field in the z direction. The quantity ∂_{xx} is the modified two-dimensional dynamical conductivity given by

$$\partial_{xx}(\omega) = \frac{e^2}{m^*} (-i\omega) n_s \sum_i \frac{\tilde{f}_i}{E_i^2 - (\hbar\omega)^2 - 2i\hbar\omega/\tau}, \quad (4)$$

where we have introduced a phenomenological relaxation time τ , and

$$\tilde{f}_i = \left[\sum_{n,n'} \left[\frac{2m^*}{\hbar^2} (\epsilon_n - \epsilon_{n'}) \right]^{1/2} Z_{n'n} \left[\frac{N_n - N_{n'}}{n_s} \right]^{1/2} U_{n'n,i} \right]^2. \quad (5)$$

Here, $Z_{n'n}$ is the matrix element of the position operator z between the states $\varphi_{n'}$ and φ_n , n_s is the two-dimensional electron density, and N_i is the number of electrons per unit area in the i th subband. \tilde{E}_i^2 in Eq. (4) and $U_{n'n,i}$ in Eq. (5) are the eigenvalues and eigenvectors of the matrix

$$\Lambda_{nn',mm'} = E_{n'n}^2 \delta_{n'n} \delta_{mm'} + (N_n - N_{n'})^{1/2} (N_m - N_{m'})^{1/2} (E_{m'm} E_{n'n})^{1/2} (\alpha_{nn',mm'} - \beta_{nn',mm'}). \quad (6)$$

In the above expressions the indexes n , n' , m , and m' refer to the eigenvalues and eigenvectors of the one-dimensional Hamiltonian given in Eq. (2). The matrix elements α and β in Eq. (6) represent the depolarization and excitonic effect, respectively, and are given by the expressions

$$\alpha_{nn',mm'} = -2 \frac{4\pi e^2}{\epsilon} \int_{-\infty}^{+\infty} dz \varphi_n(z) \varphi_n^*(z) \int_{-\infty}^z dz' \int_{-\infty}^{z'} dz'' \varphi_m(z'') \varphi_m^*(z''), \quad (7)$$

$$\beta_{nn',mm'} = -2 \int_{-\infty}^{+\infty} \varphi_n(z) \varphi_n^*(z) \frac{\partial V_{xc}}{\partial n(z)} \varphi_m(z) \varphi_m^*(z) dz, \quad (8)$$

where $n(z)$ is the electron density. It is also easy to prove that the two-dimensional dynamical conductivity satisfies the sum rule

$$\int \sigma_{xx}(\omega) d\omega = \frac{e^2 \pi}{m^*} n_s. \quad (9)$$

It is important to note that, to be consistent, the use of the Hartree potential in the calculation of the depolarization effect must be accompanied by the inclusion of V_H in the one-dimensional Schrödinger equation, and vice versa.¹⁵ Also, the inclusion of the excitoniclike effect in the response function needs to be accompanied by the inclusion of the exchange-correlation potential in the one-dimensional Schrödinger equation.¹⁵

III. RESULTS

A parabolic potential $V(z) = Az^2$ mimics the potential created by a uniform slab of positive charge of density $n_0 = A\epsilon/2\pi e^2$. In this expression e is the electron charge and ϵ is the (uniform) static dielectric constant of the host semiconductor. The actual parabolic potential profile $V_{\text{PQW}}(z)$ used in the calculations was modified to model the experimental WPQW samples more closely. Specifically, a finite parabolic well was chosen of thickness W and height Δ_1 , bounded by an additional potential barrier of height Δ_2 ,

$$V_{\text{PQW}}(z) = \frac{4\Delta_1 z^2}{W^2} \Theta(W/2 - |z|) + (\Delta_1 + \Delta_2) \Theta(|z| - W/2), \quad (10)$$

where Θ is the unit-step function. We define the fractional occupation of the WPQW as $\eta = n_s/n_d W$, where n_s is the number of electrons per unit area in the system. The thickness of the electron layer increases linearly with n_s , and for $\eta = 1$ the thickness will be W . When η is larger than one, the excess of electronic charge will be concentrated at the edges of the WPQW and the charge-density distribution will no longer be uniform. We are interested in the cases of uniform charge distribution and we restrict ourselves to $\eta = 0.6$. Size effects in a parabolic quantum well for η near 1 are investigated in Ref. 16. In the present calculations we use the following set of parameters: $\epsilon = 12.5$, $\Delta_1 = 150$ meV, $\Delta_2 = 75$ meV, and $m^*/m_0 = 0.067$, with m_0 the free-electron mass. The positively charged donor impurities are in two layers of equal charge density, 200 Å thick, located just outside the well on either side. We have checked that our results are insensitive to the precise location of the positive charges for reasonable choices of the parameters.

The superimposed superlattice potential $V_{\text{SL}}(z)$ used in the present work is the Kronig-Penney potential consisting of rectangular barriers of width b and height V_0 , and

wells of width a . In our calculations V_0 was taken to be 15 meV and the barrier and well thicknesses were taken to be equal ($a = b$). The position of the superlattice is chosen such that there is a barrier at the center of the parabolic well ($z = 0$) and the superlattice retains inversion symmetry about $z = 0$.

A. Electronic structure

In this subsection we study the electronic structure of a combined SL potential $V_{\text{SL}}(z)$ and parabolic well potential $V_{\text{PQW}}(z)$. In Fig. 1 we compare the initial potential, the self-consistent potential, and the charge-density profile in both the absence [Fig. 1(a)] and presence [Fig. 1(b)] of the superlattice potential $V_{\text{SL}}(z)$. The specific superlattice period used in this illustration was 300 Å. In the absence of the superlattice potential [Fig. 1(a)], the charge is almost uniform in the occupied part of the well. The small bumps at the edges of the slab are Friedel-type oscillations.¹⁶ In the presence of the superlattice potential [Fig. 1(b)], additional oscillations of the charge-density profile appear with the same periodicity as the superlattice. It is interesting to note from the self-consistent total potential that, although $V_{\text{PQW}}(z)$ is well screened by the electron gas, $V_{\text{SL}}(z)$ is not.

Figure 2 shows the self-consistent subband energies ϵ_s ,

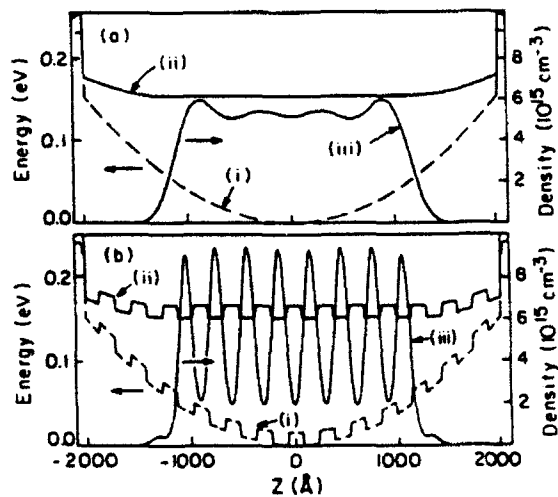


FIG. 1. Potential and charge density in a parabolic quantum well in (a) the absence and (b) the presence of an additional superlattice potential of period 300 Å. The fractional occupation $\eta = 0.6$, and the barrier height in the superlattice potential is 15 meV. Curve (i) shows the bare potential $V(z)$ for the well, and curve (ii) shows the total self-consistent potential $V_T(z)$. Curve (iii) shows the self-consistent charge-density profile $n(z)$. The parameters of the parabolic quantum well are given in the text.

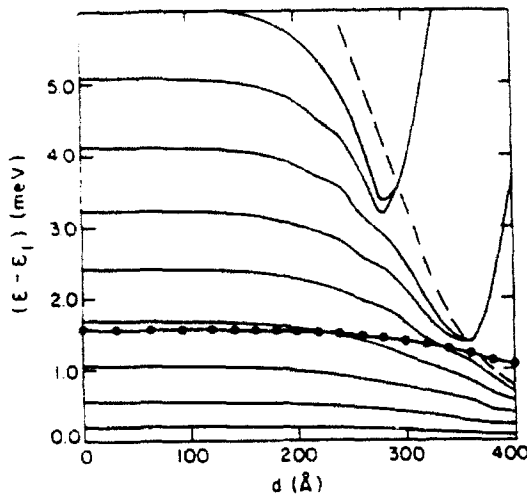


FIG. 2. Fermi level, $\epsilon_F - \epsilon_1$ (line with solid dots), and energy-level separation, $\epsilon_i - \epsilon_1$ (solid line), as a function of the superlattice period d . The fractional occupation η is 0.6. The bandwidth of the lowest conduction miniband of the superlattice is shown dashed. The parameters of the parabolic quantum well and superlattice are given in the text.

measured with respect to the lowest subband ($i=1$) as a reference, for the combined parabolic and superlattice potentials as a function of the SL period d . The dramatic variation of ϵ_i for large SL period d can be understood by comparing the following two quantities associated with the constituent parabolic and superlattice potentials, respectively: (i) the spacing of self-consistent subband energy levels in an ideal parabolic quantum well $V_{\text{PQW}}(z)$, and (ii) the bandwidth of the lowest miniband in the superlattice $V_{\text{SL}}(z)$ (indicated by a dashed line in Fig. 2). We will only be considering the bandwidth of the *unscreened* SL potential since the electron gas cannot effectively screen $V_{\text{SL}}(z)$ (see Fig. 1). For small d the superlattice bandwidth¹⁷ (dashed line) is much larger than the spacing of the parabolic-quantum-well levels, and the energy levels ϵ_i for the total potential are essentially the same as those calculated for an ideal parabolic quantum well where the electron effective mass in the perpendicular direction (m_\perp) is taken to be equal to the mass at the bottom of the superlattice conduction band. These latter levels for an ideal parabolic quantum well $V_{\text{PQW}}(z)$ are indicated by the $d \rightarrow 0$ limit in Fig. 2. Therefore, in this small- d regime the effects of the superlattice potential can be described by a renormalization of the electron effective mass just as in the well-known effective-mass approximation. As d increases, the bandwidth of the SL decreases, and the perpendicular superlattice effective mass m_\perp increases. Within a one-electron picture, an increase in m_\perp leads to a decrease in the electron energy of confinement ($\sim m_\perp^{-1}$). The separation of the subband energies therefore decreases as d increases, as shown in Fig. 2. The position of the Fermi level decreases as d increases, and the number of occupied subbands increases. An interesting situation arises when $\epsilon_i - \epsilon_1$ becomes comparable to the underlying SL bandwidth. It is no longer appropriate to

describe the SL by an effective medium with a renormalized mass equal to the band-edge SL mass, and the effective-mass approximation begins to break down. As each subband (solid line) crosses the bandwidth (dashed line), a more appropriate value of the electron mass becomes the *negative* mass at the top of the first SL miniband. The energy ϵ_i therefore starts to *increase* with increasing d . For larger d these subbands lie in the SL gap. The corresponding eigenstates are evanescent and are only allowed because of the presence of the parabolic potential which breaks the Bloch condition. Since an evanescent state can occur at the left and right walls of the parabolic potential, a symmetric (bonding) or antisymmetric (antibonding) linear combination of the two can be formed. These two "gap" states become degenerate as d increases, as can be seen from Fig. 2 since the decay length eventually becomes much less than the well width.

It is interesting to consider the SL potential to be an external probe for investigating the screening properties of the electron gas in a PQW. The presence of such an external periodic perturbation yields the total self-consistent potential $V_T(z)$ and charge density shown in Fig. 1(b). For a given SL period d , we can then define a screening factor $\epsilon(q, z)$, where $q = 2\pi/d$, given by

$$\epsilon(q, z) = V_{\text{SL}}(z) / V_T(z),$$

where $V_{\text{SL}}(z)$ is the unscreened SL potential with period d . We choose to evaluate $\epsilon(q, z)$ at the center of the parabolic well ($z=0$) and define $\epsilon(q, 0) = \epsilon(q)$. In fact, $\epsilon(q, z)$ is only a weak function of z in the central region of the parabolic quantum well. For values of q where the system responds linearly to the perturbation, this definition of an effective screening factor $\epsilon(q)$ is consistent with the definition of a static dielectric function. Figure 3 shows $\epsilon(q)$ as a function of q . For comparison, we have also plotted the Bohm-Pines random-phase-approximation (RPA) static dielectric function $\epsilon_{\text{RPA}}^{\text{3D}}(q)$ for a three-dimensional (3D) electron gas of the same concentration, same effective mass, and same background dielectric constant. The magnitudes of $\epsilon(q)$ and $\epsilon_{\text{RPA}}^{\text{3D}}(q)$ both increase as q becomes smaller, since the electron gas is better at screening external perturbations of longer wavelength. Hence the SL potential for large d is reasonably well screened. The deviation at small q between $\epsilon(q)$ and $\epsilon_{\text{RPA}}^{\text{3D}}(q)$ is due to the finite extent of the SL (i.e., size effects become important). For large q the screening of the periodic potential is ineffective. Hence for small d , the SL potential is essentially unscreened (see Fig. 1). It is important to note that in the calculation of $\epsilon(q)$ there is a contribution from the self-consistent treatment of the exchange-correlation potential that is not included in $\epsilon_{\text{RPA}}^{\text{3D}}(q)$.

B. Optical properties

In this subsection we study the optical properties of the combined PQW and SL potentials using the formalism outlined in Sec. II. In Fig. 4 we show the real part of the dynamical conductivity for different values of the superlattice period d . It was shown in Ref. 7 that in the ab-

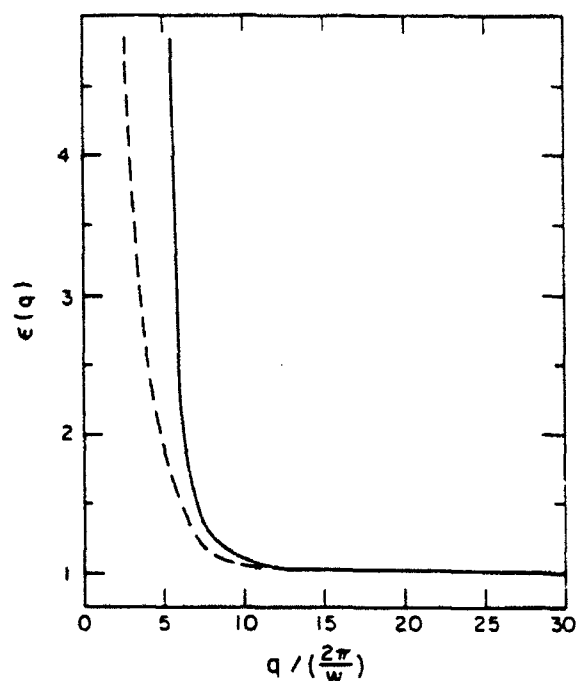


FIG. 3. Solid line shows the screening factor $\epsilon(q)$, defined in the text, as a function of $q=2\pi/d$, where d is the superlattice period. Dashed line shows the static dielectric function ϵ_{RPA}^{D} , calculated within the random-phase approximation, for a three-dimensional electron gas of the same concentration.

sence of the superlattice potential the system only absorbs light at the bare parabolic well frequency $\omega_0=(8\Delta_1/W^2m^*)^{1/2}$ independently of the number of electrons in the system and of the form of the electron-electron interaction. In the parabolic potential the depolarization term plus the vertex-correction term cancel ex-

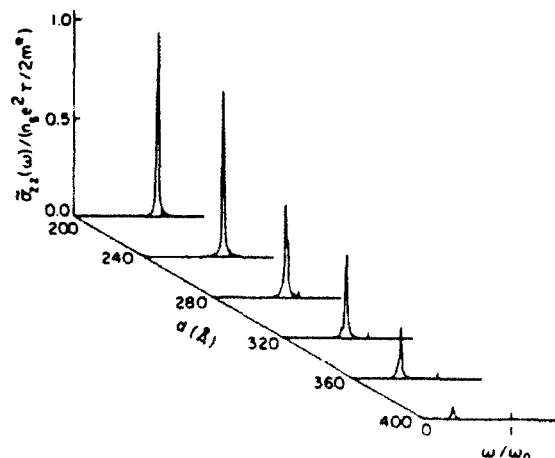


FIG. 4. Calculated real part of the dynamical conductivity $\sigma_1(\omega)$ in a combined superlattice and parabolic potential for different values of the superlattice period d . The fractional occupation η is 0.6. The value of the phenomenological relaxation time, τ , is $0.01\omega_0$.

actly the corrections to the quasiparticle energy spacing due to the Hartree potential and exchange-correlation potential, respectively.^{15,16} Therefore, for small SL periods d such that the SL bandwidth is much greater than the Fermi energy of the electrons in the parabolic well, the system only absorbs light at one frequency. As shown in Fig. 4, increasing the SL period d has two main effects.

(i) The fundamental absorption peak ω_0 shifts to a lower frequency and the intensity of the peak decreases. This can be understood qualitatively in terms of a one-particle picture.

(ii) Satellites begin to appear around ω_0 , which can only be understood in a many-particle picture and arise because the electric field of the incident light can now, in the presence of the superlattice potential, couple to the internal motion of the electrons as well as to the motion of the center of mass. This suggests that a superimposed superlattice potential in a wide parabolic quantum well could be used to investigate the internal excitations of a quasi-three-dimensional electron gas.

We now consider the effects mentioned in (i) in more detail. As discussed in connection with Fig. 2, the presence of a short-period superlattice in a parabolic quantum well can be described by a renormalization of the electron effective mass in the growth direction. Since this mass increases with increasing period d , the absorption peak will occur at lower frequencies. Since optical absorption involves the absorption of photons by electrons below the Fermi energy ϵ_F , we expect the optical absorption of a combined superlattice and parabolic potential to deviate from that of an ideal parabolic well when ϵ_F is of the order of the superlattice bandwidth. From Fig. 2 this situation occurs for $d > 350$ Å, which is consistent with the rapid decrease in the magnitude of the absorption peak in Fig. 4 as $d \rightarrow 400$ Å. From the position of the absorption peak ω_0 , we can use the expression for the bare-parabolic-well frequency to define an effective mass m_p , i.e., $\omega_0=(8\Delta_1/W^2m_p)^{1/2}$. In Fig. 5 we have plotted m_p versus the superlattice band-edge mass¹⁷ m_1 corresponding to different superlattice periods. For small d , where m_1 is essentially the GaAs bulk mass, the SL bandwidth is large and $m_p \approx m_1$. Since m_1 increases with increasing d , the fundamental absorption peak occurs at lower frequencies with increasing d . For large periods d , the effective mass m_p becomes larger than the band-edge mass m_1 due to nonparabolicity of the lowest SL conduction miniband and the eventual breakdown of the effective-mass approximation.

Additional analysis is possible using the sum rule (9). This essentially states that individual electrons contribute to absorption with an average oscillator strength m/m^* , and comes from ignoring interband transitions in the host semiconductors (i.e., only processes involving states in the host conduction band are considered). If we have a superlattice with no parabolic quantum well, then this total oscillator strength is divided among (a) all possible transitions between superlattice conduction minibands,¹⁷ and (b) free-electron absorption (peaked at $\omega=0$) within a superlattice miniband, with oscillator strength m/m_1 . Now consider the presence of a PQW such that band-

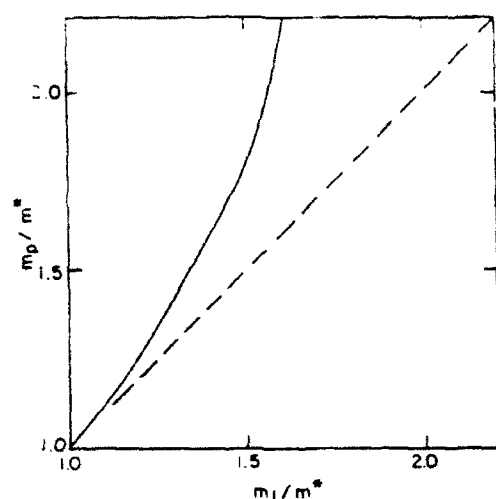


FIG. 5. Solid line shows a comparison between the effective mass m_p obtained from the position of the fundamental absorption peak, and the superlattice band-edge mass m_1 corresponding to different superlattice periods. The dashed line corresponding to $m_p = m_1$ is also shown for comparison.

width of the SL is much larger than the spacing between PQW levels, i.e., d is small. The free-electron absorption at $\omega=0$ will now shift to ω_p due to quantum confinement by the parabolic potential. Assuming all the electrons are in the lowest SL conduction miniband before adding the PQW, the integrated absorption under the fundamental peak at ω_p should be reasonably well described by

$$\int \bar{\sigma}_x(\omega) d\omega \sim \frac{e^2 \pi}{m_1} n_s. \quad (11)$$

As the SL period d increases, the SL mass m_1 decreases

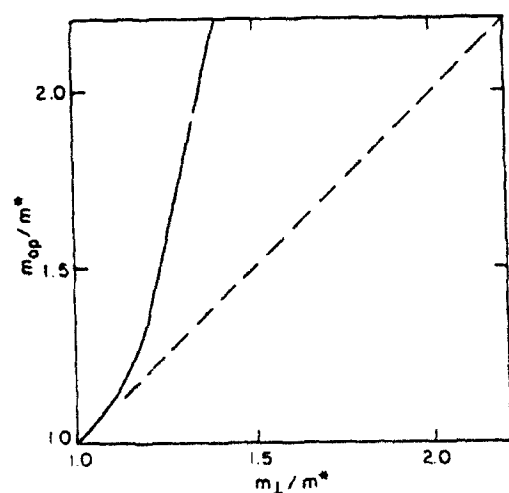


FIG. 6. Solid line shows a comparison between the effective mass m_{op} obtained from the area under the fundamental absorption peak, and the superlattice band-edge mass m_1 corresponding to different superlattice periods. The dashed line corresponding to $m_{op} = m_1$ is also shown for comparison.

and the total oscillator strength at ω_p must decrease. Eventually, as m_1 goes to infinity the SL bandwidth goes to zero and the ω_p peak will disappear (see Fig. 4), leaving transitions between the isolated quantum-well levels of the superlattice. All the oscillator strength now lies in the intersubband transitions of the isolated quantum wells of the superlattice. We can define an optical mass m_{op} from the area under the fundamental absorption peak as follows:

$$\int \bar{\sigma}_x(\omega) d\omega = \frac{e^2 \pi}{m_{op}} n_s. \quad (12)$$

It is interesting to ask how well m_{op} agrees with the effective mass at the bottom of the superlattice miniband m_1 . Figure 6 compares these two masses. For small d , where m_1 is essentially the GaAs bulk mass, the SL bandwidth is large and $m_{op} \approx m_1$. As the SL period increases, both masses increase. However, the optical mass m_{op} eventually exceeds the band-edge SL mass m_1 because of nonparabolicity of the lowest superlattice miniband, and eventual breakdown of the effective-mass approximation.

IV. SUMMARY

We have studied the changes that a superlattice perturbation induces on the electronic and optical properties of wide parabolic quantum wells. When the period of the superlattice is small, such that the bandwidth of the lowest superlattice miniband is much larger than the spacing of the ideal parabolic-quantum-well levels, the properties of the combined superlattice and parabolic potential are well described by those of an ideal parabolic quantum well with a renormalized electron mass equal to the lowest superlattice miniband mass. In particular, the combined superlattice and parabolic-quantum-well potential only absorbs light at one frequency.

When the period of the superlattice increases, the bandwidth of the superlattice becomes comparable to the spacing of the ideal-parabolic-quantum-well levels, and the properties are no longer well described by the "effective-mass approximation." In this case, additional peaks appear around the fundamental peak in the optical-absorption spectra.

ACKNOWLEDGMENTS

It is a pleasure to acknowledge B. I. Halperin for fruitful discussions and a critical reading of the manuscript. We also thank S. Das Sarma, H. Ehrenreich, and R. D. Meade for useful discussions. Two of us (L.B. and N.F.J.) wish to acknowledge support from the Ministerio de Educación y Ciencia (Spain) and from St. John's College, Cambridge (United Kingdom), respectively. This work was supported by the U.S. National Science Foundation (NSF) through the Harvard University Materials Research Laboratory and Grant No. DMR-88-17291, and the U.S. Defense Advanced Projects Agency (DARPA) through Office of Naval Research (ONR) Contract No. N00014-86-K-0033.

- ¹A. C. Gossard, B. I. Halperin, and R. M. Westervelt (unpublished); B. I. Halperin, *Jpn. J. Appl. Phys.* **26**, Suppl. 26-3, 1913 (1987).
- ²M. Sundaram, A. C. Gossard, J. H. English, and R. M. Westervelt, *Superlatt. Microstruct.* **4**, 683 (1988); E. G. Gwinn, R. M. Westervelt, P. F. Hopkins, A. J. Rimberg, M. Sundaram, and A. C. Gossard, *Phys. Rev. B* **39**, 6260 (1989); E. G. Gwinn, P. F. Hopkins, A. J. Rimberg, R. M. Westervelt, M. Sundaram, and A. C. Gossard, in *High Magnetic Fields in Semiconductors Physics II*, edited by G. Landwehr (Springer-Verlag, New York, 1989).
- ³M. Shayegan, T. Sajoto, M. Santos, and C. Silvestre, *Appl. Phys. Lett.* **53**, 791 (1988); T. Sajoto, J. Jo, L. Engel, M. Santos, and M. Shayegan, *Phys. Rev. B* **39**, 10464 (1989); M. Shayegan, T. Sajoto, J. Jo, M. Santos, and H. D. Drew, *ibid.* **40**, 3476 (1989).
- ⁴L. Brey and B. I. Halperin, in *Proceedings of the Eighth International Conference on the Electronic Properties of Two-Dimensional Systems*, Grenoble, 1989 [*Surf. Sci.* (to be published)]; *Phys. Rev. B* **40**, 11 634 (1989).
- ⁵M. P. Stopa and S. Das Sarma, *Phys. Rev. B* **40**, 10048 (1989).
- ⁶K. Karrai, H. D. Drew, M. W. Lee, and M. Shayegan, *Phys. Rev. B* **39**, 1426 (1989); K. Karrai, X. Ying, H. D. Drew, and M. Shayegan, *ibid.* **40**, 12 020 (1989).
- ⁷L. Brey, N. F. Johnson, and B. I. Halperin, *Phys. Rev. B* **40**, 10 647 (1989).
- ⁸Some preliminary magnetotransport results on this heterostructure were presented at the 1990 March Meeting of the American Physical Society by J. Jo, T. Sajoto, M. Santos, and M. Shayegan (unpublished).
- ⁹P. Hohenberg and W. Kohn, *Phys. Rev.* **136**, B864 (1964); W. Kohn and L. J. Sham, *ibid.* **140**, A1133 (1965).
- ¹⁰L. J. Sham and W. Kohn, *Phys. Rev.* **145**, 561 (1966).
- ¹¹See, e.g., T. Ando, A. B. Fowler, and F. Stern, *Rev. Mod. Phys.* **54**, 437 (1982).
- ¹²F. Stern and S. Das Sarma, *Phys. Rev. B* **30**, 840 (1984).
- ¹³We use the exchange-correlation potential suggested by L. Hedin and B. I. Lundqvist, *J. Phys. C* **4**, 2064 (1971). Since we suppose a constant effective mass and dielectric constant, this potential is continuous across the heterostructure.
- ¹⁴T. Ando, *Z. Phys. B* **26**, 263 (1977).
- ¹⁵L. Brey, N. F. Johnson, Jed Dempsey, and B. I. Halperin, in *Light Scattering in Semiconductor Structures and Superlattices* (Plenum, New York, in press); S. Das Sarma, *ibid.*
- ¹⁶L. Brey, Jed Dempsey, N. F. Johnson, and B. I. Halperin, *Phys. Rev. B* (to be published).
- ¹⁷N. F. Johnson, H. Ehrenreich, P. M. Hui, and P. M. Young, *Phys. Rev. B* **41**, 3655 (1990).

Additional evidence concerning the valence-band offset in HgTe/CdTe

P. M. Young and H. Ehrenreich*

Division of Applied Sciences, Harvard University, Cambridge, Massachusetts 02138

(Received 17 September 1990)

The consistency of large values of the valence-band offset, Λ , in HgTe/CdTe superlattices with magneto-optical experiments is examined in light of data on a 90-Å HgTe/40-Å CdTe superlattice. The data are shown to be consistent with values $\Lambda = 400 \pm 40$ meV rather than the much smaller cited values. This analysis, when considered with photoemission experiments, leaves intact the conclusion that HgTe/CdTe superlattices are best explained by a large offset.

The controversy concerning the value of the valence-band offset, Λ , in HgTe/CdTe superlattices (SL's) arose from the different values obtained by photoemission¹ ($\Lambda \approx 350 \pm 60$ meV) and magneto-optical experiments ($\Lambda \approx 40$ meV).² In a previous paper, Johnson *et al.*³ resolved this controversy by showing that the magneto-optical data obtained by Berroir *et al.*² from an experiment on a 100-Å HgTe/36-Å CdTe SL were consistent with a 350-meV offset due to the existence of a second semiconducting regime at larger Λ . Recently, Choi *et al.*⁴ presented results of a similar experiment on a 90-Å HgTe/40-Å CdTe SL sample, which were claimed to be consistent with $\Lambda = 40$ meV, but not $\Lambda = 350$ meV. The present work shows that the data are in fact consistent with $\Lambda = 400 \pm 40$ meV, in agreement with the photoemission values.

Since the appearance of Ref. 3, in which the offset controversy was initially resolved, several articles confirming a large offset, $\Lambda \gtrsim 350$ meV, have appeared in the literature. A few of the most pertinent references are summarized here. In addition to the 58-Å HgTe/42-Å Hg_{0.15}Cd_{0.85}Te SL absorption coefficient calculations of Ref. 5, analyses of other HgCdTe SL's performed by Cesar *et al.*⁶ have concluded $\Lambda \approx 400$ meV. Hoffman and co-workers⁷ have confirmed the large offset and the existence of a second semiconducting regime as predicted by Refs. 3 and 8, using the results of magnetotransport measurements for a set of three HgTe/Hg_{0.15}Cd_{0.85}Te SL's with varying well and barrier widths. Berroir *et al.*⁹ performed cyclotron-resonance experiments on Hg_{0.95}Zn_{0.05}Te/Hg_{0.15}Cd_{0.85}Te SL's and found electron mass anisotropy corresponding to $\Lambda = 350$ meV for HgTe/CdTe systems.

The sample examined by Choi *et al.*⁴ consists of twelve double layers of 90-Å HgTe/40-Å CdTe. The cyclotron effective mass is found to be $m_c^* \approx 0.011m$, close to the value $m_c^* = 0.015 \pm 0.003m$ of the 100-Å HgTe/36-Å CdTe sample (in the limit of vanishing magnetic field).¹⁰

As in previous work,^{5,11,12} the present theoretical results are obtained within the envelope function approximation. Although this approach relies on $k \cdot p$ perturbation theory applied to a bulk $k=0$ basis set limited to that of the Kane model, its validity was verified by comparison with extended basis models employing ~ 50 bulk

wave functions.¹³ Quantitative results for effective masses and optical absorption coefficients for a variety of 3–5 and 2–6 SL's have been obtained, which are in excellent agreement with experiment.^{5,11} The analysis of the 90-Å HgTe/40-Å CdTe sample in this paper uses the same bulk parameters as those of Ref. 3, and neglects the effects of strain.

Figure 1 shows the behavior of the band gap for HgTe/CdTe SL's with CdTe barrier width of 40 Å and HgTe well widths ranging from 70 to 130 Å. (Similar results for 36-Å barrier width appear in Ref. 8.) We find that the 90-Å HgTe/40-Å CdTe SL becomes semimetallic at $\Lambda \approx 300$ meV, in agreement with Choi *et al.*,⁴ but that semiconducting behavior reappears at $\Lambda \approx 350$ meV, a value lower than that implied by the inset of Fig. 3 of Choi *et al.*⁴

The appearance of the semimetallic region is explained by the offset-dependent behavior of the SL bands at SL wave vector $K=0$. The qualitative behavior of the bands

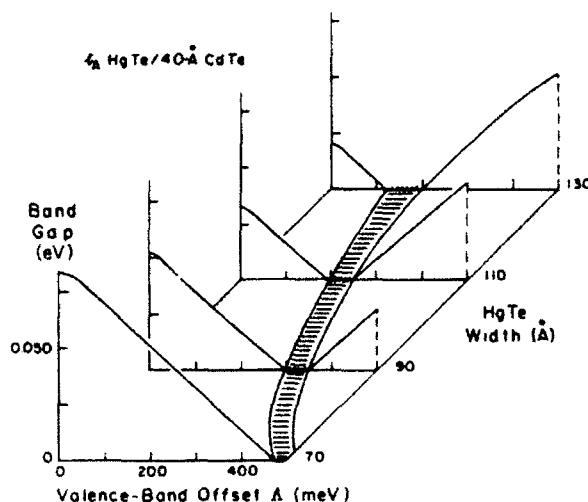


FIG. 1. Variation of band gap E_g between $C1$ and $HH1$ as a function of band offset Λ and HgTe layer width for fixed CdTe width of 40 Å. The shaded region represents the regime in which the superlattice is semimetallic.

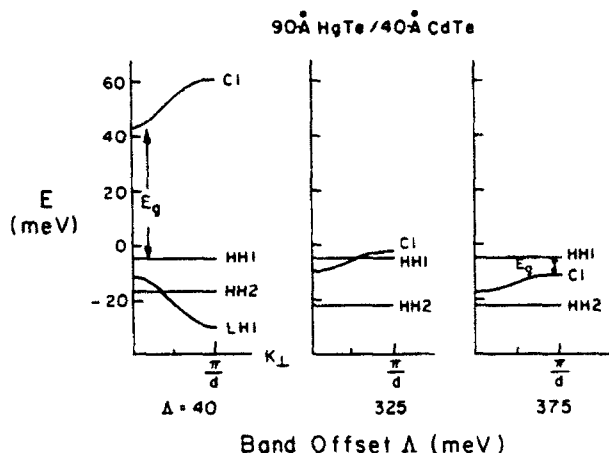


FIG. 2. Band structure for 90-Å HgTe/40-Å CdTe superlattice along K_1 as a function of band offset Δ . As Δ increases the superlattice changes from semiconducting to semimetallic and back to semiconducting as C1 crosses and then passes through HH1.

is given in Fig. 2 of Ref. 3 and Fig. 3 of Choi *et al.*⁴ The main feature, common to the 100-Å HgTe/36-Å CdTe and 90-Å HgTe/40-Å CdTe SL's, is that C1 falls roughly 20 meV as Δ increases by 100 meV, while HH1 is unaffected for $\Delta > 100$ meV. In the analysis of Choi *et al.*⁴ C1 lies at an energy ≈ 20 meV lower than the present analysis, and HH1 falls to a lower energy (-29 meV versus -5 meV) before flattening out, due to differences in parametrization and the inclusion of strain. In both analyses C1 and HH1 cross at $\Delta \approx 300$ meV. The SL becomes semiconducting again for larger Δ when C1 passes entirely through HH1.

Figure 2 illustrates the three regimes, semiconducting, semimetallic, and semiconducting, corresponding to $\Delta = 40, 325$, and 375 meV, respectively, for the 90-Å HgTe/40-Å CdTe SL. Note that for the second semiconducting region the SL gap is at the Brillouin zone face. Figure 2 indicates the width of the semimetallic region to be proportional to the K_z dispersion of C1. (HH1 is nearly dispersionless.) As Δ increases the decay length of the C1 envelope function in the CdTe barrier decreases since the effective barrier height due to the CdTe layer becomes larger. Specifically, the Γ_8 band edge in the CdTe falls approximately five times as fast as the energy of C1 relative to the Γ_8 edge in the HgTe with increasing Δ , so that C1 moves deeper into the CdTe gap. Thus with increasing Δ the dispersion of C1 decreases to ≈ 10 meV when $\Delta \approx 350$ meV. This value is sensitive to the input parameters, increasing by ≈ 10 meV as the bulk HgTe electron mass varies from $0.031m$, the present input value, to $0.025m$, the value implied by the parameters of Choi *et al.*⁴ if just the $k \cdot p$ interaction between Γ_8 and Γ_6 is considered.

Figure 3 shows the in-plane effective mass $m_{||}$ at $K=0$ for the 90-Å HgTe/40-Å CdTe SL as a function of Δ . Also plotted are theoretical values of the cyclotron mass in the limit of zero field for carrier densities $n = 10^{16}$ and $6 \times 10^{16} \text{ cm}^{-3}$ for $\Delta = 40$ and 350 meV and the experi-

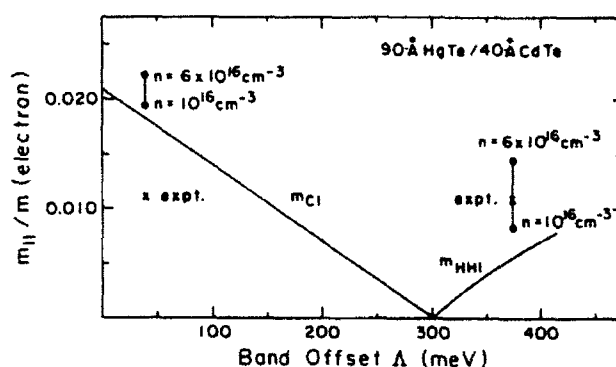


FIG. 3. In-plane electron effective mass at $K=0$ as a function of band offset Δ for the 90-Å HgTe/40-Å CdTe superlattice at the band edge. The experimental value (crosses) of the cyclotron mass m_c^*/m in the limit of zero magnetic field is shown together with theoretical values (solid dots) for doping concentrations between 10^{16} and $6 \times 10^{16} \text{ cm}^{-3}$ for $\Delta = 40$ and 375 meV.

mental value, $m_c^* = 0.011m$. For $\Delta = 40$ meV the theoretical cyclotron mass is $0.02m$, too large to match experiment. The discrepancy with Choi *et al.*⁴ is presumably due in part to the different parametrization of the bulk HgTe as discussed above. As illustrated the experimental value $m_c^* = 0.011m$ agrees with $\Delta = 375$ for doping of $n = 3 \times 10^{16} \text{ cm}^{-3}$. If the reported surface carrier density of order 10^{12} cm^{-2} is assumed uniformly distributed throughout the ≈ 1600 -Å-wide SL, a density on the order of $5 \times 10^{16} \text{ cm}^{-3}$ is obtained. Agreement of theoretical and experimental values of the cyclotron mass with doping levels of $1-6 \times 10^{16} \text{ cm}^{-3}$ is found for $\Delta = 400 \pm 40$ meV, with the lower values of offset corresponding to higher doping levels.

The present value of $\Delta = 400 \pm 40$ meV is consistent both with the previous value, $\Delta \geq 350$ meV, resulting from the analysis of the 100-Å HgTe/36-Å CdTe SL, and with the photoemission data of Shih and Spicer,¹ $\Delta = 350 \pm 60$ meV. We conclude that the magneto-optical results for this 90-Å HgTe/40-Å CdTe SL sample are consistent with a valence-band offset of $\Delta \approx 400$ meV and not small values such as $\Delta \approx 40$ meV.

Tersoff¹⁴ has found that the average of several theoretical predictions for the offset is $\Delta = 400 \pm 90$ meV, and argued by analogy with theory and experiment in the AlAs/GaAs system that a value of $\Delta \approx 480$ meV would be appropriate for the HgTe/CdTe system. Although the value of $\Delta \approx 480$ meV is too large according to the evidence cited here, the original analysis of Choi *et al.*⁴ may be consistent with that value.

We are grateful to K. C. Hass for bringing Ref. 4 to our attention. We have benefited from helpful discussions with N. F. Johnson and P. M. Hui. This work was supported by the U.S. Joint Service Electronic Program (JSEP) through U.S. Office of Naval Research (ONR) Contract No. N00014-89-J-1023 and by the U.S. Defense Advanced Research Projects Agency (DARPA) through ONR Contract No. N00014-86-K-0033. One of us (P.M.Y.) acknowledges the financial support of the Fannie and John Hertz Foundation.

*Author to whom all correspondence should be sent.

- ¹S. P. Kowalczyk, J. T. Cheung, E. A. Kraut, and R. W. Grant, Phys. Rev. Lett. **56**, 1605 (1986); T. M. Duc, C. Hsu, and J. P. Faurie, *ibid.* **58**, 1127 (1987); C. K. Shih and W. E. Spicer, *ibid.* **58**, 2594 (1987).
- ²J. M. Berroir, Y. Guldner, J. P. Vieren, M. Voos, and J. P. Faurie, Phys. Rev. B **34**, 891 (1986).
- ³N. F. Johnson, P. M. Hui, and H. Enrenreich, Phys. Rev. Lett. **61**, 1993 (1988).
- ⁴J. B. Choi, L. Ghenim, R. Mani, H. D. Drew, K. H. Yoo, and J. T. Cheung, Phys. Rev. B **41**, 10872 (1990).
- ⁵N. F. Johnson, H. Ehrenreich, P. M. Hui, and P. M. Young, Phys. Rev. B **41**, 3655 (1990).
- ⁶C. L. Cesar, M. N. Islam, R. D. Feldman, R. Spitzer, R. F. Austin, A. E. DiGiovanni, J. Shah, and J. Orenstein, Appl. Phys. Lett. **54**, 745 (1989); C. L. Cesar, M. N. Islam, R. D. Feldman, R. F. Austin, D. S. Chemla, L. C. West, and A. E. DiGiovanni, *ibid.* **56**, 283 (1990).
- ⁷C. A. Hoffman, J. R. Meyer, F. J. Bartoli, Y. Lansari, J. W. Cook, Jr., and J. F. Schetzina, Phys. Rev. B **40**, 3867 (1989); J. R. Meyer, R. J. Wagner, F. J. Bartoli, C. A. Hoffman, and L. R. Ram-Mohan, *ibid.* **40**, 1388 (1989).
- ⁸P. M. Hui, H. Enrenreich, and N. F. Johnson, J. Vac. Sci. Technol. A **7**, 424 (1989).
- ⁹J. M. Berroir, Y. Guldner, J. P. Vieren, M. Voos, X. Chu, and J. P. Faurie, Phys. Rev. Lett. **62**, 2024 (1989).
- ¹⁰The smaller value of m_e^* in Ref. 4, relative to the value of the 100-Å HgTe/36-Å CdTe sample, is consistent with a large offset. By contrast, for a small offset the effective mass in Ref. 4 should be larger according to the trends exhibited by Fig. 4 of Ref. 8.
- ¹¹N. F. Johnson, H. Enrenreich, K. C. Hass, and T. C. McGill, Phys. Rev. Lett. **59**, 2352 (1987).
- ¹²N. F. Johnson, H. Ehrenreich, and R. V. Jones, Appl. Phys. Lett. **53**, 180 (1988).
- ¹³N. F. Johnson, H. Ehrenreich, G. Y. Wu, and T. C. McGill, Phys. Rev. B **38**, 13095 (1988).
- ¹⁴J. Tersoff, Phys. Rev. B **40**, 10615 (1989).

Excitons and interband transitions in III-V semiconductor superlattices

P. M. Young, P. M. Hui,* and H. Ehrenreich†

Division of Applied Sciences, Harvard University, Cambridge, Massachusetts 02138

(Received 25 July 1991)

The fundamental optical absorption of $\text{In}_{1-x}\text{Ga}_x\text{As}/\text{In}_{1-y}\text{Al}_y\text{As}$ and $\text{GaAs}/\text{Ga}_{1-x}\text{Al}_x\text{As}$ superlattices is calculated quantitatively using superlattice $\mathbf{K}\cdot\mathbf{p}$ theory. Electron-hole Coulomb interactions yielding excitons and interband-transition Sommerfeld enhancement are incorporated. These fast, non-variational calculations yield optical structure within 2–3 meV and absolute absorption coefficients within 10% of experimental results for all but one of the twelve samples analyzed. Constituent bulk parameters and band offsets constitute the only input. Computer requirements are very modest. Calculations for different band offsets and other interface parameters using this versatile approach permit estimates of physically important quantities of relatively unexplored heterostructure systems, for example, II-VI superlattices.

I. INTRODUCTION

This theoretical study treats the effects of the electron-hole Coulomb attraction on the electronic and optical properties of III-V semiconductor superlattices (SL's) with emphasis on the remarkable quantitative agreement with the experimentally measured absolute optical-absorption spectra of several SL's. The present approach is an extension of previous work^{1–3} which developed the $\mathbf{K}\cdot\mathbf{p}$ formalism to exploit the perfect periodicity of the SL heterostructure for determination of the electronic structure. Johnson⁴ has briefly reported the transformation of the resulting SL crystal momentum representation (CMR) into a SL crystal coordinate representation (CCR) in connection with a calculation of the lowest bound exciton binding energies of the $\text{GaAs}/\text{Ga}_{1-x}\text{Al}_x\text{As}$ SL system. In the present work, all Coulomb effects, including those on the continuum states, are treated to understand the excitation energies and the optical absorption in absolute terms.

The optical absorption has been generally calculated for the isolated-quantum-well (QW) regime.^{3–8} Of notable exception is the work of Chu and Chang,^{9,10} who have employed computationally intensive \mathbf{k} -space sampling techniques to study the SL absorption. Because of very significant computational simplification, the present work permits highly detailed quantitative comparison with experiment over broad energy ranges and for a variety of systems. In addition, it leads to verification (or prediction) of band offsets in systems like the II-VI SL's, where values are uncertain. For the III-V systems illustrated here, exciton peaks are shown to lie within 2–3 meV of their experimental locations and the overall absorption coefficient agrees within 10%.

As in previous work,² the SL band structure is obtained from the envelope function approach applied to a modified Kane model for the band structure of the constituent bulk materials. The only required input to the calculations consists of those parameters required to specify the Kane model in the constituents (gaps, heavy-

hole masses, and a momentum matrix element), a valence-band offset which determines the lineup of the Γ_8 edges, and the index of refraction in the vicinity of the energy gap.

As described in Sec. II, which summarizes the formalism, the electron-hole Coulomb interaction is treated within an independent subband approximation that associates each exciton with a single conduction and a single valence band. This approach, together with a simple model for the SL Wannier functions, leads to an analytic form for the electron-hole interaction which permits solution for the exciton wave function without resorting to a variational approach. This nonvariational approach allows accurate determination of the exciton oscillator strength, and is not limited to bound states. Corrections involving the SL Sommerfeld factor also follow from the same formalism. A comparison with variationally obtained exciton binding energies is presented to verify the accuracy of the present approach.

In Sec. III the formalism is implemented and compared to experimental data published by several different groups. As already pointed out, agreement between experiment and theory is excellent. All of the major features displayed in the experiments are positively identified within the present theory. The final section discusses some implications of the present work with respect to band offsets and possible growth imperfections.

II. FORMALISM

This section summarizes the formalism for calculating the excitonic spectra and fundamental optical absorption of a SL. The one-electron band structure is described within the crystal momentum representation using the envelope function approach.² The SL wave function, depending on the SL band index L and wave vector \mathbf{K} , is expressed in terms of the bulk-basis Bloch functions $\langle \mathbf{r} | n, 0 \rangle$ corresponding to bulk band n at $\mathbf{k} = 0$, and the envelope functions $F_n(L, \mathbf{K}; \mathbf{r})$ by

$$\langle \mathbf{r} | L, \mathbf{K} \rangle = \sum_n F_n(L, \mathbf{K}; \mathbf{r}) \langle \mathbf{r} | n, 0 \rangle. \quad (1)$$

$F(L, \mathbf{K}; \mathbf{r})$, having components $F_n(L, \mathbf{K}; \mathbf{r})$, is obtained from

$$H_{A(B)}^{k,p}(k_x, k_y, k_z \rightarrow -i\partial/\partial z)F(L, \mathbf{K}; \mathbf{r}) = E_L(\mathbf{K})F(L, \mathbf{K}; \mathbf{r}). \quad (2)$$

$H_{A(B)}^{k,p}$ is a $\mathbf{k} \cdot \mathbf{p}$ Hamiltonian modeling the band structure utilizing a modified Kane model including the uppermost six valence bands with finite heavy-hole mass and the lowest pair of conduction bands at $\mathbf{k} = 0$ in the bulk materials A and B . (A denotes the well and B the barrier material.) Equation (2) is solved for $\mathbf{K} = 0$ yielding SL zone-center energies, $E_L(0)$, and SL cell periodic envelope functions. These zone-center envelope functions determine the SL $\mathbf{K} \cdot \mathbf{p}$ matrix elements which are used to set up a secular equation whose solution at finite \mathbf{K} yields the full band structure and momentum matrix elements $\langle L, \mathbf{K} | \mathbf{p} | L', \mathbf{K} \rangle$.

The optical absorption from the ground state $|G\rangle$ to excited states $|E\rangle$ associated with a photon of energy $\hbar\omega$ is

$$\alpha(E) = \frac{2\pi^2 e^2 \hbar}{n(E)mc} f_{EG} \rho(E), \quad (3)$$

where m is the free-electron mass, $\rho(E)$ is the density of excited continuum states $[(1/V)\delta(E - \hbar\omega)]$ for discrete states, $n(E)$ is the index of refraction, and $f_{EG} = 2|\langle E | \mathbf{p} | G \rangle|^2 / (mE)$ is the oscillator strength containing the momentum matrix element. The index will be approximated by an average n of the values for the constituent bulk semiconductors at the band gap.

In the absence of electron-hole interactions¹¹ $\langle E | \mathbf{p} | G \rangle = \langle L, \mathbf{K} | \mathbf{p} | L', \mathbf{K} \rangle$ and

$$\alpha(E) = \frac{2\pi^2 e^2 \hbar}{Vnmc} \sum_{L,L'} \sum_{\mathbf{K}} \frac{2}{m} \frac{|\langle L, \mathbf{K} | \mathbf{p} | L', \mathbf{K} \rangle|^2}{E_L(\mathbf{K}) - E_L(\mathbf{K})} \times \delta(E - E_L(\mathbf{K}) + E_L(\mathbf{K})), \quad (4)$$

$$\sum_{\rho} \left[\frac{1}{N} \sum_{\mathbf{K}} e^{i\mathbf{K} \cdot (\mathbf{R}_\rho - \mathbf{R}_\rho')} [E_L(\mathbf{K}) - E_L(\mathbf{K})] \right] U_{LL'}(\mathbf{R}_\rho) - V(\mathbf{R}_\rho) U_{LL'}(\mathbf{R}_\rho) = E_{ex}^{LL'} U_{LL'}(\mathbf{R}_\rho). \quad (9)$$

Here $V(\mathbf{R}_\rho)$ is the direct Coulomb term

$$V(\mathbf{R}_\rho) = \int d\mathbf{r}_e \int d\mathbf{r}_h |\langle \mathbf{r}_e | L', \mathbf{R}_\rho \rangle|^2 \frac{e^2}{\epsilon |\mathbf{r}_e - \mathbf{r}_h|} \times |\langle \mathbf{r}_h | L, 0 \rangle|^2. \quad (10)$$

The absorption in the presence of the Coulomb interaction will be modified with respect to Eq. (4) by the presence of the SL Sommerfeld factor and energetically discrete exciton peaks. Evaluation of the Sommerfeld factor and exciton spectra requires the solution of Eq. (9) for $U_{LL'}(\mathbf{R}_\rho)$. It can be determined both simply and accurately by approximating the Coulomb integral $V(\mathbf{R}_\rho)$ so as to be expressible in closed form. This calculation is facilitated by using a SL model band structure which is

where V is the sample volume.

The electron-hole correlation due to the Coulomb interaction changes the absorption both qualitatively (discrete exciton peaks appear) and quantitatively (the continuum absorption is enhanced by the Sommerfeld factor). Because of the additional term in the Hamiltonian,

$$H_{e,h} = -e^2 / \epsilon |\mathbf{r}_e - \mathbf{r}_h|, \quad (5)$$

where ϵ is the dielectric constant, and \mathbf{r}_e and \mathbf{r}_h are electron and hole coordinates, respectively, it will be most convenient to work in the SL-CCR.⁴ A basis of SL Wannier functions is defined by

$$\langle \mathbf{r} | L, \mathbf{R}_\mu \rangle = N^{-1/2} \sum_{\mathbf{K}} e^{-i\mathbf{K} \cdot \mathbf{R}_\mu} \langle \mathbf{r} | L, \mathbf{K} \rangle, \quad (6)$$

where \mathbf{R}_μ is a lattice site. The Coulomb interaction couples *all* bands, but by imposing an independent subband approximation the coupling is restricted to single pairs of conduction and valence bands. All singlet excitonic states can then be expressed in a basis of two-particle Wannier states $|L, \mathbf{R}_\nu; L', \mathbf{R}_\mu\rangle$ corresponding to a hole in band L at \mathbf{R}_ν and an electron in band L' at \mathbf{R}_μ .

The optical matrix elements are calculated for excitons having vanishing center-of-mass total momentum. The appropriate basis states

$$|\mathbf{R}_\rho; L, L'\rangle = N^{-1/2} \sum_{\mu} |L, \mathbf{R}_\mu - \mathbf{R}_\rho; L', \mathbf{R}_\mu\rangle, \quad (7)$$

depend only on the electron-hole relative coordinate \mathbf{R}_ρ . The exciton state is

$$|E_{ex}^{LL'}\rangle = \sum_{\rho} U_{LL'}(\mathbf{R}_\rho) |\mathbf{R}_\rho; L, L'\rangle, \quad (8)$$

where $U_{LL'}$ is the exciton wave function which obeys the CCR equation⁴

separable, parabolic in-plane, and tight-binding-like along the growth axis:

$$E_L(\mathbf{K}) - E_L(\mathbf{K}) = E_g^{LL'} + \frac{\hbar^2 \mathbf{K}_\parallel^2}{2\mu_{\parallel}^{LL'}} - \sum_{n=1}^{\infty} 2W^{LL'}(n) [\cos(n\mathbf{K}_\perp d) - 1]. \quad (11)$$

The directions \parallel and \perp are defined with respect to the growth planes and are identified with the x - y and z directions, respectively. $E_g^{LL'}$ is the interband gap given by $E_L(0) - E_L(0)$, $\mu_{\parallel}^{LL'}$ is the reduced mass for the pair of

bands, and d is the SL period along the growth direction. The $W^{LL'}(n)$ are the hopping matrix elements involving n th nearest neighbors in the tight-binding model. For all but the thinnest barrier SL's ($L_B \lesssim 20$ Å), a nearest-neighbor model suffices. The parabolic in-plane approximation, which may be questionable for the valence-band structure in view of anticrossing effects in the closely spaced bands, is nevertheless adequate since only the reduced mass, which is dominated by the conduction bands, is required.

The Coulomb interaction between electron and hole cannot be treated within the normal effective-mass ap-

proximation in the growth direction since the SL unit cell in that direction is comparable to the bulk exciton Bohr radius. However, along the in-plane directions the effective-mass approximation for Wannier excitons, as used in the bulk problem, is appropriate.

The model employed is that introduced by Johnson,⁴ who calculated very satisfactory binding energies for the lowest bound excitons of the GaAs/Ga_{1-x}Al_xAs system within a SL-CCR framework. The electron and hole Wannier functions are modeled by one-dimensional rods of lengths L_e and L_h along the z axis. Within this model the Coulomb integral can be expressed in closed form:¹²

$$V(\mathbf{R}_\rho) \approx \frac{e^2}{\epsilon L_e L_h} \int_{-L_h/2}^{L_h/2} dz_h \int_{\rho_z - L_e/2}^{\rho_z + L_e/2} dz_e \frac{1}{[(z_e - z_h)^2 + \rho_{xy}^2]^{1/2}}. \quad (12)$$

Here ρ_z and ρ_{xy} are the growth direction and in-plane components of the electron-hole relative coordinate \mathbf{R}_ρ , respectively (measured with respect to the hole position). For the present calculations the rod lengths, L_e and L_h , have been taken to be equal to the width of the well layer.¹³ Figure 1 schematically illustrates the present model where electron and hole rods are localized in wells separated by ρ_z along the growth direction.

This model interaction reduces properly to the appropriate limiting cases, for example the two-dimensional hydrogenic limit in narrow quantum wells. The independent subband approximation is seen to fail when the quantum-well size is much larger than the exciton Bohr radius, a case that falls outside the parameter range of interest here.

The wave functions obtained as solutions of Eq. (9) correspond to bound excitons and resonant states having a continuum density of states. The momentum matrix ele-

ment for singlet states with energy E_{ex} is given by

$$\begin{aligned} \langle E_{ex} | p | G \rangle &= N^{-1/2} \sum_{\rho} U_{LL'}(\mathbf{R}_\rho) \sum_{\mu} \langle L, \mathbf{R}_\mu - \mathbf{R}_\rho | p | L', \mathbf{R}_\mu \rangle \\ &= N^{-1/2} \sum_{\rho} U_{LL'}(\mathbf{R}_\rho) \sum_{\mathbf{K}} e^{i\mathbf{K} \cdot \mathbf{R}_\rho} \langle L, \mathbf{K} | p | L', \mathbf{K} \rangle \end{aligned} \quad (13)$$

[cf. Eqs. (7) and (8)].

In the Wannier exciton limit the Fourier transform,

$$g(\mathbf{K}) = N^{-1/2} \sum_{\rho} e^{-i\mathbf{K} \cdot \mathbf{R}_\rho} U_{LL'}(\mathbf{R}_\rho) \quad (14)$$

of $U_{LL'}(\mathbf{R}_\rho)$, is strongly peaked about a particular in-plane \mathbf{K} value, $\mathbf{K} = \mathbf{K}_\parallel$. For bound excitons $\mathbf{K} \approx 0$. For the continuum states it is approximately $E_{ex} \approx \hbar^2 K_\parallel^2 / 2\mu_{LL'}$. For the range of parameters of interest the electron and hole are located in the same or nearly adjacent wells. The momentum matrix elements can therefore be averaged over the Brillouin zone along the \mathbf{K}_\parallel direction. Equation (13) can thus be expressed in terms of the SL momentum matrix element:

$$\begin{aligned} \langle E_{ex} | p | G \rangle &= \sum_{\mathbf{K}} g(\mathbf{K}) \langle L, \mathbf{K} | p | L', \mathbf{K} \rangle \\ &\approx N^{1/2} U_{LL'}(0) \langle L, \mathbf{K}_\parallel | p | L', \mathbf{K}_\parallel \rangle. \end{aligned} \quad (15)$$

The Sommerfeld factor is defined as

$$\mathcal{S}(E) = N |U_{LL'}(0)|^2. \quad (16)$$

In the absence of electron-hole interactions $U_{LL'}(0) = N^{-1/2}$ and $\mathcal{S}(E) = 1$.

Figure 2 illustrates the effects of the electron-hole interaction on the absorption of an (80-Å In_{1-x}Ga_xAs)/(114-Å In_{1-y}Al_yAs) SL. The absorption in the absence of electron-hole interactions, the contributions due to the bound exciton peaks, and the enhance-

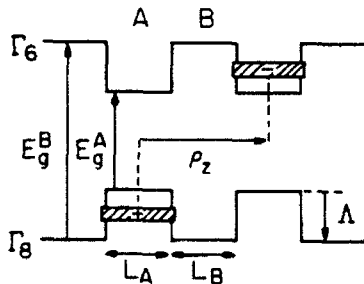


FIG. 1. Schematic illustration of relative band alignments and the representation of electron and hole Wannier functions by rods localized in the wells. A is the well material, B is the barrier material, and the Γ_8 valence-band edges are offset by Λ .

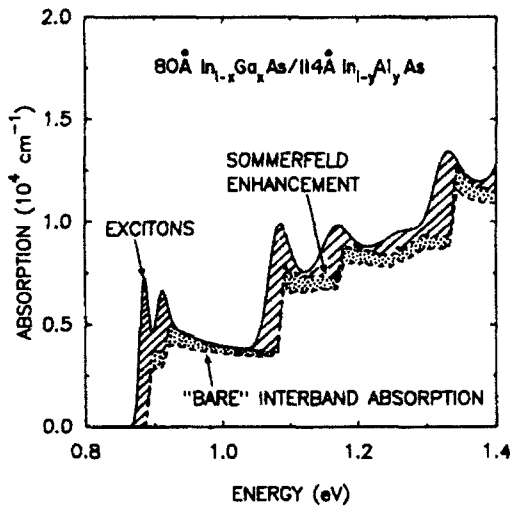


FIG. 2. The effect of the electron-hole interaction on SL absorption. Theory for the absorption of an (80-Å $\text{In}_{0.53}\text{Ga}_{0.47}\text{As}$)/(114-Å $\text{In}_{0.52}\text{Al}_{0.48}\text{As}$) superlattice is plotted with (solid line) and without (dashed line) electron-hole Coulomb interaction. Contributions due to Sommerfeld factor enhancement of continuum transitions (dotted region) and due to bound exciton peaks (crosshatched region) are separately identified.

ment due to the SL Sommerfeld factor for the continuum states are separately identified. The Coulomb interaction strengthens the overall absorption by about 20% and emphasizes the quasi-two-dimensional density of states steps with bound exciton peaks.

The behavior of the Sommerfeld factor is examined in more detail in Fig. 3 for the QW limit. The Sommerfeld factor is plotted as a function of energy above the band

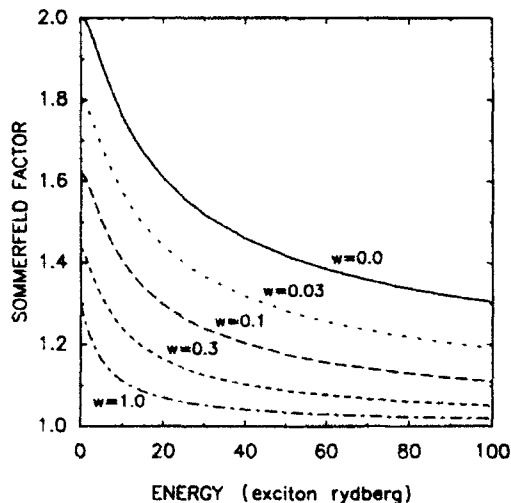


FIG. 3. Quantum-well Sommerfeld factor as a function of energy above the band edge (in exciton rydbergs) for several values of reduced well width, $w = L_A/a_B^*$, including the ideal 2D case $w=0$.

gap in exciton rydbergs $(E - E_G^{LL'})/R_H^{ex}$, where $R_H^{ex} = \mu_{LL'}^{LL} R_H/\epsilon^2$, for several values of the reduced well width, $w = L_A/a_B^*$. For the systems examined in this paper w is between 0.2 and 1.0. The 2D limit, $w=0$, corresponds to the case examined by Shinada and Sugano,¹⁴ who found $\mathcal{S}(E) = e^{\pi\alpha}/\cosh(\pi\alpha)$, where $\alpha^{-2} = (E - E_G)/R_H^{ex}$. The 3D limit, $\mathcal{S}(E) = \pi\alpha e^{\pi\alpha}/\sinh(\pi\alpha)$, is not obtained within the present formalism since it requires explicit consideration of the interaction of the subbands as they merge into a 3D density of states. The result obtained here is seen to differ from the ideal 2D limit even for monolayer confinements, $w \approx 0.03$, which motivated the work discussed in Ref. 14.

Figure 4 compares the results for QW exciton binding energies obtained from variational calculations with the results of the present formalism. Binding energies are in units of exciton rydbergs and well widths are normalized by the exciton radius a_B^* . The variational approach utilizes the effective-mass approximation along all axes; barrier layers are treated as step potential terms in the Hamiltonian. Separable solutions in Ref. 15 are obtained with trial wave functions that are products of profiles resembling envelope functions associated with particular conduction and valence subbands of the quantum well and trial in-plane profiles, e.g., decaying exponentials, that contain a variational parameter. The nonseparable trial wave function is a product of envelope functions and a decaying exponential in all directions in the well, including the growth axis. The resulting growth axis profile is no longer just a product of QW envelope functions, and thus cannot be uniquely associated with a single valence and single conduction band. Binding energies for the 1s exciton in exciton rydbergs, as obtained in Ref. 15 using separable and nonseparable variational models, are plotted together with results from the present formalism as a function of the reduced well width, w . The separable variational model yields results substantially identical to

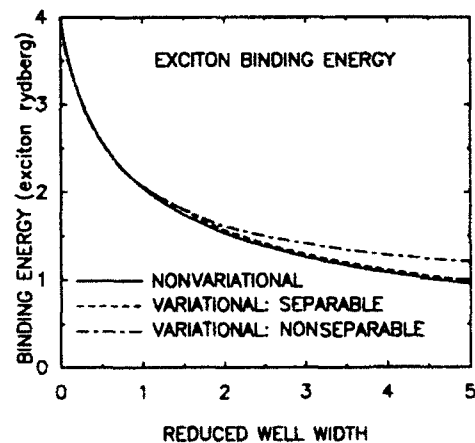


FIG. 4. Comparison of the present theory for exciton binding energies with variational calculations. The 1s exciton binding energy (in exciton rydbergs) is plotted as a function of the reduced well width (see text) for the present nonvariational theory (solid line), and for variational calculations based on separable and nonseparable trial wave functions.

the present formalism, which also agrees with the nonseparable model for reduced well widths, $w \leq 1.0$, the values of interest in the experimental results to be considered here. For wells of width significantly greater than the bulk exciton radius, the expected 3D bulk limit is obtained for the nonseparable model, but the separable and nonvariational binding energies slowly vanish because the separability approximation is not valid for very wide wells.

The above theory yields perfectly sharp exciton linewidths. We introduce a simple model based on monolayer well-width fluctuations to obtain a finite linewidth at low temperatures, ($T \approx 5$ K).¹⁶ This model is based on the notion that a SL interface plane consists of islands containing materials of the adjacent layers. Excitonic transition energies are calculated for a SL of nominal layers width, and also for SL's whose layer widths vary by ± 1 monolayer while preserving the period, d . This generates a set of lines which are convoluted to produce a linewidth which is then multiplied by a single constant (of order unity and the same for all excitons calculated) chosen to best represent the experimental results.¹⁷ This assumption concerning widths introduces the only arbitrary element into the present calculations. The model is supported by the fact that in the samples examined here, Gaussian line shapes match experiments more closely than Lorentzians, which would be expected if lifetime effects were responsible for the width at low temperature.¹⁸⁻²⁰

III. IMPLEMENTATION OF FORMALISM

This section centers on comparison of the present theory with a broad selection of absolute optical-absorption spectra for the GaAs/Ga_{1-x}Al_xAs and In_{1-x}Ga_xAs/In_{1-y}Al_yAs systems. We have analyzed 12 sets of experiments by different groups and have obtained detailed agreement with 11. (The number of absolute measurements is actually quite limited.) In the In_{1-x}Ga_xAs/In_{1-y}Al_yAs system the spectral range extends between 0.8 and 1.4 eV. Nonparabolic band effects

must therefore be included. These are contained within the Kane model used to calculate the underlying band structures. Table I provides a summary of the parameters used to describe the relevant bulk semiconductors.

Experiment and theory are compared for the In_{0.53}Ga_{0.47}As/In_{0.52}Al_{0.48}As system in Fig. 5.²⁴ The samples considered experimentally²¹ have respective well and barrier widths of (34 Å)/(114 Å), (80 Å)/(114 Å), and (138 Å)/(115 Å), and are lattice matched. Strain effects, therefore, play no role. The present calculations include the contributions of all s symmetry bound excitons associated with each pair of bands. The 1s transition accounts for roughly 90% of the total oscillator strength of each family, and has the largest binding energy by a factor of about 6 for the present case. As a result none of the higher excitons is clearly resolved in the presence of the line broadening.

The major structure in the spectra is due to pairs consisting of transitions $HHn \rightarrow Cn$, and at slightly higher energy $LHn \rightarrow Cn$ for $n = 1, 2, 3$, and 4. As n increases, the spacing between the pairs increases due to the different masses of the HH and LH bulk bands and the fact that the confinement energy goes roughly as n^2 . All of the major features in the experiments, i.e., the absorption steps and excitons associated with the "allowed" transitions $HHn \rightarrow Cn$ and $LHn \rightarrow Cn$ and the associated absorption coefficients, are accurately predicted by the theory. In the case of the 138-Å well no fewer than eight such strong transitions exist in the photon energy range of 0.6 eV under examination.

Above 1.2 eV the theory is no longer quantitative. Results fall below experiment for all samples. This behavior is possibly associated with an Urbach tailing effect due to the InP substrate on which the samples are grown, and whose band gap, at 1.42 eV, limits the energy range which can be examined experimentally.

Optical-absorption experiments for the GaAs/Ga_{1-x}Al_xAs system require etching off the GaAs substrate on which the sample is grown, since GaAs has strong absorption in the relevant energy range. As a result there are relatively few measurements of absolute op-

TABLE I. Summary of the bulk semiconductor $k \cdot p$ parameters and the valence-band offsets, Λ , used in the present calculations. E_g is the fundamental gap, Δ is the spin-orbit splitting, and m_{HH} is the heavy-hole mass along the [100] axis.

Parameter	In _{0.53} Ga _{0.47} As	In _{0.52} Al _{0.48} As	Ga _{1-x} Al _x As
E_g (eV) (4 K)	0.813 ^a	1.508 ^a	1.519 + 1.247x
E_g (eV) (300 K)			1.424 + 1.247x ^b
Δ (eV) ^c	0.36	0.33	0.34 - 0.06x
m_{HH}/m	0.5	0.5	0.45
E_p (eV) ^d	22.0	22.0	24.0
Λ (eV)		0.200 ^a	0.374x ^e

^aReference 21.

^bLinear variation (Ref. 22) valid only for $0.0 < x < 0.45$ due to band-gap bowing.

^cLinear interpolation of values in Ref. 23.

^d E_p is defined as $(2/m)|\langle S|p_z|Z \rangle|^2$; its value is deduced from the $k \cdot p$ model using electron masses from Ref. 21 for the InAs alloys and $m_e = 0.067m$ for GaAs.

^eCorresponding to a 70%-30% conduction- to valence-edge offset distribution between pure GaAs and the alloy.

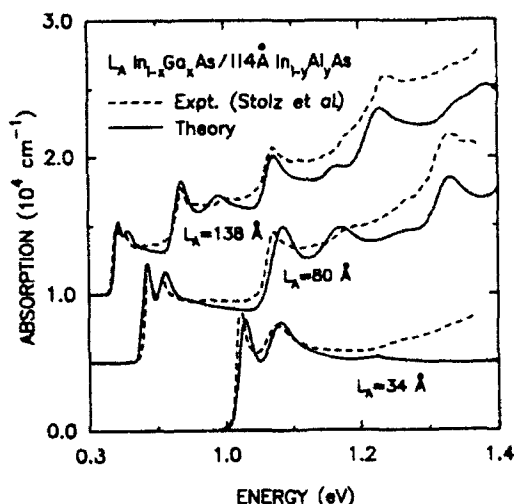


FIG. 5. Comparison of theory (solid lines) and experiment (dashed lines) for absorption in three samples in the $\text{In}_{0.53}\text{Ga}_{0.47}\text{As}/\text{In}_{0.52}\text{Al}_{0.48}\text{As}$ system with well and barrier widths as given. For clarity the curves for the 80-Å well were displaced upward by $0.5 \times 10^4 \text{ cm}^{-1}$, and those for the 138-Å well by $1.0 \times 10^4 \text{ cm}^{-1}$. Experimental data are from Ref. 21.

tical absorption for this system despite its importance. The lattice mismatch between GaAs and $\text{Ga}_{1-x}\text{Al}_x\text{As}$ is 0.13x% and the biaxial deformation potential is of order 1 eV. The effects of strain, which are at most one or two meV, may therefore be neglected.

Figure 6 compares theory to experiment²⁵ for a (116-Å GaAs)/(100-Å $\text{Ga}_{1-x}\text{Al}_x\text{As}$) SL. While the agreement between theory and experiment is still excellent, it is not quite as satisfactory as that in the In-based system. The exciton peaks are also sharper in this system, which may be due in part to the absence of alloy compositional fluctuations in the well.²¹ Note that the total-energy range

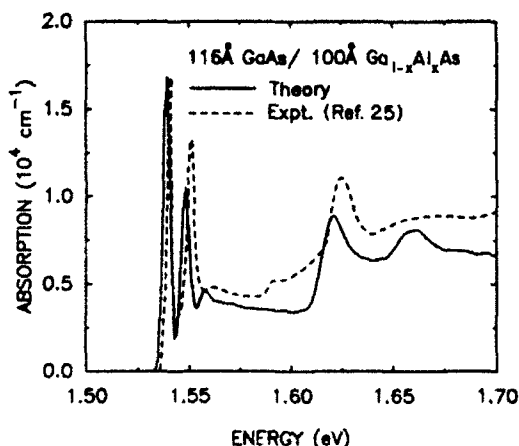


FIG. 6. Comparison of theory (solid line) and experiment (dashed line) for absorption in a (116-Å GaAs)/(100-Å $\text{Ga}_{0.75}\text{Al}_{0.25}\text{As}$) superlattice. Experimental data are from Ref. 25.

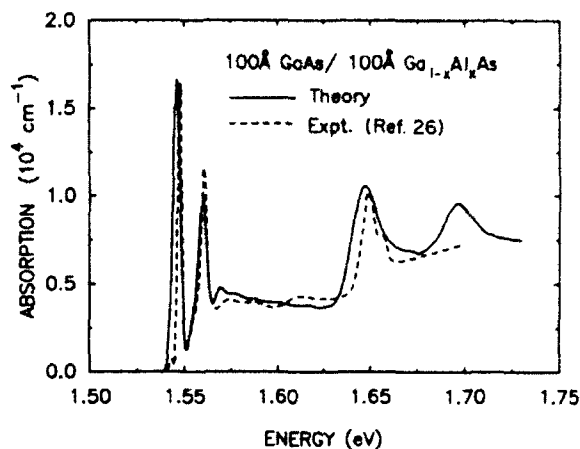


FIG. 7. Comparison of theory (solid line) and experiment (dashed line) for absorption in a (100-Å GaAs)/(100-Å $\text{Ga}_{0.7}\text{Al}_{0.3}\text{As}$) superlattice. Experimental data are from Ref. 26.

here is only 0.2 eV as opposed to the data in Fig. 5 which spanned a 0.6-eV range. The major optical structure is satisfactorily explained except for one feature, often called a "forbidden" transition. This feature, consisting of a step between the $\text{LH1} \rightarrow \text{C1}$ and $\text{HH2} \rightarrow \text{C2}$ peaks, will be discussed in Sec. IV.

A more recent spectrum²⁶ for a (100-Å GaAs)/(100-Å $\text{Ga}_{1-x}\text{Al}_x\text{As}$) SL is shown in Fig. 7. The agreement with theory is better than that of Fig. 6, despite similarities in the layer widths. The forbidden transition is comparatively small. The experimental $\text{HH2} \rightarrow \text{C2}$ peak is seen to be split. This feature, which is not reproduced by the theory, arises because some oscillator strength is passed to the nominally forbidden $\text{LH1} \rightarrow \text{C2}$ transition via the $\mathbf{k} \cdot \mathbf{p}$ interaction of the nearly degenerate LH1 and HH2 bands. This occurs because of the \mathbf{K} mixing in the exci-

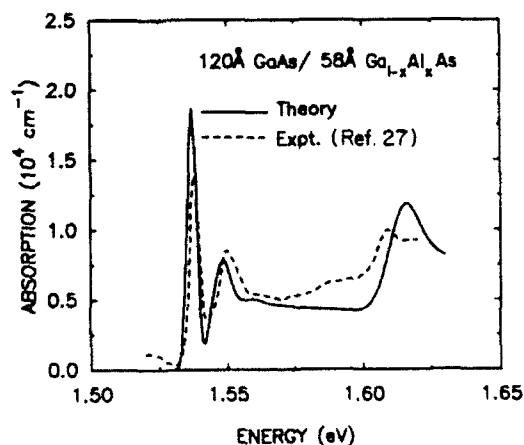


FIG. 8. Comparison of theory (solid line) and experiment (dashed line) for absorption in a (120-Å GaAs)/(58-Å $\text{Ga}_{0.71}\text{Al}_{0.29}\text{As}$) superlattice. Experimental data are from Ref. 27.

ton state which has been neglected here. The observed structure could be obtained theoretically using an improved optical matrix element in this spectral range.

Another sample,²⁷ (120-Å GaAs)/(58-Å $\text{Ga}_{1-x}\text{Al}_x\text{As}$), is examined in Fig. 8. Here, satisfactory agreement is once again obtained. Note that this sample contains somewhat wider wells and narrower barriers than most others, yet agreement is still good.

IV. IMPLICATIONS

The above discussion has focused on two well-known III-V systems because of their intrinsic importance and because much of the most reliable data on SL and QW heterostructures exists for these materials. The quality of the agreement between experiment and theory suggests that absolute optical-absorption measurements may be useful as an aid in SL characterization. Here, we shall briefly describe two specific examples relevant to (1) determination of valence-band offsets, particularly for wide-band-gap II-VI systems where the offsets are largely unknown; and (2) characterization of effects resulting from possible growth defects.

To illustrate the dependence of absorption on the valence-band offset Λ we consider the 80-Å well In system SL described above. Absorption curves for offsets of $\Lambda=30, 100, 200$, and 300 meV are shown in Fig. 9. (Figure 5 shows the results corresponding to the solid line.) For $\Lambda=30$ meV, the $\text{HH1} \rightarrow \text{C1}$ and $\text{LH1} \rightarrow \text{C1}$ exciton peaks are not resolved from one another. This is to be expected for common-anion-rule (near zero) values of the offset (given that the system is strain free). As Λ in-

creases from 30 to 100 meV the LH-HH degeneracy at $\text{K}=0$ is split and the lowest peaks separate. (The inset provides a magnification of this region.) For $\Lambda \approx 150$ meV this separation saturates at a value characteristic of perfect confinement. Between $\Lambda=30$ and 100 the $\text{HH2} \rightarrow \text{C2}$ and $\text{LH2} \rightarrow \text{C2}$ peaks appear and become resolved. For $\Lambda > 150$ meV HH2 and LH2 become increasingly confined and stronger. This is particularly noticeable for the $\text{LH2} \rightarrow \text{C2}$ exciton peak. For $\Lambda \geq 200$ meV the $\text{HH2} \rightarrow \text{C2}$ exciton peak slowly falls in energy as HH2 is now fully confined and C2 begins to relax due to the decreasing value of the conduction-band offset.

The above analysis supports the accepted value of Λ in the In system of 200 meV within an uncertainty of perhaps ± 30 meV. Thus it is expected that such calculations will be useful in characterizing less well understood systems. Work is presently under way to exploit this sort of analysis for the $\text{Zn}_{1-x}\text{Cd}_x\text{Se}/\text{ZnSe}$ SL system, which is being examined as a candidate for an emitter in the blue-green region of the spectrum.²⁸

Optical absorption may also be useful in characterizing SL growth defects. The so-called "forbidden" transition observed in the $\text{GaAs}/\text{Ga}_{1-x}\text{Al}_x\text{As}$ sample is not explained by the present theory. Other calculations of SL absorption, such as those of Chu and Chang,¹⁰ have also failed to explain the strength of this transition. This feature has been associated with the $\text{HH3} \rightarrow \text{C1}$ transition and used to infer properties of the bulk heavy-hole mass.²⁹ The size and shape of the optical absorption in this energy range is inconsistent with this interpretation. Furthermore, the magnitude of the structure is sample dependent. Work currently under way on the absorption of quantum wells in the presence of electric fields suggests that such a feature could be associated with intrinsic internal electric fields which could be introduced during the growth process. If correct, this interpretation would suggest that the effect of miscuts be examined more carefully.³⁰

Not considered in this paper, but also relevant to the present theory, are superlattices having lattice-mismatched barriers and wells. These systems are complicated by effects such as the lifting of the Γ_8 degeneracy of the constituent bulk materials at the valence-band edge. Deformation potentials, which are less well determined in the II-VI's than in the III-V's, come into play, as does the question of the effect of strain on the valence-band offset. Mismatch effects have already been incorporated into the present calculations.

We emphasize that exploration of such effects is possible only because of the modest computer requirements for this type of systematic analysis. While the present theory does not necessarily improve upon the quality of the best calculations already published in the literature (although to our knowledge none of them compares with experimental absolute absorption coefficients), the approach is sufficiently versatile and accurate that a detailed survey of the dependence of properties of band offset and strain effects of potentially important systems on parameters such as alloy concentration is entirely feasible. This fact is of importance in candidate materials like $\text{Zn}_{1-x}\text{Cd}_x\text{Se}/\text{ZnSe}$, mentioned above, and related

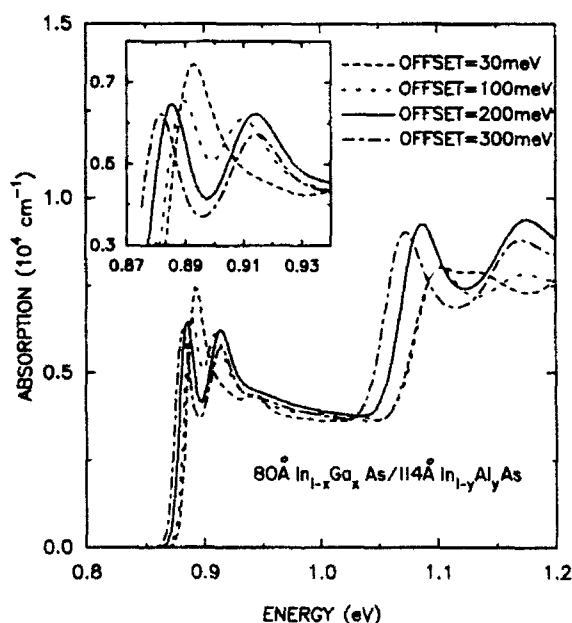


FIG. 9. Calculated fundamental optical absorption for several values of valence-band offset in an (80-Å $\text{In}_{0.33}\text{Ga}_{0.47}\text{As}$)/(114-Å $\text{In}_{0.52}\text{Al}_{0.48}\text{As}$) superlattice (see Fig. 5). The inset details the region of the spectrum around the $\text{HH1} \rightarrow \text{C1}$ - $\text{LH1} \rightarrow \text{C1}$ doublet.

systems such as CdTe/MnTe which are of interest as blue-green emitters and for which reliable experimental data are only now becoming available.

ACKNOWLEDGMENTS

We are grateful to N. F. Johnson for providing details not presented in Ref. 4 and for helpful discussions during

the early stages of this work. This research was supported by the U.S. Joint Services Electronics Program (JSEP) through U.S. Office of Naval Research (ONR) Contract No. N00014-89-J-1023 and by the U.S. Defense Advanced Research Projects Agency (DARPA) through ONR Contract No. N00014-86-K-0033. One of us (P.M.Y.) would like to acknowledge the Fannie and John Hertz Foundation for partial financial support.

*Permanent address: Department of Physics, National Central University, Chung-li, Taiwan 32054, R.O.C.

[†]To whom all correspondence should be sent.

¹N. F. Johnson, H. Ehrenreich, K. C. Hass, and T. C. McGill, *Phys. Rev. Lett.* **59**, 2352 (1987).

²N. F. Johnson, H. Ehrenreich, P. M. Hui, and P. M. Young, *Phys. Rev. B* **41**, 3655 (1990).

³N. F. Johnson, H. Ehrenreich, G. Y. Wu, and T. C. McGill, *Phys. Rev. B* **38**, 13095 (1988).

⁴N. F. Johnson, *J. Phys. Condens. Matter* **2**, 2099 (1990).

⁵Y.-C. Chang and J. N. Schulman, *Appl. Phys. Lett.* **43**, 536 (1983).

⁶Y.-C. Chang and J. N. Schulman, *Phys. Rev. B* **31**, 2069 (1985). This reference and the previous reference consider the effects of well coupling on the band-to-band transitions, but not on the electron-hole interaction.

⁷G. D. Sanders and Y.-C. Chang, *Phys. Rev. B* **31**, 6892 (1985).

⁸G. D. Sanders and Y.-C. Chang, *Phys. Rev. B* **35**, 1300 (1987).

⁹H. Chu and Y.-C. Chang, *Phys. Rev. B* **36**, 2946 (1987).

¹⁰H. Chu and Y.-C. Chang, *Phys. Rev. B* **39**, 10861 (1989).

¹¹E. O. Kane, *J. Phys. Chem. Solids* **1**, 249 (1957). See also T. S. Moss and T. D. F. Hawkins, *Infrared Phys.* **1**, 111 (1961), who apply Kane's theory for the absorption to GaAs.

¹²P. M. Young, N. F. Johnson, P. M. Hui, and H. Ehrenreich (unpublished).

¹³Note that the rod lengths employed in the present calculations differ from those of Ref. 4. The present choice reproduces the results of variational calculations more accurately.

¹⁴M. Shinada and S. Sugano, *J. Phys. Soc. Jpn.* **21**, 1936 (1966).

¹⁵G. Bastard, E. E. Mendez, L. L. Chang, and L. Esaki, *Phys. Rev. B* **26**, 1974 (1982).

¹⁶C. Weisbuch, R. Dingle, A. C. Gossard, and W. Wiegmann, *Solid State Commun.* **38**, 709 (1981).

¹⁷In the limit of perfect square-well confinement the present method of assigning linewidths reduces to the model em-

ployed in Ref. 8 and elsewhere, where the linewidths are taken to be proportional to the squares of the quantum numbers, n , of the states.

¹⁸D. S. Chemla, D. A. B. Miller, and S. Schmitt-Rink, in *Optical Nonlinearities and Instabilities in Semiconductors*, edited by H. Haug (Academic, New York, 1988), pp. 91 and 92.

¹⁹J. S. Weiner, D. S. Chemla, D. A. B. Miller, T. H. Wood, D. Sivco, and A. Y. Cho, *Appl. Phys. Lett.* **46**, 619 (1985).

²⁰D. A. B. Miller, D. S. Chemla, D. J. Eilenberger, P. M. Smith, A. C. Gossard, and W. T. Tsang, *Appl. Phys. Lett.* **41**, 679 (1982).

²¹W. Stolz, J. C. Maan, M. Altarelli, L. Tapfer, and K. Ploog, *Phys. Rev. B* **36**, 4301 (1987).

²²H. C. Casey, Jr., *J. Appl. Phys.* **49**, 3684 (1978).

²³P. Lawaetz, *Phys. Rev. B* **4**, 3460 (1971).

²⁴The absorption coefficient α is approximately given by $I/I_0 = e^{-\alpha D}$, where I/I_0 is the ratio of transmitted to incident intensity, and D is the thickness of the sample. For multiple-quantum-well systems, D is often taken to be the total thickness of well material traversed. In this paper D is identified with the total sample thickness, i.e., as the sum of well and barrier thicknesses. See also the discussion in Ref. 25.

²⁵W. T. Masselink, P. J. Pearsall, J. Klem, C. K. Peng, H. Morkoç, G. D. Sanders, and Y.-C. Chang, *Phys. Rev. B* **32**, 8027 (1985).

²⁶D. M. Huang, J.-I. Chyi, and H. Morkoç, *Phys. Rev. B* **42**, 5147 (1990).

²⁷H. Iwamura, T. Saku, and H. Okamoto, *Jpn. J. Appl. Phys.* **24**, 104 (1985).

²⁸P. M. Young, M. Ziegler, and H. Ehrenreich (unpublished).

²⁹R. C. Miller, D. A. Kleinman, and A. C. Gossard, *Phys. Rev. B* **29**, 7085 (1984).

³⁰F. Spaepen (private communication).

Response and transit times in quantum-well structures

E. Runge and H. E. Enreich

Division of Applied Sciences, Harvard University, Cambridge, Massachusetts 02138

(Received 7 January 1992)

The response of a biased double-barrier quantum well to a small ac voltage with characteristic time τ_{resp} and the transit or dwell time τ_{trans} are calculated using nonequilibrium Green's-function techniques. The tunneling process is shown to be predominantly sequential for an $\text{In}_x\text{Ga}_{1-x}\text{As}/\text{In}_y\text{Al}_{1-y}\text{As}$ structure due to only well alloy scattering treated in the coherent-potential approximation. The magnitudes of τ_{resp} and τ_{trans} are in close agreement and about the same for either sequential or coherent tunneling.

This paper introduces a technically significant time for tunneling in a double-barrier quantum well (DBQW), viewed as a response time τ_{resp} to a weak oscillatory field applied to a biased structure along any point of its current-voltage (I - V) characteristic. Its magnitude is calculated using nonequilibrium Green's-function techniques. It is shown to be nearly the same as the transit time τ_{trans} defined and measured by Chemla and co-workers.^{1,2} Furthermore, the paper demonstrates that sequential tunneling strongly dominates resonant tunneling^{3,4} as a result only of weak III-V alloy scattering, for example, in the well of a lattice-matched $\text{In}_x\text{Ga}_{1-x}\text{As}/\text{In}_y\text{Al}_{1-y}\text{As}$ structure described within the coherent-potential approximation (CPA).^{5,6} The magnitude of τ_{resp} or τ_{trans} , however, is only weakly dependent on the details of the tunneling process.

Aside from their intrinsic physical interest, these results are important since negative-differential-resistance diodes or DBQW are prototypical circuit components in cellular automata in which each cell is required to have high-frequency response and to be "locally interacting," i.e., decoupled from all but its nearest neighbors. Decoupling can be achieved if wave-function coherence between adjacent cells is eliminated. The dominance of sequential tunneling processes, which eliminate coherence, is therefore important.

Specifically, τ_{resp}^{-1} is defined as the frequency, ω_{resp} , for which the imaginary part of the conductivity $\sigma(\omega)$ is maximum. This response time, which is appropriate for high-frequency applications, is physically different from the transit time τ_{trans} defined as the ratio of the charge density in the well to the current density, ρ_W/j_{dc} , at arbitrary bias.

The model of a biased symmetric DBQW to be used in this analysis is shown in Fig. 1. The well having width d_W is surrounded by two barriers having height Δ_S and width d_S where $S=L$ (left) or R (right). The Fermi levels μ_L and μ_R in the leads represent the effect of charge accumulation in L and depletion in R . The semiconductor alloys ($\text{In}_x\text{Ga}_{1-x}\text{As}$) in the L, R and well (W) regions are assumed to be the same, as are those of the barriers ($\text{In}_y\text{Al}_{1-y}\text{As}$). The potential drop across the structure is modeled by a stepwise constant potential energy having values $\Phi_L = eV_{\text{dc}}$, where V_{dc} is the voltage drop, $\Phi_W = \frac{1}{2}\Phi_L$ for a symmetric DBQW, and $\Phi_R = 0$. The

tunneling matrix element through the barrier, h_{SW} , is given within the WKB approximation. The well is assumed to contain only one resonant level E_0 in the absence of alloying effects. E_0 represents the edge of a two-dimensional conduction band (CB) with energy $\Phi_W + E_0 + \epsilon_k$, where k_{\parallel} are associated with the two-dimensional continuum perpendicular to the growth axis and $\epsilon_k = \hbar^2 k_{\perp}^2 / 2m^*$.

The Hamiltonian is given as a sum of terms H_S^0 unperturbed by barrier tunneling and well scattering and others, H_{SW}^{un} and H_W^{scat} , describing the remaining effects. Explicitly, in terms of appropriately labeled creation and annihilation operators,

$$H_S^0 = \begin{cases} \sum_k (E_k + \Phi_S) c_{Sk}^\dagger c_{Sk}, & S=L, R \\ \sum_{k_{\parallel}} (E_0 + \epsilon_k + \Phi_W) c_{Wk_{\parallel}}^\dagger c_{Wk_{\parallel}}, & S=W, \end{cases} \quad (1)$$

where $\mathbf{k}=(k_{\parallel}, k_{\perp})$ refers to the L and R regions and

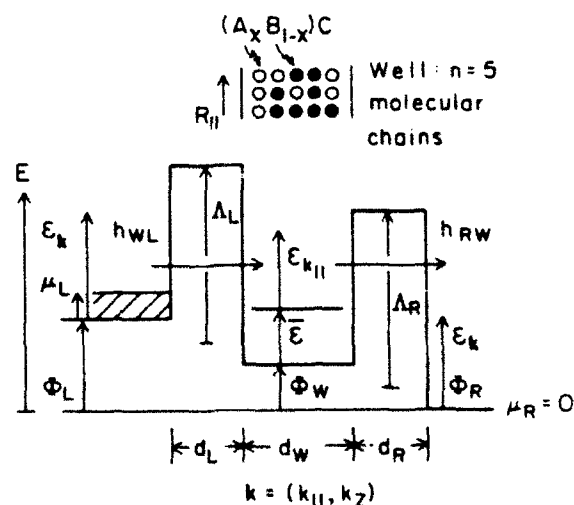


FIG. 1. Model of biased DBQW structure. Barrier and well dimensions defined in text; alloy well resonance level E_0 ; Fermi level μ_L, μ_R ; tunneling amplitudes h_{WL}, h_{RW} . Inset: Arrangement of random molecular chains having $n=5$ AC (open) or BC (closed) molecules for $(A_x B_{1-x})C$ well alloy.

$\epsilon_k = \hbar^2 k^2 / 2m^*$. Further

$$H_{WS}^{\text{un}} = \sum_{k_s, k_R} (h_{WS} c_{Wk_s}^\dagger c_{Sk} + \text{H.c.}) \quad (2)$$

and

$$H_W^{\text{scat}} = \sum_{R_s} (\epsilon_{R_s} - E_0) c_{WR_s}^\dagger c_{WR_s} \quad (3)$$

in a representation using two-dimensional Wannier creation operators $c_{WR_s}^\dagger$. As indicated in the inset of Fig. 1, a row of atoms along the growth direction is visualized as an n -membered molecular chain consisting of randomly disordered AC and BC molecules constituting the $(A_x B_{1-x})C$ alloy. The position of each chain is defined by a value of R_s as indicated in Fig. 1. The resulting two-dimensional alloy scattering associated with each of the randomly distributed chains is the only scattering effect to be considered here. Even though scattering is weak for III-V alloys, it causes tunneling to be largely sequential. The scattering potential due to the configuration-dependent energy

$$\epsilon_{R_s} = \bar{\epsilon} + \sum_i |\phi(z_i)|^2 (\epsilon_i - \bar{\epsilon}) \quad (4)$$

for each chain, where $i = 1, 2, \dots, n$ labels the sequence of AC and BC molecules with on-site electronic energies ϵ_A, ϵ_B , respectively, is much weaker than the confinement kinetic energy E_0 . Here $\bar{\epsilon} = x\epsilon_A + (1-x)\epsilon_B$ denotes the virtual crystal CB edge; $\bar{\epsilon}$ replaces E_0 in the alloy case; $\epsilon_A - \epsilon_B$ is the CB offset between the AC and BC crystals.

Equation (4) gives the chain energies to first order in the scattering. $\phi(z_i)$ is the normalized envelope function along the growth axis. The ϵ_{R_s} are assumed to have a Gaussian distribution with probability $(\Delta\sqrt{2\pi})^{-1} \exp[-(\epsilon_{R_s} - \bar{\epsilon})^2 / 2\Delta^2]$ and a variance

$$\Delta^2 = x(1-x)(\epsilon_A - \epsilon_B)^2 \left\{ (d_W/n) \int_W dz |\phi(z)|^4 \right\},$$

where the integral extends over the well width d_W and has the value $3/(2d_W)$ for deep wells. The CPA description of Gaussian disorder has been considered previously.⁷

A nonequilibrium Green's-function formalism must be used to calculate the current since inelastic-scattering processes are neglected here, and are insufficient to achieve equilibrium in the well region at low T in any case. The advanced and retarded Green's functions G^a , G^r , and also $G^<$ are related by Dyson's equations.^{8,9} The quantities of particular physical interest obtained from a solution of these equations are the matrix elements of the configuration averaged well Green's functions

$$\begin{aligned} G^<(Wk, Wk'; E) &= \delta_{k, k'} [E - (\bar{\epsilon} + \epsilon_k + \Phi_W) \\ &\quad - \Sigma_L(k; E) - \Sigma_R(k; E) \\ &\quad - \Sigma_{\text{CPA}}(E)]^{-1} \end{aligned} \quad (5)$$

and

$$\begin{aligned} G^<(Wk, Wk'; E) &= -\phi_W(E) [G^<(Wk, Wk'; E) \\ &\quad - G^a(Wk, Wk'; E)] \\ &= 2\pi i \phi_W(E) A(k, E). \end{aligned} \quad (6)$$

In Eq. (5), Σ_L and Σ_R are the self-energies associated with tunneling processes out of the well W to L and R , respectively, and Σ_{CPA} is associated with disorder scattering in the well. We shall assume the self-energy shift to be absorbed in $\bar{\epsilon}$. The remaining part,

$$\begin{aligned} i \text{Im}[\Sigma_{S=L,R}] &= -i\pi |h_{WS}|^2 \sum_{k_s} \delta(E - \epsilon_k - \Phi_S) \\ &\equiv -\frac{1}{2} i \Gamma_S \end{aligned} \quad (7)$$

and $i \text{Im}[\Sigma_{\text{CPA}}] = -\frac{1}{2} i \Gamma_{\text{scat}}$ describes the broadening due to tunneling and scattering, respectively. Γ_S is the resonant level width associated with the escape time through the barrier at side $S=L, R$. Γ_{CPA} (not defined explicitly here) is the energy-dependent level width associated with scattering. It is obtained from a numerical solution of the CPA equations. The tunneling process through the DBQW is seen to be largely coherent if $\Gamma_{\text{CPA}} \ll \Gamma_L, \Gamma_R$ and sequential in the opposite limit.

Equation (6) contains $\phi_W(E)$, the nonequilibrium distribution of electrons in the well. This form⁹ is analogous to $G_0^<(Sk, Sk; E)$, the unperturbed function in the L and R regions, in which $\phi_W(E)$ is replaced by the equilibrium Fermi distributions $f_L(E - \Phi_L)$ and $f_R(E)$.¹⁰ $A(k, E)$ is the spectral density associated with the state k .

The dc current density (per unit area) j_{dc} is obtained by calculating the $S \rightarrow W$ current density $j_{S \rightarrow W} = 2e(\partial/\partial t) \hat{N}_S$ where $\hat{N}_S = \sum_{k_s} c_{k_s}^\dagger c_{k_s}$ and expressing the result in terms of the Green's functions. The well distribution is obtained from current conservation $j_{L \rightarrow W} = j_{W \rightarrow R}$:

$$\phi_W(E) = [\Gamma_L f_L(E - \Phi_L) + \Gamma_R f_R(E)] / (\Gamma_L + \Gamma_R). \quad (8)$$

The remarkably simple formal result is

$$j_{\text{dc}} = \frac{2e}{\hbar} \int_{-\infty}^{\infty} dE \frac{\Gamma_L \Gamma_R}{\Gamma_L + \Gamma_R} g_W(E) [f_L(E - \Phi_L) - f_R(E)], \quad (9)$$

where $g_W(E) = \int A(k, E) d^2 k / (2\pi)^2$ is the two-dimensional well density of states. We note that the form of Eqs. (8) and (9) is that expected when the tunneling is purely sequential. The same formal result is obtained by considering the purely coherent tunneling limit obtained by setting $\Sigma_{\text{CPA}} = 0$. The bias dependence of this nonlinear I - V dependence is indicated explicitly. Except for its dependence on V_{dc} , the Γ_S may be assumed constant since the resonance width is < 1 meV, except when V_{dc} is such that the well CB edge coincides energetically with that of the CB on the left (in the negative-resistance region).

The level broadening associated with tunneling and scattering is contained entirely in $g_W(E)$. The spectral densities with and without scattering, $A(k=0, E)$, are compared in Fig. 2 for the state at the well CB edge when

it lies just above (0.2 meV) the left CB edge in the absence of scattering for a lattice matched $\text{In}_{0.53}\text{Ga}_{0.47}\text{As}/\text{In}_{0.52}\text{Al}_{0.48}\text{As}$ DBQW with $d_w = 45$ Å and $d_L = d_R = 56$ Å. This illustrative example corresponds to sample A of Ref. 1 which was measured at 10 K. We set $\mu_L = 50$ meV. Scattering effects shift the CB edge by $\text{Re}[\Sigma_{\text{CPA}}]$ as indicated. To permit comparison, the Lorentzian resonant peak associated with tunneling has been shifted by $\text{Re}[\Sigma_{\text{CPA}}]$. The shape of $A(0, E)$ including scattering is strongly asymmetric. This behavior results from the Gaussian distribution of states that blur the CB edge: The high-energy tail results from the increasing density of state available for scattering; the sharp cutoff at low energies is primarily associated with the energy dependence of $\text{Re}[\Sigma_{\text{CPA}}]$. Both widths are small compared to eV_{dc} . Since the f_S and Γ_S in Eq. (9) are weakly dependent on energy when eV_{dc} lies well within the Ohmic (positive-differential-resistance) region, the energy integral reduces to $\int dE g_w(E + \Phi_w)$ and is the same for all reasonable alloy scattering strengths. As a result j_{dc} in these regions is unaffected by scattering,¹¹ and will be the same regardless of whether the transport is coherent or sequential. Thus, neither τ_{resp} nor τ_{trans} will be appreciably affected by the tunneling

mechanisms. Note also that I - V measurements cannot be used to distinguish between coherent and sequential tunneling.

For a given V_{dc} , the factor $\Gamma_L \Gamma_R / (\Gamma_L + \Gamma_R)$ may be removed from the integral in Eq. (9). Similarly, the contribution to the current from unscattered electrons can be shown to be $j_{\text{dc}} \propto \Gamma_L \Gamma_R / (\Gamma_L + \Gamma_R + \Gamma_{\text{scat}})$. The fraction of coherent tunneling is thus $(\Gamma_L + \Gamma_R) / (\Gamma_L + \Gamma_R + \Gamma_{\text{scat}})$. Its value is about 1% for sample A of Ref. 1.

The transit time, $\tau_{\text{trans}} = \rho_w / j_{\text{dc}}$, where

$$\rho_w = \int_{-\infty}^{\infty} dE \phi_w(E) g_w(E) \quad (10)$$

is the charge density in the well, was measured by Chemla and co-workers¹ using differential absorption spectroscopy. Figure 3 compares the measured and calculated τ_{trans} in the Ohmic region as a function of current density for sample A of Ref. 1. The range of current densities for the experimental points is larger than that for the calculations because the experimental maximum current density exceeds the calculated value. The factor of 3–4 difference is reasonable in view of the approximations inherent in the model, the neglect of other scattering effects,¹² and the exponential dependence of h_{wS} on input parameters.

τ_{trans} may be estimated simply when \bar{e} is aligned with filled states on the left and empty states on the right. Equations (8)–(10) yield $\tau_{\text{trans}} \sim \hbar / \Gamma_R \approx 75$ ps in the present case when $j_{\text{dc}} = 100$ A/cm², in agreement with the physical expectation that the transit time is controlled by the effective height of the right barrier.

The importance of the frequency response of a DBQW operating as a negative-differential-resistance diode characterized by the response time τ_{resp} has already been noted. Operationally, the appropriately biased DBQW,

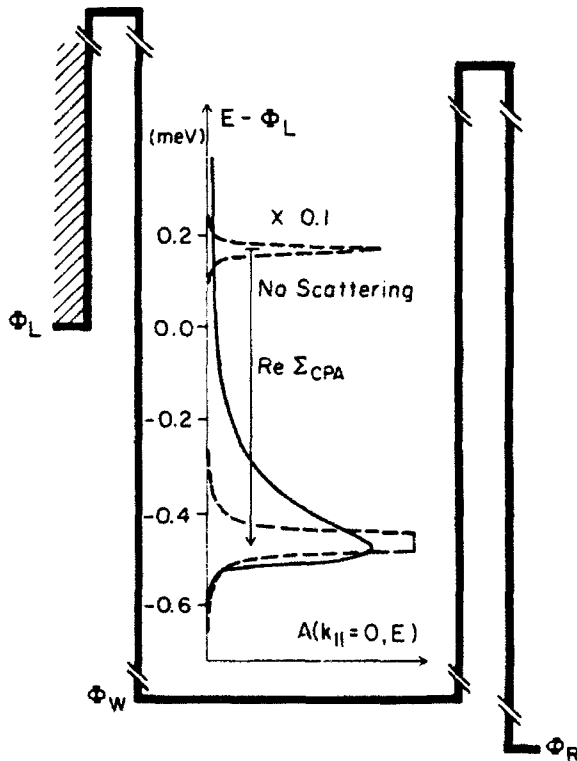


FIG. 2. Spectral density $A(k=0, E)$ for biased DBQW at far end of negative-differential-resistance regime with (solid curve) and without (dashed curve) alloy scattering. Resonance is sharper and located in positive-differential-resistance region for the case of well lifetime broadening alone (upper dashed curve; multiplied by 0.1). Shift by $\text{Re}[\Sigma_{\text{CPA}}]$ and scale change permits comparison between line shapes. DBQW is indicated schematically. Dashed region on left occupied by electrons.

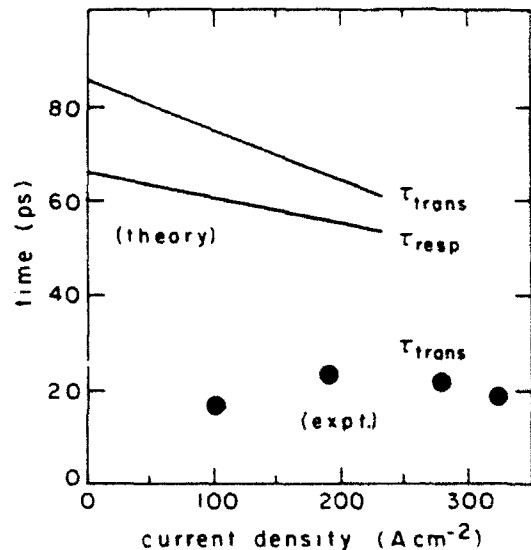


FIG. 3. Theoretical response and transit times vs current density compared with experiment, sample A, Ref. 1, in positive-differential-resistance region.

acted upon by an additional small ac field having frequency ω with Hamiltonian

$$H_{ac} = \frac{1}{2} e V_{ac} (\hat{N}_L - \hat{N}_R) e^{-i\omega t}$$

responds linearly to that field. For frequencies $\omega > \omega_{resp}$, as defined above, the current is no longer able to follow H_{ac} without phase lag. The upper frequency limit of de-

vice operation is thus given by $\omega_{resp} = \tau_{resp}^{-1}$. (The frequency limit is depressed due to circuit capacitance effects and other scattering mechanisms.)

The derivation of $\sigma(\omega)$ is lengthy, since a Bethe-Salpeter equation must be solved to include vertex corrections properly.¹³ The result, valid for the Ohmic region in which the energy dependence of the Γ_S can be neglected, is

$$\sigma(\omega) = \frac{e^2}{2\hbar^2\omega} \int_{-\infty}^{\infty} dE g_W(E; \omega) \frac{(\hbar\omega + 2i\Gamma_R)\Gamma_L(\Delta f_L) + (\hbar\omega + 2i\Gamma_L)\Gamma_R(\Delta f_R)}{\hbar\omega + i(\Gamma_L + \Gamma_R)}, \quad (11)$$

where

$$g_W(E; \omega) = (-2\pi i)^{-1} [F'_{CPA}(E + \hbar\omega) - F'_{CPA}(E)],$$

$$F'_{CPA}(E) = \langle 0 | G_{CPA}^{r(a)}(E) | 0 \rangle,$$

the single-chain diagonal matrix element of the CPA retarded (advanced) Green's function, and $\Delta f_S = f_S(E + \hbar\omega - \Phi_S) - f_S(E - \Phi_S)$ ($S = L, R$). Note that $g_W(E; 0) = g_W(E)$, the well density of states in Eq. (9), and that $\sigma(0) = dj_{dc}/dV_{dc}$ at a given V_{dc} in the present case. The applied dc voltage remains even when V_{ac} , which is much smaller than V_{dc} , has vanishing frequency.

The results for τ_{resp} are also shown in Fig. 3. Even though the physical ingredients in the definitions of τ_{trans} and τ_{resp} are quite different, the numerical values are seen

to be in remarkably close agreement. Calculations for a typical current of $j_{dc} = 100$ A/cm² in the negative-differential-resistance region (not indicated in Fig. 3) show that τ_{trans} and τ_{resp} have values about 60 ps and differ by only 7 ps, as in the Ohmic region. This result confirms that the experimentally accessible time defined and measured in Ref. 1 is, in fact, useful in device applications of current interest.

We are grateful to D. S. Chemla, D. K. Ferry, and P. M. Hui for useful discussions. This work was supported by the U.S. Joint Services Electronics Program (JSEP) through ONR Contract No. N00014-89-J-1023 and by the DARPA through ONR Contract No. N00014-86-K-0033.

¹I. Bar-Joseph, T. K. Woodward, D. S. Chemla, D. Sivco, and A. Y. Cho, Phys. Rev. B **41**, 3264 (1990).

²I. Bar-Joseph *et al.*, Superlatt. Microstruct. **8**, 409 (1990).

³S. Luryi, in *Heterojunction Band Discontinuities: Physics and Device Applications*, edited by F. Capasso and G. Margaritondo (Elsevier, Amsterdam, 1987), p. 489.

⁴B. Ricco and M. Ya. Azbel, Phys. Rev. B **29**, 1970 (1984).

⁵For example, H. Ehrenreich and L. M. Schwartz, in *Solid State Physics*, edited by H. Ehrenreich, F. Seitz, and D. Turnbull (Academic, New York, 1976), Vol. 31, p. 149.

⁶B. Velický, Phys. Rev. **184**, 614 (1969).

⁷H. Sumi and Y. Toyozawa, J. Phys. Soc. Jpn. **31**, 342 (1971).

⁸For example, J. Rammer and H. Smith, Rev. Mod. Phys. **58**, 323 (1986).

⁹L. Y. Chen and C. S. Ting, Phys. Rev. Lett. **64**, 3159 (1990); Phys. Rev. B **41**, 8533 (1990); **43**, 2097 (1991).

¹⁰Note that in the S regions both G' and G^a also assume their unperturbed values.

¹¹This fact was previously noted for a simple resonance model by T. Weil and B. Vinter, Appl. Phys. Lett. **50**, 1281 (1987); M. Jonson and A. Grincwajg, *ibid.* **51**, 1729 (1987).

¹²For example, F. Chevoir and B. Vinter, Appl. Phys. Lett. **55**, 1859 (1989); H. A. Fertig, S. He, and S. Das Sarma, Phys. Rev. B **41**, 3596 (1990); J. Leo and A. H. MacDonald, *ibid.* **43**, 9763 (1991); N. S. Wingreen, K. W. Jacobsen, and J. W. Wilkins, *ibid.* **40**, 11 834 (1989).

¹³E. Runge and H. Ehrenreich (unpublished).

Evidence for quantum well asymmetry in optical absorption

P. M. Young and H. Ehrenreich

Division of Applied Sciences, Harvard University, Cambridge, Massachusetts 02138

(Received 14 April 1992; accepted for publication 19 June 1992)

Some previously unexplained features of the experimentally determined optical spectra of GaAs/Ga_{1-x}Al_xAs heterostructures are theoretically explained in terms of unintentionally introduced asymmetries in the shape of semiconductor quantum wells which break the usual optical selection rules. Various mechanisms that may be responsible for well asymmetries are suggested. Their measurement may be a useful characterization tool in quantum well fabrication.

Several absolute optical absorption and photoluminescence excitation (PLE) experiments have been performed on GaAs/Ga_{1-x}Al_xAs superlattices (SLs) and quantum wells (QWs).¹⁻⁴ Some unexpected features in the otherwise well-understood spectra of these heterostructures have been seen.⁵⁻⁷ Recent calculations⁷ of optical absorption for both the In_{1-x}Ga_xAs/In_{1-x}Al_xAs and the GaAs/Ga_{1-x}Al_xAs systems showed better agreement with experiment for the former due, in part, to the absence of these features. We propose that the unexpected features, which are more pronounced in the Ga than in the In_{1-x}Ga_x based system, arise from asymmetries in the heterostructures and the associated breaking of the usual optical selection rules for such structures.

Most QWs are designed to have conduction and valence band edges with flat, symmetric energy profiles as in Fig. 1(a). QW asymmetry arises from imperfections introduced during the growth of the heterostructure. Figures 1(b)-1(d) illustrate three simple models for this asymmetry.

The first model, illustrated in Fig. 1(b), includes the effects of a built-in electric field extending over the QW. A field of this kind could be created, for example, by a doping imbalance between the buffer and capping layers of the QW sample. In the extreme case of an *n*- to *p*-type transition, this would impose a field over the sample of strength 1.5×10^4 V/cm for a 10^4 Å sample. The second possibility, illustrated in Fig. 1(c), is a field spanning only the well region. Such a field could occur if an intentional miscut in one of the high symmetry growth planes resulted in dangling bonds at the two interfaces⁸ having opposite charge. The third possibility, illustrated in Fig. 1(d), involves compositional gradients which may exist in the barriers, in the wells, or in both. Such compositional gradients could result during the molecular beam epitaxy (MBE) growth process in which the flux of the Al in the Ga_{1-x}Al_xAs system deviates briefly from its nominal value when shutters are opened or closed. Upon switching from barrier growth to well growth the Al flux may persist briefly after the Al source has been closed. Upon initiation of barrier growth, the Al flux may overshoot its nominal value when the shutter is first opened due to built up pressure in the Al chamber.⁹ The dotted profile in Fig. 1(d) illustrates the situation qualitatively; the solid line corresponds to a simplified model. Variation in the Al concentration of 1% over

100 Å mimics the effects of an electric field of about 10^4 V/cm.

To investigate the effects of asymmetry, we have performed absorption calculations based on the uniform field model of Fig. 1(b). Investigations of the other models lead to results that differ by less than the experimental differences between nominally identical samples. The key point is that the selection rules of a symmetric QW are broken in asymmetric wells since the electronic states no longer have even and odd parity. Calculations for a field of 3×10^4 V/cm are presented below, which according to the third possibility discussed above, correspond to a variation in the Al concentration of about 3% over the well. The size of the field was selected to lie within bounds consistent with the uncertainty in field strengths of about 10^4 V/cm associated with experiments investigating the quantum-confined stark effect.¹⁰

The optical absorption spectra of SLs and QWs are dominated by the discrete exciton peaks and the staircase-like continuum absorption due to transitions from the valence subband states *n* associated with the light holes (LHn) and heavy holes (HHn) to the conduction subbands (Cn). Allowed transitions consist of the HHn, LHn → Cn pairs, which obey the selection rule $\Delta n = 0$. These features are clearly seen in Fig. 2, which compares

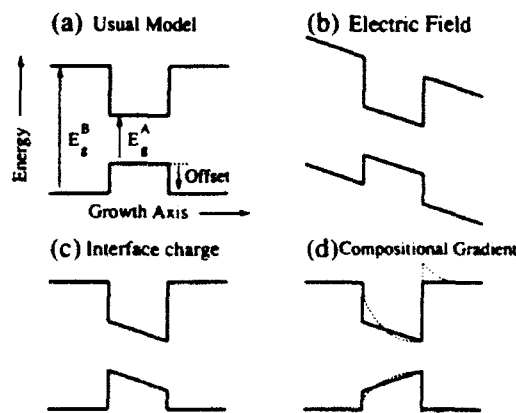


FIG. 1. The usual QW model, (a), and three simple models for QW asymmetry, resulting from (b) an electric field over the entire structure, (c) a field extending only over the well, and (d) a gradient in the Al concentration. The band gaps, E_g^A and E_g^B are indicated, as is the valence band offset. Gradients in Al concentration can arise from MBE growth, illustrated qualitatively with the dashed profile in (d).

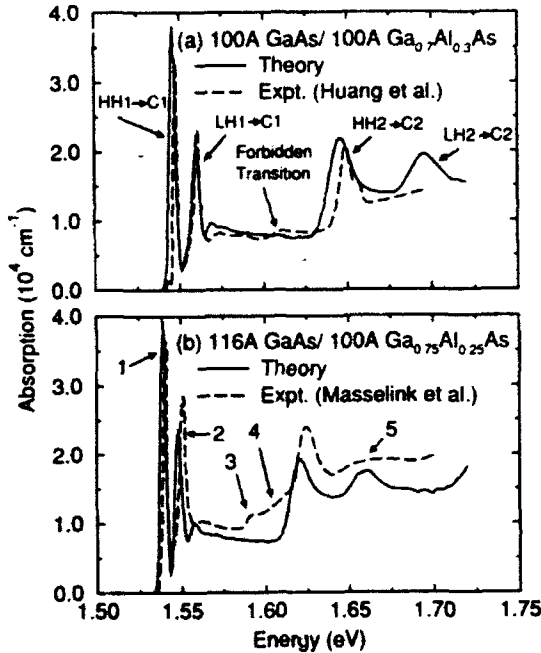


FIG. 2. Comparison of theoretical (solid) and experimental (dashed) absorption of SLs of (a) 100 Å GaAs/100 Å Ga_{0.7}Al_{0.3}As; and (b) 116 Å GaAs/Ga_{0.75}Al_{0.25}As. (See footnotes 2 and 3 for experimental information.) Major allowed transitions and a "forbidden" transition are identified. The disagreement between experiment and theory in (b) is indicated by five characteristic features discussed in the text.

theoretical absorption for symmetric wells^{7,11} to two experiments on 100 Å GaAs/100 Å Ga_{0.7}Al_{0.3}As and 116 Å GaAs/100 Å Ga_{0.75}Al_{0.25}As SLs. The major allowed excitonic transitions and a forbidden transition are identified in Fig. 2(a). In Fig. 2(b) five points of disagreement between experiment and theory are identified. These same points of disagreement are also present, albeit to a lesser extent, in Fig. 2(a), and are characteristic of all but one of the twenty absorption and PLE measurements on GaAs samples that we have encountered in the published literature. Chu and Chang¹² have also calculated SL absorption but compared to PLE experiments. Their results exhibit the same points of disagreement. We conclude that these features are not a shortcoming of the absorption theory of Ref. 7, nor are they a peculiarity of any particular sample.

The first two features to note, 1 and 2 in Fig. 2(a), are that theory predicts a stronger HH1→C1 transition than is observed in experiment, while it predicts a weaker LH1→C1 peak than is actually seen. Thus, the approximately two to one ratio of oscillator strengths predicted by theory is experimentally significantly smaller. Feature 3 is the distinct "forbidden transition" in the absorption spectrum between the $n=1$ and $n=2$ HHn, LHn→Cn doublets. Various authors have associated this feature with the HH3→C1 transition,^{1,4,6,12,13} which is forbidden by the selection rule $\Delta n=0$, but not strictly forbidden in real GaAs QWs since the Ga_{1-x}Al_xAs barriers are only of finite height. However, absorption calculations^{6,7} have found the HH3→C1 transition to be too weak to explain the experimentally observed feature. It is also interesting that this

transition appears as a "step" without a distinct associated peak. Feature 4 is the low energy shoulder observed just below the HH2→C2 peak, which makes the transition seem broader than expected. Feature 5 is that the LH2→C2 peak is only poorly resolved, and sometimes barely visible at all.

The present calculations for asymmetric wells are performed using an eight-band Kane model modified to include finite HH mass, which determines envelope functions for the QW structure.^{14,15} The calculations include an asymmetric potential, $V_{\text{asym}} = -e\mathcal{E}z$, linear in the growth axis coordinate of the structure, z . Here \mathcal{E} is the built-in electric field. The QW states, $|L, K\rangle$, are defined in terms of the envelope functions, F_n , and the eight $k=0$ states of the Kane model, $\langle r|n0\rangle$, by $\langle r|L, K\rangle = \sum_n F_n(L, K; r) \langle r|n0\rangle$. These states include the effects of the electric field as does the equation determining the envelope functions at $K=0$,

$$H^{k=0}[k_x=0, k_y=0, k_z \rightarrow -i(\partial/\partial z)]F(L, 0; z) - e\mathcal{E}zF(L, 0; z) = E_L(K=0)F(L, 0; z). \quad (1)$$

Here $H^{k=0}$ is the $k \cdot p$ Hamiltonian appropriate to the constituent bulk semiconductors of the heterostructure. Because the asymmetric term diverges at large distances, hard-wall boundary conditions are imposed on both sides of the QW at points 100 Å outside the well. The states and optical matrix elements for finite heterostructure wave vector K , which lies in the x - y , or QW, plane, are determined from a SL $K \cdot p$ theory¹⁵ applied to the zone center $K=0$ states.

The optical absorption at zero temperature between valence band L and conduction band L' in the absence of electron-hole interactions is given by

$$\alpha_{LL'}(E) = \frac{2\pi^2 e^2 \hbar}{V n m c} \sum_K \frac{2}{m} \frac{|\langle L, K | p | L', K \rangle|^2}{E_{L'}(K) - E_L(K)} \times \delta[E - E_{L'}(K) + E_L(K)], \quad (2)$$

where n is the refractive index and V is the volume of the well. The effect of the electron-hole Coulomb interaction is incorporated using the heterostructure crystal coordinate representation (CCR) and a simple model for the electron-hole interaction.^{7,16} The results are expressed in terms of a Sommerfeld enhancement factor $\mathcal{S}(E)$ for the continuum interband absorption, bound exciton energies, E_n , and oscillator strengths, $f_i = (2/m) |\langle L, 0 | p | L', 0 \rangle|^2 |U(0)|^2 / [E_{L'}(0) - E_L(0)]$, where $U(R)$ is the CCR exciton wave function. The absorption is then¹⁷

$$\alpha(E) = \frac{2\pi^2 e^2 \hbar}{n m c} \sum_i f_i \delta(E - E_i) + \sum_{LL'} \mathcal{S}(E) \alpha_{LL'}(E). \quad (3)$$

The results for a 100 Å GaAs/Ga_{0.7}Al_{0.3}As QW are illustrated in Fig. 3 for the theory with and without an asymmetric potential term of $e\mathcal{E} = 30$ meV/100 Å. The asymmetry is seen to provide exactly those features whose absence caused disagreement between experiment and the theory for symmetric QWs.

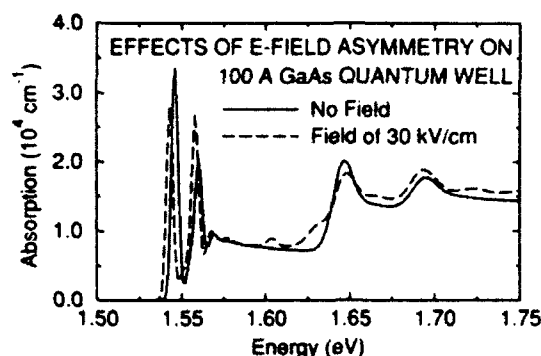


FIG. 3. Comparison of theoretical calculations of absorption in a 100 Å GaAs QW with $\text{Ga}_{0.7}\text{Al}_{0.3}\text{As}$ barriers with (dashed) and without (solid) an electric field of 3×10^5 V/cm. The effects of the asymmetric potential furnish those features whose absence caused disagreement between experiment and theory in Fig. 2.

When inversion symmetry is broken, the optical selection rule $\Delta n=0$ is no longer applicable, and the oscillator strengths of the various transitions change. Miller, Weiner, and Chemla¹⁸ have discussed approximate absorption sum rules which require that the total integrated absorption from the heavy- and the light-hole subbands to a single conduction subband should be independently preserved when a field is introduced. These sum rules suggest that the field induced changes result from a *transfer* of oscillator strength between the various $\text{LH}n \rightarrow \text{C}n$ and the various $\text{HH}n \rightarrow \text{C}n$ transitions.

More specifically, introduction of the field results in oscillator strength being lost from the $\text{HH}1 \rightarrow \text{C}1$ transition to the formerly forbidden $\text{HH}2 \rightarrow \text{C}1$ and $\text{HH}3 \rightarrow \text{C}1$ transitions. The $\text{HH}2 \rightarrow \text{C}1$ transition occurs at nearly the same energy as the $\text{LH}1 \rightarrow \text{C}1$ transition, explaining why experimental measurements show a weaker $\text{HH}1 \rightarrow \text{C}1$ and stronger $\text{LH}1 \rightarrow \text{C}1$, [cf. Figs. 2(a) and 2(b)]. Oscillator strength is shifted from $\text{LH}1 \rightarrow \text{C}1$ to $\text{LH}2 \rightarrow \text{C}1$, so that this transition and the $\text{HH}3 \rightarrow \text{C}1$ contribute to the experimentally observed forbidden transition of Fig. 2(a). The transfer of oscillator strength from allowed to forbidden transitions is more important for states away from the zone center than for those at $\text{K}=0$, so violation of the selection rules is more important for the continuum than for the exciton peaks. Thus, the experimentally observed step, feature 3 of Fig. 2(b), results because the forbidden transition corresponds to a 10%–20% increase in continuum absorption rather than an exciton peak. The previously forbidden $\text{HH}1 \rightarrow \text{C}2$ transition acquires oscillator strength and appears as the low energy shoulder, feature 4, on the $\text{HH}2 \rightarrow \text{C}2$ peak. Other forbidden transitions around the $\text{LH}2 \rightarrow \text{C}2$ peak also acquire oscillator strength, obscuring the allowed peak associated with feature 5.

While the effects of QW asymmetry on optical absorption are significant, asymmetry has so far received little attention in comparisons of band structure theories to experiment. This is because the effects of the asymmetry on the transition energies are rather small, as can be seen in Fig. 3, and are comparable to the uncertainty introduced by monolayer fluctuations in the nominal well width. The

fact that asymmetry has a large effect on the absorption, yet a small effect on the transition energies, is best understood by considering $V_{\text{asym}} = -e\mathcal{E}z$ as a perturbation. Since the unperturbed well is symmetric, the energies of all interband transitions are affected only in *second* order of the antisymmetric perturbing potential. However, the oscillator strengths of *forbidden* transitions involving states of opposite parity (which is a good quantum number for the symmetric well) are affected in *first* order. Therefore, calculations which compare only interband transition energies but not absorption coefficients are unable to account for the five effects of QW asymmetry which are here explained.

In view of the relatively small conduction and valence band barrier heights in the GaAs/ $\text{Ga}_{1-x}\text{Al}_x\text{As}$ system (200 and 100 meV, respectively) compared to those of $\text{In}_{1-x}\text{Ga}_x\text{As}/\text{In}_{1-y}\text{Al}_y\text{As}$ (500 and 200 meV), effects associated with electric field asymmetry of the well (≈ 30 meV) are expected to be small in the latter system, as observed. For systems with sufficiently small band offsets optical absorption measurements can therefore serve as a characterization tool for testing growth perfection.

We acknowledge fruitful discussions with F. Spaepen and members of the DARPA Defense Sciences Research Council, in particular, J. P. Hirth, E. Hu, and D. A. B. Miller. This research was supported by JSEP and DARPA through ONR Contract Nos. N00014-89-J-1023 and N00014-86-K-0033, respectively. One of us (P.M.Y.) acknowledges the Fannie and John Hertz Foundation for partial financial support.

¹R. C. Miller, D. A. Kleinman, W. A. Nordland, Jr., and A. C. Gossard, *Phys. Rev. A* **22**, 863 (1980).

²D. Huang, J. I. Chyi, and H. Markoc, *Phys. Rev. B* **42**, 5147 (1990).

³W. T. Masselink, P. J. Pearah, J. Klem, C. K. Peng, H. Markoc, G. D. Sanders, and Y. C. Chang, *Phys. Rev. B* **32**, 8027 (1985).

⁴R. C. Miller, A. C. Gossard, G. D. Sanders, Y. C. Chang, and J. N. Schulman, *Phys. Rev. B* **32**, 8452 (1985).

⁵G. D. Sanders and Y. C. Chang, *Phys. Rev. B* **31**, 6892 (1985); **35**, 1300 (1987); H. Chu and Y. C. Chang, *ibid.* **36**, 2946 (1987).

⁶H. Chu and Y. C. Chang, *Phys. Rev. B* **39**, 10861 (1989).

⁷P. M. Young, P. M. Hui, and H. Ehrenreich, *Phys. Rev. B* **44**, 12969 (1991).

⁸J. P. Hirth and F. Spaepen (private communications).

⁹D. A. B. Miller (private communication).

¹⁰D. A. B. Miller, D. S. Chemla, T. C. Damen, A. C. Gossard, W. Wiegmann, T. H. Wood, and C. A. Burrus, *Phys. Rev. Lett.* **53**, 2173 (1984).

¹¹The absorption coefficient is given approximately by $(I/I_0) = e^{-\alpha D}$, where (I/I_0) is the ratio of transmitted to incident intensity. Here, D is taken as the total thickness of the well material only. This is in contrast to note 24 of Ref. 7.

¹²Y. C. Chang and J. N. Schulman, *Appl. Phys. Lett.* **43**, 536 (1983).

¹³R. C. Miller, D. A. Kleinman, and A. C. Gossard, *Phys. Rev. B* **29**, 7085 (1984).

¹⁴N. F. Johnson, H. Ehrenreich, K. C. Hass, and T. C. McGill, *Phys. Rev. Lett.* **59**, 2352 (1987).

¹⁵N. F. Johnson, H. Ehrenreich, P. M. Hui, and P. M. Young, *Phys. Rev. B* **41**, 3655 (1990).

¹⁶N. F. Johnson, *J. Phys. Condens. Matter* **2**, 2099 (1990).

¹⁷Fano resonances are neglected in the independent subband approximation. The calculations of Ref. 6 show Fano resonances to be weak in this system.

¹⁸D. A. B. Miller, J. S. Weiner, and D. S. Chemla, *IEEE J. Quantum Electron.* **22**, 1816 (1986).

Non-equilibrium Transport in Alloy Based Resonant Tunneling Systems

E. RUNGE AND H. EHRENREICH

*Division of Applied Sciences, Harvard University,
Cambridge, Massachusetts 02138*

Received May 15, 1992

The transit and dynamic response times for a semiconductor alloy-based double barrier quantum well structure are calculated within the coherent potential approximation. The formalism is based on a non-equilibrium Green's function formulation of the transport process including vertex corrections. The tunneling current is expressed as a sum of coherent and sequential distributions respectively corresponding to tunneling with and without multiple alloy scattering in the well region. This distinction is significant in nanostructures exhibiting quantum interference effects. The calculated characteristic times are of practical importance because they determine the achievable high frequency performance of device structures.

© 1992 Academic Press, Inc.

I. INTRODUCTION

Resonant tunneling structures that exhibit negative differential resistance are promising candidates for various applications such as ultrahigh-frequency ac-generators or very fast switching elements [1-3]. Furthermore, they are useful for the investigation of fundamental transport processes in nanostructures. Double barrier quantum well systems (DBQW) are prototypical tunneling structures. This paper examines the influence of scattering in the *well* region on the DBQW steady-state dc-current and the dynamic response to an ac-field. We concentrate on disorder scattering due to alloying or impurities. This is the dominant scattering mechanism at low temperatures in many Group III-V $A_xB_{1-x}C$ compounds such as $In_{0.47}Ga_{0.53}As$ [4]. The calculations presented here apply to elastic scattering mechanisms, but not to inelastic phonon scattering, giving rise to phonon sidepeaks in the current-voltage characteristic.

A biased DBQW as a whole is a system *far from equilibrium*, even though the electron systems on both sides of the barriers will be assumed to be in thermal equilibrium with distinct reservoirs on either side (see Section II). Furthermore, the dc-current represents a highly nonlinear response to the applied bias. The formalism therefore uses non-equilibrium Green's function techniques (see Sections III and V). These techniques have been previously applied to a one-dimensional DBQW structure [5]. We treat here a three-dimensional model that includes elastic

alloy scattering of practical interest in III-V alloy structures, within the coherent potential approximation (CPA). Elastic scattering has been previously considered in low order perturbation theory [6]. The CPA provides a simple yet quite accurate description of alloy scattering beyond either the weak scattering limit or the dilute impurity limit [7].

Coherent and sequential tunneling processes have been widely discussed [8]. In the former, resonant tunneling is visualized in analogy to the optical Fabry-Pérot spectrometer as coherent transmission through the entire structure. In the latter case the particle first tunnels into the well and then to the other side in a separate step. Section IV derives the total current as a sum of a coherent contribution of electrons that remain in their momentum eigenstate and of a sequential contribution of electrons that are scattered in the well. The ratio of the coherent and the sequential contributions depends very sensitively on parameters like the barrier thickness. Coherent electron transport is shown to be dominant only in DBQWs that are smaller than those currently in use.

One of the driving forces for the investigation of DBQWs is to develop devices that can be operated at very high frequencies. This application requires understanding of the dynamic behavior of DBQWs and, in particular, of their linear current response to an applied ac-field. The current response is calculated in Section V. The results significantly generalize earlier model calculations that neglected scattering [5, 9, 10]. Other aspects of the time-dependent response have been investigated theoretically in Refs. [11-14] and numerically in Refs. [15-19].

Two characteristic time scales for tunneling are of concern here [20, 21]. The steady state dc-current density, j_{dc} , and the charge density ρ_w stored in the well define a characteristic time, the *dwell* or *transit time*: $\tau_{trans} \equiv \rho_w/j_{dc}$ [20]. This time has been measured experimentally [22, 23]. The transit time is an intrinsically static quantity. The *response time*, τ_{resp} , which is introduced here, is directly relevant for high frequency response. It is defined as the inverse frequency $\omega_{resp} = \tau_{resp}^{-1}$ at which the systems fails to follow the external ac-field, or more precisely as the frequency for which $\text{Im } \sigma(\omega_{resp})$ is maximum. These characteristic times differ both conceptually and quantitatively. The calculations of Section V show that the inverse response time is dominated by the escape rate out of the well to *either* side. By contrast, the dwell time is determined by the escape rate to the collector side only.

The present authors have recently published a brief physical discussion of the principal results [21]. Here we focus on the underlying theory and, in addition, present some new results.

II. MODEL AND ASSUMPTIONS

A biased DBQW structure is depicted schematically in Fig. 1. We consider electron tunneling involving a single conduction band which is described within the effective mass approximation. The semiconductor materials on both sides of the

structure are assumed the same. An external dc-bias shifts the conduction band edges Φ_L and Φ_R of the left (emitter) and the right (collector) side relative to each other; $\Phi_L = eV_{dc}$ and $\Phi_R = 0$. Resonant tunneling and a resulting current maximum occurs for dc-bias when well states are lined up with occupied states in the emitter and empty states in the collector. The I-V-characteristic, i.e., the current as a function of the applied dc-bias, typically shows a slow increase, a sudden drop, a broad valley, and finally an approximately exponential increase.

The Hamiltonian for the sides $S = L, R$ is

$$\hat{H}_S^0 = \sum_{S=L,R} \sum_{\mathbf{k}} (\epsilon_{\mathbf{k}} + \Phi_S) c_{S\mathbf{k}}^\dagger c_{S\mathbf{k}} \quad (1)$$

with crystal momentum $\mathbf{k} = (k_{||}, k_z)$, kinetic energy $\epsilon_{\mathbf{k}} = \hbar^2 \mathbf{k}^2 / 2m^*$ and appropriately labelled creation operators $c_{S\mathbf{k}}^\dagger$. Both leads are assumed to be in separate thermal equilibrium at temperature T and characterized by chemical potentials μ_R and μ_L relative to Φ_L and Φ_R ,

$$f_S(E - \Phi_S) = \frac{1}{e^{(E - \Phi_S - \mu_S)/(k_B T)} + 1} \quad (2)$$

The chemical potential μ_L is typically of the order 50 meV reflecting the increased electron density in the accumulation layer. For simplicity, we use $\mu_L = \mu_R$. Note that V_{dc} differs from the external bias because of the voltage drops across the accumulation and depletion layers.

We restrict attention to only one subband within the well region (W), which

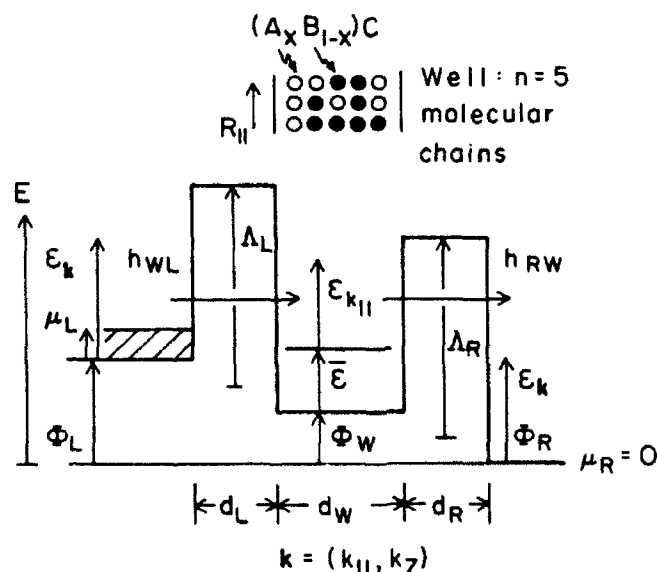


FIG. 1. Schematic representation of a biased double barrier quantum well system. Symbols are introduced in the text. The inset shows three random chains of $n = 5$ AC or BC units (from Ref. [21]).

gives rise to one resonance peak in the I-V-characteristic. The Hamiltonian for the well region in the absence of tunneling and scattering is

$$\hat{H}_w^0 = \sum_{k_{||}} (\bar{\epsilon} + \epsilon_{k_{||}} + \Phi_w) c_{wk_{||}}^\dagger c_{wk_{||}}, \quad (3)$$

describing the two-dimensional band starting at energy $\bar{\epsilon}$ above the the bottom of the well Φ_w . The effective mass is assumed the same in the well region and the leads. For simplicity, flat potentials are assumed in each spatial region. The well potential Φ_w results from a linear interpolation between Φ_L and Φ_R ; in particular, $\Phi_w = eV_{dc}/2$ for symmetric structures.

The barriers regions are described by transfer Hamiltonians

$$\hat{H}^{\text{tun}} = \sum_{S=L,R} \hat{H}_{wS}^{\text{tun}} = \sum_{S=L,R} \sum_{k_z, k_{||}} (h_{wS} c_{wk_{||}}^\dagger c_{Sk} + \text{h.c.}). \quad (4)$$

The tunneling matrix elements h_{wS} are closely related to the Golden rule rates for the escape of an electron out of the well to side S

$$\Gamma_S = 2\pi \sum_{k_z} |h_{wS}|^2 \delta(E - \epsilon_{k_{||}} - \epsilon_{k_z} - \Phi_S). \quad (5)$$

If h_{wS} only depends on k_z , Γ_S is a function of the "perpendicular" energy $E - \epsilon_{k_{||}}$. The matrix elements h_{wS} need not be specified explicitly, since they are always subsumed in Γ_S . The tunneling rates Γ_S are given by the WKB expression for tunneling through rectangular barriers with heights shown in Fig. 1:

$$\Gamma_S \approx \left(\frac{E - \epsilon_{k_{||}} - \Phi_w}{\pi} \right) \Theta(E - \epsilon_{k_{||}} - \Phi_S) \times \exp \left\{ -\frac{2}{\hbar} d_S \sqrt{2m_B^* \left(A_S + \frac{\Phi_S + \Phi_w}{2} - E + \epsilon_{k_{||}} \right)} \right\}. \quad (6)$$

Here $A_L = A_R$ is the conduction band offset between the barriers and the well. The first factor $\sqrt{2(E - \epsilon_{k_{||}} - \Phi_w)/m^*}/(2d_w)$, describes the classical collision frequency of a well electron with the wall separating the well from side S . The exponential describes the tunneling probability-amplitude through the barrier region of width d_S and effective electron mass m_B^* . The theta function cuts off the escape probability at the conduction band edge. We frequently assume Γ_S to be slowly varying on the energy scale given by the width of the tunneling resonance (typically a fraction of a meV). Since the spectral density of well states is sharply peaked around $\Phi_w + \bar{\epsilon} + \epsilon_{k_{||}}$, this amounts to replacing $E - \epsilon_{k_{||}} - \Phi_w$ by $\bar{\epsilon}$ everywhere in (6).

Equation (6) is not appropriate for energies close to the top or above the barriers, since the assumption of a single subband in the well region breaks down. The current contributions in this energy range are accounted for here by adding a classical Richardson current for all states with energies higher than the emitter

barrier. Other mechanisms that contribute to the current (e.g., leakage currents due to deep donor levels), particularly in the valley region, are neglected.

The full Hamilton operator

$$\hat{H} = \hat{H}_S^0 + \hat{H}_W^0 + \hat{H}^{\text{tun}} + \hat{H}^{\text{scat}} \quad (7)$$

also involves a term \hat{H}^{scat} describing the alloy scattering in the well. The specification of \hat{H}^{scat} requires more detailed discussion. At low temperatures the dominant scattering process in an $(A_x B_{1-x})C$ semiconductor alloy like $(\text{In}_x \text{Ga}_{1-x})\text{As}$ is scattering associated with the different on-site energies ϵ_A and ϵ_B on the cations [24]. For the difference $\epsilon_A - \epsilon_B$ we take the conduction band offset between the AC and the BC bulk material.

For typical well parameters the kinetic energy due to the confinement in the growth (z) direction is large compared with the effects of alloy scattering. Therefore the z -dependence of the wavefunction is determined by the confinement to a good approximation and can be expressed by a normalized disorder-independent factor $\phi(z)$. For high barriers, $\phi(z) \sim \cos(\pi z/d_w)$ for z within the well with the origin at the well center.

Electrons freely moving in the parallel directions experience the randomly varying potential. The alloy disorder is best described in terms of chains of atoms centered at $R_{||}$ and extending along the z direction. The inset of Fig. 1 shows these chains schematically. The electron energy of a chain at $R_{||}$ is

$$\epsilon_{R_{||}} = \sum |\phi(z_i)|^2 \epsilon(R_{||}, z_i), \quad (8)$$

where the sum runs over all the cations in the chain since the conduction band edge states are predominately of cation character. The factor $\epsilon(R_{||}, z_i)$ is either ϵ_A or ϵ_B , depending on the type of cation at $(R_{||}, z_i)$. The energies $\epsilon_{R_{||}}$ are approximately Gaussian distributed with the average energy

$$\bar{\epsilon} = \langle \epsilon_{R_{||}} \rangle_{\text{av}} = x\epsilon_A + (1-x)\epsilon_B \quad (9)$$

and variance

$$\langle (\epsilon_{R_{||}} - \bar{\epsilon})^2 \rangle_{\text{av}} = x(1-x)(\epsilon_A - \epsilon_B)^2 a^{-1} \int_{\text{well}} |\phi(z)|^4 dz, \quad (10)$$

where a^3 is the spatial extent of the anion cation unit. For high barriers the integral is approximately $3/2n$, where n is the number of atomic layers in the well.

Formally, the chain at $R_{||}$ corresponds to the Wannier state

$$c_{WR_{||}}^\dagger = a^2 \sqrt{N} \int_{BZ} \frac{d^2 k_{||}}{(2\pi)^2} e^{-ik_{||} \cdot R_{||}} c_{Wk_{||}}^\dagger. \quad (11)$$

Thus the scattering term of the Hamiltonian is

$$\hat{H}^{\text{scat}} = \sum_{R_{||}} \varepsilon_{R_{||}} c_{WR_{||}}^\dagger c_{WR_{||}}, \quad (12)$$

where the $\varepsilon_{R_{||}}$ are Gaussian distributed random variables with average and variance given by (9) and (10).

III. ELECTRON PROPAGATION IN THE WELL

Since a biased DBQW is far from thermal equilibrium, it is necessary to use non-equilibrium quantum transport theory [25] for the description of the electron propagation in the well. The retarded and advanced Green's functions for any two fermion operators c_α^\dagger and c_β (e.g., $\alpha = Lk$, $\beta = Wk_{||}$) are the expectation values:

$$G^r(\beta t_2, \alpha t_1) = -i\Theta(t_2 - t_1) \langle c_\beta(t_2) c_\alpha^\dagger(t_1) + c_\alpha^\dagger(t_1) c_\beta(t_2) \rangle \quad (13)$$

$$G^a(\beta t_2, \alpha t_1) = G^r(\alpha t_1, \beta t_2)^*. \quad (14)$$

An additional distribution Green's function

$$G^<(\beta t_2, \alpha t_1) = +i \langle c_\alpha^\dagger(t_1) c_\beta(t_2) \rangle \quad (15)$$

describes the occupation of the individual states. For $t_1 = t_2$ the distribution Green's function is the actual density matrix of the system.

For a steady state, the distribution Green's function depends only on the difference of its time arguments. For non-interacting fermion systems in thermal equilibrium $G^<$ is not an independent quantity, but its Fourier transform

$$G^<(\beta, \alpha | E) = \int_{-\infty}^{\infty} dt e^{+iE(t_2 - t_1)/\hbar} G^<(\beta t_2, \alpha t_1) \quad (16)$$

is given by

$$G^<(\beta, \alpha | E) = -f(E)[G^r(\beta, \alpha | E) - G^a(\beta, \alpha | E)], \quad (17)$$

where f is the appropriate Fermi function.

The results of this paper can be derived using Dyson's equation with a perturbation of the simple form $V_{\gamma\delta} c_\gamma^\dagger c_\delta$. The relevant Dyson's equations are

$$G^r(\beta t_2, \alpha t_1) = G_0^r(\beta t_2, \alpha t_1) + \int_{-\infty}^{\infty} dt_3 G_0^r(\beta t_2, \gamma t_3) V_{\gamma\delta} G^r(\delta t_3, \alpha t_1) \quad (18)$$

$$G^<(\beta t_2, \alpha t_1) = G_0^<(\beta t_2, \alpha t_1) + \int_{-\infty}^{\infty} dt_3 [G_0^r(\beta t_2, \gamma t_3) V_{\gamma\delta} G^<(\delta t_3, \alpha t_1) + G_0^<(\beta t_2, \gamma t_3) V_{\gamma\delta} G^a(\delta t_3, \alpha t_1)]. \quad (19)$$

The presence of *two* terms in the integral of (19) reflects that the perturbation influences $G^<$ by modifying the propagation *and* the occupation of states. Used iteratively, these equations lead to a systematic perturbation expansion for G' and $G^<$ in terms of G'_0 and $G^<_0$. For steady states, the Fourier transforms of (18) and (19) have the simple form

$$G'(\beta\alpha | E) = G'_0(\beta\alpha | E) + G'_0(\beta\gamma | E) V_{\gamma\delta} G'(\delta\alpha | E) \quad (20)$$

$$G^<(\beta\alpha | E) = G^<_0(\beta\alpha | E) + G'_0(\beta\gamma | E) V_{\gamma\delta} G^<(\delta\alpha | E) + G^<_0(\beta\gamma | E) V_{\gamma\delta} G^a(\delta\alpha | E). \quad (21)$$

In the case of interest, we neglect any influence of the well on the leads $S = L, R$. The leads are described by the *unperturbed* Green's functions and Fermi distributions (2):

$$G'(Sk_z k_{||} | E) = \frac{1}{E + i0^+ - \varepsilon_{k_z} - \varepsilon_{k_{||}} - \Phi_S} \quad (22)$$

$$G^<(Sk_z k_{||} | E) = 2\pi i f_S(E - \Phi_S) \delta(E - \varepsilon_{k_z} - \varepsilon_{k_{||}} - \Phi_S). \quad (23)$$

(We write $G(Sk_z k_{||} | E)$ instead of $G(Sk_z k_{||}, Sk_z k_{||} | E)$, since these Green's functions are diagonal in all their quantum numbers. For the well Green's functions, only the average $\langle G(Wk_{||}, Wk'_{||} | E) \rangle$ is diagonal in the momentum variable.)

Particles in the well have a finite lifetime expressed by the finite imaginary part of the self-energy

$$\Sigma_0 = \Sigma_L + \Sigma_R, \quad (24)$$

even in the absence of scattering, since they can escape to either side [26]. Specifically, Σ_S describes tunneling out of the well, propagation in S , and tunneling back into the well. Its form (see Fig. 2a)

$$\Sigma'_S(k_{||} | E) \equiv \sum_{k_z} h_{wS} G'(Sk_z k_{||} | E) h_{wS}^*, \quad (25)$$

and correspondingly for $\Sigma_S^<$ and Σ_S^a , follows from the once-iterated Dyson's equation (20) with \hat{H}^{tun} as perturbation. We assume that the real part of the tunneling self-energy has been incorporated into the energy $\bar{\varepsilon}$ denoting the resonance level. Its effect is to lower $\bar{\varepsilon}$ relative to that in an isolated quantum well having the same width and depth. The remaining imaginary parts have the familiar form expected from perturbation theory,

$$\begin{aligned} \Sigma_S^<(k_{||} | E) &= 2\pi i \sum_{k_z} f_S(E - \Phi_S) |h_{wS}|^2 \delta(E - \varepsilon_{k_z} - \varepsilon_{k_{||}} - \Phi_S) \\ &= f_S(E - \Phi_S) i\Gamma_S \end{aligned} \quad (26)$$

$$\Sigma'_S(k_{||} | E) = \Sigma_S^a(k_{||} | E)^* = -i\Gamma_S/2. \quad (27)$$

$$\begin{aligned}
\text{a) } \Sigma_S(k_{||}|E) &= \textcircled{\Sigma_S} = x \xleftarrow{E} x \\
\text{b) } \xleftarrow{E} x \xleftarrow{E} x - x \xleftarrow{E} x \xleftarrow{E} x &= \xleftarrow{E} \textcircled{\Sigma_S} - \textcircled{\Sigma_S} \xleftarrow{E} \\
\text{c) } \Sigma_S^{[1]}(k_{||}|E+\hbar\omega, E) &= \textcircled{\Sigma_S^{[1]}} = x \xleftarrow{E+\hbar\omega} \cdot \xleftarrow{E} x \\
\text{d) } \xleftarrow{E+\hbar\omega} x \xleftarrow{E+\hbar\omega} \cdot \xleftarrow{E} x - x \xleftarrow{E+\hbar\omega} \cdot \xleftarrow{E} x \xleftarrow{E} &= \xleftarrow{E+\hbar\omega} \textcircled{\Sigma_S^{[1]}} - \textcircled{\Sigma_S^{[1]}} \xleftarrow{E} \\
\text{e) } \xleftarrow{E+\hbar\omega} x \xleftarrow{E+\hbar\omega} \cdot \xleftarrow{E} x \xleftarrow{E} x \xleftarrow{E} x - x \xleftarrow{E+\hbar\omega} x \xleftarrow{E+\hbar\omega} x \xleftarrow{E+\hbar\omega} \cdot \xleftarrow{E} x \xleftarrow{E} &= \xleftarrow{E+\hbar\omega} \textcircled{\Sigma_{S'}^{[1]}} \xleftarrow{E} \textcircled{\Sigma_S} - \textcircled{\Sigma_S} \xleftarrow{E+\hbar\omega} \textcircled{\Sigma_{S'}^{[1]}} \xleftarrow{E}
\end{aligned}$$

FIG. 2. (a) Diagrammatic representation of the tunneling self-energy $\Sigma_S(k_{||}|E)$; (b) dc-current; (c) first-order correction $\Sigma_S^{[1]}(k_{||}|E+\hbar\omega, E)$ to the tunneling self-energy; (d) and (e): the two classes of first-order corrections to the current. Single arrows represent lead Green's functions, double arrows are well Green's functions. Crosses stand for the tunneling through the individual barriers. Dots indicate bare ac-vertices (m). Diagrams are read from the right to the left.

In order to calculate the self-energy contributions due to scattering, we invoke the coherent potential approximation.

The CPA replaces the propagation in the disordered medium by the propagation in an effective homogeneous medium described by an energy-dependent, momentum-independent complex self-energy Σ_{CPA} [27]

$$G(Wk_{||}, Wk'_{||}|E) \xrightarrow{\text{CPA}} \delta_{k_{||}, k'_{||}} G_{\text{CPA}}(k_{||}|E) = \delta_{k_{||}, k'_{||}} G_0(Wk_{||}|E - \Sigma_{\text{CPA}}(E)), \quad (28)$$

where G_0 is the Green's function in the absence of scattering, but including the tunneling self-energies:

$$G_0^{\prime a}(Wk_{||}|E) = \frac{1}{E - \bar{E} - \epsilon_{k_{||}} - \Phi_W \pm i(\Gamma_L + \Gamma_R)/2}. \quad (29)$$

The arguments W for G_{CPA} are omitted, since the subscript "CPA" will be used only for well Green's functions (for the component $\Sigma_{\text{CPA}}^<$ see Appendix A).

The CPA self-energy is defined by the condition that the average of the effective t -matrix t_R for a single scattering site $R_{||}$, embedded in the effective CPA medium vanishes:

$$\langle t_{R_{||}} \rangle_{\text{av}} = \left\langle \frac{\epsilon_{R_{||}} - \Sigma_{\text{CPA}}}{1 - (\epsilon_{R_{||}} - \Sigma_{\text{CPA}}) F_{\text{CPA}}} \right\rangle_{\text{av}} = 0. \quad (30)$$

Here $\langle \rangle_{av}$ denotes the average over all scatterer configurations. The on-site CPA-Green's function

$$F'_{CPA}(E) = G'_{CPA}(R_{||}, R_{||} | E) = G'_0(R_{||}, R_{||} | E - \Sigma'_{CPA}(E)) \quad (31)$$

depends on Σ_{CPA} , but it is independent of $R_{||}$. A constant average value of Γ_L and Γ_R is used to calculate F_{CPA} . Equation (30) is then readily solved numerically.

If the occupation function ϕ_w is momentum-independent in the absence of alloy scattering, this will also be the case within the CPA with scattering included. Since $\langle t_{R||}^< \rangle_{av}$ vanishes within the CPA (cf., Appendix A),

$$G_{CPA}^<(k_{||} | E) = -2\pi i \phi_w(E) \text{Im} \left[\frac{1}{E - \bar{\epsilon} - \epsilon_{k_{||}} - \Phi_w - \Sigma'_w} \right], \quad (32)$$

where the total self-energy of well electrons is denoted by

$$\Sigma_w = \Sigma_{CPA} + \Sigma_0. \quad (33)$$

The CPA, as described here, permits calculation of all properties that are related to averages of the single-particle Green's function. The evaluation of quantities, like dynamic response functions, containing averages of the two-particle Green's function or averages of products of single-particle Green's functions, must include vertex corrections.

IV. STEADY STATE AND dc-CURRENT

The current from side $S = L, R$ into well W for electrons of both spins is given by

$$I_{S \rightarrow W} = 2e \left\langle \left\langle \frac{\partial}{\partial t} \hat{N}_S \right\rangle \right\rangle_{av}, \quad (34)$$

where $\hat{N}_S = \sum_{\mathbf{k}} c_{S\mathbf{k}}^\dagger c_{S\mathbf{k}}$ ($S = L, R$). Since

$$\hbar \frac{\partial}{\partial t} \hat{N}_S = i[\hat{H}, \hat{N}_S] = -i \sum_{k_z, k_{||}} [h_{WS}^* c_{Sk_z, k_{||}}^\dagger c_{Wk_{||}} - h_{WS} c_{Wk_{||}}^\dagger c_{Sk_z, k_{||}}], \quad (35)$$

the current at time t is, according to the definition (15), given by

$$\begin{aligned} I_{S \rightarrow W} &= -\frac{2e}{\hbar} \sum_{k_z, k_{||}} [\langle G^<(Wk_{||}t, Sk_z, k_{||}t) \rangle_{av} h_{WS}^* - \text{h.c.}] \\ &= -\frac{2e}{\hbar} \int \frac{dE}{2\pi} \sum_{k_z, k_{||}} [\langle G^<(Wk_{||}, Sk_z, k_{||} | E) \rangle_{av} h_{WS}^* - \text{h.c.}]. \end{aligned} \quad (36)$$

With the help of (20) and (21) the propagator $G(Wk_{||}, Sk_z k_{||} | E)$ can be expressed as an unperturbed propagator in S , a tunneling matrix element, and a full propagator in the well (see Fig. 2b). Two tunneling matrix elements and the propagator in the lead combine into a tunneling self-energy. Thus,

$$\begin{aligned} \sum_{k_z} G^<(Wk_{||}, Sk_z k_{||} | E) h_{WS}^* \\ = G^<(Wk_{||}, Wk_{||} | E) \Sigma_S^<(k_{||} | E) + G^<(Wk_{||}, Wk_{||} | E) \Sigma_S^a(k_{||} | E), \end{aligned} \quad (37)$$

and correspondingly for the same quantity involving $G^<(Sk_z k_{||}, Wk_{||} | E)$.

Writing the well distribution Green's function,

$$G^<(Wk_{||}, Wk_{||} | E) = -\phi_w [G^<(Wk_{||}, Wk_{||} | E) - G^a(Wk_{||}, Wk_{||} | E)], \quad (38)$$

in a form analogous to (17) yields the current

$$\begin{aligned} I_{S \rightarrow W} = \frac{2e}{h} \int \frac{dE}{2\pi} \\ \times \sum_{k_{||}} \langle -i\Gamma_S [f_S(E - \Phi_S) - \phi_w] [G^<(Wk_{||}, Wk_{||} | E) - \text{h.c.}] \rangle_{av}. \end{aligned} \quad (39)$$

Clearly, ϕ_w plays the role of a well occupation function. It is determined by the steady state condition

$$\Gamma_R(f_R - \phi_w) + \Gamma_L(f_L - \phi_w) = 0 \quad (40)$$

which balances the net influx from the left into each of the well states and the net outflux to the right. The result

$$\phi_w = \frac{\Gamma_L f_L + \Gamma_R f_R}{\Gamma_L + \Gamma_R} \quad (41)$$

represents a weighted average of the occupation functions of the left and the right sides. Substituting into (39) yields the current per unit area,

$$j_{dc} = |j_{S \rightarrow W}| = 2 \frac{e}{h} \int dE |f_S(E - \Phi_S) - \phi_w(E)| \Gamma_S g_w(E) \quad (42)$$

$$= 2 \frac{e}{h} \int dE [f_L(E - eV_{dc}) - f_R(E)] \frac{\Gamma_L \Gamma_R}{\Gamma_L + \Gamma_R} g_w(E), \quad (43)$$

where

$$g_w(E) = -\frac{1}{2\pi i} \int \frac{d^2 k_{||}}{(2\pi)^2} [\langle G'_{CPA}(Wk_{||}, Wk_{||} | E) \rangle_{av} - \text{h.c.}] \quad (44)$$

is the average well density of states per spin direction.

The fact that the dc-conductance (43) can be calculated using only the single particle Green's function appears surprising. The reason for the difference is that in the resonant tunneling case the relevant distribution functions are known (2) or easy to calculate (41), whereas in the usual case they have to be determined by solving a transport equation.

Equation (43) reduces correctly to the two limiting cases representing sequential and coherent scattering, respectively. In the limit of strong scattering, tunneling is sequential; the tunneling processes through the individual barriers are effectively decoupled by the scattering processes. In that case, Eq. (42) can be written directly, and the steady state condition immediately yields the total current (43).

In the absence of scattering the electrons traverse the well coherently. The parallel momentum $k_{||}$ is conserved, and resonant tunneling is best understood in analogy with the optical Fabry-Pérot interferometer. The t -matrix for the transfer of an electron through the entire structure is

$$T_{L \rightarrow R}(k_{||}, k'_{||}) = h_{WR}^* G(Wk'_{||}, Wk_{||} | E) h_{WL}. \quad (45)$$

According to Fermi's Golden rule, the coherent tunneling current, i.e., the contribution due to scattering-free tunneling events with $k_{||} = k'_{||}$, is

$$\begin{aligned} j_{dc}^{coh} &= \frac{4\pi e}{\hbar} \int \frac{dE d^2 k_{||}}{(2\pi)^2} \sum_{k_z, k'_z} [f_L(E - eV_{dc}) - f_R(E)] \\ &\quad \times \langle \delta(E - \epsilon_{k_{||}} - \epsilon_{k'_z}) |T_{L \rightarrow R}(k_{||}, k_{||})|^2 \delta(E - \epsilon_{k_{||}} - \epsilon_{k'_z} - eV_{dc}) \rangle_{av} \\ &= \frac{e}{\pi \hbar} \int \frac{dE d^2 k_{||}}{(2\pi)^2} \Gamma_L \Gamma_R |G'_{CPA}(k_{||} | E)|^2 [f_L(E - eV_{dc}) - f_R(E)] \\ &= \frac{2e}{\hbar} \int dE \frac{\Gamma_L \Gamma_R}{\Gamma_L + \Gamma_R + 2 |\text{Im } \Sigma'_{CPA}|} g_W(E) [f_L(E - eV_{dc}) - f_R(E)]. \quad (46) \end{aligned}$$

Equation (46) is obtained from definition (5) and by noting that

$$|G'_{CPA}(k_{||} | E)|^2 = -\text{Im } G'_{CPA}(k_{||} | E) / (\frac{1}{2} \Gamma_L + \frac{1}{2} \Gamma_R - \text{Im } \Sigma'_{CPA}). \quad (47)$$

In the absence of scattering, $\text{Im } \Sigma'_{CPA} = 0$, the coherent contribution (47) is the total current. Figure 3 represents the partition of the total current as calculated within the CPA into coherent and sequential contributions diagrammatically. The

$$\left[G(Wk_{||}, Wk'_{||} | E) \right]_{CPA} = \text{coherent term} + \left[\text{sequential terms} + \dots \right]$$

FIG. 3. Graphical representation of the partition of $\langle |G(Wk_{||}, Wk'_{||} | E)|^2 \rangle_{av}$ into a coherent tunneling contribution (first term) and a sequential tunneling contribution (ladder sum). Bold arrows are CPA Green's functions. Crosses stand for scattering events (on-site t -matrices). The crosses are connected by dashed lines if they belong to the same effective site.

first term corresponds to the coherent contribution and the remainder, involving scattering events, contribute to sequential tunneling. A comparison of (46) with (43) shows that the coherent current is unimportant if the scattering time is much smaller than the lifetime due to tunneling, i.e., if

$$\tau_{\text{scatter}} = \hbar / |\text{Im } \Sigma'_{\text{CPA}}| \ll \hbar / (\Gamma_L + \Gamma_R). \quad (48)$$

This criterion is analogous to one first discussed by Price [28]. In the case of a 45\AA $\text{In}_{0.47}\text{Ga}_{0.53}\text{As}/56\text{\AA}$ $\text{In}_{0.48}\text{Al}_{0.52}\text{As}$ DBQW which is discussed in Ref. [21], the tunneling current is almost completely sequential. Another example is given in Fig. 4 for an asymmetric DBQW (50\AA and 70\AA $\text{Al}_{0.30}\text{Ga}_{0.70}\text{As}$ barriers and a 45\AA GaAs well) at room temperature. The dashed curve shows the relatively small coherent contribution. The inset exhibits the peak to valley ratio as a function of the Al concentration. The contribution to the current in the valley and beyond is approximated by a Richardson term.

Equation (43) shows the dc-current to be rather insensitive to scattering, since Γ_S and f_S are slowly varying functions of energy (except near the band edges) and the main effect of the scattering is to smear out the density of states [29, 30]. The decrease of the peak to valley ratio (inset of Fig. 4) with decreasing scattering strength is primarily due to larger valley currents. If both the tunneling width and the scattering width are small, $g_W(E)$ is the s-p-like two-dimensional density of states. At $T=0$ (43) then yields the well-known triangular shaped I-V-characteristic [31]. The sudden drop of the current from its maximum-value to almost zero, in this case results from the use of the same effective masses in (1) and (3), a fact often overlooked when modelling DBQW.

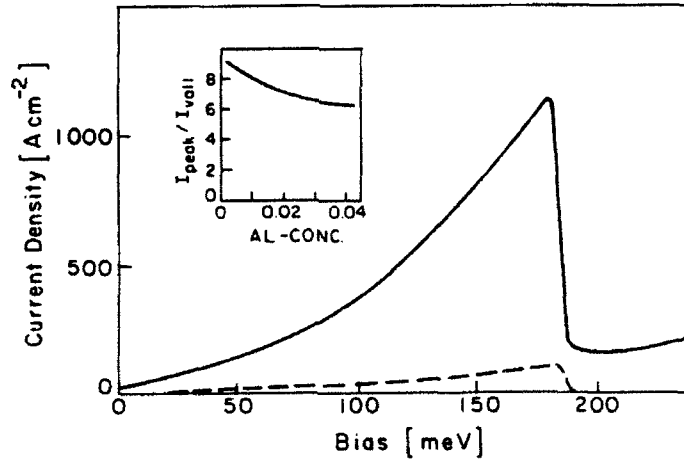


FIG. 4. I-V-characteristic for an asymmetric DBQW ($d_L = 50\text{\AA}$ and $d_R = 70\text{\AA}$ $\text{Al}_{0.30}\text{Ga}_{0.70}\text{As}$ barriers and a $d_W = 45\text{\AA}$ GaAs well) with $T = 300\text{ K}$, $\mu_L = \mu_R = 50\text{ meV}$. A small amount of Al, $x = 1\%$, is assumed to be present in the well region. The dashed line indicates the coherent tunneling contribution to the current. Inset: Peak to valley ratio for different Al concentrations in the well.

For later reference, we note the charge density ρ_w in the well. It is derived from the expectation value

$$\langle\langle c_{wk_{||}}^\dagger c_{wk_{||}} \rangle\rangle_{av} = \left\langle -i \int \frac{dE}{2\pi} G^<(Wk_{||}, Wk_{||} | E) \right\rangle_{av}$$

and takes the form

$$\rho_w = 2e \int dE \varphi_w(E) g_w(E) = 2e \int dE \frac{\Gamma_L f_L + \Gamma_R f_R}{\Gamma_L + \Gamma_R} g_w(E). \quad (49)$$

V. DYNAMICAL RESPONSE

The ac-response function $\sigma(\omega)$ is defined as the current response to a small ac field $V_{ac} e^{-i\omega t}$ superimposed on the dc-bias. The additional term in the Hamiltonian, \hat{H}_{ac} , shifts the energy levels on the left and the right side up and down periodically. For symmetric DBQW,

$$\hat{H}_{ac} = eV_{ac} e^{-i\omega t} (\frac{1}{2}\hat{N}_L - \frac{1}{2}\hat{N}_R) = \frac{1}{2}eV_{ac} e^{-i\omega t} \sum_{S'=L,R} \eta_{S'} \hat{N}_{S'}. \quad (50)$$

Here, $\hat{N}_{S'}$ is the number operator for the side $S' = L, R$, and $\eta_L = 1$, $\eta_R = -1$.

We next calculate the linear current response to \hat{H}_{ac} . The incoming and outgoing currents do not balance at each instant. According to the Ramo-Shockley theorem, the measured current is given by the average

$$I(t) = \frac{I_{L \rightarrow w}(t) - I_{R \rightarrow w}(t)}{2} = \frac{1}{2} \sum_{S=L,R} \eta_S I_{S \rightarrow w}(t). \quad (51)$$

The ac-current in linear response (cf., (36)) is

$$\begin{aligned} I_{ac}(\omega) = & \frac{1}{2} \sum_{S=L,R} \eta_S \frac{-2e}{h} \int_{-\infty}^{\infty} \frac{dt}{2\pi} e^{i\omega t} \\ & \times \sum_{k_z, k_{||}} [\langle G^{<[1]}(Wk_{||}t, Sk_z k_{||}t) \rangle_{av} h_{wS}^* \\ & - h_{wS} \langle G^{<[1]}(Sk_z k_{||}t, Wk_{||}t) \rangle_{av}]. \end{aligned} \quad (52)$$

Here and in the following the superscript "[1]" denotes the first-order corrections due to \hat{H}_{ac} . The unperturbed Green's functions G now include both the self-energy

due to tunneling *and* the self-energy due to scattering. The current (52) is most easily evaluated using a Fourier representation. For the retarded Green's function

$$\begin{aligned} & \iint dt_1 dt_2 e^{i(E + \hbar\omega)t_2/\hbar} e^{-iEt_1/\hbar} G^{r[1]}(Wk_{||}t_2, Wk_{||}t_1) \\ &= 2\pi \sum_{S'=L,R} G'(Wk_{||}, Wk_{||} | E + \hbar\omega) \\ & \quad \times \Sigma_{S'}^{r[1]}(k_{||} | E + \hbar\omega, E) G'(Wk_{||}, Wk_{||} | E). \end{aligned} \quad (53)$$

Three terms of the form $(G' \Sigma^{r[1]} G^< + G' \Sigma^{<[1]} G^a + G^< \Sigma^{a[1]} G^a)$ contribute to the distribution Green's function $G^{<[1]}$. The first-order correction $\Sigma_{S'}^{[1]}$ to the self-energies $\Sigma_{S'}$ (see Fig. 2c for a diagrammatic representation) is, according to Eqs. (18)–(20) and (22)–(23),

$$\begin{aligned} \Sigma_{S'}^{r[1]}(k_{||} | E + \hbar\omega, E) &= \eta_{S'} \frac{eV_{ac}}{2} \sum_{k_z} h_{WS'} G'(S'k_z k_{||} | E + \hbar\omega) G'(S'k_z k_{||} | E) h_{WS'}^* \\ &= \frac{-eV_{ac}}{2\hbar\omega} \eta_{S'} [\Sigma_{S'}^r(k_{||} | E + \hbar\omega) - \Sigma_{S'}^r(k_{||} | E)] \\ &\approx \frac{i eV_{ac}}{4\hbar\omega} \eta_{S'} \Delta\Gamma_{S'} \end{aligned} \quad (54)$$

and

$$\Sigma_{S'}^{<[1]}(k_{||} | E + \hbar\omega, E) \approx \frac{-i eV_{ac}}{2\hbar\omega} \eta_{S'} (\overline{f_{S'}} \Delta\Gamma_{S'} + \overline{\Gamma_{S'}} \Delta f_{S'}), \quad (55)$$

where $\Delta f_S = f_S(E + \hbar\omega - \Phi_S) - f_S(E - \Phi_S)$, $\overline{f_S} = (f_S(E + \hbar\omega - \Phi_S) + f_S(E - \Phi_S))/2$ and similarly for $\Delta\Gamma_S$. The relationship

$$\begin{aligned} & G'(S'k_z k_{||} | E + \hbar\omega) G'(S'k_z k_{||} | E) \\ &= -\frac{1}{\hbar\omega} (G'(S'k_z k_{||} | E + \hbar\omega) - G'(S'k_z k_{||} | E)) \end{aligned} \quad (56)$$

has been used. Only the imaginary part of the tunneling self-energies has been retained explicitly.

The perturbation acts directly only on the *L*- and *R*-states. The well-Green's functions are affected only indirectly via their tunneling self-energies. When (52) is rewritten in analogy to (37), the first-order self-energy is seen to enter in two different ways corresponding to Figs. 2d and e. These are the contributions from the Σ_S explicitly shown in Fig. 2b and from corrections to the self-energy implicitly contained in the well Green's function, respectively.

Equations (52) and (53) yield the frequency-dependent conductivity

$$\begin{aligned} \sigma(\omega) = & \sum_{S=L,R} \eta_S \frac{e^2}{\hbar} \int \frac{dE}{2\pi} \int \frac{d^2 k_{\parallel}}{(2\pi)^2} \frac{1}{eV_{ac}} \\ & \times \left[\langle G'(Wk_{\parallel}, Wk_{\parallel} | E + \hbar\omega) \Sigma_S^{[1]}(k_{\parallel} | E + \hbar\omega, E) \pm \dots \rangle_{av} \right. \\ & + \sum_{S'=L,R} \langle G'(Wk_{\parallel}, Wk_{\parallel} | E + \hbar\omega) \Sigma_{S'}^{[1]}(k_{\parallel} | E + \hbar\omega, E) \\ & \left. \times G'(Wk_{\parallel}, Wk_{\parallel} | E) \Sigma_S^<(k_{\parallel} | E) \pm \dots \rangle_{av} \right], \end{aligned} \quad (57)$$

where the dots represent more terms of the same structure which arise from the repeated application of (19). The resulting expression is lengthy but straightforward to evaluate in the absence of scattering. The one-dimensional case is discussed in Ref. [5] (see also Refs. [9, 10]).

The expression (57) for the dynamic response contains averages of *products* of Green's functions of the form $\langle G'(\beta, \mu | E + \hbar\omega) m_{\mu\nu} G^a(\nu, \alpha | E) \rangle_{av}$. Such expressions are represented graphically in Fig. 5a. The average of the two-particle Green's

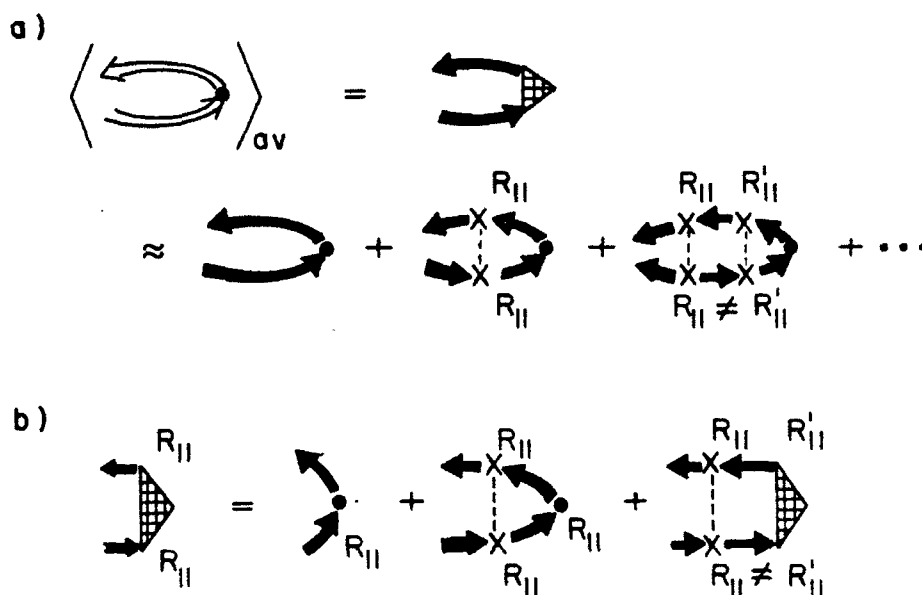


FIG. 5. Vertex corrections for CPA: (a) m is the bare vertex of interest; M includes the bare vertex and the vertex corrections represented in the CPA by ladder diagrams shown. (b) Bethe-Salpeter-like equation for CPA corrections to a vertex that is diagonal in R_{\parallel} -representation. Light double arrows represent unaveraged Green's functions, bold arrows are CPA Green's functions. Crosses stand for on-site t -matrices. They are connected by dashed lines if they belong to the same effective site. Dots are bare vertices (m), shaded triangles include vertex corrections (M).

function and a bare vertex $m_{\mu\nu}$ can be expressed in terms of averaged single-particle Green's functions and a dressed vertex $M_{\mu\nu}$,

$$\begin{aligned} & \langle G'(\beta, \mu | E + \hbar\omega) m_{\mu\nu} G^a(\nu, \alpha | E) \rangle_{\text{av}} \\ & \approx \langle G'(\beta, \mu | E + \hbar\omega) \rangle_{\text{av}} M_{\mu\nu} \langle G^a(\nu, \alpha | E) \rangle_{\text{av}}. \end{aligned} \quad (58)$$

In the present case, $m_{\mu\nu}$ stands for the time-dependent quantity $\Sigma_S^{[1]}$. Velický *et al.* [32] showed that the vertex corrections appropriate for the single-particle CPA is the sum of the ladder diagrams of Fig. 5. Each pair of the effective on-site t -matrices constituting a rung of the ladder is averaged independently of the others. Subsequent pairs belong to different sites. The propagation between rungs is described by the effective medium propagation G_{CPA} . This yields a Bethe-Salpeter equation (Fig. 5b) for the diagonal elements of the real-space representation of the full retarded vertex $M_{R_{||}}$ in terms of the diagonal terms of $m_{R_{||}}$

$$\begin{aligned} M'_{R_{||}} &= m'_{R_{||}} + \langle t'_{R_{||}}(E + \hbar\omega) t'_{R_{||}}(E) \rangle_{\text{av}} G'_{\text{CPA}}(R_{||}, R_{||} | E + \hbar\omega) G'_{\text{CPA}}(R_{||}, R_{||} | E) m'_{R_{||}} \\ &+ \sum_{R'_{||} \neq R_{||}} \langle t'_{R_{||}}(E + \hbar\omega) t'_{R_{||}}(E) \rangle_{\text{av}} \\ &\times G'_{\text{CPA}}(R_{||}, R'_{||} | E + \hbar\omega) G'_{\text{CPA}}(R'_{||}, R_{||} | E) M'_{R'_{||}}. \end{aligned} \quad (59)$$

In the case of interest, where the bare vertex $\Sigma_S^{[1]}$ is $k_{||}$ -independent, (59) reduces to

$$M' = \frac{m'(1 + F'_{\text{CPA}}(E + \hbar\omega) F'_{\text{CPA}}(E) \langle t'_{R_{||}}(E + \hbar\omega) t'_{R_{||}}(E) \rangle_{\text{av}})}{\left[1 - \sum_{R'_{||} \neq R_{||}} G'_{\text{CPA}}(R_{||}, R'_{||} | E + \hbar\omega) \times G'_{\text{CPA}}(R'_{||}, R_{||} | E) \langle t'_{R_{||}}(E + \hbar\omega) t'_{R_{||}}(E) \rangle_{\text{av}} \right]}. \quad (60)$$

The quantity $\langle t'_{R_{||}}(E + \hbar\omega) t'_{R_{||}}(E) \rangle_{\text{av}}$ takes a particularly simple form in the CPA. Purely algebraic manipulation of Eq. (30) leads to

$$\begin{aligned} \frac{1}{\langle t'_{R_{||}}(E + \hbar\omega) t'_{R_{||}}(E) \rangle_{\text{av}}} &= \frac{F'_{\text{CPA}}(E + \hbar\omega) - F'_{\text{CPA}}(E)}{\Sigma'_{\text{CPA}}(E + \hbar\omega) - \Sigma'_{\text{CPA}}(E)} \\ &- F'_{\text{CPA}}(E + \hbar\omega) F'_{\text{CPA}}(E), \end{aligned} \quad (61)$$

and correspondingly for expectation values of the form $\langle t'^a t^a \rangle_{\text{av}}$ or $\langle t'^a t^a \rangle_{\text{av}}$. Thus the retarded (or advanced) vertex corrections take the form

$$\frac{M'^{r/a}}{m'^{r/a}} = \frac{\hbar\omega - (\Sigma'^{r/a}_W(E + \hbar\omega) - \Sigma'^{r/a}_W(E))}{\hbar\omega - (\Sigma'^{r/a}_0(E + \hbar\omega) - \Sigma'^{r/a}_0(E))}. \quad (62)$$

The result for the "<" component, derived in Appendix A, is most simply written in the form

$$\frac{M^< + \varphi_w(E) M' - \varphi_w(E + \hbar\omega) M^a}{m^< + \varphi_w(E) m' - \varphi_w(E + \hbar\omega) m^a} = \frac{\hbar\omega - (\Sigma'_w(E + \hbar\omega) - \Sigma^a_w(E))}{\hbar\omega - (\Sigma'_0(E + \hbar\omega) - \Sigma^a_0(E))}. \quad (63)$$

Equations (62) and (63) show that Velický's vertex corrections satisfy the Ward identities even when generalized to non-equilibrium situations.

The conductivity (52) can be calculated with the help of (62) and (63). This is done for biases: (a) well below the negative resistance region and (b) in the negative resistance region. In the first case the left conduction band edge lies below the resonance. For constant Γ_L and Γ_R , the square bracket in (57) contains only four nonvanishing terms

$$\begin{aligned} & \left[\langle G'(Wk_{||}, Wk_{||} | E + \hbar\omega) - G^a(Wk_{||}, Wk_{||} | E) \rangle_{av} \left(\frac{-ieV_{ac}}{2\hbar\omega} \eta_S \Gamma_S \Delta f_S \right) \right. \\ & + 2 \left\langle \left(\frac{i}{2} \Gamma_S \right) G'(Wk_{||}, Wk_{||} | E + \hbar\omega) \right. \\ & \left. \times \left(\frac{-ieV_{ac}}{2\hbar\omega} \sum_{S'} \eta_{S'} \Gamma_{S'} \Delta f_{S'} \right) G^a(Wk_{||}, Wk_{||} | E) \right\rangle_{av} \left. \right]. \quad (64) \end{aligned}$$

The averages are evaluated using (58), (62), and (63) with $m' = m^a = 0$ and $m^< = -i\eta_S \Gamma_S \Delta f_S$ (see (54)–(55)) and using the CPA Green's functions. With identities like (47) the frequency dependent conductivity can be written as

$$\begin{aligned} \sigma(\omega) = & -\frac{1}{2} \frac{e^2}{\hbar} \frac{1}{\hbar\omega} \int dE g_w(E; \hbar\omega) \\ & \times \frac{[\hbar\omega + 2i\Gamma_R] \Gamma_L \Delta f_L + [\hbar\omega + 2i\Gamma_L] \Gamma_R \Delta f_R}{\hbar\omega + i\Gamma_L + i\Gamma_R} \quad (65) \end{aligned}$$

$$g_w(E; \hbar\omega) = \frac{F'_{CPA}(E + \hbar\omega) - F^a_{CPA}(E)}{-2\pi i a^2}. \quad (66)$$

Scattering effects enter this expression only via the real-space matrix elements of the CPA Green's function (31)

$$F_{CPA}(E) = a^2 \int \frac{d^2 k_{||}}{(2\pi)^2} G_{CPA}(k_{||} | E). \quad (67)$$

In the low frequency limit

$$\sigma(\omega \rightarrow 0) = e \left. \frac{\partial}{\partial x} \right|_{x=0} \times \left[\frac{2e}{\hbar} \int dE [f_L(E - eV_{dc} - x/2) - f_R(E + x/2)] \frac{\Gamma_L \Gamma_R}{\Gamma_L + \Gamma_R} g_W(E) \right] \quad (68)$$

and the adiabatic response dj_{dc}/dV_{dc} of Eq. (43) subject to a slow change of the dc-voltage is recovered. For comparison, the ac-response in a classical rate-equation picture is derived in Appendix B.

In the second case involving the negative differential resistance region, the occupation functions can be taken as $f_L = 1$ and $f_R = 0$, but the energy dependence of the tunneling rate Γ_L must be taken into account. It drops abruptly from some finite value Γ_L^+ to zero at the energy of the left conduction band edge. The non-vanishing first-order tunneling self-energies (54)–(55) are

$$\Sigma_L^{<[1]} = -2\Sigma_L^{r[1]} = 2\Sigma_L^{a[1]} = -(ieV_{ac}\Gamma_L^+)/(2\hbar\omega). \quad (69)$$

The resulting conductivity can be calculated from (57) analogously to (65)–(67):

$$\begin{aligned} \sigma(\omega) = & -\frac{1}{2} \frac{e^2}{\hbar} \frac{1}{\hbar\omega} \int_{E \leq \Phi_W \leq E + \hbar\omega} dE \frac{\Gamma_L^+(\hbar\omega + 2i\Gamma_R)}{\Gamma_L^+ + \Gamma_R} \\ & \times \left(g_W(E; \hbar\omega) \frac{\Gamma_R + \Gamma_L^+/2}{\hbar\omega + i\Gamma_R + i\Gamma_L^+/2} \right. \\ & \left. + [g_W(E; \hbar\omega) - g_W(E + \hbar\omega)] \frac{\Gamma_L^+/2}{\hbar\omega - i\Gamma_L^+/2} \right). \end{aligned} \quad (70)$$

The results for the real and imaginary parts of the conductivity ratio $\sigma(\omega)/\sigma_0$ based on Eqs. (65)–(67) are shown in Figs. 6a and b, respectively, as a function of frequency for various ratios Γ_L/Γ_R with Γ_R fixed. The parameters including the dc conductivity σ_0 characterize sample A of Ref. [22] (see Fig. 6 caption). The results of the dashed line have been previously discussed in some detail [21] by the present authors. The imaginary part of the conductance, $|\text{Im}[\sigma(\omega)]|$, exhibits a maximum at a finite frequency ω_{resp} . For frequencies larger than ω_{resp} the ac-current cannot follow the applied voltage without a phase lag. This frequency therefore defines a characteristic time scale defined by the response time $\tau_{\text{resp}} = 1/\omega_{\text{resp}}$. For frequencies $\omega\tau_{\text{resp}} < 1$ the current is able to follow the ac voltage; ω_{resp} therefore defines the upper frequency limit for DBQW. The inverse response time ω_{resp} is indicated by the dashed line in Fig. 6b. For the present sample its magnitude is 60 ps. For fixed Γ_R the response time increases with decreasing Γ_L for $\Gamma_L > \Gamma_R$ and is approximately constant for $\Gamma_L < \Gamma_R$.

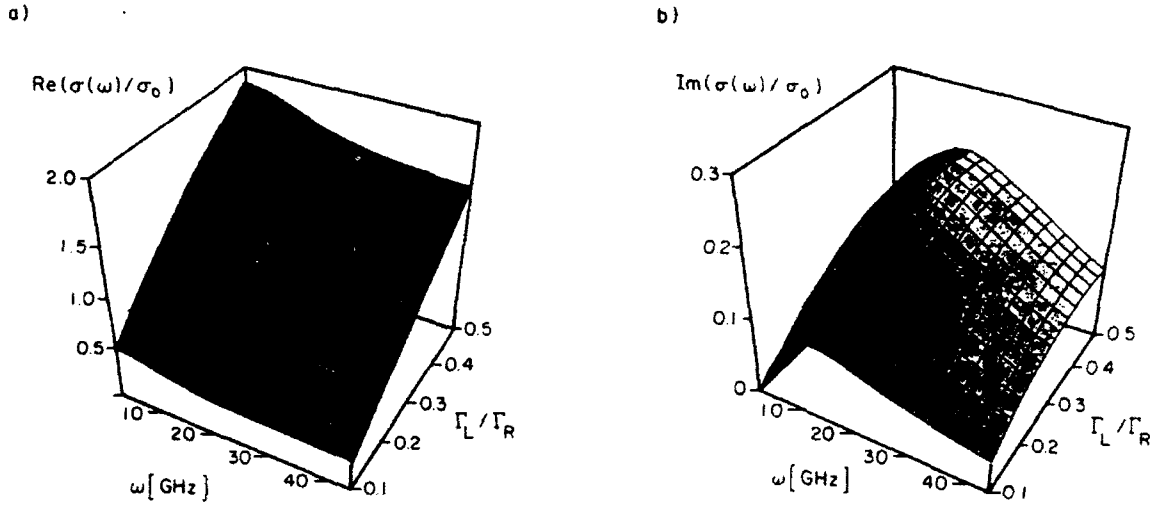


FIG. 6. Real (a) and imaginary (b) parts of the dynamic conductivity ratio $\sigma(\omega)/\sigma_0$ in the positive resistance region ($V_{dc} = 240$ meV) vs ω for different ratios Γ_L/Γ_R . The other parameters of the DBQW structure $d_L = d_R = 56 \text{ \AA}$, $d_W = 45 \text{ \AA}$, $\mu_L = 50$ meV are chosen to represent the lattice matched $\text{In}_{0.53}\text{Ga}_{0.47}\text{As}/\text{In}_{0.52}\text{Al}_{0.48}\text{As}$ sample A of Ref. [22] (dotted line). σ_0 is the zero frequency conductivity corresponding to sample A. The dashed line in (b) indicates $\text{Im } \sigma(\omega)$ for $\omega = 1/\tau_{\text{resp}}$.

For applied voltages high enough that $f_L \gg f_R$ for the energies of interest and with $g_W(E; \hbar\omega) \approx g_W(E)$,

$$\begin{aligned} \text{Im}[\sigma(\omega)] &\sim \text{Im} \int dE g_W(E) \frac{(\hbar\omega + 2i\Gamma_R) \Gamma_L \Delta f_L}{\hbar\omega(\hbar\omega + i\Gamma_L + i\Gamma_R)} \\ &= \int dE g_W(E) \frac{(\Gamma_R - \Gamma_L) \Gamma_L \Delta f_L}{(\hbar\omega)^2 + (\Gamma_L + \Gamma_R)^2}. \end{aligned} \quad (71)$$

This expression estimates the response time as

$$\tau_{\text{resp}} = 1/\omega_{\text{resp}} \approx \hbar/(\Gamma_L + \Gamma_R). \quad (72)$$

Both barriers (Γ_L, Γ_R) enter (72) symmetrically, as one would expect for a quantity characteristic for the response of the whole structure.

In Ref. [21] we compare the response time with the experimentally measurable transit or dwell time [22],

$$\tau_{\text{trans}} = \rho_W/j_{dc}. \quad (73)$$

By its definition, the transit time is a static quantity. In the same limit, $f_L \gg f_R$ for the energies of interest, (43) and (49) indicate that

$$\tau_{\text{trans}} \approx \hbar/\Gamma_R. \quad (74)$$

The transit time τ_{trans} does not show the same R - L symmetry, since the time

duration for remaining in the well is determined by the opacity of the right barrier. For most experimentally considered DBQW structures $\Gamma_L \ll \Gamma_R$ near the peak tunneling current and the numerical values of τ_{trans} and τ_{resp} differ by about 10%. As a consequence, the experimentally accessible quantity τ_{trans} yields information about the fundamental quantity τ_{resp} determining the high frequency behavior directly.

APPENDIX A: SOME USEFUL IDENTITIES WITHIN THE CPA

The retarded CPA self-energy and the CPA Green's function are defined by the condition that the disorder average of the retarded t -matrix $t'_{R_{||}}(E)$ of a single impurity in the CPA effective medium vanishes. The natural generalization of the CPA condition (30) is

$$\langle t'_{R_{||}} \rangle_{\text{av}} = 0. \quad (\text{A.1})$$

Equation (19) is used to generate a perturbation series for $t'_{R_{||}}$. Distinguishing between contributions, where the "<"-factor refers to a scattering event or where it refers to a propagation, the perturbation series can be rearranged with the result that

$$t'_{R_{||}} = t'_{R_{||}} F_0^< t_{R_{||}}^a - (1 + t'_{R_{||}} F_0^r) \Sigma_{\text{CPA}}^< (1 + F_0^a t_{R_{||}}^a). \quad (\text{A.2})$$

For the case of a momentum independent unperturbed occupation function, i.e., $G_0^< = -\varphi_w(E)[G_0^r - G_0^a]$, Eqs. (A.1), (A.2), and (61) yield

$$\Sigma_{\text{CPA}}^< = (-\varphi_w)[\Sigma_{\text{CPA}}^r - \Sigma_{\text{CPA}}^a] \quad (\text{A.3})$$

and, finally,

$$t'_{R_{||}} = (-\varphi_w)[t'_{R_{||}} - t_{R_{||}}^a]. \quad (\text{A.4})$$

We next write down explicitly the vertex equation of Fig. 5b for the <-component with a $R_{||}$ -independent vertex m . Application of rule (19) and writing G_+ and G_- for $G_{\text{CPA}}(R_{||}, R'_{||} | E + \hbar\omega)$ and $G_{\text{CPA}}(R'_{||}, R_{||} | E)$ and, similarly, F_+ , F_- , t_+ , and t_- , yields

$$\begin{aligned} M^< &= m^< + \langle t'_+ t_-^a \rangle_{\text{av}} (F'_+ m' F_-^< + F'_+ m^< F_-^a + F_+^< m^a F_-^a) \\ &+ \langle t'_+ t_-^< \rangle_{\text{av}} F'_+ m' F_-^r + \langle t_+^< t_-^a \rangle_{\text{av}} F_+^a m^a F_-^a \\ &+ \sum_{R'_{||} \neq R_{||}} \langle t'_+ t_-^a \rangle_{\text{av}} (G'_+ M' G_-^< + G'_+ M^< G_-^a + G_+^< M^a G_-^a) \\ &+ \sum_{R'_{||} \neq R_{||}} \langle t'_+ t_-^< \rangle_{\text{av}} G'_+ M' G_-^r \\ &+ \sum_{R'_{||} \neq R_{||}} \langle t_+^< t_-^a \rangle_{\text{av}} G_+^a M^a G_-^a. \end{aligned} \quad (\text{A.5})$$

Using the corresponding simpler equations for the retarded and advanced component (see (62)), this can be rewritten as an equation for the combination $M^< + \varphi_w(E) M^r - \varphi_w(E + \hbar\omega) M^a$. With (A.4), (61), and (62), one obtains

$$\frac{M^< + \varphi_w(E) M^r - \varphi_w(E + \hbar\omega) M^a}{m^< + \varphi_w(E) m^r - \varphi_w(E + \hbar\omega) m^a} = \frac{\hbar\omega - (\Sigma'_w(E + \hbar\omega) - \Sigma_w^a(E))}{\hbar\omega - (\Sigma'_0(E + \hbar\omega) - \Sigma_0^a(E))}. \quad (\text{A.6})$$

This is the desired result, Eq. (63). If the vertex consists only of a "<"-component, the left-hand side of (A.6) is just $M^</m^<$.

APPENDIX B. "CLASSICAL" ac-RESPONSE

In this appendix, the ac-response is derived in a "classical" rate equation picture and compared with the quantum mechanical result (65)–(67). In the current context, the concept of rate equations implies the notion of completely sequential tunneling.

A group of well states $2g_w \Delta E$ at energy E with time-dependent occupation function φ_w is considered. The left and right sides are moved relatively to the well periodically up and down by η_S (eV_{ac}/2) $\cos \omega t$. With single barrier tunneling rates Γ_S/\hbar , the current from side S is

$$\Delta j_{S \rightarrow w} = -e \frac{\Gamma_S}{\hbar} \left[f \left(E - \frac{\eta_S e V_{ac}}{2} \cos \omega t - \Phi_S \right) - \varphi_w(t) \right] 2g_w \Delta E. \quad (\text{B.1})$$

The time derivative of the charge density is

$$(-2eg_w \Delta E) \frac{\partial \varphi_w}{\partial t} = \Delta j_{L \rightarrow w} + \Delta j_{R \rightarrow w}. \quad (\text{B.2})$$

Assuming Γ_L and Γ_R to be constant, expansion of f_S to first order in V_{ac} and Fourier transformation yields

$$\varphi_w(\omega) = -\frac{eV_{ac}}{2} \left(\sum_S \eta_S \Gamma_S \frac{\partial f_S}{\partial E} \right) / (-i\hbar\omega + \Gamma_L + \Gamma_R). \quad (\text{B.3})$$

The result (B.3) for the time-dependent occupation functions leads to the current

$$\begin{aligned} \Delta j(\omega) &= \frac{1}{2} (\Delta j_{R \rightarrow w}(\omega) - \Delta j_{L \rightarrow w}(\omega)) \\ &= \frac{e^2}{2\hbar} \frac{\sum_S (\partial f_S / \partial E) (\hbar\omega \Gamma_S + 2i\Gamma_R \Gamma_L)}{\hbar\omega + i\Gamma_L + i\Gamma_R} g_w \Delta E V_{ac}. \end{aligned} \quad (\text{B.4})$$

Equation (B.4) differs from the quantum mechanical result (65)–(67) only insofar

as $\Delta f_S/\hbar\omega$ is replaced by the derivative $\partial f/\partial E$ and $g_w(E;\hbar\omega)$ is replaced by the density of states $g_w(E)$. The first difference is a trivial consequence of the Taylor expansion. The other difference is associated with the fact that classically the well states have no intrinsic dynamics and are completely described by the intrinsically static density of states.

ACKNOWLEDGMENTS

We are grateful to D. S. Chemla, P. H. Hui, H. Pastawski, and C. Grein for useful discussions. This work was supported by the U.S. Joint Services Electronics Program (JSEP) through ONR Contract N00014-89-J-1023 and by DARPA through ONR Contract N00014-86-K-0033.

REFERENCES

1. S. LURYI, in "Heterojunction Band Discontinuities: Physics and Device Applications" (F. Capasso and G. Margaritondo, Eds.), p. 489, Elsevier, Amsterdam, 1987.
2. D. D. COON AND K. M. S. V. BANDARA, in "Physics of Thin Films" (M. H. Francomb and J. L. Vossen, Eds.), Vol. 15, p. 219, Academic Press, New York, 1991.
3. E. R. BROWN, C. D. PARKER, AND T. C. L. G. SOLLNER, *Appl. Phys. Lett.* **54** (1989), 934; E. R. BROWN, W. D. GOODHUE, AND T. C. L. G. SOLLNER, *J. Appl. Phys.* **64** (1988), 1519.
4. W. WALUKIEWICZ, H. E. RUDA, J. LAGOWSKI, AND H. C. GATOS, *Phys. Rev. B* **30** (1984), 4571.
5. L. Y. CHEN AND C. S. TING, *Phys. Rev. B* **41** (1990), 8533; *Phys. Rev. Lett.* **64** (1990), 3159; *Phys. Rev. B* **43** (1991), 2097.
6. H. A. FERTIG AND S. DAS SARMA, *Phys. Rev. B* **40** (1989), 7410; H. A. FERTIG, S. HE, AND S. DAS SARMA, *Phys. Rev. B* **41** (1989), 3596.
7. F. YONEZAWA, in "The Structure and Properties of Matter" (T. Matsubara, Ed.), Solid-State Sciences, Vol. 45, p. 383, Springer-Verlag, Berlin, 1982.
8. For example, S. LURYI, *Superlatt. Microstruct.* **5** (1989), 375; A. N. KHONDKER, *J. Appl. Phys.* **67** (1990), 6432; O. VANBESSEN AND D. LIPPENS, *Solid-State Electron.* **32** (1989), 1533.
9. P. PRICE, *Superlatt. Microstruct.* **2** (1986), 213, 593; C. JACOBONI AND P. J. PRICE, in "Resonant Tunneling in Semiconductors" (L. L. Chang *et al.*, Eds.), p. 351, Plenum, New York, 1991.
10. W. R. FRENSLEY, *Superlatt. Microstruct.* **4** (1988), 497; *Appl. Phys. Lett.* **51** (1987), 448; N. C. KLUKSDAHL *et al.*, *Phys. Rev. B* **39** (1989), 7720.
11. H. PASTAWSKI, preprint MIT, 1992.
12. D. SOKOLOWSKI, *Phys. Rev. B* **37** (1988), 4201; *J. Phys. C* **21** (1988), 639; P. JOHANSSON, *Phys. Rev. B* **41** (1990), 9882.
13. H. Y. SHENG AND J. SINKKONEN, *Superlatt. Microstruct.* **9** (1991), 537.
14. F. W. SHEARD AND G. A. TOOMBS, *Solid State Electron.* **32** (1989), 1443.
15. S. C. KAN AND A. YARIV, *J. Appl. Phys.* **64** (1988), 3098.
16. A. P. JAUHO AND M. M. NIETO, *Superlatt. Microstruct.* **2** (1986), 407.
17. H. C. LIU, *J. Appl. Phys.* **67** (1990), 593.
18. K. L. JENSEN AND F. A. BUOT, *J. Appl. Phys.* **67** (1990), 7602.
19. K. L. JENSEN AND F. A. BUOT, *Phys. Rev. Lett.* **66** (1991), 1078.
20. M. BÜTTIKER, *Phys. Rev. B* **27** (1983), 6178; E. H. HAUGE AND J. A. STØVNENG, *Rev. Mod. Phys.* **61** (1989), 917.
21. E. RUNGE AND H. EHRENREICH, *Phys. Rev. B* **45** (1992), 9145.
22. I. BAR-JOSEPH, T. K. WOODWARD, D. S. CHEMLA, D. SIVCO, AND A. Y. CHO, *Phys. Rev. B* **41** (1990), 3264; I. BAR-JOSEPH *et al.*, *Superlatt. Microstruct.* **8** (1990), 409.

23. J. F. YOUNG *et al.*, *Phys. Rev. Lett.* **60** (1988), 2085; C. H. YANG, M. J. YANG, AND Y. C. KAO, *Phys. Rev. B* **40** (1989), 6272; H. YOSHIMURA, J. N. SCHULMAN, AND H. SAKAKI, *Phys. Rev. Lett.* **64** (1990), 2422.
24. K. C. HASS, H. EHRENREICH, AND B. VELICKÝ, *Phys. Rev. B* **27** (1983), 1088.
25. J. RAMMER AND H. SMITH, *Rev. Mod. Phys.* **58** (1986), 323; D. C. LANGRETH, in "Linear and Nonlinear Electron Transport in Solids," Nato Advanced Studies Series B, (J. T. Devreese and E. van Doren, Eds.), Vol. 17, p. 3, Plenum, New York/London, 1976; V. KORENMAN, *Ann. Phys. (N.Y.)* **39** (1966), 72; L. P. KADANOFF AND B. BAYM, "Quantum Statistical Mechanics," Benjamin, New York, 1962.
26. M. TSUCHIYA, T. MATSUSUE, AND H. SAKAKI, *Phys. Rev. Lett.* **59** (1987), 2356.
27. For example, H. EHRENREICH AND L. M. SCHWARTZ, in "Solid State Physics" (H. Ehrenreich, F. Seitz, and D. Turnbull, Eds.), Vol. 31, p. 149, Academic Press, New York, 1976.
28. P. PRICE, *Phys. Rev. B* **36** (1987), 1314.
29. T. WEIL AND B. VINTER, *Appl. Phys. Lett.* **50** (1987), 1281.
30. M. JONSON AND A. GRINCWAIG, *Appl. Phys. Lett.* **51** (1987), 1729.
31. H. C. LIU AND G. C. ARES, *Solid State Commun.* **67** (1988), 1131.
32. B. VELICKÝ, *Phys. Rev.* **184** (1969), 614; K. LEVIN, B. VELICKÝ, AND H. EHRENREICH, *Phys. Rev. B* **2** (1970), 1771.

Minority carrier lifetimes in ideal InGaSb/InAs superlattices

C. H. Grein, P. M. Young, and H. Ehrenreich

Division of Applied Sciences, Harvard University, Cambridge, Massachusetts 02138

(Received 6 July 1992; accepted for publication 5 October 1992)

Calculations of band-to-band Auger and radiative recombination lifetimes of the recently proposed $\text{In}_x\text{Ga}_{1-x}\text{Sb}/\text{InAs}$ superlattices (SL) show them to be promising infrared detectors. Several superlattices with energy gaps in the 5–11 μm range exhibit suppressed p -type Auger recombination rates due to a large light hole–heavy hole splitting. The p -type Auger lifetime at 77 K of an 11 μm $\text{In}_x\text{Ga}_{1-x}\text{Sb}/\text{InAs}$ SL is found to be, respectively, three and five orders of magnitude longer than those of bulk and superlattice HgCdTe with the same energy gap. The n -type lifetimes are comparable.

The thin-layered type II staggered $\text{In}_x\text{Ga}_{1-x}\text{Sb}/\text{InAs}$ superlattice (SL) has been proposed as an infrared (IR) detector candidate.¹ It has been suggested² that p -type Auger recombination rates are suppressed in some of these SLs due to a large strain-induced light hole–heavy hole splitting. In this letter we calculate both band-to-band Auger and radiative recombination lifetimes using accurate band structure and numerical techniques, and compare the results with similar calculations for SL and bulk HgCdTe . We show that the p -type Auger lifetime τ_A of a 11 μm $\text{InGaSb}/\text{InAs}$ SL is somewhat larger than that of bulk HgCdTe and very significantly better (by five orders of magnitude for unintentionally p -type doped material) than that of SL HgCdTe at $T=77$ K having the same energy gap. Between 77 and 90 K the temperature dependence of τ_A is seen to be weak for n -type $\text{InGaSb}/\text{InAs}$, but moderately strong for p -type material. The above properties, combined with their compatibility with III-V device technology, suggest that well-fabricated III-V SLs are excellent candidates as a new class of IR detectors.

In an IR detector, a nonequilibrium distribution of minority carriers is created by means of optical absorption. Since phonon scattering times are of the order of picoseconds,³ several orders of magnitude shorter than the Auger and radiative lifetimes, the minority carrier distribution function employed in recombination calculations may be taken to be an equilibrium Fermi distribution. We calculate the lifetimes of a single excess carrier in the region of highest occupation, that is, an electron at the bottom of the conduction band (C1 in Fig. 1) in a p -type material, and hole at the top of the heavy hole band (HH1 in Fig. 1) in an n -type material. In the latter case, the lifetime is averaged over hole positions in HH1 in the growth direction (\perp) due to the flatness of this portion of the band, implying equal occupation probabilities along its length.

The methods for calculating band-to-band Auger recombination^{4–6} are here extended to superlattices. Since the proposed III-V IR detectors employ thin layered (~ 25 Å) SLs, electrons in the C1 band have significant dispersion in the \perp direction requiring a three-dimensional calculation, in contrast with earlier two-dimensional calculations of Auger lifetimes of electrons confined in quantum wells.⁷ An envelope function formalism⁸ is used to describe the SL states, and SL $\mathbf{k}\cdot\mathbf{p}$ theory⁹ is used to obtain the energy bands and the wave functions $\langle \mathbf{r} | L, \mathbf{K} \rangle$ for band L and

wave vector \mathbf{K} . The overlap integrals required to evaluate the screened Coulomb potential matrix elements were obtained to first order in $|\mathbf{K}_1 - \mathbf{K}'_1|^2$ in a manner similar to that described in Refs. 4, 10, and 11. Due to the highly nonparabolic nature of the band structure (see Fig. 1), parabolic approximations are not applicable. The p -type Auger lifetime (i.e., the lifetime of the photoexcited minority electron 1') is given by

$$\frac{1}{\tau_A} = \frac{3e^4 \hbar^3}{2\epsilon^2 \pi^4 m^4} \int \int f_p(\mathbf{K}_1) f_p(\mathbf{K}_2) \times \frac{\beta_{\text{C1,HH1}}(\mathbf{K}_1, \mathbf{K}'_1) \beta_{\text{LH1,HH1}}(\mathbf{K}_2, \mathbf{K}'_2)}{|\lambda^2 + |\mathbf{K}_1 - \mathbf{K}'_1|^2|^2} \times \delta[E_{\text{C1}}(\mathbf{K}'_1) + E_{\text{LH1}}(\mathbf{K}'_2) - E_{\text{HH1}}(\mathbf{K}_1) - E_{\text{HH1}}(\mathbf{K}_2)] d^3\mathbf{K}_1 d^3\mathbf{K}_2, \quad (1)$$

in the absence of exchange interactions.¹² The \mathbf{K}_i refer to the superlattice states defined in Fig. 1, $E_L(\mathbf{K})$ are the band energies, and ϵ , m , f_p and λ^{-1} are the dc dielectric constant of the barrier layers, the free electron mass, the hole Fermi function, and the Debye screening length, respectively. The quantity

$$\beta_{LL'}(\mathbf{K}, \mathbf{K}') = |\langle L, \mathbf{K}' | (\mathbf{K} - \mathbf{K}') \cdot \nabla | L', \mathbf{K}' \rangle|^2 / [E_L(\mathbf{K}') - E_{L'}(\mathbf{K}')]^2$$

involves the superlattice momentum matrix elements. \mathbf{K}'_1 denotes the minority carrier 1', and crystal momentum conservation determines $\mathbf{K}'_2 = \mathbf{K}_1 + \mathbf{K}_2 - \mathbf{K}'_1$. A similar expression applies to n -type Auger recombination. The calculation of radiative lifetimes follows Ref. 13.

These expressions were evaluated numerically for realistic SL band structures. Figure 1 shows the calculated band structure of 25 Å $\text{In}_{0.25}\text{Ga}_{0.75}\text{Sb}/41$ Å InAs for the in-plane (\parallel) and growth (\perp) directions. This superlattice has been studied experimentally at 77 K as a candidate material for 11 μm IR detectors.¹ Auger transitions involve limited regions of \mathbf{K} space due both to restrictions imposed by energy and crystal momentum conservation and occupation probabilities. Typical transitions which satisfy the constraints are shown. In the n -type material, electrons 1 and 2 are in regions of high occupation, implying a fast recombination rate. In the p -type material, hole 1 is in a

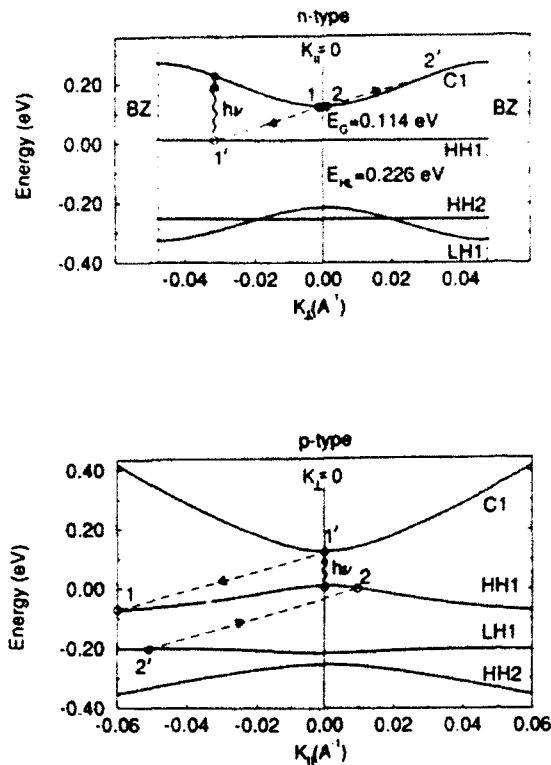


FIG. 1. The calculated band structure of a 25 Å $\text{In}_{0.25}\text{Ga}_{0.75}\text{Sb}/41$ Å InAs superlattice in the growth (\parallel) and in-plane (\perp) directions. C1, HH1, HH2, and LH1 refer to conduction, heavy, and light hole bands. BZ indicates the Brillouin zone boundary in the \parallel direction. Wavy lines indicate possible IR photon absorptions; diagonal dashed lines show typical Auger recombination transitions. E_G is the energy gap, and E_{HL} is the zone-center light hole-heavy hole splitting. The perpendicular width of the C1 band is 0.149 eV.

region of low occupation, thus suppressing Auger transitions. This suppression, a consequence of the large strain-induced LH1-HH1 splitting, accounts in part for the promise of $\text{In}_{0.25}\text{Ga}_{0.75}\text{Sb}/\text{InAs}$ for IR detectors.¹

Figure 2 shows the regions of \mathbf{K} space important for

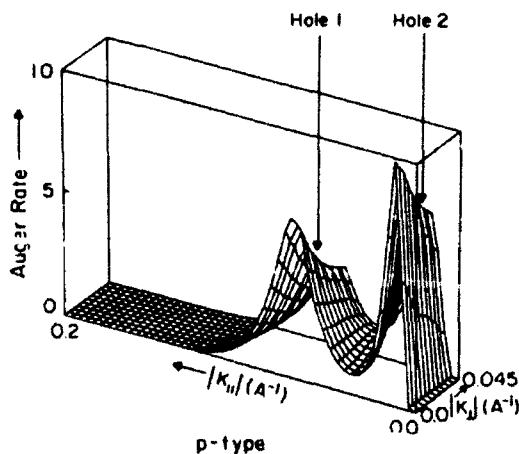


FIG. 2. The p -type Auger rate for holes 1 and 2 (cf. Fig. 1) in arbitrary units for 25 Å $\text{In}_{0.25}\text{Ga}_{0.75}\text{Sb}/41$ Å InAs SL with $p = 10^{16} \text{ cm}^{-3}$ and $T = 77$ K in \mathbf{K} space.

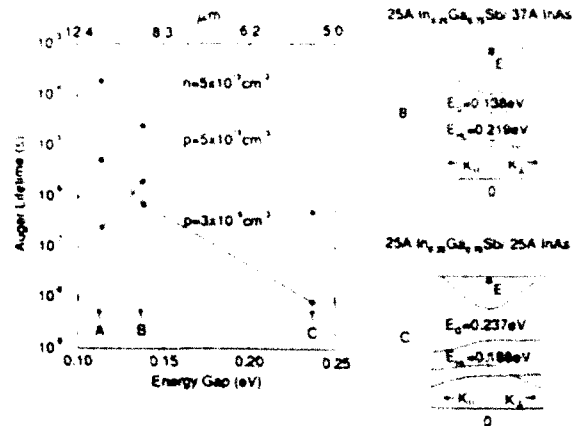


FIG. 3. Calculated Auger recombination lifetimes at 77 K of 25 Å $\text{In}_{0.25}\text{Ga}_{0.75}\text{Sb}/41$ Å InAs (A), 25 Å $\text{In}_{0.25}\text{Ga}_{0.75}\text{Sb}/37$ Å InAs (B), and 25 Å $\text{In}_{0.25}\text{Ga}_{0.75}\text{Sb}/25$ Å InAs (C) superlattices as a function of energy gap for the indicated doping levels. Solid circles are the calculated points. Insets on right show band structures of the B and C superlattices; A is shown in Fig. 1. The perpendicular widths of the C1 band of the B and C superlattices are 0.161 and 0.231 eV, respectively.

p -type Auger recombination in 25 Å $\text{In}_{0.25}\text{Ga}_{0.75}\text{Sb}/41$ Å InAs for $p = 10^{16} \text{ cm}^{-3}$ at 77 K. The structures marked "Hole 1" and "Hole 2" indicate the positions in \mathbf{K} space of holes 1 and 2 (defined in Fig. 1) taking part in the same transition, which provide the largest contributions to the recombination rate. The Auger rate is approximately independent of K_x due to the flatness of the HH1 and LH bands in the \parallel direction. The \mathbf{K} space volumes associated with "Hole 1" and "Hole 2" are equal. The "Hole 1" structure is broader because the HH1 band is flatter near hole 1 (see Fig. 1). Transitions for which the positions of holes 1 and 2 are reversed are suppressed by a smaller overlap of the electron and hole wave functions. For n -type recombination, the important region of \mathbf{K} space for both electrons 1 and 2 (defined in Fig. 1) is a sharp peak centered at the zone center of width 0.012 Å^{-1} for $n \approx 10^{17} \text{ cm}^{-3}$.

Figure 3, exhibiting the Auger lifetimes of three $\text{In}_{0.25}\text{Ga}_{0.75}\text{Sb}/\text{InAs}$ superlattices of different layer thicknesses, illustrate the IR multispectral characteristics. The energy gaps of the three superlattices A, B, and C are 10.9, 9.0, and 5.2 μm , respectively. The experimentally studied SL¹ A has background doping levels $n = 5 \times 10^{15} \text{ cm}^{-3}$ and $p = 3 \times 10^{16} \text{ cm}^{-3}$ and corresponds to the band structure of Fig. 1. SLs B and C refer to the insets. The lifetimes are plotted for the fixed carrier concentrations shown to illustrate phase space effects on Auger lifetimes. The dashed line permits comparison of τ_A for equal n and p doping levels. The n -type lifetimes increase with increasing energy gap because the \parallel bandwidth of the C1 band becomes less than the energy gap E_G . The n -type transition of Fig. 1 is no longer possible since 2' cannot be accommodated in the C1 band. By contrast, the p -type lifetimes decrease with increasing gap because the zone center HH1-LH1 splitting E_{HL} becomes less than E_G . A greater volume of phase space is thus available for 2' in the LH1 band. The flatness of the HH1 and LH1 bands gives rise to a maximal p -type

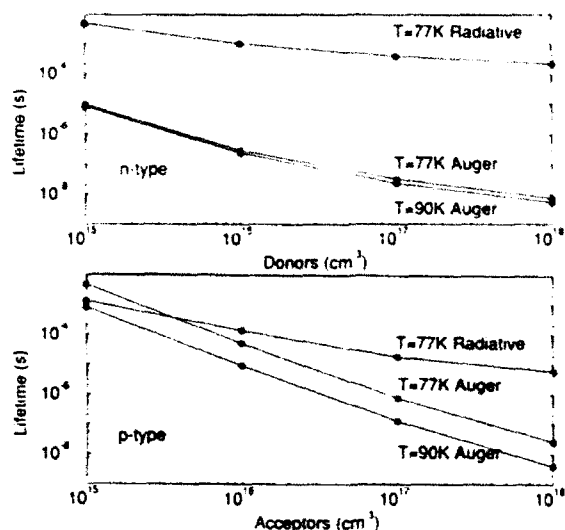


FIG. 4. Calculated *n*-type and *p*-type Auger and radiative recombination lifetimes of a 25 Å $\text{In}_{0.25}\text{Ga}_{0.75}\text{Sb}/41$ Å InAs superlattice as a function of doping at $T=77$ K and $T=90$ K.

Auger rate when $E_G \approx E_{HL}$ because energy and crystal momentum conservation conditions can be easily satisfied by carriers in regions of high occupation.

The Auger lifetimes of a 37 Å $\text{HgTe}/16$ Å CdTe SL and bulk $\text{Hg}_{0.79}\text{Cd}_{0.21}\text{Te}$ having the same energy gap, 0.114 eV, as the 25 Å $\text{In}_{0.25}\text{Ga}_{0.75}\text{Sb}/41$ Å InAs SL have also been calculated. The II-VI SL has the same axial electron effective mass ($0.025 m$) as the III-V SL. For $n=5 \times 10^{15} \text{ cm}^{-3}$ and $T=77$ K, the II-VI SL has an Auger lifetime of 9×10^{-8} s and the II-VI bulk has a lifetime of 1×10^{-7} s, both somewhat less than the value of 2×10^{-7} s of the III-V SL. More significant differences are found in the *p*-type lifetimes due to the different valence band structures. For $p=3 \times 10^{16} \text{ cm}^{-3}$ and $T=77$ K, the II-VI SL and bulk II-VI material have Auger lifetimes of 9×10^{11} and 5×10^{-9} s, respectively, compared to 5×10^{-6} s for III-V SL. The extremely short lifetime of the II-VI SL results from the approximate equality of the energy gap and the HH1-LH1 splitting. The II-VI bulk lifetime is shorter compared to the III-V SL because the small effective-mass light hole band provides phase space for recombination transitions that is absent for larger masses. It should be noted that other choices of II-VI SL barrier and well widths and compositions may result in improved Auger rates.

The calculated Auger and radiative lifetimes of a single band edge minority carrier in the 25 Å $\text{In}_{0.25}\text{Ga}_{0.75}\text{Sb}/41$ Å InAs superlattice are plotted in Fig. 4 as a function of doping levels for $T=77$ K and $T=90$ K. The decreasing lifetimes with increasing doping levels are due to more probable carrier-carrier collisions. We note that the radiative lifetimes are almost always longer than the Auger lifetimes. The *n*-type lifetimes are only weakly temperature dependent because the near zone center electrons 1 and 2 of Fig. 1 are almost statistically degenerate for the doping levels considered. The *p*-type lifetimes decrease by a factor of five to six as T is changed from 77 to 90 K. Hole 1 of

Fig. 1 lies in the tail of the hole Fermi distribution. Its occupation probability is therefore strongly temperature dependent. The lifetime obeys an approximate power law relationship with the carrier concentration: $\tau_A \sim n^{-1.7}$ and $\tau_A \sim p^{-2.1}$ for carrier densities between 5×10^{15} and 10^{17} cm^{-3} . In the simplest parabolic band case, in which carriers involved in Auger recombination are located at the band edges, $\tau_A \sim n^{-2}$ and p^{-2} . The deviations found here are associated with band structure and occupation number effects.

In summary, we find on the basis of carrier lifetime calculations that $\text{In}_{1-x}\text{Ga}_x\text{Sb}/\text{InAs}$ is a promising superlattice for IR detector applications in the 5–11 μm range. The 11 μm SL has an *n*-type Auger lifetime somewhat larger than those of bulk HgCdTe and a HgTe/CdTe SL with the same energy gap. In superlattices, the *n*-type Auger recombination may be suppressed by reducing the bandwidth of the conduction band to a value less than the energy gap. The *p*-type Auger lifetime of the 11 μm $\text{InGaSb}/\text{InAs}$ SL is approximately three orders of magnitude longer than bulk HgCdTe and five orders of magnitude longer than the HgTe/CdTe SL with the same energy gap. The suppression of *p*-type recombination is due to the flatness of the light and heavy hole bands whose splitting exceeds the energy gap, thus limiting phase space for recombination transitions. This splitting can be increased further (without changing the energy gap) through the choice of other alloy compositions and layer thicknesses, which will further suppress *p*-type recombination in $\text{In}_x\text{Ga}_{1-x}\text{Sb}/\text{InAs}$ superlattices.

The authors are grateful to T. C. McGill for stimulating this work and to R. H. Miles for making data available prior to publication. Helpful discussions with both are greatly appreciated. This work was supported by DARPA and JSEP through ONR Contract Nos. N00014-86-K-0033 and N00014-89-J-1023, respectively.

¹ D. H. Chow, R. H. Miles, J. N. Schulman, D. A. Collins, and T. C. McGill, *Semi. Sci. Tech.* 6, C47 (1991); R. H. Miles (private communication).

² The idea for this SL and its properties originated with D. Smith and C. Mailhot in association with T. C. McGill. We thank the referee and T. C. McGill for drawing our attention to this fact.

³ R. Ferreira and G. Bastard, *Phys. Rev. B* 40, 1074 (1989).

⁴ A. R. Beattie and P. T. Landsberg, *Proc. R. Soc. London, Ser. A* 249, 16 (1959).

⁵ A. R. Beattie and G. Smith, *Phys. Status Solidi* 19, 577 (1967).

⁶ P. T. Landsberg, *Solid-State Electron.* 30, 1107 (1987).

⁷ Y. Jiang, M. C. Teich, and W. I. Wang, *J. Appl. Phys.* 69, 836 (1991).

⁸ G. Bastard, in *Proceedings of the NATO Advanced Study Institute on Molecular Beam Epitaxy in Heterostructures*, Erice, Italy, 1983, edited by L. L. Chang and K. Ploog (Martinus-Nijhoff, Dordrecht, 1984), p. 381.

⁹ N. F. Johnson, H. Ehrenreich, P. M. Hui, and P. M. Young, *Phys. Rev. B* 41, 3655 (1990).

¹⁰ E. Antonik and P. T. Landsberg, *Proc. Phys. Soc.* 82, 337 (1963).

¹¹ M. Takeshima, *J. Appl. Phys.* 43, 4114 (1972).

¹² The lifetime would differ by less than 33% if exchange interactions were included.

¹³ G. P. Agrawal and N. K. Dutta, *Long Wavelength Semiconductor Lasers* (Van Nostrand-Reinhold, New York, 1986).

Noise in alloy-based resonant-tunneling structures

E. Runge

Division of Applied Sciences, Harvard University, Cambridge, Massachusetts 02138

(Received 30 July 1992)

The noise properties of semiconductor alloy-based resonant-tunneling double-barrier quantum-well structures are calculated within a nonequilibrium Green's-function formulation. Alloy scattering is treated in the coherent-potential approximation including vertex corrections. Different noise characteristics are found depending on applied bias, scattering strength, and the transparency of the barriers. A characteristic frequency for the noise current power spectrum $S(\omega)$ is given by the inverse response time.

I. INTRODUCTION

Noise gets relatively more important with decreasing device dimensions and lower operating currents. Double-barrier quantum-well (DBQW) structures are prototypical for a wide class of small and very fast switching resonant-tunneling devices currently designed and, in part, already realized. The first measurements of low-frequency noise in DBQW's have been published recently.¹

Noise properties are investigated here as an extension of previous quantum transport calculations^{2,3} for alloy-based DBQW's. Different noise characteristics are found depending on applied bias, scattering strength, and the transparency of the barriers. The fluctuation-dissipation theorem states generally that for small bias, thermal Johnson-Nyquist noise, proportional to the resistance, dominates. For finite bias, the DBQW as a whole is no longer in thermal equilibrium. Thus it is appropriate to employ nonequilibrium Green's-function techniques in the general case. In a semiconductor alloy such as $(\text{In}_x\text{Ga}_{1-x})\text{As}$ alloy scattering is the main scattering mechanism at low temperatures. The scattering is incorporated within the coherent-potential approximation (CPA) including vertex corrections.

For systems with *asymmetric* barriers and for large bias, frequency-independent shot noise is present. In the case of barriers with about the *same* transparency, a frequency dependence of the noise current power spectrum is observed. A crossover from a low-frequency regime to a high-frequency regime takes place at a frequency equal to the inverse response time τ_{resp}^{-1} earlier identified as limiting the high-speed performance of DBQW devices.²

The frequency dependence of the noise current power spectrum in this case reflects temporal correlation between electrons tunneling into and out of the well. For strong scattering, where tunneling is completely incoherent, the noise spectrum can be derived by classical rate-equation considerations. The suppression of shot noise in DBQW's is therefore not a manifestation of the quantum-mechanical Pauli principle, as has been stated recently.⁴

An early calculation of noise in quantum systems was performed by Yurke and Kochanski.⁵ Within the

Büttiker-Landauer formalism, a general expression for the noise in open conductors has recently been given in terms of the global T matrix.^{6,7} A microscopic model for a perfect DBQW without scattering has been considered in Ref. 4. Scattering effects must be included in the modeling of real systems because scattering in semiconductor alloy DBQW's is strong enough that tunneling is predominantly sequential.²

In Sec. II the noise problem for DBQW's is formulated in terms of nonequilibrium Green's functions. The effects of alloy scattering in the CPA are incorporated in Sec. III. Section IV gives the results and examines special cases that allow an interpretation in terms of thermal noise, shot noise, and generation-recombination noise.

II. NOISE IN DBQW's

We are interested in the noise properties of alloy-based double-barrier quantum-well structures. These are described by the Hamiltonian (see Refs. 2 and 3, which use the same notation, for details)

$$\hat{H} = \sum_{S=L,R,W} \hat{H}_S^0 + \hat{H}^{\text{tun}} + \hat{H}^{\text{scat}}. \quad (1)$$

Here, \hat{H}_S^0 refers to either side of the DBQW structure [$S=L$ (left), R (right)] or the well region ($S=W$). The case of a single conduction band and a single resonant subband in the well region is considered. The bands are treated within the effective-mass approximation. The tunneling Hamiltonian is

$$\hat{H}^{\text{tun}} = \sum_{S=L,R} \hat{H}_{WS}^{\text{tun}} = \sum_{S=L,R} \sum_{k_z, k_{\parallel}} (h_{WS} c_{Wk_{\parallel}}^{\dagger} c_{Sk_z} + \text{H.c.}) \quad (2)$$

in terms of appropriately labeled creation and annihilation operators with momentum quantum numbers $\mathbf{k}=(k_{\parallel}, k_z)$ in $S=L, R$ and k_{\parallel} in $S=W$. A simple WKB estimate for tunneling through rectangular barriers is used for the tunneling matrix element h_{WS} . The tunneling operator gives rise to a self-energy Σ_S of well electrons. We keep only the imaginary part of the retarded tunneling self-energy Σ_S^r and denote it by $-i\Gamma_S/2$:

$$\begin{aligned} \Sigma_S^r(k_{\parallel}|E) &\approx -i\pi \sum_{k_z} |h_{WS}|^2 \delta(E - \epsilon_{k_{\parallel}} - \epsilon_{k_z} - \Phi_S) \\ &\equiv -i\Gamma_S/2. \end{aligned} \quad (3)$$

Here, Φ_S is the energy of the conduction-band edge in S . The electron distribution functions in $S = L, R$ at temperature T and for chemical potentials μ_S are

$$f_S(E - \Phi_S) = \frac{1}{e^{(E - \Phi_S - \mu_S)/(k_B T)} + 1} \quad (4)$$

(see Ref. 2 for an explicit diagram). It can be shown that the steady-state distribution function of the well region for this model is independent of momentum k_{\parallel} and is given by [Eq. (8) of Ref. 2]

$$f_W = \frac{\Gamma_L f_L + \Gamma_R f_R}{\Gamma_L + \Gamma_R} \quad (5)$$

The alloy scattering term in the well region takes the form of site-diagonal scattering from a two-dimensional arrangement of effective sites given by the Wannier orbitals within the one subband considered. For an $(A_x B_{1-x})C$ semiconductor alloy such as $(\text{In}_x \text{Ga}_{1-x})\text{As}$, the scattering strength ϵ is approximately Gaussian, distributed with the average energy

$$\bar{\epsilon} = \langle \epsilon \rangle_{av} = x\epsilon_A + (1-x)\epsilon_B \quad (6)$$

and disorder strength

$$\langle (\epsilon - \bar{\epsilon})^2 \rangle_{av} = x(1-x)(\epsilon_A - \epsilon_B)^2 \int_{\text{well}} a|\phi(z)|^4 dz, \quad (7)$$

where ϵ_A and ϵ_B are the on-site energies for the cations A and B , $\langle \rangle_{av}$ denotes the average over all scattered configurations, a^3 is the spatial extent of the anion cation unit, and $\phi(z)$ is the envelope wave function for the well states.

From the commutator of the number operators for $S = L, R$ with the tunneling operator (2), one gets the operator for the externally measurable current (assuming $h_{WS} = h_{WS}^*$ for ease of notation),

$$I = 2 \frac{e}{\hbar} \sum_{S=L,R} \frac{\eta_S}{2} \sum_{\mathbf{k}=(k_{\parallel}, k_{\perp})} (-ih_{WS} c_{S\mathbf{k}_{\parallel}}^{\dagger} c_{W\mathbf{k}_{\parallel}} + ih_{WS} c_{W\mathbf{k}_{\parallel}}^{\dagger} c_{S\mathbf{k}_{\parallel}}), \quad (8)$$

with $\eta_L \equiv +1$ and $\eta_R \equiv -1$ for convenient bookkeeping. Note a factor of 2 coming from the spin degeneracy.

Noise is characterized by the current-current correlation function

$$S(t) = \langle \langle \delta I(t) \delta I(0) \rangle + \langle \delta I(0) \delta I(t) \rangle \rangle_{av}, \quad (9)$$

where δI is the current fluctuation operator

$$\delta I(t) = I(t) - \langle I(t) \rangle \quad (10)$$

and the inner brackets in (9) indicate the quantum-mechanical expectation value.

For any two fermion operators c_{α}^{\dagger} and c_{β} (e.g., $\alpha = L\mathbf{k}$, $\beta = W\mathbf{k}_{\parallel}$), retarded (r), advanced (a), and distribution ($<$

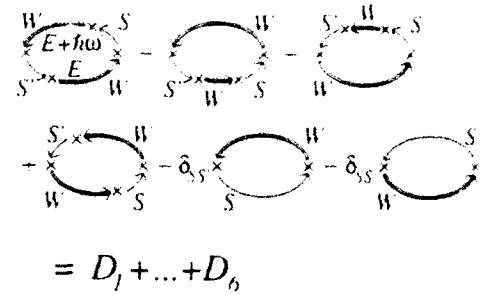


FIG. 1. Diagrams contributing to $\langle \delta I(t) \delta I(t') \rangle$. Thin arrows represent lead Green's functions; double arrows are well Green's functions. Crosses stand for the tunneling through the individual barriers (h_{WS}). Diagrams are read from the right to the left.

and $>$) Green's functions⁸ are defined by

$$G'(\beta t_2, \alpha t_1) \equiv -i \Theta(t_2 - t_1) \langle c_{\beta}(t_2) c_{\alpha}^{\dagger}(t_1) + c_{\alpha}^{\dagger}(t_1) c_{\beta}(t_2) \rangle, \quad (11)$$

$$G^a(\beta t_2, \alpha t_1) \equiv G'(\alpha t_1, \beta t_2)^*, \quad (12)$$

$$G^>(\beta t_2, \alpha t_1) \equiv -i \langle c_{\beta}(t_2) c_{\alpha}^{\dagger}(t_1) \rangle, \quad (13)$$

$$G^<(\beta t_2, \alpha t_1) \equiv +i \langle c_{\alpha}^{\dagger}(t_1) c_{\beta}(t_2) \rangle. \quad (14)$$

Equation (8) in (9) yields

$$S(t) = \sum_{S,S'} 2 \left[\frac{-ie}{2\hbar} \right]^2 \eta_S \eta_{S'} (D_1 + \dots + D_6), \quad (15)$$

where D_1 to D_6 correspond to the six diagrams of Fig. 1. That figure shows all possibilities of connecting the two fermion operators in $\delta I(t)$ with those in $\delta I(0)$ [unconnected parts are canceled by the subtraction of $\langle I(t) \rangle$ in the definition (10) of the fluctuations]. In the diagrams, Green's-function lines have been subdivided by tunneling events (the operator \hat{H}^{tun} is marked by crosses) so as to show as few Green's-function lines as possible with the restrictions that (i) no Green's function contains arguments referring to two different spatial regions L , R , or W and (ii) the well Green's functions are dressed by tunneling self-energies, whereas *unperturbed* Green's functions are used for the leads L and R . Two crosses at either end of the diagrams stem from the factors h_{WS} and h_{WS}^* in the current operator (8). Spin indices are not explicitly given, but are included by factors of 2 where appropriate.

As an example, the term D_6 reads

$$\begin{aligned} D_6 &= -\delta_{S,S'} \sum_{\mathbf{k}=(k_{\parallel}, k_{\perp})} \langle \langle c_{W\mathbf{k}_{\parallel}}^{\dagger}(t) c_{W\mathbf{k}_{\parallel}}(0) \rangle h_{WS} \langle c_{S\mathbf{k}}(t) c_{S\mathbf{k}}^{\dagger}(0) \rangle h_{WS} + \langle c_{W\mathbf{k}_{\parallel}}(0) c_{W\mathbf{k}_{\parallel}}^{\dagger}(t) \rangle h_{WS} \langle c_{S\mathbf{k}}^{\dagger}(t) c_{S\mathbf{k}}(0) \rangle h_{WS} \rangle_{av} \\ &= -\delta_{S,S'} \sum_{\mathbf{k}=(k_{\parallel}, k_{\perp})} \langle -i^2 G^<(W\mathbf{k}_{\parallel}t, W\mathbf{k}_{\parallel}0) G^>(S\mathbf{k}0, S\mathbf{k}t) | h_{WS} |^2 - i^2 G^>(W\mathbf{k}_{\parallel}t, W\mathbf{k}_{\parallel}0) G^<(S\mathbf{k}0, S\mathbf{k}t) | h_{WS} |^2 \rangle_{av}. \end{aligned} \quad (16)$$

The coherent-potential approximation replaces the Green's functions of the alloy region by the CPA Green's functions $G_{\text{CPA}}(k_{\parallel}, t=0)$. These are best described as functions of energy rather than as functions of time arguments. They have the same form as the Green's function for the corresponding ordered system, but with the self-energy Σ_0 , in our case

$$\Sigma_0 = \Sigma_{(L)} + \Sigma_{(R)}, \quad (17)$$

replaced by

$$\Sigma_W = \Sigma_0 + \Sigma_{\text{CPA}}, \quad (18)$$

with a suitably determined energy-dependent, but momentum-independent, self-energy contribution Σ_{CPA} due to scattering.⁹ Further, the CPA density of states

$$g_W(E) = \frac{1}{-2\pi i \mathcal{A}} \sum_{k_{\parallel}} \{G'_{\text{CPA}}(k_{\parallel}, E) - G^c_{\text{CPA}}(k_{\parallel}, E)\} \quad (19)$$

and the more general quantity

$$g_W(E; \omega) = \frac{1}{-2\pi i \mathcal{A}} \sum_{k_{\parallel}} \{G'_{\text{CPA}}(k_{\parallel}, E + \hbar\omega) - G^a_{\text{CPA}}(k_{\parallel}, E)\} \quad (20)$$

are introduced, where \mathcal{A} is the cross section of the DBQW. Note that $g_W(E; 0) = g_W(E)$ and $\int_{-\infty}^{+\infty} g_W(E; \omega) dE = 1$.

The Green's functions for $S=L, R$ combine with the tunneling matrix elements $|h_{WS}|^2$ to give $\Sigma_S^>$ and $\Sigma_S^<$. Thus,

$$(D_6)_{\text{CPA}} = \delta_{S,S'} \sum_{k_{\parallel}} [G^<_{\text{CPA}}(k_{\parallel}, t) \Sigma_S^>(k_{\parallel}, -t) + G^>_{\text{CPA}}(k_{\parallel}, t) \Sigma_S^<(k_{\parallel}, -t)]. \quad (21)$$

For D_5 one gets the same result with t and $-t$ interchanged.

The explicit evaluation of (15) is best done in Fourier space,

$$\begin{aligned} S(\omega) &\equiv \int_{-\infty}^{\infty} S(t) e^{-i\omega t} dt \\ &= \int_{-\infty}^{\infty} \langle \langle \delta I(t) \delta I(0) + \delta I(0) \delta I(t) \rangle \rangle_{av} e^{-i\omega t} dt \\ &= 4 \int_0^{\infty} \cos(\omega t) S(t) dt. \end{aligned} \quad (22)$$

With this convention for the Fourier transforms, $S(\omega)$ is the noise current power per frequency range $d\omega/2\pi$.

As an example, the contribution (21) becomes

$$\begin{aligned} D_6(\omega) &= \delta_{S,S'} \int \frac{dE}{2\pi} \sum_{k_{\parallel}} [\Sigma_S^>(k_{\parallel}|E + \hbar\omega) G^<_{\text{CPA}}(k_{\parallel}, E) \\ &\quad + \Sigma_S^<(k_{\parallel}|E + \hbar\omega) G^>_{\text{CPA}}(k_{\parallel}, E)]. \end{aligned} \quad (23)$$

Within the approximation (3), this yields

$$\begin{aligned} &\sum_{S,S'} \eta_S \eta_{S'} D_6(\omega) \\ &= \int \frac{dE}{2\pi} 2\pi \mathcal{A} g_W(E) (\Gamma_L + \Gamma_R) \\ &\quad \times [2\varphi_W(E + \hbar\omega) \varphi_W(E) - \varphi_W(E + \hbar\omega) - \varphi_W(E)]. \end{aligned} \quad (24)$$

D_5 gives a similar expression with E and $E + \hbar\omega$ interchanged, i.e., $g_W(E)$ replaced by $g_W(E + \hbar\omega)$. For ideal systems without scattering, the other terms D_1 to D_4 are equally straightforward to evaluate (see Ref. 4). However, those terms all contain products of well Green's functions, the disorder average of which cannot be simply replaced by the product of two CPA Green's functions without any additional adjustments. Such a procedure would violate particle conservation. Many years ago, Velický realized that for transport properties of thermal equilibrium alloy systems, one has to sum the ladder diagrams of repeated scattering of particle-hole pairs in order to be consistent with the single-particle CPA.¹⁰ This is done in Sec. III.

III. RESUMMATION OF LADDER DIAGRAMS IN THE CPA FOR NONEQUILIBRIUM SYSTEMS

The first four diagrams of Fig. 1 contain products of well Green's functions. The averages of these products over all disorder configurations can only be done approximately. Extending the work of Velický¹⁰ to nonequilibrium Green's functions we argued in Refs. 2 and 3 that the contributions to keep and sum correspond to ladder diagrams. The ladders contain two well Green's functions running in different "time" directions and are interconnected by rungs, each consisting of two on-site t matrices at the same site. Successive rungs correspond to different sites (multiple scattering exclusion) (see Fig. 2).

The averages of the form $\langle G \cdots G \cdots \rangle_{av}$ can be written in this approximation as the product of two CPA Green's functions times a factor u including the scattering effects: $(\langle G \rangle_{av} \cdots \langle G \rangle_{av} \cdots) u$. Four different cases u^{ar} , $u^{a<}$, $u^{>r}$, and $u^{><}$ have to be considered depending on which component of the "upper" and "lower" Green's function in Fig. 1 one is interested in. In each case, the ladder diagrams can be summed by a

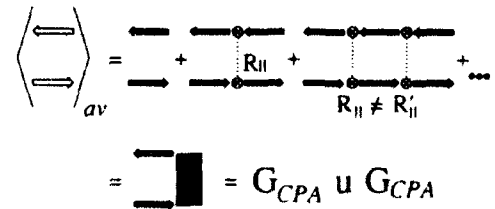


FIG. 2. Approximation of the particle-hole propagator by ladder diagrams. Double arrows indicate (configuration-dependent) well Green's functions, bold arrows represent CPA well Green's functions, hatched boxes stand for the vertex correction factors u , and encircled crosses symbolize on-site t matrices. These are connected if they belong to the same scattering site.

Bethe-Salpeter-like equation (see Ref. 3).

Figure 3(a) shows the equation for u^{ar} . Note that averages have to be taken over all configurations of each pair of t matrices separately and that the multiple scattering exclusion is incorporated by subtracting a suitable term compensating for repeated scattering at the same site.

This equation corresponds to Fig. 5 of Ref. 3. As in that figure, the Bethe-Salpeter equation can be easily solved for the site-diagonal terms. For energy arguments $E + \hbar\omega$ (upper Green's-function line) and E (lower line), the quantity u^{ar} reduces to a simple diagonal term,

$$u^{ar} \equiv \frac{\hbar\omega - \Sigma_W^a(E + \hbar\omega) + \Sigma_W^r(E)}{\hbar\omega - \Sigma_0^a(E + \hbar\omega) + \Sigma_0^r(E)}. \quad (25)$$

In practice, this implies replacing terms of the form

$$\langle G^a(Wk_{\parallel} Wk_{\parallel} | E + \hbar\omega) \cdots G^r(Wk_{\parallel} Wk_{\parallel} | E) \cdots \rangle_{av} \quad (26)$$

by

$$-\frac{G_{CPA}^a(k_{\parallel} | E + \hbar\omega) - G_{CPA}^r(k_{\parallel} | E)}{\hbar\omega - \Sigma_0^a(E + \hbar\omega) + \Sigma_0^r(E)} (\cdots), \quad (27)$$

with the denominator *not* containing the full self-energy but only the part Σ_0 excluding scattering contributions.

Using the equation of motion method or diagrammatic rules, one gets slightly more complicated equations for the other components, e.g., for $u^{>r}$ in Fig. 3(b). After adding $[1 - \varphi_W(E + \hbar\omega)]$ times the equation of Fig. 3(a) to Fig. 3(b), the latter is easily solved along the same lines as the equation of Fig. 3(a). The result is tantamount to replacing

$$\begin{aligned} &\langle G^>(Wk_{\parallel} Wk_{\parallel} | E + \hbar\omega) \cdots G^r(Wk_{\parallel} Wk_{\parallel} | E) \cdots \\ &\quad + [1 - \varphi_W(E + \hbar\omega)] G^a(Wk_{\parallel} Wk_{\parallel} | E + \hbar\omega) \\ &\quad \times \cdots G^r(Wk_{\parallel} Wk_{\parallel} | E) \cdots \rangle_{av} \end{aligned} \quad (28)$$

by

$$-\frac{G_{CPA}^r(k_{\parallel} | E + \hbar\omega) - G_{CPA}^r(k_{\parallel} | E)}{\hbar\omega - \Sigma_0^r(E + \hbar\omega) + \Sigma_0^r(E)} (\cdots). \quad (29)$$

In other words, averages of products of Green's functions can be written in the usual way as differences of Green's functions *provided* the unperturbed denominators not including scattering contributions to the self-energy are used. Corresponding statements can be proven for the quantities $u^{a<}$ and $u^{><}$. These are generalizations of a well-known property of the retarded CPA Green's function (see Ref. 10). Most important, particle conservation is satisfied only with these scattering corrections included.

IV. RESULTS AND DISCUSSION

A. Evaluation of the noise current power-density expression

The evaluation of the Fourier transform of the expression (8) for the noise current power density is now

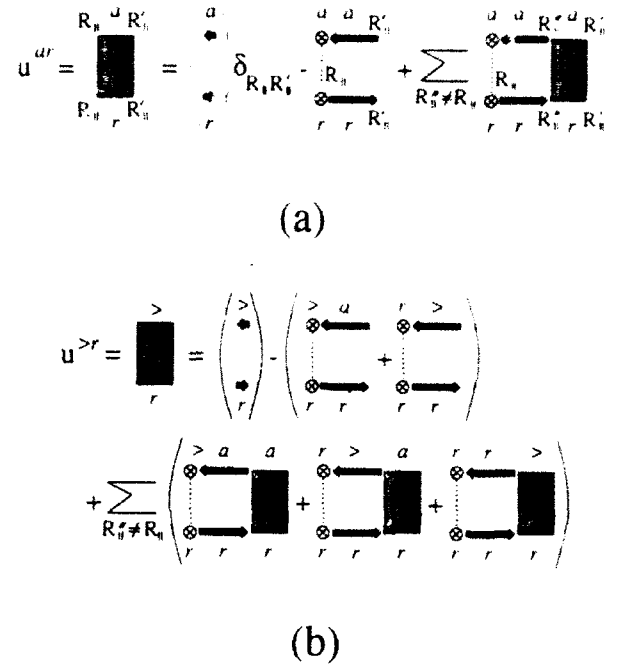


FIG. 3. Ladder diagrams for repeated scattering of a particle-hole pair at different sites are summed by means of Bethe-Salpeter-like equations: (a) for u^{ar} and (b) for $u^{>r}$.

straightforward. Let us first consider in detail the first term D_1 . The Green's functions of the leads $S=L,R$ combine with the tunneling matrix elements t_{WS} to form the tunneling self-energies Σ_S . All remaining Green's functions are well Green's functions. It has been shown in Refs. 2 and 3 that even in the presence of scattering, the well Green's function $G^<$ factorizes into

$$G_{CPA}^<(k_{\parallel} | E) = -\varphi_W(E) [G_{CPA}^r(k_{\parallel} | E) - G_{CPA}^a(k_{\parallel} | E)]. \quad (30)$$

Analogously,

$$G_{CPA}^>(k_{\parallel} | E) = [1 - \varphi_W(E)] [G_{CPA}^r(k_{\parallel} | E) - G_{CPA}^a(k_{\parallel} | E)]. \quad (31)$$

From equations of motion, one easily derives the simple rules

$$\begin{aligned} (g_1 g_2)^< &= g_1^< g_2^< + g_1^r g_2^<, \\ (g_1 g_2)^> &= g_1^> g_2^> + g_1^r g_2^>, \end{aligned}$$

and similarly for products containing three or more terms.⁸ We omit unnecessary arguments and indicate energy arguments $E + \hbar\omega$ and E by indices "+" and "-", respectively. Thus

$$\begin{aligned}
D_1(\omega) &= \int \frac{dE}{2\pi} \sum_{k_{\parallel}} \langle (G + \Sigma_{S+})^> (G - \Sigma_{S'-})^< + (G + \Sigma_{S+})^< (G - \Sigma_{S'-})^> \rangle_{av} \\
&= \int \frac{dE}{2\pi} \sum_{k_{\parallel}} \langle (G + \Sigma_{S+}^a + G' + \Sigma_{S+}^z) (G - \Sigma_{S'-}^a + G' - \Sigma_{S'-}^z) + \dots \rangle_{av} \\
&= \int \frac{dE}{2\pi} \sum_{k_{\parallel}} \left\{ -(1 - \varphi_+) (-\varphi_-) \frac{G'_+ - G'_-}{\hbar\omega - \Sigma'_{0+} + \Sigma'_{0-}} \Sigma_{S+}^a + \Sigma_{S'-}^a + \dots \right\}. \quad (32)
\end{aligned}$$

The ellipses indicate more terms of similar structure. The last step involves the results of Sec. III. Within the approximation (3), the resulting numerous terms can nicely be combined with $D_2 - D_4$. It is convenient to use the abbreviations

$$\Gamma_0 = \Gamma_L + \Gamma_R, \quad \tilde{\Gamma} = \frac{\Gamma_L \Gamma_R}{\Gamma_L + \Gamma_R}, \quad \Delta\Gamma = \Gamma_L - \Gamma_R, \quad (33)$$

and to introduce factors $a_{SS'}$ containing the statistical factors for fluctuations between S and S' ,

$$a_{WR} = a_{RW} = f_R(E + \hbar\omega)[1 - \varphi_W(E)] + [1 - f_R(E + \hbar\omega)]\varphi_W(E) + f_R(E)[1 - \varphi_W(E + \hbar\omega)] + [1 - f_R(E)]\varphi_W(E + \hbar\omega), \quad (34)$$

and correspondingly for a_{WL} , a_{WW} , a_{LL} , a_{LR} , and a_{RR} . The final result can be written as

$$\begin{aligned}
S(\omega) &= 2 \left[\frac{-ie}{2\hbar} \right]^2 \mathcal{A} \sum_{S,S'} \eta_S \eta_{S'} \{ D_1(\omega) + \dots + D_6(\omega) \} \\
&= \frac{e^2}{2\hbar} \mathcal{A} \int dE \left\{ \frac{g_W(E + \hbar\omega) + g_W(E)}{2} \Gamma_0 \left[a_{WW} - \frac{\Delta\Gamma}{(\hbar\omega)^2 + \Gamma_0^2} [4\tilde{\Gamma}(a_{LW} - a_{RW}) + (\Delta\Gamma)a_{WW}] \right] \right. \\
&\quad \left. + \text{Im}[g_W(E; \hbar\omega)] \left[\frac{4\tilde{\Gamma}^2}{\hbar\omega} (a_{LL} - 2a_{LR} + a_{RR}) + \frac{\hbar\omega(\Delta\Gamma)}{(\hbar\omega)^2 + \Gamma_0^2} [4\tilde{\Gamma}(a_{LW} - a_{RW}) + (\Delta\Gamma)a_{WW}] \right] \right\}. \quad (35)
\end{aligned}$$

It is noteworthy that the scattering described by Σ_{CPA} enters the final result only via the Green's functions contained implicitly in $g_W(E; \hbar\omega)$ and in the density of states $g_W(E)$. In the absence of scattering and for one dimension, Eq. (35) reduces to the result of Ref. 4.

The evaluation of Eq. (35) requires the numerical solution of the CPA equation for the scattering self-energy. Once g_W is known, the remaining integrals can easily be done numerically. Results are shown for an illustrative example in Fig. 4. The different curves correspond to different dc currents. The parameters are the same as in Ref. 2 and are chosen to represent a 45-Å $\text{In}_{0.47}\text{Ga}_{0.53}\text{As}$ -56-Å $\text{In}_{0.48}\text{Al}_{0.52}\text{As}$ DBQW used for measurements of the transit time in Ref. 11. Vertical arrows mark the response time and horizontal arrow mark the asymptotic large- ω values derived from the approximation (37) discussed below. $S(\omega)$ is approximately proportional to the current and decreases with frequencies.¹²

B. Discussion of special cases

The result (35) is easily understood in the limit of strong scattering, when the tunneling into the well and out of the well can be considered as independent events coupled only by the availability of empty or occupied states, i.e., by the number of electrons in the well. Disregarding the difference between the Green's functions and occupation factors evaluated at energies E and $E + \hbar\omega$, Eq. (35) then reduces to

$$\begin{aligned}
S(\omega) &\approx \frac{e^2}{2\hbar} \mathcal{A} \int dE g_W(E) \Gamma_0 \left[a_{WW} - \frac{\Delta\Gamma}{(\hbar\omega)^2 + \Gamma_0^2} [4\tilde{\Gamma}(a_{LW} - a_{RW}) + (\Delta\Gamma)a_{WW}] \right] \\
&= \frac{e^2}{2\hbar} \mathcal{A} \int dE g_W(E) 2\Gamma_0 \left[2\varphi_W(1 - \varphi_W) - \frac{\Delta\Gamma}{(\hbar\omega)^2 + \Gamma_0^2} [4\tilde{\Gamma}(f_L - f_R)(1 - 2\varphi_W) + (\Delta\Gamma)\varphi_W(1 - \varphi_W)] \right]. \quad (36)
\end{aligned}$$

In the sequential tunneling limit, where tunneling events can be treated classically and rate equation arguments apply, Eq. (36) can be derived by simple probabilistic arguments. As in Appendix B of Ref. 3, one takes the current from side S to the well as proportional to the well density

of states and the difference of the (time-dependent) occupation functions of S and W ,

$$j_{S \rightarrow W} \sim \int dE (f_S - \varphi_W) g_W,$$

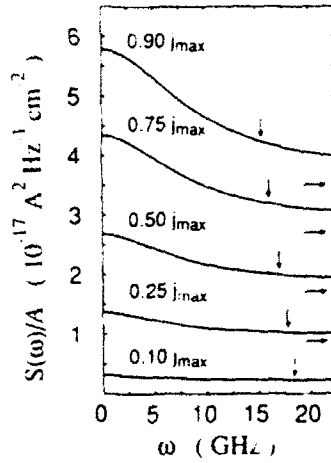


FIG. 4. Noise current power density per area $S(\omega)/\mathcal{A}$ as a function of frequency ω for sample A of Ref. 11 and different dc currents j_{dc} corresponding to, from top to bottom, about 90%, 75%, 50%, 25%, and 10% of the peak dc current j_{max} . Horizontal arrows mark the asymptotic values $S(\omega)/\mathcal{A} \approx e j_{dc}$; vertical arrows indicate the response time τ_{resp} (from Ref. 2).

and solves the resulting differential equation. Such a picture, where each tunneling event into the well increases the chance to observe a tunneling event out of the well approximately \hbar/Γ_0 later, resembles the well-known generation-recombination noise,¹³ where each generation event increases the chance for a recombination event soon after. This similarity was pointed out by the authors of Ref. 1 in the course of explaining their experimental results. The case of noise in a DBQW results in a lengthier expression. The additional complications come from the fact that both tunneling events can increase or decrease the current, depending on through which barrier the electron tunnels. The interpretation of Eq. (36) for incoherent tunneling, in terms of a simple coupling between fluctuations of the charge in the well and fluctuations of the current, makes it likely that the interpretation of Ref. 4 for a scattering-free coherent tunneling model as a manifestation of the quantum-mechanical Pauli principle is unnecessarily complicated. It should be mentioned as an aside that in the limit of a well coupled weakly only to one lead ($\Gamma_R \rightarrow 0$), the average current vanishes, but not the noise $S(\omega)$. In that case the well acts as a capacitor and

$$S(\omega) = \frac{e^2}{2\hbar} \mathcal{A} \int dE a_{LL} \Gamma_L \text{Re}[g_W(E; \hbar\omega) / (\hbar\omega + i\Gamma_L)] .$$

It is illuminating to discuss the general result (35) in more detail for the two limiting cases of (i) large dc bias and (ii) very small dc bias. We first assume that in a large-bias situation the resonant subband is lined up with empty states on the right-hand side so that $f_L \equiv 1$, $f_R \equiv 0$, and $\varphi_W \equiv \Gamma_L/\Gamma_0$ for the states that contribute to the current. For systems other than one dimensional, the as-

sumption of a constant f_L is not valid for a small-energy region around the Fermi energy. In general, this gives only a small correction to both the expression for the noise and for the dc current. In the case under consideration, the energy integral becomes trivial and we get

$$S(\omega) = e j_{dc} \mathcal{A} \left[1 + \frac{(\Delta\Gamma)^2}{(\hbar\omega)^2 + \Gamma_0^2} \right] , \quad (37)$$

where j_{dc} is the current density²

$$j_{dc} = 2 \frac{e}{\hbar} \int dE [f_L(E - eV_{dc}) - f_R(E)] \frac{\Gamma_L + \Gamma_R}{\Gamma_L \Gamma_R} g_W(E) . \quad (38)$$

For barriers of approximately the same transparencies, $\Delta\Gamma/\Gamma_0 \approx 0$, the noise is suppressed by up to a factor of 2 compared to the shot-noise result⁴

$$S^{\text{shot}}(\omega) = 2e j_{dc} \mathcal{A} . \quad (39)$$

For large ω , corresponding to short times, the noise $S(\omega)$ is reduced by this factor of 2 independent of the actual values of Γ_L and Γ_R (the horizontal arrows in Fig. 4 marked $S(\omega)/\mathcal{A} = e j_{dc}$). The reason is simply that the large- ω behavior is determined by the equal-time correlation part of (9). Each tunneling event corresponds to the transfer of half an electron through the DBQW (Ramo-Shockley theorem), yielding a factor $(e/2)^2$. Only one factor $\frac{1}{2}$ is compensated for by the fact that there are twice as many tunneling events as there would be in a single-barrier tunneling system. The characteristic time scale for this noise suppression is $\hbar/(\Gamma_L + \Gamma_R)$, the same as that we identified as the response time τ_{resp} describing the ac conductivity.

Interestingly, the form (37) is valid independent of the scattering strength as long as the scattering broadening of the well states is small compared with energies characterizing the electron distributions in the leads—in particular, μ_L . In the coherent tunneling limit treated in Ref. 4, an interpretation of the characteristic time $1/\Gamma_0$ as a quantum-mechanical time delay in the Wigner-Eisenbud sense is possible. It is therefore not surprising to find it governing the frequency dependence of the noise spectrum.

In the opposite limit (iii) of very small dc bias, all distribution functions can be replaced by a common thermal equilibrium Fermi function f_0 . With

$$\begin{aligned} & f_0(E + \hbar\omega) + f_0(E) - 2f_0(E + \hbar\omega)f_0(E) \\ &= -\coth \left[\frac{\hbar\omega}{2k_B T} \right] [f_0(E + \hbar\omega) - f_0(E)] \end{aligned} \quad (40)$$

for all factors a_{SS} , we get

$$S(\omega) = 2\hbar\omega \coth \left[\frac{\hbar\omega}{2k_B T} \right] \mathcal{A} \\ \times \left\{ \frac{-e^2}{2\hbar^2\omega} \int dE [f_0(E + \hbar\omega) - f_0(E)] \Gamma_0 \right. \\ \left. \times \operatorname{Re} \left[\frac{\hbar\omega + 4i\tilde{\Gamma}}{\hbar\omega + i\Gamma_0} g_W(E; \omega) \right] \right\}. \quad (41)$$

As is to be expected on general grounds (fluctuation-dissipation theorem), the expression in the curly brackets

is exactly the dynamic conductivity $\operatorname{Re}[\sigma(\omega)]$ (discussed in detail in Ref. 3) in the same limit. This is the usual thermal or Nyquist-Johnson noise.

ACKNOWLEDGMENTS

The author is very grateful to Professor H. Ehrenreich for his active interest in this research and to C. H. Grein for invaluable discussions. This work was supported by the U.S. Joint Services Electronics Program (JSEP) through ONR Contract No. N00014-89-J-1023 and by the DARPA through ONR Contract No. N00014-86-K-0033.

¹Y. P. Li, A. Zaslavsky, D. C. Tsui, M. Santos, and M. Shayegan, Phys. Rev. B **41**, 8388 (1990).

²E. Runge and H. Ehrenreich, Phys. Rev. B **45**, 9145 (1992).

³E. Runge and H. Ehrenreich, Ann. Phys. (N.Y.) **219**, 55 (1992).

⁴L. Y. Chen and C. S. Ting, Phys. Rev. B **43**, 4534 (1991); see also, in *Physics of Hot Electron Transport in Semiconductors*, edited by C. S. Ting (World Scientific, Singapore, 1992), p. 295.

⁵B. Yurke and G. P. Kochanski, Phys. Rev. B **41**, 8184 (1990).

⁶M. Büttiker, Phys. Rev. Lett. **65**, 2901 (1990).

⁷M. Büttiker, Phys. Rev. B **45**, 3807 (1992).

⁸For example, J. Rammer and H. Smith, Rev. Mod. Phys. **58**, 323 (1986); D. C. Langreth, in *Linear and Nonlinear Transport in Solids*, Vol. 17 of *NATO Advanced Study Institute*,

Series B: Physics, edited by J. T. Devreese and E. van Doren (Plenum, New York, 1976), p. 3.

⁹For example, H. Ehrenreich and L. M. Schwartz, in *Solid State Physics*, edited by H. Ehrenreich, F. Seitz, and D. Turnbull (Academic, New York, 1976), Vol. 31, p. 149.

¹⁰B. Velický, Phys. Rev. **184**, 614 (1969).

¹¹I. Bar-Joseph, T. K. Woodward, D. S. Chemla, D. Sivco, and A. Y. Cho, Phys. Rev. B **41**, 3264 (1990).

¹²Reference 7 points out that for the particle-current fluctuations (i.e., not including displacement currents) in each of the leads *L* and *R* individually, an increase with frequency is found.

¹³For example, A. van der Ziel, *Noise in Solid State Devices and Circuits* (Wiley, New York, 1986).

Phonon assisted transport in
double-barrier resonant-tunneling structures

C.H. Grein, E. Runge, and H. Ehrenreich

Division of Applied Sciences and Department of Physics

Harvard University

Cambridge, MA 02138

Abstract

The dc current in a biased double barrier resonant tunneling structure is calculated using a non-equilibrium Green's function formalism. Realistic models involving well, barrier, and interface modes are employed to evaluate the phonon-assisted components of the current. The calculated dc current agrees well with experimental data for a GaAs/AlGaAs resonant tunneling structure. The observed phonon replica peak in the I-V characteristics is attributed to the emission of GaAs confined modes in the well and AlAs-like symmetric interface modes. The effect of the non-equilibrium well occupation function is shown to be small. For the InAlAs/InGaAs resonant tunneling structure, phonon scattering becomes comparable to alloy well scattering at about 200K.

PACS: 73.40.Gk, 72.10.Di, 85.30.-z

I. Introduction

Resonant tunneling in double barrier resonant tunneling structures (DBRTS) is attracting considerable attention due to interest in the study of quantum transport processes in nanostructures, and in potential device applications such as high frequency ac generators¹ and bipolar transistors.² Since inelastic phonon scattering may play a substantial role in such applications, phonon-assisted tunneling in DBRTS and other heterostructures has been the subject of a number of recent theoretical studies.³⁻¹² These studies neglect the modifications to the phonon spectra resulting from interfaces. Recently, Turley and Teitsworth¹³ have examined tunneling in GaAs/AlAs DBRTS involving the emission of confined and interface phonons, but have employed a formalism which neglects the non-zero occupation probabilities of well states. Here, we employ non-equilibrium (Keldysh) Green's function techniques to calculate the dc current associated with phonon-assisted tunneling in DBRTS. Emission and absorption processes involving well, barrier, and interface phonons are considered. By employing the Keldysh formalism, the non-equilibrium occupation function of the well states is calculated and Fermi statistics are included which limit available phase space in the well. This general approach shows the effects of a non-equilibrium occupation function in the well to be relatively small for the cases considered by Turley and Teitsworth. The present work permits direct comparison to the results of Refs. 14 and 15, which were devoted to elastic alloy scattering, and, in particular, an assessment of the relative importance of the two scattering mechanisms. Our calculations combine realistic phonon models with a rigorous formalism to make quantitative comparisons with experimental data.

Experimental data clearly reveals at least one replica peak associated with phonon emission in the dc I-V curves of high quality DBRTS. This replica peak appears at bias

voltages greater in magnitude than the main elastic tunneling peak. Goldman *et al.*¹⁶ find a broad shoulder to the main elastic tunneling peak and associate it with the emission of a bulk AlAs-like phonon of energy ≈ 45 meV in the barrier layers of their $\text{Al}_{0.4}\text{Ga}_{0.6}\text{As}/\text{GaAs}$ DBRTS. Leadbeater *et al.*¹⁷ have performed magnetotunneling spectroscopic investigations of $\text{Al}_{0.4}\text{Ga}_{0.6}\text{As}/\text{GaAs}$ DBRTS and find two replica peaks corresponding to phonons of energy ≈ 35 and 48 meV being emitted. Both sets of observations have not been explained by theories which consider only bulk phonons. The coupling of the tunneling electron to barrier bulk AlAs-like phonons is very weak. The replica peak at $\hbar\omega_{\text{AlAs-like}} \approx 48\text{meV}$ would therefore be absent. Its presence can be explained by the emission of an interface phonon. The 35 meV replica peak is interpreted as being due to the emission of a confined GaAs phonon in the well. The Goldman *et al.* data is of lower resolution and therefore fails to separate the contributions of the 35 and 48 meV phonons. Nevertheless, the width of the replica peak suggests that both of these phonons contribute.

Section II discusses the nature of confined phonon modes in a DBRTS, and the corresponding electron-phonon interaction Hamiltonians. An expression for the resonant tunneling dc current associated with the absorption and emission of phonons is derived in Section III, and results are discussed in that section. Section IV compares the relative importance of phonon and alloy scattering, assesses the importance of the non-equilibrium well occupation function, and shows how to obtain Turley and Teitsworth's results for the phonon-assisted dc current in a DBRTS. The results are summarized in Section V.

II. Phonons and electron-phonon interactions in heterostructures

The presence of interfaces in semiconductor heterostructures will modify the vibrational spectra and the electronic spectra of the heterostructures with respect to their bulk constituents. The interfaces may lead to the confinement of optical modes within each

layer and the formation of interface modes which are localized near the interfaces. The use of the usual bulk Fröhlich Hamiltonian is inappropriate under such circumstances.

To calculate the vibrational modes in a double barrier heterostructure we employ an extension of the continuum theory described by Born and Huang.¹⁸ A number of phenomenological continuum models have been proposed,¹⁹⁻²⁸ usually differing in the choice of boundary conditions at the interfaces. We employ a model which is a combination of the better features of several models previously considered, and describe it below. In order to obtain more accurate mode frequencies our work includes dispersion of the interface modes. The discussion is restricted to polar optical phonons since the coupling of electrons to acoustic modes is very weak.

The dynamical variable $\vec{u}(\vec{x}, t)$ is defined as the relative sublattice displacement field times $\sqrt{\bar{M}/V_c}$; $\bar{M} = M_+M_-/(M_+ + M_-)$ is the reduced mass; M_+ and M_- are the anion and cation masses respectively and V_c is the volume of a unit cell. We consider the equation of motion

$$\ddot{\vec{u}}(\vec{x}, t) = -\omega_T^2 \vec{u}(\vec{x}, t) + \left[\frac{\epsilon_0 - \epsilon_\infty}{4\pi} \right]^{1/2} \omega_T \vec{E}(\vec{x}, t) - v_a^2 \nabla[\nabla \cdot \vec{u}(\vec{x}, t)] - v_\beta^2 \nabla^2 \vec{u}(\vec{x}, t), \quad (2.1)$$

where \vec{E} is the macroscopic electric field, ω_T is the frequency of bulk TO phonons, and ϵ_0 and ϵ_∞ are the zero and high frequency dielectric constants respectively. The last two terms in (2.1) are introduced to incorporate dispersion into the model. Their form is determined by symmetry considerations. The velocity parameters v_a and v_β are averaged over the Brillouin zone and can be shown to be of the same order of magnitude as the speed of LA phonons in the material.²⁸

The macroscopic polarization field is given by

$$\vec{P}(\vec{x}, t) = \left[\frac{\epsilon_0 - \epsilon_\infty}{4\pi} \right]^{1/2} \omega_T \vec{u}(\vec{x}, t) + \frac{\epsilon_\infty - 1}{4\pi} \vec{E}(\vec{x}, t). \quad (2.2)$$

The prefactors of \vec{u} and \vec{E} in (2.1) and (2.2) are chosen to be the same as those considered by Born and Huang. We consider only LO modes, which are characterized by $\vec{D}(\vec{x}, t) = \vec{E}(\vec{x}, t) + 4\pi\vec{P}(\vec{x}, t) = 0$.

The effects of heterostructure interfaces are discussed next. Different materials are labeled with integer index i . If the growth direction is parallel to the z axis, translational invariance parallel to the interfaces permits one to write the LO displacement field as $\vec{u}^L(\vec{x}) = \vec{f}(z)e^{i\vec{q}_\parallel \cdot \vec{x}_\parallel}$, where $\vec{x} = (\vec{x}_\parallel, z)$. The equation of motion is

$$\left(\frac{d^2}{dz^2} + q_i^2\right)\vec{f}(z) = 0, \quad (2.3a)$$

where

$$q_i^2 = \frac{\omega_{L,i}^2 - \omega^2}{v_i^2} - q_\parallel^2, \quad (2.3b)$$

$\omega_{L,i}$ are the bulk longitudinal mode frequencies, and $v_i^2 = v_{\alpha,i}^2 + v_{\beta,i}^2$. For example, for the case of a single quantum well extending from $z = 0$ to $z = a$ with $i = 1$ labeling the well material and $i = 2$ labeling the barrier regions, the general solution is

$$\vec{f}(z) = \begin{cases} A_2 \left[\hat{q}_\parallel + \left(\frac{q_2}{q_\parallel} \right) \hat{z} \right] e^{iq_2 z} & \text{for } a \leq z \\ A_1 \left[\hat{q}_\parallel + \left(\frac{q_1}{q_\parallel} \right) \hat{z} \right] e^{iq_1 z} + B_1 \left[\hat{q}_\parallel - \left(\frac{q_1}{q_\parallel} \right) \hat{z} \right] e^{-iq_1 z} & \text{for } 0 \leq z \leq a \\ B_2 \left[\hat{q}_\parallel - \left(\frac{q_2}{q_\parallel} \right) \hat{z} \right] e^{-iq_2 z} & \text{for } z \leq 0 \end{cases}, \quad (2.4)$$

where the curl-free nature of longitudinal phonons ($\nabla \times \vec{u}^L = 0$) has been exploited to obtain the prefactors.

Since electrostatics is the underlying physics of the above model, it should be appropriate to choose dielectric boundary conditions,^{19,24,27} that is, continuity of \vec{E}_\parallel and $\epsilon(\omega)E_z$ across each interface. However, this is not the only choice of boundary conditions considered previously. For confined modes, a model considering "jellium" between rigid walls has been employed.^{20,21} Here, the z component of the displacement field is assumed

to vanish at the interfaces (thereby preventing the formation of interface modes). Phonon displacements obtained from this choice of boundary conditions are completely confined in the well and are in better agreement than dielectric boundary conditions with experimental data²⁹ for the extent of confinement. We employ these boundary conditions for confined modes and dielectric boundary conditions for interface modes. A discussion of the physical foundations of different choices of boundary conditions is given in Ref. 30.

In the calculations to be described in the next section for $\text{Al}_x\text{Ga}_{1-x}\text{As}/\text{GaAs}$ heterostructures, electron-phonon scattering is considered due to the following phonon types: GaAs confined modes in the well, AlAs-like confined modes in the barriers, symmetric and antisymmetric interface modes, and GaAs-like extended modes.³¹ To treat confined modes, we employ the interface boundary conditions corresponding to "jellium" between rigid walls. Applying these boundary conditions to the general solution (2.4) leads to the lattice displacement field

$$\vec{u}^L(\vec{x}) = \sum_{\vec{q}_{\parallel}} \sum_{n=-N}^N \left[\frac{\hbar}{2\omega_{\vec{q}_{\parallel},n} A a} \right]^{1/2} \frac{\vec{q}}{|\vec{q}|} (e^{i\vec{q} \cdot \vec{x}} a_{\vec{q}_{\parallel},n} + \text{h.c.}), \quad (2.5)$$

for $0 \leq z \leq a$. Equation (2.5) describes confined LO modes ("guided modes") with crystal momentum $\vec{q} = (\vec{q}_{\parallel}, n\pi/a)$, annihilation operator $a_{\vec{q}_{\parallel},n}$, and dispersion $\omega_{\vec{q}_{\parallel},n}^2 = \omega_L^2 - v^2(q_{\parallel}^2 + [n\pi/a]^2)$. N is the largest value of n such that $\omega_L^2 \geq v^2(q_{\parallel}^2 + [n\pi/a]^2)$, and A is the interface area.

The symmetric interface mode centered on the interior interfaces ($z = 0$ and a) of the double heterostructure has, with dielectric boundary conditions, the displacement pattern

$$\vec{u}_{(S)}^L(\vec{x}) = \sum_{\vec{q}_{\parallel}} \sum_{n=-1}^1 |n| \left[\frac{\hbar}{2\omega_{\vec{q}_{\parallel},n} A a} \right]^{1/2} \frac{\vec{q}_{\parallel} + i q_1 \hat{z}}{|\vec{q}|} (e^{i\vec{q}_{\parallel} \cdot \vec{x}_{\parallel} + n q_1 (z-a/2)} a_{\vec{q}_{\parallel},n} + \text{h.c.}), \quad (2.6)$$

for $0 \leq z \leq a$. Here, the frequencies of vibration $\omega_{\vec{q}_{\parallel}}$ for the interface modes with $\vec{q} = (\vec{q}_{\parallel}, i n q_1)$ are given by the solutions of $q_2 \epsilon_2(\omega) + q_1 \epsilon_1(\omega) \tanh(q_1 a/2) = 0$. The dielectric

functions $\epsilon_1(\omega)$ and $\epsilon_2(\omega)$ for the case of alloys with two-mode behavior in their phonon spectra (such as $\text{Al}_x\text{Ga}_{1-x}\text{As}$) are defined in Ref. 32. More complete discussions of the number and types of interface modes that can arise are given in Refs. 19 and 32.

The electron-phonon interaction is obtained from the Hamiltonian³³

$$H_{el-ph}(\vec{x}) = -e \int \frac{\nabla' \cdot \vec{P}(\vec{x}')}{|\vec{x} - \vec{x}'|} e^{-|\vec{x} - \vec{x}'|/\lambda} d^3 \vec{x}'. \quad (2.7)$$

where a screening length λ has been introduced. The standard Fröhlich Hamiltonian for bulk phonon modes is

$$H_{el-ph}(\vec{x}) \approx \left[\frac{2\pi\hbar\omega_L e^2}{V_c} \left(\frac{1}{\epsilon_\infty} - \frac{1}{\epsilon_0} \right) \right]^{1/2} \frac{q e^{i\vec{q} \cdot \vec{x}}}{|q^2 + 1/\lambda^2|}. \quad (2.8)$$

For the confined modes described above, the corresponding Hamiltonian is²⁰

$$H_{el-ph}(\vec{x}) \approx \left[\frac{2\pi\hbar\omega_L^2 e^2}{\omega_{q\parallel, n} a} \left(\frac{1}{\epsilon_\infty} - \frac{1}{\epsilon_0} \right) \right]^{1/2} \frac{Q e^{i\vec{q}_\parallel \cdot \vec{x}_\parallel}}{[Q^2 + (\frac{n\pi}{a})^2]} \Phi_{q\parallel}(z), \quad (2.9a)$$

where

$$\Phi_{q\parallel}(z) = e^{in\pi z/a} - \frac{1}{2} \left[e^{-Qz} + (-1)^n e^{Q(z-a)} \right], \quad (2.9b)$$

$Q^2 = q_\parallel^2 + 1/\lambda^2$, and $0 \leq z \leq a$. For the case of symmetric interface modes,

$$H_{el-ph}(\vec{x}) \approx \left[\frac{\hbar e^2}{2A} \right]^{1/2} [\epsilon'_1(\omega) \tanh(q_1 a/2) + \epsilon'_2(\omega)]^{-1/2} \frac{e^{i\vec{q}_\parallel \cdot \vec{x}_\parallel}}{\sqrt{Q}} \frac{\cosh q_1(z - a/2)}{\cosh q_1 a/2}, \quad (2.10)$$

for $0 \leq z \leq a$, where ϵ' denotes the derivative with respect to ω .

III. DC Current

In this section, the non-equilibrium Keldysh Green's function formalism is employed to calculate the phonon-assisted dc current in DBRTS. Phonon emission and absorption processes in the well and in both barriers are considered.

We consider a DBRTS with a single conduction band (see Fig. 1) and treat the electron dynamics in an effective mass approximation. If the dc bias voltage moves the left conduction band edge up with respect to the right conduction band edge, then resonant tunneling without phonon assistance occurs when occupied states in the left lead are resonant with unoccupied states in the well. Phonon assisted tunneling will occur when the occupied states in the left lead differ in energy by integer multiples of a phonon energy from unoccupied states in the well.

The unperturbed Hamiltonian for the DBRTS is the same as that considered in Refs. 14 and 15. The left ($S = L$) and right ($S = R$) leads are described by

$$\hat{H}_S^0 = \sum_{S=L,R} \sum_{\vec{k}} (\epsilon_{\vec{k}} + \Phi_S) c_{S\vec{k}}^\dagger c_{S\vec{k}}, \quad (3.1)$$

where $\vec{k} = (\vec{k}_\parallel, k_z)$ is the electron's crystal momentum, $\epsilon_{\vec{k}} = \hbar^2 k^2 / 2m_S^*$ its energy, and $c_{S\vec{k}}^\dagger$ the electron creation operator. Further definitions of the notation are found in the caption of Fig. 1, and in Ref. 15. Both leads are assumed to be in separate thermal equilibrium with Fermi-Dirac distribution functions defined by $f_S(E) = [\exp(E - \mu_S - \Phi_S) / k_B T + 1]^{-1}$. Considering only a single subband in the well, the unperturbed electronic states in the well are described by

$$\hat{H}_W^0 = \sum_{\vec{k}_\parallel} (\bar{\epsilon} + \epsilon_{\vec{k}_\parallel} + \Phi_W) c_{W\vec{k}_\parallel}^\dagger c_{W\vec{k}_\parallel}, \quad (3.2)$$

where $\epsilon_{\vec{k}_\parallel} = \hbar^2 k_\parallel^2 / 2m_W^*$ is the in-plane component of the energy.

Elastic tunneling through the barriers is described by the transfer Hamiltonian

$$\hat{H}^{tun} = \sum_{S=L,R} \hat{H}_{WS}^{tun} = \sum_{S=L,R} \sum_{\vec{k}_\parallel, k_z} (\hbar_{WS}^e c_{W\vec{k}_\parallel}^\dagger c_{S\vec{k}} + h.c.), \quad (3.3)$$

where the escape rates out of the well are given by Fermi's Golden Rule

$$\Gamma_S / \hbar = \frac{2\pi}{\hbar} \sum_{k_z} |\hbar_{WS}^e|^2 \delta(E - \epsilon_{\vec{k}_\parallel} - \epsilon_{k_z} - \Phi_S). \quad (3.4)$$

Here h_{WS}^e describes elastic tunneling and is to be distinguished from the phonon-assisted inelastic process h_{WS}^{ph} to be introduced below. Assuming that the density of states in lead S varies little over energy ranges comparable to phonon energies (≈ 50 meV), the escape rates may be obtained from the WKB expression

$$\Gamma_S = \left(\frac{E - \epsilon_{\vec{k}_\parallel} - \Phi_W}{\pi} \right) \Theta(E - \epsilon_{\vec{k}_\parallel} - \Phi_S) \times \exp(-2d_S \sqrt{2m_B^* (\Lambda_S + (\Phi_S + \Phi_W)/2 - E + \epsilon_{\vec{k}_\parallel})} / \hbar). \quad (3.5)$$

Since the well spectral density is peaked at $\bar{\epsilon} + \epsilon_{\vec{k}_\parallel} + \Phi_W$, this means that $E - \epsilon_{\vec{k}_\parallel} - \Phi_W$ can be replaced by $\bar{\epsilon}$ everywhere in (3.5).

The electron-phonon interaction in the well is described by the Hamiltonian

$$\hat{H}_{el-ph}^W = \sum_{\vec{k}_\parallel, \vec{q}_\parallel, n} (M_{\vec{q}_\parallel, n} c_{W\vec{k}_\parallel + \vec{q}_\parallel}^\dagger c_{W\vec{k}_\parallel} a_{\vec{q}_\parallel, n} + h.c.), \quad (3.6)$$

where $M_{\vec{q}_\parallel, n} = \langle W\vec{k}_\parallel + \vec{q}_\parallel | H_{e-ph}(\vec{x}) | W\vec{k}_\parallel \rangle$, the $|W\vec{k}_\parallel\rangle$ are the portions of the electronic states in the well obtained by solving a one-dimensional Schrödinger equation. Similarly, the electron-phonon interaction in the barriers is described by the Hamiltonian

$$\hat{H}_{el-ph}^B = \sum_{S=L,R} \sum_{k_z, \vec{k}_\parallel, \vec{q}_\parallel, n} (M'_{\vec{q}_\parallel, n} c_{S\vec{k}_z, \vec{k}_\parallel + \vec{q}_\parallel}^\dagger c_{S\vec{k}_z, \vec{k}_\parallel} a_{\vec{q}_\parallel, n} + h.c.), \quad (3.7)$$

where $M'_{\vec{q}_\parallel, n} = \langle B\vec{k}_\parallel + \vec{q}_\parallel | H_{e-ph}(\vec{x}) | B\vec{k}_\parallel \rangle$, and $|B\vec{k}_\parallel\rangle$ are the portions of the electronic eigenstates in the barrier, also obtained by solving a one-dimensional Schrödinger equation. Note that Hamiltonian (3.7) describes phonon-assisted tunneling. In analogy with Eq. (3.3) the phonon-assisted tunneling matrix elements h_{WS}^{ph} are given by $M'_{\vec{q}_\parallel, n}$.

We employ the non-equilibrium Keldysh Green's function formalism to compute transport properties due to the non-equilibrium nature of carriers in a biased DBRTS. The retarded and advanced Green's functions for the electron creation and annihilation operators

c_α^\dagger and c_β are

$$G^r(\beta t_2, \alpha t_1) = -i\Theta(t_2 - t_1)\langle c_\beta(t_2)c_\alpha^\dagger(t_1) + c_\alpha^\dagger(t_1)c_\beta(t_2) \rangle, \quad (3.8)$$

and

$$G^a(\beta t_2, \alpha t_1) = G^r(\alpha t_1, \beta t_2)^*. \quad (3.9)$$

In addition, the distribution Green's functions are defined as

$$G^<(\beta t_2, \alpha t_1) = i\langle c_\alpha^\dagger(t_1)c_\beta(t_2) \rangle, \quad (3.10)$$

and

$$G^>(\beta t_2, \alpha t_1) = -i\langle c_\beta(t_2)c_\alpha^\dagger(t_1) \rangle. \quad (3.11)$$

The Fourier transforms of the above Green's functions are

$$G(\beta, \alpha|E) = \int_{-\infty}^{\infty} \frac{dE}{2\pi} e^{-iE(t_2-t_1)/\hbar} G(\beta t_2, \alpha t_1). \quad (3.12)$$

where E is the energy.

Due to the weakness of electron-phonon interactions, we assume that in any given scattering channel phonon scattering occurs in the barriers or the well but not simultaneously in both. Then the total current density can be written $j_{dc} = j^{(1)} + j^{(2)} + j^{(3)}$, where $j^{(1)}$ is the current density in the absence of phonon scattering, $j^{(2)}$ is the current density due to phonon scattering in the well, and $j^{(3)}$ is the current density due to phonon scattering in the barriers.

The current from lead S into the well W is given by

$$I_{S-W} = 2e \left\langle \frac{\partial \hat{N}_S}{\partial t} \right\rangle, \quad (3.13)$$

where the number of electrons in lead S is $\hat{N}_S = \sum_{\vec{k}} c_{S\vec{k}}^\dagger c_{S\vec{k}}$. Use of the Heisenberg equation of motion

$$\hbar \frac{\partial \hat{N}_S}{\partial t} = -i \sum_{\vec{k}_\parallel, \vec{k}_\perp} [h_{WS}^* c_{S\vec{k}_\perp}^\dagger c_{W\vec{k}_\parallel} - h_{WS} c_{W\vec{k}_\parallel}^\dagger c_{S\vec{k}_\perp}], \quad (3.14)$$

where $h_{WS} = h_{WS}^e$ for elastic tunneling (contributing to $j^{(1)}$ and $j^{(2)}$), and $h_{WS} = h_{WS}^{ph}$ for phonon-assisted tunneling (contributing to $j^{(3)}$), leads to the current

$$I_{S \rightarrow W} = \frac{2e}{\hbar} \int \frac{dE}{2\pi} \sum_{\vec{k}, \vec{k}_\parallel} [G^<(W\vec{k}_\parallel, S\vec{k}_\perp \vec{k}_\parallel | E) h_{WS}^* - h_{WS} G^<(S\vec{k}_\perp \vec{k}_\parallel, W\vec{k}_\parallel | E)]. \quad (3.15)$$

Considering the tunneling Hamiltonian as a perturbation, the first order Dyson equation relating the full Green's function to the unperturbed propagators is

$$\begin{aligned} G^<(W\vec{k}_\parallel, S\vec{k}_\perp \vec{k}_\parallel | E) &= G^r(W\vec{k}_\parallel, W\vec{k}_\parallel | E) h_{WS} G_0^<(S\vec{k}_\perp \vec{k}_\parallel | E) \\ &+ G^<(W\vec{k}_\parallel, W\vec{k}_\parallel | E) h_{WS} G_0^a(S\vec{k}_\perp \vec{k}_\parallel | E). \end{aligned} \quad (3.16)$$

Here, the $G_0(S\vec{k}_\perp \vec{k}_\parallel | E)$ include no self-energy corrections. Insertion of (3.16) into (3.13) yields

$$\begin{aligned} I_{S \rightarrow W} &= \frac{2e}{\hbar} \int \frac{dE}{2\pi} \sum_{\vec{k}, \vec{k}_\parallel} |h_{WS}|^2 [G_0^<(S\vec{k}_\perp \vec{k}_\parallel | E) G^>(W\vec{k}_\parallel, W\vec{k}_\parallel | E) \\ &- G_0^>(S\vec{k}_\perp \vec{k}_\parallel | E) G^<(W\vec{k}_\parallel, W\vec{k}_\parallel | E)] \end{aligned} \quad (3.17)$$

To obtain $j^{(1)}$ and $j^{(2)}$, we set $h_{WS} = h_{WS}^e$ (as given by Eq. (3.5)), and calculate $G^<(W\vec{k}_\parallel, W\vec{k}_\parallel | E)$ and $G^>(W\vec{k}_\parallel, W\vec{k}_\parallel | E)$ including self-energy corrections due to the electron-phonon interaction in the well. In order to accomplish this, Dyson's equation with \hat{H}_{e-ph}^W as the perturbation is iterated to give

$$\begin{aligned}
G^<(W\vec{k}_{\parallel}, W\vec{k}_{\parallel}|E) \approx & G_0^<(W\vec{k}_{\parallel}, W\vec{k}_{\parallel}|E) + G_0^r(W\vec{k}_{\parallel}, W\vec{k}_{\parallel}|E)\Sigma_{ph,w}^<(\vec{k}_{\parallel}|E)G_0^a(W\vec{k}_{\parallel}, W\vec{k}_{\parallel}|E) \\
& + G_0^r(W\vec{k}_{\parallel}, W\vec{k}_{\parallel}|E)\Sigma_{ph,w}^r(\vec{k}_{\parallel}|E)G_0^<(W\vec{k}_{\parallel}, W\vec{k}_{\parallel}|E) \\
& + G_0^<(W\vec{k}_{\parallel}, W\vec{k}_{\parallel}|E)\Sigma_{ph,w}^a(\vec{k}_{\parallel}|E)G_0^a(W\vec{k}_{\parallel}, W\vec{k}_{\parallel}|E), \quad (3.18a)
\end{aligned}$$

where the self energy correction to the electron to lowest order in the electron-phonon interactions is

$$\begin{aligned}
\Sigma_{ph,w}^<(\vec{k}_{\parallel}|E) = & \sum_{\vec{q}_{\parallel}, n} [(N(\hbar\omega_{\vec{q}_{\parallel}, n}) + 1)|M_{\vec{q}_{\parallel}, n}|^2 G_0^<(W\vec{k}_{\parallel} + \vec{q}_{\parallel}, W\vec{k}_{\parallel} + \vec{q}_{\parallel}|E + \hbar\omega_{\vec{q}_{\parallel}, n}) \\
& + N(\hbar\omega_{\vec{q}_{\parallel}, n})|M_{-\vec{q}_{\parallel}, n}|^2 G_0^<(W\vec{k}_{\parallel} - \vec{q}_{\parallel}, W\vec{k}_{\parallel} - \vec{q}_{\parallel}|E - \hbar\omega_{\vec{q}_{\parallel}, n})], \quad (3.18b)
\end{aligned}$$

and $\Sigma^{r,a}$ are the retarded and advanced self-energies. In (3.18b), the Bose-Einstein occupation function is $N(E) = [\exp(E/k_B T) - 1]^{-1}$, and n enumerates the phonon modes discussed in section II. The well Green's functions $G_0(W\vec{k}_{\parallel}, W\vec{k}_{\parallel}|E)$ include self energy corrections due to tunneling through the barriers, but do not include self energy corrections due to phonon scattering. To obtain $j^{(3)}$ we let $\hbar\omega_S = \hbar\omega_{WS}^p$ in Eq. (3.17) and neglect phonon scattering in the well (that is, $G^{(<, >)}(W\vec{k}_{\parallel}, W\vec{k}_{\parallel}|E) = G_0^{(<, >)}(W\vec{k}_{\parallel}, W\vec{k}_{\parallel}|E)$).

The final two terms in (3.18a) may be neglected in the valley region of I-V curves (where the phonon replica peaks are observed) due to the three dimensional nature of the calculation. Described physically, the electron tunnels into a virtual state in the well because \vec{k}_{\parallel} conservation prohibits it from tunneling into a real state. It then emits a phonon to drop into a real state. This is reflected in the final two terms in (3.18a) (which describe tunneling into real well states) being negligible due to the smallness of $G_0^<(W\vec{k}_{\parallel}, W\vec{k}_{\parallel}|E)$ for E values corresponding to V_{bias} in the valley region.

The final expression for the dc current is

$$I_{dc} = I^{(1)} + I^{(2)} + I^{(3)}, \quad (3.19a)$$

where the phonon independent contributions to the current are

$$I^{(1)} = -\frac{ei}{\hbar} \int \frac{dE}{2\pi} \sum_{\vec{k}_{\parallel}} \{ [f_L(E) - \varphi_W(E)] \Gamma_L - [f_R(E) - \varphi_W(E)] \Gamma_R \} \\ \times \{ G_0^r(W\vec{k}_{\parallel}, W\vec{k}_{\parallel}|E) - G_0^a(W\vec{k}_{\parallel}, W\vec{k}_{\parallel}|E) \}, \quad (3.19b)$$

the inelastic contributions associated with phonon scattering in the well are

$$I^{(2)} = -\frac{e}{\hbar} \int \frac{dE}{2\pi} \sum_{\vec{k}_{\parallel}} \left[\frac{G_0^r(W\vec{k}_{\parallel}, W\vec{k}_{\parallel}|E) - G_0^a(W\vec{k}_{\parallel}, W\vec{k}_{\parallel}|E)}{\Gamma_L + \Gamma_R} \right] \\ \times \{ [f_L(E) \Gamma_L - f_R(E) \Gamma_R] \Sigma_{ph,W}^>(\vec{k}_{\parallel}|E) \\ - [(f_L(E) - 1) \Gamma_L - (f_R(E) - 1) \Gamma_R] \Sigma_{ph,W}^<(\vec{k}_{\parallel}|E) \}, \quad (3.19c)$$

and the inelastic contributions associated with phonon scattering in the barriers are

$$I^{(3)} = -\frac{e}{\hbar} \int \frac{dE}{2\pi} \sum_{\vec{k}_{\parallel}} [G_0^r(W\vec{k}_{\parallel}, W\vec{k}_{\parallel}|E) - G_0^a(W\vec{k}_{\parallel}, W\vec{k}_{\parallel}|E)] \\ \times \{ [\Sigma_{ph,L}^<(\vec{k}_{\parallel}|E) - \Sigma_{ph,R}^<(\vec{k}_{\parallel}|E)] [\varphi_W(E) - 1] - [\Sigma_{ph,L}^>(\vec{k}_{\parallel}|E) - \Sigma_{ph,R}^>(\vec{k}_{\parallel}|E)] \varphi_W(E) \}. \quad (3.19d)$$

The non-equilibrium occupation function of the well, $\varphi_W(E)$, has been introduced through the relation $G_0^<(W\vec{k}_{\parallel}, W\vec{k}_{\parallel}|E) = -\varphi_W(E)[G_0^r(W\vec{k}_{\parallel}, W\vec{k}_{\parallel}|E) - G_0^a(W\vec{k}_{\parallel}, W\vec{k}_{\parallel}|E)]$. The $\Sigma_{ph,\{L,R\}}^<$ are defined by (3.18b) with the well Green's function replaced by a lead ($S = L$ or R) Green's function and well electron-phonon matrix elements $M_{\vec{q}\vec{n},n}$ replaced by their barrier counterparts $M'_{\vec{q}\vec{n},n}$.

The phonons are assumed to be in thermal equilibrium. That this is actually the case may be shown as follows. The experimental Raman linewidth of confined GaAs phonons

in $\text{Al}_{0.33}\text{Ga}_{0.67}\text{As}/\text{GaAs}$ superlattices is $\sim 4\text{cm}^{-1}$.³⁴ This implies a phonon lifetime of approximately 10^{-12}s . A calculation similar to that of Menendez and Cardona³⁵ of the anharmonic decay rate of GaAs confined phonons yields a lifetime of approximately 10^{-11}s . Both of these lifetimes are considerably shorter than the electron transit times of $\sim 10^{-9}\text{s}$ (see below and Fig. 3), implying that the phonons can relax to thermal equilibrium during tunneling time scales.

The nonequilibrium occupation function in the well is specified by a rate equation which requires the occupation function of the well at energy E to be constant:

$$\begin{aligned}
 0 = & \Gamma_L(f_L(E) - \varphi_W(E))/\hbar + \Gamma_R(f_R(E) - \varphi_W(E))/\hbar \\
 & - \frac{2\pi}{\hbar} \sum_{\vec{q}_{\parallel} n k_{\parallel}, \vec{k}_{\parallel}} [1 - f_L(E + \hbar\omega_{\vec{q}_{\parallel} n})] \varphi_W(E) N(\hbar\omega_{\vec{q}_{\parallel} n}) |M'_{\vec{q}_{\parallel}, n}|^2 \\
 & \times \delta(E - \epsilon_{k_{\parallel}} - \epsilon_{\vec{k}_{\parallel} + \vec{q}_{\parallel}} - \Phi_L + \hbar\omega_{\vec{q}_{\parallel} n}) \\
 & + \frac{1}{\hbar} \sum_{\vec{q}_{\parallel} n \vec{k}_{\parallel}} f_L(E + \hbar\omega_{\vec{q}_{\parallel} n}) [1 - \varphi_W(E)] [1 + N(\hbar\omega_{\vec{q}_{\parallel} n})] \\
 & \times \frac{\Gamma_L}{\Gamma_L + \Gamma_R} |M_{\vec{q}_{\parallel}, n}|^2 \{-\text{Im}G'_0(W\vec{k}_{\parallel}, W\vec{k}_{\parallel}|E + \hbar\omega_{\vec{q}_{\parallel} n})\} \\
 & + \dots,
 \end{aligned} \tag{3.20}$$

where the ellipsis denotes 14 other terms describing other phonon scattering channels. The first two terms in (3.20) describe coherent tunneling. The third term describes an electron absorbing phonons while tunneling through the left barrier from the well into the left lead. The fourth term describes an electron tunneling through the left barrier from the left lead into the well, and then emitting phonons in the well. The remaining terms are obtained by permuting phonon emissions with absorptions, electron propagation directions, and the left with the right barrier.

Equations (3.19) and (3.20) were numerically evaluated for the various phonon types

discussed in section II. The results of the calculation of the dc I-V characteristics are presented in Fig. 2 for temperatures $T=4\text{K}$ and $T=300\text{K}$, and compared with the data of Goldman *et al.*¹⁶ at $T=4\text{K}$. The dimensions and composition of the DBRTS were chosen to be the same as those employed in Ref. 16. The experimental peak height has been scaled to agree with the calculated one (a factor of approximately 21), and the data is shifted by $\Delta V_{bias} \approx 50\text{meV}$ with respect to the calculated results. The emitter chemical potential was chosen to be 23meV . The current due to thermionic emission above the barriers is described by the classical Richardson expression. At $T=4\text{K}$, the theory predicts a broad replica peak (labeled "ph" in Fig. 2) occurring over bias voltages between about 175 to 275 meV in addition to the main elastic tunneling peak (labeled "e" in Fig. 2). The agreement between theory and experiment is very good, even with the scaling of the peak height and the shifting of the bias voltage. The need for such adjustments is not surprising since the voltage drops in the leads and in depletion and accumulation layers are neglected, and the effective DBRTS area is not well known. The theory is not expected to reproduce the external circuit related hysteretic behavior in the negative differential resistance region ranging from approximately 150 to 180 meV.

The broad phonon replica peak is clearly visible in the experimental data and matches the calculated one in shape and position. We find that the dominant phonons which contribute to the calculated peak are the $n=1$ GaAs LO phonons of energy 36.2 meV confined in the well and AlAs-like symmetric interface phonons of energy 45.7 meV. Barrier phonons do not contribute due to the weak coupling. At $T=300\text{K}$, the replica peak is seen to be superimposed on the Richardson current background. The phonon absorption replica peak (which would appear at low bias voltages) is too weak to be visible at $T=300\text{K}$.

Figure 3 shows the calculated transit times for the same structure. The transit time, defined by $\tau_{trans} = \rho_W / j_{dc}$,³⁶ the ratio of the charge density in the well and the dc current density (excluding the Richardson component), is a measure of the dwell time of the electron in the well. Here, τ_{trans} is comparatively long due to the rather thick barriers. We find that for low current densities τ_{trans} for $T=300K$ is longer than that at $T=4K$. This is mainly due to the broader Fermi distribution of the electrons at $T=300K$, which implies that a given current density can be attained with a lower bias voltage than at $T=4K$. The lower bias voltage leads to increased trapping of electrons in the well since the effective right barrier height is greater, and hence to a larger dwell time.

IV. General Conclusions

In this section we compare the relative importance of phonon and alloy scattering,^{14,15} assess the importance of the non-equilibrium well occupation function φ_W , and show how to obtain Turley and Teitsworth's¹³ results for the phonon-assisted dc current in a DBRTS.

Figure 4 compares the phonon scattering self-energy correction (3.18b) and the alloy scattering self energy derived in Refs. 14 and 15 employing the coherent potential approximation for the 56\AA $\text{In}_{0.52}\text{Al}_{0.48}\text{As}$ / 45\AA $\text{In}_{0.53}\text{Ga}_{0.47}\text{As}$ DBRTS studied by Chemla *et al.*³⁶ (The sample of Goldman *et al.*¹⁶ is unsuitable because of the absence of well alloy scattering). The self-energy corrections due to temperature independent well alloy scattering in this sample was reported in Ref. 15, and is indicated in Fig. 4. The self-energy corrections due to phonon scattering were computed using the phonon models discussed in Section 2. Phonon frequencies for bulk $\text{In}_{0.53}\text{Ga}_{0.47}\text{As}$ were obtained from Ref. 37, and for bulk $\text{In}_{0.52}\text{Al}_{0.48}\text{As}$ from Ref. 38. In computing the confined and interface modes in the DBRTS, we approximated the two-mode behavior of $\text{In}_{0.53}\text{Ga}_{0.47}\text{As}$ by the single GaAs-like mode. This is a good approximation due to the small energy difference between

the two modes, and simplifies the calculations. The chemical potential was again chosen to be 23 meV, and V_{bias} was set to 330 meV. Figure 4 shows that alloy scattering dominates at low temperatures, but phonon scattering becomes more important at $T \approx 200K$. This crossover temperature is higher than that familiar from electronic transport in bulk semiconductors. For bulk samples the final density of states for inelastic phonon absorption processes is greater than the density of states probed by elastic alloy scattering, whereas in two dimensions, characteristic of DBRTS, phonon and alloy scattering processes probe an energy-independent density of states.

In order to assess the importance of the non-equilibrium well occupation function φ_W , we set $\varphi_W=0$ in (3.19d). The component of the current associated with phonon emission in the left barrier may be written as

$$I^{(3)} \rightarrow \frac{2Ve}{(2\pi)^3} \int W(\vec{k}; n) f_L(E(\vec{k})) d\vec{k}, \quad (4.1a)$$

where

$$W(\vec{k}; n) = \frac{2\pi}{\hbar} \sum_{\vec{q}_\parallel, n} |M'_{\vec{q}_\parallel, n}|^2 [1 + N(\hbar\omega_{\vec{q}_\parallel, n})] \delta(E(\vec{k}) - \bar{\epsilon} - \epsilon_{\vec{k}_\parallel - \vec{q}_\parallel} - \Phi_W - \hbar\omega_{\vec{q}_\parallel, n}). \quad (4.1b)$$

This equation is identical to (4) of Turley and Teitsworth¹³. Equation (3.19c) for the current associated with phonon scattering in the well can also be reduced to (4.1). As discussed below, both equations are quite accurate. In agreement with Ref. 13, we find the dominant phonon scattering channels to involve symmetric interface modes and GaAs modes confined in the well.

The Keldysh formalism properly includes the well non-equilibrium occupation function, thereby taking Fermi statistics into account during resonant tunneling. For the device parameters employed to obtain Fig. 2 and 3, we find that effect of the non-zero occupation

of the well states is to decrease the peak current obtained from (3.19) by 11% at $T=4K$ and by 28% at $T=300K$. The current decreases due to fewer available states in the well for tunneling electrons. The small magnitudes of these decreases may be understood by noting that at the bias voltages near resonance the right barrier is comparatively transparent. Hence $\varphi_W \approx 0$ in any case. At higher temperatures the well occupation function is greater than at low temperatures due to the broader collector Fermi distribution.

V. Summary

This paper and two earlier ones^{14,39} have employed the Keldysh non-equilibrium Green's function formalism to study transport and noise properties of DBRTS, including the effects of alloy and phonon scattering, systematically. Alloy scattering is dominant in alloy based DBRTS at low temperature, and phonon scattering is dominant at room temperature or high bias. The Keldysh technique provides a systematic methodology for incorporating the complex effects associated with non-equilibrium occupation functions^{14,15} which is of particular importance for the calculation of two-particle correlation functions needed to obtain the ac response. Under normal operating conditions of a DBRTS, the distribution function may be determined from rate equations and thus an equilibrium Green's function steady state calculation provides a good approximation (see Appendix B of Ref. 15). For the dc current, the effects of a non-equilibrium distribution function in the well are small due to the low occupation probability of well states in a biased DBRTS. Thus intuitive expressions for the dc current which assume a vanishing well occupation function such as those employed in Ref. 13 are good approximations.

The present paper has employed realistic phonon models to calculate the phonon-assisted resonant tunneling dc current in a $Al_{0.4}Ga_{0.6}As/GaAs$ DBRTS. Results for the phonon replica peak position and width in the I-V characteristics agree well with the

experimental results of Goldman *et al.*¹⁶ This verifies our conclusion that the strongest phonon scattering channels at low temperature in the valley region of the I-V curve are the emission of AlAs-like symmetric interface phonons and the emission of confined GaAs phonons. For a $\text{In}_{0.52}\text{Al}_{0.48}\text{As}/\text{In}_{0.53}\text{Ga}_{0.47}\text{As}$ DBRTS, we find that alloy scattering is dominant at low temperature, but phonon scattering will dominate at room temperature.

Acknowledgements

This work was supported by DARPA and JSEP through ONR contract Nos. N00014-86-K-0033 and N00014-89-J-1023, respectively.

References

1. E.R. Brown, C.D. Parker, and T.C.L.G. Sollner, Appl. Phys. Lett. **54**, 934 (1989).
2. M.A. Reed, W.R. Frensley, R.J. Matyi, J.N. Randall, and A.C. Seabaugh, Appl. Phys. Lett. **54**, 1034 (1989).
3. N.S. Wingreen, K.W. Jacobsen, and J.W. Wilkins, Phys. Rev. B **40**, 11834 (1989).
4. W. Cai, T.F. Zheng, P. Hu, B. Yudanin, and M. Lax, Phys. Rev. Lett. **63**, 418 (1989).
5. M. Jonson, Phys. Rev. B **39**, 5924 (1989).
6. F. Chevoir and B. Vinter, Appl. Phys. Lett. **55**, 1859 (1989).
7. B.Y. Gelfand, S. Schmitt-Rink, and A.F.J. Levi, Phys Rev. Lett. **62**, 1683 (1989).
8. E.V. Anda and F. Flores, J. Phys.: Condens. Matter **3**, 9087 (1991).
9. R. Lake and S. Datta, Phys. Rev. B **45**, 6670 (1992).
10. S. Hershfield, J.H. Davies, and J.W. Wilkins, Phys. Rev. Lett. **67**, 3270 (1991).
11. Y. Meir and N.S. Wingreen, Phys. Rev. Lett. **68**, 2512 (1992).
12. H. Pastawski, Phys. Rev. B **46**, 4053 (1992), and references therein.
13. P.J. Turley and S.W. Teitsworth, Phys. Rev. B **44**, 8181 (1991).
14. E. Runge and H. Ehrenreich, Phys. Rev. B **45**, 9145 (1992);
15. E. Runge and H. Ehrenreich, Annals of Physics (NY) **219**, 55 (1992).
16. V.J. Goldman, D.C. Tsui, and J.E. Cunningham, Phys. Rev. B **36**, 7635 (1987).
17. M.L. Leadbeater, E.S. Alves, L. Eaves, M. Henini, O.H. Hughes, A. Celeste, J.C. Portal, G. Hill and M.A. Pate, Phys. Rev. B **39**, 3438 (1989).
18. M. Born and K.K Huang, "Dynamical Theory of Crystal Lattices" (Clarendon, Oxford, 1968).
19. N. Mori and T. Ando, Phys. Rev. B **40**, 61175 (1989).

20. C. Trallero Giner and F. Comas, *Phys. Rev. B* **37**, 4583 (1988).
21. B.K. Ridley, *Phys. Rev. B* **39**, 5282 (1989).
22. F. Bechsted, and R. Enderlein, *Phys. Stat. Sol. (B)* **131**, 53 (1985).
23. N. Sawaki, and I. Akasaki, *Physica* **134B**, 494 (1985).
24. A.A. Lucas, E. Kartheuser, and R.G. Badro, *Phys. Rev. B* **2**, 2488 (1970).
25. L. Wendler, *Phys. Stat. Sol. (B)* **129**, 513 (1985).
26. N. Sawaki, *Surface Science* **170**, 537 (1986).
27. R. Haupt and L. Wendel, *Phys. Rev. B* **44**, 1850 (1991).
28. M. Babiker, *J. Phys. C: Solid State Phys.* **19**, 683 (1986).
29. A.K. Sood, J. Menendez, M. Cardona, and K. Ploog, *Phys. Rev. Lett.* **54**, 2111 (1985).
30. C. Trallero-Giner, F. Garcia-Moliner, V.R. Velasco, and M. Cardona, *Phys. Rev. B* **45**, 11944 (1992).
31. B. Jusserand, D. Paquet, and A. Regreny, *Superlattices and Microstructures* **1**, 61 (1985).
32. K.W. Kim and M.A. Stroscio, *J. Appl. Phys.* **68**, 6289 (1990).
33. H. Ehrenreich, *J. Phys. Chem. Solids* **8**, 130 (1959).
34. Z.P. Wang, H.X. Han, and G.H. Li, *Phys. Rev. B* **2**, 9693 (1990).
35. J. Menendez and M. Cardona, *Phys. Rev. B* **29**, 2051 (1984).
36. I. Bar-Joseph, T.K. Woodward, D.S. Chemla, D. Sivco, and A.Y. Cho, *Phys. Rev. B.* **41**, 3264 (1990).
37. U.D. Venkateswaran, L.J. Cui, M. Li, B.A. Weinstein, K. Elcess, C.G. Fonstad, and C. Mailhoit, *Appl. Phys. Lett.* **56**, 286 (1990).
38. A. Ksendzov, P. Parayanthal, F.H. Pollak, D. Welch, G.W. Wicks, and L.F. Eastman,

Phys. Rev. B. 36, 7646 (1987).

39. E. Runge, submitted to Phys. Rev. B.

Figure Captions

Figure 1. Schematic drawing of double barrier resonant tunneling structure defining the symbols employed in the text (from Ref. 14). The external dc bias shifts the conduction band edges $\Phi_L (= eV_{bias})$ of the left lead, Φ_W of the well, and Φ_R of the right lead relative to one another. The chemical potentials of the left and right leads are μ_L and μ_R . The band offsets of the left and right barriers are Λ_L and Λ_R , and the electron tunneling matrix elements through these barriers are h_{WL} and h_{RW} . The bottom of the two-dimensional subband in the well is at energy $\bar{\epsilon}$ above the bottom of the well, and the energy of a state with parallel (in-plane) momentum \vec{k}_{\parallel} is $\epsilon_{\vec{k}_{\parallel}}$ above $\bar{\epsilon}$.

Figure 2. Calculated dc current-voltage characteristics of a 85\AA $\text{Al}_{0.4}\text{Ga}_{0.6}\text{As}/56\text{\AA}$ GaAs double barrier resonant tunneling structure at $T=4\text{K}$ and 300K (solid lines), and the experimental data at $T=4\text{K}$ obtained from Ref. 16 (dashed line). The calculated and experimental curves at $T=4\text{K}$ for $V_{bias} \geq 180\text{meV}$ are multiplied by 2 in order to show more detail. Also, the $T=300\text{K}$ curve has been shifted upwards by 3 A/cm^2 for clarity. Phonon emissions are responsible for the broad shoulder marked "ph" extending approximately over $175 \leq V_{bias} \leq 275\text{ meV}$. The peak marked "e" corresponds to elastic tunneling contributions.

Figure 3. Calculated transit times for phonon-assisted electrons tunneling through a 85\AA $\text{Al}_{0.4}\text{Ga}_{0.6}\text{As}/56\text{\AA}$ GaAs double barrier resonant tunneling structure at $T=4\text{K}$ and 300K .

Figure 4. Imaginary part of the retarded electron self-energy due to phonon absorption

plotted as a function of temperature for a 56\AA $\text{In}_{0.52}\text{Al}_{0.48}\text{As}$ / 45\AA $\text{In}_{0.53}\text{Ga}_{0.47}\text{As}$ double barrier resonant tunneling structure biased by 330 meV. The imaginary part of the alloy scattering self-energy obtained (from Ref. 15) in the coherent potential approximation for this structure is marked.

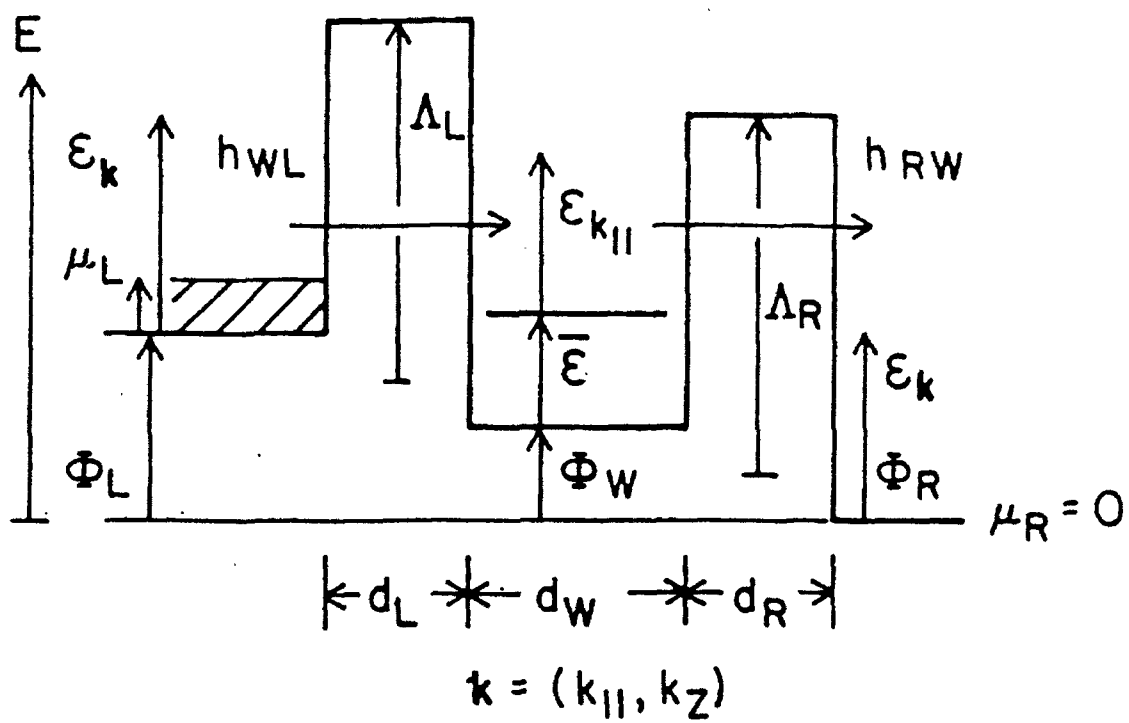


Fig. 1

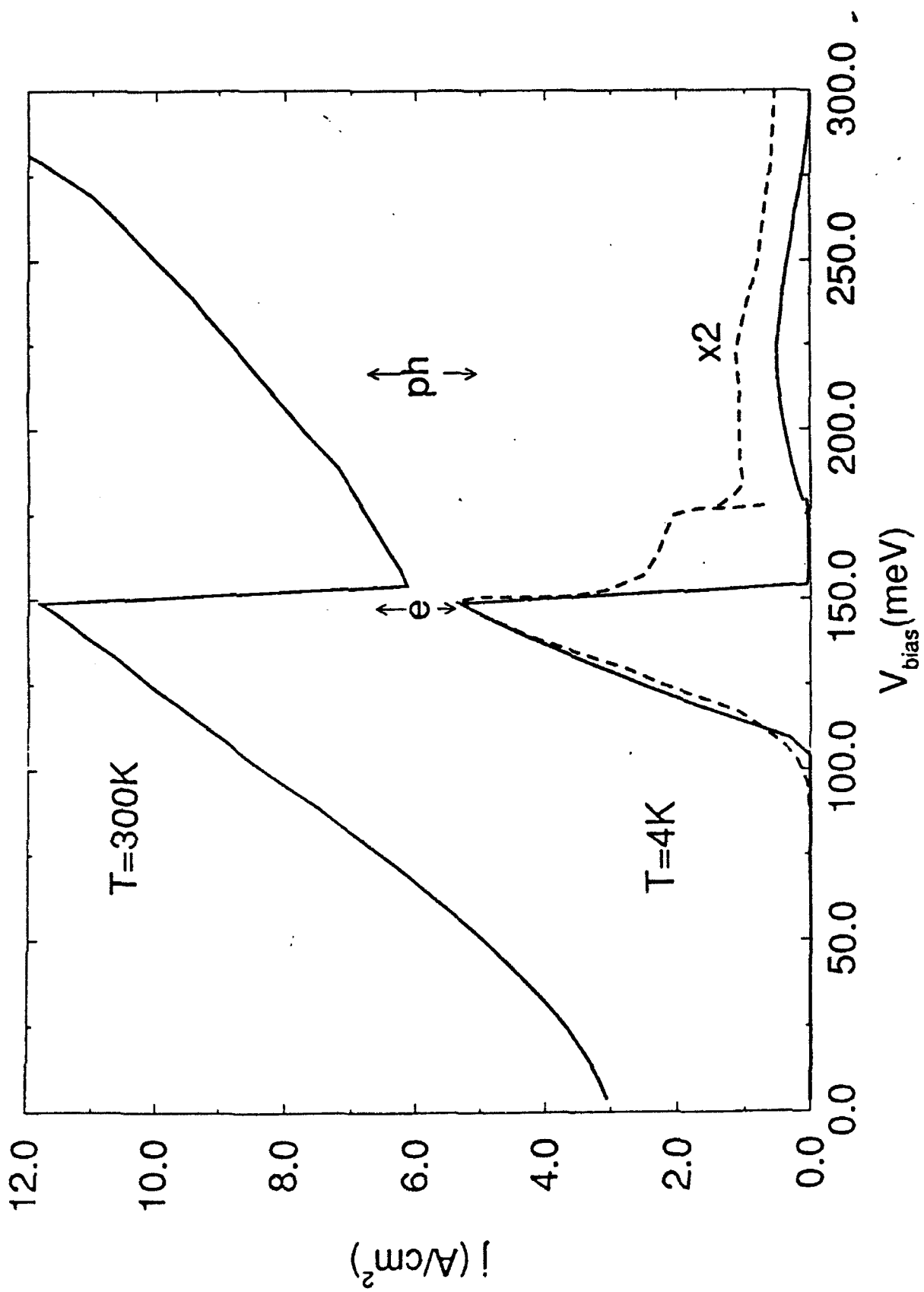


Fig. 2

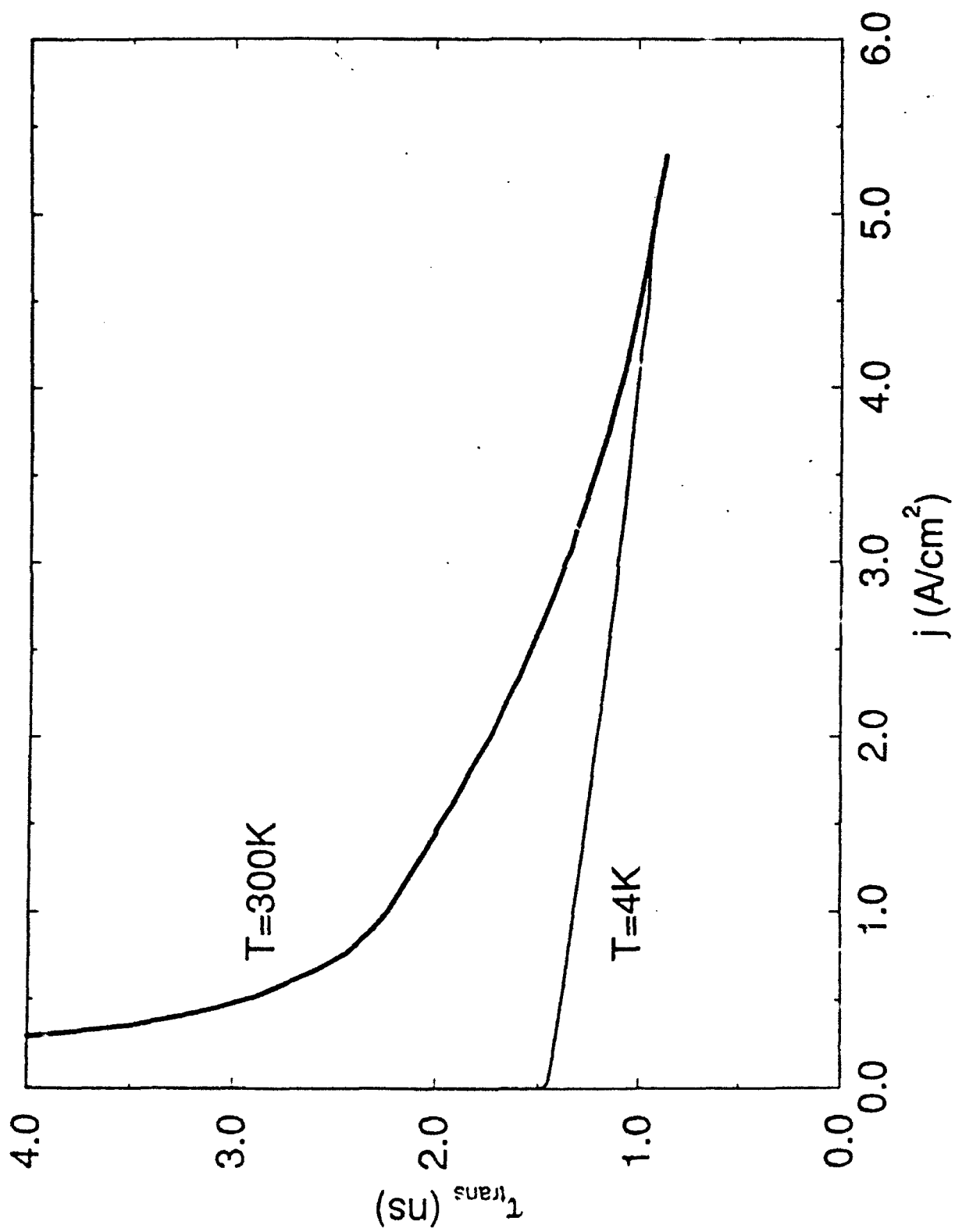


Fig. 3

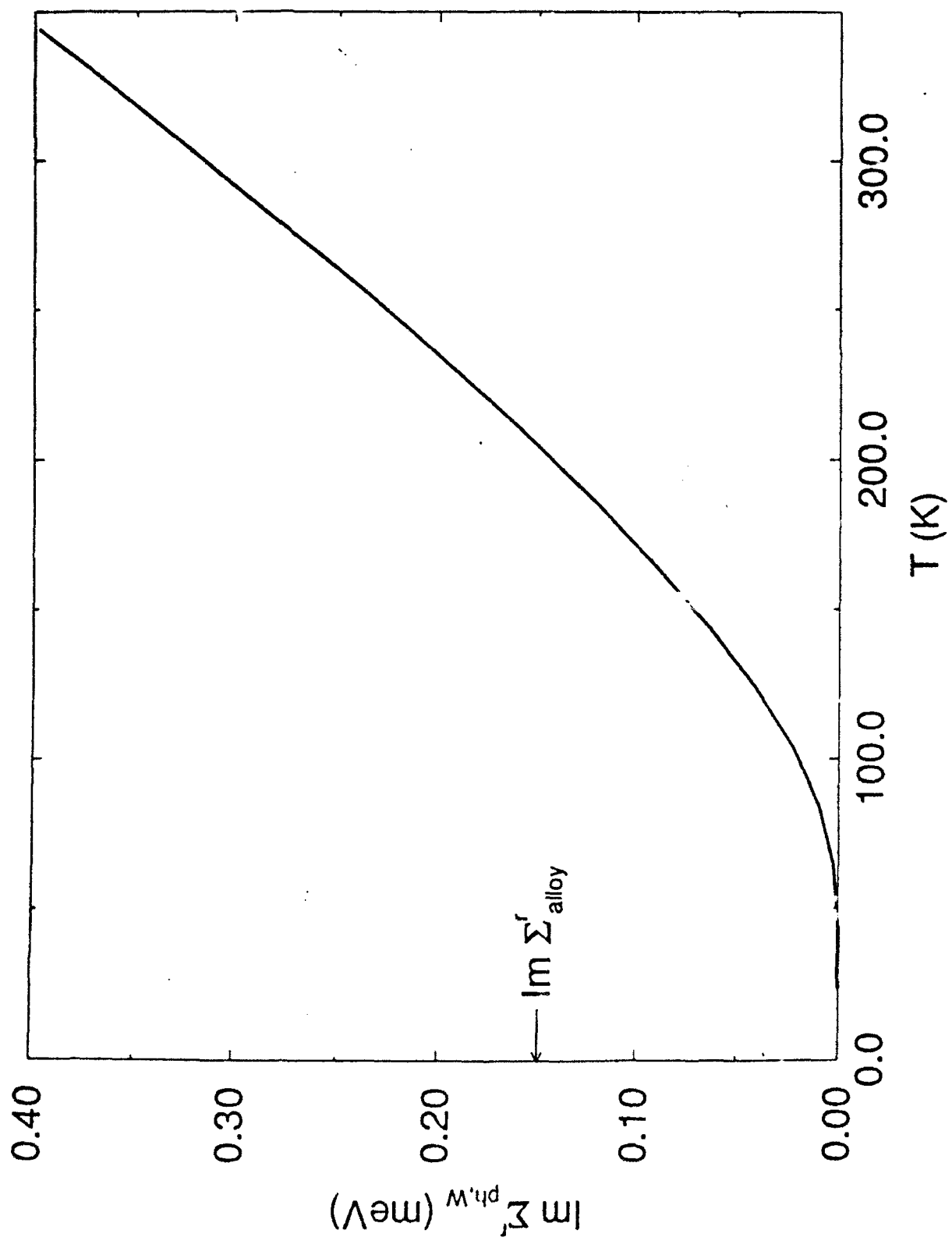


Fig. 4

Auger Lifetimes in Ideal InGaSb/InAs Superlattices

C.H. Grein, P.M. Young and H. Ehrenreich

Division of Applied Sciences, Harvard University, Cambridge, Massachusetts 02138

and

T.C. McGill

*California Institute of Technology, Pasadena, California 91125***Abstract**

Quantitative calculations are reported of both band-to-band Auger and radiative recombination lifetimes in thin-layered type II $\text{In}_x\text{Ga}_{1-x}\text{Sb}/\text{InAs}$ superlattices with energy gaps in the 5-17 μm range, using accurate band structure and numerical techniques. Results for a 11 μm superlattice are compared with similar calculations for bulk HgCdTe and a HgTe/CdTe superlattice having the same energy gap. The results show the n-type Auger rates to be comparable and the p-type rates to be suppressed by three orders of magnitude in some experimentally realizable structures. Thus well fabricated III-V SLs appear to be excellent candidates as a new class of IR detectors.

PACS #'s: 72.15.Lh, 72.40.+w, 78.60.-b, 85.60.Gz

The thin-layered type II staggered $\text{In}_x\text{Ga}_{1-x}\text{Sb}/\text{InAs}$ superlattice (SL) has been proposed as an infrared (IR) detector candidate.¹ It has been suggested² that p-type Auger recombination rates are suppressed in some of these SL's due to a large strain-induced light hole-heavy hole splitting. We perform quantitative calculations of band to-band Auger and radiative recombination rates, employing realistic non-parabolic band structures.³ The results verify that p-type Auger recombination rates are suppressed relative to those of bulk HgCdTe and SL HgTe/CdTe with the same energy gap due to the absence of strain splitting in the latter two systems. Auger recombination rates of n-type $\text{InGaSb}/\text{InAs}$ SL's are comparable to those of n-type bulk HgCdTe and SL HgTe/CdTe with the same energy gap. Radiative recombination rates are almost always smaller than Auger recombination rates for unintentionally doped samples. Superlattice based IR detectors are versatile because of their multi-spectral response and their ability to suppress both n- and p-type Auger recombination rates in samples with properly chosen alloy composition ratios, and well and barrier widths.

The minority carrier distribution function in an IR detector relevant to calculations of Auger and radiative recombination rates is an equilibrium Fermi distribution. This is a consequence of energy relaxation times⁴ of photoexcited carriers ($\sim 10^{-12}\text{s}$) being several orders of magnitude shorter than Auger and radiative lifetimes ($\sim 10^{-4}$ to 10^{-10}s) for carrier densities of experimental interest. We calculate the lifetimes of a single excess non-equilibrium minority carrier in the region of highest occupation. For an n-type material the excess carrier is a hole at the top of the heavy hole band (HH1 in Fig. 1), and results are averaged over the flat portions of this band. For a p-type material, the excess carrier is an electron at the bottom of the conduction band (C1 in Fig. 1).

The established methods for calculating band-to-band Auger recombination⁵⁻⁷ are

here extended to superlattices. Since the proposed III-V IR detectors employ thin layered (~ 25 Å) SLs, electrons in the C1 band have significant dispersion in the \perp direction requiring a three dimensional calculation, in contrast with earlier two dimensional calculations of Auger lifetimes of electrons confined in quantum wells.⁸ An envelope function formalism⁹ is used to describe the SL states, and SL $\mathbf{K} \cdot \mathbf{p}$ theory¹⁰ is used to obtain the energy bands and the wave functions $\langle \mathbf{r} | L, \mathbf{K} \rangle$ for band L and wave vector \mathbf{K} . The overlap integrals required to evaluate the screened Coulomb potential matrix elements were obtained to first order in $|\mathbf{K}_1 - \mathbf{K}'_1|^2$ in a manner similar to that described in Refs. 5, 11 and 12. Due to the highly non-parabolic nature of the band structure (see Fig. 1), parabolic approximations are not applicable. The p-type Auger lifetime (i.e. the lifetime of the photoexcited minority electron $1'$) is given by

$$\frac{1}{\tau_A} = \frac{3e^4 \hbar^3}{2\epsilon^2 \pi^3 m^4} \int \int f_p(\mathbf{K}_1) f_p(\mathbf{K}_2) \frac{\beta_{C1,HH1}(\mathbf{K}_1, \mathbf{K}'_1) \beta_{LH1,HH1}(\mathbf{K}_2, \mathbf{K}'_2)}{|\lambda^2 + |\mathbf{K}_1 - \mathbf{K}'_1|^2|^2} \times \delta(E_{C1}(\mathbf{K}'_1) + E_{LH1}(\mathbf{K}'_2) - E_{HH1}(\mathbf{K}_1) - E_{HH1}(\mathbf{K}_2)) d^3 \mathbf{K}_1 d^3 \mathbf{K}_2, \quad (1)$$

in the absence of exchange interactions.¹³ The \mathbf{K}_i refer to the superlattice states defined in Fig. 1, $E_L(\mathbf{K})$ are the band energies, and ϵ , m , f_p and λ^{-1} are the dc dielectric constant of the barrier layers, the free electron mass, the hole Fermi function, and the Debye screening length respectively. The quantity $\beta_{L,L'}(\mathbf{K}, \mathbf{K}') = |\langle L, \mathbf{K}' | (\mathbf{K} - \mathbf{K}') \cdot \mathbf{p} | L', \mathbf{K}' \rangle|^2 / [E_L(\mathbf{K}') - E_{L'}(\mathbf{K}')]^2$ involves the superlattice momentum matrix elements. \mathbf{K}'_1 denotes the minority carrier $1'$, and crystal momentum conservation determines $\mathbf{K}'_2 = \mathbf{K}_1 + \mathbf{K}_2 - \mathbf{K}'_1$. A similar expression applies to n-type Auger recombination. Following Ref. 14, the p-type radiative lifetime of electron $1'$ is given by

$$\frac{1}{\tau_R} = \frac{n e^2}{\pi \hbar^2 c^3 m^2 \epsilon} |\langle C1, \mathbf{K}'_1 | \mathbf{p} | HH1, \mathbf{K}'_1 \rangle|^2 f_p(\mathbf{K}'_1) [E_{C1}(\mathbf{K}'_1) - E_{HH1}(\mathbf{K}'_1)], \quad (2)$$

where n is the index of refraction. A similar expression applies to n-type radiative recombination.

These expressions were evaluated numerically for realistic SL band structures. Equation (1) involves six integrals. One integral, over the energy conserving delta function, was performed analytically. If the minority carrier has no component of its momentum in the \parallel direction, then rotational symmetry in the plane permits the analytical evaluation of a second integral. Thus four to five nested integrals were evaluated numerically. This task is at the limits of what can be performed with distributed desktop computing. The error in the lifetime due to numerical integrations on a finite mesh was no more than 40%.

Figure 1 shows the calculated band structure of 25\AA $\text{In}_{0.25}\text{Ga}_{0.75}\text{Sb}/41\text{\AA}$ InAs for the in-plane (\parallel) and growth (\perp) directions. This superlattice has been studied experimentally at 77K as a candidate material for $11\text{ }\mu\text{m}$ IR detectors.¹ Auger transitions involve limited regions of \mathbf{K} space due both to restrictions imposed by energy and crystal momentum conservation and occupation probabilities. Typical transitions which satisfy the constraints are shown. In the n-type material, transitions dominantly involve crystal momentum changes in the \perp direction. Here, electrons 1 and 2 are in regions of high occupation, implying a fast recombination rate. In the p-type material, transitions dominantly involve crystal momentum changes in the \parallel direction. Here, hole 1 is in a region of low occupation, thus suppressing Auger transitions. This suppression, a consequence of the large strain-induced LH1-HH1 splitting, accounts in part for the promise of $\text{In}_{0.25}\text{Ga}_{0.75}\text{Sb}/\text{InAs}$ for IR detectors.¹

Figure 2 shows the regions of \mathbf{K} space important for n- and p-type Auger recombination in 25\AA $\text{In}_{0.25}\text{Ga}_{0.75}\text{Sb}/41\text{\AA}$ InAs for $p = 10^{16}\text{ cm}^{-3}$ at 77K. The structures marked "Hole 1" and "Hole 2" indicate the positions in \mathbf{K} space of holes 1 and 2 (defined in Fig. 1) taking part in the same transition, which provide the largest contributions to the recombination rate. The Auger rate is approximately independent of \mathbf{K}_{\perp} due to the flatness of the HH1

and LH1 bands in the \perp direction. The K space volumes associated with "Hole 1" and "Hole 2" are equal, as is required by detailed balance. The "Hole 1" structure is broader because the HH1 band is flatter near hole 1 (see Fig. 1). Transitions for which the positions of holes 1 and 2 are reversed are suppressed by a smaller overlap of the electron and hole wave functions. For n-type recombination, the important region of K space for both electrons 1 and 2 (defined in Fig. 1) is a sharp peak centered at the zone center of width 0.012\AA^{-1} for $n \approx 10^{16}\text{cm}^{-3}$.

Figure 3, exhibiting the Auger lifetimes of five $\text{In}_{0.25}\text{Ga}_{0.75}\text{Sb}/\text{InAs}$ superlattices of different layer thicknesses, illustrate the IR multi-spectral characteristics. The energy gaps of the five superlattices A, B, C, D and E are 17.0, 13.8, 10.9, 9.0 and $5.2\text{ }\mu\text{m}$ respectively. The experimentally studied SL¹ C has background doping levels $n = 5 \times 10^{15}\text{ cm}^{-3}$ and $p = 3 \times 10^{16}\text{ cm}^{-3}$ and corresponds to the band structure of Fig. 1. The lifetimes are plotted for the fixed carrier concentrations shown to illustrate phase space effects on Auger lifetimes. The dashed line permits comparison of τ_A for equal n and p doping levels. The n-type lifetimes increase with increasing energy gap because the \perp bandwidth of the C1 band becomes less than the energy gap E_G . The n-type transition of Fig. 1 is no longer possible since $2'$ cannot be accommodated in the C1 band. By contrast, the p-type lifetimes decrease with increasing gap because E_G becomes greater than the zone center HH1-LH1 splitting E_{HL} . A greater volume of phase space is thus available for $2'$ in the LH1 band. The flatness of the HH1 and LH1 bands gives rise to a maximal p-type Auger rate when $E_G \approx E_{HL}$ because energy and crystal momentum conservation conditions can be easily satisfied by carriers in regions of high occupation.

The Auger lifetimes of a 37\AA $\text{HgTe}/16\text{\AA}$ CdTe SL and bulk $\text{Hg}_{0.79}\text{Cd}_{0.21}\text{Te}$ having the same energy gap, 0.114 eV, as the 25\AA $\text{In}_{0.25}\text{Ga}_{0.75}\text{Sb}/41\text{\AA}$ InAs SL have also been

calculated. The II-VI SL has the same axial electron effective mass ($0.025 m$) as the III-V SL. For $n=5 \times 10^{15} \text{cm}^{-3}$ and $T=77\text{K}$, the II-VI SL has an Auger lifetime of $9 \times 10^{-8} \text{s}$ and the II-VI bulk has a lifetime of $1 \times 10^{-7} \text{s}$, both somewhat less than the value of $2 \times 10^{-7} \text{s}$ of the III-V SL. More significant differences are found in the p-type lifetimes due to the different valence band structures. For $p=3 \times 10^{16} \text{cm}^{-3}$ and $T=77\text{K}$, the II-VI SL and bulk II-VI material have Auger lifetimes of $9 \times 10^{-11} \text{s}$ and $5 \times 10^{-9} \text{s}$ respectively compared to $5 \times 10^{-6} \text{s}$ for the III-V SL. The extremely short lifetime of the II-VI SL results from the approximate equality of the energy gap and the HH1-LH1 splitting. The II-VI bulk lifetime is shorter compared to the III-V SL because the small effective-mass light hole band provides phase space for recombination transitions that is absent for larger masses. It should be noted that other choices of II-VI SL barrier and well widths and compositions may result in improved Auger rates.

The calculated Auger and radiative lifetimes of a single band edge minority carrier in the 25\AA $\text{In}_{0.25}\text{Ga}_{0.75}\text{Sb}/41\text{\AA}$ InAs superlattice are plotted in Fig. 4 as a function of doping levels for $T=77\text{K}$ and $T=90\text{K}$. The decreasing lifetimes with increasing doping levels are due to more probable carrier-carrier collisions. We note that the radiative lifetimes are almost always longer than the Auger lifetimes. The n-type lifetimes are only weakly temperature dependent because the near zone center electrons 1 and 2 of Fig. 1 are almost statistically degenerate for the doping levels considered. The p-type lifetimes decrease by a factor of five to six as T is changed from 77 to 90K. Hole 1 of Fig. 1 lies in the tail of the hole Fermi distribution. Its occupation probability is therefore strongly temperature dependent. The lifetime obeys an approximate power law relationship with the carrier concentration: $\tau_A \sim n^{-1.7}$ and $\tau_A \sim p^{-2.1}$ for carrier densities between 5×10^{15} and 10^{17}cm^{-3} . In the simplest parabolic band case, in which carriers involved in Auger recombination are located

at the band edges, $\tau_A \sim n^{-2}$ and p^{-2} . The deviations found here are associated with band structure and occupation number effects.

In summary, we find on the basis of carrier lifetime calculations that $\text{In}_{1-x}\text{Ga}_x\text{Sb}/\text{InAs}$ is a promising superlattice for IR detector applications in the 5-17 μm range. The 11 μm SL has an n-type Auger lifetime somewhat larger than those of bulk HgCdTe and a HgTe/CdTe SL with the same energy gap. In superlattices, the n-type Auger recombination may be suppressed by reducing the \perp bandwidth of the conduction band (by increasing the barrier thickness) to a value less than the energy gap. The p-type Auger lifetime of the 11 μm InGaSb/InAs SL is approximately 3 orders of magnitude longer than bulk HgCdTe and 5 orders of magnitude longer than the HgTe/CdTe SL with the same energy gap. The suppression of p-type recombination is due to the flatness of the light and heavy hole bands whose splitting exceeds the energy gap, thus limiting phase space for recombination transitions. This splitting can be increased further (without changing the energy gap) through the choice of other alloy compositions and layer thicknesses, which will further suppress p-type recombination in $\text{In}_x\text{Ga}_{1-x}\text{Sb}/\text{InAs}$ superlattices.

The authors are grateful to R.H. Miles for making data available prior to publication. Helpful discussions with him are also greatly appreciated. This work was supported by DARPA and JSEP through ONR contract Nos. N00014-86-K-0033 and N00014-89-J-1023, respectively.

References

1. D.H. Chow, R.H. Miles, J.N. Schulman, D.A. Collins, and T.C. McGill, *Semi. Sci. Tech.* **6**, C47, (1991); R.H. Miles, private communication.
2. The idea for this SL and its properties originated with D. Smith and C. Mailhot in association with T.C. McGill.
3. A shorter version of the paper has been accepted for publication in *Appl. Phys. Lett.*
4. R. Ferreira and G. Bastard, *Phys. Rev. B* **40**, 1074 (1989).
5. A.R. Beattie and P.T. Landsberg, *Proc. R. Soc. Lond. Ser. A* **249**, 16 (1959).
6. A.R. Beattie and G. Smith, *Phys. Stat. Sol.* **19**, 577 (1967).
7. P.T. Landsberg, *Solid State Electronics* **30**, 1107 (1987).
8. Y. Jiang, M.C. Teich, and W.I. Wang, *J. Appl. Phys.* **69**, 836 (1991).
9. G. Bastard in *Proceedings of the NATO Advanced Study Institute on Molecular Beam Epitaxy in Heterostructures*, Erice, Italy, 1983, edited by L.L. Chang and K. Ploog (Martinus-Nijhoff, Dordrecht, 1984), p.381.
10. N.F. Johnson, H. Ehrenreich, P.M. Hui, and P.M. Young, *Phys. Rev. B* **41**, 3655 (1990).
11. E. Antončik and P.T. Landsberg, *Proc. Phys. Soc.* **82**, 337 (1963).
12. M. Takeshima, *J. App. Phys.* **43**, 4114 (1972).
13. The lifetime would differ by less than 33% if exchange interactions were included.
14. G.P. Agrawal and N.K. Dutta, *Long Wavelength Semiconductor Lasers* (Van Nostrand Reinhold Co., New York, 1986).

Figure Captions

Figure 1. The calculated band structure of a 25\AA $\text{In}_{0.25}\text{Ga}_{0.75}\text{Sb}/41\text{\AA}$ InAs superlattice in the growth (\perp) and in-plane (\parallel) directions. C1, HH1, HH2 and LH1 refer to conduction, heavy and light hole bands. BZ indicates the Brillouin zone boundary in the \perp direction. Wavy lines indicate possible IR photon absorptions; diagonal dashed lines show typical Auger recombination transitions. E_G is the energy gap, and E_{HL} is the zone-center light hole-heavy hole splitting. The perpendicular width of the C1 band is 0.149 eV.

Figure 2. The p-type Auger rate for holes 1 and 2 (cf. Fig. 1) in arbitrary units for 25\AA $\text{In}_{0.25}\text{Ga}_{0.75}\text{Sb}/41\text{\AA}$ InAs SL with $p = 10^{16}\text{cm}^{-3}$ and $T=77\text{K}$ in K-space.

Figure 3. Calculated Auger recombination lifetimes at 77K of 30\AA $\text{In}_{0.25}\text{Ga}_{0.75}\text{Sb}/48\text{\AA}$ InAs (A), 28\AA $\text{In}_{0.25}\text{Ga}_{0.75}\text{Sb}/45\text{\AA}$ InAs (B), 25\AA $\text{In}_{0.25}\text{Ga}_{0.75}\text{Sb}/41\text{\AA}$ InAs (C), 25\AA $\text{In}_{0.25}\text{Ga}_{0.75}\text{Sb}/37\text{\AA}$ InAs (D), and 25\AA $\text{In}_{0.25}\text{Ga}_{0.75}\text{Sb}/25\text{\AA}$ InAs (E) superlattices as a function of energy gap for the indicated doping levels. Solid circles are the calculated points. The band structure for C is given in Fig. 1. The heavy hole-light hole splittings for superlattices A,B, D, and E are 0.201, 0.227, 0.219, and 0.188 eV respectively.

Figure 4. Calculated n-type and p-type Auger and radiative recombination lifetimes of a 25\AA $\text{In}_{0.25}\text{Ga}_{0.75}\text{Sb}/41\text{\AA}$ InAs superlattice as a function of doping at $T=77\text{K}$ and $T=90\text{K}$.

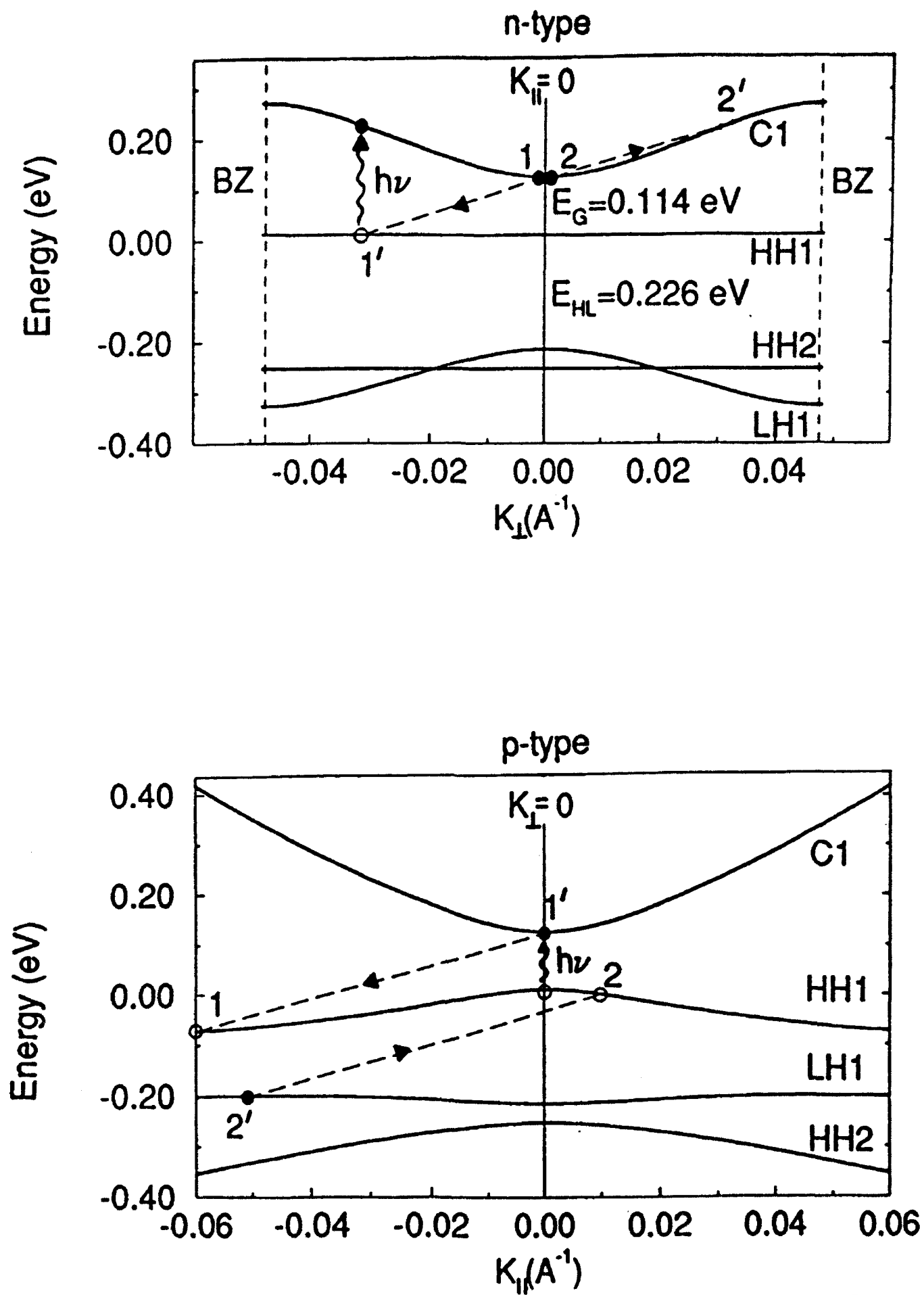


Fig. 1

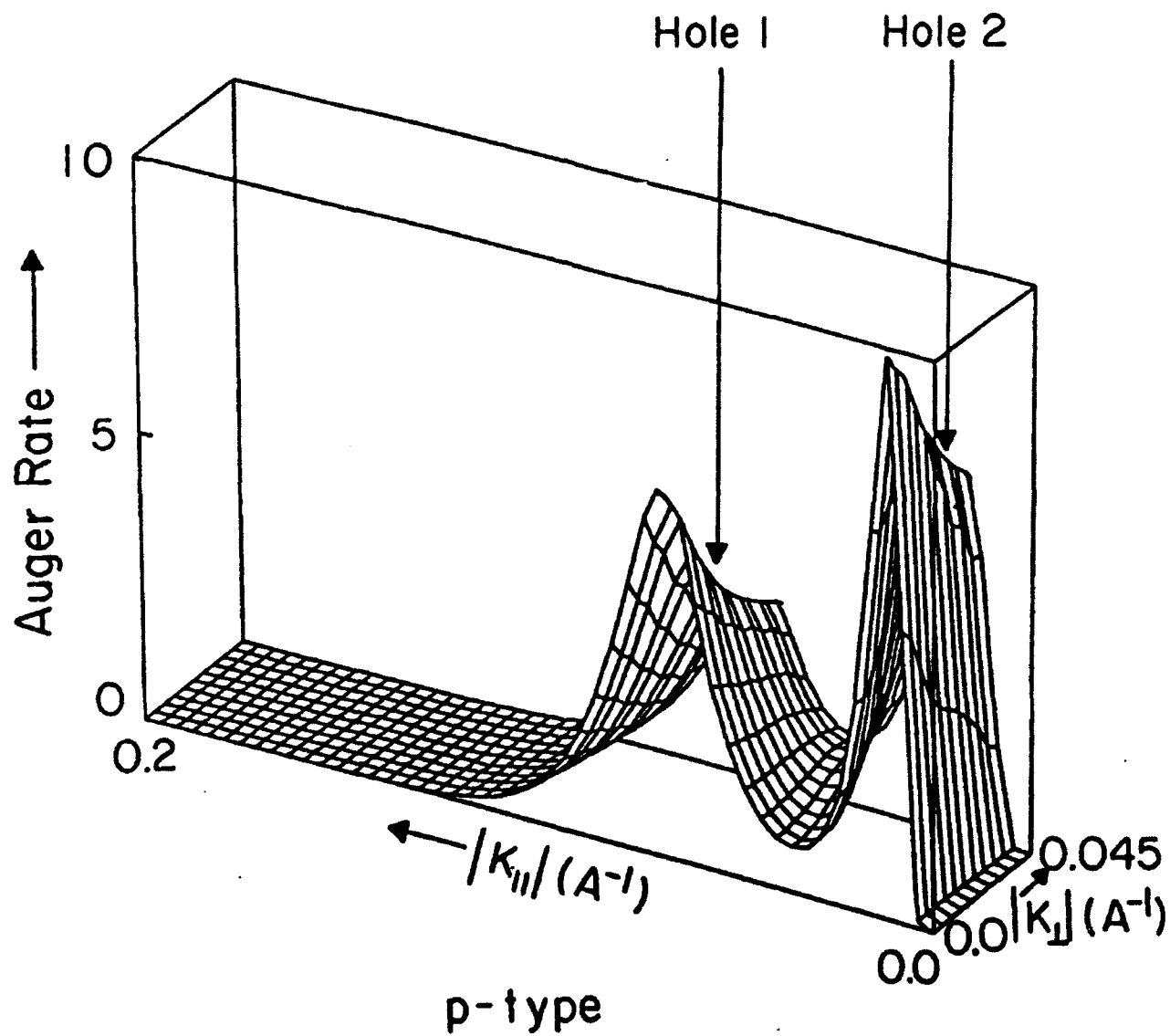


Fig. 2

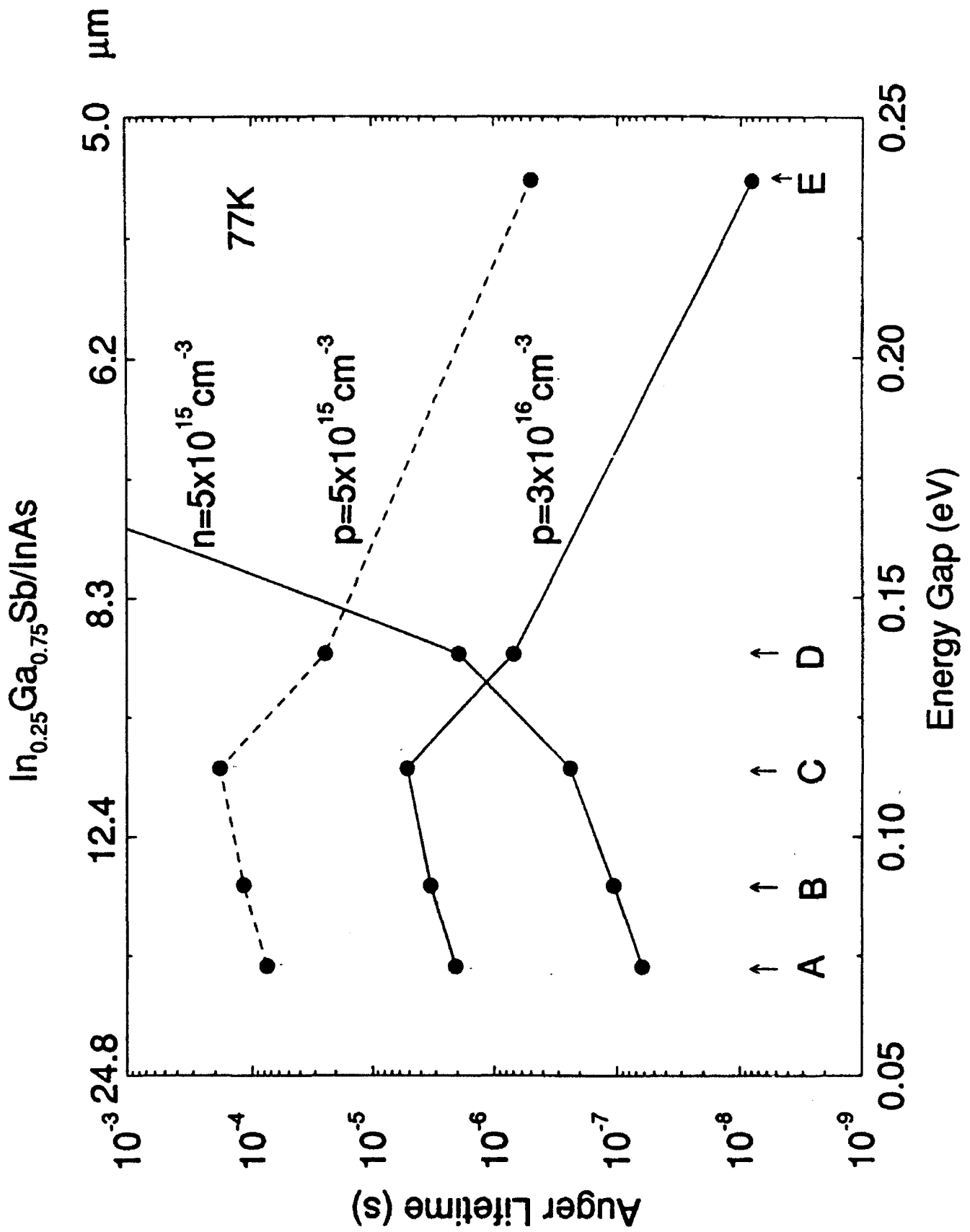


Fig. 3

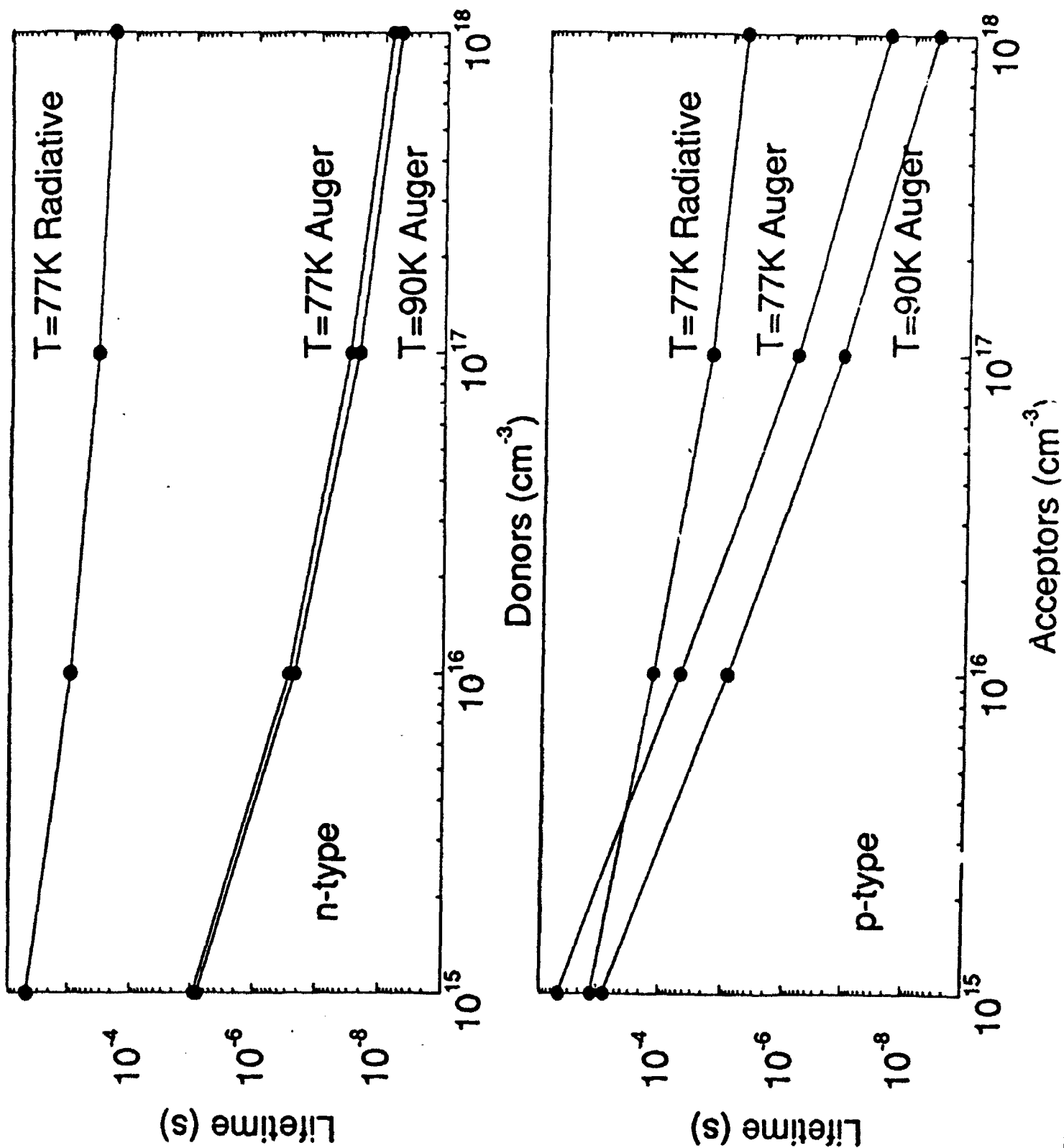


Fig. 4

**Temperature Limits on Infrared Detectivities of
InAs/In_xGa_{1-x}Sb Superlattices and Bulk Hg_xCd_{1-x}Te**

P.M. Young^{a)}, C.H. Grein^{b)}, H. Ehrenreich^{a)}, and R.H. Miles^{c)}

^{a)} Division of Applied Sciences, Harvard University, Cambridge, MA 02138

^{b)} Physics Department M/C 273, University of Illinois at Chicago, Chicago, IL 60607-7059

^{c)} Hughes Research Laboratories, Malibu, CA 90265

Abstract

Detailed theoretical calculations of Auger and radiative recombination rates for an optimized InAs/In_xGa_{1-x}Sb superlattice (SL) and bulk Hg_xCd_{1-x}Te (MCT) show that 300K background limited operation for a 60 degree field of view can be theoretically achieved up to 130K for the 11 μm SL and up to 185K for 5 μm MCT. The SL structure is theoretically superior to MCT for 11 μm operation. The converse is true at 5 μm.

PACS #'s: 72.15.Lh, 72.40.+w, 78.60.-b

Modern high performance infrared (IR) detector technology based on photon absorption in narrow gap semiconductors requires the use of extensive detector cooling in order to achieve background limited performance (BLIP). Even modest gains in detector operating temperatures will translate into large gains in the power consumption, size, weight, and lifetime of coolers. In this letter, we explore theoretical limits for high temperature operation of photovoltaic (PV) and photoconductive (PC) detectors based on bulk $\text{Hg}_x\text{Cd}_{1-x}\text{Te}$ (MCT) alloys and the recently proposed¹ type II broken band alignment $\text{InAs}/\text{In}_x\text{Ga}_{1-x}\text{Sb}$ superlattices (SLs). Detector performance is compared at 5 and 11 μm wavelengths. MCT is the current standard for 8-12 μm defense applications, and will be considered here also for commercial applications at 5 μm where higher temperature operation, 200 - 300K, even without achieving the BLIP condition, may provide satisfactory signal to noise ratios. The III-V SL promises a number of advantages over $\text{Hg}_x\text{Cd}_{1-x}\text{Te}$ alloys beyond 8 μm ,² including lower nonradiative recombination rates.³ In this letter, these lower rates will be shown to lead to a 40K increase in the operating temperature T_{BLIP} at which 300K BLIP with a 60 degree field of view may be attained at 11 μm . This background condition is typical for 11 μm strategic military applications. MCT is superior for 5 μm applications.

Earlier calculations of Auger recombination rates in ideal $\text{InAs}/\text{In}_x\text{Ga}_{1-x}\text{Sb}$ SLs³ with energy gaps in the 8 to 12 μm range demonstrated the possibility of suppressing Auger recombination in both n- and p-doped samples relative to bulk $\text{Hg}_x\text{Cd}_{1-x}\text{Te}$ with the same energy gap and majority carrier concentrations. The calculations employed the accurate highly non-parabolic superlattice $\mathbf{K} \cdot \mathbf{p}$ band structures and included possible degenerate carrier statistics to evaluate carrier lifetimes. Here,

the same methods are employed to examine a number of $\text{InAs}/\text{In}_x\text{Ga}_{1-x}\text{Sb}$ SLs and $\text{Hg}_x\text{Cd}_{1-x}\text{Te}$ alloys and, for the case of $\text{InAs}/\text{In}_x\text{Ga}_{1-x}\text{Sb}$ SLs, to identify the alloy composition and choice of well and barrier widths which will best suppress Auger recombination. To obtain the total Auger recombination rate, the contributions of majority carrier-majority carrier and minority carrier-minority carrier collisions are added to give a reciprocal Auger lifetime $\tau_A^{-1} = \tau_{A,ee}^{-1} + \tau_{A,hh}^{-1}$. The first term corresponds to electron-electron collisions and the second to hole-hole collisions.

The limiting values of specific detectivities D^* for photoconductors and n-on-p photodiodes are given by

$$D_{PC}^* = \frac{\eta}{2h\nu} \left[\frac{(n+p)\tau}{npt} \right]^{1/2}, \quad D_{PV}^* = \frac{\eta}{2h\nu} \left[\frac{\tau}{n_p L_n} \right]^{1/2}, \quad (1)$$

respectively.⁴ Here ν is the photon frequency; τ is the minority carrier lifetime, given by $\tau^{-1} = \tau_A^{-1} + \tau_R^{-1}$, where τ_R is the radiative lifetime; t is the thickness of the photoconductor, taken to be 10^{-3} cm based on the optical absorption, α , in both $\text{InAs}/\text{In}_x\text{Ga}_{1-x}\text{Sb}$ SLs and bulk $\text{Hg}_x\text{Cd}_{1-x}\text{Te}$; n and p are the PC equilibrium concentrations of electrons and holes; n_p is the PV density of electrons in the p-type layer; L_n is the PV minority electron diffusion length; and η is the quantum efficiency, assumed to be 0.7 for PC devices and given by $\eta = L_n\alpha/(L_n\alpha + 1)$ for PV devices. The diffusion length $L_n = \sqrt{D\tau}$ is determined by the electron diffusion constant $D = (kT/e)\mu_e$, where μ_e is the electron mobility estimated to be 3.5×10^4 $\text{cm}^2/\text{V-s}$ for $\text{InAs}/\text{In}_x\text{Ga}_{1-x}\text{Sb}$ SLs and taken from experimentally determined values⁵ as a function of T and x for $\text{Hg}_x\text{Cd}_{1-x}\text{Te}$. Equation (1) for the PV case assumes the dominant dark current above 77K to be due to electron diffusion from the p-type side of the junction. Intrinsic theoretical limits for D^* will be obtained from these expressions by considering only Auger and radiative processes to limit carrier lifetimes.

Only photovoltaics will be considered at $11\mu\text{m}$ because high performance focal plane arrays benefit from the low power dissipation associated with these devices relative to that of PC detectors. As a result PV devices are preferred over PC devices. We shall consider structures having n-on-p geometry. The parameters of interest for $\text{InAs}/\text{In}_x\text{Ga}_{1-x}\text{Sb}$ SLs therefore are those leading to the lowest Auger rates in the p-type layers. The strain induced splitting of the heavy hole (HH) and light hole (LH) valence band edges of the constituent bulk $\text{In}_x\text{Ga}_{1-x}\text{Sb}$ of the $\text{InAs}/\text{In}_x\text{Ga}_{1-x}\text{Sb}$ SLs leads to a large (200 to 300 meV) splitting of the two highest valence bands of the SL, HH1 and LH1, at the center of the Brillouin zone.³ This impedes hole-hole scattering Auger processes and thus improves Auger limited minority carrier lifetimes in p-type material,³ which in turn leads to improved D^* and T_{BLIP} values in n-on-p geometry devices.

The $11\mu\text{m}$ D^* of $\text{InAs}/\text{In}_x\text{Ga}_{1-x}\text{Sb}$ SLs was optimized by maximizing the lifetime enhancement. The strain induced splitting increases with alloy composition ratio x . For the purposes of this study, SLs with $x \leq 0.4$ and layers no thinner than 15\AA were considered. While growth beyond these limits may be possible, practical constraints associated with tolerable lattice mismatches and nonuniformities will limit the utility of structures employing high strains or thin layers. In order to suppress Auger recombination pathways involving transitions between the flat portions of the HH1 and HH2 bands³ the zone center splitting of the HH1 and HH2 bands must be greater than the energy gap. Suppression is best achieved if the second valence band has light hole character. Auger lifetimes were calculated for several SLs satisfying these constraints. The SL found to have the lowest p-type rates is $39.8\text{\AA}\text{InAs}/15\text{\AA}\text{In}_{0.4}\text{Ga}_{0.6}\text{Sb}$.

Figure 1 shows the calculated values of Auger lifetimes in the optimized $39.8\text{\AA}\text{InAs}/$

15ÅIn_{0.4}Ga_{0.6}Sb SL with acceptor concentrations N_A of 10^{15} and 10^{17} cm⁻³ respectively (dashed curves). The Auger lifetime for bulk Hg_xCd_{1-x}Te with $N_A = 10^{17}$ cm⁻³ (solid line) is plotted for comparison. The results for Hg_xCd_{1-x}Te are found to be in good agreement, within a factor of two, with those calculated by Casselman.⁶ The basic mechanisms of lifetime suppression have been discussed in Ref. [3]. The same mechanisms dominate here. Most important is the suppression of hole-hole scattering due to the low occupation probability of one of the hole states at low temperature. For the SL with the lower acceptor concentration the hole-hole scattering has been suppressed to the point where the minority electron-electron scattering dominates the Auger lifetime. At the higher level of doping, hole-hole scattering dominates since its rate increases with the higher hole population. At the same time the electron-electron scattering rate decreases because the electron population falls to keep the np product roughly constant.⁷ Auger rates for $N_A = 10^{17}$ cm⁻³ at T=77K are found to be as much as seven orders of magnitude smaller in the optimized SL than in Hg_xCd_{1-x}Te.

The calculated values of D^* in the temperature range of 77 to 200K of the optimized 39.8ÅInAs/15ÅIn_{0.4}Ga_{0.6}Sb SL, a 41ÅInAs/25ÅIn_{0.25}Ga_{0.75}Sb SL (currently under experimental study²), and bulk Hg_xCd_{1-x}Te are plotted in Fig. 2. All materials have the same p-side acceptor concentration of 10^{17} cm⁻³ and energy gap of 0.114 eV or 11 μm. The gap is assumed to be temperature independent. This is a reasonable assumption because SLs and alloys with slightly different compositions may be selected to provide the chosen gap for different temperatures without significantly affecting detectivity values. The calculated values of D^* for Hg_xCd_{1-x}Te are found to be in good agreement with previously calculated values at T=77K.⁴ The figure indicates that T_{BLIP} for a 300K background and a 60 degree field of view is 130K

for $39.8\text{\AA}\text{InAs}/15\text{\AA}\text{In}_{0.4}\text{Ga}_{0.6}\text{Sb}$, substantially higher than the 90K for $\text{Hg}_x\text{Cd}_{1-x}\text{Te}$ at $11\text{ }\mu\text{m}$. The non-optimum $41\text{\AA}\text{InAs}/25\text{\AA}\text{In}_{0.25}\text{Ga}_{0.75}\text{Sb}$ SL still offers almost 20K improvement in T_{BLIP} over $\text{Hg}_x\text{Cd}_{1-x}\text{Te}$. As previously emphasized, these improvements result from the suppression of Auger recombination pathways in the SLs.

Note that the D^* advantage of the $39.8\text{\AA}\text{InAs}/15\text{\AA}\text{In}_{0.4}\text{Ga}_{0.6}\text{Sb}$ SL over bulk $\text{Hg}_x\text{Cd}_{1-x}\text{Te}$ decreases from almost two orders of magnitude at 77K to less than one order of magnitude at 200K. This is a consequence of the carrier recombination suppression mechanism referred to above becoming weaker at higher temperatures.³ Specifically, the hole occupation probability away from zone center increases with increasing temperature; hence more carriers are available for Auger recombination. For this reason, $\text{InAs}/\text{In}_x\text{Ga}_{1-x}\text{Sb}$ SLs are not expected to offer an advantage over bulk $\text{Hg}_x\text{Cd}_{1-x}\text{Te}$ detectors at elevated temperatures. At room temperature cheaper thermal detectors are better than either system for most applications.

At $5\text{ }\mu\text{m}$, $\text{InAs}/\text{In}_x\text{Ga}_{1-x}\text{Sb}$ SLs are less attractive than bulk $\text{Hg}_x\text{Cd}_{1-x}\text{Te}$ due to their short Auger lifetimes. They cannot be designed to suppress p-type Auger lifetimes because the energy gap (0.248 eV) exceeds the strain-induced splitting of the HH1 and LH1 bands for SLs with the range of layer thicknesses and compositions considered here.

Possible room temperature operation of $5\text{ }\mu\text{m}$ bulk $\text{Hg}_x\text{Cd}_{1-x}\text{Te}$ detectors in a device limited mode is also of interest. The calculated D^* values of $5\text{ }\mu\text{m}$ n-on-p geometry PV and n-type PC $\text{Hg}_x\text{Cd}_{1-x}\text{Te}$ detectors are plotted in Fig. 3 as a function of temperature in the range 100 to 300K. The p-on-n PV and p-type PC detectors are not considered here. The figure indicates that the 300K BLIP condition cannot be met above approximately 185K. However, the optimal D^* values at 300K are approx-

imately 3×10^9 cm Hz^{1/2}/watt, just below the ideal D^* of 1.5×10^{10} cm Hz^{1/2}/watt of thermal detectors. Nevertheless, room temperature 5 μ m Hg_xCd_{1-x}Te detectors are expected to fill niche applications such as those requiring superior frequency response.

The authors are grateful to T.C. McGill for helpful discussions. One of us (RM) acknowledges helpful discussions with D.H. Chow and R. Baron. This work was supported by DARPA and JSEP through ONR contracts Nos. N00014-86-K-0033, N0001492-C-022A and N00014-89-J-1023.

References

- [1] C. Mailhot and D.L. Smith, *J. Vac. Sci. Technol. A* **7**, 445 (1989).
- [2] D.H. Chow, R.H. Miles, J.N. Schulman, D.A. Collins, and T.C. McGill, *Semi. Sci. Technol.* **6**, C47 (1991).
- [3] C.H. Grein, P.M. Young, and H. Ehrenreich, *Appl. Phys. Lett.* **61**, 2905 (1992).
- [4] M.A. Kinch and S.R. Borrello, *Infrared Physics* **15**, 111 (1974).
- [5] M.W. Scott, *J. Appl. Phys.* **43**, 1055 (1972).
- [6] T.N. Casselman, *J. Appl. Phys.* **52**, 848 (1980).
- [7] The np product is not constant for degenerate statistics.

Figure Captions

FIG. 1. Auger lifetimes for 11 μm 39.8ÅInAs/15ÅIn_{0.4}Ga_{0.6}Sb superlattices with acceptor concentrations N_A of 10^{15} and 10^{17} cm^{-3} and for 11 μm Hg_xCd_{1-x}Te (MCT), with $N_A = 10^{17} \text{ cm}^{-3}$, as a function of temperature. For $N_A = 10^{17} \text{ cm}^{-3}$ Auger lifetimes are determined by hole-hole scattering, but for $N_A = 10^{15} \text{ cm}^{-3}$ electron-electron scattering dominates.

FIG. 2. D^* of 39.8ÅInAs/15ÅIn_{0.4}Ga_{0.6}Sb, 41ÅInAs/25ÅIn_{0.25}Ga_{0.75}Sb, and Hg_xCd_{1-x}Te (MCT) ideal n-on-p geometry PV detectors at 11 μm , as a function of temperature. The p-layer doping level is $N_A = 10^{17} \text{ cm}^{-3}$. D_{BLIP}^* is the 300K background limited detectivity at 11 μm for a 60 degree field of view. The maximum temperatures for D_{BLIP}^* are indicated.

FIG. 3. D^* of ideal PC and PV 5 μm MCT photodetectors as a function of temperature. D_{BLIP}^* is the 300K background limited detectivity at 5 μm for a 60 degree field of view. The maximum temperature for D_{BLIP}^* is indicated.

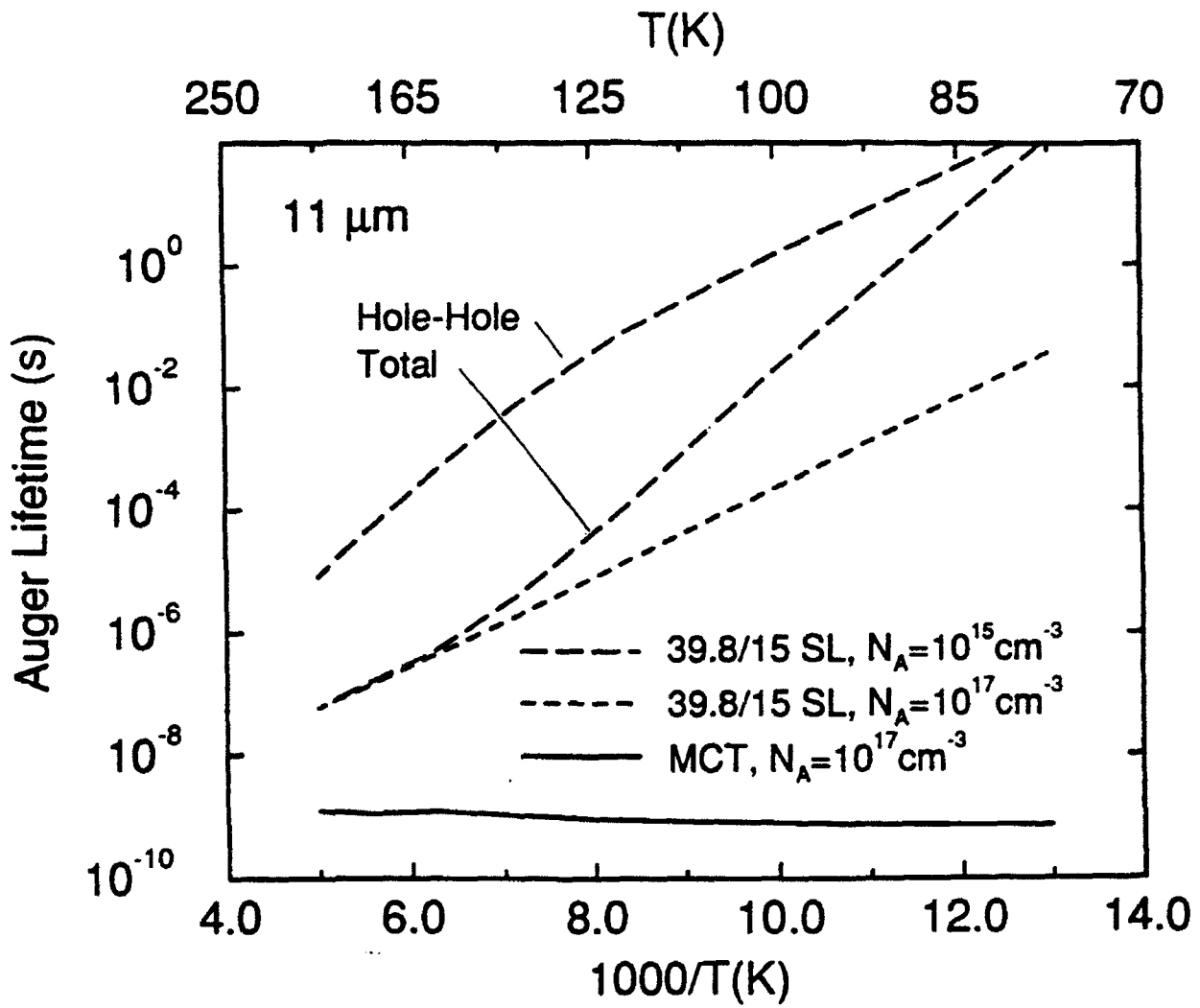


Fig. 1

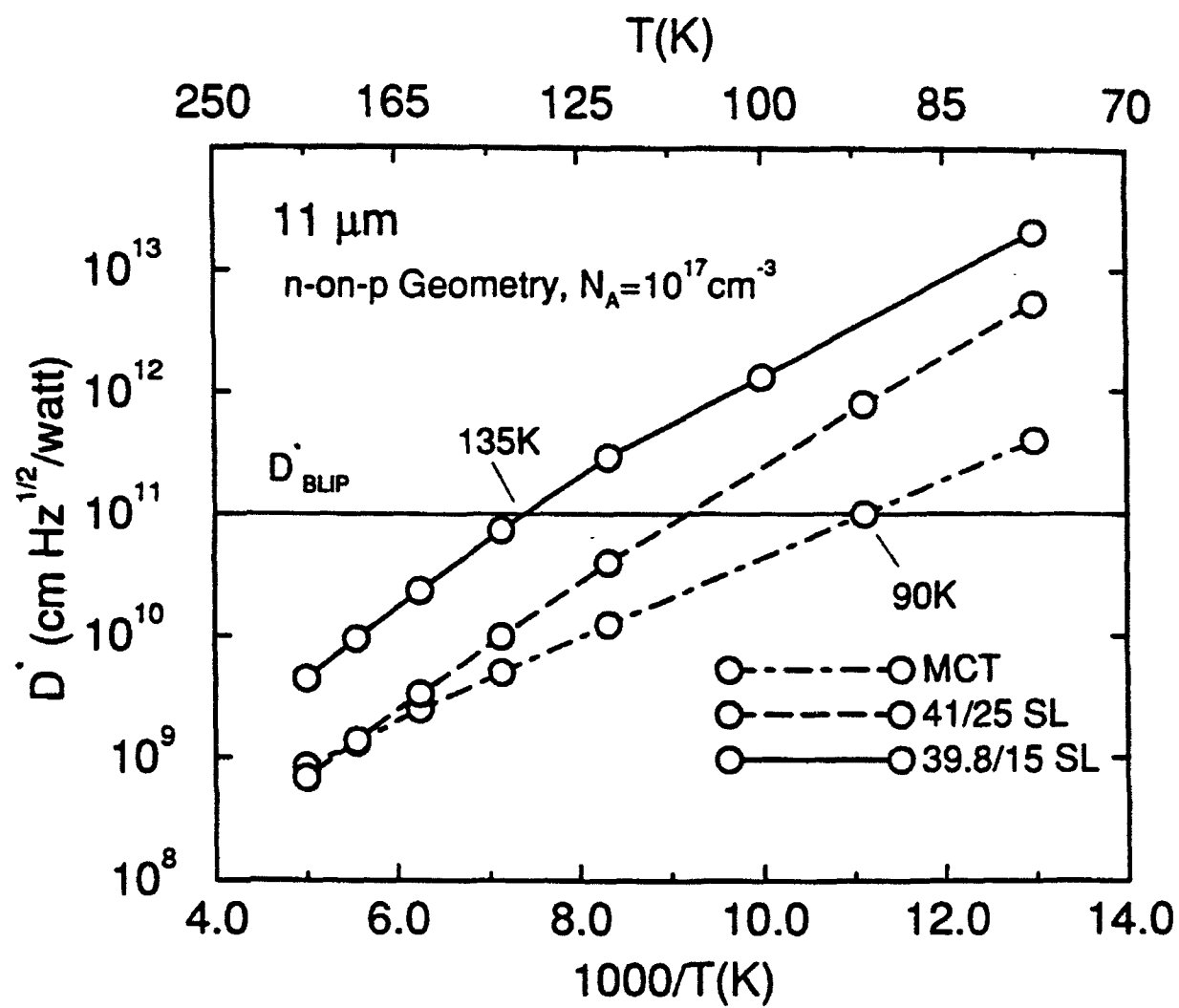


Fig 2

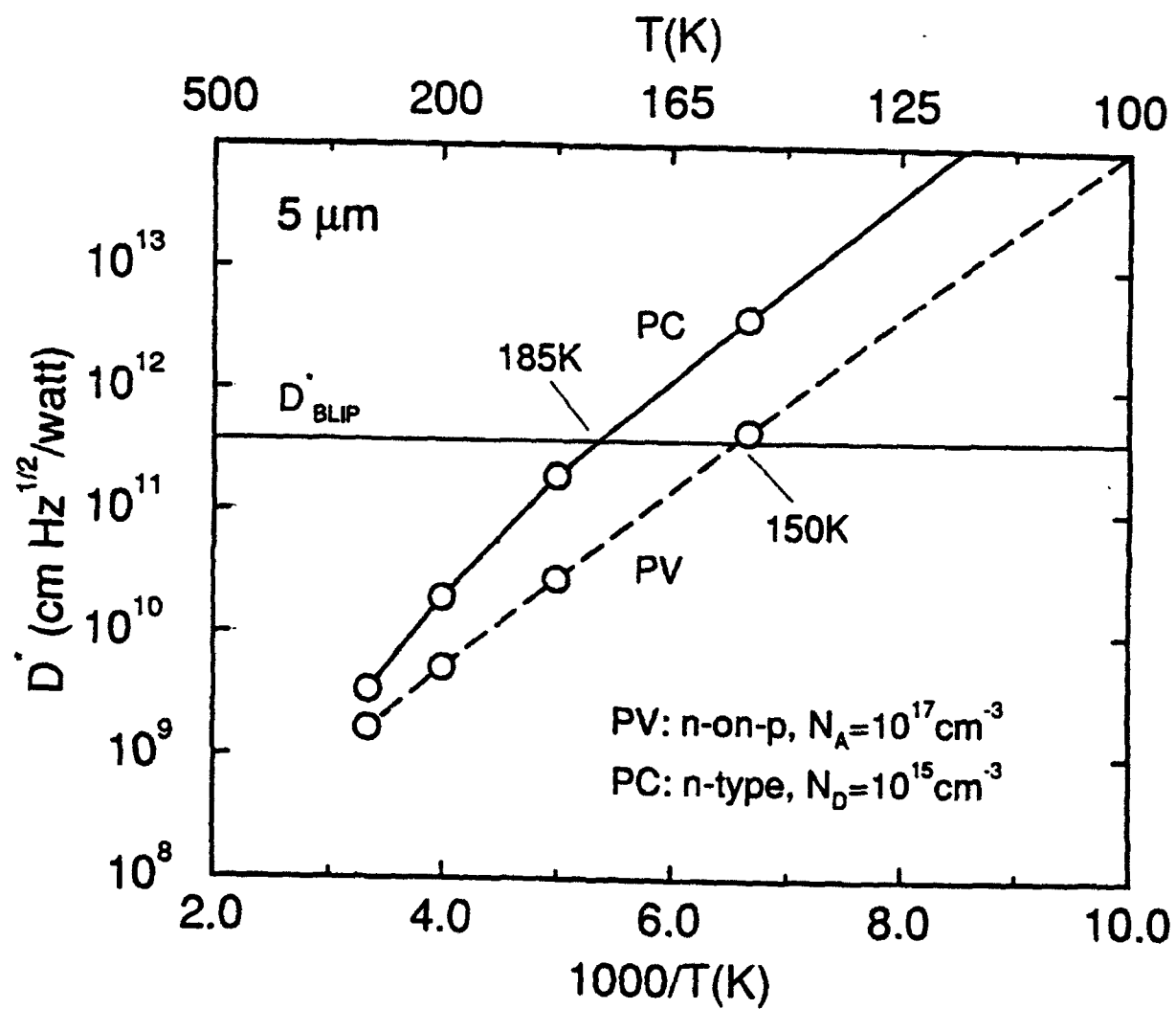
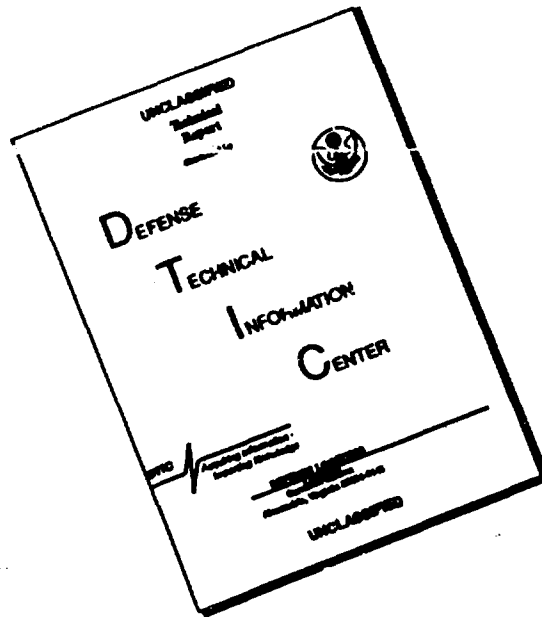


Fig. 3

DISCLAIMER NOTICE



**THIS DOCUMENT IS BEST
QUALITY AVAILABLE. THE COPY
FURNISHED TO DTIC CONTAINED
A SIGNIFICANT NUMBER OF
PAGES WHICH DO NOT
REPRODUCE LEGIBLY.**